

# Neuroimaging Techniques in Clinical Practice

Physical Concepts and Clinical  
Applications

Manoj Mannil  
Sebastian F.-X. Winklhofer  
*Editors*

---

# Neuroimaging Techniques in Clinical Practice

---

Manoj Mannil • Sebastian F.-X. Winklhofer  
Editors

# Neuroimaging Techniques in Clinical Practice

Physical Concepts and Clinical  
Applications

 Springer

*Editors*

Manoj Mannil  
University Clinic for Radiology  
University Hospital of Münster  
Münster  
Germany

Sebastian F.-X. Winklhofer  
Department of Neuroradiology  
University Hospital Zurich  
Zurich  
Switzerland

ISBN 978-3-030-48418-7      ISBN 978-3-030-48419-4 (eBook)  
<https://doi.org/10.1007/978-3-030-48419-4>

© Springer Nature Switzerland AG 2020

This work is subject to copyright. All rights are reserved by the Publisher, whether the whole or part of the material is concerned, specifically the rights of translation, reprinting, reuse of illustrations, recitation, broadcasting, reproduction on microfilms or in any other physical way, and transmission or information storage and retrieval, electronic adaptation, computer software, or by similar or dissimilar methodology now known or hereafter developed.

The use of general descriptive names, registered names, trademarks, service marks, etc. in this publication does not imply, even in the absence of a specific statement, that such names are exempt from the relevant protective laws and regulations and therefore free for general use.

The publisher, the authors, and the editors are safe to assume that the advice and information in this book are believed to be true and accurate at the date of publication. Neither the publisher nor the authors or the editors give a warranty, express or implied, with respect to the material contained herein or for any errors or omissions that may have been made. The publisher remains neutral with regard to jurisdictional claims in published maps and institutional affiliations.

This Springer imprint is published by the registered company Springer Nature Switzerland AG  
The registered company address is: Gewerbestrasse 11, 6330 Cham, Switzerland

---

## Preface

The textbook *Neuroimaging Techniques in Clinical Practice* was conceptualized due to the ever-increasing complexity of neuroimaging in today's clinical practice. The first edition of the book is the result of the work of numerous expert authors and author groups, consisting of some of the most recognized, brilliant, and accomplished experts in the field of neuroimaging from all over the world. Many of the chapters are written by pioneers in their field of expertise, such as the chapters about CT-Perfusion, Photon Counting CT, Susceptibility Weighted Imaging (SWI), or Intravoxel Incoherent Motion (IVIM). This book also covers the basics and recent advancements of the modalities plain film radiography, ultrasound, digital subtraction angiography (DSA), computed tomography (CT), magnetic resonance imaging (MRI), positron emission tomography (PET), and electroencephalography (EEG) for an interested reader without assumed prior knowledge in medical physics. Therefore, the book is suitable for physicians who would like to improve their understanding of the underlying imaging techniques and at the same time it allows non-clinicians and students to understand the clinical applications of neuroradiological modalities and techniques.

Since the discovery of X-rays in 1895, imaging has undergone a substantial evolution and is now an integral part of modern medicine. Today's available imaging techniques allow researchers and clinicians alike to visualize the brain and spinal cord in unimagined detail, shedding light on one of the most fascinating structures of the human body. The field of neuroimaging is rapidly advancing; this includes newer and faster scanners, improved image quality, higher spatial and temporal resolution, and advanced methods of image acquisition and analysis.

This textbook aims to make these complex neuroimaging techniques less intimidating. Next to the classical morphological and structural imaging, this book deals with advanced functional and quantitative imaging approaches such as perfusion imaging, fMRI, or quantitative imaging techniques. The latter, for instance, shows great potential for an improved characterization of pathologies with their underlying tissue. The same is valid for artificial intelligence, a topic, which may substantially revolutionize future medical imaging. Combining all these technical achievements, which are currently progressing so rapidly, highly fascinating possibilities will arise, ranging from molecular imaging to radiogenomics.

Neuroradiological textbooks often deal with clinical topics, and the technical aspects of imaging are just briefly described or even neglected. That is

how this book is supposed to differ from others. With our comprehensive single volume textbook, we would like to demystify the complexity of advanced imaging techniques and gently introduce the interested reader to the technical background, followed by the clinical applications thereof.

A clinical case at the end of each chapter supplements the provided theoretical content and highlights the potential of the respective technique. The main focuses of the textbook are computed tomography and magnetic resonance imaging, with their many new applications ranging from dual-energy CT to arterial spin labelling MRI. However, the intention of the book remains to present techniques with established or potential clinical applications.

The process of editing this book has taken a considerable amount of time and effort. We would like to thank all contributing authors for sharing their expertise, providing assistance, advice, and investing their time into this project. We would also like to thank our project coordinator Mrs. Sasirekka Nijanthan and associate editor Mrs. Anna-Lena Buchholz for their guidance and support.

Münster, Germany  
Zurich, Switzerland  
August 2020

Manoj Mannil  
Sebastian F.-X. Winklhofer

---

# Contents

<b>1</b>	<b>Ultrasound in Neuroimaging</b> .....	<b>1</b>
	Thomas Witton-Davies, Marion Witton-Davies, and Gernot Schulte-Altedorneburg	
<b>2</b>	<b>Conventional Radiography</b> .....	<b>19</b>
	Michael H. Schönfeld and Sebastian F.-X. Winklhofer	
<b>3</b>	<b>Digital Subtraction Angiography</b> .....	<b>23</b>
	Eef J. Hendriks, Jesse M. Klostranec, and Timo Krings	
<b>4</b>	<b>Basics of Computed Tomography</b> .....	<b>31</b>
	Manoj Mannil and Natalia Saltybaeva	
<b>5</b>	<b>Computed Tomography Angiography</b> .....	<b>45</b>
	Jan W. Dankbaar, Ewoud J. Smit, and Birgitta K. Velthuis	
<b>6</b>	<b>CT Perfusion</b> .....	<b>61</b>
	Douglas Joseph Martin and Max Wintermark	
<b>7</b>	<b>Dual-Energy CT</b> .....	<b>69</b>
	Can Ozan Tan, Daan Kuppens, and Rajiv Gupta	
<b>8</b>	<b>Photon-Counting Detector-Based Computed Tomography</b> ....	<b>87</b>
	Kishore Rajendran and Cynthia H. McCollough	
<b>9</b>	<b>Basics of Magnetic Resonance Imaging</b> .....	<b>95</b>
	Franciszek Hennel, Roger Luechinger, and Marco Piccirelli	
<b>10</b>	<b>Magnetic Resonance Angiography</b> .....	<b>123</b>
	Benjamin Peters, Sven Dekeyzer, Omid Nikoubashman, and Paul Marie Parizel	
<b>11</b>	<b>MRI Perfusion Techniques</b> .....	<b>141</b>
	Kyrre E. Emblem, Christopher Larsson, Inge R. Groote, and Atle Bjørnerud	
<b>12</b>	<b>Susceptibility Weighted Imaging</b> .....	<b>165</b>
	Jürgen R. Reichenbach	
<b>13</b>	<b>Diffusion-Weighted Imaging</b> .....	<b>189</b>
	Tarini Ratneswaren and Tomasz Matys	

---

<b>14</b>	<b>Diffusion Tensor Imaging</b> . . . . .	203
	Samira N. Kashefi and Gavin P. Winston	
<b>15</b>	<b>Diffusion Kurtosis Imaging</b> . . . . .	215
	Jiachen Zhuo and Rao P. Gullapalli	
<b>16</b>	<b>Intravoxel Incoherent Motion (IVIM)</b> . . . . .	229
	Denis Le Bihan and Sebastian F.-X. Winkelhofer	
<b>17</b>	<b>Magnetic Resonance Spectroscopy</b> . . . . .	239
	Lucy McGavin and Amoolya Mannava	
<b>18</b>	<b>Magnetization Transfer Imaging</b> . . . . .	253
	Paula Trujillo, Daniel O. Claassen, and Seth A. Smith	
<b>19</b>	<b>Functional Magnetic Resonance Imaging</b> . . . . .	263
	N. Hainc, J. Reinhardt, and C. Stippich	
<b>20</b>	<b>Positron Emission Tomography</b> . . . . .	285
	Martin W. Huellner, Daniele A. Pizzuto, Philipp C. Mächler, and Tetsuro Sekine	
<b>21</b>	<b>Electroencephalography</b> . . . . .	313
	L. Michels	
<b>22</b>	<b>Artificial Intelligence and Radiomics: Outlook into the Future</b> . . . . .	335
	Tommaso Di Noto, Manoj Mannil, Hugo Aerts, and Chandini Kadian	





# Ultrasound in Neuroimaging

# 1

Thomas Witton-Davies, Marion Witton-Davies,  
and Gernot Schulte-Altendorneburg

## Contents

1.1	<b>Introduction</b> .....	1
1.2	<b>Technical Background</b> .....	3
1.2.1	Sound Waves.....	3
1.2.2	Ultrasound.....	3
1.2.3	Transducer.....	4
1.2.4	Resolution.....	4
1.2.5	Doppler Effect.....	4
1.2.6	Angulation.....	5
1.2.7	Turbulences and Disturbed Flow.....	5
1.2.8	Time–Frequency Spectrum.....	5
1.2.9	Ultrasound Settings.....	5
1.3	<b>Examination Technique</b> .....	7
1.3.1	Pulsatile Flow in Arteries.....	7
1.3.2	Ultrasound Representation of Arterial Stenosis.....	7
1.3.3	Pulsatility Index.....	8
1.3.4	Requirements for Examiners and Reporting.....	9
1.3.5	Safety of Diagnostic Ultrasound.....	9
1.3.6	Contrast-Enhanced Ultrasound (CEUS).....	9
1.4	<b>Clinical Application</b> .....	10
1.4.1	Extracranial.....	10
1.4.2	Intracranial.....	12
1.5	<b>Future Developments</b> .....	16
1.5.1	Brain-Focused Ultrasound.....	16
1.5.2	Neurological Applications.....	16
1.6	<b>Clinical Case</b> .....	17
	<b>References</b> .....	17

T. Witton-Davies (✉) · M. Witton-Davies  
G. Schulte-Altendorneburg  
Department of Diagnostic and Interventional  
Radiology and Neuroradiology, München Klinik  
Harlaching, Munich, Germany  
e-mail: [Thomas.Witton-Davies@muenchen-klinik.de](mailto:Thomas.Witton-Davies@muenchen-klinik.de);  
[gernot.schulte-altendorneburg@muenchen-klinik.de](mailto:gernot.schulte-altendorneburg@muenchen-klinik.de)

## 1.1 Introduction

Ultrasound is a fast, low-cost and non-invasive diagnostic tool in neurological diseases. Unlike other neuroimaging techniques (i.e. computed

tomography (CT) and computed tomography angiography (CTA), magnetic resonance imaging (MRI) and magnetic resonance angiography (MRA), digital subtraction angiography (DSA)), ultrasound allows for simultaneous high spatial resolution in parenchymal imaging and high temporal resolution in accurate measurement of blood flow velocities. Furthermore, ultrasound is as often repeatable as wanted by the sonographer. Thus, ultrasound is an excellent technique for elective examinations, emergency diagnostics, intraoperative imaging and monitoring examinations in intensive care or stroke units.

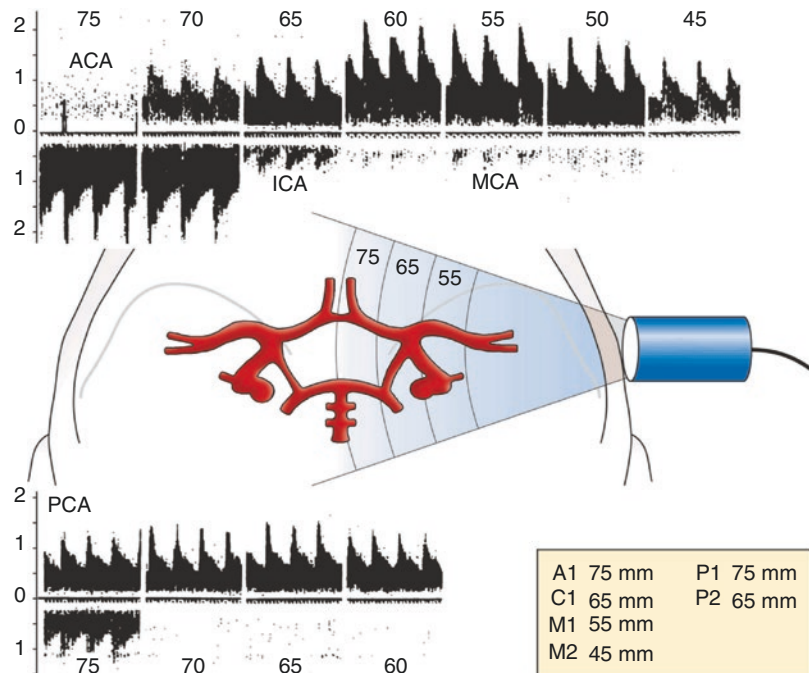
Extracranial neurological ultrasound mainly comprises the visualization of the vessel wall and measurement of blood flow velocities of the brain-supplying arteries. The detection and evaluation of steno-occlusive carotid artery plaques have a high importance for clinical decisions regarding correct risk stratification and a subsequent adequate therapy.

In 1982, Aaslid and co-workers first described transcranial Doppler sonography (TCD) and its application in vasospasm, intracranial stenosis and

cerebral autoregulation [1]. A low-frequency (2 MHz) pulsed-wave probe was used for insonation through the thin portion of the temporal bone as well as via cranial foramina, i.e. foramen magnum and orbital fissures. Eight years later, Bogdahn and co-workers introduced transcranial colour-coded duplex sonography (TCCS) which combines parenchymal B-mode, colour-coded flow and spectral Doppler [2]. By TCCS, bony and parenchymal landmarks visible by B-mode via transtemporal, transnuchal and transorbital insonation facilitate differentiation of the arteries of the circle of Willis (Figs. 1.1 and 1.2). Besides this, colour-coded vessel imaging allows for more precise measurement of blood flow velocities, since the angle correction can be carried out reliably. However, both TCD and TCCS are limited by an insufficient temporal window in up to 20% [3]. In these cases, transpulmonary ultrasound contrast agent (UCA) enables to overcome these limitations [4].

This chapter describes the basic principles of ultrasound, instrumentation, examination techniques as well as important clinical applications in neurological diseases.

**Fig. 1.1** Transtemporal insonation of basal cerebral arteries and their expected depths in millimetres. *ACA* Anterior communicating artery, *ICA* Internal carotid artery, *MCA* Medial cerebral artery, *PCA* Posterior cerebral artery (from [5])



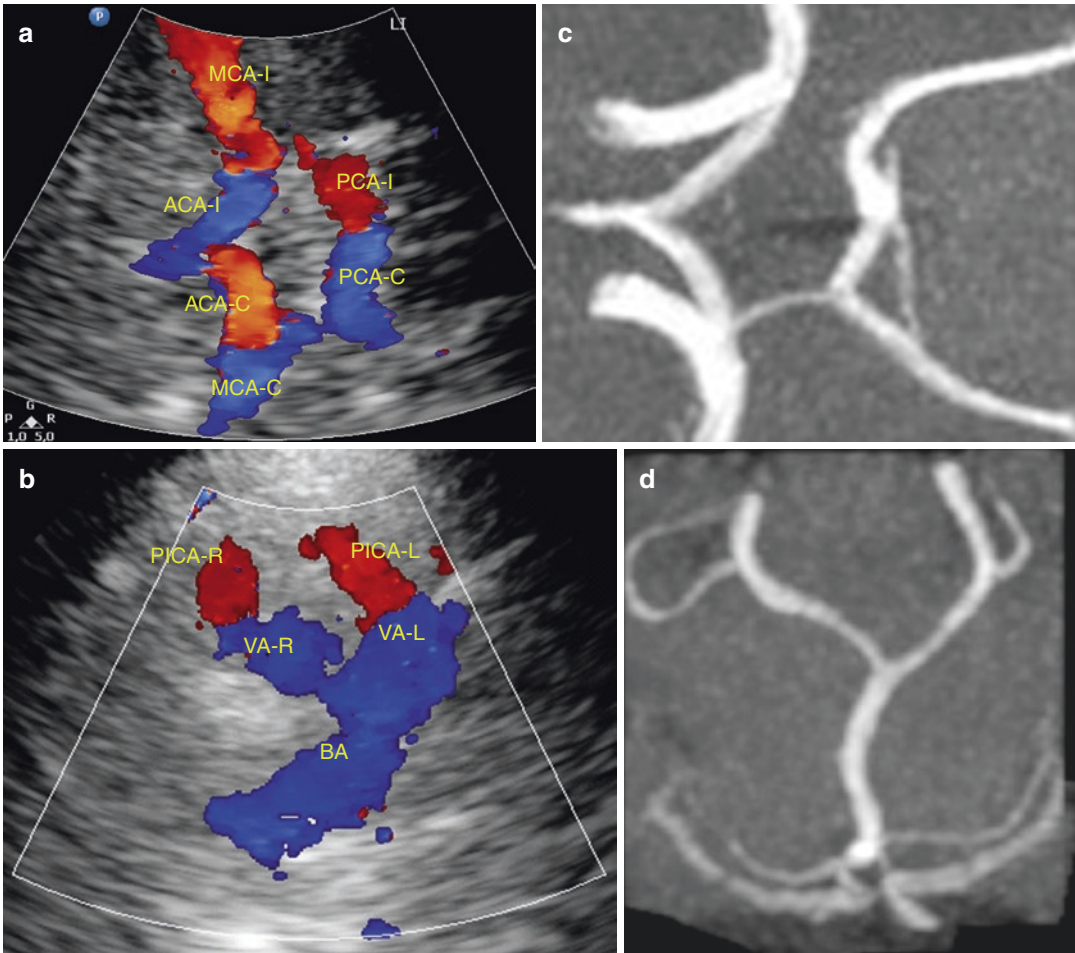


**Fig. 1.2** Normal TCCS of (a) the circle of Willis and (b) the vertebrasystem with corresponding (c, d) TOF-MRA in the same plane. Arteries with flow towards the ultrasound probe are coded red while those with flow away from the probe are coded blue. *MCA-I* Ipsilateral middle cerebral artery, *ACA-I* Ipsilateral anterior cerebral artery,

*PCA-I* Ipsilateral posterior cerebral artery, *MCA-C* Contralateral middle cerebral artery, *ACA-C* Contralateral anterior cerebral artery, *PCA-C* Contralateral posterior cerebral artery, *VA-R* Right distal vertebral artery, *VA-L* Left distal vertebral artery, *PICA-R* Right posterior cerebellar artery, *PICA-L* Left posterior cerebellar artery, *BA* Basilar artery

## 1.2 Technical Background

### 1.2.1 Sound Waves

Leonardo da Vinci already compared the characteristics of sound waves emitted by a bell with the waves being formed by a stone which was thrown into water. Physically, surface waves are in fact very demanding to characterize. For convenience, we will be considering a standing elastic wave travelling at speed  $c$  with the frequency  $f$ . The wavelength  $\lambda$  is then calculated by  $\lambda = c/f$ .

### 1.2.2 Ultrasound

Sound waves with frequencies reaching from the threshold of hearing (15–20 kHz) up to 10 GHz are called ultrasound. In the upper part of this spectrum, the wavelength is comparable to that of light. Accordingly, diffraction, which complicates sound waves in the hearable range, plays a less important role. Ultrasound can therefore be bundled just like light and the reflection of this directional beam is used to localize objects (e.g. sonar in nautics). In neurovascular ultrasound,

typically linear array transducers (5–13 MHz) and phased array transducers (2–8 MHz) are being used.

### 1.2.3 Transducer

Ultrasound produced mechanically with sirens may reach 500 kHz. A more effective way is to use the piezoelectric effect in certain crystals or ceramics, where an electric charge is “transduced” to mechanical stress or vice versa. Piezoelectric materials have a defined arrangement of aligned electric dipoles. Multi-element array transducers (Fig. 1.3) can simultaneously emit and receive ultrasound. The excitation of one element may produce a single wavelet. Combining the excitation of hundreds (typically 128–512) of elements enables to generate different shapes of ultrasound beams. In the linear array transducer, a simultaneous excitation would produce a wavefront perpendicular to the transducer surface. Variation of the time delay between

the individual excitation of the elements makes it possible to steer the wave front, to focus the beam or generally to configure the shape of the ultrasound beam. Simple transducers operate in resonance mode. Their frequency is determined by the thickness of the piezoelectric material. In a 5-MHz transducer, it measures 0.4 mm. The emitted wavelength is twice its thickness. In multifrequency transducers, the design is more complex. Here ultrasound pulses can be emitted in one frequency and received at another, for example, higher frequency.

### 1.2.4 Resolution

The ultrasound beam is three-dimensional. Volume elements can be defined (axial, lateral and depth resolution). Geometric considerations subdivide the ultrasound beam into near field and far field. Lateral resolution is best in the distal near field where optimal collimation of the ultrasound beam can be achieved. It is worst very close or very far from the transducer surface. Axial resolution is restricted by half of the spatial pulse length and is approximately 0.5 mm at 5 MHz. It does not change with depth.

### 1.2.5 Doppler Effect

In transcranial Doppler sonography, the technique to measure the velocity of intracranial blood flow relies on the Doppler effect. An outgoing sound wave of frequency  $f$  and velocity  $c$  (which is approx. 1.540 m/s in soft tissue) is being reflected by a moving blood cell of velocity  $v$ . This changes its frequency by the magnitude of  $\Delta f$ . The latter is termed Doppler shift or Doppler frequency. Ideally, the sound wave and blood movement would be parallel, but most commonly there will be an angle  $\alpha$  between both. The Doppler frequency is then calculated as follows:

$$\Delta f = \frac{v * 2 * f * \cos \alpha}{c}.$$



**Fig. 1.3** Left, broadband sector array transducer with a frequency range of 5 – 1 MHz for trans-/intracranial insonation. Right, broadband linear array transducer with a frequency range of 12 – 3 MHz for transcutaneous/extracranial insonation

### 1.2.6 Angulation

According to the calculation of the Doppler frequency, the maximum  $\Delta f$  is measured if the angle of insonation is  $0^\circ$ . At  $90^\circ$  it is not possible to measure a Doppler frequency. At  $60^\circ$  the angle error leads to 3% discrepancy ( $\cos 60^\circ \div \cos (60^\circ + 1^\circ)$ ) in the measurement of the velocity. This can still be tolerated in clinical practice. Larger angles of insonation should be avoided.

While using a linear array transducer, it is possible to steer the beam up to  $25^\circ$  to either side without losing too much on sensitivity. In colour flow imaging, this helps to improve colour coding of the image especially in vessels with low flow which runs parallel to the skin surface.

### 1.2.7 Turbulences and Disturbed Flow

In smoothly lined vessels, the velocities of blood cells are distributed parabolically. The fastest cells are found centrally; peripheral cells have a strong adherence to the vessel wall and are therefore much slower. In laminar flow, they move in parallel lines. If blood flow increases, turbulences occur first peripherally and later also centrally. Disturbed flow is normal in bifurcations or at side branches. Abnormal disturbed flow caused by stenosis can be detected intra- and poststenotically. In disturbed flow, flow lines are regularly not parallel and have to adjust to the specific geometry.

### 1.2.8 Time–Frequency Spectrum

Doppler–sonographic measurements of a vessel segment do not consist of a single Doppler shift but a continuous spectrum of frequency shifts. After being registered in the ultrasound transducer, the Doppler signal is processed using mathematical techniques like the fast Fourier transformation. The result is a velocity distribution which can be displayed in real time on the ultrasound monitor. In this pulsatile diagram, the Doppler signal of blood cells moving towards the

transducer is represented as a positive value (above the baseline of Doppler spectrum) and that of cells moving away as a negative value (below the baseline of Doppler spectrum).

It is a useful coincidence that the extracted Doppler frequencies are in the audible range. They can be made hearable by using a loud speaker. The combined audio-visual output enables the examiner to perceive flow disturbances like turbulences and also disturbed flow more easily.

### 1.2.9 Ultrasound Settings

To be able to carry out an ultrasound examination correctly it is necessary to have good knowledge about ultrasound machine adjustments.

#### 1.2.9.1 Frequency

Higher ultrasound frequencies are being attenuated more quickly in tissue than lower frequencies. In order to penetrate the skull, ultrasound transducers need to have lower frequencies ranging between 1.8 and 2.5 MHz. Penetration depth is reached when noise supersedes reflection and back scatter. It decreases with  $f$ .

#### 1.2.9.2 Pulse Repetition Frequency

The pulse repetition frequency (PRF) describes the frequency at which the ultrasound pulses are being emitted. It is adjusted by the machine setting called “scale”. The scale needs to be adapted to the estimated blood velocity, otherwise erroneous measurements may occur. For lower blood velocities, the PRF should be reduced and vice versa. To precisely locate an object the returning pulse needs to be registered before a new pulse is emitted. Measurements in increasing depths are therefore limited by the PRF. This reduces the possibility to detect high intrastenotic Doppler frequencies correctly, if the according vessel is deeply located. As soon as the Doppler frequency exceeds half the pulse repetition frequency ( $PRF/2 = \text{Nyquist frequency}$ ) aliasing occurs. Due to insufficient sampling of the signal, its exact position cannot be determined. The systolic peaks are cut off and inserted below the baseline

giving the impression of a flow reversal. In transcranial colour-coded duplex sonography aliasing can be identified by a change of colour between red and blue with intermediate white speckles.

### 1.2.9.3 Output Power and Receiver Gain

Power and gain are two different options to directly increase the amplitude of the returning Doppler signal. Power describes the emitted energy per time. An increase in output power directly exposes the patient to more energy. Increasing the receiver gain helps to amplify low-amplitude signals from deep within the tissue, but it also increases background noise. Output power and receiver gain need to be adjusted continuously on- or off-line throughout the entire examination to ensure an optimized spectral display.

### 1.2.9.4 Sample Volume and Depth

The range gate represents the time during which the received signal is measured. Its axial extent or length can be adjusted by the operator and determines the sample volume size. The depth of the sample volume along the ultrasound beam is defined by the time the ultrasound system waits before the measurement starts. The sample volume increases when the receiver gain is raised.

### 1.2.9.5 Amplitude Modulation: (A)-Mode

A-Mode gives a reminiscence of an oscilloscope. The strength of the signal registered by the transducer is represented on the vertical axis and time on the horizontal axis. A-Mode is not widely used in neurosonography and will not be further discussed.

### 1.2.9.6 Brightness: (B)-Mode

B-Mode was a major step to the practical use of ultrasound. The echo strength and its depth are assigned to a two-dimensional black and white image. This way a representative image of the anatomy is created. Line density is determined by the distance of the piezoelectric elements. In order to compensate for signal loss with increasing depth, gain can be individually regulated by

several sliding knobs, also known as time gain compensation (TGC). The range of signals is characterized by the decibel scale and is usually too extensive to be displayed on the ultrasound monitor. Therefore, the signal needs to be transformed with compression curves; the examiner influences this by selecting a “preset”.

### 1.2.9.7 Motion: (M)-Mode

In M-Mode, the depth of the reflector is displayed on the vertical axis and time is displayed on the horizontal axis. This is particularly useful to illustrate and evaluate cardiac motion.

### 1.2.9.8 Continuous-Wave (CW) Doppler

Continuous-wave (CW) Doppler continuously emits a specific frequency while the receiving element continuously detects any echoes from the sensitive region of the beam. It is the oldest and simplest ultrasound technique used to detect flow velocity and direction. The sensitive region may cover several centimetres. It is effectively used in the examination of the extracranial cerebral vessels and the supratrochlear artery. A flow reversal in the latter (normally from intracranial to extracranial) is an important indicator of severe extracranial stenosis (>80% lumen diameter reduction) of the internal carotid artery (ICA). Due to absent range resolution, it is not possible to gather information about the depth from which the Doppler signal is returning. Thus, simultaneous detection of two or more vessels within the ultrasound beam might worsen differentiation of the cervical vessels and prolong examination duration.

### 1.2.9.9 Pulsed-Wave (PW) Doppler

Pulsed-wave (PW) Doppler enables to localize the depth from which the Doppler signal originates. The same piezoelectric element within the ultrasound transducer is used to emit and to receive the signal alternately. The signal travelling at speed  $c$  needs time  $t$  to reach depth  $d$  before it returns back the same way. The depth  $d$  can therefore be calculated as:

$$d = \frac{t * c}{2}$$

To be able to determine precisely, it is necessary to reduce the time interval during which the reflected signal is measured to a minimum. During the examination, this can be done by adjusting the range gate. Any other signals outside the gate will not be registered.

### 1.2.9.10 Colour Flow Imaging

In colour flow imaging, a box- or diamond-shaped region of interest is chosen where the pixel-wise information of blood flow is superimposed on the grey-scale image. Flow direction and velocity are colour-coded and displayed. This process is time-consuming and the frame rate is remarkably longer than in B-mode. It increases with depth. Width should be kept as small as possible. It has to be pointed out, that colour flow imaging is not a precise map of spectral Doppler measurements, but an estimated map of mean velocities which are obtained by auto-correlation of consecutive pulses.

A colour flow image helps to identify the course of vessels and to focus on where to gather precise spectral Doppler measurements with PW Doppler.

### 1.2.9.11 Power Doppler Imaging

Unlike colour flow imaging, Power Doppler uses the amplitude of the Doppler signal to detect blood flow. Therefore, power Doppler is independent of velocity and flow direction and enables to detect lower and slower flow than Doppler-dependent colour flow imaging. It gives a clearer outline of the vessel wall than colour flow imaging. Another drawback is the high degree of frame-averaging used to improve sensitivity. Therefore, flash (motion) artefacts may occur which can be avoided by moving the transducer more carefully and slowly during the examination.

intracranial arteries is usually feasible. Occasionally it is necessary though to apply compression manoeuvres of the extracranial carotid artery (avoiding the bifurcation due to thromboembolic danger or parasympathetic reaction) or vertebral artery at the C2 level. In order to obtain Doppler signals of the intracranial arteries, it is recommendable to first use a relatively large range gate of 10–13 mm and to start searching at a typical depth (5–6 cm). Comparing both sides is often more helpful than referring to standard values. After a stabilizing period of half a minute, the documentation of the Doppler signals should last for at least ten cardiac cycles [6, 7].

## 1.3.1 Pulsatile Flow in Arteries

In the healthy aorta pressure is always positive due to the “windkessel function”. The pulsatile heartbeat causes pressure waves which are reflected peripherally. The reflexion depends on peripheral resistance. If it is high, the reflected pressure amplitude will also be high. As blood flow is determined by the pressure gradient the reflected pulse-wave causes periodic local back-flow, comparable to water waves being reflected from the seashore. This characterizes high pulsatility. If peripheral resistance is low, there is continuous antegrade flow. In general, arteries supplying parenchymal organs (e.g. ICA supplies the brain parenchyma) have a low pulsatility, while arteries supplying skin and muscle (e.g. external carotid artery) have a high pulsatility.

The evaluation of pulsatility is crucial in describing vessel pathologies like stenosis, which represent circumscribed reductions of the vessel diameter.

## 1.3 Examination Technique

For the extracranial examination, the patient is lying supine with a (moderately) hyperextended neck. In transcranial ultrasound, three commonly employed acoustic windows are temporal, orbital and nuchal (Fig. 1.4). The identification of the

### 1.3.2 Ultrasound Representation of Arterial Stenosis

A stenosis of >50% lumen reduction leads to higher Doppler frequencies (up to fivefold) within the narrowed vessel, acoustically represented by a hissing sound. Aliasing can be indicative of stenosis. Poststenotic turbulences are

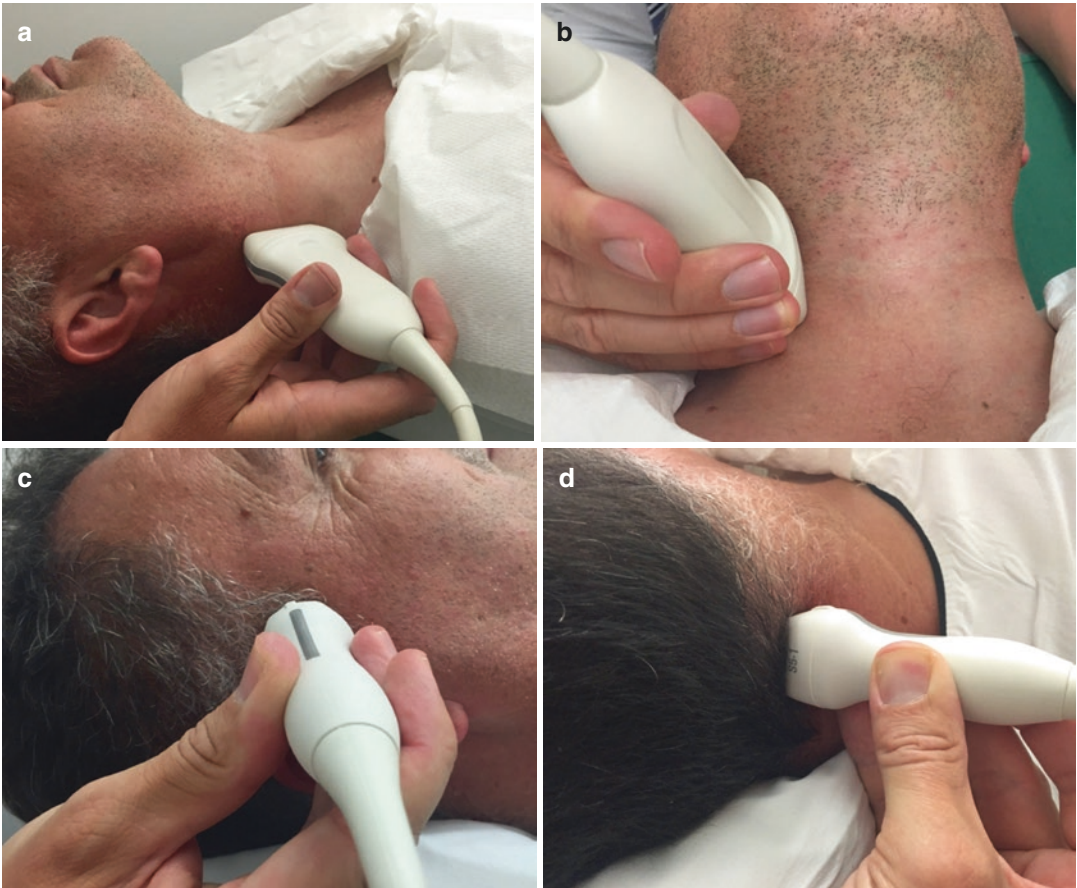


**Fig. 1.4** Most relevant transducer positions in cerebrovascular ultrasound. **(a, b)** Top, extracranial examination with patient lying supine and patient's neck hyperextended. **(a)** Top left, examination of the carotid arteries placing the transducer on the sternocleidomastoid muscle. **(b)** Top right, examination of the vertebral artery by scanning from anterior to the sternocleidomastoid muscle. **(c,**

**d)** Bottom, intracranial examination. **(c)** Bottom left, transtemporal insonation with patient lying supine in comfortable position. **(d)** Bottom right, transnuchal/suboccipital insonation via the foramen magnum with patient lying on the side; alternatively, patient might be lying supine head turned comfortably to one side

dominated by lower frequencies and irregular regions of flow reversal. In very short stenosis, it is difficult to measure the highest flow acceleration precisely (so-called stenotic jet) as the ultrasound beam always partly registers poststenotic flow. Pulsatility may increase up to threefold compared to normal values. In high-grade stenosis pulsatility will be reduced.

### 1.3.3 Pulsatility Index

Pulsatility describes the difference in the maximum systolic ( $S$ ) and diastolic ( $D$ ) velocities [8].

In order to put the value into perspective, it is either related to the systolic velocity itself (Pourcelot's resistance index [RI]) or to the mean velocity  $v_{\text{mean}}$  (Gosling's Pulsatility Index [PI]).

$$\text{RI} = \frac{S - D}{S}$$

$$\text{PI} = \frac{S - D}{v_{\text{mean}}}$$

A pulsatility index is usually automatically given by the ultrasound machine when measuring velocities. It is also important in the detection of intracranial hypertension or an upstream high-



grade stenosis which cannot be directly visualized due to bony structures (e.g. near the skull base).

### 1.3.4 Requirements for Examiners and Reporting

Precise and reproducible reporting can only be achieved if the examiner carries out transcranial Doppler sonographies on a regular basis. The results need to be compared to other diagnostic procedures like DSA, MRA or CTA, if available.

The time–frequency spectrum has to be documented over a period of several heart beats. Documentation of maximum systolic and diastolic frequency is obligatory, while the additional documentation of the maximum mean Doppler shift (arithmetic average of the signal envelope) is helpful, especially in detecting and quantifying vasospasm. Additionally, transcranial colour-coded duplex sonography should include colour- and cross-sectional images. The transtemporal examination should include the anterior-, middle- and posterior cerebral artery as well as the carotid-T on both sides. Comparative documentation of the distal vertebral arteries and basilar artery as distal as possible are recommended via the transnuchal approach.

### 1.3.5 Safety of Diagnostic Ultrasound

As is known from ionizing radiation the ALARA rule (As Low As Reasonably Achievable) can also be applied to diagnostic ultrasound. Local heating is the most important biophysical effect. It can affect the cranial bone especially during long examinations. Nevertheless, a dangerous temperature rise of the brain parenchyma is unlikely to happen for several reasons: The healthy temporal bone reduces ultrasound energy significantly and intracranial blood flow has a cooling effect. Dynamic angulation of the transducer also helps to spread the thermal energy. Output power should be reduced when using skull defects (i.e. after craniectomy) or to avoid

damage of the eye lens during transorbital insonation. Another theoretical danger results from cavitation, when tissue cohesion is exceeded in the low-pressure cycle of the sound pressure. This may be exacerbated by the use of ultrasound contrast agent. So far, there are no definite reports about negative side effects in transcranial ultrasound, but it is recommended to keep the mechanical index as low as possible [9].

### 1.3.6 Contrast-Enhanced Ultrasound (CEUS)

Contrast agents used in ultrasound are blood pool agents, of which some are taken up by Kupffer cells in the liver. They consist of microbubbles filled with gas and stabilized by a shell of proteins or lipids. Their diameter ranges from 2.5 to 3  $\mu\text{m}$  in order to enable capillary passage. After intravenous injection they significantly increase not only the back-scatter signal of vascularized structures but also of multiples of the original frequency, so-called harmonics. Amplification is described as up to 1000-fold. The microbubbles are easily destroyed by the energy of the ultrasound beam. Therefore, the acoustic energy delivered needs to be minimized. This requires specific ultrasound settings. A dual-image display is necessary which simultaneously shows two images, one in B-mode for general anatomic orientation and a second one in contrast mode. Both images use the same information but are compressed differently in order to show different parts of the dynamic range. After the injection of the contrast agent, the diagnostic effect lasts up to 5 min. Advantages of CEUS include the visualization of slow perfusion (e.g. cerebral perfusion or high-grade carotid stenosis). Focal destruction (“burst”) of microbubbles may help to apply specific drugs locally, which is currently under investigation. Apart from extremely low rates of anaphylactic reactions ultrasound contrast agents are considered to be safe [10]. Unlike other radiologic contrast agents, the renal and thyroid function does not need to be checked in advance.

## 1.4 Clinical Application

### 1.4.1 Extracranial

#### 1.4.1.1 Arterial Wall Imaging

The extracranial brain-supplying arteries, especially the carotid arteries, lie superficially and can be easily visualized by means of a high-frequency linear transducer (7.5–10 MHz). The arterial wall has a typical appearance imaged by B-mode: It is defined by two parallel echogenic lines which are separated by an echolucent line. These lines do not represent the histological layers of the vessel wall but the interfaces between blood flow, intima, media and adventitia, which cause differences in acoustic impedance [11]. The inner echogenic line together with the adjacent echolucent line (“double-line-pattern”) is called Intima–Media–Thickness (IMT) complex (Fig. 1.5). IMT increases with age. IMT can also be changed in size and appearance by different diseases. (Early) atherosclerotic changes are most frequent, but large vessel vasculitis, radiation-induced vasculopathy and dissections are also accompanied with changes of IMT and the entire vessel wall, respectively.

IMT measurements “in plaque-free-zones” were shown to be an appropriate tool to estimate the cardiovascular risk, since IMT was found to be a predictor for coronary heart disease and stroke [12]. However, in more recent meta-analysis, the authors disapproved of this, since IMT measurements only slightly improved the prediction of cardiovascular risk compared with the Framingham Risk score alone [13]. Thus, the future role of MRI is emphasized in non-invasive risk stratification of cardiovascular diseases by several authors [14]. Several limitations of IMT measurements have been identified as causes for conflicting results: First, the current resolution of the usually applied 7-MHz transducer is lower than IMT changes per year (about 0.3 mm vs. 0.04 mm). Second, there is no final consensus concerning the site of IMT measurement (CCA vs. ICA vs. carotid bulb). Third, IMT measurement captures only the increase in (sub)-millimetres but not the complexity of the (early) atherosclerotic changes. Furthermore, it remains

unclear whether semi-automated border detection is more accurate and reproducible than manual positioning of the caliper.

Unlike IMT, the presence and morphology of carotid artery plaques are undoubtedly closely associated with coronary heart disease, coronary events and stroke. In contrast to IMT, a plaque is defined as a focal wall thickening that is at least 50% greater than that of the surrounding vessel wall or a protrusion of more than 1.5 mm into the lumen [15]. It is well known that the plaque vulnerability is as important as the severity of stenosis [16]. Thus, carotid plaque morphology has to be defined by ultrasound which is the first-line imaging modality. The evaluation of carotid artery plaque comprises the analysis and description of the plaque surface morphology (regular vs. irregular; with/without niche/ulceration), the intraplaque structure (echogenic vs. echolucent; homogenous vs. heterogenous) and ultrasonic shadowing (due to calcification). Plaque echolucency and disruption or absence of plaque surface (echogenic cap) are established plaque features associated with an increased thromboembolic risk (Fig. 1.5).

#### 1.4.1.2 Stenosis and Occlusion

The arteriosclerotic stenosis of the extracranial ICA at the carotid bifurcation has a high frequency in Caucasians. Its significance is greatest amongst all vascular pathologies of the brain-supplying arteries. ICA stenosis is responsible for 10–20% of strokes and transient ischemic attacks (TIA). The results of the North American Symptomatic Carotid Endarterectomy Trial (NASCET) showed an absolute risk reduction (ARR) of 16% for any ipsilateral stroke after 5 years in patients with symptomatic high-grade stenosis (70–99%) following carotid endarterectomy (CEA). In patients with moderate stenosis (50–69%) the 5-year ARR was 4.6%. Therefore, the rapid detection and correct characterization of the extracranial ICA stenosis are mandatory especially in the symptomatic stroke patient.

The criteria of multiparametric ultrasound were revised by the members of the German Society of Ultrasound in Medicine and Biology on the basis of the angiographic measurement of

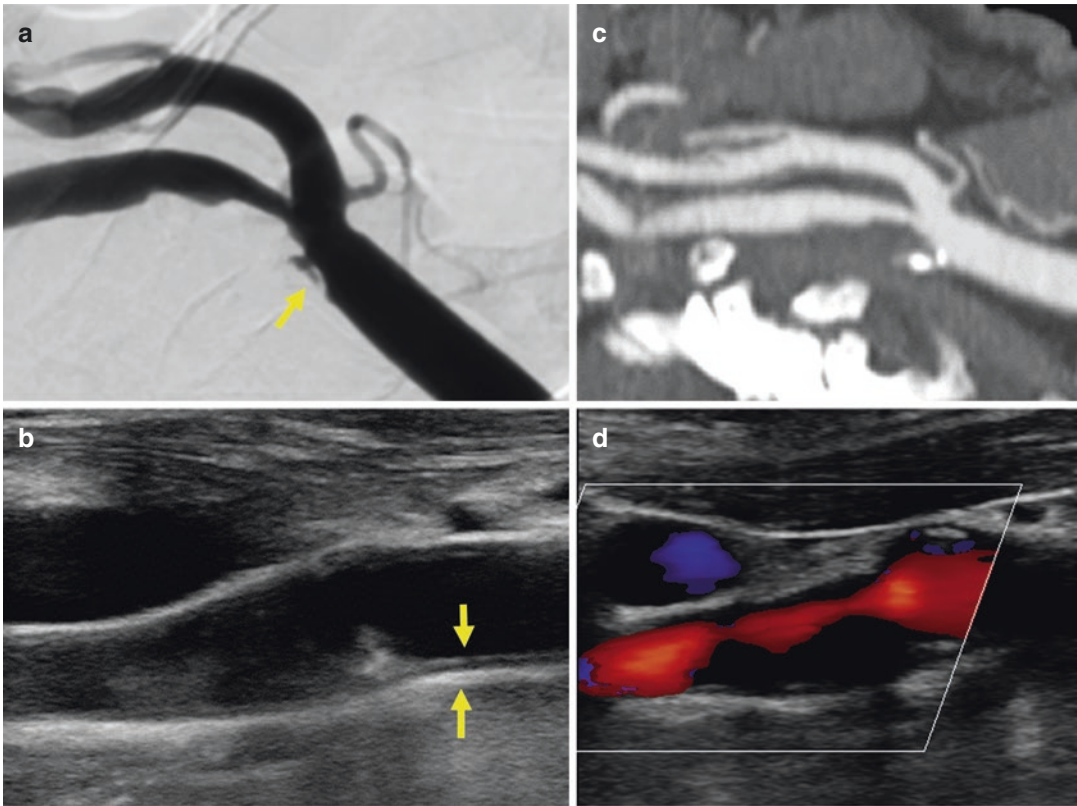


**Fig. 1.5** Complex plaque located at the distal common carotid artery and proximal internal carotid artery. **(a)** Top left, intra-arterial angiography shows the irregular plaque surface (*arrow*). **(c)** Top right, maximal intensity projection (MIP) of CTA visualizes partial calcification within

the proximal portion of the plaque. **(b)** Bottom, B-mode ultrasound and **(d)** colour mode enables delineation of the plaque and residual lumen. Double-line pattern of the IMT complex is also visible in the far wall of the distal CCA (*arrows in b*)

carotid stenosis as utilized in NASCET. For this, the predominantly Doppler sonographic major and minor criteria, which originally corresponded to the angiographic European Carotid Surgery Trial measurement (ECST), were adapted to NASCET (Table 1.1). Overall, the flow velocities corresponding to a specific degree of stenosis were replaced by lower values.

A reliable and precise grading of stenosis involves B-mode measurements in various angles, direct peri- and intrastenotic measurements of flow velocities as well as indirect hemodynamic parameters (e.g. detection of collaterals). Therefore, the diagnostic significance of Doppler sonographic determination of stenosis goes far beyond a “screening tool”.

Approximately one-third of ischemias in the vertebrobasilar system are caused by vascular stenosis [18]. The origin of the vertebral artery is most commonly affected. Due to its elongated proximal segment and anatomic restrictions (short strong neck) a reliable and angle-corrected measurement is often challenging. Hence, a rough distinction between the exclusion of stenosis and high-grade stenosis (>50%) as well as an occlusion is all that might be achieved.

However, occlusion and pseudo-occlusion of the proximal extracranial ICA can usually be differentiated. This is especially the case if the ICA occlusion is localized at the level of the bifurcation and the downstream vessel wall and Doppler spectrum are clearly visualized.

**Table 1.1** Graduation of stenosis in the internal carotid artery (modified from [17])

Stenosis (NASCET definition)		10	20–40	50	60	70	80	90	Occlusion
Stenosis (ECST definition)		45	50–60	70	75	80	90	95	Occlusion
Major criteria	1. B-mode	+++	+						
	2. Colour flow	+	+++	+	+	+	+	+	+++
	3. Intrastenotic peak systolic Velocity (cm/s)			200	250	300	350–400	100–500	
	4. Poststenotic peak systolic velocity (cm/s)					>50	<50	<30	
	5. Collaterals and precursors (periorbital artery/ACA)					(+)	++	+++	+++
Minor criteria	6. Diastolic prestenotic flow reduction (CCA)					(+)	++	+++	+++
	7. Poststenotic disturbed flow			+	+	++	+++	(+)	
	8. End diastolic flow velocity in maximum stenosis (cm/s)			≤100	≤100	>100	>100		
	9. Confetti-sign				(+)	++	++		
	10. Stenosis index (ICA/CCA)			≥2	≥2	≥4	≥4		

Under limited ultrasound conditions, accuracy can be improved by using ultrasound contrast agents or the Doppler- and angle-independent B-flow technique [19]. Ultrasound may even be superior to CTA, MRA and DSA in the detection of occlusions of the extracranial vertebral artery. Whereas the latter merely depict the contrast-filled vessel lumen, B-Mode can help to distinguish frequent vessel hypo- or aplasia from occlusion by displaying the vessel wall of no-flow or low-flow arteries.

Juvenile stroke (<45 years) may be caused by spontaneous dissection of the extracranial carotid artery and vertebral artery in about 20%. Risk factors include connective tissue disorders, fibromuscular dysplasia, collagenosis and possibly kinking or looping of the affected vessel. Primary diagnosis can either be made with CT, MRI or ultrasound. Ultrasound is well suited for follow-up. Dissection may lead to extended hypoechoic or crescent-shaped luminal narrowing, circumscribed flow velocity acceleration, the detection of a membrane separating true and false lumen or the detection of a pseudo-aneurysm. It has to be stated, that the proximity of the base of the skull is one predilection site for extracranial

dissections and is methodically only partially visible by ultrasound. Indirect signs like increased prestenotic pulsatility may be useful.

## 1.4.2 Intracranial

### 1.4.2.1 Parenchymal Sonography

Transcranial parenchymal sonography is an established diagnostic tool in neurodegenerative diseases. Already in 1995, Becker and co-worker first described a hyperechogenic area within the substantia nigra (SN) in patients with Parkinson's disease (PD) [20]. This patchy, band-like or sometimes wide oval appearing hyperechogenicity is found in more than 90% of PD patients but then again also in 10% of healthy adults [21]. It is recommended to use the following ultrasound system settings: *Image depth* starts with 14–16 cm and has to be adapted as needed, *dynamic range* is 45–55 dB, image brightness and time gain compensation have to be adapted manually as needed or, if available, optimized automatically. An adequately qualified investigator and a sufficient temporal window are of great importance to achieve a reliable diagnostic accu-

racy. In a 5-year follow-up study, Berg and co-workers found the risk for PD to be 21 times increased in participants with a hyperechogenicity of the SN. Furthermore, SN is a sonographic landmark in PD patients to control correct position of deep brain stimulation electrodes within the subthalamic nucleus [22].

Enlargement of the third ventricle and frontal horns can also be monitored by transtemporal sonography. This is of high clinical relevance in patients with acute obstructive hydrocephalus following intraventricular haemorrhage [23] as well as in the elderly with cognitive impairment [24].

In stroke patients with a space-occupying supratentorial process (i.e. intracranial bleeding and/or malignant ischemic MCA-infarction), TCCD allows for reliable monitoring of midline shift [25] and consecutively avoids repeated CT examinations with high-risk transport of intensive care patients and considerable cumulative radiation dose (Fig. 1.6).

#### 1.4.2.2 Stenosis, Occlusion and Vasospasm

In acute stroke, detection of the underlying brain vessel occlusion is of great importance. Ultrasound is a unique diagnostic modality which

even allows emergency assessment using a portable duplex machine [26]. In order to diagnose a middle cerebral artery or distal ICA occlusion there needs to be an adequate temporal window. This is the case if there is clear visualization of the contralateral MCA and of the ipsilateral P1 and P2-segment of the posterior cerebral artery while a flow signal in the lateral fissure is lacking (M1-occlusion) or minimal (distal ICA occlusion). In general, the detection of an occlusion of the intracranial vertebrobasilar system is frequently not possible with a reliable accuracy, especially under emergency conditions (i.e. basilar artery, distal vertebral artery [V4 segment] and proximal posterior cerebral artery [P1 segment] occlusion).

Due to interindividual differences in intracranial blood flow velocity, there are no widely accepted thresholds for the detection and quantification of intracranial stenosis. Similar to the sonographic diagnosis of extracranial stenosis, the main criteria are the detection of a circumscribed elevation of blood flow velocity (PSV > 120 cm/s [= suspicious on stenosis]; >160 cm/s [= definitely pathological]), prestenotic elevated pulsatility and poststenotic flow changes (i.e. turbulences, decreased pulsatility)

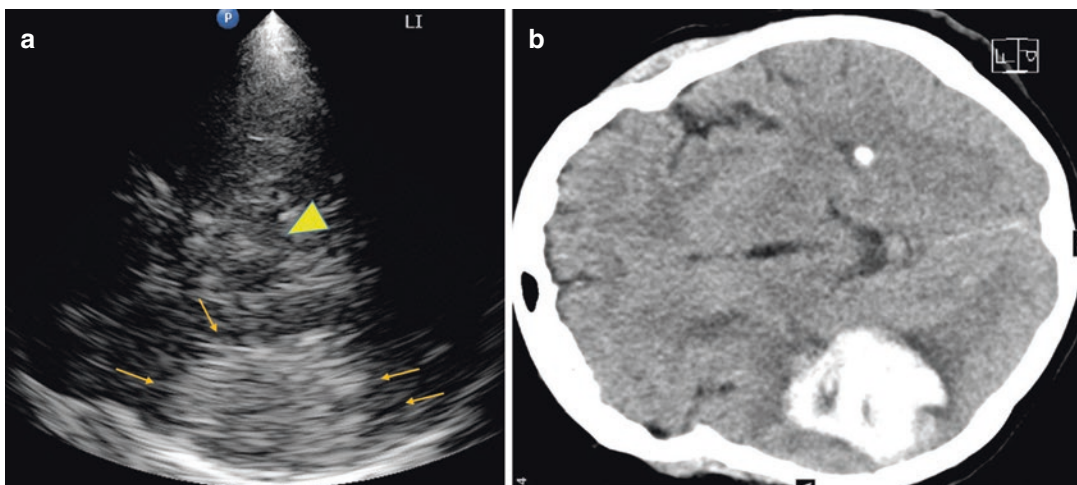


**Fig. 1.6** Acute intracerebral bleeding into the right temporal lobe. (a) Left, transcranial B-mode, insonated from the left temporal window showing the intraparenchymal hematoma close to the right temporal skull (*small arrows*).

Butterfly-shaped hypoechoenic mesencephalon (*arrowhead*). (b) Right, corresponding plain CT (rotated by 90° to the left)

as well as an elevated flow velocity of >30% compared with the contralateral side (except basilar artery). Regarding the vertebrobasilar system, it has to be considered that the blood flow velocity is generally about 20–30% lower than in the anterior circulation.

Another frequent and important reason for a circumscribed increased blood flow velocity of an intracranial artery (segment) or even a reversed flow (i.e. the A1- or P1-segment) is a collateral flow due to an extracranial high-grade stenosis or occlusion. Thus, knowledge of extracranial steno-occlusive lesions is necessary to avoid misdiagnosis of the intracranial vasculature.

A major and potentially lethal complication after subarachnoid bleeding is circumscribed or general vasospasm of the intracranial arteries which may cause ischemic infarcts in about 25–30% of patients. The early detection and monitoring of vasospasm of the basal arteries have been a domain of TCD (and TCCD) for more than 30 years. Whereas the measurement of flow velocity is used to characterize arteriosclerotic stenosis, the intensity-weighted mean flow velocity (“mean velocity”) is used to detect vasospasm. The thresholds for mean velocities are >120 cm/s (“suspected vasospasm”) and >160 cm/s (“definitive vasospasm”) in the carotid territory, and >80 cm/s (“suspected”) and >95 cm/s (“definitive”) in the vertebrobasilar territory, respectively. Another important and pathognomonic criterion for the diagnosis of vasospasm is the increase of blood flow velocity of 50% and/or of 30–40 cm/s within 24 h. Thus, daily TCD is mandatory following subarachnoid bleeding.

#### 1.4.2.3 Cerebral Autoregulation and Functional TCD (Neurovascular Coupling)

Cerebral brain perfusion is being kept constant in a wide range of cerebral perfusion pressures, reaching from 50 to 150 mmHg. This mechanism is called cerebral autoregulation. Despite intense clinical research, the investigation of autoregulation remains insufficient. Most studies showed technical shortcomings and focused on the middle cerebral artery, leaving out cortical and posterior arteries [6].

Cerebral autoregulation comprises the change of regional blood flow induced by neuronal activ-

ity (neurovascular coupling) as well as the change of blood flow resulting from alterations in the partial pressures of blood gases (cerebrovascular reactivity) [27]. The adaptation of the cerebral blood flow is a result of the adjustment in the pre-capillary arterioles diameter. Unlike in other small vessels, the diameter of the basal cerebral arteries remains constant. Thus, blood flow velocities measured by TCD/TCCD are directly proportional to the cerebral blood flow.

In healthy individuals, hypercapnic stimulation of the highly CO<sub>2</sub>-sensitive pre-capillary arterioles leads to further dilation (Fig. 1.7). If the pre-capillary arterioles in the middle cerebral artery territory are already at maximum dilatation, i.e. in a patient with insufficient collateralization of an ICA occlusion, additional hypercapnic stimulation does not lead to continuing measurable dilatation because the reserve capacity has already been exhausted. Thus, testing cerebral autoregulation might help to decide on the indication for extracranial-intracranial bypass surgery. Besides this, the potential risk of hemodynamically induced ischemia during carotid endarterectomy or cardiopulmonary surgery can be assessed.

#### 1.4.2.4 Microemboli Detection and Diagnosis of Patent Foramen Ovale (PFO)

Clinically silent circulating cerebral microemboli produce a visible and audible signal (“click, chirp, whistle”) and can be detected by TCD [28]. These signals, called microembolic signals (MES), are of short duration and high intensity (Fig. 1.8). MES might originate from microemboli composed of different material such as atheromatous debris, clotted blood, platelets, fat or air. The presence of MES is indicative for emboligenic activity into the cerebral arteries [29]. Thus, microemboli detection is used to determine the emboligenic potential of an embolic source (e.g. carotid artery stenosis or prosthetic heart valves) or to monitor antithrombotic treatment [30].

*Technique:* For microemboli detection, TCD monitoring is performed for 30–60 min using a pulsed Doppler machine with a 2-MHz probe and a sample volume of 4–10 mm [31]. After

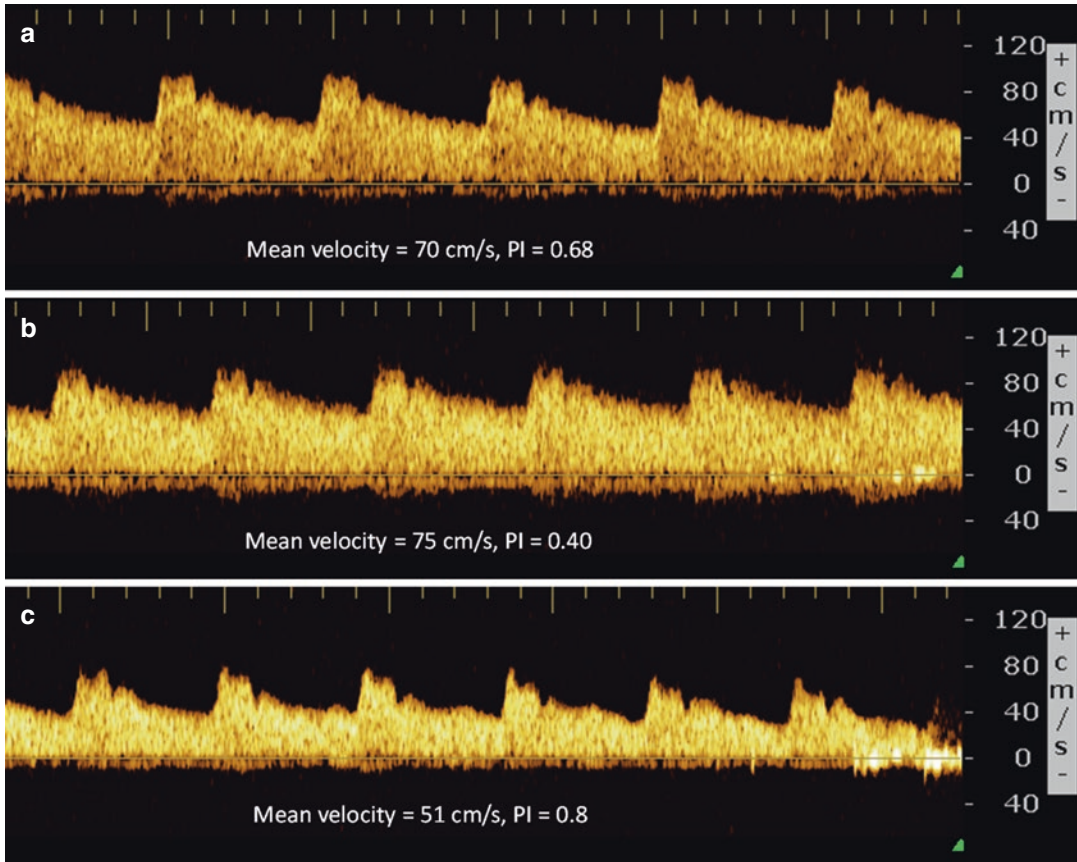


**Fig. 1.7** Effect of slight  $\text{PCO}_2$  changes on flow velocity and pulsatility index of the MCA in a healthy subject. (a) During regular breathing. (b) Holding the breath for several seconds. (c) During hyperventilation

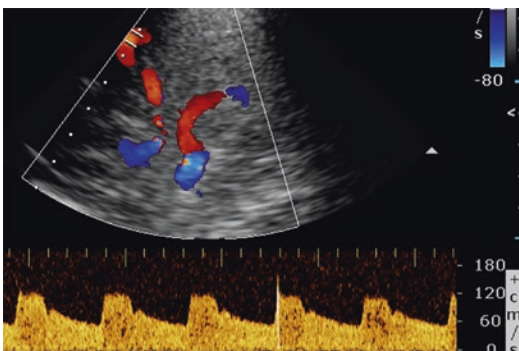


**Fig. 1.8** Microembolic signals detected in the ipsilateral M2-segment of the middle cerebral artery immediately following extracranial carotid artery stenting

identification of the target vessel (mostly the M1-segment of the middle cerebral artery), the probe is fixed on the temporal skull with an elas-

tic band in order to minimize artefacts. The prefast Fourier transformation signal is recorded on digital audio tape (DAT) for off-line analysis and later re-evaluation of regions of interest. Since microemboli detection is time-consuming, attempts towards automatic microemboli detection by trained neural networks have been undertaken.

The most frequent cardiac right-to-left-shunt (RLS) is the patent foramen ovale (PFO). PFO is a well-recognized cause of stroke due to paradoxical thromboembolism. Thus, the correct diagnosis of RLS is of high clinical significance in patients without other embolic sources.

The sensitivity and specificity of the non-/semi-invasive contrast TCD in detecting intracardiac RLS is similar to transoesophageal echocardiography (TEE) [32].

*Technique:* Similar to microemboli detection (see above), a 2-MHz probe is mounted on the temporal bone and fixed. A contrast mixture consisting of normal saline, air and the patient's own blood is agitated by means of a three-way stopcock. Then, the mixture is applied intravenously via an 18–21 gauge needle according to a standardized protocol. A Valsalva manoeuvre is performed 4–6 s after injection in order to raise the pressure within the right atrium. If a PFO is present, MES can be detected regularly within a few seconds and up to 20–30 s after injection, sometimes even as a cluster or “shower”. Depending on the number of MES counted an estimation of the size of the RLS is possible. Previously, a galactose-based contrast agent that generates air-filled microbubbles was used instead of the above-mentioned mixture.

## 1.5 Future Developments

### 1.5.1 Brain-Focused Ultrasound

Magnetic resonance-guided focused ultrasound surgery (MRgFUS) is being studied in various clinical applications. It uses non-invasive thermal ablation to treat soft tissue tumours, but also other neurodegenerative diseases like essential tremor and Parkinson's disease. Several clinical trials have demonstrated feasibility and a favourable safety profile [33].

Ultrasound waves are focused onto the target area. This leads to local thermal destruction with high spatial accuracy. As known from TCD the skull bone absorbs most of the energy and distorts the focused beam. The use of large-sized phased array transducers and adjusted focusing techniques in combination with MR thermometry has made real-time therapy guidance possible [34].

Depending on the tremor aetiology a reduction of tremor intensity of up to 80% after 6–12 months follow-up has been reported without the disadvantages of open brain surgery. First data on the treatment of lesions of the thalamic ventral intermediary nucleus as well as subthalamic fibre tracts have been published [35].

### 1.5.2 Neurological Applications

There is increasing knowledge that focused ultrasound (FUS) combined with microbubbles enables to cross the blood–brain barrier (BBB) and to deliver diagnostic and therapeutic agents into the CNS in animals [36]. Additional diagnostic ultrasound allows precise targeting of the brain lesion as well as to introduce a broader range of BBB disruption than FUS alone. Zhao and co-workers demonstrated that the extent of BBB disruption is increased by microbubble dose, mechanical index and duration of insonation [37]. By simultaneous application of diagnostic ultrasound, BBB disruption could be enhanced and accompanying tissue damage could be minimized.

*Ultrasound perfusion imaging* in acute stroke has been introduced in the late 1990s. Despite this, it has not been established in routine clinical practice yet. Recently, a novel technique, the so-called real-time low mechanical index imaging, has been introduced. It allows a simpler and more precise acquisition of perfusion parameters. Unlike the previous technique which uses a high mechanical index leading to rapid disruption of the microbubbles, real-time low mechanical index imaging enables to study refill kinetics by the replacement of new bubbles in the ultrasound plane [38].

Currently, CEUS is also tested for target *imaging in vulnerable artery plaques*. Antibodies against membrane proteins which are involved in the plaque formation are conjugated to modified microbubbles. These conjugated microbubbles can be visualized non-invasively by CEUS in rabbits. This might serve as a marker for plaque vulnerability in the future [39].

*Contrast-enhanced sonothrombolysis* (CEST) is the combination of intravenously administered thrombolytic drug, transcranial ultrasound and intravenously administered microbubbles for acute treatment of ischemic stroke. The current rapid evolution of endovascular mechanical recanalization in acute stroke seems to pre-empt CEST. However, recent studies suggest that CEST might be effective (potentially as an adjuvant therapy) in patients with M1-segment occlusion as well as in patients with smaller thrombi [40, 41].



## 1.6 Clinical Case (Fig. 1.9)

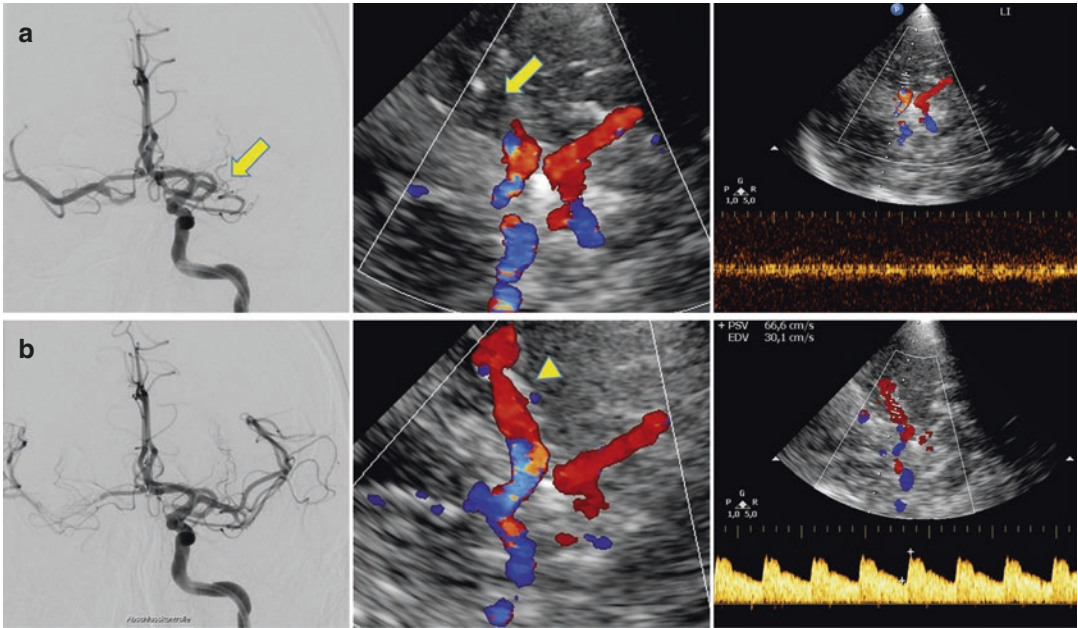


**Fig. 1.9** Cerebral angiography in a.-p. projection and transtemporal TCCS (colour mode and Doppler waveform) (a) before and (b) after mechanical recanalization of an acute M1-occlusion. (a) Absent filling of the M1-segment with contrast agent and colour (arrow),

respectively. Doppler spectrum shows minimal blunted flow. (b) After thrombectomy there is complete recanalization (arrowhead) of the MCA and a normal Doppler waveform

## References

1. Aaslid R, et al. Noninvasive transcranial Doppler ultrasound recording of flow velocity in basal cerebral arteries. *J Neurosurg.* 1982;57(6):769–74.
2. Bogdahn U, et al. Transcranial color-coded real-time sonography in adults. *Stroke.* 1990;21(12):1680–8.
3. Kollár J, et al. Image quality of the temporal bone window examined by transcranial Doppler sonography and correlation with postmortem computed tomography measurements. *Cerebrovasc Dis.* 2004;17(1):61–5.
4. Nabavi DG, et al. Potential and limitations of echocontrast-enhanced ultrasonography in acute stroke patients: a pilot study. *Stroke.* 1998;29:949–54.
5. Widder B. Doppler- und Duplexsonographie der hirnversorgenden Arterien. 6th ed. Berlin: Springer; 2004. p. 128.
6. D’Andrea A, et al. Transcranial Doppler ultrasound: physical principles and principal applications in neurocritical care unit. *J Cardiovasc Echogr.* 2016;26(2):28–41. <https://doi.org/10.4103/2211-4122.183746>.
7. Nedelmann M, et al. Consensus recommendations for transcranial color-coded duplex sonography for the assessment of intracranial arteries in clinical trials on acute stroke. *Stroke.* 2009;40(10):3238–44. <https://doi.org/10.1161/STROKEAHA.109.555169>.
8. Naqvi J, et al. Transcranial Doppler ultrasound: a review of the physical principles and major applications in critical care. *Int J Vasc Med.* 2013;2013:629378. <https://doi.org/10.1155/2013/629378>.
9. Harrer JU, et al. Neurosonografie in der neurologischen Notfall- und Intensivmedizin: Grundlagen, vaskuläre Schlaganfalldiagnostik und Monitoring—Teil 1. *Ultraschall Med.* 2012;33:218–35.
10. Dietrich CF, et al. How to perform contrast-enhanced ultrasound (CEUS). *Ultrasound Int Open.* 2018;4(1):E2–E15. <https://doi.org/10.1055/s-0043-123931>.
11. Schulte-Altendorfer G, et al. Accuracy of in vivo carotid B-mode ultrasound compared with pathological analysis. Intima media-thickening, lumen diameter, and cross-sectional area. *Stroke.* 2001;32:1520–4.
12. Simon A, et al. The value of carotid intima-media thickness for predicting cardiovascular risk. *Arterioscler Thromb Vasc Biol.* 2010;30(2):182–5. <https://doi.org/10.1161/ATVBAHA.109.196980>.
13. Den Ruijter HM, et al. Common carotid intima-media thickness measurements in cardiovascular risk prediction: a meta-analysis. *JAMA.* 2012;308(8):796–803. <https://doi.org/10.1001/jama.2012.9630>.

14. Zhang Y, et al. Is carotid intima-media thickness as predictive as other noninvasive techniques for the detection of coronary artery disease? *Arterioscler Thromb Vasc Biol.* 2014;34:1341–45.
15. Stein JH, et al. Use of carotid ultrasound to identify subclinical vascular disease and evaluate cardiovascular disease risk: a consensus statement from the American Society of Echocardiography carotid intima-media thickness task force. Endorsed by the Society for Vascular Medicine. *J Am Soc Echocardiogr.* 2008;21(2):93–111; quiz 189–90. <https://doi.org/10.1016/j.echo.2007.11.011>.
16. Brinjikji W, et al. Contemporary carotid imaging: from degree of stenosis to plaque vulnerability. *J Neurosurg.* 2016;124:27–42.
17. Arning C, et al. Ultraschallkriterien zur Graduierung von Stenosen der A. carotis interna—Revision der DEGUM-Kriterien und Transfer in NASCET-Stenosierungsgrade. *Ultraschall in der Medizin—Eur J Ultrasound.* 2010;31(03):251–7. <https://doi.org/10.1055/s-0029-1245336>.
18. Savitz SI, Caplan LR. Vertebrobasilar disease. *N Engl J Med.* 2005;352(25):2618–26.
19. Jung EM, et al. Diagnostics characterisation of preocclusive stenoses and occlusions of the internal carotid artery with B-flow. *Eur Radiol.* 2007;17:439–47.
20. Becker G, et al. Degeneration of substantia nigra in chronic Parkinson's disease visualized by transcranial color-coded real-time sonography. *Neurology.* 1995;45(1):182–4.
21. Walter U. How to measure substantia nigra hyperechogenicity in Parkinson disease: detailed guide with video. *J Ultrasound Med.* 2013;32(10):1837–43. <https://doi.org/10.7863/ultra.32.10.1837>.
22. Berg D, et al. Enlarged hyperechogenic substantia nigra as a risk marker for Parkinson's disease. *Mov Disord.* 2013;28:216–9.
23. Kiphuth IC, et al. Sonographic monitoring of ventricle enlargement in posthemorrhagic hydrocephalus. *Neurology.* 2011;76(10):858–62. <https://doi.org/10.1212/WNL.0b013e31820f2e0f>.
24. Wollenweber FA, et al. Width of the third ventricle assessed by transcranial sonography can monitor brain atrophy in a time- and cost-effective manner—results from a longitudinal study on 500 subjects. *Psychiatry Res.* 2011;191(3):212–6. <https://doi.org/10.1016/j.psychres.2010.09.010>.
25. Martí-Fàbregas J, et al. Relationship between transcranial Doppler and CT data in acute intracerebral hemorrhage. *AJNR Am J Neuroradiol.* 2005;26(1):113–8.
26. Schlachetzki F, et al. Transcranial ultrasound from diagnosis to early stroke treatment: part 2: prehospital neurosonography in patients with acute stroke: the Regensburg stroke mobile project. *Cerebrovasc Dis.* 2012;33:262–71.
27. Willie CK, et al. Utility of transcranial Doppler ultrasound for the integrative assessment of cerebrovascular function. *J Neurosci Methods.* 2011;196(2):221–37. <https://doi.org/10.1016/j.jneumeth.2011.01.011>.
28. Spencer MP. Detection of middle cerebral artery emboli during carotid endarterectomy using transcranial Doppler ultrasonography. *Stroke.* 1990;21(3):415–23.
29. Poppert H, et al. Embolic signals in unselected stroke patients: prevalence and diagnostic benefit. *Stroke.* 2006;37(8):2039–43.
30. Markus HS, et al. Dual antiplatelet therapy with clopidogrel and aspirin in symptomatic carotid stenosis evaluated using Doppler embolic signal detection. The clopidogrel and aspirin for reduction of emboli in symptomatic carotid stenosis (CARESS) trial. *Circulation.* 2005;111(17):2233–40.
31. Ringelstein EB, et al. Consensus on microembolus detection by TCD. *Stroke.* 1998;29:725–9. <https://doi.org/10.1161/01.STR.29.3.725>.
32. Mojadidi MK, et al. Accuracy of transcranial Doppler for the diagnosis of intracardiac right-to-left shunt: a bivariate meta-analysis of prospective studies. *JACC Cardiovasc Imag.* 2014;7(3):236–50. <https://doi.org/10.1016/j.jcmg.2013.12.011>.
33. Bretszajn L, Gedroyc W. Brain focused ultrasound: what's the 'FUS' all about? A review of current and emerging neurological applications. *Br J Radiol.* 2018;6:20170481. <https://doi.org/10.1259/bjr.20170481>.
34. Jenne JW. Non-invasive transcranial brain ablation with high-intensity focused ultrasound. *Front Neurol Neurosci.* 2015;36:94–105. <https://doi.org/10.1159/000366241>.
35. Schreglmann SR, Hägele-Link S, Werner B, et al. Focused ultrasound ablation as tremor treatment. *Nervenarzt.* 2018;89:674–81. <https://doi.org/10.1007/s00115-017-0470-4>.
36. Meairs S. Facilitation of drug transport across the blood-brain barrier with ultrasound and microbubbles. *Pharmaceutics.* 2015;7(3):275–93. <https://doi.org/10.3390/pharmaceutics7030275>.
37. Zhao B, et al. Blood-brain barrier disruption induced by diagnostic ultrasound combined with microbubbles in mice. *Oncotarget.* 2018;9(4):4897–914. <https://doi.org/10.18632/oncotarget.23527>.
38. Seidel G, Meairs S. Ultrasound contrast agents in ischemic stroke. *Cerebrovasc Dis.* 2009;27(Suppl 2):25–39. <https://doi.org/10.1159/000203124>.
39. Zhang YJ. Ultrasound-guided imaging of junctional adhesion molecule-A-targeted microbubbles identifies vulnerable plaque in rabbits. *Biomaterials.* 2016;94:20–30. <https://doi.org/10.1016/j.biomaterials.2016.03.049>.
40. Nacu A, et al. NOR-SASS (norwegian sonothrombolysis in acute stroke study): randomized controlled contrast-enhanced sonothrombolysis in an unselected acute ischemic stroke population. *Stroke.* 2017;48(2):335–41. <https://doi.org/10.1161/STROKEAHA.116.014644>.
41. Reinhard M, et al. Endovascular treatment versus Sonothrombolysis for acute ischemic stroke. *Cerebrovasc Dis.* 2015;40(5–6):205–14. <https://doi.org/10.1159/000439142>.



# Conventional Radiography

# 2

Michael H. Schönfeld and Sebastian F.-X. Winklhofer

## Contents

2.1	<b>Introduction</b> .....	19
2.2	<b>Technical Background</b> .....	19
2.3	<b>Clinical Applications</b> .....	20
2.4	<b>Clinical Case</b> .....	21

## 2.1 Introduction

Less than a month after Wilhelm Conrad Röntgen published his first article about X-rays in 1895, his discovery was put into medical practice and “radiology” as a medical specialty was born (Fig. 2.1). Conventional radiography, where electromagnetic radiation at a certain wavelength passes a body and creates a two-dimensional image on film or a digital detector depending on the amount of X-rays absorbed on its way, has been the mainstay of radiology since. The advent of computed tomography (CT) in 1971 however, rendered most conventional radiography tech-

niques in neuroradiology as a subspecialty obsolete. Today the majority of X-ray applications in diagnostic neuroradiology like the pneumencephalography—a milestone at its time—have been replaced primarily by CT or magnetic resonance imaging (MRI).

## 2.2 Technical Background

X-rays are generated in an X-ray tube with its cathode and its anode as main components. The cathode is the source of the electrons, which are accelerated and which are hitting the anode, resulting in the generation of an X-ray beam. The anode, which usually consists of tungsten, includes the focal spot, a tiny area on the anodes surface, where the X-rays are generated. Hereby, two main types of ionizing radiation interactions can be found: The Bremsstrahlung (due to the electron deceleration) and the characteristic radiation. Basic parameters influencing the quantity and quality of the produced

---

M. H. Schönfeld (✉)  
Department of Diagnostic and Interventional  
Radiology, University Hospital Cologne, Cologne,  
Germany  
e-mail: [michael.schoenfeld@uk-koeln.de](mailto:michael.schoenfeld@uk-koeln.de)

S. F.-X. Winklhofer  
Department of Neuroradiology, University Hospital  
Zurich, Zurich, Switzerland  
e-mail: [Sebastian.Winklhofer@usz.ch](mailto:Sebastian.Winklhofer@usz.ch)



**Fig. 2.1** Conventional radiography of the left hand of Anna Bertha Ludwig, the wife of Wilhelm Conrad Röntgen. This image is considered the first medical radiographic examination (1895)

X-rays include the tube current (milliamperes, mA), the tube voltage (peak kilovoltage, kVp), and the exposure time (seconds). When the resulting X-ray beam is passing through the object of interest (e.g., the human skull) a certain amount of the X-ray beam gets absorbed, depending, among others, on the density and

the atomic number of the objects tissue. The X-rays which pass through the object can then be detected by either a conventional film or by a digital detector.

### 2.3 Clinical Applications

Even though conventional radiography is used only rarely in diagnostic radiology, some applications are still established in clinical routine. Conventional radiography is often the first-line imaging modality for a variety of traumatic and non-traumatic conditions of the osseous spine, especially if functional imaging is required, allowing for the assessment of position-related changes of the vertebral bodies to each other (lithesis) (Fig. 2.2). Another frequent application of conventional radiography is to rule out foreign bodies prior to magnetic resonance imaging (MRI) in suspected ferromagnetic particles. This is of relevance, for example in the orbita, where the magnetic field of MRI could induce movement of the foreign body and therefore potentially could injure sensitive structures. Furthermore, plain film radiography is the gold standard for the control of shunt continuity and valve adjustment (see Sect. 2.4). In pediatric neuroradiology, it can be considered an alternative imaging technique to diagnose cranio-cervical abnormalities in children since it uses less radiation than CT and may not require sedation compared to MRI.

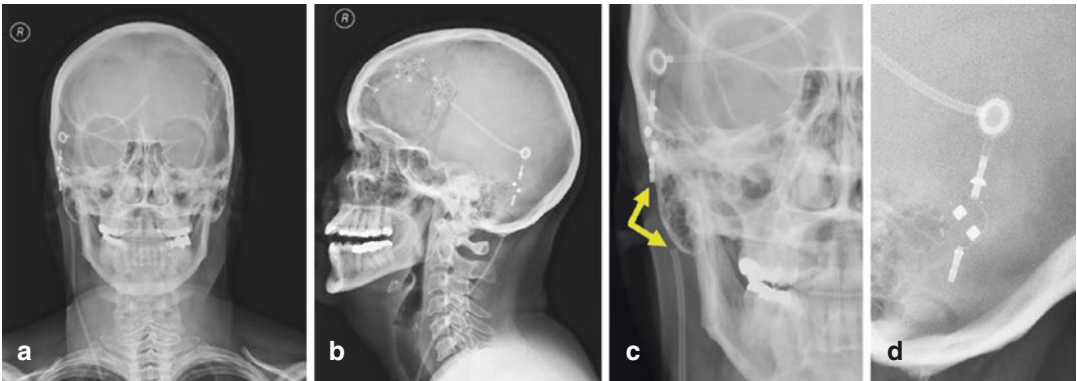
Other applications of conventional radiography, such as fracture detection or imaging in sinusitis, are increasingly being replaced by CT because of its superior diagnostic capabilities.



**Fig. 2.2** MRI (a) and conventional radiography (b, c) of a patient with previously surgically decompressed lumbar spinal stenosis. MRI shows only a mild spinal stenosis at

the level L4/5. Functional radiography, however, demonstrates progressive anterolisthesis of L4/5 from reclination (middle) to inclination

## 2.4 Clinical Case



(a, b) AP and lateral conventional radiograph of the skull in a patient with a ventriculoperitoneal shunt due to hydrocephalus. In this follow-up examination, a discontinuity of the tube distal from the valve over a length of about 2.8 cm can be seen (arrows) (c). This finding was confirmed

during surgery the next day, where a shunt revision was performed. Conventional radiographs furthermore allow us to assess the adjusting of the valve; in this case, a “Sophy” valve was set to 30 mm H<sub>2</sub>O (d)



# Digital Subtraction Angiography

# 3

Eef J. Hendriks, Jesse M. Klostranec,  
and Timo Krings

## Contents

3.1	<b>Technical Background</b> .....	23
3.2	<b>Clinical Applications</b> .....	25
3.3	<b>Clinical Case</b> .....	27
	<b>References</b> .....	29

## 3.1 Technical Background

The technique of subtraction angiography was first reported on by Ziedses Des Plantes in 1935 [1]. With the introduction of the “Seldinger” technique, safe intravascular access for angiography became available [2], paving the way for application of subtraction angiography in radiology in the 1950s [3], neuroradiology in the 1960s [4] and eventually digital subtraction angiography (DSA) in the late 1970s [5, 6].

E. J. Hendriks  
Radiology and Nuclear Medicine, Amsterdam  
University Medical Centers—Location VU  
University Medical Center,  
Amsterdam, The Netherlands  
e-mail: [e.hendriks@vumc.nl](mailto:e.hendriks@vumc.nl)

J. M. Klostranec · T. Krings (✉)  
Division of Neuroradiology, Joint Department of  
Medical Imaging, Toronto Western Hospital,  
University Health Network, University of Toronto,  
Toronto, Canada  
e-mail: [jesse.klostranec@uhn.ca](mailto:jesse.klostranec@uhn.ca);  
[timo.krings@uhn.ca](mailto:timo.krings@uhn.ca)

This minimally invasive technique has had a major impact on the field of radiology in general, and more specifically acute stroke and intracranial aneurysm treatment with the subspecialty evolution of interventional neuroradiology.

The purpose of DSA is to obtain images of blood vessels as they fill with injected radiographic dye, isolated from other overlapping tissues (e.g. bone) and extracorporeal structures. Advantages of subtractions include providing image enhancement and improving detail in areas hidden by overlying bone or poor contrast. This results in improved clarity in the imaging of blood vessels and requires a lower dose of contrast medium. Most commonly used radiographic dye is one from a variety of iodinated contrast media, selected due to iodine’s K-shell binding energy of 33.2 keV that closely coincides with the mean energy of the X-ray beam used in DSA to provide significant beam attenuation and therefore, image contrast. Images of the same region are acquired before and after injection of the contrast medium. For this reason, movement of the

patient or equipment between acquired images is to be avoided, as patient motion or respiration, peristalsis of gut, swallowing, cardiac motion, or change in caliber of vessels during the cardiac cycle will result in an incomplete subtraction and may cause artifacts degrading the appearance of vessels. Accordingly, the images are acquired in rapid succession (i.e., at least two “frames” per second) [7, 8]. The process of DSA in neuroradiology is schematically illustrated in Fig. 3.1.

First, a non-contrast image (a) is taken even before the contrast medium has reached the imaging field of view, in this case, the left cerebral hemisphere. Only the osseous anatomy of the cranium is shown on this “mask” image frame. A second contrast “enhanced” image (b) is taken when the intracranial vessels have begun filling with contrast medium. The filled vessels are shown superimposed on the osseous anatomy of the cranium and stored as the second frame.

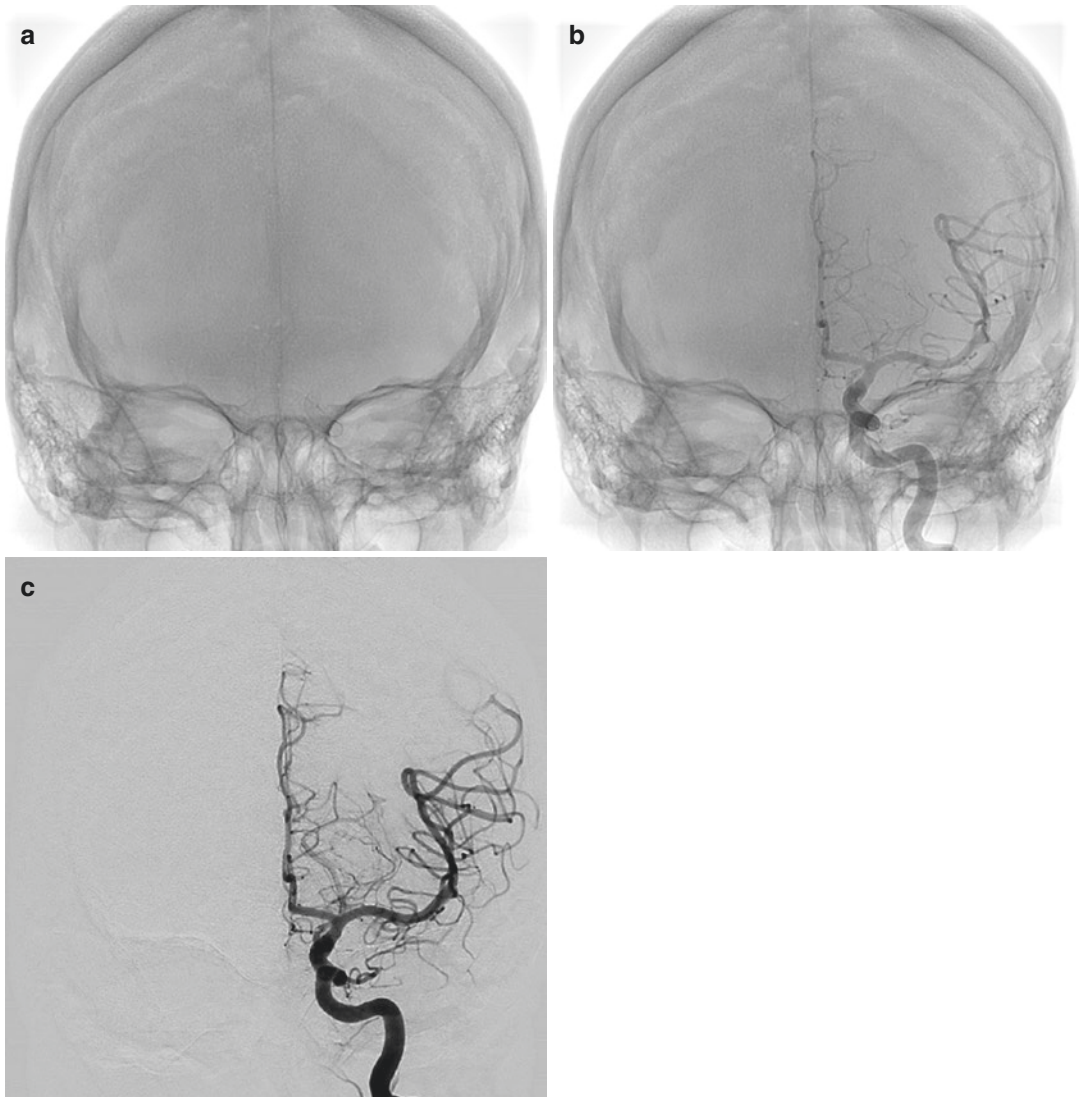


**Fig. 3.1** Digital subtraction angiography (DSA) illustrating (a) the precontrast mask image, i.e. anterior–posterior view of the cranium without contrast, (b) the unsubtracted

image showing contrast injection, and (c) the subtracted DSA image, giving high-resolution contrast imaging of the anterior circulation on the left side

Finally, the “mask” is subtracted from the second image on a pixel by pixel basis. This results in a subtracted image, on which only filled vessels are demonstrated. Recording can continue providing a sequence of subtracted images based on the original mask, documenting the flow of contrast dye from arteries, through the parenchyma, to the veins.

Certain interventional procedures may be operated with a monoplane angiography system (i.e., one spatial plane), whereas in interventional neuroradiology, the use of biplane systems has become widespread since the early 2000s. Biplane devices typically display two spatial orthogonal planes in real time simultaneously, most commonly a combined anterior–posterior and lateral view of the cranium. Advantages of this configuration include reduced ionizing radiation exposure and medical complications, as well as shortened procedure times [9]. Furthermore, significantly fewer contrast-agent injections are required; one injection for both planes.

DSA is also being used for more complex techniques such as rotational angiography [10]. With this technique images are acquired at angles covering 180°, by first taking mask images at

several angles for a rotational angle of the X-ray tube and intensifier around the patient. Subsequently, a post-contrast rotation acquisition is performed during which the contrast filled vessels are imaged. Finally, these images can be used for three-dimensional reconstruction of the vessels, which can be analyzed from any angle, called 3D rotational angiography (3DRA). The primary advantage of 3DRA is the ability to select an ideal imaging projection to view vessels and pathology that otherwise might be hidden behind adjacent vessels, essential when using DSA to treat neurovascular lesions (Fig. 3.2).

### 3.2 Clinical Applications

Currently, DSA is applied for a broad spectrum of indications in interventional neuroradiology, both for diagnostic and therapeutic purposes, for example, mechanical thrombectomy in acute stroke, coiling of intracranial aneurysms, and embolization of cerebrospinal arteriovenous shunting lesions.

In acute ischemic stroke patients, a large-vessel occlusion is routinely diagnosed using



**Fig. 3.2** DSA of the right anterior circulation (a) and left anterior circulation (b) after contrast injection to the internal carotid artery. Rotation angiography of the right side reveals a carotid cave aneurysm (c and d; arrow) located

at the right carotid siphon, pointing medially and inferiorly. This aneurysm is difficult to appreciate on the anterior–posterior projection (a). Note the configuration of the subtracted aneurysm clips and staples on both sides



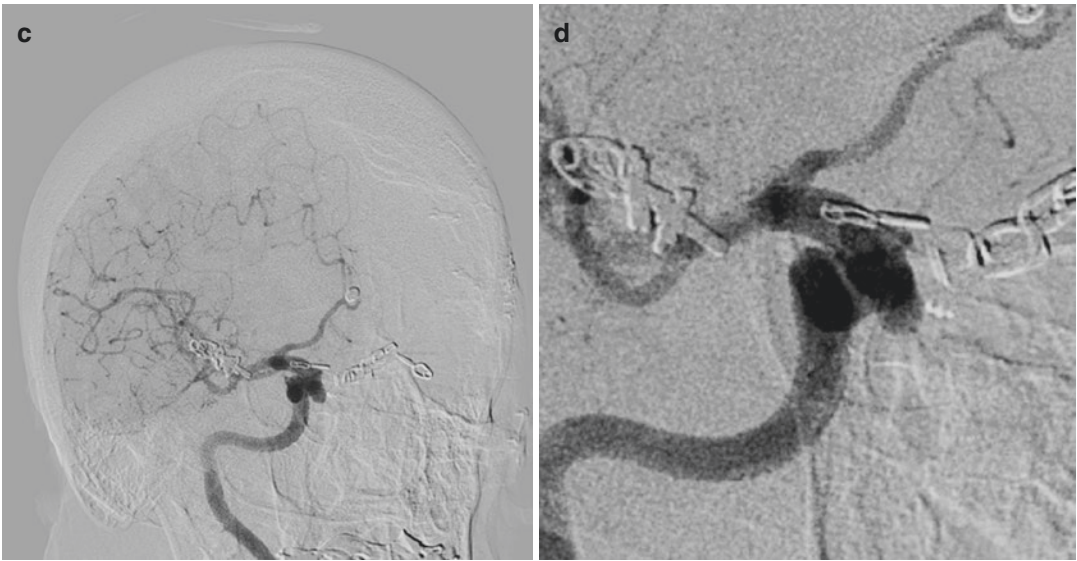


**Fig. 3.2** (continued)

CT-angiography images. If within the appropriate time frame (e.g., within 6 h after symptom onset) or meeting criteria on physiologic cerebral perfusion imaging, endovascular thrombectomy is recommended as standard of care [11]. Two techniques are generally accepted: (1) direct aspiration by advancing a large-bore catheter to the face of the thrombus, followed by its removal with aspiration alone or withdrawal of the catheter while aspirating or (2) stent-retriever thrombectomy that dislodges the clot using a removable stent. Both methods are associated with comparable final reperfusion rates and functional outcomes. Stent-retriever thrombectomy is found superior in achieving reperfusion as a stand-alone first-line technique, with lower use of rescue devices but a longer groin-to-reperfusion time [12]. In stroke treatment, DSA is used to identify the intra-arterial occlusion, maneuver the aspiration device or stent-retriever into position (i.e., against or at the site of the clot, respectively), and monitor the therapeutic result. In case of a difficult route to the intracranial circulation, a “road-map” may be used. This application provides the neuro-interventionalist the ability to view the subtracted image with the screening image superimposed to facilitate catheter manipulation [7].

A second major application of DSA concerns the treatment of intracranial aneurysms.

Indications for treatment include symptomatic aneurysms, after a rupture causing a subarachnoid hemorrhage or by neurovascular compression inducing a cranial nerve palsy, or incidental aneurysms with risk factors for rupture present related to size, location, and age [13, 14]. In case of a symptomatic aneurysm, very early (<1 day) aneurysm treatment is favored [15]. Both endovascular (such as coiling) and surgical (clipping) treatments aim to isolate the aneurysm from the blood circulation. With coiling, the most common endovascular treatment, the aim is to permanently occlude the aneurysm by densely packing the lumen with platinum coils. As with stroke treatment, access to the vessel is usually obtained through the femoral artery, into which a guiding catheter is inserted and navigated to the intracranial arteries using DSA. Through this guiding catheter, a small flexible microcatheter can be inserted and navigated into the aneurysm with the assistance of a microwire. Once the microcatheter is in the aneurysm, a coil is inserted into the aneurysm sac. Using different shapes and lengths of coils, dense packing of the aneurysm can be achieved [16].

Where conscious (moderate) sedation seems to favor outcome in treatment of acute ischemic stroke [17], general anesthesia is essential for endovascular treatment of aneurysms. Advantage

of the latter is a fixed stable position of the patient without unforeseen movement, minimizing artifacts during DSA and reducing the risk of motion-induced coil luxation or migration.

Risks related to cerebral angiography are temporary and permanent neurological deficits (0.5%) due to thromboembolic events, allergic cutaneous reactions (0.1%), and hematomas at the puncture site (0.4%). Age-related vascular disease appears to account for the majority of the neurologic complication rate. Renal failure as a consequence of angiography is uncommon [18].

### 3.3 Clinical Case

A 52-year-old female underwent investigations for pulsatile tinnitus that spontaneously improved. An MR angiogram revealed a dural arteriovenous fistula (DAVF) centered within the left transverse sinus (Fig. 3.3), for which the patient underwent catheter angiography and endovascular treatment. A 2D DSA of the left common carotid artery (Fig. 3.4) and combined 3DRA of the left internal and external carotid

arteries (Fig. 3.5) were performed. This confirmed a left transverse sinus DAVF with arterial supply from a transosseous branch of the left occipital artery. Spontaneous occlusion of the left internal jugular vein caused retrograde venous drainage of the left hemisphere via the contralateral dural venous system. No cortical venous reflux was demonstrated. The treatment strategy of this DAVF consisted of a combined transarterial and transvenous approach. First, a balloon was placed in the left proximal transverse sinus, via the contralateral internal jugular vein. Second, a microcatheter was advanced through to the distal left occipital artery DAVF feeder. By delivering three microcoils into the fistulous compartment, a “plug” was formed. After inflation of the balloon in the left proximal transverse sinus, complete embolization of the DAVF with Onyx could be achieved. Control angiogram showed complete occlusion of the fistula (Fig. 3.4), without thromboembolic or hemorrhagic complications. Follow-up MR angiogram after 10 weeks demonstrated no residual arteriovenous shunting into the left transverse sinus.

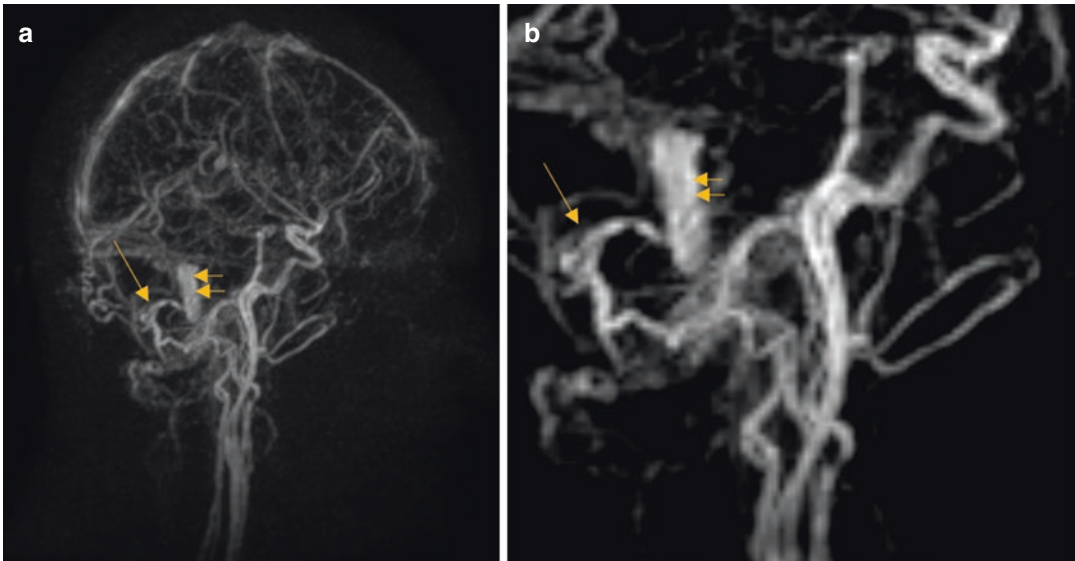


**Fig. 3.3** Dynamic MR angiography, the time-resolved imaging of contrast kinetics (TRICKS) sequence, demonstrates a left-sided dural arteriovenous fistula (DAVF) centered within the left transverse sinus (a, b). A transos-

seous branch (*large arrow*) of the occipital artery is suspected to be the major contributor to the dural shunt. The arterial phase reveals early filling of the transverse sinus (*small arrows*)

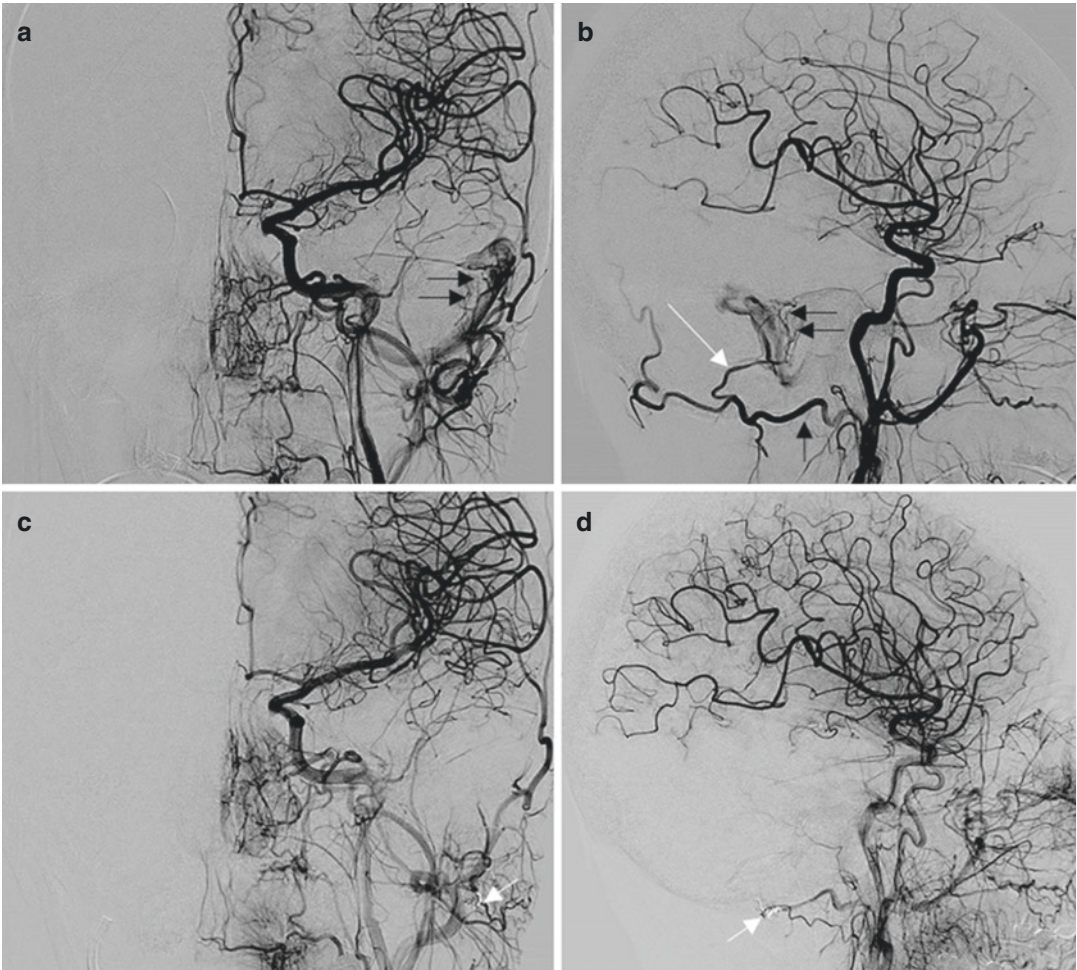


**Fig. 3.4** Left common carotid artery (CCA) angiogram in anterior–posterior (a) and lateral view (b) confirm main arterial supply from a transosseous branch (white arrow) of a hypertrophic occipital artery (small black arrow),

with early filling of the left transverse sinus (small black arrows). After embolization of the DAVF with microcoils and Onyx (small white arrow), a final control angiogram showed complete occlusion of the fistula (c and d)

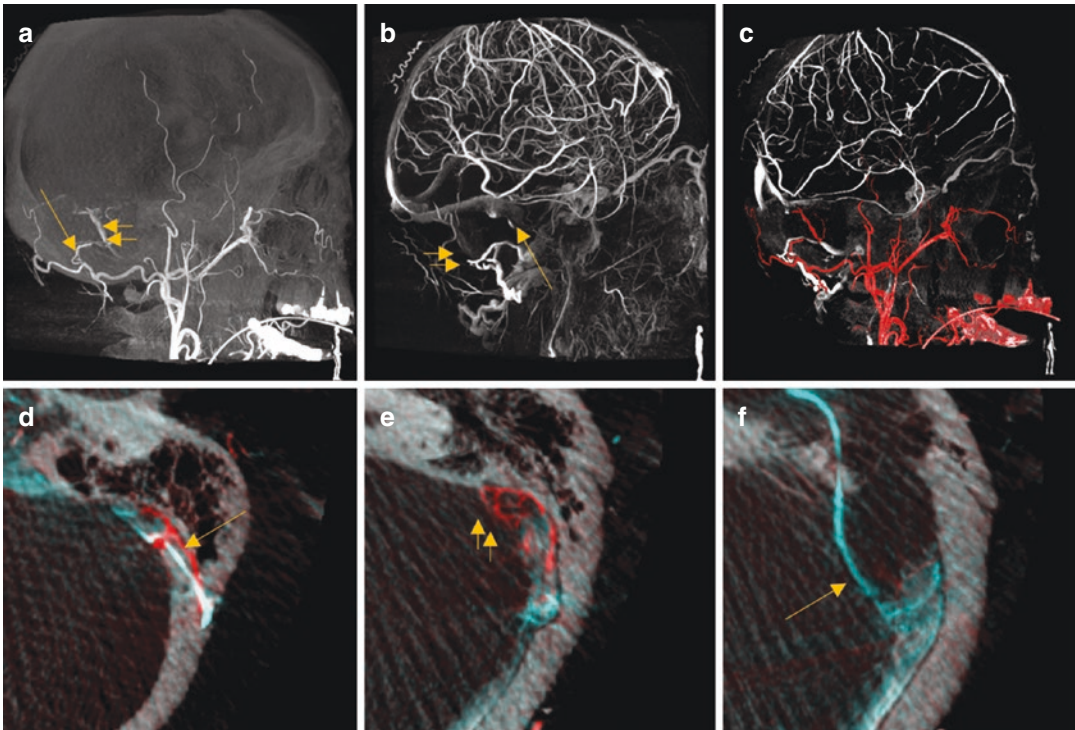


**Fig. 3.5** 3D rotational angiography (3DRA) of the left external carotid artery (ECA; **a**; *arterial phase*), left internal carotid artery (ICA; **b**; *venous phase*), and combined projection (**c**). The arterial phase demonstrates the transosseous branch (*arrow*) of the occipital artery with arterial filling of the left transverse sinus (*small arrows*). In the venous phase, occlusion of the left jugular bulb prohibits antegrade flow in the left transverse sinus (*arrow*), redirecting venous drainage of the left hemisphere via the

contralateral internal jugular vein (*small arrows*). Overlay of both 3DRAs on the angio-CT at three caudocranial levels (**d–f**) illustrate separate arterial flow from the ECA injection (in red) and venous drainage from the ICA injection (in blue). The transosseous arterial feeder (**d**; *arrow*) of the occipital artery and dural fistulous compartment (**e**; *small arrows*) can be identified at distance from a draining proximal cortical vein (**f**; *arrow*), ensuring a safety margin for endovascular treatment

## References

1. Ziedses Des Plantes BG. Subtraktion. eine röntgenographische Methode zur separaten Abbildung bestimmter Teile des Objekts. *Fortschritte auf dem Gebiete der Röntgenstrahlung*. 1935;52:69–79.
2. Seldinger SI. Catheter replacement of the needle in percutaneous arteriography; a new technique. *Acta Radiol*. 1953;39(5):368–76.
3. Ziedses Des Plantes BG. Use of subtraction in the radiography of the heart and the great blood vessels. *Ned Tijdschr Geneesk*. 1959;103:2554–61.
4. Djindjian R. Application to cerebral angiography of the subtraction method of Ziedses des Plantes. *Concours Med*. 1962;84:3839–45.
5. Kruger RA, Mistretta CA, Houk TL, Riederer SJ, Shaw CG, Goodsitt MM, et al. Computerized fluoroscopy in real time for noninvasive visualization of the cardiovascular system. *Prelim Stud Radiol*. 1979;130(1):49–57.
6. Meaney TF, Weinstein MA, Buonocore E, Pavlicek W, Borkowski GP, Gallagher JH, et al. Digital subtraction angiography of the human cardiovascular system. *AJR Am J Roentgenol*. 1980;135(6):1153–60.
7. Jeans WD. The development and use of digital subtraction angiography. *Br J Radiol*. 1990;63(747):161–8.
8. Allisy-Roberts PJ, Williams J. *Farr's physics for medical imaging*. Philadelphia, PA: Saunders Elsevier; 2008.
9. Bellemare CA, Poder TG. Effectiveness of biplane angiography compared to monoplane angiography for vascular neuro-interventions: a systematic review of the literature. *Clin Radiol*. 2017;72(7):612.e1–5.
10. Hoff DJ, Wallace MC, terBrugge KG, Gentili F. Rotational angiography assessment of cerebral aneurysms. *AJNR Am J Neuroradiol*. 1994;15(10):1945–8.

11. Powers WJ, Rabinstein AA, Ackerson T, Adeoye OM, Bambakidis NC, Becker K, et al. 2018 guidelines for the early management of patients with acute ischemic stroke: a guideline for health-care professionals from the American Heart Association/American Stroke Association. *Stroke*. 2018;49(3):e46–e110.
12. Tsang COA, Cheung IHW, Lau KK, Brinjikji W, Kallmes DF, Krings T. Outcomes of stent retriever versus aspiration-first thrombectomy in ischemic stroke: a systematic review and meta-analysis. *AJNR Am J Neuroradiol*. 2018;39:2070.
13. Brinjikji W, Pereira VM, Khumtong R, Kostensky A, Tymianski M, Krings T, et al. PHASES and ELAPSS scores are associated with aneurysm growth: a study of 431 unruptured intracranial aneurysms. *World Neurosurg*. 2018;114:e425–e32.
14. Greving JP, Wermer MJ, Brown RD Jr, Morita A, Juvola S, Yonekura M, et al. Development of the PHASES score for prediction of risk of rupture of intracranial aneurysms: a pooled analysis of six prospective cohort studies. *Lancet Neurol*. 2014;13(1):59–66.
15. Rawal S, Alcaide-Leon P, Macdonald RL, Rinkel GJ, Victor JC, Krings T, et al. Meta-analysis of timing of endovascular aneurysm treatment in subarachnoid haemorrhage: inconsistent results of early treatment within 1 day. *J Neurol Neurosurg Psychiatry*. 2017;88(3):241–8.
16. Krings T, Mandell DM, Kiehl TR, Geibprasert S, Tymianski M, Alvarez H, et al. Intracranial aneurysms: from vessel wall pathology to therapeutic approach. *Nat Rev Neurol*. 2011;7(10):547–59.
17. Wijayatilake DS, Ratnayake G, Ragavan D, Anaesthesia for neuroradiology: thrombectomy: ‘one small step for man, one giant leap for anaesthesia’. *Curr Opin Anaesthesiol*. 2016;29(5):568–75.
18. Willinsky RA, Taylor SM, TerBrugge K, Farb RI, Tomlinson G, Montanera W. Neurologic complications of cerebral angiography: prospective analysis of 2,899 procedures and review of the literature. *Radiology*. 2003;227(2):522–8.



# Basics of Computed Tomography

# 4

Manoj Mannil and Natalia Saltybaeva

## Contents

4.1	<b>A Brief History of Computed Tomography</b> .....	31
4.1.1	Spiral CT .....	32
4.1.2	Dual-Energy CT .....	32
4.2	<b>Basic Principles</b> .....	33
4.2.1	CT Detectors .....	33
4.2.2	Flat Panel Detector CT .....	33
4.2.3	Image Reconstruction .....	34
4.2.4	Image (Post-)Processing .....	35
4.2.5	CT Artefacts .....	36
4.3	<b>Radiation Dose in CT</b> .....	37
4.3.1	Dose Metrics .....	38
4.3.2	Technical Parameters Influencing the Dose in CT .....	39
4.3.3	Non-Technical Parameters Influencing the Dose in CT .....	41
4.3.4	Dose Reduction Techniques .....	41
	<b>References</b> .....	43

## 4.1 A Brief History of Computed Tomography

Computed tomography (CT) is based on ionizing electromagnetic radiation known as X-rays. Wilhelm Röntgen, a German physics professor, discovered them in 1895 and quickly realized its

potential for medical imaging. The mathematical foundation for modern-day CT is the *Radon transform*, an integral transform used for the generation of tomographic images from X-ray attenuation images. Johann Radon, an Austrian mathematician, first published this concept in 1917. Five decades later, the first patient scan of the Neurocranium was obtained at Atkinson Morley's Hospital, London, UK. The first-generation CT scanner was produced by EMI, a record company, which led a research division (EMI Central Research Laboratories) in Hayes, UK. The first commercial CT scanner used a translate and rotate method, in which a focused X-ray beam and the detector moved laterally to

---

M. Mannil  
University Clinic for Radiology, University Hospital  
Münster, Münster, Germany  
e-mail: [Manoj.Mannil@ukmuenster.de](mailto:Manoj.Mannil@ukmuenster.de)

N. Saltybaeva (✉)  
Institute of Diagnostic and Interventional Radiology,  
University of Zurich, Zurich, Switzerland  
e-mail: [Natalia.Saltybaeva@usz.ch](mailto:Natalia.Saltybaeva@usz.ch)

**Table 4.1** Evolution of CT scanners

Scanner generation	Detectors ( <i>n</i> )	X-ray beam	Average scan duration
First	1	Pencil beam	25–30 min
Second	30	Fan shaped	<90 s
Third	288–700	Fan shaped	5 s
Fourth	>2000	Fan shaped	<4 s

cover the whole region of interest. Afterwards, the gantry rotated by approximately  $1^\circ$  and the process was repeated. In order to obtain a single axial slice of the brain, this procedure was repeated 180 times ( $180^\circ$ ). Using this method, a single axial slice of the brain took approximately 5 min to obtain. Second-generation CT scanners, introduced in 1972, used a small X-ray fan beam and up to 30 detectors. As a result, image acquisition was substantially faster, and an entire scan of the neurocranium took about 90 s using the same translate and rotate method (Table 4.1).

The hallmark of third-generation CT scanner systems was a full X-ray fan beam that covered the complete field of view and a simultaneously rotating tube and detector array introduced in 1975. A similar architecture is still used in current generation CT systems. Sir Godfrey Hounsfield and Alan MacLeod Cormack independently contributed to the invention of CT and were jointly awarded the Nobel Prize in Medicine in 1979. In fourth-generation systems, detectors were removed from the rotating gantry and put in a stationary ring outside the gantry bore. With a full 360-degree detector ring and a rotating X-ray tube ring, artefacts could be avoided. However, the use of detectors was less efficient as less than one-fourth are used at any point during scanning. These scanners are also more susceptible to scatter artefacts than third-generation types, since they cannot use anti-scatter grid. As a result, fourth-generation CT scanners were widely replaced by further developments in third-generation-type CT systems. In 1987, novel slip-ring technology enabled continuously rotating systems with a gantry rotation time of approxi-

mately 1 s. Slip-rings are electromechanical devices consisting of circular electrical conductive rings and brushes that transmit electrical energy across a moving interface. All power and control signals from the stationary parts of the scanner system are communicated to the rotating frame through the slip-ring [1].

#### 4.1.1 Spiral CT

The currently used spiral (or helical) mode of image acquisition was introduced in 1989, enabling true 3D image acquisition within a single breath hold. This technique involves the continuous acquisition of projection data through a 3D volume by continuous rotation of the X-ray tube and detectors and simultaneous translation of the patient through the gantry opening. Three technological developments were required: slip-ring gantry designs, interpolation algorithms to handle the non-coplanar projection data and high-power X-ray tubes. These tubes used oil-cooled rotating anodes for efficient thermal dissipation. Heat storage capacities varied from 1 to 3 million heat units in early third-generation CT scanners. Extreme heat capacities in modern X-ray tubes are achieved, among other factors, by use of thick graphite backing of target disks, anode diameters of 200 mm or more, improved high-temperature rotor bearings, and metal housings with ceramic insulators [1–3].

#### 4.1.2 Dual-Energy CT

In dual-energy CT (DECT), a second attenuation measurement is obtained, allowing the differentiation of the two materials. Alternatively, this allows quantification of mass density of two or three materials in a mixture with known elemental composition (Fig. 4.1) [4]. Depending on the vendor, DECT can be implemented by using, for example rapid tube potential switching technique, multilayer detectors or dual X-ray sources. More information on DECT is provided in chapter Dual-Energy CT.

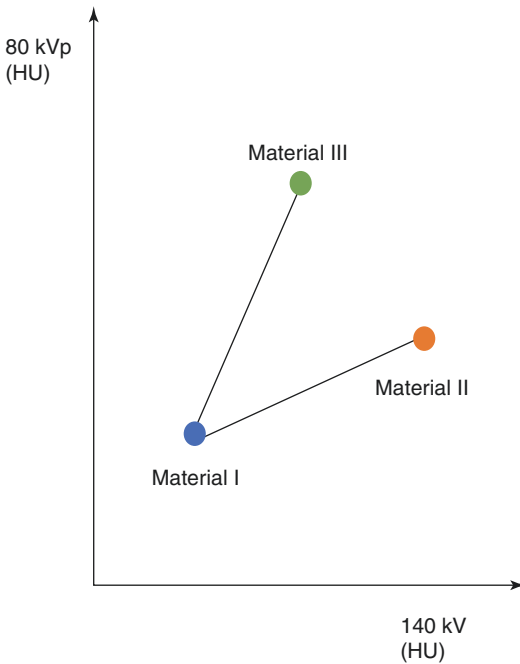


**Fig. 4.1** CT numbers of three different materials in high- and low-energy conditions, respectively. Unknown materials are then mapped onto this plot to determine the percentage composition of each of the three basis materials

## 4.2 Basic Principles

### 4.2.1 CT Detectors

Standard CT detectors are indirect energy converters, in which the X-ray energy is first converted into visible light and then detected by a photodiode and converted into electric current. Indirectly converting detectors in clinical CT systems are usually based on gadolinium oxysulfide ( $Gd_2O_2S$ ) ceramic scintillators, which have the advantage of high-dose efficiency, low cross-talk and low afterglow. Recent developments have further optimized electronic noise, intrinsic to the detector. Electronic noise adds to the X-ray quantum noise. While quantum noise cannot be altered much, by reducing the distance between the photodiode and the analogue-to-digital converter electronics, electronic noise can be minimized. For this reason, more compact electronics are installed close to the detector pixels, which

require less analogue wiring. Silicon vias contacting technology can reduce the analogue distance to millimetres [1, 5]. Further developments in CT detector technology have led to photon-counting detectors (see Chap. 8).

### 4.2.2 Flat Panel Detector CT

#### 4.2.2.1 Flat Panel Detector

A flat panel detector (FD) consists of a film of caesium iodide scintillator crystals that is cast onto a matrix of photographic detectors made of amorphous silicon. The scintillator converts the X-ray energy into light. The needle-shaped caesium iodide crystals act as fibreoptic channels and guide the light to the photodiodes to be converted into an electrical charge. The close interface between the caesium iodide crystals and the photosensitive diodes preserves the high-fidelity transfer of the projection data from photon energy to digitized signals. Because of the size of the matrix and the unique flat-panel design, flat-panel volume CT yields ultra-high isotropic spatial resolution compared to conventional multidetector CT [6].

#### 4.2.2.2 Flat Panel Detector Computed Tomography

Incorporation of the above-mentioned detector technology in CT scanners led to FDCT. These provide higher spatial resolution but have inherent disadvantages, ranging from lower dose efficiency, smaller field of view to lower temporal resolution compared to conventional CT scanner systems. However, dedicated CT scanners have emerged for imaging of the maxillo-facial and temporal bone region and micro-CT research applications [7]. Furthermore, FD-CT shows less artefacts from metal implants with potential benefits in dental imaging or follow-up examinations of temporal bone after cochlea implant surgery [8].

#### 4.2.2.3 C-Arm-Based Flat Panel Detector Computed Tomography

Combining FD with C-arm angiography systems allows for angiographic or C-arm-based FDCT

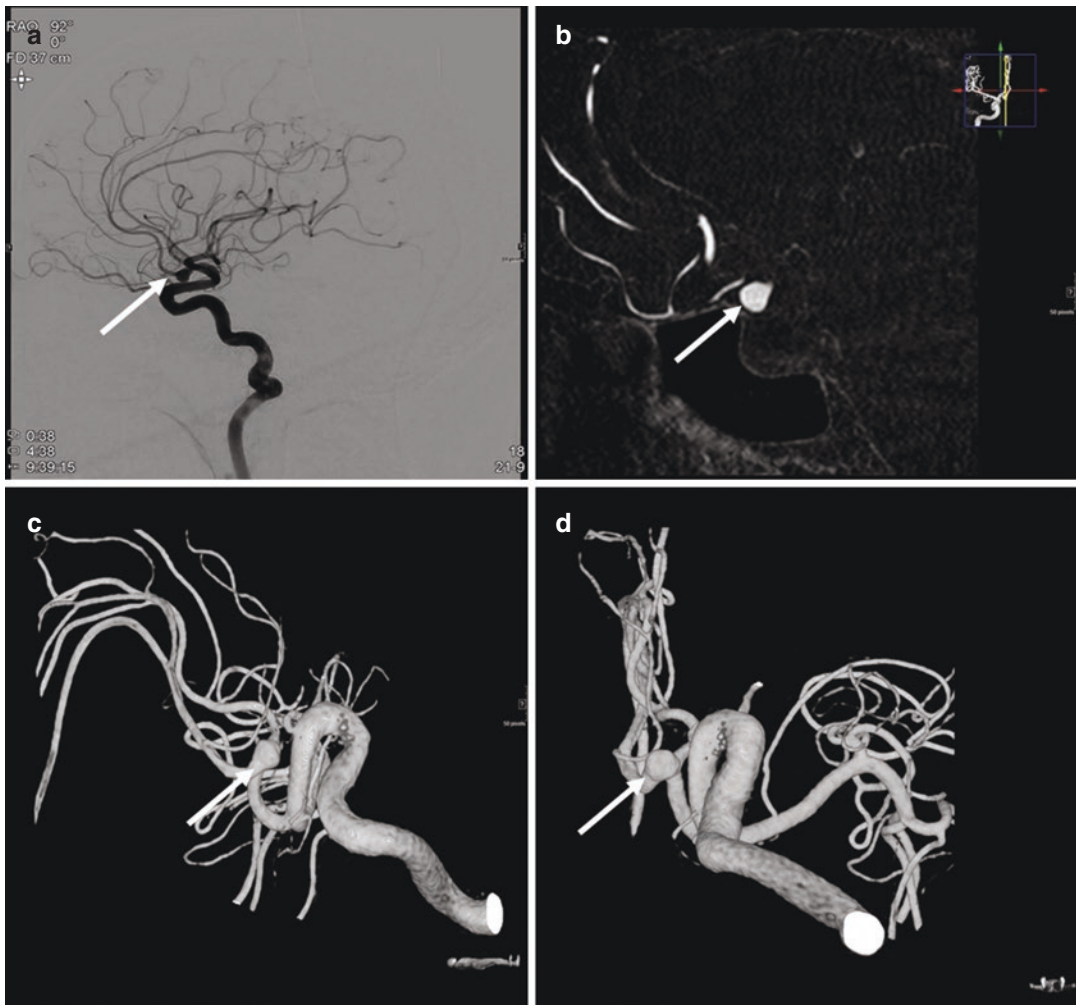


image acquisition. Apart from their advanced fluoroscopic capabilities, they offer a greater flexibility in orientation around the patient. However, they usually are less mechanically stable, have geometric inaccuracies, a less sharply defined isocentre and therefore an overall compromised spatial resolution compared to traditional CT scanners [6]. Nevertheless, angiographic FDCT is widely used during various neurointerventional procedures, ranging from treatment of aneurysms to arteriovenous malformations (Fig. 4.2). Due to its inherently high spatial resolution, it allows for imaging of

stent struts while also providing morphologic images of the brain within the angiography suite. For this reason, periprocedural complications such as an intracranial haemorrhage may be detected more quickly [7].

### 4.2.3 Image Reconstruction

Different algorithms can be used to reconstruct the images from the raw data acquired by a CT system. The primary technique for image reconstruction in CT is called Filtered back projection



**Fig. 4.2** 58-year-old male patient with incidental berry aneurysm (GGF arrows) of the anterior communicating artery. (a) Source images of cerebral angiography. (b)

C-arm-based FD-CT in sagittal plane. (c, d) Intraoperative 3D reconstructions acquired during the procedure

(FBP). It was used since the introduction of CT in the early 1970s and is still in use. Although FBP method is very fast and robust, it is prone to streak artefacts, high noise and poor low contrast detectability, especially at lower doses. FBP is a so-called analytical image reconstruction algorithm, an inversion formula for a simplified measurement model. X-rays are collected in sets, called projections, which are made across the patient in a particular direction in the section plane. There may be thousands of photons in a single projection. To reconstruct the image from the ray measurements, each voxel must be viewed from multiple different directions. A complete data set requires many projections at rotational intervals of  $1^\circ$  or less around the cross section. Back-projection effectively reverses the attenuation process by adding the attenuation value of each ray in each projection back through the reconstruction matrix. As this process generates a blurred image, the data from each projection are mathematically filtered prior to back-projection, eliminating the intrinsic blurring effect. FBP has desirable properties such as linearity and translational invariance that make image quality easily understandable. However, FBP cannot optimally account for a number of physical effects, such as the photon statistics, beam polychromaticity, or finite width X-ray beams. To account for the photon statistics empirical sinogram restoration approaches, so-called adaptive filters have been developed. With the introduction of multirow detector CT, the efficiency of such adaptive filtering improved tremendously owing to the possibility of filtering across detector rows or even across projections [1, 9].

Other reconstruction algorithms are more sophisticated and allow for significant noise reduction. The reconstruction algorithm based on the use of maximum likelihood is called iterative technique or iterative reconstruction (IR). The newest model-based IR starts with an initial guess of the object and iteratively improves the initial estimate of the attenuation value by comparing the theoretical projection data with the acquired one to make an incremental change to the previous guess.

This iterative estimation requires a series of iterations. Every iteration step consists of a for-

ward projection, followed by a comparison of the forward-projected data with the measured raw data and a back projection. The first iterative image reconstruction algorithms that became available commercially were adaptive statistical iterative reconstruction (ASIR, General Electric), adaptive iterative dose reduction (AIDR/ADIR 3D, Toshiba), iterative reconstruction in image space (IRIS, Siemens Healthineers), and iDose (Philips). These post-processing algorithms represent so-called edge-preserving filters, which reduce preserve spatial resolution at edges and perform noise reduction in homogeneous regions. This approach is computationally demanding, but it serves for significant decrease in image noise comparing to FBP technique [1, 10].

## 4.2.4 Image (Post-)Processing

### 4.2.4.1 Maximum- and Minimum-Intensity Projections

In the maximum-intensity projection method, only the relative maximum value detected along each ray path is retained by the computer. This method tends to display bone and contrast material-filled structures preferentially, and other lower attenuation structures are not well visualized. Similarly, minimum-intensity projection involves detecting the minimum value along the ray paths in each view. Both methods can add different and important information to the original axial sequences [11].

### 4.2.4.2 Volume Rendering

In volume rendering, the CT numbers that makeup the image are assigned to be either visible or invisible, to be displayed with varying colours and often to be displayed with varying opacity levels (transparency). The assignment of these characteristics to the voxels can be defined for specific imaging protocols and organ systems [11].

### 4.2.4.3 Cinematic Rendering

Cinematic rendering (CR) generates realistic depictions of human anatomy by using random sampling of computational algorithms combined with different light maps. CR integrates light scattered from any directions along a ray to solve

the multidimensional and non-continuous rendering equation. Randomized subset of light paths with an adequate distribution is generated by use of Monte-Carlo simulations. By iteratively averaging multiple Monte Carlo samples, which represent radiance at random positions with light scattered in random directions, a CR image is obtained. Combined with high dynamic range (HDR) rendering used for light maps, a natural illumination of the rendered data is achieved [12].

## 4.2.5 CT Artefacts

CT artefacts may degrade the image quality and thus negatively impact the diagnostic information. The term is applied to any systematic discrepancy between the CT numbers and the true attenuation coefficients of the object. The most common sources of artefacts are mentioned below.

### 4.2.5.1 Patient Motion

The most often occurring and most detrimental form of CT artefacts can be observed in case of patient movements during scanning. The result-

ing misregistration artefacts appear as shading or streaking (Fig. 4.3).

### 4.2.5.2 Metal Artefacts

The presence of metal objects in the field of view may lead to streaking artefacts. They occur as the density of the metal is beyond the range of normal attenuation, resulting in incomplete attenuation profiles (Fig. 4.4).

### 4.2.5.3 Beam Hardening

Individual photons with a range of energies compose an X-ray beam. As the beam traverses through any object, it becomes “harder,” as the higher energy photons are absorbed more slowly than the low-energy photons. Two artefacts may result from beam hardening: Cupping artefacts and the appearance of dark bands with streaks between dense objects in the image. On a side note, Cupping artefacts can be counteracted by the use of bow-tie filter.

### 4.2.5.4 Partial Volume

*Partial volume artefacts occur when a dense object is located off-centre and protrudes into the slice in one projection but not in the opposing projection. This causes the object to appear*

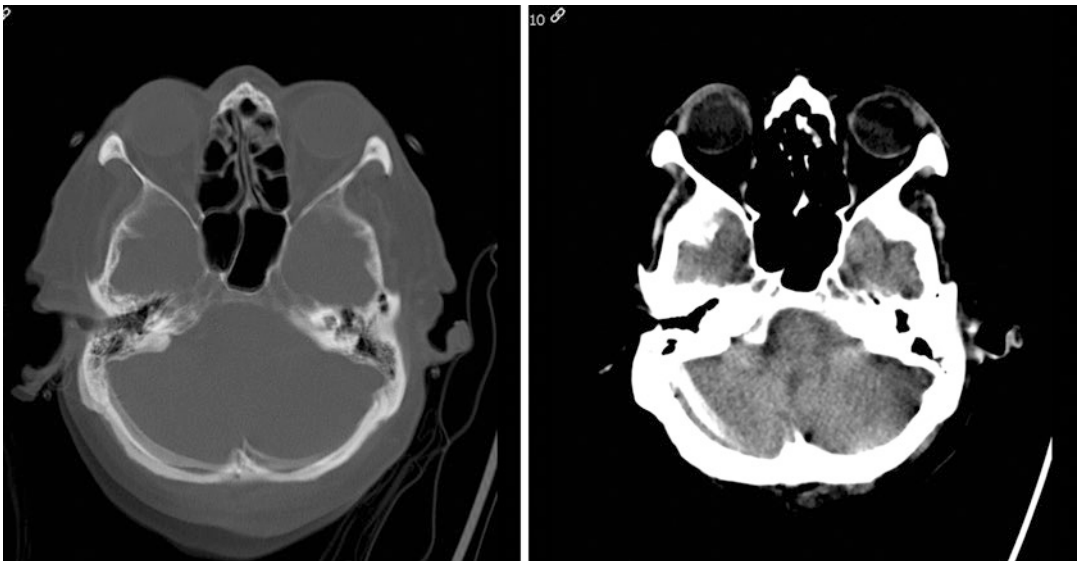


**Fig. 4.3** Patient motion in bone (left) and soft tissue (right) window. The patient motion may mimic an infratentorial subdural hematoma

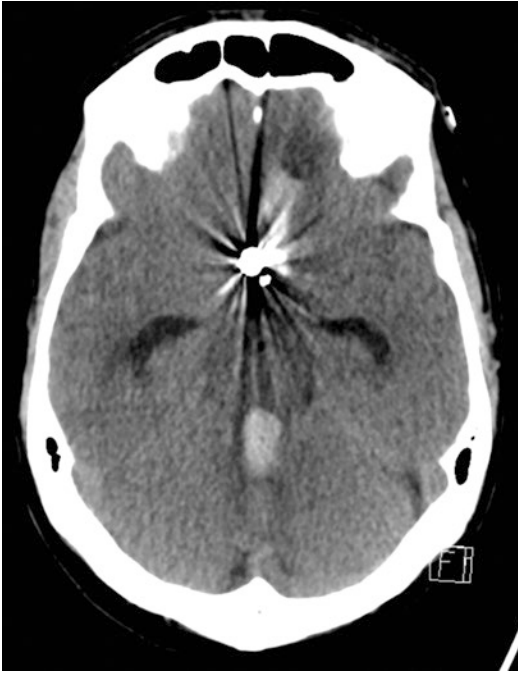


**Fig. 4.4** Example of extensive metal artefacts due to an aneurysm coiling of the communicating anterior artery. Note the star-burst appearance

*streaked due to the inconsistencies produced during imaging.* Partial volume artefacts can best be avoided by using a thin acquisition section width. Note that partial volume artefacts should not be confused with partial volume averaging effects, which occur when tissues of widely different absorption rates are included in the same voxel, producing a beam attenuation proportional to the average value of their densities.

#### 4.2.5.5 Photon Starvation

Photon starvation occurs in highly attenuating areas such as the temporal bones. When the X-ray beam is traveling horizontally through both temporal bones, the attenuation is greatest and too few photons reach the detectors, resulting in very low signal and thus noisy images. The reconstruction process has the effect of greatly magnifying the noise, resulting in horizontal streaks in the image. Photon starvation can be overcome by increasing the tube current. To avoid unnecessarily high doses when the beam is passing through less attenuating parts, manufacturers have imple-

mented technologies such as automatic tube current modulation.

#### 4.2.5.6 Undersampling

A large interval between projections used to reconstruct a CT image is called *undersampling*. It may result in misregistration of information relating to sharp edges and small objects. This leads to an effect known as *view aliasing*, in which fine stripes appear radiating with a small distance from the edge of a dense structure. Stripes appearing close to the structure are likely to be caused by undersampling within a projection, which is known as *ray aliasing*.

#### 4.2.5.7 Ring Artefacts

If a single detector in a third-generation CT scanner system is out of calibration, it will give a consistently erroneous reading at each angular position. This results in a circular artefact. When central detectors are affected, a smudge-like stain is visible in the centre of the acquired images [13].

## 4.3 Radiation Dose in CT

Despite substantial clinical benefits, computed tomography is usually associated with «high-dose» radiological procedures, comparing, for example, to conventional radiography. While CT examinations make up a relatively low percentage of all radiological procedures, their contribution to the total population dose is considerably high. Meanwhile, the radiation exposure from single CT procedure might vary a lot depending on the specific procedure and clinical indications. In case of low-dose CT procedures, such as lung cancer screening, for example, CT contributes in few submillisieverts effective dose, while, for instance, multi-phases brain perfusion would result in up to a hundred of millisievert. Interestingly, the great majority of patient exposure nowadays arises from practices that barely existed even two decades ago.

With the introduction of faster scan techniques and improved software and hardware technologies the number of CT examinations has been growing rapidly. As a consequence, radiation dose from CT

became a subject of concern to radiologists, referring physicians and patients. Organizations such as the International Atomic Energy Agency, the European Society of Radiology and International Commission on Radiological Protection (ICRP) have recommended dose tracking for individual patients as well as the possible dose reduction and optimization. The most common CT metrics which are used for radiation dose assessment and recommended to be tracked are computed tomography dose index (CTDI) and dose-length product (DLP).

### 4.3.1 Dose Metrics

#### 4.3.1.1 CTDI

CTDI was first introduced by Shope et al. in 1981 as a metric to quantify the radiation output from a CT examination consisting of multiple contiguous CT scans. This new dosimetric method was required because the irradiation geometry of the CT scan was quite different from other X-ray modalities that were in use at the time. Unlike conventional radiography, where the dose is determined by the impact of a single projection and can be well described by the exponential function, the dose in CT represents the sum of all projections, resulting in non-uniform dose distribution with a difference of about 20–40% between the surface and the centre of the irradiated object, so the overall dose needs to be estimated based on measurements in several points. These measurements are usually performed using a 100-mm-long ionization chamber inserted in the centre and periphery of the CTDI phantom, a cylinder made of polymethylmethacrylate (PMMA) with a diameter of 16 and 32 cm for average head and body, respectively. When the measurements are performed the CTDI weighted ( $CTDI_w$ ) is calculated as follows:

$$CTDI_w = \frac{1}{3}CTDI_{center} + \frac{2}{3}CTDI_{periphery}$$

The SI units of  $CTDI_w$  are milligray (mGy).

To represent the dose for a specific scan protocol, which generally includes several rotations

and potentially a pitch factor different from 1 it is essential to take all gaps or overlaps of the X-ray beam from these consecutive rotations into account. This is accomplished by a dose descriptor known as the volume CTDI or  $CTDI_{vol}$ . This  $CTDI_{vol}$  can be expressed as:

$$CTDI_{vol} = \frac{CTDI_w}{Pitch}$$

The  $CTDI_{vol}$  provides a single CT dose metric, which can be directly measured and represents the average dose within the scan volume for a standard phantom. It can be used to compare different CT protocols on a single CT scanner or as a metric to compare protocols across different scanners.

#### 4.3.1.2 Dose-Length Product

Another common metric for dose assessment in CT is dose-length product (DLP), which reflects the total energy deposited into the entire scan volume.

$$DLP = CTDI_{vol} \times \text{Scan length}$$

It is important to say that although both  $CTDI_{vol}$  and DLP values are included in patient radiation dose report, they represent the scanner-specific radiation output but not the radiation dose received by a particular patient.

#### 4.3.1.3 Effective Dose

The concept of effective dose was developed by Wolfgang Jacobi in the middle of the 1970s and was incorporated into ICRP Publication 26. Effective dose ( $E$ ) reflects the differences in biological tissue sensitivity to ionizing radiation and thus can be used for risk evaluation. By definition, effective dose is a weighted sum of measured organ dose values

$$E = \sum_{T,R} W_T \times W_R \times D_{T,R}$$

where dose-weighting factors  $W_R$  and  $W_T$  account for different types of radiation (equal to one for X-ray and gamma-ray) and different irradiated tissue types (e.g. for lungs  $W_T = 0.12$ ), respectively, and  $D_{T,R}$  is an average absorbed dose to tissue  $T$ . ICRP defines the weighting factors for 30 organs and tissues.

There are two common approaches to calculate effective dose: The first is based on Monte Carlo methods, and the second was developed as a simplified method for quick effective dose estimation using the dose-length product (DLP) and sets of age- and body region-specific conversion coefficients ( $k$ ).

Monte Carlo simulations are usually performed on virtual anthropomorphic models and assume precise modelling of the CT system, including the source location and scanner geometry. The Monte Carlo methods were extensively investigated by several groups and are currently considered to be a gold standard for dose assessment in diagnostic imaging due to its capacity to accurately describe the physical interactions between radiation and matter. However, this approach requires significant computational resources, specialized software, and skilled staff.

The approach based on the conversion factors ( $k$ ), on the other hand, is much more lightweight and is commonly used for effective dose assessment in clinical practice. In Europe, respective  $k$ -factors have been first tabulated and published for several scanned body regions: head, neck, chest, abdomen and pelvis. The original values did not account for different age and gender. Later the set of the coefficients was extended by Deak et al. in order to include adult and paediatric patients of different genders following the recommendations of ICRP publication 103. A recent study performed by Saltybaeva et al. additionally provided conversion factors for the lower extremities [14]. By means of  $k$ -factors effective dose can be estimated for arbitrary CT examination as follows:

$$E = \text{DLP} \times k \left( \text{in } \frac{\text{mSv}}{\text{mGy} \times \text{cm}} \right).$$

The effective doses values calculated for standard CT examinations typically vary between 1 and 20 mSv. Modern CT allows very high-quality imaging with effective dose values in the low mSv or even sub-mSv range. This metric can be used for a comparison between different CT examinations as well as between different diagnostic modalities (conventional radiography, CT, etc.). It also facilitates communication with

patients regarding potential risk from a radiological examination. However, it is important to notice here, that effective dose is not intended to describe the radiation dose received by particular individuals.

### 4.3.2 Technical Parameters Influencing the Dose in CT

Radiation dose as well as image quality depends on several parameters which can be selected by the clinician. The main factors that contribute to radiation dose are the duration of the scan and the selected X-ray spectrum. The effect of the latter can be very complex, but the three main defining factors are tube voltage (kV), tube current (mA) and filtration.

#### 4.3.2.1 Tube Current

The relationship between tube current and radiation dose is linear, that is doubling the tube current increases the radiation dose twofold. In diagnostic imaging, it is quite common to describe the intensity of the X-ray beam in terms of *tube current-time product* measured in milliamperes-second, or mAs, which represents the tube current (in milliamperes) multiplied by the CT scanner exposure time per rotation (in seconds). Modern CT scans are performed with the rotation time of about 0.3–0.5 s per rotation, with the fastest rotation time of about 0.27 s. Note that this definition assumes a constant tube current throughout the examination, which is rarely used in practice—modern techniques such as tube current modulation (TCM) automatically adjust the mAs based on the patient attenuation, significantly reducing the overall dose.

It should be also stated that the decrease in mAs results not only in radiation dose reduction but also can negatively influence the image quality due to fewer photons on the detector and thus increased noise.

#### 4.3.2.2 Tube Voltage

Tube voltage (kVp) refers to the peak energy of the photons in X-ray spectra. Meanwhile, the average energy of the beam is usually much

lower. Unlike tube current, the relationship between kilovoltage and dose is nonlinear. For instance, when the kVp is decreased from 140 to 120 kVp (14%), the radiation dose is reduced approximately by 35%. Despite this strong effect of tube voltage on dose, these values in CT usually remain in a range of 80–140 kVp. Lower kVp values appeared impractical, at least for the adult patients, because they entail higher power demands, while the values above 160 kVp result in undesired reduction in contrast and the high radiation dose to the patient. Current CT technology does not allow the tube voltage to be modulated during a CT scan; however, the kVp still can be optimized based on the patient size and specific clinical indication.

#### 4.3.2.3 Pitch

Pitch is defined as a ratio of table feed per rotation to the total slice collimation.

$$\text{Pitch} = \text{Table feed (mm)} / NT,$$

where  $N$  is number of detector rows and  $T$  slice collimation in mm. Pitch factor plays a significant role in improving spatial resolution but at the same time has a dramatic effect on the radiation dose. In general, radiation dose is inversely proportional to the pitch and high pitch values allow for substantial dose reduction and lower acquisition time. Despite these benefits, pitch values in spiral CT cannot be arbitrarily increased, since gapless data sampling along the  $z$ -axis has to be ensured. Therefore, typical pitch value used in single-source CT examinations should not exceed the value of 1.5. Cardiac imaging requires the pitch to be as low as 0.2–0.4 in order to guarantee high spatial and temporal resolution and reduce potential motion artefacts. This results in beam overlapping and respective increase in radiation dose of up to 5 $\times$  compared to a pitch 1. To overcome this disadvantage, the dual-source spiral CT with pitch of up to 3.2 and 75 ms temporal resolution was introduced recently and has already demonstrated significantly lower doses than other existing methods in cardiac CT. It also should be taken into account that in some CT systems (Siemens, Philips) the variation in pitch is automatically compensated by the changes in

tube current to maintain the same image quality, so pitch does not directly affect the radiation dose.

#### 4.3.2.4 Filtration

X-ray beam filtration is an important consideration for the dose efficiency of the CT system. The filter represents a physical object that partly attenuates photons so that the lower energy component is removed from the spectra and the X-ray beam gets harder. It allows for more efficient penetration of the remaining photons through the patient's body and lower dose, while still providing sufficient contrast information.

Since the cross section of a patient has an approximately oval shape, the attenuation on the periphery of the beam is less than in the central projection. In order to keep the intensity of the attenuated beam constant and also to minimize the patient's surface dose, a bow-tie filter has been introduced by several CT manufacturers (Fig. 4.5). Depending on the clinical application the system can select one or a combination of several different filter sizes. Usually, the large/wide bow-tie filter is used for performing adult body CT scan, while the small/narrow one is used for head CTs, paediatric and cardiac examinations.

Another type of filtration used in CT is the selective photon shield usually made of high-attenuating material such as tin. The tin filter was

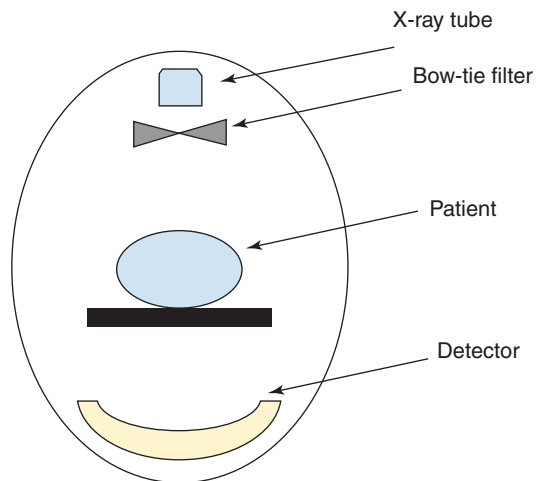


**Fig. 4.5** Schematic representation of a bow-tie filter in CT system

initially introduced by the vendors for dual-energy CT in order to minimize the spectral overlap when the two tubes are operated at different tube potentials. Recent studies have demonstrated potential for radiation dose reduction when selective photon shield is used in single energy mode [15, 16]. The tin filter cuts out low-energy beam component that does not contribute to the image quality, but only to the patient dose, allowing for significant dose reduction in non-contrast-enhanced CT scans. This has direct benefits in lungs or colon imaging. Recent clinical experience has also shown that tin filter allows for beam hardening artefacts reduction in bony structures, making it also useful in orthopaedic or head and neck CTs.

### 4.3.3 Non-Technical Parameters Influencing the Dose in CT

Apart from technical parameters such as kVp or mAs, the dose is significantly affected by other factors, several of which are controlled by the technologist performing the CT examination.

#### 4.3.3.1 Patient Positioning

Although this may seem to be of only minimal importance, improper positioning can have a significant impact on both image noise and radiation dose received by the patient.

It can be explained by the fact that patient size in CT localizers varies with localizer type and patient positioning in the CT gantry. When, for example, the patient is positioned too close to the X-ray source, the patient size is overestimated on the localizer radiograph (LR) image due to a magnification, resulting in higher tube current values applied by the TCM system. In contrast, when patients are placed further away from the X-ray source the LR image becomes smaller and patient size is underestimated, which leads to the lower dose prescribed by the system, substantial increases in image noise and unreliability of the CT attenuation values. Thus, inappropriate patient positioning impacts the automatic tube current modulation function which consequently affects both image quality and patient radiation

dose Patient off-centring of about 6 cm towards the X-ray tube can increase the radiation dose by up to 38% [17, 18].

It is especially important for paediatric patients and patients with smaller body habitus. Since TCM techniques tend to reduce dose in smaller patients and increase dose in larger patients, smaller patients are more likely to have an unintentional increase in image noise caused by inappropriate beam attenuation from bow-tie filters as a result of off-centring.

In general, the off-centring errors can be prevented through active training of technologists. Additionally, the first CT system with automatic patient positioning was recently developed and introduced to the market (Fig. 4.6). The algorithm is based on the three-dimensional (3D) depth sensor of the camera employing infrared light to measure the distance of objects to the camera and to define ideal vertical position based on the individual patient size and shape.

#### 4.3.3.2 Scan Length

In some cases, radiation dose can be optimized without any changes in the scanning parameters but by reducing the scan length to the needed minimum. Particularly, when imaging structures such as heart or brain, where an increased scan range is unnecessary.

### 4.3.4 Dose Reduction Techniques

#### 4.3.4.1 Tube Current Modulation

Among all dose reduction strategies in CT Tube current modulation technique is one of the most important. The TCM algorithm automatically adapts the tube current based on the attenuation of the body region. The first efforts at tube current modulation (TCM) aimed at reducing the exposure by adjusting the tube current in a sinusoidal fashion based on the assumption that attenuation in the lateral direction was higher than in the antero-posterior one. That time no substantial improvements in patient dose relative to the given noise level were reported. Modern CT systems utilize more complex approaches including both angular ( $\alpha$ ) and longitudinal



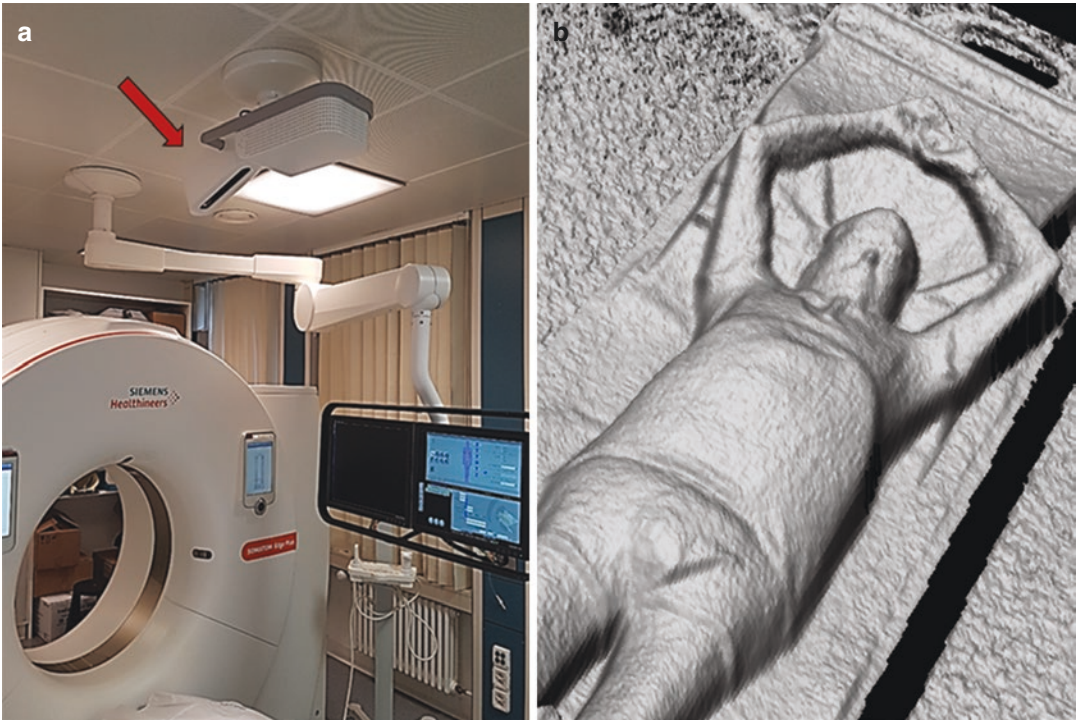


**Fig. 4.6** The CT system equipped by 3D camera (arrow) placed above the patient table (a); surface image of a patient obtained by the 3D depth camera (b)

modulations ( $z$ ). Angular modulation addresses the variation in tube current as the X-ray tube rotates around the patient according to the information from the localizer radiographer or even in real time, based on the attenuation measured from the previous  $180^\circ$  projection. Longitudinal modulation refers to the variation in tube current along the  $z$ -axis of the patient reflecting the variation in patient anatomy (e.g. shoulders versus abdomen). Angular and longitudinal modulation can be combined resulting in the most comprehensive approach since the exposure is adjusted according to the patient attenuation in all three dimensions. TCM allows for significant dose reduction by up to 60% without compromising the image quality. However, the dose savings always depend on the pre-selected level of the desired image quality.

#### 4.3.4.2 Kilovoltage Adaptation

Comparing to the adaptation of the tube current, relatively little attention has been given to the

optimization of the energy spectra. In the past, the settings of 120 kVp were used as a default value. It is still used in 90% of all CT examinations. Meanwhile, the adaptation of kVp to the specific imaging task as well as to the patient size is a promising tool for dose optimization. Recently, technology for automatic tube voltage selection and respective software has been introduced by CT manufacturers. The software aids tube voltage selection based on the patient's attenuation profile from the CT localizer radiograph and the examination type predefined by the user (e.g. routine CT, contrast-enhanced CT, renal calculi, etc.). The studies have reported that automated tube voltage selection frequently suggests a tube potential between 80 and 110 kVp instead of 120 kVp in contrast-enhanced CT examinations, resulting in both lower radiation dose and higher contrast due to the superior enhancement of iodine at lower energies [19]. However, it must be taken into account that images obtained at lower kVp tend to be much noisier, due to the higher absorp-

tion of low-energy photons. Therefore, a trade-off between image noise and contrast enhancement should be made, especially in patients with bigger diameters. Overall, the automatic kVp selection technique allows for radiation dose reduction while providing diagnostically acceptable image quality.

#### 4.3.4.3 Image Reconstruction Algorithms

Unlike parameters such as tube voltage and tube current, reconstruction algorithms do not directly affect the radiation dose; however, they can reduce the image noise and thus enable CT acquisitions at lower doses without sacrificing image quality. For instance, iterative reconstruction algorithms mentioned above allow for a dose reduction of up to 50% compared to standard FBP technique.

## References

1. Lell MM, Wildberger JE, Alkadhi H, Damlakis J, Kachelriess M. Evolution in computed tomography: the battle for speed and dose. *Investig Radiol*. 2015;50(9):629–44.
2. Mahesh M. Search for isotropic resolution in CT from conventional through multiple-row detector. *Radiographics*. 2002;22(4):949–62.
3. Goldman LW. Principles of CT and CT technology. *J Nucl Med Technol*. 2007;35(3):115–28. quiz 29–30
4. McCollough CH, Leng S, Yu L, Fletcher JG. Dual- and multi-energy CT: principles, technical approaches, and clinical applications. *Radiology*. 2015;276(3):637–53.
5. Mahesh M. AAPM/RSNA physics tutorial for residents: digital mammography: an overview. *Radiographics*. 2004;24(6):1747–60.
6. Gupta R, Cheung AC, Bartling SH, Lisauskas J, Grasruck M, Leidecker C, et al. Flat-panel volume CT: fundamental principles, technology, and applications. *Radiographics*. 2008;28(7):2009–22.
7. Kalender WA, Kyriakou Y. Flat-detector computed tomography (FD-CT). *Eur Radiol*. 2007;17(11):2767–79.
8. Kennedy TA, Connell N, Szczykutowicz T, Schafer S, Royalty K, Nace S, et al. Flat-panel CT for cochlear implant electrode imaging: comparison to multi-detector CT. *Otol Neurotol*. 2016;37(10):1646–53.
9. Willemink MJ, Noel PB. The evolution of image reconstruction for CT—from filtered back projection to artificial intelligence. *Eur Radiol*. 2019;29(5):2185–95.
10. Geyer LL, Schoepf UJ, Meinel FG, Nance JW Jr, Bastarrica G, Leipsic JA, et al. State of the art: iterative CT reconstruction techniques. *Radiology*. 2015;276(2):339–57.
11. Cody DD. AAPM/RSNA physics tutorial for residents: topics in CT. Image processing in CT. *Radiographics*. 2002;22(5):1255–68.
12. Dappa E, Higashigaito K, Fornaro J, Leschka S, Wildermuth S, Alkadhi H. Cinematic rendering—an alternative to volume rendering for 3D computed tomography imaging. *Insights Imaging*. 2016;7(6):849–56.
13. Shetty CM, Barthur A, Kambadakone A, Narayanan N, Kv R. Computed radiography image artifacts revisited. *AJR Am J Roentgenol*. 2011;196(1):W37–47.
14. Saltybaeva N, Jafari ME, Hupfer M, Kalender WA. Estimates of effective dose for CT scans of the lower extremities. *Radiology*. 2014;273(1):153–9.
15. Gordic S, Morsbach F, Schmidt B, Allmendinger T, Flohr T, Husarik D, et al. Ultralow-dose chest computed tomography for pulmonary nodule detection: first performance evaluation of single energy scanning with spectral shaping. *Investig Radiol*. 2014;49(7):465–73.
16. Martini K, Higashigaito K, Barth BK, Baumüller S, Alkadhi H, Frauenfelder T. Ultralow-dose CT with tin filtration for detection of solid and sub solid pulmonary nodules: a phantom study. *Br J Radiol*. 2015;88(1056):20150389.
17. Saltybaeva N, Alkadhi H. Vertical off-centering affects organ dose in chest CT: evidence from Monte Carlo simulations in anthropomorphic phantoms. *Med Phys*. 2017;44(11):5697–704.
18. Kaasalainen T, Palmu K, Reijonen V, Kortensniemi M. Effect of patient centering on patient dose and image noise in chest CT. *AJR Am J Roentgenol*. 2014;203(1):123–30.
19. Higashigaito K, Husarik DB, Barthelmes J, Plass AR, Manka R, Maisano F, et al. Computed tomography angiography of coronary artery bypass grafts: low contrast media volume protocols adapted to tube voltage. *Investig Radiol*. 2016;51(4):241–8.



# Computed Tomography Angiography

# 5

Jan W. Dankbaar, Ewoud J. Smit,  
and Birgitta K. Velthuis

## Contents

5.1	<b>Introduction</b> .....	45
5.2	<b>Technique</b> .....	47
5.2.1	Contrast Timing.....	47
5.2.2	Image Acquisition.....	48
5.2.3	Reconstruction.....	49
5.3	<b>Clinical Applications</b> .....	49
5.3.1	Ischemic Stroke.....	49
5.3.2	Haemorrhagic Stroke.....	50
5.3.3	Venous Sinus Thrombosis.....	52
5.3.4	Vasculopathy.....	52
5.3.5	Dissection.....	53
5.4	<b>Clinical Case</b> .....	55
	<b>References</b> .....	55

## 5.1 Introduction

On unenhanced computed tomography (CT) images, the density of blood is similar to brain and other soft tissues. Detailed evaluation of vascular structures is therefore not possible if no intravascular contrast is administered. Computed tomography angiography (CTA) visualizes vas-

cular structures with CT after intravascular injection of a radiopaque contrast material (Figs. 5.1 and 5.2). With the introduction of multi-detector-row spiral CT, CTA has become the standard technique for fast and accurate vascular imaging. By using different delays after contrast injection, different phases of the circulating blood can be imaged. As angiography is literally defined as the visualization of vessels, CTA techniques can be referred to as arterial-CTA and venous-CTA depending on the phase of the circulating contrast material. When CTA is performed at multiple time points to assess dynamic angiography, the terms dynamic-CTA, 4D-CTA or multi-phase CTA are used. CTA has proven to be highly valuable in neuro-imaging

J. W. Dankbaar (✉) · B. K. Velthuis  
Department of Radiology, University Medical Center  
Utrecht, Utrecht, The Netherlands  
e-mail: [j.w.dankbaar@umcutrecht.nl](mailto:j.w.dankbaar@umcutrecht.nl);  
[B.K.Velthuis@umcutrecht.nl](mailto:B.K.Velthuis@umcutrecht.nl)

E. J. Smit  
Department of Radiology, Radboud University  
Medical Center Nijmegen,  
Nijmegen, The Netherlands

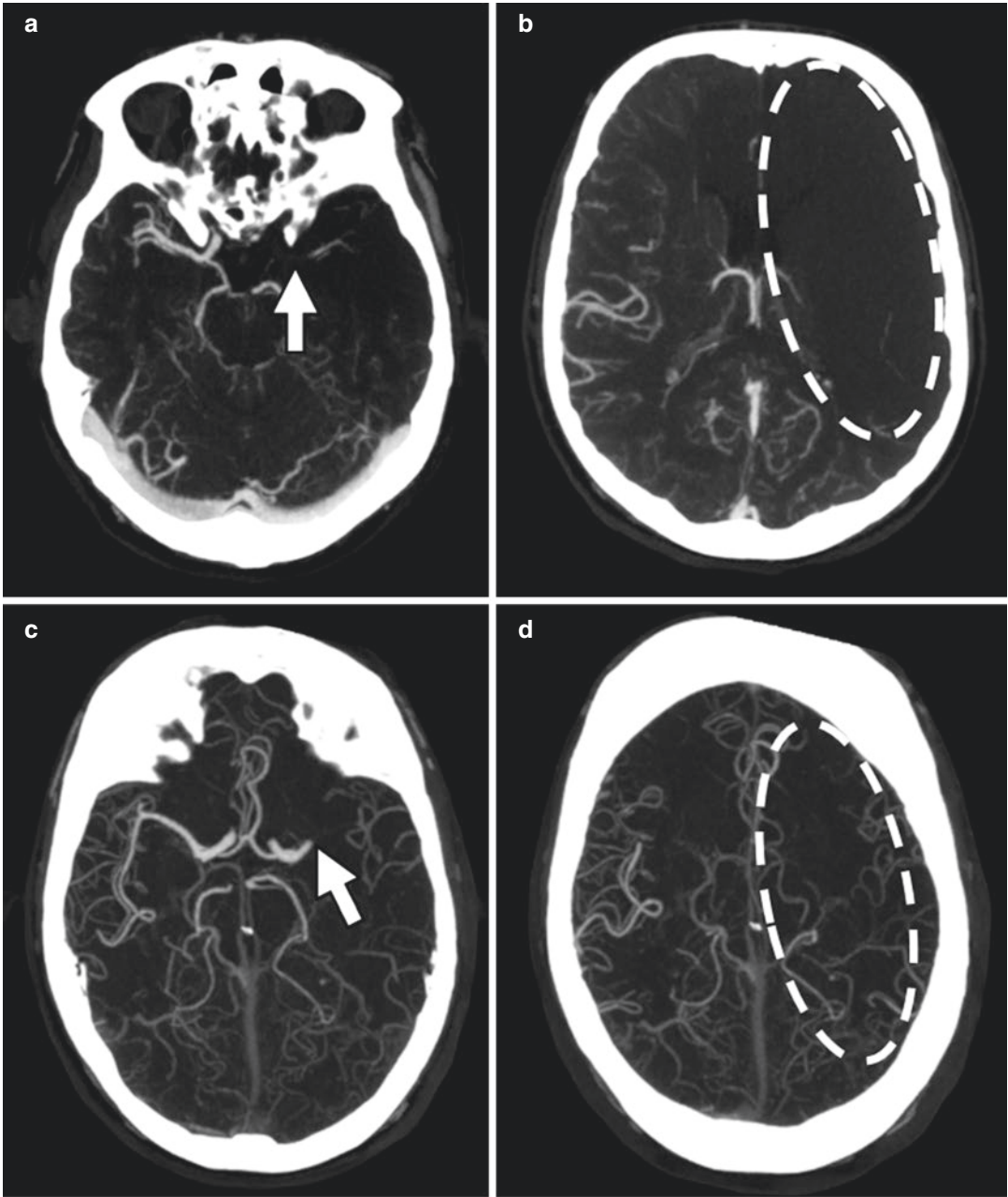


**Fig. 5.1** Axial 10 mm maximum intensity projections of a patient showing a distal left internal carotid artery occlusion (arrow in **a**) and absent collateral filling (white oval

in **b**); another example showing a proximal left middle cerebral artery occlusion (arrow in **c**) and good collateral filling (white oval in **d**)

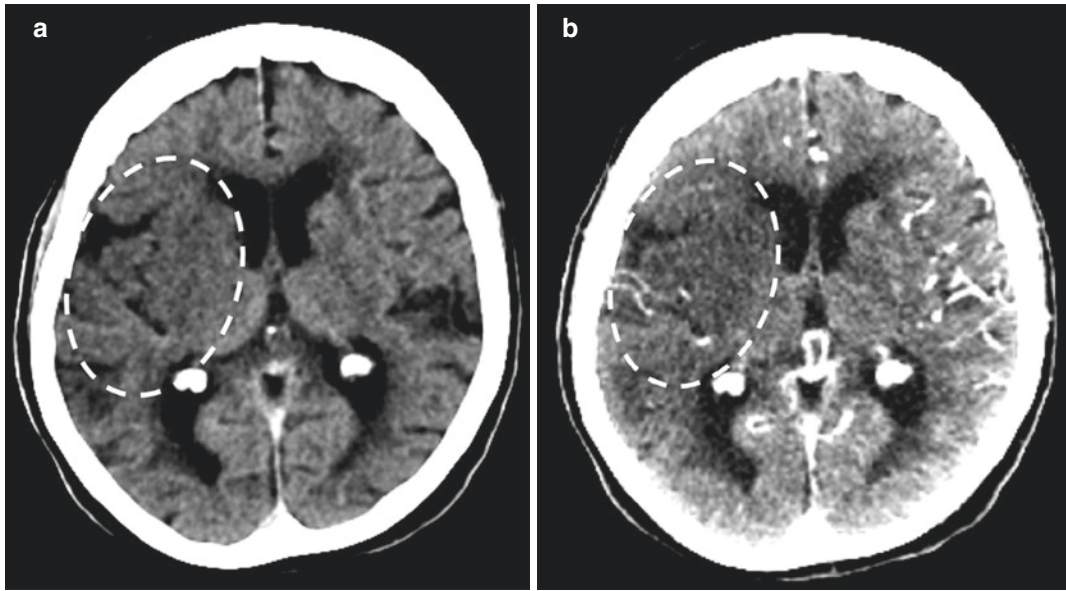


**Fig. 5.2** Example of the difference in the conspicuity of hypoattenuation in the flow territory of an occluded right middle cerebral artery on NCCT (a) and CTA (b) in a

patient with acute ischemic stroke. The hypoattenuation is more conspicuous on the CTA

but also in non-invasive vascular imaging of other parts of the body. Thin slice acquisition makes multi-planar reconstructions, maximum-intensity projections (MIP), and 3D volume-rendered images possible. In this chapter, the acquisition and technical details of CTA will be discussed, followed by the different applications of CTA in neuro-imaging.

## 5.2 Technique

### 5.2.1 Contrast Timing

The main challenge in CTA is to provide a sufficient amount of contrast material in the vasculature at the time of scanning to ensure reliable diagnostic assessment. Variations in cardiac output in critically ill patients will result in different arrival times of contrast material in the brain. Therefore, it is insufficient to simply apply a fixed delay between the time of contrast injection and scanning. To ensure adequate contrast enhancement, bolus tracking may be used. In

bolus tracking, multiple low-dose single-slab images are performed, generally at the level of the common carotid artery or descending aorta. As soon as contrast arrives, imaging starts automatically by moving the table to the starting position and performing a spiral acquisition. Automatic bolus tracking may fail if the threshold for contrast arrival is set too low (scan too early) or too high (scan too late) or if the sampling interval is too long (scan too late). Settings for automatic bolus tracking vary between vendors as some define absolute thresholds, while others define thresholds for relative enhancement. Alternatively, scanning may be started manually by positioning the region-of-interest of bolus tracking outside the patient and visually monitoring contrast arrival. Although more prone to human error, in good hands, this manual approach may be more robust and reduce contrast material usage. The scan delay after contrast injection can also be calculated from the time to peak of the arterial enhancement curve on CT perfusion (CTP), if this is performed. When exams seem to have failed because of insufficient

contrast enhancement of the intracranial arteries, it is important to assess the extracranial arteries to ensure appropriate timing, as contrast material may not arrive to the brain in case of increased intracranial pressure resulting from swelling.

Typically, spiral arterial-CTA exams of the brain and cervical arteries can be performed using 50–80 mL of intravenously injected contrast material at a flow rate of 6 mL/s followed by 40 mL of saline. For venous-CTA, a set post-injection delay of 30–45 s can be used after injection of 100 mL of iodinated contrast material at a rate of 3 or 4 mL/s [1, 2]. In acute trauma patients, a split bolus technique can be used to visualize the cervical arteries in combination with thoracic and abdominal scans. Typically, this requires injection of a bolus of about 100 mL of iodinated contrast at a flow rate of 5 mL/s followed 50 s later by a second bolus of about 65–100 mL at a flow rate of 5 mL/s. The acquisition should be triggered with a bolus tracker at the aortic arch at a threshold of 160 HU without a post-threshold delay [3].

## 5.2.2 Image Acquisition

Standard CTA is performed by using spiral CT scanning in which the table is quickly moved through the gantry allowing for flexible scan ranges. Image quality can be improved by using low tube voltage as contrast between contrast material and soft tissue is greater at lower energies (e.g. 80–100 kVp) [4]. Radiation dose can be reduced by using dose modulation and iterative reconstruction techniques [5]. Dual-energy scanners provide the opportunity of monoenergetic reconstructions at high- and low-energy levels to improve contrast-to-noise ratio. Additionally, subtraction CT and dual energy can be used to reduce metal implant artefacts, enable bone and metal removal and create iodine maps [6, 7].

With the increasing width of the multi-detector-row scanners, dynamic CTA techniques can be used to optimize timing and reduce the amount of intravenous contrast needed (Fig. 5.3). In dynamic CTA, multiple low-dose scans are performed over time after contrast injection. This

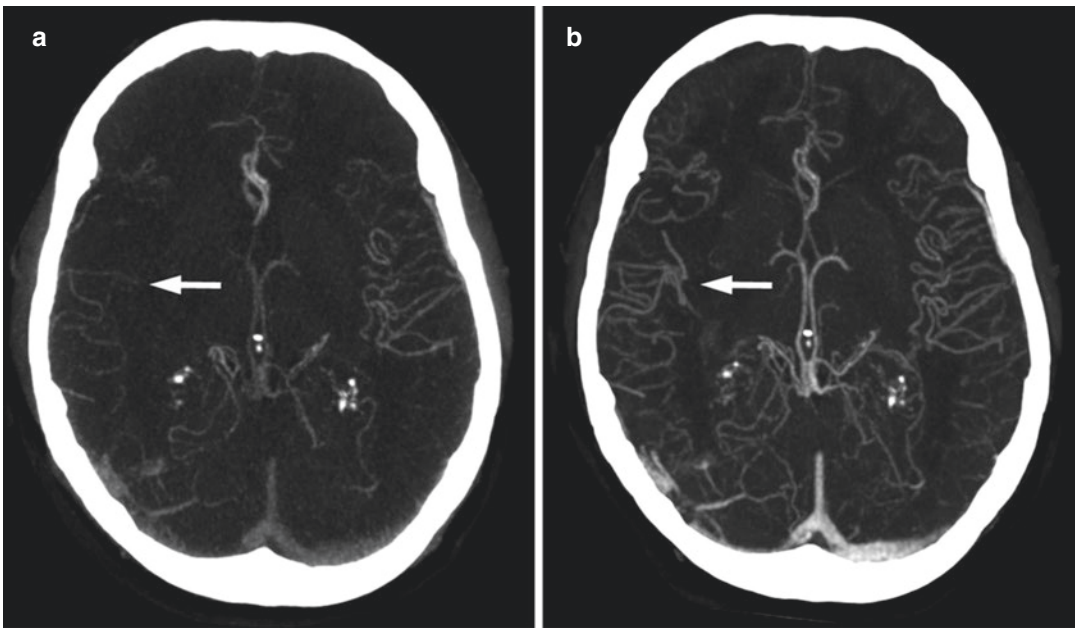


**Fig. 5.3** Timing-invariant CTA better estimates the extent of collateral circulation in a patient with right middle cerebral artery occlusion. Conventional CTA (a) shows poor collateral circulation and suggests a poor

prognosis. The timing-invariant CTA (b) shows good collateral filling and suggests a good prognosis. In this case, the patient had a good recovery

allows for the assessment of arterial and venous phases as well as timing differences in contrast filling, for example in delayed collateral blood supply and vascular malformations [8]. The dynamic CTA images serve as the source images from which CTP maps can be calculated. In other words, if CTP imaging is performed the source images can be reviewed as dynamic CTA images. Since in dynamic CTA multiple scans are performed over time of the same region, there is a trade-off between scan interval and scan volume, which is mainly affected by the number of detector rows of the scanner (z-coverage of the detector elements). The use of dynamic CTA is therefore restricted to modern scanners with large spatial coverage. Some vendors provide scanners with whole-brain coverage in a single volumetric acquisition allowing for flexible scan intervals without table movement. Other vendors extend spatial coverage by using a toggling table technique (table moves between two positions) or continuous table feed (continues back and forth table movement). In these techniques, the minimum scan interval is limited by the time the scanner needs to get back to its starting position. On large coverage scanners, the toggling table technique may also be used to acquire an interleaved volumetric acquisition of the carotids, allowing for a combined head and neck exam [9, 10]. Since multiple scans are performed over time, the radiation dose in dynamic CTA may be modestly to substantially higher than in standard CTA. The individual images over time should therefore be performed at an ultra-low dose level to limit total radiation dose to the patient. Dose modulation should not be used, since it may not be optimized for the ultra-low dose acquisitions of the scans over time. Imaging is best performed at low tube voltage combined with iterative reconstruction methods to improve image quality as well as reduce radiation dose and noise [11]. Assessment of vascular morphology and occlusions on the individual images is limited by the substantial image noise on the individual images over time [12]. A delay-insensitive (or timing-invariant) CTA scan may be reconstructed from the dynamic CTA data providing a high-quality overview of the vasculature [13]. Instead of dynamic CTA, a

multi-phase approach, in which a CTA is acquired at different points in the time attenuation curve CTA (peak arterial phase, peak venous phase and delayed or late venous phase CTA), can also be performed [14]. In contrast to dynamic CTA, multi-phase CTA is however limited to the acquired time points without a decrease in radiation dose [15].

### 5.2.3 Reconstruction

CTA acquisition with multidetector row scanners can result in sub-millimetre isometric voxels. This large quantity of volumetric data enables the use of multiplanar and three-dimensional reconstructions like volume rendering and maximum intensity projections (MIP) [16]. These reconstruction techniques permit the visualization of anatomical details, which would be difficult to evaluate using axial reconstructions alone. To obtain these reconstructions, dedicated computer software is needed, which is generally provided by the CT scanner manufacturer. With CTA, MIP reconstructions are easily obtained due to the high density of the intravascular contrast material compared to the surrounding tissue. In neuroimaging, MIP and other three-dimension evaluations of CTA images are of high value for the detection of small intracranial aneurysms, arterial stenosis grading and determining the morphology of aneurysm and vascular malformations.

---

## 5.3 Clinical Applications

### 5.3.1 Ischemic Stroke

The incidence of ischemic stroke is about 143 per 100,000 per year and a leading cause of death and disability in the Western world [17]. It is caused by an acute occlusion of one of the cerebral arteries. Recanalization can be achieved with intravenous thrombolysis within a limited time window [18]. About 30% of patients have an intracranial large artery occlusion, and they may benefit more from endovascular (intra-arterial) thrombectomy than intravenous thrombolysis alone [19]. Most

hospitals use CT for acute stroke imaging evaluation [20]. An acute stroke CT protocol typically comprises a non-contrast CT (NCCT) to rule out haemorrhage and a CTA to determine the occlusion site, thrombus extent and collateral status of the patient [21]. Additional CTP may be performed to assess focal perfusion deficits and extend the time window for endovascular thrombectomy treatment [22, 23]. Imaging in acute ischemic stroke patients should not delay administration of intravenous thrombolysis, since “*time is brain*” [24]. Therefore, decision-making regarding the administration of intravenous thrombolysis is usually made immediately after haemorrhage is excluded on NCCT. To decide whether a patient is eligible for endovascular treatment the required CTA can be performed while intravenous thrombolysis is being administered. CTA has a high sensitivity (97–100%) and specificity (98–100%) for detecting intracranial stenosis and occlusions [25–28]. Additional information regarding the extent of the area deprived of contrast and thereby blood can be obtained with the CTA source images [29]. Hypodense regions on CTA source images represent diminished vascular filling and tissue enhancement and thereby ischemic tissue. The conspicuity of the ischemic area depends on the timing of the CTA [30], but it is usually more conspicuous than on NCCT [31]. Although the area of hypoattenuation has a good correlation to final infarct volumes [32], CTP is superior in predicting presence and extent of infarction [33]. An important predictor of outcome in acute ischemic stroke patients is the extent of collateral blood supply behind the arterial occlusion. Collateral filling has been shown to enhance recanalization and reperfusion, reduce the size of the ischemic lesion growth, decrease the risk of haemorrhagic transformation and improve outcomes with intravenous and endovascular treatment [34–37]. CTA can help visualize filling through collateral vessels but is again dependent on timing. Collateral filling may be slow and therefore not yet visible on a single-phase CTA timed to image the arteries of the circle of Willis. To overcome this problem, dynamic CTA (or CTP) can be used to obtain a timing invariant CTA [38–41]. Alternatively, collateral filling can be visualized

with multiphase CTA [42]. However, CTP has a higher temporal resolution and is already frequently acquired in acute ischemic stroke patients to determine the extent of the ischaemia and treatment selection [23]. It is thereby already available for a timing invariant CTA reconstruction. The timing invariant and multiphase CTA may not just improve the visualization of collateral filling but also the visualization of the extent and location of the occlusion [12, 43, 44]. Extent of the occlusion (thrombus length) is another important determinant of efficacy of intravenous thrombolysis [45, 46]. In addition to determining the occlusion site, thrombus extent and collateral filling, CTA can be used to evaluate the possible cause of the stroke and plan the endovascular treatment procedure. With CTA, cardiac thrombus can be identified, which is defined as a homogeneous filling defect with low HU-values (<100 HU) and a well-defined border [47]. In the aortic arch, raised plaques with a thickness >4 mm on CTA are an important risk factor for stroke [48, 49]. Additionally, ulcerations with a depth of 2 mm or more result in an increased risk of stroke [50]. In the carotid arteries, atherosclerotic plaques are classified on CTA, according to their HU density, as fatty (<60 HU), mixed (60–130 HU) and calcified (>130 HU) plaques [51]. Irregular plaques and plaques with fatty content are associated with increased stroke risk [52, 53]. Very hypodense plaques (<30 HU) and plaque ulcerations of  $\geq 2$  mm are associated with the presence of intraplaque haemorrhage which is another important risk factor for stroke [51, 52, 54]. The grade of the stenosis caused by atherosclerotic plaques in the carotid arteries also determines the risk of stroke. High-grade stenosis can be accurately determined on CTA [55].

### 5.3.2 Haemorrhagic Stroke

About one-third of haemorrhagic strokes are caused by subarachnoid haemorrhage (SAH) with an incidence of 6–9 per 100,000 per year [17, 56]. It has a case fatality of 40–50% in the first month [57]. The cause of SAH is mostly (85%) rupture of a cerebral aneurysms [58] (Fig. 5.4). It has been shown that the location,



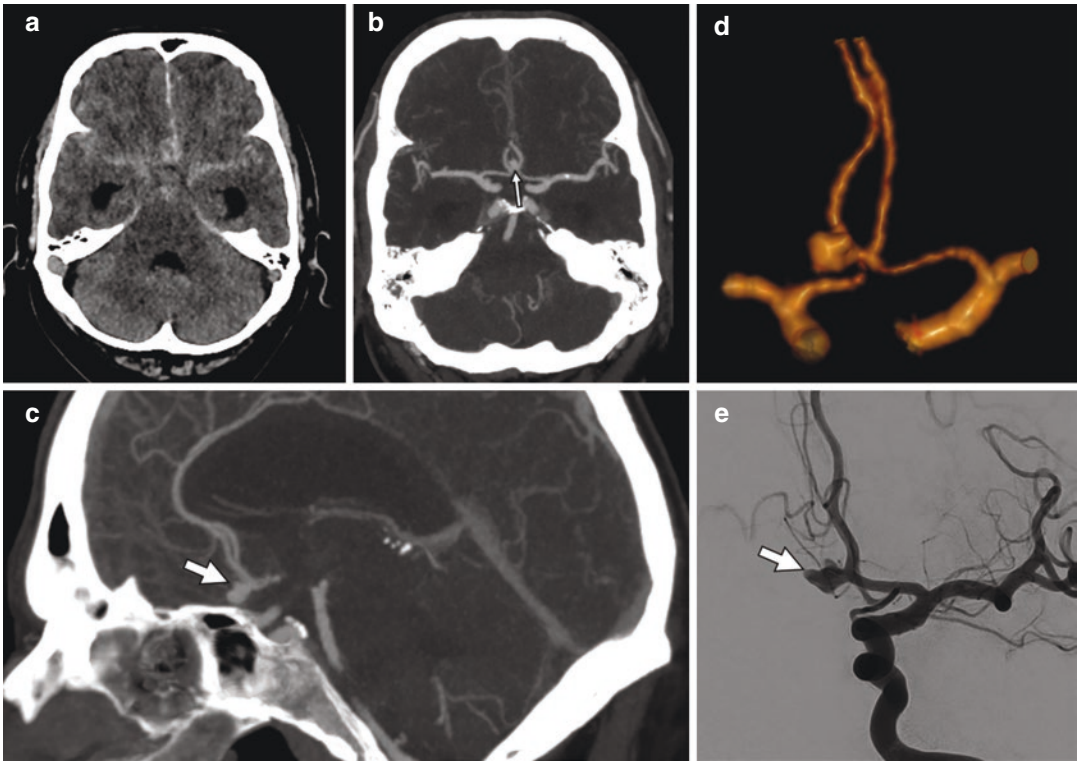


**Fig. 5.4** A patient with subarachnoid haemorrhage on NCCT (a) with an anterior communicating artery aneurysm (arrow) visualized on axial and sagittal CTA (b and c), a 3D volume-rendered CTA (d) and DSA (e)

size and morphology of unruptured cerebral aneurysms predict future rupture [59–63]. The six-item PHASES risk score, including size and location of the unruptured aneurysm, can be used to predict the 5-year absolute risk of rupture and identify patients with a high risk of aneurysm growth [64, 65]. The prevalence of unruptured aneurysms is around 3% in the general population. Not all unruptured aneurysms require treatment, as the risk of treatment complication is sometimes higher than the estimated risk of rupture. The choice between conservative, endovascular or neurosurgical treatment is again influenced by the different features of cerebral aneurysm. This emphasizes the importance of accurate characterization of cerebral aneurysms.

The three major imaging methods that are used for imaging of cerebral aneurysms are CTA, magnetic resonance angiography (MRA) and digital subtraction angiography (DSA). Since a NCCT is almost always performed to rule out intracranial haemorrhage in acute stroke patients,

CTA is the first modality of choice to image ruptured intracranial aneurysms in patients with SAH. It has been reported that the negative-predictive value of NCCT followed by CTA is 99.4% for aneurysmal SAH [66]. Multi-detector spiral CT scanners with sub-millimetre slice thickness allowing for multi-planar reformats have a sensitivity of 97% for the detection of cerebral aneurysm of all sizes [67]. With future advances in CT technology, it is likely that a sensitivity of 100% will be reached. Currently, DSA is still superior to 64- and 256-detector-row CTA, in detecting small aneurysms (<3 mm) and visualizing small branching arteries [68]. DSA should therefore be used when CTA does not identify an aneurysm in the setting of a spontaneous subarachnoid haemorrhage with an aneurysmal bleeding pattern. In patients meeting the strict imaging criteria for peri-mecencephalic pattern of SAH, a negative high-quality CTA may obviate the additional use of DSA or further imaging follow-up [69, 70].

For screening purposes and to evaluate aneurysmal growth, MRA has comparable diagnostic properties to CTA with the advantage of non-contrast imaging without ionizing radiation. MRA shows a good diagnostic performance for the evaluation of aneurysms treated with endovascular coiling [71], both with and without contrast at 1.5- and 3-Tesla field strength [53]. CTA is less suited for this purpose due to severe streak artefacts caused by the metal coils. On the other hand, CTA is better at visualizing aneurysms treated by neurosurgical clipping, while the clip induced artefact prevents evaluation with MRA. With iterative reconstruction or the use of monoenergetic high energy level (100–140 KeV) reconstructions from dual-energy scanning metal artefacts in CTA can be significantly reduced [72]. In combination with the possibility of bone removal this aids in the assessment of aneurysms near the skull base [73].

Intracerebral haemorrhage (ICH) accounts for the other two-thirds of haemorrhagic stroke. About 20% of intracerebral haemorrhages are caused by an underlying macrovascular abnormality like arteriovenous malformations (AVM) or dural fistula. Standard CTA can adequately visualize these macrovascular causes [74, 75]. CTA is however less suited to identify the feeding vessels and determine the flow dynamics. For this purpose, dynamic CTA can be used [76]. Dynamic CTA may also help identify aneurysms within the nidus of the arteriovenous malformation (AVM) [77].

Haematoma expansion occurs in about one-third of patients with ICH and worsens outcome. Early prediction of hematoma expansion could possibly help timely management of these patients. Identification of extravasation of contrast material (a spot sign) in the haematoma on CTA has prognostic implications. More spot signs are identified on dynamic or multi-phase CTA [78, 79]. Although the sensitivity for spot signs and the negative-predictive value for hematoma expansion increase on later CTA phases, the positive-predictive value for hematoma expansion is highest for spot signs seen on early (arterial) phase CTA and on CTA scans acquired early after onset [80].

### 5.3.3 Venous Sinus Thrombosis

Cerebral venous sinus thrombosis (CVST) is a rare but life-threatening disease. It can lead to haemorrhagic venous infarction and has a mortality rate of about 15% [81]. The estimated annual incidence is less than 1 per 100,000 in adults [82]. The most common causes are oral contraceptive use, vascular malformations, infection and malignancy [83]. Pregnancy and other prothrombotic states are also risk factors for the development of CVST [82]. The initial symptoms are mostly non-specific and are most often a headache. If CVST is suspected, both CTA and MRI can be used. Patients with non-specific symptoms such as headache are frequently scanned by CT for initial screening. Within the same session, a venous CTA can be acquired. Other advantages of CT over MRI are that the imaging acquisition time is shorter, it is less prone to (flow related) artefacts, more accessible for critical patients and better in depicting small vessels [84]. The disadvantage of CT is of course the use of ionizing radiation that can be especially harmful to the unborn child in pregnant women. In a head-to-head comparison between CTA and MRI, no difference was found in the detection rate of CVST [85]. The preferred modality will therefore be dictated by the experience and resources of the individual institutions. On NCCT, CVST results in an increased density of the affected venous structures. On CTA, CVST results in filling defects in the affected sinuses and veins with or without expansion of the vessel. Common pitfalls, that need to be taken into account when looking for CVST on CTA, are venous anatomic variants that mimic occlusion (sinus atresia or hypoplasia), asymmetric or variations in sinus drainage (occipital sinuses and sinus duplication) and normal sinus filling defects (arachnoid granulations and septa within the sinus) [86] (Figs. 5.5 and 5.6).

### 5.3.4 Vasculopathy

The imaging findings of vasculopathy are various and depend on the site and type of blood vessels that are affected. In general, MRI with MRA is

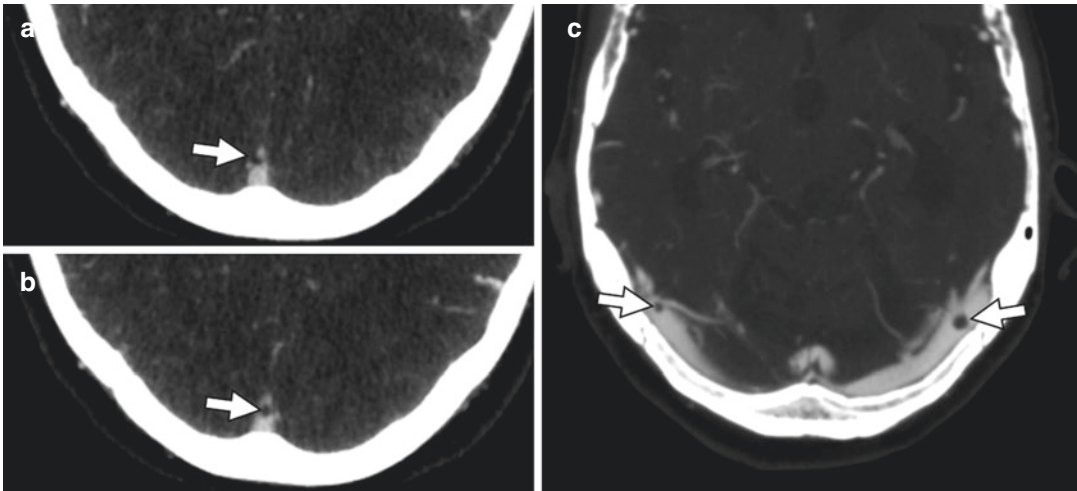


**Fig. 5.5** Normal sinus filling defects on axial venous-CTA caused by arachnoid granulations (arrows) in the superior sagittal sinus (a and b) and the transverse sinuses (c), not to be confused with thrombosis

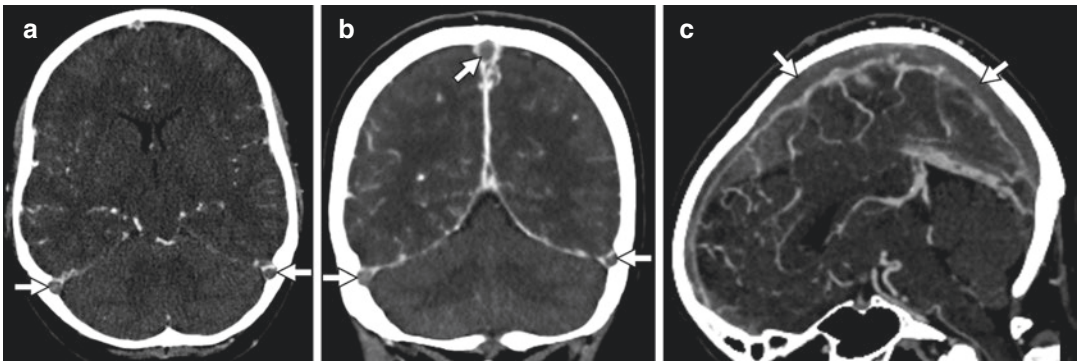


**Fig. 5.6** Axial (a), coronal (b) and sagittal (c) venous-CTAs showing extensive venous sinus thrombosis in the superior sagittal sinus and the transverse sinuses. Filling

defects with expansion of the venous sinus due to the mass effect of the thrombus are seen (arrows)

used to evaluate vasculopathies, since evaluation of the brain tissue is as essential as evaluation of the pathological vessels. MRA however tends to overestimate the grade of stenosis in patients with steno-occlusive vasculopathies, especially when time-of-flight techniques without contrast are used [87]. In Moyamoya disease, it has been shown that CTA is superior to MRA in detecting affected vessels [88]. Dynamic CTA also shows a strong correlation with DSA in determining vascular stenosis but is insufficient in the evaluation of the collateral circulation in Moyamoya patients [89] (Fig. 5.7). Patients with severe steno-occlusive vasculopathies in the proximal cerebral

arteries and the circle of Willis can be treated by extracranial to intracranial bypass surgery to prevent ischemia [90]. Evaluation of the patency of these bypasses can be done non-invasively with CTA. It is as accurate as DSA and superior to MRA in depicting vessels with slow flow and small calibre [87, 91, 92].

### 5.3.5 Dissection

Dissection of the cervical arteries has become increasingly recognized as a cause of stroke in young and middle-aged patients. It can occur

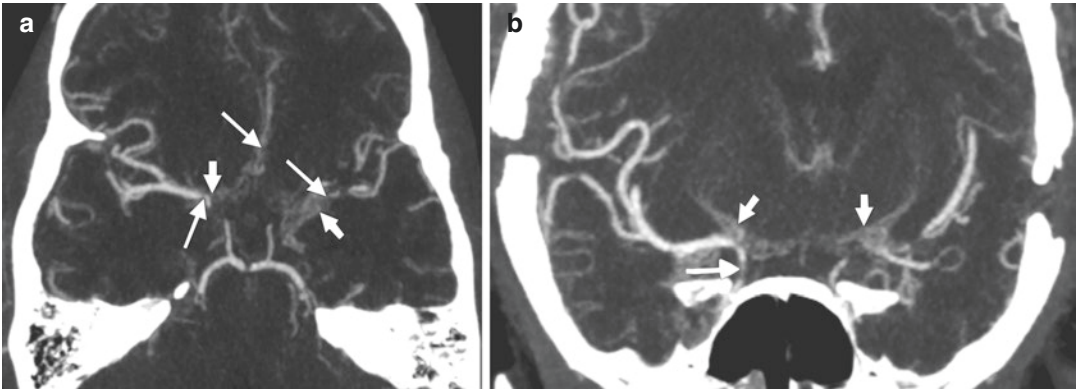


**Fig. 5.7** A patient with severe Moyamoya disease with an axial (a) and coronal (b) 10-mm maximum intensity projection showing narrowing of the distal internal carotid arteries and proximal anterior and middle cerebral arteries

(long arrows) in combination with extensive collateral filling around the affected vessel segments (short arrows). Note the skull defects resulting from neurosurgical extracranial to intracranial bypass surgery

spontaneously, due to trauma, or secondary to diseases of the connective tissue, such as Marfan syndrome and fibromuscular dysplasia. Up to 20% of patients with traumatic osseous cervical spine injury suffer from vertebral artery dissection [93, 94]. Imaging of the cervical arteries is therefore strongly indicated in cases of cervical spine trauma. CTA of the cervical arteries is a fast and accurate method for detecting dissection of the craniocervical region and can be easily integrated into a whole-body trauma CT protocol [95]. To achieve optimal cervical artery visibility without losing vital information on other traumatic soft tissue injury, a spilt bolus technique can be used [3, 96]. For the evaluation of suspected non-traumatic cervical artery dissection, a standard CTA of the cervical and cerebral vessels can be used.

The performance of CTA for the detection of cervical artery dissection is similar to MRI/MRA [97]. However, intimal flaps and pseudoaneurysms are better seen on CTA than MRI/MRA [98]. Compared to the gold standard DSA a very high sensitivity and specificity can be achieved when using multi-detector row CT [99]. On CTA, there are several important findings that indicate cervical artery dissection [100]. Dissection of the carotid arteries is mostly limited to the part of the internal carotid artery (ICA) between the bifurcation and the skull base [101]. The ICA dissection is characterized by a long segment of eccentric luminal narrowing with an increase of the external diameter of the artery [100]. Other typical findings are an intimal flap and a dissecting aneurysm. In vertebral artery dissection, an increased external diameter and crescent-shaped mural thickening have been found in 100% and 79% of patients, respectively [102].

## 5.4 Clinical Case (Fig. 5.8)

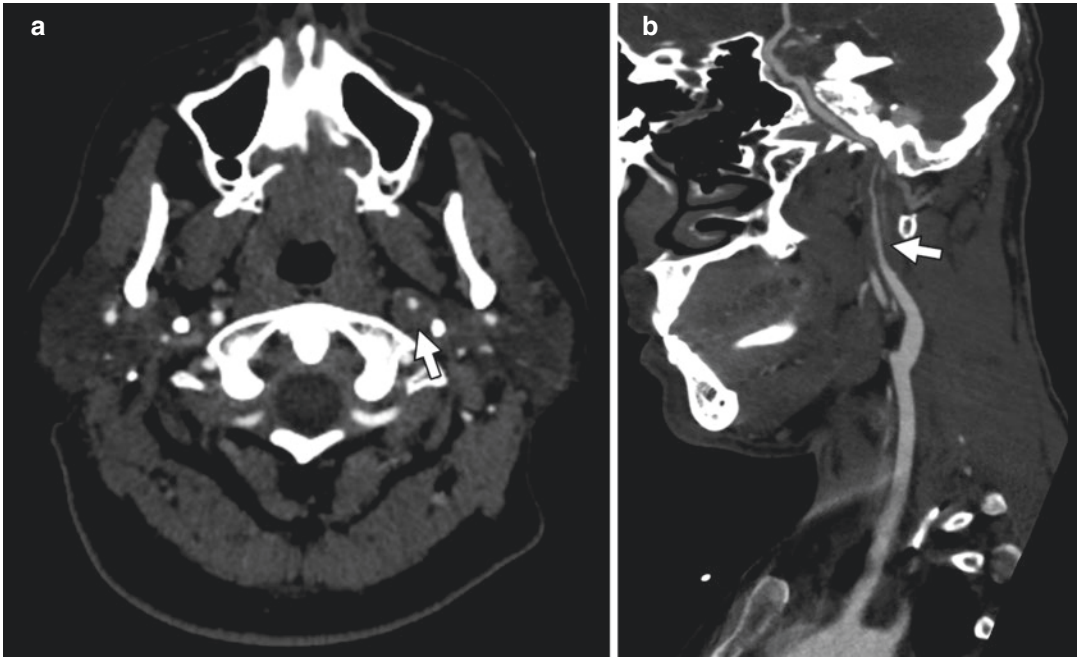


**Fig. 5.8** A patient with an extracranial left internal carotid artery dissection. **(a)** Axial CTA image showing eccentric luminal narrowing with an increase of the external

diameter of the artery (arrow). **(b)** The curved reformat of the CTA shows the long segment of eccentric luminal narrowing typical for a dissection (arrow)

## References

- Rodallec MH, Krainik A, Feydy A, Helias A, Colombani JM, Julles MC, et al. Cerebral venous thrombosis and multidetector CT angiography: tips and tricks. *Radiographics*. 2006;26(Suppl 1):S5–18; discussion S42–3. Epub 2006/10/20.
- Biswas S, Chandran A, Roughley S, Bhojak M, Das K. Cerebral CT venography using a 320-MDCT scanner with a time-density curve technique and low volume of contrast agent: comparison with fixed time-delay technique. *AJR Am J Roentgenol*. 2015;205(6):1269–75; Epub 2015/11/21.
- Beenen LF, Sierink JC, Kolkman S, Nio CY, Saltzherr TP, Dijkgraaf MG, et al. Split bolus technique in polytrauma: a prospective study on scan protocols for trauma analysis. *Acta Radiol*. 2015;56(7):873–80; Epub 2014/07/19.
- Waaijer A, Prokop M, Velthuis BK, Bakker CJ, de Kort GA, van Leeuwen MS. Circle of Willis at CT angiography: dose reduction and image quality—reducing tube voltage and increasing tube current settings. *Radiology*. 2007;242(3):832–9; Epub 2007/01/19.
- Smith AB, Dillon WP, Gould R, Wintermark M. Radiation dose-reduction strategies for neuro-radiology CT protocols. *AJNR Am J Neuroradiol*. 2007;28(9):1628–32; Epub 2007/09/26.
- Postma AA, Das M, Stadler AA, Wildberger JE. Dual-energy CT: what the neuroradiologist should know. *Curr Radiol Rep*. 2015;3(5):16; Epub 2015/03/31.
- Faby S, Kuchenbecker S, Sawall S, Simons D, Schlemmer HP, Lell M, et al. Performance of today's dual energy CT and future multi energy CT in virtual non-contrast imaging and in iodine quantification: a simulation study. *Med Phys*. 2015;42(7):4349–66; Epub 2015/07/03.
- Kortman HG, Smit EJ, Oei MT, Manniesing R, Prokop M, Meijer FJ. 4D-CTA in neurovascular disease: a review. *AJNR Am J Neuroradiol*. 2015;36(6):1026–33; Epub 2014/10/31.
- Oei MTH, Meijer FJA, van der Woude WJ, Smit EJ, van Ginneken B, Prokop M, et al. Interleaving cerebral CT perfusion with neck CT angiography part I. proof of concept and accuracy of cerebral perfusion values. *Eur Radiol*. 2017;27(6):2649–56; Epub 2016/10/09.
- Oei MTH, Meijer FJA, van der Woude WJ, Smit EJ, van Ginneken B, Manniesing R, et al. Interleaving cerebral CT perfusion with neck CT angiography. Part II: clinical implementation and image quality. *Eur Radiol*. 2017;27(6):2411–8; Epub 2016/09/22.

11. Niesten JM, van der Schaaf IC, Riordan AJ, de Jong HW, Horsch AD, Eijspaart D, et al. Radiation dose reduction in cerebral CT perfusion imaging using iterative reconstruction. *Eur Radiol.* 2014;24(2):484–93; Epub 2013/10/16.
12. Smit EJ, Vonken EJ, Meijer FJ, Dankbaar JW, Horsch AD, van Ginneken B, et al. Timing-invariant CT angiography derived from CT perfusion imaging in acute stroke: a diagnostic performance study. *AJNR Am J Neuroradiol.* 2015;36(10):1834–8; Epub 2015/06/27.
13. Smit EJ, Vonken EJ, van der Schaaf IC, Mendrik AM, Dankbaar JW, Horsch AD, et al. Timing-invariant reconstruction for deriving high-quality CT angiographic data from cerebral CT perfusion data. *Radiology.* 2012;263(1):216–25; Epub 2012/02/15.
14. Menon BK, d’Esterre CD, Qazi EM, Almekhlafi M, Hahn L, Demchuk AM, et al. Multiphase CT angiography: a new tool for the imaging triage of patients with acute ischemic stroke. *Radiology.* 2015;275(2):510–20; Epub 2015/01/31.
15. Aviv RI, Parsons M, Bivard A, Jahromi B, Wintermark M. Multiphase CT angiography: a poor man’s perfusion CT? *Radiology.* 2015;277(3):922–4; Epub 2015/11/26.
16. Fishman EK, Ney DR, Heath DG, Corl FM, Horton KM, Johnson PT. Volume rendering versus maximum intensity projection in CT angiography: what works best, when, and why. *Radiographics.* 2006;26(3):905–22; Epub 2006/05/17.
17. Benjamin EJ, Blaha MJ, Chiuve SE, Cushman M, Das SR, Deo R, et al. Heart disease and stroke statistics-2017 update: a report from the American Heart Association. *Circulation.* 2017;135(10):e146–603; Epub 2017/01/27.
18. Hacke W, Kaste M, Bluhmki E, Brozman M, Davalos A, Guidetti D, et al. Thrombolysis with alteplase 3 to 4.5 hours after acute ischemic stroke. *N Engl J Med.* 2008;359(13):1317–29; Epub 2008/09/26.
19. Berkhemer OA, Fransen PS, Beumer D, van den Berg LA, Lingsma HF, Yoo AJ, et al. A randomized trial of intraarterial treatment for acute ischemic stroke. *N Engl J Med.* 2015;372(1):11–20; Epub 2014/12/18.
20. Wintermark M, Luby M, Bornstein NM, Demchuk A, Fiehler J, Kudo K, et al. International survey of acute stroke imaging used to make revascularization treatment decisions. *Int J Stroke.* 2015;10(5):759–62; Epub 2015/04/03.
21. Wintermark M, Sanelli PC, Albers GW, Bello J, Derdeyn C, Hetts SW, et al. Imaging recommendations for acute stroke and transient ischemic attack patients: a joint statement by the American Society of Neuroradiology, the American College of Radiology, and the Society of NeuroInterventional Surgery. *AJNR Am J Neuroradiol.* 2013;34(11):E117–27; Epub 2013/08/03.
22. Albers GW, Marks MP, Kemp S, Christensen S, Tsai JP, Ortega-Gutierrez S, et al. Thrombectomy for stroke at 6 to 16 hours with selection by perfusion imaging. *N Engl J Med.* 2018;378:708–18; Epub 2018/01/25.
23. Nogueira RG, Jadhav AP, Haussen DC, Bonafe A, Budzik RF, Bhuva P, et al. Thrombectomy 6 to 24 hours after stroke with a mismatch between deficit and infarct. *N Engl J Med.* 2017;378:11–21; Epub 2017/11/14.
24. Saver JL. Time is brain—quantified. *Stroke.* 2006;37(1):263–6; Epub 2005/12/13.
25. Hirai T, Korogi Y, Ono K, Nagano M, Maruoka K, Uemura S, et al. Prospective evaluation of suspected stenooclusive disease of the intracranial artery: combined MR angiography and CT angiography compared with digital subtraction angiography. *AJNR Am J Neuroradiol.* 2002;23(1):93–101; Epub 2002/02/06.
26. Katz DA, Marks MP, Napel SA, Bracci PM, Roberts SL. Circle of Willis: evaluation with spiral CT angiography, MR angiography, and conventional angiography. *Radiology.* 1995;195(2):445–9; Epub 1995/05/01.
27. Nguyen-Huyh MN, Wintermark M, English J, Lam J, Vittinghoff E, Smith WS, et al. How accurate is CT angiography in evaluating intracranial atherosclerotic disease? *Stroke.* 2008;39(4):1184–8; Epub 2008/02/23.
28. Verro P, Tanenbaum LN, Borden NM, Sen S, Eshkar N. CT angiography in acute ischemic stroke: preliminary results. *Stroke.* 2002;33(1):276–8; Epub 2002/01/10.
29. Sharma M, Fox AJ, Symons S, Jairath A, Aviv RI. CT angiographic source images: flow- or volume-weighted? *AJNR Am J Neuroradiol.* 2011;32(2):359–64; Epub 2010/11/06.
30. Dave P, Lum C, Thornhill R, Chakraborty S, Dowlatshahi D. Hypoattenuation on CTA images with large vessel occlusion: timing affects conspicuity. *Neuroradiology.* 2017;59(5):471–5; Epub 2017/04/02.
31. van Seeters T, Biessels GJ, Niesten JM, van der Schaaf IC, Dankbaar JW, Horsch AD, et al. Reliability of visual assessment of non-contrast CT, CT angiography source images and CT perfusion in patients with suspected ischemic stroke. *PLoS One.* 2013;8(10):e75615; Epub 2013/10/12.
32. d’Esterre CD, Trivedi A, Pordeli P, Boesen M, Patil S, Hwan Ahn S, et al. Regional comparison of multiphase computed tomographic angiography and computed tomographic perfusion for prediction of tissue fate in ischemic stroke. *Stroke.* 2017;48(4):939–45; Epub 2017/03/16.
33. van Seeters T, Biessels GJ, Kappelle LJ, van der Schaaf IC, Dankbaar JW, Horsch AD, et al. CT angiography and CT perfusion improve prediction of infarct volume in patients with anterior circulation stroke. *Neuroradiology.* 2016;58(4):327–37; Epub 2016/01/16.
34. Tan IY, Demchuk AM, Hopyan J, Zhang L, Gladstone D, Wong K, et al. CT angiography clot burden score and collateral score: correlation with

- clinical and radiologic outcomes in acute middle cerebral artery infarct. *AJNR Am J Neuroradiol*. 2009;30(3):525–31; Epub 2009/01/17.
35. Tan JC, Dillon WP, Liu S, Adler F, Smith WS, Wintermark M. Systematic comparison of perfusion-CT and CT-angiography in acute stroke patients. *Ann Neurol*. 2007;61(6):533–43.
  36. Bang OY, Saver JL, Kim SJ, Kim GM, Chung CS, Ovbiagele B, et al. Collateral flow predicts response to endovascular therapy for acute ischemic stroke. *Stroke*. 2011;42(3):693–9; Epub 2011/01/15.
  37. Berkhemer OA, Jansen IG, Beumer D, Fransen PS, van den Berg LA, Yoo AJ, et al. Collateral status on baseline computed tomographic angiography and intra-arterial treatment effect in patients with proximal anterior circulation stroke. *Stroke*. 2016;47(3):768–76; Epub 2016/02/24.
  38. Smit EJ, Vonken EJ, van Seeters T, Dankbaar JW, van der Schaaf IC, Kappelle LJ, et al. Timing-invariant imaging of collateral vessels in acute ischemic stroke. *Stroke*. 2013;44(8):2194–9; Epub 2013/06/14.
  39. Frolich AM, Wolff SL, Psychogios MN, Klotz E, Schramm R, Wasser K, et al. Time-resolved assessment of collateral flow using 4D CT angiography in large-vessel occlusion stroke. *Eur Radiol*. 2014;24(2):390–6; Epub 2013/10/01.
  40. van den Wijngaard IR, Holswilder G, Wermer MJ, Boiten J, Algra A, Dippel DW, et al. Assessment of collateral status by dynamic CT angiography in acute MCA stroke: timing of acquisition and relationship with final infarct volume. *AJNR Am J Neuroradiol*. 2016;37:1231–6; Epub 2016/04/02.
  41. Menon BK, O'Brien B, Bivard A, Spratt NJ, Demchuk AM, Miteff F, et al. Assessment of leptomeningeal collaterals using dynamic CT angiography in patients with acute ischemic stroke. *J Cereb Blood Flow Metab*. 2013;33(3):365–71; Epub 2012/11/15.
  42. Garcia-Tornel A, Carvalho V, Boned S, Flores A, Rodriguez-Luna D, Pagola J, et al. Improving the evaluation of collateral circulation by multiphase computed tomography angiography in acute stroke patients treated with endovascular reperfusion therapies. *Interv Neurol*. 2016;5(3–4):209–17; Epub 2016/10/27.
  43. Byrne D, Sugrue G, Stanley E, Walsh JP, Murphy S, Kavanagh EC, et al. Improved detection of anterior circulation occlusions: the “delayed vessel sign” on multiphase CT angiography. *AJNR Am J Neuroradiol*. 2017;38(10):1911–6; Epub 2017/08/12.
  44. Yu AY, Zerna C, Assis Z, Holodinsky JK, Randhawa PA, Najm M, et al. Multiphase CT angiography increases detection of anterior circulation intracranial occlusion. *Neurology*. 2016;87(6):609–16; Epub 2016/07/08.
  45. Rohan V, Baxa J, Tupy R, Cerna L, Sevcik P, Friesl M, et al. Length of occlusion predicts recanalization and outcome after intravenous thrombolysis in middle cerebral artery stroke. *Stroke*. 2014;45(7):2010–7; Epub 2014/06/12.
  46. Riedel CH, Zimmermann P, Jensen-Kondering U, Stingele R, Deuschl G, Jansen O. The importance of size: successful recanalization by intravenous thrombolysis in acute anterior stroke depends on thrombus length. *Stroke*. 2011;42(6):1775–7; Epub 2011/04/09.
  47. Teunissen C, Habets J, Velthuis BK, Cramer MJ, Loh P. Double-contrast, single-phase computed tomography angiography for ruling out left atrial appendage thrombus prior to atrial fibrillation ablation. *Int J Cardiovasc Imaging*. 2017;33(1):121–8; Epub 2016/09/08.
  48. Amarenco P, Cohen A, Tzourio C, Bertrand B, Hommel M, Besson G, et al. Atherosclerotic disease of the aortic arch and the risk of ischemic stroke. *N Engl J Med*. 1994;331(22):1474–9; Epub 1994/12/01.
  49. Chatzikonstantinou A, Krissak R, Fluchter S, Artemis D, Schaefer A, Schoenberg SO, et al. CT angiography of the aorta is superior to transesophageal echocardiography for determining stroke subtypes in patients with cryptogenic ischemic stroke. *Cerebrovasc Dis*. 2012;33(4):322–8; Epub 2012/02/22.
  50. Di Tullio MR, Russo C, Jin Z, Sacco RL, Mohr JP, Homma S. Aortic arch plaques and risk of recurrent stroke and death. *Circulation*. 2009;119(17):2376–82; Epub 2009/04/22.
  51. de Weert TT, Ouhlous M, Meijering E, Zondervan PE, Hendriks JM, van Sambeek MR, et al. In vivo characterization and quantification of atherosclerotic carotid plaque components with multidetector computed tomography and histopathological correlation. *Arterioscler Thromb Vasc Biol*. 2006;26(10):2366–72; Epub 2006/08/12.
  52. Gupta A, Baradaran H, Schweitzer AD, Kamel H, Pandya A, Delgado D, et al. Carotid plaque MRI and stroke risk: a systematic review and meta-analysis. *Stroke*. 2013;44(11):3071–7; Epub 2013/08/31.
  53. Rothwell PM, Gibson R, Warlow CP. Interrelation between plaque surface morphology and degree of stenosis on carotid angiograms and the risk of ischemic stroke in patients with symptomatic carotid stenosis. On behalf of the European Carotid Surgery Trialists' Collaborative Group. *Stroke*. 2000;31(3):615–21; Epub 2000/03/04.
  54. U-King-Im JM, Fox AJ, Aviv RI, Howard P, Yeung R, Moody AR, et al. Characterization of carotid plaque hemorrhage: a CT angiography and MR intraplaque hemorrhage study. *Stroke*. 2010;41(8):1623–9; Epub 2010/06/26.
  55. Wardlaw JM, Chappell FM, Best JJ, Wartolowska K, Berry E. Non-invasive imaging compared with intra-arterial angiography in the diagnosis of symptomatic carotid stenosis: a meta-analysis. *Lancet*. 2006;367(9521):1503–12; Epub 2006/05/09.
  56. de Rooij NK, Linn FH, van der Plas JA, Algra A, Rinkel GJ. Incidence of subarachnoid haemor-

- rhage: a systematic review with emphasis on region, age, gender and time trends. *J Neurol Neurosurg Psychiatry*. 2007;78(12):1365–72; Epub 2007/05/02.
57. Nieuwkamp DJ, Setz LE, Algra A, Linn FH, de Rooij NK, Rinkel GJ. Changes in case fatality of aneurysmal subarachnoid haemorrhage over time, according to age, sex, and region: a meta-analysis. *Lancet Neurol*. 2009;8(7):635–42; Epub 2009/06/09.
  58. van Gijn J, Kerr RS, Rinkel GJ. Subarachnoid haemorrhage. *Lancet*. 2007;369(9558):306–18.
  59. Wiebers DO, Whisnant JP, Huston J 3rd, Meissner I, Brown RD Jr, Piegras DG, et al. Unruptured intracranial aneurysms: natural history, clinical outcome, and risks of surgical and endovascular treatment. *Lancet*. 2003;362(9378):103–10; Epub 2003/07/18.
  60. Bousset L, Rayz V, McCulloch C, Martin A, Acevedo-Bolton G, Lawton M, et al. Aneurysm growth occurs at region of low wall shear stress: patient-specific correlation of hemodynamics and growth in a longitudinal study. *Stroke*. 2008;39(11):2997–3002; Epub 2008/08/09.
  61. Dhar S, Tremmel M, Mocco J, Kim M, Yamamoto J, Siddiqui AH, et al. Morphology parameters for intracranial aneurysm rupture risk assessment. *Neurosurgery*. 2008;63(2):185–96; discussion 96–7. Epub 2008/09/18.
  62. Morita A, Kirino T, Hashi K, Aoki N, Fukuhara S, Hashimoto N, et al. The natural course of unruptured cerebral aneurysms in a Japanese cohort. *N Engl J Med*. 2012;366(26):2474–82; Epub 2012/06/29.
  63. Raghavan ML, Ma B, Harbaugh RE. Quantified aneurysm shape and rupture risk. *J Neurosurg*. 2005;102(2):355–62; Epub 2005/03/03.
  64. Backes D, Vergouwen MDI, Groenestege ATT, Bor ASE, Velthuis BK, Greving JP, et al. PHASES score for prediction of intracranial aneurysm growth. *Stroke*. 2015;46(5):1221–6.
  65. Greving JP, Wermer MJH, Brown RD, Morita A, Juvela S, Yonekura M, et al. Development of the PHASES score for prediction of risk of rupture of intracranial aneurysms: a pooled analysis of six prospective cohort studies. *Lancet Neurol*. 2014;13(1):59–66.
  66. McCormack RF, Hutson A. Can computed tomography angiography of the brain replace lumbar puncture in the evaluation of acute-onset headache after a negative noncontrast cranial computed tomography scan? *Acad Emerg Med Off J Soc Acad Emerg Med*. 2010;17(4):444–51; Epub 2010/04/08.
  67. Guo W, He XY, Li XF, Qian DX, Yan JQ, Bu DL, et al. Meta-analysis of diagnostic significance of sixty-four-row multi-section computed tomography angiography and three-dimensional digital subtraction angiography in patients with cerebral artery aneurysm. *J Neurol Sci*. 2014;346(1–2):197–203; Epub 2014/09/10.
  68. Bechan RS, van Rooij SB, Sprengers ME, Peluso JP, Sluzewski M, Majoie CB, et al. CT angiography versus 3D rotational angiography in patients with subarachnoid hemorrhage. *Neuroradiology*. 2015;57(12):1239–46; Epub 2015/09/06.
  69. Kalra VB, Wu X, Matouk CC, Malhotra A. Use of follow-up imaging in isolated perimesencephalic subarachnoid hemorrhage: a meta-analysis. *Stroke*. 2015;46(2):401–6; Epub 2014/12/20.
  70. Rinkel GJ, Wijndicks EF, Vermeulen M, Ramos LM, Tanghe HL, Hasan D, et al. Nonaneurysmal perimesencephalic subarachnoid hemorrhage: CT and MR patterns that differ from aneurysmal rupture. *AJNR Am J Neuroradiol*. 1991;12(5):829–34; Epub 1991/09/01.
  71. Schaafsma JD, Velthuis BK, Majoie CB, van den Berg R, Brouwer PA, Barkhof F, et al. Intracranial aneurysms treated with coil placement: test characteristics of follow-up MR angiography—multi-center study. *Radiology*. 2010;256(1):209–18; Epub 2010/05/28.
  72. Roele ED, Timmer V, Vaassen LAA, van Kroonenburgh A, Postma AA. Dual-energy CT in head and neck imaging. *Curr Radiol Rep*. 2017;5(5):19; Epub 2017/04/25.
  73. Luo Z, Wang D, Sun X, Zhang T, Liu F, Dong D, et al. Comparison of the accuracy of subtraction CT angiography performed on 320-detector row volume CT with conventional CT angiography for diagnosis of intracranial aneurysms. *Eur J Radiol*. 2012;81(1):118–22; Epub 2011/06/03.
  74. Josephson CB, White PM, Krishan A, Al-Shahi SR. Computed tomography angiography or magnetic resonance angiography for detection of intracranial vascular malformations in patients with intracerebral haemorrhage. *Cochrane Database Syst Rev*. 2014;9:CD009372; Epub 2014/09/02.
  75. van Asch CJ, Velthuis BK, Rinkel GJ, Algra A, de Kort GA, Witkamp TD, et al. Diagnostic yield and accuracy of CT angiography, MR angiography, and digital subtraction angiography for detection of macrovascular causes of intracerebral haemorrhage: prospective, multicentre cohort study. *BMJ*. 2015;351:h5762; Epub 2015/11/11.
  76. Willems PW, Taeshineetanakul P, Schenk B, Brouwer PA, Terbrugge KG, Krings T. The use of 4D-CTA in the diagnostic work-up of brain arteriovenous malformations. *Neuroradiology*. 2012;54(2):123–31; Epub 2011/04/06.
  77. Chandran A, Radon M, Biswas S, Das K, Puthuran M, Nahser H. Novel use of 4D-CTA in imaging of intracranial aneurysms in an acutely ruptured arteriovenous malformation: is this the way forward? *J Neurointerv Surg*. 2016;8(9):e36; Epub 2015/07/17.
  78. Rodriguez-Luna D, Coscojuela P, Rodriguez-Villatoro N, Juega JM, Boned S, Muchada M, et al. Multiphase CT angiography improves prediction of intracerebral hemorrhage expansion. *Radiology*. 2017;285(3):932–40; Epub 2017/07/06.
  79. Rodriguez-Luna D, Dowlatshahi D, Avivi RI, Molina CA, Silva Y, Dzialowski I, et al. Venous phase of computed tomography angiography increases spot sign detection, but intracerebral hemorrhage expansion is greater in spot signs detected in arterial phase. *Stroke*. 2014;45(3):734–9; Epub 2014/02/01.



80. Dowlatshahi D, Brouwers HB, Demchuk AM, Hill MD, Aviv RI, Uffholz LA, et al. Predicting intracerebral hemorrhage growth with the spot sign: the effect of onset-to-scan time. *Stroke*. 2016;47(3):695–700; Epub 2016/02/06.
81. Dentali F, Gianni M, Crowther MA, Ageno W. Natural history of cerebral vein thrombosis: a systematic review. *Blood*. 2006;108(4):1129–34; Epub 2006/04/13.
82. Stam J. Thrombosis of the cerebral veins and sinuses. *N Engl J Med*. 2005;352(17):1791–8; Epub 2005/04/29.
83. Gosk-Bierska I, Wysokinski W, Brown RD Jr, Karnicki K, Grill D, Wiste H, et al. Cerebral venous sinus thrombosis: incidence of venous thrombosis recurrence and survival. *Neurology*. 2006;67(5):814–9; Epub 2006/09/13.
84. Poon CS, Chang JK, Swarnkar A, Johnson MH, Wasenko J. Radiologic diagnosis of cerebral venous thrombosis: pictorial review. *AJR Am J Roentgenol*. 2007;189(6 Suppl):S64–75; Epub 2007/12/06.
85. Khandelwal N, Agarwal A, Kochhar R, Bapuraj JR, Singh P, Prabhakar S, et al. Comparison of CT venography with MR venography in cerebral sinovenous thrombosis. *AJR Am J Roentgenol*. 2006;187(6):1637–43; Epub 2006/11/23.
86. Leach JL, Fortuna RB, Jones BV, Gaskill-Shipley MF. Imaging of cerebral venous thrombosis: current techniques, spectrum of findings, and diagnostic pitfalls. *Radiographics*. 2006;26(Suppl 1):S19–41; discussion S2–3. Epub 2006/10/20.
87. Ishimaru H, Ochi M, Morikawa M, Takahata H, Matsuoka Y, Koshiishi T, et al. Accuracy of pre- and postcontrast 3D time-of-flight MR angiography in patients with acute ischemic stroke: correlation with catheter angiography. *AJNR Am J Neuroradiol*. 2007;28(5):923–6; Epub 2007/05/15.
88. Sugino T, Mikami T, Ohtaki S, Hirano T, Iihoshi S, Houkin K, et al. Assessment of moyamoya disease using multidetector row computed tomography. *J Stroke Cerebrovasc Dis*. 2013;22(5):644–9; Epub 2012/03/01.
89. Tian B, Jiang Y, Kang Q, Xu B, Liu R, Liu Q, et al. Comparative study of 4D CTA and DSA for vascular assessment in moyamoya disease. *Clin Imaging*. 2017;48:74–8; Epub 2017/10/22.
90. Okada Y, Shima T, Nishida M, Yamane K, Yamada T, Yamanaka C. Effectiveness of superficial temporal artery-middle cerebral artery anastomosis in adult moyamoya disease: cerebral hemodynamics and clinical course in ischemic and hemorrhagic varieties. *Stroke*. 1998;29(3):625–30; Epub 1998/03/20.
91. Besachio DA, Ziegler JI, Duncan TD, Wanebo JS. Computed tomographic angiography in evaluation of superficial temporal to middle cerebral artery bypass. *J Comput Assist Tomogr*. 2010;34(3):437–9; Epub 2010/05/26.
92. Teksam M, McKinney A, Truwit CL. Multi-slice CT angiography in evaluation of extracranial-intracranial bypass. *Eur J Radiol*. 2004;52(3):217–20; Epub 2004/11/17.
93. Fleck SK, Langner S, Baldauf J, Kirsch M, Rosenstengel C, Schroeder HW. Blunt cranio-cervical artery injury in cervical spine lesions: the value of CT angiography. *Acta Neurochir*. 2010;152(10):1679–86; Epub 2010/05/25.
94. Fleck SK, Langner S, Baldauf J, Kirsch M, Kohlmann T, Schroeder HW. Incidence of blunt cranio-cervical artery injuries: use of whole-body computed tomography trauma imaging with adapted computed tomography angiography. *Neurosurgery*. 2011;69(3):615–23; discussion 23–4. Epub 2011/04/19.
95. Langner S, Fleck S, Kirsch M, Petrik M, Hosten N. Whole-body CT trauma imaging with adapted and optimized CT angiography of the cranio-cervical vessels: do we need an extra screening examination? *AJNR Am J Neuroradiol*. 2008;29(10):1902–7; Epub 2008/09/12.
96. Nguyen D, Platon A, Shanmuganathan K, Mirvis SE, Becker CD, Poletti PA. Evaluation of a single-pass continuous whole-body 16-MDCT protocol for patients with polytrauma. *AJR Am J Roentgenol*. 2009;192(1):3–10; Epub 2008/12/23.
97. Provenzale JM, Sarikaya B. Comparison of test performance characteristics of MRI, MR angiography, and CT angiography in the diagnosis of carotid and vertebral artery dissection: a review of the medical literature. *AJR Am J Roentgenol*. 2009;193(4):1167–74; Epub 2009/09/23.
98. Vertinsky AT, Schwartz NE, Fischbein NJ, Rosenberg J, Albers GW, Zaharchuk G. Comparison of multidetector CT angiography and MR imaging of cervical artery dissection. *AJNR Am J Neuroradiol*. 2008;29(9):1753–60; Epub 2008/07/19.
99. Eastman AL, Chason DP, Perez CL, McNulty AL, Minei JP. Computed tomographic angiography for the diagnosis of blunt cervical vascular injury: is it ready for primetime? *J Trauma*. 2006;60(5):925–9; discussion 9. Epub 2006/05/12.
100. Rodallec MH, Marteau V, Gerber S, Desmottes L, Zins M. Cranio-cervical arterial dissection: spectrum of imaging findings and differential diagnosis. *Radiographics*. 2008;28(6):1711–28; Epub 2008/10/22.
101. Schievink WI. Spontaneous dissection of the carotid and vertebral arteries. *N Engl J Med*. 2001;344(12):898–906; Epub 2001/03/22.
102. Chen CJ, Tseng YC, Lee TH, Hsu HL, See LC. Multisession CT angiography compared with catheter angiography in diagnosing vertebral artery dissection. *AJNR Am J Neuroradiol*. 2004;25(5):769–74; Epub 2004/05/14.



# CT Perfusion

# 6

Douglas Joseph Martin and Max Wintermark

## Contents

6.1	<b>Introduction</b> .....	61
6.2	<b>Image Acquisition</b> .....	62
6.3	<b>Image Processing</b> .....	62
6.4	<b>Applications</b> .....	63
6.5	<b>Case</b> .....	64
	<b>References</b> .....	66

## 6.1 Introduction

The brain is highly metabolically active but has virtually no internal energy reserves, instead depending on a constant high level of blood flow in order to maintain its function. As a result, it is of critical importance that cerebral blood flow, or CBF, is maintained in the optimal range. A decrease in brain perfusion, as is seen in stroke, results in rapid loss of function followed by irreversible tissue injury [1]. Conversely, an abnormal elevation of perfusion can be a marker of pathology as is seen with high-grade glial tumours such as glioblastoma [2]. The CBF is determined by the balance between the cerebral perfusion pressure, determined from the mean

arterial pressure and intracranial pressure, and the cerebrovascular resistance [3]. Because of its critical importance in health and disease, a variety of methods, using both computed tomography (CT) and magnetic resonance imaging (MRI), have been developed for measuring CBF and other indicators of brain perfusion. CT perfusion is a commonly used non-invasive technique for determining the CBF as well as its related parameters, cerebral blood volume (CBV) and mean transit time (MTT) [4–7]. Following a bolus injection of intravenous contrast, serial CT scans of the head are performed as the contrast arrives and passes through the brain tissue. Based on the change in attenuation, the CBF and CBV can be calculated with a high degree of accuracy. In this chapter, we will review the technical aspects of CT perfusion and highlight clinical applications of the technique, with particular emphasis on its role in the diagnosis and treatment of acute ischaemic stroke.

---

D. J. Martin · M. Wintermark (✉)  
Department of Radiology, Stanford University,  
Stanford, CA, USA  
e-mail: [dougjoemartin@stanford.edu](mailto:dougjoemartin@stanford.edu); [mwinterm@stanford.edu](mailto:mwinterm@stanford.edu)

## 6.2 Image Acquisition

The theoretical basis of CT perfusion imaging and important technical considerations are well described in the literature [3–5]. CT perfusion requires a bolus of intravenous contrast followed by rapid sequential CT scans of the head. The contrast bolus must be large enough to be easily detected and tight enough to approximate an instantaneous bolus in order to satisfy key mathematical assumptions [4, 5, 7]. This is achieved by injecting 35–50 mL of a contrast agent with an iodine concentration of at least 300 mg/mL at a rate of 4–7 mL/s followed by a 20–40 mL saline flush. These injection rates and volumes necessitate use of a large-bore (18–20 gauge) intravenous line in the antecubital fossa. After a brief delay, images of the head are acquired in two phases; an initial rapid acquisition phase with images obtained every second for 30–45 s and a washout phase with images taken every 2–3 s for an additional 30–45 s. The initial rapid acquisition phase is necessary to accurately describe the initial inflow of contrast; once the contrast concentration has peaked on the arterial side, the washout phase can be acquired with less frequent images in order to reduce radiation dose. Radiation dose is further reduced by lowering the tube voltage of the CT scanner to 80 keV and reducing the tube current to the lowest value that gives an acceptable signal-to-noise ratio (typically 100 mAs). Once these measures have been implemented, the additional radiation dose for CT perfusion is approximately 3 mSv, only slightly more than a non-contrast head CT and comparable to the annual background radiation dose from environmental sources [8].

Beyond the bolus timing and image acquisition parameters, it is critical that the CT perfusion includes the relevant brain regions for analysis. The latest generation of CT scanners is capable of covering the entire brain in a single scan. However, while older CT scanners are also capable of performing CT perfusion, their smaller coverage area requires that they acquire the images in multiple sections. This can either be done by repeating the scan at the next level with a second contrast bolus or by operating the scanner in “toggling” mode,

where the scanner table is toggled back and forth between two positions [8, 9]. With the former, the acquisition parameters can be identical to an ideal scan at the cost of additional contrast and radiation. With the latter, temporal resolution is decreased (each position is scanned every 2–3 s), but the contrast dose is unchanged and radiation dose is slightly decreased.

## 6.3 Image Processing

Once the images have been acquired, the data must be processed to generate perfusion maps. Accurate calculation of CBF and CBV first requires identification of regions of interest to define the arterial input and venous outflow [4, 5]. The arterial input is typically defined from one of the arteries of the circle of Willis, and the venous outflow is typically defined from the superior sagittal sinus. These functions are then compared with the CT density of each region of the brain, or voxel, as a function of time. After correcting for several parameters, including the attenuation of the underlying brain tissue and differences in haematocrit between the arteries and capillary bed, this yields the CBV for each voxel of brain tissue. Calculation of CBF is slightly more complex mathematically. One of the key assumptions in calculating the CBF in CT perfusion is that the contrast bolus is *instantaneous*, reaching its maximum intensity at  $t = 0$ . This will clearly never be true in a real patient; a variety of techniques have been proposed to account for this shortcoming, the most widely accepted and validated of which is known as deconvolution [10–12]. This technique removes the effect of the arterial input function on the bolus, creating a theoretical residue function that more closely approximates the CBF after an ideal bolus (Fig. 6.1). While this process is computationally demanding, advances in computer technology have allowed its widespread adoption. Once CBF and CBV have been determined, maps of the mean transit time and  $T_{\max}$  (time to maximum contrast enhancement) can be calculated.

These perfusion maps can be generated in a manual, semiautomated or fully automated fash-

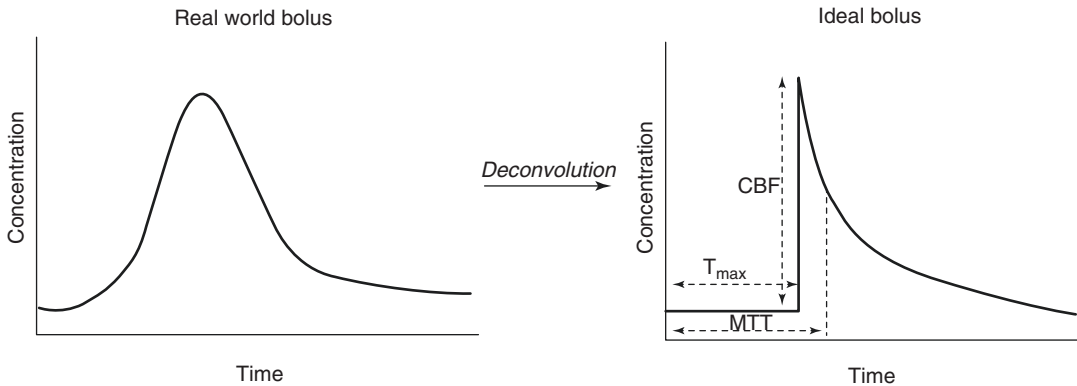


**Fig. 6.1** Schematic illustration of conversion of a real-world concentration–time curve to an idealized curve for calculation of CBF. Deconvolution is the mathematical

process by which the time dependence of the arterial input function is removed, creating a single tracer input

ion on a number of native or third-party platforms. While CT perfusion has been extensively validated, it is worth noting that there are multiple potential sources of variation in the CBV/CBF calculation, particularly the choice of the arterial input function and the precise algorithm selected [7, 10, 13–19]. Studies comparing both interobserver variability in a single platform and different software platforms have shown differences of up to 30% in the size of a target volume on the perfusion map. One of the driving forces behind the development of fully automated processing software has been the standardization of the perfusion maps within an institution. While this does not address the issue of variability between platforms, it ensures application of a uniform standard for clinical decision making within an institution.

## 6.4 Applications

While CT perfusion has been applied to numerous areas of neuroradiology, including the study of vasospasm after subarachnoid haemorrhage [20, 21], Moyamoya disease [22, 23], primary brain tumours [2, 24] and head and neck malignancy [25], the primary driver of its development has been and continues to be ischaemic stroke [8, 11, 19, 26]. Ischaemic strokes are caused by disruption of arterial blood flow to the brain. The resultant hypoxia rapidly leads to neuronal dysfunction, ulti-

mately resulting in permanent disability or death. Treatment for acute ischaemic stroke depends on restoring blood flow to the affected tissue before cell death occurs. Because of the exquisite sensitivity of neurons to hypoxia, the process of cell death begins mere minutes after the loss of blood flow.

CT perfusion plays a key role in the care of stroke patients, both in the initial diagnosis of stroke and in the selection of patients for advanced therapy [6, 8, 11, 26, 27]. Head CT, while exquisitely sensitive for the detection of intracranial haemorrhage, has poor sensitivity and specificity for stroke in the acute setting. MRI offers increased sensitivity and specificity but at a cost of time and availability. CT perfusion is much more sensitive and specific than non-contrast CT during the acute phase, with ischaemic strokes characterized by decreased CBF with increased  $T_{\max}$  and MTT [26]. This would be of limited utility if CT perfusion were only able to identify irreversibly infarcted tissue; however, the study of brain perfusion in ischaemic stroke has introduced the concept of ischaemic penumbra [1, 9, 11, 28, 29]. The penumbra is a region of brain tissue, typically at the periphery of an infarct, where the CBF is reduced below the level for normal neuronal function but not yet to the point where irreversible cell death occurs. By restoring blood flow to this tissue, it is possible to prevent further infarction and preserve brain function.

For the past 20 years, the mainstay of stroke therapy has been the so-called ‘clot-buster’ drugs, typified by tissue plasminogen activator (tPA). First approved for clinical use in 1995 [30], tPA works through the body’s natural clot lysing mechanisms to open thrombosed vessels. While the use of tPA has been a revolution in the treatment of stroke, its success comes with many qualifiers. Significantly, tPA is only effective if administered quickly after the onset of symptoms (initially within 3 h, later expanded to 4.5 h in select patients), and it performs relatively poorly when there is occlusion of one of the large proximal intracranial arteries [30, 31]. These limitations, and the success of angiographic intervention in cardiology, have led to the development of mechanical thrombectomy, an angiographic technique whereby clot is physically removed from the affected arteries. Developed shortly after the introduction of tPA, initial trials of mechanical thrombectomy failed to show any benefit relative to the use of intravenous tPA [32, 33]. Despite the initially underwhelming results, multiple lines of evidence continued to suggest that thrombectomy remained a viable strategy, and subsequent trials have vindicated its use [33–39]. Two key changes in the past decade have seen a revival of the technique—the development of second-generation stentriever devices and the use of advanced imaging, including CT and MR perfusion, for patient selection. By targeting patients with a significant volume of ischaemic penumbra, the DEFUSE 3 trial has shown a significant benefit for stroke patients beyond the tPA window, up to 16 h after the onset of symptoms [27]. Along with the DAWN trial [40], this has opened the door for a new era in stroke therapy.

---

## 6.5 Case

To illustrate the role of CT perfusion in the diagnosis and treatment of acute ischaemic stroke, we offer two companion cases. In the first case, a 40-year-old man with a history of rheumatic heart disease status post-aortic and mitral valve

replacement was found down at work. By the time paramedics arrived, he had regained consciousness but was aphasic with a right hemiplegia. He was brought to the emergency department as a stroke code and was found to have an NIH stroke scale of 17. He received tPA after an initial non-contrast head CT was negative for haemorrhage, and CT perfusion as well as a CTA of the head and neck were obtained. On CTP, there was a large area of delayed perfusion with a smaller area of decreased CBF and CBV (Fig. 6.2), and CTA showed a proximal left MCA occlusion. The patient was taken for mechanical thrombectomy and following successful revascularization and a short inpatient stay, his NIH stroke scale improved to 2.

Our second patient is an 89-year-old woman with a history of atrial fibrillation on warfarin who was heard to fall from her bed at approximately 7:30 a.m. She was brought to the emergency department, where she was noted to have altered mental status with some facial bruising when the clinical team noted that she was not moving her left side (NIH stroke scale 22). An initial head CT was negative, and she underwent CT perfusion and head and neck CTA. This showed delayed perfusion involving both the right MCA and ACA territories with corresponding vascular occlusions; however, unlike the first patient, the area of delayed perfusion had a matching decrease in CBF and CBV in those territories (Fig. 6.3), consistent with an established infarct. No therapy was given and in accordance with the patient’s prior health care directives she was transitioned to hospice.

In both cases, CT perfusion rapidly confirmed the clinical diagnosis and facilitated appropriate triage. While the outcome in the second case was poor, CT perfusion confirmed that, although the head CT was unrevealing at presentation, the patient had a large stroke that had already progressed beyond the point where intervention was likely to show any benefit. As stroke therapy continues to evolve, CT perfusion will continue to play an active role in guiding clinical decision-making.

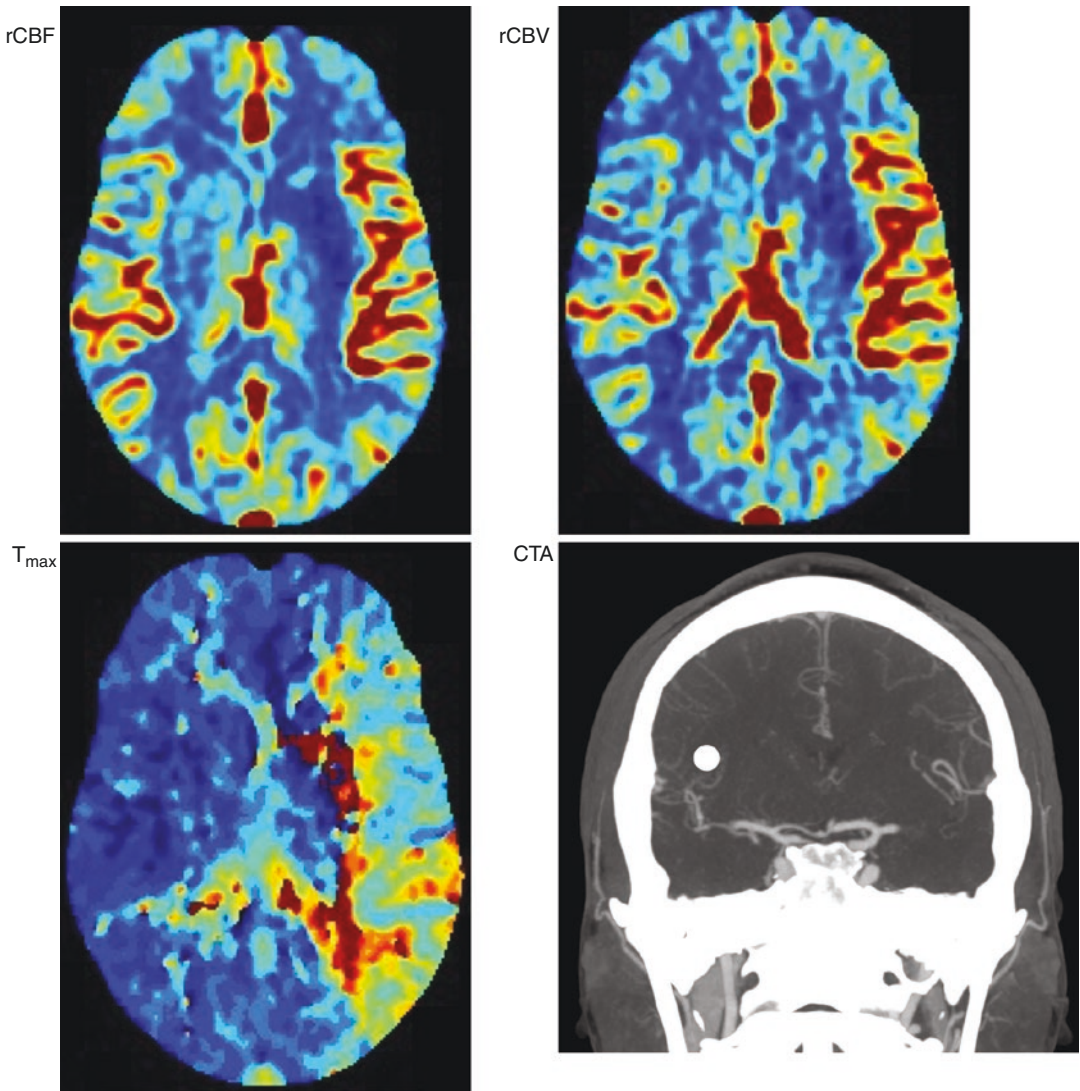


**Fig. 6.2** CT perfusion maps and CTA images for a patient with a left MCA occlusion. The colour gradient is arranged so that shades of blue represent low values and shades of red represent high values. There is a small area of decreased rCBV and rCBF in the left basal ganglia,

however the  $T_{\max}$  map shows delayed perfusion throughout the left MCA territory (most pronounced posteriorly). A single coronal MIP image of the CTA shows the occluded vessel

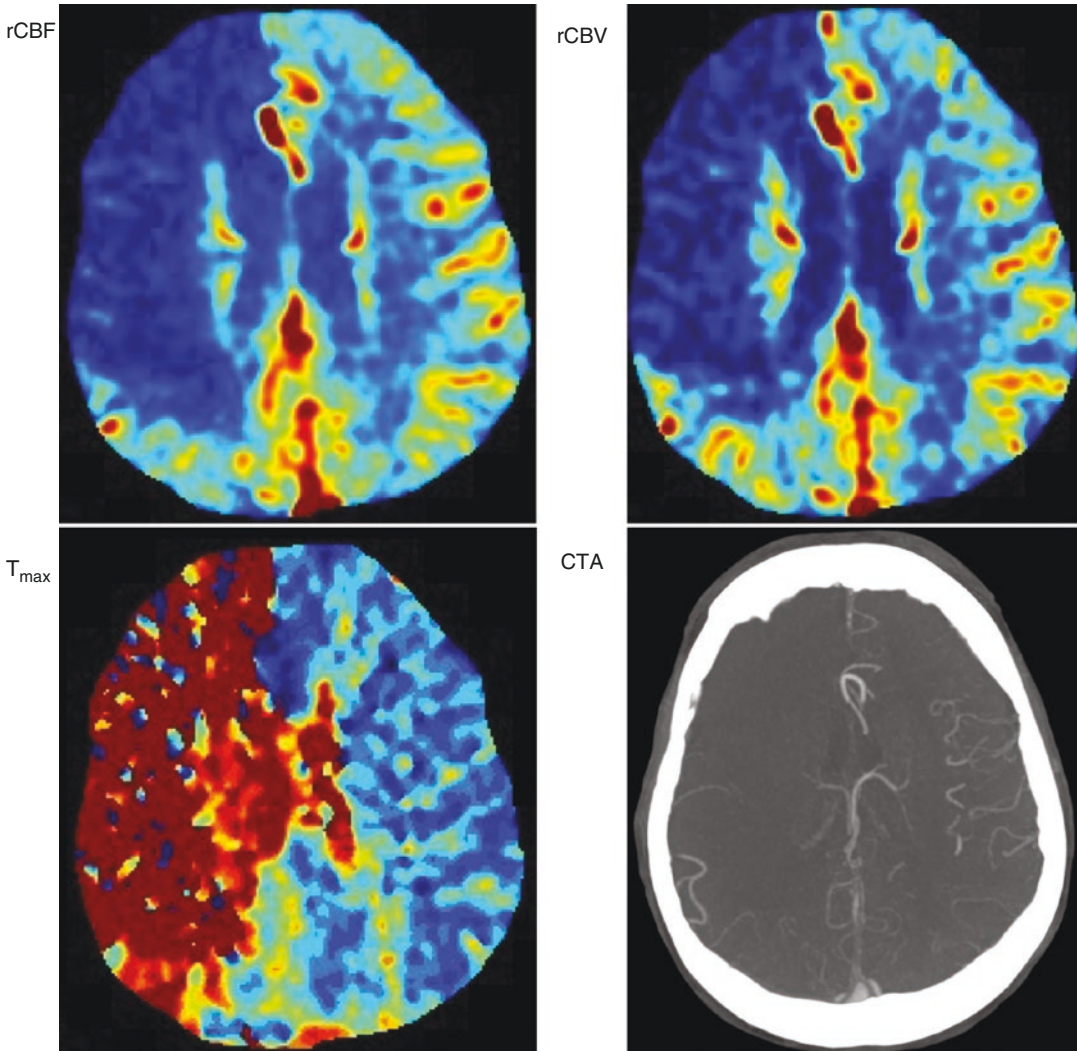


**Fig. 6.3** CT perfusion maps and CTA images for a patient with tandem right ACA and MCA occlusions. The colour gradient is arranged so that shades of blue represent low values and shades of red represent high values.

There is decreased rCBV and rCBF and increased  $T_{\max}$  throughout the right MCA and ACA territories. A single axial MIP image shows absent vascular flow in these territories

## References

1. Hossmann KA. Viability thresholds and the penumbra of focal ischemia. *Ann Neurol*. 1994;36(4):557–65.
2. Jain R, Gutierrez J, Narang J, Scarpace L, Schultz LR, Lemke N, et al. In vivo correlation of tumor blood volume and permeability with histologic and molecular angiogenic markers in gliomas. *AJNR Am J Neuroradiol*. 2011;32(2):388–94.
3. Axel L. Cerebral blood flow determination by rapid-sequence computed tomography: theoretical analysis. *Radiology*. 1980;137(3):679–86.
4. Konstas AA, Goldmakher GV, Lee TY, Lev MH. Theoretic basis and technical implementations of CT perfusion in acute ischemic stroke, part 1: theoretic basis. *AJNR Am J Neuroradiol*. 2009;30(4):662–8.
5. Konstas AA, Goldmakher GV, Lee TY, Lev MH. Theoretic basis and technical implementations of CT perfusion in acute ischemic stroke, part 2: technical implementations. *AJNR Am J Neuroradiol*. 2009;30(5):885–92.
6. Donahue J, Wintermark M. Perfusion CT and acute stroke imaging: foundations, applications, and literature review. *J Neuroradiol*. 2015;42(1):21–9.

7. Cenic A, Nabavi DG, Craen RA, Gelb AW, Lee TY. Dynamic CT measurement of cerebral blood flow: a validation study. *AJNR Am J Neuroradiol*. 1999;20(1):63–73.
8. Konstas AA, Wintermark M, Lev MH. CT perfusion imaging in acute stroke. *Neuroimaging Clin N Am*. 2011;21(2):215–38. ix
9. Heit JJ, Wintermark M. Perfusion computed tomography for the evaluation of acute ischemic stroke: strengths and pitfalls. *Stroke*. 2016;47(4):1153–8.
10. Abels B, Klotz E, Tomandl BF, Kloska SP, Lell MM. Perfusion CT in acute ischemic stroke: a qualitative and quantitative comparison of deconvolution and maximum slope approach. *AJNR Am J Neuroradiol*. 2010;31(9):1690–8.
11. Bivard A, Levi C, Spratt N, Parsons M. Perfusion CT in acute stroke: a comprehensive analysis of infarct and penumbra. *Radiology*. 2013;267(2):543–50.
12. Wittsack HJ, Wohlschläger AM, Ritzl EK, Kleiser R, Cohnen M, Seitz RJ, et al. CT-perfusion imaging of the human brain: advanced deconvolution analysis using circulant singular value decomposition. *Comput Med Imaging Graph*. 2008;32(1):67–77.
13. Wintermark M, Thiran JP, Maeder P, Schnyder P, Meuli R. Simultaneous measurement of regional cerebral blood flow by perfusion CT and stable xenon CT: a validation study. *AJNR Am J Neuroradiol*. 2001;22(5):905–14.
14. Abels B, Villablanca JP, Tomandl BF, Uder M, Lell MM. Acute stroke: a comparison of different CT perfusion algorithms and validation of ischaemic lesions by follow-up imaging. *Eur Radiol*. 2012;22(12):2559–67.
15. Copen WA, Deipolyi AR, Schaefer PW, Schwamm LH, González RG, Wu O. Exposing hidden truncation-related errors in acute stroke perfusion imaging. *AJNR Am J Neuroradiol*. 2015;36(4):638–45.
16. Fahmi F, Marquering HA, Streekstra GJ, Beenen LF, Velthuis BK, VanBavel E, et al. Differences in CT perfusion summary maps for patients with acute ischemic stroke generated by 2 software packages. *AJNR Am J Neuroradiol*. 2012;33(11):2074–80.
17. Ibaraki M, Ohmura T, Matsubara K, Kinoshita T. Reliability of CT perfusion-derived CBF in relation to hemodynamic compromise in patients with cerebrovascular steno-occlusive disease: a comparative study with 15O PET. *J Cereb Blood Flow Metab*. 2015;35(8):1280–8.
18. Kudo K, Sasaki M, Yamada K, Momoshima S, Utsunomiya H, Shirato H, et al. Differences in CT perfusion maps generated by different commercial software: quantitative analysis by using identical source data of acute stroke patients. *Radiology*. 2010;254(1):200–9.
19. Wintermark M, Smith WS, Ko NU, Quist M, Schnyder P, Dillon WP. Dynamic perfusion CT: optimizing the temporal resolution and contrast volume for calculation of perfusion CT parameters in stroke patients. *AJNR Am J Neuroradiol*. 2004;25(5):720–9.
20. Dankbaar JW, de Rooij NK, Rijdsdijk M, Velthuis BK, Frijns CJ, Rinkel GJ, et al. Diagnostic threshold values of cerebral perfusion measured with computed tomography for delayed cerebral ischemia after aneurysmal subarachnoid hemorrhage. *Stroke*. 2010;41(9):1927–32.
21. Washington CW, Zipfel GJ. Hemorrhage PitIM-dCCotCCMoS. detection and monitoring of vasospasm and delayed cerebral ischemia: a review and assessment of the literature. *Neurocrit Care*. 2011;15(2):312–7.
22. Smith LM, Elkins JS, Dillon WP, Schaeffer S, Wintermark M. Perfusion-CT assessment of the cerebrovascular reserve: a revisit to the acetazolamide challenges. *J Neuroradiol*. 2008;35(3):157–64.
23. Hashimoto A, Mikami T, Komatsu K, Noshiro S, Hirano T, Wanibuchi M, et al. Assessment of hemodynamic compromise using computed tomography perfusion in combination with 123I-IMP single-photon emission computed tomography without acetazolamide challenge test. *J Stroke Cerebrovasc Dis*. 2017;26(3):627–35.
24. Cenic A, Nabavi DG, Craen RA, Gelb AW, Lee TY. A CT method to measure hemodynamics in brain tumors: validation and application of cerebral blood flow maps. *AJNR Am J Neuroradiol*. 2000;21(3):462–70.
25. Srinivasan A, Mohan S, Mukherji SK. Biologic imaging of head and neck cancer: the present and the future. *AJNR Am J Neuroradiol*. 2012;33(4):586–94.
26. Merino JG, Warach S. Imaging of acute stroke. *Nat Rev Neurol*. 2010;6(10):560–71.
27. Albers GW, Marks MP, Kemp S, Christensen S, Tsai JP, Ortega-Gutierrez S, et al. Thrombectomy for stroke at 6 to 16 hours with selection by perfusion imaging. *N Engl J Med*. 2018;378(8):708–18.
28. Kamalian S, Konstas AA, Maas MB, Payabvash S, Pomerantz SR, Schaefer PW, et al. CT perfusion mean transit time maps optimally distinguish benign oligemia from true “at-risk” ischemic penumbra, but thresholds vary by postprocessing technique. *AJNR Am J Neuroradiol*. 2012;33(3):545–9.
29. Olivot JM, Mlynash M, Thijs VN, Kemp S, Lansberg MG, Wechsler L, et al. Optimal Tmax threshold for predicting penumbral tissue in acute stroke. *Stroke*. 2009;40(2):469–75.
30. Group NtONdASr-PSS. Tissue plasminogen activator for acute ischemic stroke. *N Engl J Med*. 1995;333(24):1581–7.
31. Saqqur M, Uchino K, Demchuk AM, Molina CA, Garami Z, Calleja S, et al. Site of arterial occlusion identified by transcranial Doppler predicts the response to intravenous thrombolysis for stroke. *Stroke*. 2007;38(3):948–54.
32. Flint AC, Duckwiler GR, Budzik RF, Liebeskind DS, Smith WS, Committee MaMMW. Mechanical thrombectomy of intracranial internal carotid occlusion: pooled results of the MERCI and multi MERCI part I trials. *Stroke*. 2007;38(4):1274–80.
33. Almekhlafi MA, Menon BK, Freiheit EA, Demchuk AM, Goyal M. A meta-analysis of observational intra-arterial stroke therapy studies using the Merci device, penumbra system, and retrievable stents. *AJNR Am J Neuroradiol*. 2013;34(1):140–5.



34. Wheeler HM, Mlynash M, Inoue M, Tipiririni A, Liggins J, Bammer R, et al. The growth rate of early DWI lesions is highly variable and associated with penumbral salvage and clinical outcomes following endovascular reperfusion. *Int J Stroke*. 2015;10(5):723–9.
35. Berkhemer OA, Fransen PS, Beumer D, van den Berg LA, Lingsma HF, Yoo AJ, et al. A randomized trial of intraarterial treatment for acute ischemic stroke. *N Engl J Med*. 2015;372(1):11–20.
36. Campbell BC, Mitchell PJ, Kleinig TJ, Dewey HM, Churilov L, Yassi N, et al. Endovascular therapy for ischemic stroke with perfusion-imaging selection. *N Engl J Med*. 2015;372(11):1009–18.
37. Goyal M, Demchuk AM, Menon BK, Eesa M, Rempel JL, Thornton J, et al. Randomized assessment of rapid endovascular treatment of ischemic stroke. *N Engl J Med*. 2015;372(11):1019–30.
38. Jovin TG, Chamorro A, Cobo E, de Miquel MA, Molina CA, Rovira A, et al. Thrombectomy within 8 hours after symptom onset in ischemic stroke. *N Engl J Med*. 2015;372(24):2296–306.
39. Saver JL, Goyal M, Bonafe A, Diener HC, Levy EI, Pereira VM, et al. Stent-retriever thrombectomy after intravenous t-PA vs. t-PA alone in stroke. *N Engl J Med*. 2015;372(24):2285–95.
40. Nogueira RG, Jadhav AP, Haussen DC, Bonafe A, Budzik RF, Bhuva P, et al. Thrombectomy 6 to 24 hours after stroke with a mismatch between deficit and infarct. *N Engl J Med*. 2018;378(1):11–21.



# Dual-Energy CT

# 7

Can Ozan Tan, Daan Kuppens, and Rajiv Gupta

## Contents

7.1	<b>Introduction</b> .....	70
7.2	<b>DECT System Technology</b> .....	71
7.2.1	Dual-Spin DECT .....	71
7.2.2	Dual-Source DECT .....	72
7.2.3	Single-Source Fast kVp-Switching DECT .....	72
7.2.4	“Sandwich” Detector DECT .....	73
7.2.5	Twin Beam DECT .....	73
7.2.6	Photon-Counting Multispectral CT .....	73
7.3	<b>Fundamental Principles of DECT</b> .....	74
7.4	<b>Practical Considerations</b> .....	75
7.4.1	Temporal Parameters .....	76
7.4.2	Image Reconstruction .....	76
7.4.3	Basis Material Decomposition .....	77
7.4.4	Virtual Non-Contrast (VNC) Images and Iodine Maps .....	77
7.4.5	Workflow and Other Considerations .....	78

---

C. O. Tan (✉)

Department of Radiology, Massachusetts General Hospital, Boston, MA, USA

Cerebrovascular Research Laboratory, Spaulding Rehabilitation Hospital, Boston, MA, USA

Harvard Medical School, Boston, MA, USA  
e-mail: [cotan@mgh.harvard.edu](mailto:cotan@mgh.harvard.edu)

D. Kuppens

Department of Radiology, Massachusetts General Hospital, Boston, MA, USA

Department of Technical Medicine, University of Twente, Enschede, The Netherlands

R. Gupta

Department of Radiology, Massachusetts General Hospital, Boston, MA, USA

Harvard Medical School, Boston, MA, USA

7.5	<b>Neuroradiology Applications of DECT</b> .....	78
7.5.1	Virtual Monochromatic Images .....	78
7.5.2	Material Decomposition .....	80
7.5.3	Quantification of the Contrast Medium .....	82
7.6	<b>Conclusion</b> .....	83
7.7	<b>Clinical Case</b> .....	83
	<b>References</b> .....	84

## 7.1 Introduction

X-ray computed tomography (CT) is the workhorse of modern medical imaging. Every year, millions of CT scans are performed around the world for a wide variety of indications, including acute stroke, trauma, and cancer. Majority of this imaging is done using a conventional, single-energy CT (SECT). In SECT, a single X-ray tube emitting a polychromatic X-ray beam is used to acquire a set of projection images of the patients via an energy integrating detector. The projection data are reconstructed into tomographic images reflecting X-ray attenuation. Dual-energy CT (DECT), the primary focus of this chapter, is a radical departure from this paradigm.

In DECT, multiple X-ray spectra are utilized to characterize material-specific photon attenuation. Since the atomic composition of different tissues influences the photon attenuation at different energies, the relative change in photon attenuation between different energy levels is indicative of material composition of each voxel. In other words, because tissue attenuation is both material and energy-specific, projection images acquired at different energies may be used for tissue characterization beyond what is possible with conventional SECT. This is a key advantage of DECT over SECT. Even though applications of DECT for clinical use were initially advocated in the 1970s [1–7], it is only recently that the technological and computational advances necessary for successful clinical implementation of DECT have become available.

For acquiring the projection data, the DECT scanner must use different energy spectra and separately record the high- and low-energy measurements. From a technical viewpoint, this ability has been implemented in the clinical practice using a variety of means which include the following paradigms.

1. Acquiring two independent CT scans of the same anatomy at two different energies (dual-spin DECT).
2. Simultaneous use of two different imaging chains with their own dedicated sources and detectors (dual-source DECT).
3. Using a single X-ray source that is capable of rapid switching between high- and low-energy levels and a detector with very fast readout capability (kVp Switching DECT).
4. Acquiring data sets at different energy levels using specialized detectors with two different scintillator layers, one of high-energy acquisition and the other for low-energy acquisition (Sandwich Detector DECT).
5. Splitting a single X-ray beam into high- and low-energy beams with the help of filters (TwinBeam DECT).
6. Using a so-called “photon-counting” detector that is able to count each arriving X-ray photon and sort it into different energy bins (Photon-Counting CT).

In the following section, we briefly describe these implementations.

## 7.2 DECT System Technology

### 7.2.1 Dual-Spin DECT

These CT systems acquire two independent scans sequentially using two different tube voltages [2, 6, 8], at the same table position or a range of table positions (see Fig. 7.1). This allows already established SECT technology to be used for each scan, albeit at different tube voltages. However, the time interval between the high- and low-energy acquisitions can pose a significant limitation on temporal resolution, which is critical when imaging moving organs such as heart and bowel. This temporal skew renders the two image

sets, when processed as a single dual-energy data set, susceptible to motion artifacts. The temporal skew also limits image quality when there is a change in contrast opacification such as CT angiograms or studies that involve tissue enhancement. These shortcomings can be mitigated, at least partially, by alternating scanning of different energy levels for each gantry rotation, instead of scanning the entire volume two times sequentially. Even then, the scans are at least one rotation time apart.

Dual-spin DECT is used in some scanners, such as some Aquilion ONE models (Toshiba, Tochigi, Japan) and Revolution EVO (GE Healthcare, Waukesha, WI, USA). However,

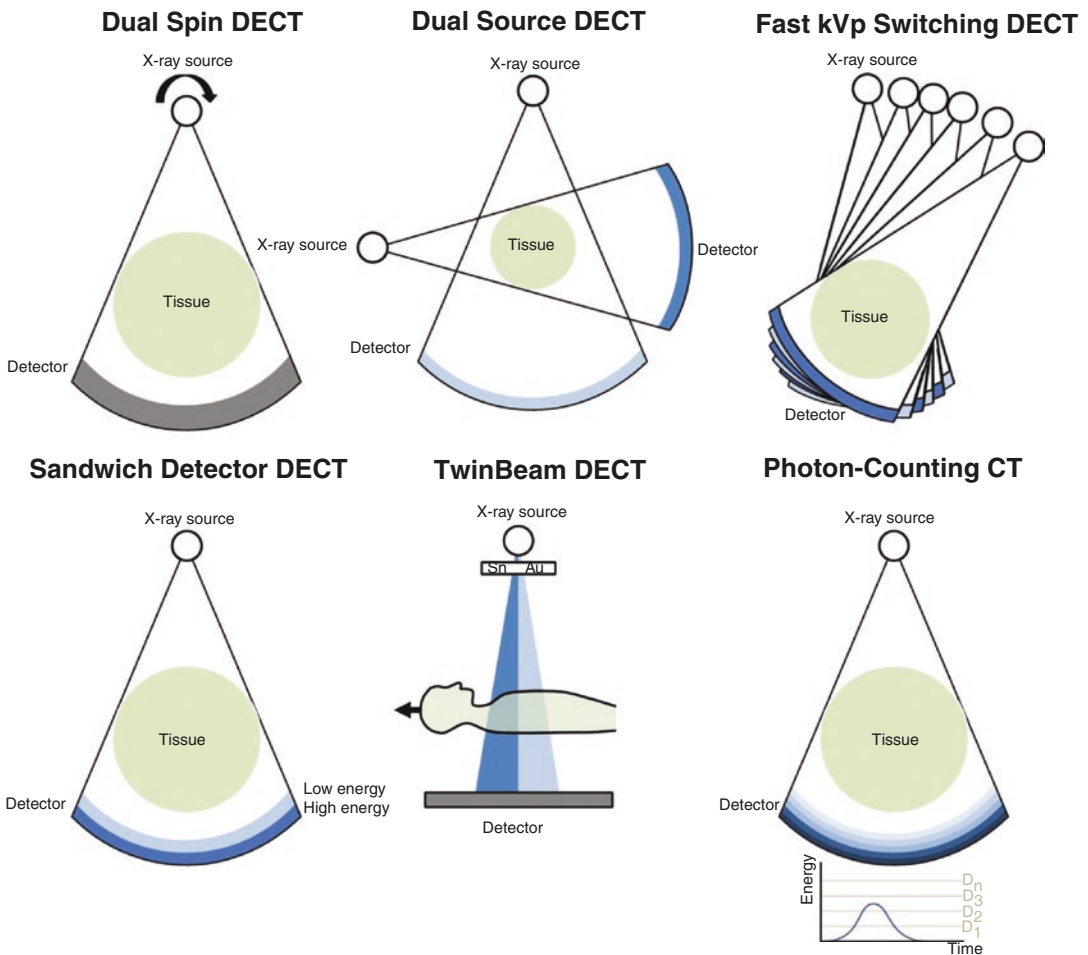


**Fig. 7.1** Schematic representation of the paradigms utilized by different DECT scanners to use different energy spectra and to separately record the high and low energy measurements

major limitations due to motion and temporal skew remain even with the more refined acquisition schemes.

### 7.2.2 Dual-Source DECT

The first DECT scanner approved for clinical use, a dual-source CT scanner, was introduced into the market in late 2006. It consisted of two source and detector combinations [1, 2, 9–11] (Siemens AG, Forchheim, Germany) at a near perpendicular angle to each other. This arrangement allowed the same volume to be scanned simultaneously with high- and low-energy spectra by setting the two X-ray sources at two different tube voltages.

A dual-source arrangement has several advantages. First, the use of separate tubes allows independent adjustment of the voltage and current for each tube, helping optimize separation of the low- and high-energy spectra and balance the total amounts of quanta emitted. Second, a filter may be applied to the tube emitting the higher energy spectrum to reduce associated low-energy photons from its polychromatic emission, thereby increasing the spectral separation between the two sources. Third, combined tubes can provide a higher total X-ray flux in a given amount of time, which is also beneficial for larger patients. Lastly, separate tubes allow application of established SECT technology and algorithms to each imaging chain independently.

A dual-source scanner also has some disadvantages. One, because of the limited space in the CT gantry, in the current generation of scanners the field of view of one of the imaging chains is smaller. This design choice places restrictions on the usable field of view of the DECT mode. Second, cross-scatter from the primary course of one source-detector pair contaminates the data of the other source detector pair. While this can be partly mitigated by technical modifications and optimization during image reconstruction, it cannot be completely eliminated. Since the two imaging chains are perpendicular to each other, this design also results in a quarter rotation “temporal skew” between the high and the corre-

sponding low energy projection. This, in turn, makes it hard to perform material decomposition in the projection domain, especially if there is any patient or organ motion. While the high- and low-energy data sets are separately reconstructed by filtered back projection, and material decomposition can be performed afterward in the image domain, this may lead to imperfect beam hardening correction and reduced material decomposition accuracy. Lastly, there are considerable additional hardware requirements for this system compared to the single-source scanners.

### 7.2.3 Single-Source Fast kVp-Switching DECT

Some of the shortcomings of a dual-source DECT are overcome by single-source design using fast kVp switching and fast detector technology employed in scanners such as the GE Gemstone Spectral CT (GE Healthcare, Waukesha, WI, USA) (Fig. 7.1) [1, 12–14]. This technology allows the generator and tube to rapidly and reliably switch between the 80 and 140 kVp voltages, with sampling periods as fast as 50  $\mu$ s. Tube voltage follows a square waveform and interleaved high- and low-voltage projection data are collected for twice the number of view angles, half at each tube voltage. Since the temporal skew or the delay between the high and low projections is low (50  $\mu$ s), spatiotemporal registration is excellent, and material decomposition is performed directly in the projection domain, making it robust against motion artifacts and beam-hardening artifacts in virtual monochromatic images (VMIs). Overall, this technology offers a cost-efficient design to increase the longitudinal detector coverage up to 160 mm, with the ability to scan over the entire full field of view of 50 cm. Furthermore, additional spectral analysis or reconstruction of different VMIs or maps can also be performed retrospectively in the reconstructed image space based on the data generated from the original projection data.

Ideally, one would like to have the same radiation dose in the low- and high-energy data sets. To address the challenges related to the relative

photon flux between the two energies, fast kVp switching scanners are designed to balance the dose, with allocation of additional time for the low kVp relative to the high kVp acquisition. This strategy provides a more balanced X-ray dose between the low- and high-energy acquisition. However, in practice, the time profile of the tube voltage has a slightly trapezoidal, rather than purely rectangular shape. In addition, tube current modulation—a technique where the tube current is increased or decreased in proportion to the attenuation through the patient—cannot be used with fast kVp switching. These factors lead to slightly increased dose as compared with single energy CT.

### 7.2.4 “Sandwich” Detector DECT

The DECT scanner implementations discussed so far change the energy of the acquired projections between a high- and low-energy setting by changing the X-ray source. Source-side energy modulation has been available for over a decade. Different scanner types have been refined for optimizing image quality, post-processing capabilities, radiation exposure, and ease of use. DECT technology, however, is continuously evolving area with continued refinements and iterations being introduced. This includes a radical departure from the source-side energy modulation to detector-side energy discrimination using a layered (“sandwich”) detector with a traditional X-ray source [1, 2, 15, 16] (Fig. 7.1). These DECT scanners use the intrinsic polychromaticity of the X-rays coming out of an X-ray tube, with the spectral separation achieved by the detector (Philips Healthcare, Andover, MA, USA). Such a set up completely eliminates the time lag between acquisitions of the different energy spectra. Because spectral separation is at the level of the detector, these systems always acquire scans in DECT mode. This allows retrospective spectral evaluation for all scan acquisitions, and noise correlation in the projection domain can be used to improve material separation and reduce noise on low-energy virtual monochromatic images. However, while this sys-

tem does not have the problems of cross-scatter discussed earlier for dual-source scanners, it is susceptible to a different type of cross-scatter between the two detector layers.

### 7.2.5 Twin Beam DECT

Unlike the fast kVp approach, the TwinBeam DECT scanner (Siemens AG, Forchheim, Germany) (Fig. 7.1) relies on the beam being pre-filtered using two different materials and split into high- and low-energy beams [17, 18]. The corresponding halves of the detector are then used for detection of the high- and low-energy spectra, respectively. This affords the ability to image the full field of view, hardware simplification, lower cost, and compatibility (as an upgrade) with some conventional scanner models. However, because a different portion of the patient is irradiated by the low- and high-energy spectra, a helical scan is needed so that each voxel scanned at one energy is eventually also scanned with the other energy, resulting in high temporal skew. There is also potential for cross-scatter originating from one side of the beam and contaminating data at the other side of the beam.

### 7.2.6 Photon-Counting Multispectral CT

One emerging approach to overcome these limitations is the photon counting scanner [2, 19, 20] (Fig. 7.1). Still under development, these scanners use of photon-counting detectors to resolve the energy of individual photons. As their name implies, photon-counting detectors count each incident X-ray photon, measure its energy, and sort it into narrow spectral subranges for robust multi-energy material characterization. Photon-counting detectors have a higher geometric efficiency than conventional energy-integrating detectors, although their efficiency is limited by the anti-scatter collimator. Furthermore, the impact of detector electronic noise can be significantly reduced, or even entirely eliminated, by applying an energy threshold just above the

electronic noise level. Theoretically, as these systems provide energy information for each individual photon, they can potentially improve characterization of energy-dependency of material attenuation and improve distinction of a material based on its specific K-edge (see Sect. 7.3)—a technique referred to as K-edge imaging—allowing classification of materials at very low concentrations. However, in practice, it is not yet clear whether energy separation in more than two bins as DECT dose will be a significant advantage. The small size of the individual detector elements—a necessity born out of keeping the photon count low for each bin so as not to overflow its counter—could also improve spatial resolution. Leveraging this advantage of photon-counting detectors, however, requires an equally small focal spot size on the X-ray source side, a design choice that limits X-ray photon flux (and consequently, increases exposure rates). A smaller detector element size also necessitates a higher dose to maintain acceptable image noise. For example, a twofold improvement in spatial resolution decreases the detector area by a factor of 4 and requires a 16-fold increase in radiation dose to achieve the same level of signal-to-noise ratio (see Sect. 7.4). Due to these and several other technical challenges with the detectors—e.g., “pulse pile up” effects, pulse sharing across multiple detector pixels—photon-counting scanners are not yet widely available for clinical use.

---

### 7.3 Fundamental Principles of DECT

DECT acquires projection data at two different energy spectra instead of one and combines them in order to evaluate tissue properties. Because materials with different elemental composition attenuate X-rays differently at different energies, DECT affords tissue characterization beyond what is possible with conventional SECT.

Two different energy X-ray beams, each composed of monochromatic energies would be ideal for material differentiation. However, current

X-ray tube technology used in the clinical setting cannot generate monochromatic X-ray spectra. Instead, clinical DECT scanners rely on polychromatic X-ray spectra with as little overlap between the different energy spectra as possible. While most systems that rely on different tube voltages for spectral separation utilize standard peak energies for scan acquisition, typically at 80 and 140 kVp, protocols may vary depending on the vendor or the specific application. For example, some dual-source scanner models may use 90 or 100 kVp with a filter, instead of 80 kVp, especially for scanning heavier patients. In addition, DECT scanners using dual-layer detectors typically use the conventional single-energy CT protocol.

For the low-energy spectrum, a tube voltage of approximately 80 kVp is typically chosen because at a lower tube voltage setting, a large proportion of photons would be absorbed by the body without generating any clinically useful information [1, 21]. For the high-energy spectrum, while 150 kVp may be used instead of 140 kVp, energies higher than 150 kVp may result in too little soft-tissue contrast, limiting applications in the clinical setting. Nonetheless, higher energies could still be useful for specialized applications and for discriminating between low and high atomic number ( $Z$ ) elements. For successful clinical application of DECT, issues beyond specific image data acquisition protocols that take into account materials or tissues of interest must be considered.

At the photon energies used for medical imaging, X-ray attenuation is governed by two main processes: Compton scattering and photoelectric effect. Rayleigh scattering—a coherent scattering process related inversely to the fourth power of the wavelength of the X-rays—also impacts attenuation; however, this process accounts for a small percentage of interactions and is typically considered negligible in conventional absorption-based CT.

Compton scattering is a function of both the electron density of the tissue and the tube voltage and spectrum. It accounts for the greatest contribution to the overall attenuation, at least at the

typical tube voltages used in CT. The electron density of the tissue is the dominant factor, as Compton effect is only minimally dependent on photon energy [9].

The photoelectric effect refers to the ejection of an electron from a shell of an atom by an incident photon. The innermost shell (K-shell) has the most strongly bound electrons. The probability of photoelectric interactions generally decreases with higher energies but increases abruptly when the incident photon energy just exceeds the binding electron energy of the K-shell electrons to enable the ejection of an electron from the K-shell. This energy represents the K-edge for a given element. There is a spike in attenuation at the K-edge followed by a rapid drop in the probability of photoelectric interactions. Photoelectric effect is strongly dependent on the atomic number or  $Z$  (i.e., the number of protons within the nucleus) of the elements that constitute the tissue under consideration and is particularly important for spectral CT [16]. Thus, the atomic number of materials of interest must be considered when planning applications of DECT in any research or clinical setting.

For elements (thus, tissues) to be distinguishable based on their spectral properties, there must be sufficient difference in their atomic number (i.e.,  $Z$ ). Common elements found in the human body have low and very similar atomic numbers. For example, hydrogen ( $Z = 1$ ), carbon ( $Z = 6$ ), nitrogen ( $Z = 7$ ), and oxygen ( $Z = 8$ ) do not have sufficient component of photoelectric interactions. Consequently, their attenuation is relatively low and very similar to each other at different energies. This precludes reliable differentiation based on their spectral properties [1, 22].

On the other hand, elements with high atomic numbers and large differences in their atomic numbers have a stronger energy-dependence. Among these elements, iodine ( $I$ ,  $Z = 53$ ) is particularly of clinical interest. Iodine has a K-edge of 33.2 keV. A drop in X-ray energy would result in an increase in iodine attenuation, with the highest attenuation at the energy closest to the K-edge of iodine. Given that most commonly used CT contrast agents are iodine-based and are widely used for a variety of indications, ranging

from oncologic imaging to angiography, iodine's strong energy-dependence can be exploited in DECT applications. Calcium ( $Ca$ ,  $Z = 20$ ) is another element intrinsic to the human body that has a relatively high atomic number. Energy dependence of  $Ca$  can also be used in a variety of clinical applications of DECT.

---

## 7.4 Practical Considerations

All DECT scanners can be operated in either SECT or DECT mode. Obviously, using a DECT scanner exclusively in SECT mode does not take advantage of its full capabilities. DECT scanning has its specific workflow requirements, and therefore, scanning must be planned and specified beforehand. The layered or "sandwich" detector scanner described above is an exception as these systems allow retrospective spectral evaluation for all scan acquisitions.

There are two basic but interrelated requirements for routine clinical use of DECT: (1) acquired image quality should be at least equivalent to those obtained using SECT mode and (2) the acquisition must be made with an acceptable (preferably, equivalent or lower) patient radiation dose. Beyond these requirements, the additional post-processing capabilities made possible by DECT mode are essentially without any image quality or dose penalty, only requiring additional post hoc image processing.

One specific factor with a significant impact on image noise, and hence on radiation dose, is the image spatial resolution. The image noise (as measured by standard deviation of the image) scales with the inverse of the square root of the dose, but with the square of the isotropic spatial resolution (assuming the slice thickness and the in-plane resolution change the same way). This implies that other factors being equal, a fourfold increase of dose would reduce image noise by a factor of 2, whereas a twofold increase isotropic spatial resolution—i.e., all three dimensions are reduced by a factor of 2—would decrease the voxel size by a factor of 8. Consequently, to keep the noise unchanged, a twofold increase in spatial resolution requires an increase in dose by a factor



64! In most clinically deployed scanners, changing from SECT to DECT does not decrease the voxel size. While increased radiation dose was a concern during earlier attempts at DECT scanning [23], this problem has been largely eliminated in the DECT systems currently in clinical use [24–30].

#### 7.4.1 Temporal Parameters

For DECT applications, total scan time, temporal resolution, and spectral projection skew or delay are the three time-related parameters of clinical importance.

The total scan time is the total elapsed time to scan a desired anatomical scan range. Its significance is related to the time of a breath hold, the time during which a patient must hold still during a scan, and the time period over which good contrast opacification must be maintained. The total scan time is heavily impacted by the scanner z-coverage and increases for TwinBeam CT (since the helical pitch must be decreased) and sequential DECT modes (since consecutive scans need to be completed).

The temporal resolution is the time during which all spectral data for a given image voxel or slice is collected. It corresponds to the time of about half a rotation (and thus, is influenced by gantry speed), and determines motion artifacts in the scan, e.g., during cardiac imaging. Most vendors offer motion compensation algorithms. For TwinBeam CT and sequential scanning, due to the delay between the high- and low-energy measurement of each given slice, the DECT temporal resolution is much poorer and these DECT approaches are not suitable for cardiac imaging.

In contrast to the total scan time and temporal resolution, the spectral skew or the delay between the high- and low-energy measurements for a given projection ray, is unique to DECT. The spectral delay affects the spectral accuracy for fast-moving objects, independent of the motion artifacts due to temporal resolution limits. It dictates the additional errors and artifacts caused by the motion of an object between the high- and low-energy measurement of a given projection

ray. This delay is inherent to the scanner design and cannot be controlled through changes in the scan protocol. Detector-based DECT systems and fast kVp switching-based systems have a clear advantage due to their smaller (<1 ms) spectral skew compared to the time span for most macroscopic biological motion (~10 ms).

#### 7.4.2 Image Reconstruction

The data from the low- and high-energy DECT acquisitions can be combined in a variety of ways to produce images for interpretation. One common type of reconstruction obtained is the virtual monochromatic image (VMI). VMI at a particular energy simulates the image that would be obtained with a monochromatic X-ray beam at that energy. Based on phantom studies and body imaging, 70 keV VMIs are similar to the standard 120 kVp SECT acquisition [24, 31, 32]. In fact, sometimes VMIs may even have a better image quality compared to an SECT acquisition at the same dose, supporting the use of conventional SECT equivalent reconstructions [24], and several observations support routine use of 65–70 keV VMIs as SECT equivalent [25, 33, 34], supplemented by VMIs constructed across a variety of energy levels [33–43].

VMIs are reconstructed by decomposing the low- and high-energy acquisitions into two equivalent images that represent the photoelectric and Compton components of the overall attenuation. Since the energy dependence of both of these components is known from physics, one can project them to any desired monochromatic energy level.

Another reconstruction routinely obtained when using DECT scanners is the weighted average image (WA), which represents a linear blend of the low- and high-energy acquisitions. Typically, a linear blend consisting of 30% of the low- and 70% of the high-energy acquisitions are considered equivalent to the standard 120 kVp SECT acquisition and generated for routine clinical interpretation [27, 44–46]. However, similar to VMIs, the proportion of the low- and high-energy data that are blended as

well as the way they are blended (e.g., linear vs. nonlinear) can be altered to accentuate different material or tissue characteristics of potential interest [44, 46]. Depending on the energy (VMI) or blending ratio (WA), VMIs and WA images can resemble images generated using conventional SECT scanning that radiologists are looking at routinely. DECT scan data can also be used to create other types of images based on material decomposition.

### 7.4.3 Basis Material Decomposition

DECT basis material decomposition is based on the fact that the X-ray attenuation of any material is a linear combination of Compton scatter attenuation and photoelectric attenuation (with negligible contribution from Rayleigh scatter, as described previously). The relative contribution of these two effects to the overall attenuation changes for different materials. Thus, these two effects form a material basis pair in which all materials can be expressed.

Water and iodine are one of the most common basis pairs. The attenuation in water is dominated by Compton scatter, with some contribution from the photoelectric effect. Iodine, on the other hand, has a much higher contribution of the photoelectric effect and its attenuation exhibits a strong energy-dependence. Using water–iodine as the material basis pair, every material can be represented as a linear combination of water and iodine. For example, water (and blood which essentially behaves as water) would, by definition, be 100% water and 0 mg/mL iodine. A mixture of iodine and blood, e.g., after iodinated contrast administration, would be 100% water and a certain concentration of iodine. All tissues (e.g., muscle, adipose, cartilage, etc.) would have their own distinct pattern when expressed using a given basis material pair. In other words, their X-ray attenuation can be expressed as a specific combination of the X-ray attenuation of water and iodine *at all X-ray energies*.

DECT has also been used to characterize three or more materials in the body, but under significant assumptions. Based on these approaches,

DECT data can also be used for material labeling, or classification of materials into predefined groups, such as renal stone characterization [11, 47, 48]. Strictly based on physical principles, DECT systems cannot exactly distinguish three or more linearly independent basis functions and there are technical limitations to this type of analysis [49].

### 7.4.4 Virtual Non-Contrast (VNC) Images and Iodine Maps

One of the most promising applications of DECT is the ability to visualize parts of the image without contrast (iodine) enhancement, to create “maps” reflecting distribution of contrast in tissues, and to suppress other tissues such as bone or calcium.

One way to suppress iodine in the DECT images is to use VMIs reconstructed at a relatively high keV, where the iodine attenuation is substantially more suppressed than other tissues due to the reduction in photoelectric interactions at energies further away from the iodine K-edge. Another way to suppress iodine in an image is to decompose it using a water–iodine basis material pair. Water is used as the reference because it is the most common constituent of the human body, there is significant spectral contrast between iodine and water, and water’s CT number remains relatively constant with respect to change in X-ray energy. After the decomposition, the iodine is captured in the iodine map and the water map represents blood and other tissues without iodine. It should be noted that all tissues are transformed into a water–iodine combination. Therefore, the water image is not the same as a regular non-contrast CT image. The iodine maps represent the iodine content within tissues. They can be used to estimate the iodine concentration or to evaluate its distribution. This approach is useful for several clinical applications, such as assessment of enhancing tumor [50] or blood pool imaging [2].

In DECT imaging, commonly performed representations include maps estimating iodine content, iodine subtraction (or VNCs), calcium or

bone subtraction, or a combination of all. These reconstructions have several uses in neuroradiology and head and neck imaging, such as differentiation of intracranial hemorrhage from iodinated contrast material [51] or evaluation of sialolithiasis [52].

#### 7.4.5 Workflow and Other Considerations

As mentioned, once scans are acquired in DECT mode, spectral analysis and material characterization can be performed retrospectively. Post-processing software that enables advanced DECT spectral analysis is typically vendor specific as it relies on details of the hardware implementation.

Integration of DECT into routine clinical workflow requires generation of specific sets of useful reconstructions for a given study at the CT console, that can then be sent to the picture archiving and communication system (PACS) so they are immediately available for review [34, 35, 40, 41]. This may be achieved by specific referral pattern (e.g., all neuro- or head and neck oncology studies), by highly specialized studies for very selective clinical questions (e.g., all studies after intra-arterial interventions for ischemic stroke to distinguish hemorrhage from iodinated contrast), or broadly based on the body area (e.g., all stroke head CTs; all neck studies). However, without the capability to do additional post-processing, the radiologist is limited to preselected reconstructions, and depending on the vendor, certain reconstructions such as material decomposition maps are also not always optimal in terms of use and manipulation. Some consoles also can generate different energy VMIs automatically, and additional advanced image analysis or reconstructions can be performed on a stand-alone dedicated image-processing workstation. Layered detector systems also enable preprogramming for the automatic generation of different DECT reconstructions that are then sent to PACS. Increasingly, different systems enable a more seamless flow which is important for widespread and routine use of DECT in the clinical setting. This is an area that is likely to evolve as

additional studies become available demonstrating applications and potential advantages of DECT technology.

### 7.5 Neuroradiology Applications of DECT

Multiple applications of DECT have been described in neuroradiologic literature. Typical applications include the following application domains.

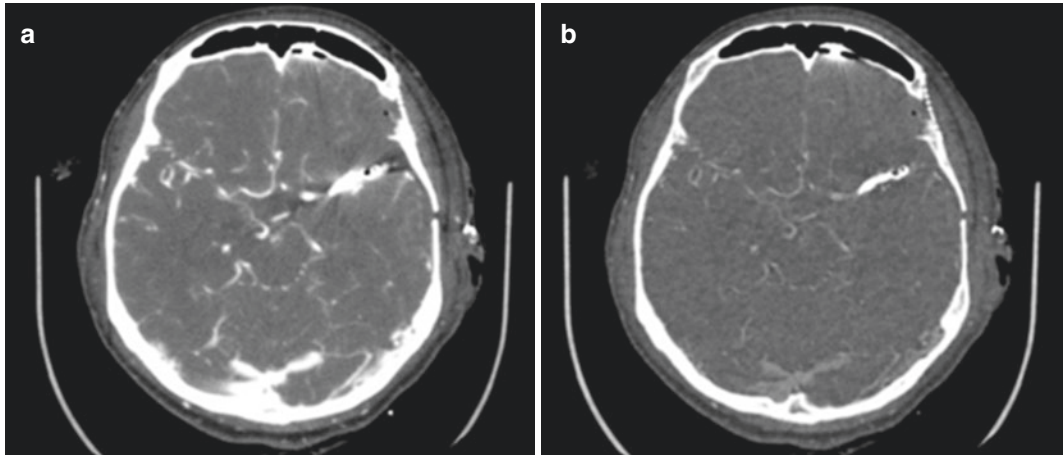
1. Bone subtraction.
2. Image contrast optimization.
3. Material characterization: Materials such as iodine, calcium, and hemorrhage can have very similar CT number. DECT may be used to distinguish tissues and materials that have similar attenuation on SECT.
4. Plaque characterization.
5. Beam hardening artifact reduction.
6. Metal artifact reduction.

In the following exposition of clinical applications, we classify them based on the principles and processing techniques described earlier.

#### 7.5.1 Virtual Monochromatic Images

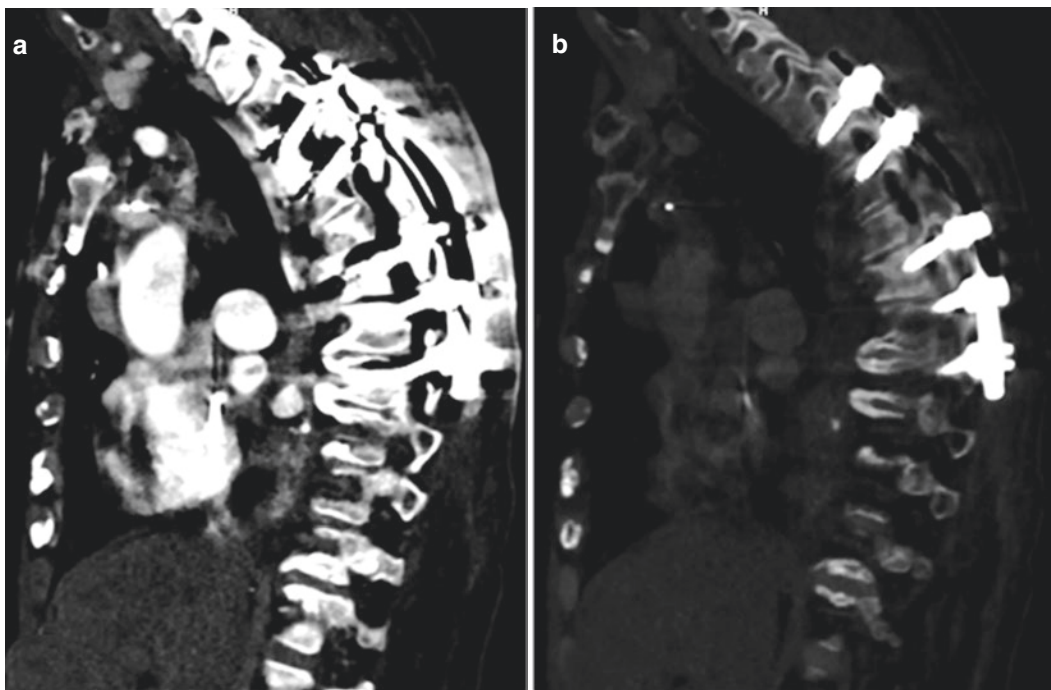
VMI generation enables one to view an image at different virtual keV levels. As can be expected, some of the artifacts that arise from polychromaticity of the beam should be diminished with virtual monochromatic images. In addition, the higher the beam energy, the more penetrating it is. Figure 7.2 shows an example of this principle for reducing metal artifacts associated with aneurysm clips. As can be seen, the metal clip and its surrounding areas are well visualized at a virtual beam energy of 140 keV.

Figure 7.3 shows another example of the same principle in a much more demanding artifact setting. In this example, the metal artifact from the posterior spinal fixation rods makes it nearly impossible to appreciate the bony anatomy and the integrity of the hardware. At 190 keV, one can appreciate



**Fig. 7.2** Dual-energy CT in a patient after a surgically clipped aneurysm in the left middle cerebral artery. Monoenergetic reconstruction at 64 keV (which matches the mean energy of standard 120 kVp) shows severe metal

artifact (**a**). Monoenergetic reconstruction at 140 keV reduced the metal artifact and enables better visualization of the surrounding brain parenchyma and vasculature (**b**)



**Fig. 7.3** Metal artifact reduction using DECT. Panel (**a**) shows a traditional single energy image, while panel (**b**) is the same image at a virtual monochromatic image level of 190 keV

that the transpedicular screws are well seated. In addition, the fracture in the vertebral body that is straddled by the transpedicular screws can be appreciated. It is worth pointing out that the iodinated

contrast, which is quite well seen at 120 keV in panel (**a**) is not visible in panel (**b**) because the attenuation of iodine drops precipitously as one moves away from the K-edge of iodine.

While high keV images are suitable for metal artifact reduction, low keV images may be used for accentuating contrast between soft tissues. In addition, as the X-ray beam energy approaches the K-edge of iodine (33.2 keV), the attenuation of iodine is disproportionately increased. This fact can be used to accentuate iodine-containing structures such as vessels and tumors.

Figure 7.4 shows an interesting application of low keV imaging technique in CT myelography for detecting a CSF leak. In this patient, there is posterior fluid collection in a surgical defect that was seen on routine single-energy CT. However, it was not clear if there was a CSF leak into this collection. Iodinated contrast was injected intrathecally in the lumbar cistern under image guidance. On routine single energy image (Fig. 7.4a), it is not apparent if any of the injected contrast extravasated into the posterior collection. As the beam energy is lowered to 50 keV, the attenuation of the intrathecal fluid as well as that of the posterior fluid collection increases (Fig. 7.4b). When the beam energy is further reduced, the CSF leak is quite apparent (Fig. 7.4c).

### 7.5.2 Material Decomposition

As described previously, DECT enables division of any image into a pair of images, each representing a single material from a predefined material pair. The material pair used for decomposition

is up to the user and can be selected based on the application. In addition, the same set of images can be retrospectively processed using different material pairs after the images have been acquired.

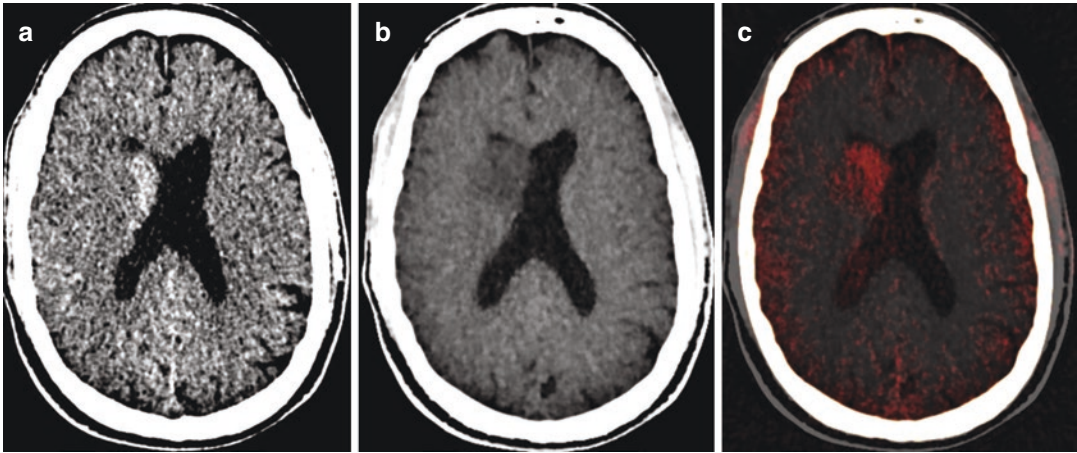
There are times when two different materials, such as diluted contrast and hemorrhage, may have the same CT number on a single-energy CT. Such overlap in CT numbers may lead to a diagnostic dilemma, for example after intra-arterial interventions for acute stroke. Figure 7.5 shows one such example.

Figure 7.5a shows a non-contrast head CT performed in a patient after a thrombectomy for a right middle cerebral artery ischemic stroke. This immediately post-procedure non-contrast CT scan shows a hyperdensity in the right caudate head and body. There was trace hyperdensity in the lentiform nuclei as well (not shown). This hyperdensity may represent one of two things: it may be a serious condition such as hemorrhagic conversion of infarct, or it may be iodine leakage into the infarcted territory from the intra-arterially administered contrast during the procedure.

Figure 7.5b shows a virtual non-contrast image derived from DECT where all iodinated contrast has been removed. In this processed image, one can only see the hypoattenuation of the infarcted territory; all the hyperdensity seen on the single-energy non-contrast scan has been eliminated. The iodine overlay image (Fig. 7.5c) demonstrates that the previously mentioned



**Fig. 7.4** Multiple virtual monochromatic image; (a) routine single-energy image (b) VMI at 50 keV; (c) VMI at 40 keV (Courtesy of Dr. Stuart Pomerantz, Massachusetts General Hospital, Boston)



**Fig. 7.5** (a) Hyperdensity involving the right caudate head and a portion of the right lentiform nucleus seen on single-energy non-contrast CT after endovascular acute ischemic stroke treatment. (b) Virtual non-contrast image

derived from dual-energy CTA shows the hypo-attenuated infarcted region. (c) Iodine-overlay image shows that the hyperdense area is actually caused by staining of iodinated contrast from the intervention

hyperdensity is attributable to iodine staining. It is worth noting that skull is present on both the VNC and iodine overlay images because calcium maps to both of the material pairs (i.e., water and iodine) chosen for this application.

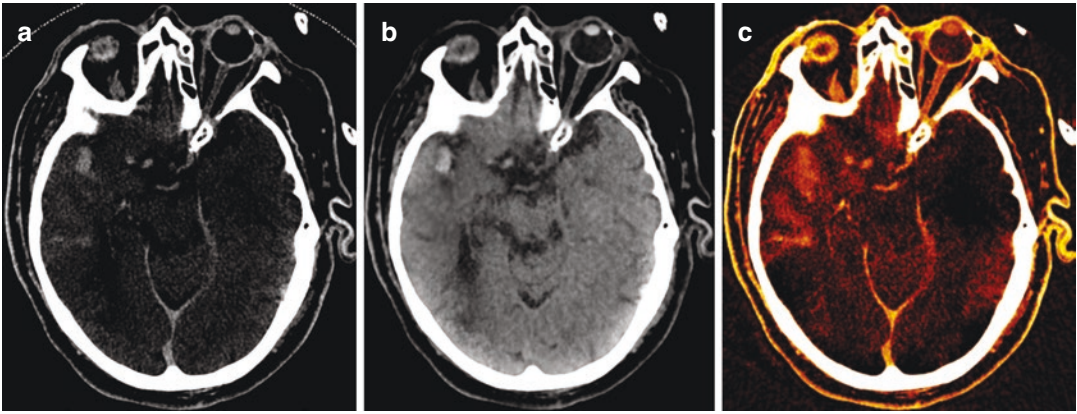
The traditional method for distinguishing these two conditions is by repeat imaging after 24 h. Iodinated contrast, being water-soluble, would nearly completely washout in 24 h. Hemorrhage, on the other hand, would persist for several days. Making the distinction between hemorrhage and contrast extravasation is very important if the patient has to be anticoagulated. DECT provides a robust method of distinguishing these materials without having to wait [51, 53].

Figure 7.6 shows another application of decomposing a single-energy CT scan into water/iodine material pair. This example shows a non-contrast CT scan (panel a) with intraparenchymal and subarachnoid hyperdensity in the right middle cerebral artery territory. When split into a VNC and iodine images (panels b and c, respectively), a portion of the previous hyperdensity persists on the VNC image. This portion likely represents thrombus in or hemorrhage in or around a right MCA bifurcation aneurysm. The

remainder of the hyperdensity, which maps on the iodine image, likely represents contrast material. This example shows that both iodine and hemorrhage are properly partitioned by the material decomposition algorithm.

One can use the ability to distinguish materials that look the same on a single-energy image in multiple different applications besides the ones illustrated above. For example, one can distinguish calcium from all soft tissues and iodine in order to automatically suppress bone in a CT dataset. Such bone subtraction algorithms have become quite common and can be used to quickly screen for aneurysms, stenoses, and dissection at the CT scanner console in CT angiograms [54].

There are instances when diffuse demineralization in the brain parenchyma may appear as acute intracranial hemorrhage, e.g., in a patient presenting for non-contrast head CT after a motor vehicle accident. In the absence of a prior CT scan for comparison, the only way to settle this question using single-energy imaging would be to perform repeat imaging and assess for progression of the presumed hematoma, or development of secondary signs such as perilesional edema. Since the spectral signature of calcium and hemorrhage is quite different, one can use



**Fig. 7.6** Single-energy non-contrast CT (a) shows hyperdensity close to the right MCA bifurcation that persists on the virtual non-contrast image (b), suggesting that it represents contained hemorrhage or a thrombotic pseudoaneurysm rather than contrast staining. (c) Extensive hyperdensity in the right MCA territory likely represents extravasated iodine from prior intervention

eurysm rather than contrast staining. (c) Extensive hyperdensity in the right MCA territory likely represents extravasated iodine from prior intervention

material decomposition to distinguish these two materials. Robust DECT techniques have been published in the literature to make this distinction [55].

### 7.5.3 Quantification of the Contrast Medium

DECT angiography enables separation of pixel intensities into hemorrhage, brain, and contrast medium through three-material decomposition, utilizing the relative attribution of the photoelectric effect and Compton scattering to the energy-specific attenuation [51, 53], as described earlier. This allows generation of separate virtual non-contrast (VNC) images and iodine-overlay images, which can be further used for quantification of contrast medium. The iodine-overlay images provide an estimate of the quantity of iodine in Hounsfield Units, which can be calibrated to known concentrations of iodine (e.g., using a prespecified phantom) for measuring the amount of iodine per unit volume of brain tissue.

For example, on SECT angiography, qualitative identification of the foci of contrast enhancement due to local extravasation of iodine—spot-sign—is a highly specific marker for hematoma expansion [56]. However, spot sign is limited in its application for expansion risk assessment due to its relatively low sensitivity [57]; almost half of the expanding hematomas do not show a visually detectable spot sign on CT angiography. Quantification of the iodine concentration in the hematoma, based on iodine-overlay images, allows a quantitative approach to identify both localized and diffuse leakage of contrast material (Fig. 7.7). Thus, both the extravasation foci (localized leakage) and the total iodine content in the hematoma (diffuse leakage) can be quantified. In fact, previous work from our group shows that this approach can improve sensitivity, and thus, the overall accuracy of hematoma expansion risk assessment compared to qualitative assessment of spot sign [58]. Thus, quantification of iodine based on DECT images (specifically, iodine-overlay images) to aid in the selection of candidates for early medical or surgical intervention.

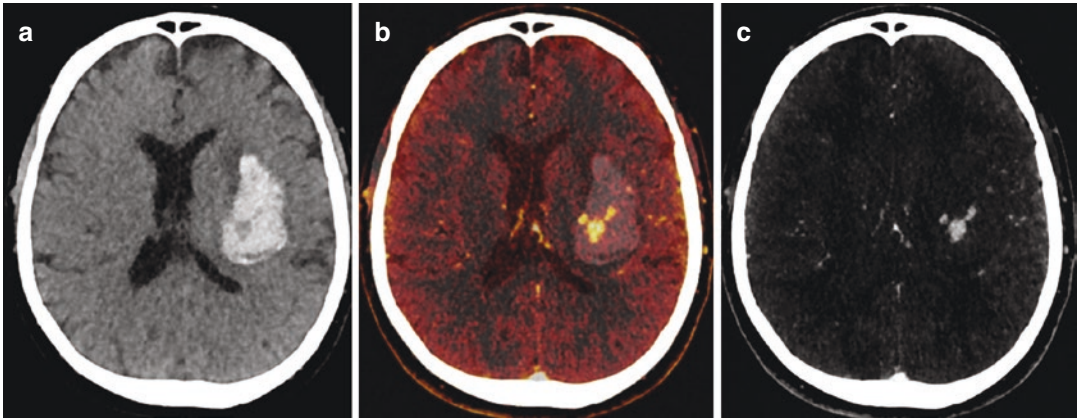


**Fig. 7.7** Detection and quantification of iodine to assess deep lobar hemorrhage for expansion. (a) Virtual non-contrast image clearly shows hematoma in the left basal ganglia and subcortical white matter. (b) Iodine-overlay image shows iodine diffusely present with the hematoma with big “spot-sign” in the center, clearly suggesting active contrast extravasation. (c) Iodine-only image shows

that there are three tiny foci of iodine present within the actual spot, increasing the chance of hematoma expansion. Follow-up single-energy non-contrast CT (not shown) a few hours later demonstrated expansion of the hematoma. A combination of the diffuse sign and spot sign derived from DECT represents a dual-energy counterpart of the single energy spot sign

## 7.6 Conclusion

In this chapter, we described the fundamental principles behind the DECT technology. Six different implementations of this type of scanner were described and their relative pros and cons compared. We also discussed practical issues related to DECT protocols and processing techniques. The chapter concluded by illustrating multiple applications of this novel imaging technique.

Besides a simulated single-energy image, DECT can also produce simulated monochromatic images as well as perform material decomposition into two (or three) predefined materials. Using a single CT Number (HU), it may be difficult to ascribe a material or tissue type to a region observed single-energy CT. For example, a routine non-contrast CT is unable to distinguish materials such as blood and dilute contrast or blood and diffuse mineralization. Such classification, when performed by human readers, relies on prior knowledge of anatomy. DECT can use the spectral signature of a material to characterize it. As we illustrated using multiple examples, DECT can aid in material discrimination. The literature describes multiple applications such as

differentiation of hemorrhage, iodinated contrast, and calcium; plaque characterization; bone removal; urinary stone characterization, and characterization and measurement of gout. DECT also provides virtual monochromatic images which may be used for optimizing image contrast, or reducing beam hardening and metal artifacts. Finally, DECT is a quantitative technique. We described one application of this modality in the assessment of hemorrhage expansion. Other applications in oncology, stroke, and blood perfusion are currently being investigated.

In conclusion, DECT is a robust technique that is currently available for routine clinical use. It has sound technical foundation and multiple implementations are currently available. It has numerous neuroradiologic applications such as bone subtraction, material characterization, plaque characterization, beam hardening and metal artifact reduction, and soft tissue contrast accentuation.

## 7.7 Clinical Case

The clinical cases show another novel application of material decomposition using DECT. Panels (a) through (c) show single energy non-contrast



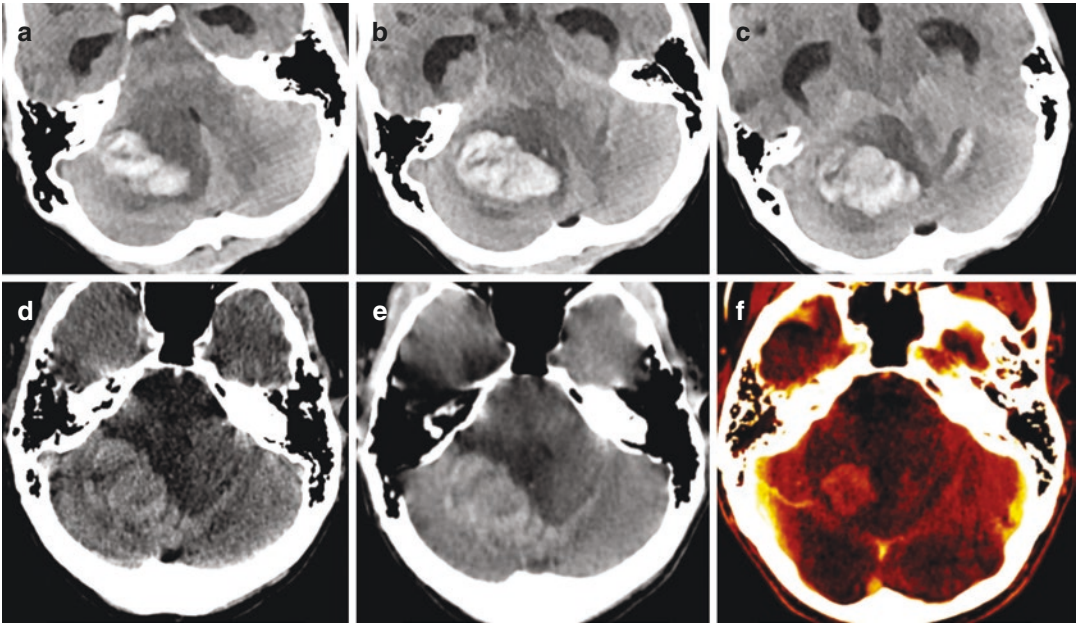


**Fig. 7.8** Single-energy head CT images (a–c) of a 37-year-old patient with a history of colon cancer and recent trauma, showing a mass in the posterior fossa on the right, surrounded with edema, indicating malignancy and/or intracranial hemorrhage. Single-energy equivalent

of dual-energy acquisition (d) and virtual non-contrast image (e) showing the same mass. (f) Iodine-overlay image shows that the center of the mass consists of tumor, surrounded by hemorrhage

head CT slices of a 37-year-old patient with a prior history of colon cancer who presented to the Emergency Department after a motor vehicle accident. The images clearly show an intraparenchymal hemorrhage in the right cerebellar hemisphere with surrounding edema and a subarachnoid component that extends to the contralateral side. A CT angiogram using a DECT scanner was performed afterward to assess for an underlying lesion. Panel (d) of Fig. 7.8 shows a single-energy equivalent image after contrast administration. This single-energy image was decomposed into a VNC image (panel e) and an iodine overlay image (panel f). On the VNC image, one can appreciate the extent of the intraparenchymal and subarachnoid hemorrhage. The iodine overlay image shows a smaller, contrast-enhancing mass centered within the hemorrhagic lesion, presumably a metastasis from patient's colon cancer. Therefore, this case likely represents hemorrhagic conversion of an intracranial metastasis rather than a purely post-traumatic hemorrhage. It should be noted that the enhance-

ment from the metastatic lesion was completely masked by the surrounding hemorrhage and the metastasis would have been missed in acute setting without the help of a DECT scan.

**Acknowledgments** The authors thank Mr. Maarten Poirot for his help in generating Fig. 7.1.

## References

1. Johnson TRC, Kalender WA. Physical background. In: Johnson TRC, et al., editors. Dual energy CT in clinical practice. Heidelberg: Springer; 2011. <https://doi.org/10.1007/174>.
2. McCollough CH, Leng S, Yu L, Fletcher JG. Dual- and multi-energy CT: principles, technical approaches, and clinical applications. *Radiology*. 2015;276:637–53.
3. Di Chiro G, et al. Tissue signatures with dual-energy computed tomography. *Radiology*. 1979;131:521–3.
4. Genant HK, Boyd D. Quantitative bone mineral analysis using dual energy computed tomography. *Investig Radiol*. 1977;12:545–51.
5. Kelcz F, Joseph PM, Hilal SK. Noise considerations in dual energy CT scanning. *Med Phys*. 2014;6:418–25.

6. Millner MR, et al. Extraction of information from CT scans at different energies. *Med Phys.* 1979;6:70–1.
7. Macovski A, Alvarez RE, Chan J-H, Stonestrom JP, Zatz M. Energy dependent reconstruction in X-ray computerized tomography. *Comput Biol Med.* 1976;6:325–36.
8. Brooks RA, Di Chiro G, Tsai CM, Cho ZH, Herman GT. Energy-selective reconstructions in X-ray computerized tomography energy-selective reconstructions in X-ray computerized. *Phys Med Biol.* 1976;21:733–44.
9. Johnson TRC, et al. Material differentiation by dual energy CT: initial experience. *Eur Radiol.* 2007;17:1510–7.
10. Petersilka M, Bruder H, Krauss B, Stierstorfer K, Flohr TG. Technical principles of dual source CT. *Eur J Radiol.* 2008;68:362–8.
11. Krauss B, Schmidt B, Flohr TG. Dual source CT. In: Johnson TRC, et al., editors. *Dual energy CT in clinical practice.* Heidelberg: Springer; 2011. <https://doi.org/10.1007/174>.
12. Chandra N, Langan DA. Gemstone detector: dual energy imaging via fast kVp switching. In: Johnson TRC, et al., editors. *Dual energy CT in clinical practice.* Heidelberg: Springer; 2011. <https://doi.org/10.1007/174>.
13. Kalender WA, Perman WH, Vetter JR, Klotz E. Evaluation of a prototype dualenergy computed tomographic apparatus. I. Phantom. *Med Phys.* 1986;13:334–9.
14. Xu D, et al. Dual energy CT via fast kVp switching spectrum estimation. *Proc SPIE.* 2009;7258:1–10.
15. Vlassenbroek A. Dual layer CT. In: Johnson TRC, et al., editors. *Dual energy CT in clinical practice.* Heidelberg: Springer; 2011. <https://doi.org/10.1007/174>.
16. Alvarez RE, Seibert JA, Thompson SK, Seibert JA, Thompson SK. Comparison of dual energy detector system performance. *Med Phys.* 2004;31:556–65.
17. Euler A, et al. Initial results of a single-source dual-energy computed tomography technique using a split-filter: assessment of image quality, radiation dose, and accuracy of dual-energy applications in an in vitro and in vivo study. *Investig Radiol.* 2016;51:491–8.
18. Kaemmerer N, et al. Dual-energy computed tomography angiography of the head and neck with single-source computed tomography a new technical (split filter) approach for bone removal. *Investig Radiol.* 2016;10:1–6.
19. Schlomka JP. Experimental feasibility of multi-energy photon-counting K-edge imaging in pre-clinical computed tomography. *Phys Med Biol.* 2006;53:4031–47.
20. Benjaminov O, Perlow E, Romman Z, Levinson R, Bashara B, Cohen M, Zelikovsky A. Novel, energy-discriminating photon counting ct system (EDCT): first clinical evaluation—CT angiography: carotid artery stenosis. In: *Radiological Society of North America 2008 scientific assembly and annual meeting, Feb 18–20 (2008).*
21. Trc J. Dual-energy CT: general principles. In: Johnson TRC, et al., editors. *Dual energy CT in clinical practice.* Heidelberg: Springer; 2012. p. 3–8. <https://doi.org/10.2214/AJR.12.9116>.
22. Michael GJ. Tissue analysis using dual energy CT. *Australas Phys Eng Sci Med.* 1992;15:25–37.
23. Ho LM, et al. Dual energy versus single energy MDCT: measurement of radiation dose using adult abdominal imaging protocols 1. *Acad Radiol.* 2009;16:1400–7.
24. Matsumoto K, et al. Imaging with fast kilovoltage switching: improved image quality as compared with that obtained with 120-kVp CT. *Radiology.* 2011;259:257–62.
25. Forghani R, et al. Low-energy virtual monochromatic dual-energy computed tomography images for the evaluation of head and neck squamous cell carcinoma: a study of tumor visibility compared with single-energy computed tomography and user acceptance. *J Comput Assist Tomogr.* 2017;41:1–7.
26. Schenzle JC, et al. Dual energy CT of the chest. *Investig Radiol.* 2010;45:347–53.
27. Tawfik A, et al. Image quality and radiation dose of dual-energy CT of the head and neck compared with a standard 120-kVp acquisition. *Am J Neuroradiol.* 2011;32:1994–9.
28. Li B, Yadava G, Hsieh J. Quantification of head and body CTDI VOL of dual-energy x-ray CT with fast-kVp switching. *Med Phys.* 2011;38:2595–601.
29. Kamiya K, Kunitatsu A. Preliminary report on virtual monochromatic spectral imaging with fast kVp switching dual energy head CT: comparable image quality to that of 120-kVp CT without increasing the radiation dose. *Jpn J Radiol.* 2013;31:293–8.
30. Hwang WD, et al. Qualitative comparison of noncontrast head dual-energy computed tomography using rapid voltage switching technique and conventional computed tomography. *J Comput Assist Tomogr.* 2016;40:320–5.
31. Pinho DF, Kulkarni NM. Initial experience with single-source dual-energy CT abdominal angiography and comparison with single-energy CT angiography: image quality, enhancement, diagnosis and radiation dose. *Eur Radiol.* 2013;23:351–9.
32. Patel BN, Thomas JV, Lockhart ME, Berland LL, Morgan DE. Single-source dual-energy spectral multidetector CT of pancreatic adenocarcinoma: Optimization of energy level viewing significantly increases lesion contrast. *Clin Radiol.* 2013;68:148–54.
33. Pomerantz SR, Shervin Kamalian S, et al. Virtual monochromatic reconstruction of dual-energy unenhanced head CT at 65–75 keV maximizes image quality compared with conventional polychromatic CT. *Radiology.* 2013;266:318–25.
34. Lam S, et al. Optimal virtual monochromatic images for evaluation of Normal tissues and head and neck cancer using dual energy CT. *Am J Neuroradiol.* 2015;36:1518–24.

35. Forghani R, et al. Different spectral Hounsfield unit curve and high-energy virtual monochromatic image characteristics of squamous cell carcinoma compared with nonossified thyroid cartilage. *Am J Neuroradiol.* 2015;36:1194–200.
36. Wichmann JL, et al. Virtual monoenergetic dual-energy computed tomography optimization of kiloelectron volt settings in head and neck cancer. *Investig Radiol.* 2014;49:735–41.
37. Tanaka R, Hayashi T, Ike M, Noto Y. Reduction of dark-band-like metal artifacts caused by dental implant bodies using hypothetical monoenergetic imaging after dual-energy computed tomography. *Oral Surg Oral Med Oral Pathol Oral Radiol.* 2013;115:833–8.
38. Srinivasan A, Parker RA, Manjunathan A, Ibrahim M. Differentiation of benign and malignant neck pathologies: preliminary experience using spectral computed tomography. *J Comput Assist Tomogr.* 2013;37:666–72.
39. Srinivasan A, et al. Utility of dual-energy CT virtual keV monochromatic series for the assessment of spinal transpedicular hardware-bone interface. *Am J Roentgenol.* 2013;201:878–83.
40. Forghani R. Advanced dual-energy CT for head and neck cancer imaging. *Expert Rev Anticancer Ther.* 2015;15:1–13. <https://doi.org/10.1586/14737140.2015.1108193>.
41. Lam S, Gupta R, Kelly H, Curtin HD, Forghani R. Multiparametric evaluation of head and neck squamous cell carcinoma using a single-source dual-energy CT with fast kVp switching: state of the multiparametric evaluation of head and neck squamous cell carcinoma using a single-source dual-energy CT with F. *Cancers (Basel).* 2015;7:2201–16.
42. Stolzmann P, Winkelhofer S. Monoenergetic computed tomography reconstructions reduce beam hardening artifacts from dental restorations. *Forensic Sci Med Pathol.* 2013;9:327–32.
43. Albrecht MH, et al. Assessment of an advanced monoenergetic reconstruction technique in dual-energy computed tomography of head and neck cancer. *Eur Radiol.* 2015;25:2493–501.
44. Scholtz J, Husers K, Lehnert T, Vogl TJ, Wichmann JL. Non-linear image blending improves visualization of head and neck primary squamous cell carcinoma compared to linear blending in dual-energy CT. *Clin Radiol.* 2015;70:168–75.
45. Graser A, et al. Dual-energy CT in patients suspected of having renal masses: can virtual nonenhanced images replace true nonenhanced images? *Radiology.* 2009;252:433–40.
46. Tawfik AM, Bauer RW, Naguib NNN, Vogl TJ, Mack MG. Dual-energy CT of head and neck Cancer. *Investig Radiol.* 2012;47:306–11.
47. Primak AN, et al. Noninvasive differentiation of uric acid versus non—uric acid kidney stones using dual-energy CT 1. *Acad Radiol.* 2007;14:1441–7.
48. Boll DT, et al. Renal stone assessment with dual-energy multidetector CT and advanced postprocessing techniques: improved characterization of renal stone composition—pilot study 1 methods: results: conclusion. *Radiology.* 2009;250:813–20.
49. Forghani R, Man BD. Dual-energy computed tomography physical principles, approaches to scanning, usage, and implementation: part 2. *Neuroimaging Clin N Am.* 2017;27:385–400.
50. Kuno H, et al. Evaluation of cartilage invasion by laryngeal and hypopharyngeal squamous cell carcinoma with dual-energy CT. *Radiology.* 2012;265:488–96.
51. Gupta R, et al. Evaluation of dual-energy CT for differentiating intracerebral hemorrhage from iodinated contrast material staining. *Radiology.* 2010;257:205–11.
52. Chawla A, et al. Dual-energy CT applications in salivary gland lesions. *Br J Radiol.* 2017;90:20160859.
53. Phan CM, Yoo AJ, Hirsch JA, Nogueira RG, Gupta R. Differentiation of hemorrhage from iodinated contrast in different intracranial compartments using dual-energy head CT. *Am J Neuroradiol.* 2012;33:1088–94.
54. Naruto N, Tannai H, Nishikawa K, Yamagishi K. Dual-energy bone removal computed tomography (BRCT): preliminary report of efficacy of acute intracranial hemorrhage detection. *Emerg Radiol.* 2017;25:29–33.
55. Aran S, Besheli LD, Gupta R, Flores EJ, Abujudeh HH. Applications of dual-energy CT in emergency radiology. *Am J Neuroradiol.* 2014;202:314–24.
56. Romero JM, et al. Prospective validation of the computed tomographic angiography spot sign score for intracerebral hemorrhage. *Stroke.* 2013;44:3097–102.
57. Demchuk AM, et al. Prediction of haematoma growth and outcome in patients with intracerebral haemorrhage using the CT-angiography spot sign (PREDICT): a prospective observational study. *Lancet Neurol.* 2012;11:307–14.
58. Tan CO, et al. Spot and diffuse signs: quantitative markers of intracranial hematoma expansion at dual-energy CT. *Radiology.* 2019;219:179–86.



# Photon-Counting Detector-Based Computed Tomography

# 8

Kishore Rajendran and Cynthia H. McCollough

## Contents

8.1	<b>Introduction</b> .....	87
8.2	<b>Multi-Energy CT Using Photon-Counting Detectors</b> .....	88
8.2.1	Energy Binning and X-Ray Attenuation.....	88
8.2.2	Electronic Noise and Artifact Reduction.....	88
8.2.3	High-Resolution Imaging.....	88
8.2.4	Material Decomposition.....	90
8.3	<b>Whole-Body PCD-CT</b> .....	90
8.4	<b>Preclinical Neurological Applications of PCD-CT</b> .....	91
8.4.1	Temporal Bone Imaging.....	91
8.4.2	Head and Neck CT Angiography.....	92
8.4.3	Spine Imaging.....	92
8.5	<b>Conclusions and Outlook</b> .....	92
8.6	<b>Clinical Case</b> .....	93
	<b>References</b> .....	94

## 8.1 Introduction

Photon-counting detectors (PCDs, also commonly known as energy-resolving, energy-discriminating, or direct conversion detectors) are a type of X-ray detector that allows multi-energy X-ray acquisitions from a single X-ray exposure. The predecessor of spectral CT imag-

ing is a dual-energy approach [1], where two X-ray acquisitions with different X-ray spectra (and effective energies) are acquired with dual-source, rapid kVp-switching, dual-layer detectors, or dual-pass methods. These dual-energy approaches make use of conventional X-ray detectors, known commonly as energy-integrating detectors (EIDs). EIDs convert X-rays to visible light, and the light to electrical signal, to record the associated attenuation. Different tissue types and contrast materials have distinct X-ray spectral signatures (a material's X-ray attenuation is dependent on the X-ray energy).

---

K. Rajendran · C. H. McCollough (✉)  
Department of Radiology, Mayo Clinic,  
Rochester, MN, USA  
e-mail: [mccollough.cynthia@mayo.edu](mailto:mccollough.cynthia@mayo.edu)

This traditional gray-scale imaging approach from EID-CT systems is useful for anatomical imaging, as demonstrated by decades of use of EIDs in commercial systems. However, an inherent limitation of EIDs is the loss of X-ray *energy* information during signal (energy) integration.

PCDs employ a direct conversion detector technology that records X-ray events without first converting them to visible light. The X-ray energies of individually detected photons are determined based on the magnitude of the electrical signal they create. Based on user-defined energy thresholds, the detected photons are binned according to their energies. This approach provides energy-resolving capabilities to the data acquisition system, which can be used to spectrally profile different materials in vivo at clinically acceptable signal-to-noise (SNR) ratios. This chapter is intended to introduce readers to the basics of using PCDs for CT imaging and their relative advantages, concluding with a case report involving a research whole-body PCD-CT system.

---

## 8.2 Multi-Energy CT Using Photon-Counting Detectors

In this section, the working principles of a typical PCD-CT system and how it benefits clinical imaging are briefly described.

### 8.2.1 Energy Binning and X-Ray Attenuation

The energy resolution of a PCD comes from its ability to assign detected X-ray photons to individual energy bins. This allows the PCD-CT system to sample the X-ray attenuation profile of different materials, such as native tissue types (fat, muscle, bone), and contrast media, such as iodine and gadolinium. One application of PCD-CT is K-edge imaging [2], where energy thresholds are specified at certain energy levels that correspond to the K-edge energy of different contrast materials (example, gadolinium with

K-edge at 50.2 keV, or gold nanoparticles with K-edge at 80.7 keV). By placing energy thresholds just below the K-edges of such materials, it is possible to measure the K-edge discontinuity in subsequent energy bins (Fig. 8.1) to identify and quantify the material type and its mass density.

### 8.2.2 Electronic Noise and Artifact Reduction

Since PCDs detect X-rays above a certain energy threshold, it is possible to set the lowest energy threshold just above the electronic noise level of the system, thereby reducing streak artifacts occurring from electronic noise in the acquired data. This property of PCDs allows for dose reduction at a specific noise level, or reduced artifacts at lower doses. Conversely, due to the lack of the ability to set a lower energy threshold in EIDs, current commercial CT systems suffer from electronic noise at low doses or when imaging large patients [4]. An extension of this approach is the ability to set an energy threshold at a higher energy, above which beam hardening is less pronounced [5, 6]. This results in a reduction of beam-hardening artifacts in the high-energy bin images arising from dense objects such as the petrous bones or metal implants. Since not all of the detected photons are used, these images exhibit relatively higher image noise levels.

### 8.2.3 High-Resolution Imaging

It is desirable to have a smaller X-ray detector pixel element to increase the spatial resolution of the CT system. Conventionally, this is achieved by reducing the size of the detector pixel. This approach is difficult to implement due to decreased geometric dose efficiency as the detectors are cut into smaller pixels. This is because a finite-width layer of light-reflecting media is required between each detector cell in order to avoid signal from one pixel spreading into neighboring pixels [7].

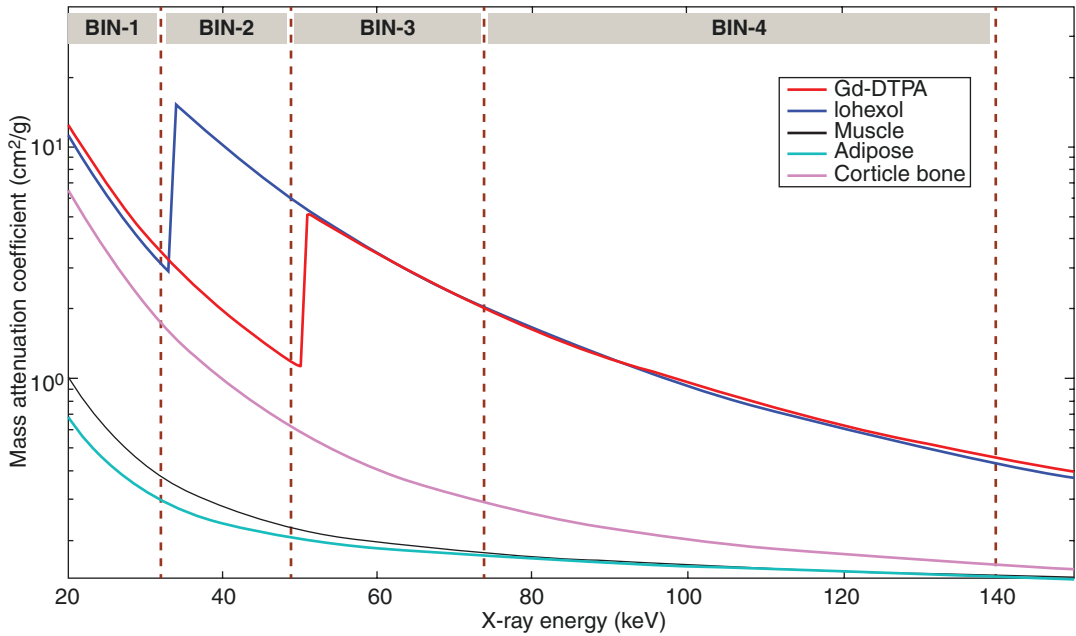


**Fig. 8.1** Energy-binning scheme for multiple contrast materials (iohexol and Gd-DTPA) and native tissue types at a 140 kV tube potential. Bins 2 and 3 are placed around the K-edges of iodine (33 keV) and gadolinium (50 keV), respectively. The K-edge energy of native tissue types

such as bone is too low (4 keV) to be imaged with the clinical X-ray energy range (20–150 keV). The mass attenuation values were obtained from the National Institute of Standards and Technology (NIST [3]) based on ICRU44

Another approach is to use a dedicated attenuating filter in front of the detector array. This ultra-high resolution (UHR) filter [8], typically designed in the form of a metallic comb or grid, reduces the effective pixel aperture size by blocking photons from entering the detector. As a result, the total pixel size is reduced, leading to an increase in spatial resolution. One of the disadvantages of this approach is the dose inefficiency due to use of the UHR filter, which blocks X-rays that have already passed through the patient.

Reducing the pixel size, whether by making a smaller detector pixel or by use of a UHR filter, also leads to a decrease in SNR, and additional measures such as increasing the acquisition dose or using noise reduction algorithms are usually warranted.

With PCD technology, it is possible to directly design smaller detector pixels, and this is an inherent benefit from the semiconductor technology and the detector fabrication processes used in

PCDs. The PCDs do not suffer from fill factor limitations of EIDs due to detector septa, and can be fabricated to sizes as small as  $450 \times 450 \mu\text{m}^2$  at the detector ( $250 \times 250 \mu\text{m}^2$  at the isocenter). It is to be noted, however, that PCDs suffer from non-ideal physical effects such as charge sharing [9, 10] at smaller pixel sizes. Hence, the use of even smaller detector pixels will degrade the spectral resolution of the imaging system if these effects are not taken into account. On the other hand, larger pixel sizes require dedicated high-speed readout electronics to deal with the increased per-pixel count rate. That is, it is difficult for PCDs to handle the high photon flux required for clinical CT at detector pixel sizes much greater than a few hundred microns. Finally, pixel binning can be used to minimize charge-sharing effects, and dedicated hardware or software-based correction schemes can be used to identify and correct charge sharing effects.

### 8.2.4 Material Decomposition

Using the spectrally resolved data acquired using PCD-CT, it is possible to transform the multi-energy CT images into material maps representative of specific anatomical and physiological processes. Currently, the spectral separation on the research whole-body PCD-CT system (Somatom CounT, Siemens Healthcare GmbH, Forchheim, Germany) is better than non-dual-source, dual-energy systems and comparable to the newer dual-source, dual-energy CT systems [11, 12]. Thus, compared to dual-energy systems with lower spectral separation (kVp switching, dual-layer detector, and dual-pass approaches), improvements in material decomposition performance can be achieved. The primary goal of material decomposition is to locate and differentiate material types *in vivo* (native tissue types and contrast media), and quantify their mass densities. The ability of PCD-CT to capture the K-edge information of contrast materials may lead to new material decomposition capabilities. One promising application of PCD-CT is the ability to locate and quantify the uptake of nanoparticles at specific targeted sites of interest. Surface-functionalized nanoparticles with antibody conjugation can be tailored to bind with certain tissue types (e.g., cancer cells, fibrotic collagenous tissue, etc.), and PCD-CT has demonstrated quantitative imaging of such targeted nanoparticles in small animal studies, potentially enabling CT-based molecular imaging [13, 14]. The use of nanoparticles as a whole-body CT contrast agent currently faces challenges such as effective surface functionalization and targeting, *in vivo* toxicity of heavy metals used in nanoparticles, sufficient uptake at target site to produce clinically acceptable sensitivity and specificity, and contrast dose optimization. For the present time, conventional contrast agents based on iodine and gadolinium have been largely used in PCD-CT research to demonstrate imaging tasks involving material decomposition [2, 15].

### 8.3 Whole-Body PCD-CT

Several prototype PCD-CT scanners have been reported in the literature, mainly designed as small-animal or bench-top scanners [13, 16], with limited field of view (FOV) size, to characterize PCD imaging performance and to carry out early-stage pre-clinical studies involving small animals or excised specimens. The world's first research whole-body PCD-CT system (Somatom CounT, Siemens Healthcare) capable of performing multi-energy imaging at clinical dose rates and dose levels is currently installed at three sites—Mayo Clinic (USA), the National Institutes of Health (USA), and the German Cancer Research Center (Germany).

The whole-body PCD-CT scanner is a modified second-generation dual-source scanner (Somatom Definition Flash, Siemens Healthcare). One of the two X-ray sources is coupled to a cadmium telluride PCD array with a 27.5-cm FOV at scan isocenter. The second source is coupled to a conventional EID array with a native FOV of 50 cm at scan isocenter as shown in Fig. 8.2. The PCD FOV is suf-

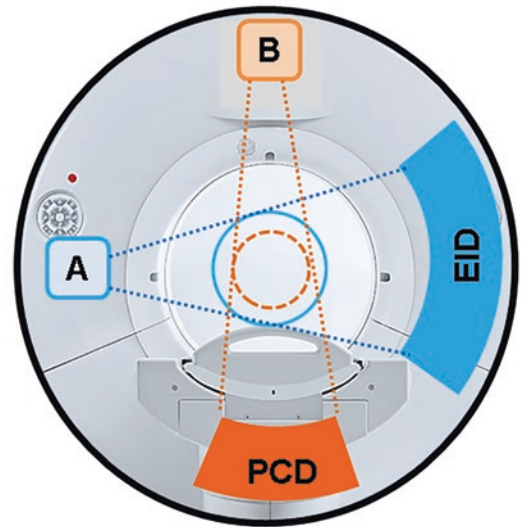


**Fig. 8.2** Whole body research PCD-CT system. The A-tube is coupled to a conventional energy-integrating detector (EID) array, while the B-tube is coupled to a photon-counting detector (PCD) array. Note the reduction in the scan FOV for PCD (inner orange circle, 27.5 cm) relative to EID (outer blue circle, 50 cm)

ficient to scan head and extremities without data truncation. When scanning the thoracic, abdominal, and pelvic regions (cross-sectional diameters  $>27.5$  cm), an additional low-dose scan (known as the data completion scan) from the EID system is required to correct the data truncation occurring from PCD subsystem's limited FOV [17].

The PCD-CT scanner offers four data acquisition modes, which are based on the number of energy thresholds available and the mode's spatial resolution. The four acquisition modes are: (i) Macro mode, (ii) Chess mode, (iii) Sharp mode, and (iv) Ultra-high resolution (UHR) mode. The differences are described in Table 8.1.

Several reports have been published evaluating the benefits of each of the above-mentioned acquisition modes. Yu et al. [18] reported the conventional CT imaging performance of the whole-body PCD-CT system involving the Macro and Chess modes. The results revealed that PCD-CT Macro and Chess mode images exhibit enhanced iodine contrast than EID-based conventional CT images due to the equal weighting applied to all detected photons, which allows a more efficient retrieval of low-energy X-ray information compared to EID CT systems. This leads to improved image contrast. The PCD-CT system also provides a slightly improved longitudinal spatial resolution due to the smaller detector pixel size compared to conventional CT, while the in-plane spatial resolution remained identical between the two systems.

Leng et al. [19] reported the benefits of the UHR and Sharp modes, namely a substantial improvement in the spatial resolution (in-plane and longitudinal) relative to the Chess and Macro modes. Additionally, noise-matched images were achievable with PCD-based high-resolution imaging at 50% lower dose compared to conventional EID-based high-resolution (UHR filter-based) imaging.

## 8.4 Preclinical Neurological Applications of PCD-CT

Clinical use of conventional dual-energy CT systems has demonstrated improved contrast enhancement and quantitative material discrimination [20] than conventional single-energy CT. Between 2015 and 2017, research studies involving the whole-body PCD-CT have demonstrated reduced blooming effects from bone, reduced beam-hardening artifacts using high-energy acquisitions, and improved temporal bone imaging using high-resolution PCD-CT. A preliminary list of neuroimaging tasks for which PCD CT demonstrated improved imaging performance is given below.

### 8.4.1 Temporal Bone Imaging

One of the challenges in temporal bone CT imaging is the detection of malleus head and incus

**Table 8.1** PCD-CT acquisition modes available on the whole-body research PCD-CT system and their properties

Mode	Collimation	Detector pixel size	No. of energy thresholds	Description
Macro	$32 \times 0.50$ mm	0.90 mm (0.50 mm at isocenter)	2	Dual-energy mode with comparable resolution to conventional CT.
Chess	$32 \times 0.50$ mm	0.90 mm (0.50 mm at isocenter)	4	Interleaved Chess pattern to extend spectral capability to four thresholds
UHR	$32 \times 0.25$ mm	0.45 mm (0.25 mm at isocenter)	2	Ultra-high resolution mode for dose-efficient scanning at increased spatial resolution
Sharp	$48 \times 0.25$ mm	0.45 mm (0.25 mm at isocenter) for lower energy threshold 0.90 mm (0.50 mm at isocenter) for high-energy threshold	2	Hybrid mode, with one threshold suited for high-resolution imaging, and another at standard resolution



body, and the stapes superstructure; this requires ultra-high resolution capabilities from the imaging system. As described earlier, conventional approaches toward achieving better spatial resolution for temporal bone imaging are dose inefficient due to the use of a septa between detectors or an X-ray blocking UHR filter in front of the detectors. PCD-CT-based UHR imaging of the temporal bone can approximately yield a 50% dose reduction at equivalent levels of image noise relative to EID-CT-based UHR imaging, as demonstrated by Leng et al. [19] using anthropomorphic phantom and cadaveric temporal bone specimens.

### 8.4.2 Head and Neck CT Angiography

The improvements in iodine contrast-to-noise ratio from PCD-CT [21] could benefit contrast-enhanced procedures such as angiography. Angiography of the head and neck, in particular, deals with assessing small to moderately sized blood vessels and the ultra-high-resolution modes of the PCD-CT system could yield better anatomical delineation and contrast differentiation. The high-resolution modes of the conventional EID CT are typically limited to bone imaging, and are not routinely employed for angiography applications. PCD-CT offers the ability to provide improved iodine contrast at ultra-high spatial resolution.

Symons et al. [22] demonstrated the use of PCD-CT for head and neck CT angiography to exploit the improved iodine contrast resolution and quantitative multi-material discrimination capabilities of the PCD-CT system. Image quality was scored in patient images obtained using the PCD-CT system based on image noise and artifacts, and delineation of segments in the internal carotid artery, vertebral artery, basilar artery, and cerebral artery. In comparison to EID-CT, PCD-CT showed significantly higher scores overall for delineating petrous and cavernous segments of the internal carotid artery, foraminal and atlantic segments of the vertebral artery, and all the three segments (anterior, posterior, and mid-

dle) of the cerebral artery. This was facilitated by the improved iodine contrast and lower subjective image noise demonstrated by the PCD-CT.

### 8.4.3 Spine Imaging

One of the major benefits of PCD-CT for spine imaging comes from its ability to reduce metal artifacts arising from dense metal spine hardware using high-energy bin images. Beam hardening occurs when soft X-rays (low-energy X-rays) are removed from the primary beam, causing beam hardening (meaning only the high-energy hard X-rays remain in the beam). This causes the mean energy of the polychromatic beam to shift toward higher X-ray energy. The high-energy X-rays can penetrate dense objects better than soft X-rays, and undergo lesser beam hardening, consequently showing lesser beam hardening artifacts (streaking). Zhou et al. [6, 23] reported the use of high energy PCD-CT images to reduce metal artifacts in phantom experiments, and in patients with metal hardware. It was found that the PCD-CT approach using a [75–140] keV bin showed substantial reduction in artifacts compared to the full spectrum image, which was similar to EID-based images.

## 8.5 Conclusions and Outlook

The studies described in this chapter demonstrate the potential benefits of PCD-CT for neuroimaging applications. Dose-efficient high-resolution CT and multi-energy acquisition for accurate quantitative material discrimination using techniques such as K-edge imaging could be considered as the primary benefits of the next-generation CT systems involving PCDs. In particular, neuroimaging tasks could benefit from improved contrast for CTA applications, reduced noise or reduced dose for temporal bone imaging, and reduced metal artifacts for imaging tasks involving metal implants. Multi-energy data from PCD-CT can be processed using conventional

dual-energy post-processing techniques to yield additional diagnostic information, or could lead to the development of new tools and techniques to process multi-energy PCD-CT images. Due to the limited availability of research whole body PCD-CT systems, additional studies are required prior to widespread clinical use, as well as the development of large-scale manufacturing techniques. Nonetheless, PCD-CT technology continues to rapidly evolve and initial results from the current research scanners clearly demonstrate the benefits of PCD-CT for diagnostic imaging.

## 8.6 Clinical Case

After IRB approval and written-informed consent, a 39-year-old male was scanned using the whole-body PCD-CT system at our institution. The PCD-CT non-contrast head scan was performed using the Sharp mode head protocol at 140 kV, 200 mAs, 0.5 s rotation time, and energy thresholds set to 25 and 75 keV. The  $CTDI_{vol}$  for the exam was 55 mGy, matching the dose of the clinical scan performed on an EID CT scanner (Somatom Force, Siemens Healthcare) for temporal bone imaging. PCD-CT images were reconstructed using weighted-filtered back projection

[24] (WFBP) using a high-resolution kernel U70f (Fig. 8.3). The EID-CT images were reconstructed using WFBP and ADMIRE (strength-2) using a high-resolution U73u kernel.

Image analysis revealed that the PCD-UHR reconstructions exhibited lower image noise for the same volume CT dose index ( $CTDI_{vol}$ ) compared to the conventional EID-UHR images, as was expected due to the absence of the grid/comb UHR filter on the PCD system. The PCD-CT image (WFBP) showed lower noise than the WFBP and ADMIRE (iterative reconstruction package from Siemens Healthcare) images from the conventional EID-UHR scan. The EID images showed a subtle increase in image sharpness, which was due to the availability of a smaller focal spot size and a flying focal spot on the EID system (such features are not yet available on the research PCD-CT system). Using the equation described by Leng et al. [19], the reduction in image noise between the two systems can be used instead to lower the PCD-CT dose, while achieving the same noise as the EID-CT system. For a noise difference of 40% between PCD (WFBP) and EID (WFBP), as shown in Fig. 8.3, matched image noise could be achieved on the two systems by reducing the PCD-CT dose by 64%.

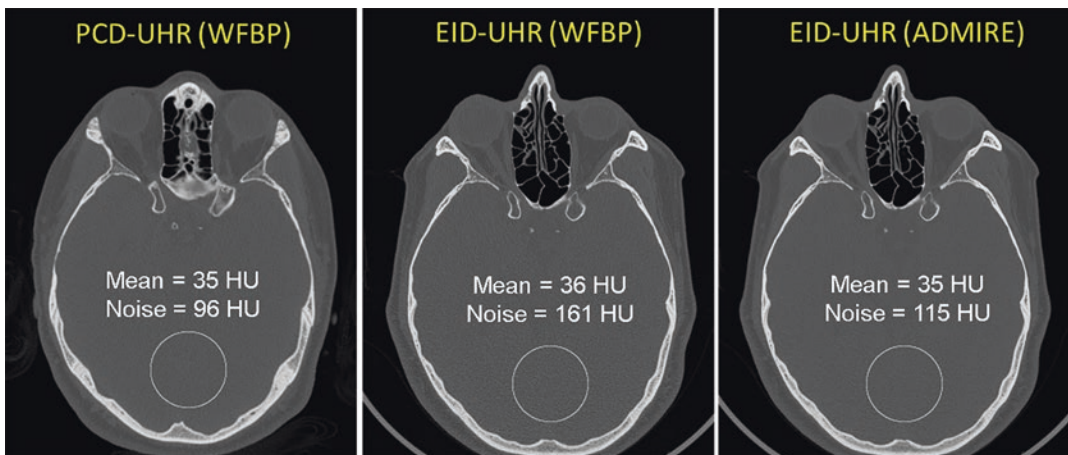


**Fig. 8.3** Head CT scan reconstructions of 140 kV PCD-UHR (Sharp mode) using U70f (WFBP kernel), and conventional EID-based UHR at 120 kV reconstructed using

Ur73u kernel (WFBP and ADMIRE-2). Reconstruction FOV = 275 mm, image matrix size = 1024×1024, display [W/L] = [2800/600] HU

## References

1. Baert AL, et al., editors. Dual energy CT in clinical practice. Medical radiology—diagnostic imaging. Heidelberg: Springer; 2011.
2. Schlomka JP, et al. Experimental feasibility of multi-energy photon-counting K-edge imaging in pre-clinical computed tomography. *Phys Med Biol*. 2008;53(15):4031–47.
3. Hubbell JH, Seltzer SM. NIST X-ray mass attenuation coefficients—NISTIR 5632; 1996.
4. Yu Z, et al. Noise performance of low-dose CT: comparison between an energy integrating detector and a photon counting detector using a whole-body research photon counting CT scanner. *J Med Imaging*. 2016;3(4):043503.
5. Rajendran K, et al. Reducing beam hardening effects and metal artefacts in spectral CT using Medipix3RX. *J Instrum*. 2014;9(03):P03015.
6. Zhou W, et al. Metal artifact reduction and dose efficiency improvement on photon counting Ct using an additional tin filter. *Med Phys*. 2017;44(6):3235.
7. Kakinuma R, et al. Ultra-high-resolution computed tomography of the lung: image quality of a prototype scanner. *PLoS One*. 2015;10(9):e0137165.
8. McCollough CH, et al. Spatial resolution improvement and dose reduction potential for inner ear CT imaging using a z-axis deconvolution technique. *Med Phys*. 2013;40(6):061904.
9. Koenig T, et al. How spectroscopic x-ray imaging benefits from inter-pixel communication. *Phys Med Biol*. 2014;59(20):6195–213.
10. Taguchi K, Iwanczyk JS. Vision 20/20: single photon counting x-ray detectors in medical imaging. *Med Phys*. 2013;40(10):100901.
11. Leng S, et al. Spectral performance of a whole-body research photon counting detector CT: quantitative accuracy in derived image sets. *Phys Med Biol*. 2017;62(17):7216–32.
12. Faby S, et al. Performance of today's dual energy CT and future multi energy CT in virtual non-contrast imaging and in iodine quantification: a simulation study. *Med Phys*. 2015;42(7):4349–66.
13. Anderson NG, Butler AP. Clinical applications of spectral molecular imaging: potential and challenges. *Contrast Media Mol Imaging*. 2014;9(1):3–12.
14. Schirra CO, et al. Spectral CT: a technology primer for contrast agent development. *Contrast Media Mol Imaging*. 2014;9(1):62–70.
15. Rink K, et al. Investigating the feasibility of photon-counting K-edge imaging at high x-ray fluxes using non-linearity corrections. *Med Phys*. 2013;40(10):101908.
16. Touch M, et al. A neural network-based method for spectral distortion correction in photon counting x-ray CT. *Phys Med Biol*. 2016;61(16):6132–53.
17. Yu Z, et al. How low can we go in radiation dose for the data-completion scan on a research whole-body photon-counting computed tomography system. *J Comput Assist Tomogr*. 2016;40(4):663–70.
18. Yu Z, et al. Initial results from a prototype whole-body photon-counting computed tomography system. *Proc SPIE Int Soc Opt Eng*. 2015;9412:94120W.
19. Leng S, et al. Dose-efficient ultrahigh-resolution scan mode using a photon counting detector computed tomography system. *J Med Imaging (Bellingham)*. 2016;3(4):043504.
20. Krauss B, Schmidt B, Flohr TG. Dual energy CT in clinical practice. In: Baert AL, et al., editors. Medical radiology—diagnostic imaging. Heidelberg: Springer; 2011. p. 11–20.
21. Gutjahr R, et al. Human imaging with photon counting-based computed tomography at clinical dose levels: contrast-to-noise ratio and cadaver studies. *Invest Radiol*. 2016;51(7):421–9.
22. Symons R, et al. Photon-counting computed tomography for vascular imaging of the head and neck: first in vivo human results. *Invest Radiol*. 2018;53(3):135–42.
23. Zhou W, et al. Reduction of metal artifacts and improvement in dose efficiency using photon-counting detector computed tomography and tin filtration. *Invest Radiol*. 2019;54(4):204–11. <https://doi.org/10.1097/RLI.0000000000000535>.
24. Stierstorfer K, et al. Weighted FBP—a simple approximate 3D FBP algorithm for multislice spiral CT with good dose usage for arbitrary pitch. *Phys Med Biol*. 2004;49(11):2209–18.



# Basics of Magnetic Resonance Imaging

# 9

Franciszek Hennel, Roger Luechinger,  
and Marco Piccirelli

## Contents

9.1	<b>Introduction</b> .....	96
9.2	<b>History</b> .....	96
9.3	<b>Principles of MRI</b> .....	98
9.3.1	The Signal.....	98
9.3.2	Excitation.....	99
9.3.3	Spatial Encoding.....	99
9.3.4	Data Sampling.....	101
9.4	<b>MRI Pulse Sequences</b> .....	103
9.4.1	Gradient Echo.....	103
9.4.2	Spin Echo.....	105
9.4.3	Fast Spin Echo.....	106
9.4.4	Echo Planar Imaging.....	106
9.4.5	Spiral Scan.....	106
9.4.6	Radial Scan.....	107
9.4.7	Ultrashort Echo Time.....	107
9.4.8	Contrast Options.....	107
9.5	<b>MR Safety</b> .....	111
9.5.1	Overview.....	111
9.5.2	MR System.....	112

---

F. Hennel · R. Luechinger  
Institute for Biomedical Engineering, University of  
Zurich and ETH Zurich, Zurich, Switzerland  
e-mail: [hennel@biomed.ee.ethz.ch](mailto:hennel@biomed.ee.ethz.ch); [luechinger@biomed.ee.ethz.ch](mailto:luechinger@biomed.ee.ethz.ch)

M. Piccirelli (✉)  
Department of Neuroradiology, University Hospital  
Zurich, Zurich, Switzerland  
e-mail: [marco.piccirelli@usz.ch](mailto:marco.piccirelli@usz.ch)

9.5.3	Potential Safety Risks of the Electromagnetic Fields.....	113
9.5.4	Potential Safety Risks Due to Contrast Agents and Medication.....	115
9.5.5	Other Potential Safety Risks Including Liquid Helium.....	116
9.5.6	MR Safety Labels for Medical Devices.....	117
9.5.7	Passive Implants.....	117
9.5.8	Active Implants.....	118
9.5.9	Site Planning.....	119
9.5.10	Training.....	120
9.5.11	Conclusion.....	120
	<b>References.....</b>	<b>120</b>

---

## 9.1 Introduction

Magnetic resonance imaging (MRI) is a widely used tomographic technique with numerous applications in all domains of medical diagnostics, animal research, and material science. Its popularity is due to the absence of ionizing radiation, which allows MRI to be used without “dose” restrictions for patients and healthy volunteers of any age, as well as to the exceptional variety of contrasts achievable with this technique. MRI is based on the phenomenon of nuclear magnetic resonance (NMR) in which magnetic moments of certain nuclei, above all the ubiquitous hydrogen (1H), placed in a strong magnetic field interact with weak electromagnetic pulses and generate a radio-frequency signal. The richness of MRI contrasts is related to the sensitivity of this phenomenon to the physical and chemical properties of the neighboring tissue. The NMR signal depends on the structure and dynamics of molecules containing the observed nuclei, the presence of paramagnetic ions, the viscosity, diffusion, and flow of the tissue—all these properties are reflected by the MR image intensity or even quantifiable in absolute units. Consequently, in addition to morphology, MRI provides further important biomedical information such as accumulation of fat, demyelination, orientation of myocytes and white matter axons, vascularization of tumors, cortical function-related blood oxygenation, vascular reactivity, cellular integrity, and blood flow.

---

## 9.2 History

The idea to use NMR for tomographic imaging was proposed in 1973 by Paul Lauterbur [1] of the Stony Brook University, New York, USA, and, independently, by Sir Peter Mansfield of The University of Nottingham, UK [2]. They were jointly awarded the Nobel Prize in Physiology and Medicine for this achievement in 2003. “NMR imaging” remained the matter of academic research in several laboratories until the construction of first clinical MRI scanners in the 1980s. Both inventors have significantly contributed to the development of MRI throughout their further career: Lauterbur advanced relaxation-based contrast mechanisms, three-dimensional reconstruction, and spectroscopic imaging; Mansfield improved numerous technical aspects from slice selection to the design of gradient coils, and, above all ultrafast imaging. His famous Echo Planar Imaging (EPI) method, demonstrated as early as 1977, is being used on all high-end scanners today with only minor modifications [3]. Another Nobel Prize laureate, Richard Ernst of the ETH Zurich, Switzerland, inventor of two-dimensional NMR spectroscopy, a technique that visualizes molecular bonds in form of two-dimensional maps, translated this idea to MRI in 1975 and laid the foundations of Fourier transform-based image reconstruction used by today’s scanners [4]. Further, Nobel Prize Laureates related to the NMR field were Otto Stern, Isidor I. Rabi, Edward M. Purcell, Felix Bloch, and Kurt Wüthrich.

Further milestones in the early MRI history originate from several academic centers. The “spin-warp” method proposed in Aberdeen, UK, in 1980 introduced basic building blocks of all modern MRI sequences: The readout- and phase-encoding gradient pulses [5]. Groups in Göttingen and, later, in Würzburg, Germany developed the “fast low-angle shot” or FLASH imaging sequence based on gradient echoes, allowing images to be acquired in a few seconds instead of usual minutes needed for spin-echo sequences at the time [6]. Juergen Hennig in Freiburg, Germany proposed a similar acceleration of the spin-echo sequence by finding the way to combine the known Carr–Purcell echo train with phase encoding gradients [7]. Interestingly, an incredible step in the development of fast MRI was made by two theoretical papers, published independently by Ljunggren [8] and Twieg [9] in 1983, who imported the now basic notion of  $k$ -space from diffraction physics to MRI. This not only explained existing approaches, such as spin-warp or EPI in simpler terms, but opened a door to the optimization of scanning strategy and resulted in “non-Cartesian” methods such as the spiral scan, the approach pioneered by Albert Macovski and colleagues in Stanford, USA [10, 11]. Beyond the work on image-generation schemes, research of the 1980s focused on the information contents of an MR image. Paul Callaghan of Massey University, New Zealand [12, 13], developed foundations of the now flourishing diffusion MRI [14], and extended the diffraction formalism to “ $q$ -space” [15], the domain reciprocal to molecular displacements. Together with the seminal work on diffusion anisotropy at the NIH in Bethesda, USA [16], this has led to the spectacular results of brain connectivity imaging we appreciate today. Further decisive steps on the way to today’s variety of MR image types include works of PR Moran at the University of Illinois, Urbana–Champaign, USA on flow quantification [17], DB Plewes in Toronto and R Muthupillai at the Mayo Clinic, Rochester, USA on MR elastography [18], and M Haacke in

Detroit, USA and JR Reichenbach, Jena, Germany on magnetic susceptibility mapping [19]. An interesting mathematical aspect was common to these new methods: the attention shift from the magnitude of an MRI image to its so far neglected phase as the source of information.

The turn of the century brought another important achievement in the quest for new information sources in MRI, which has revolutionized its further practice. At that time, the technology of parallel signal detection by a receiver coil array [20], proposed in early 1990 by PB Roemer, GE R&D Niskayuna, USA was coming into use on clinical systems. The advantage of a higher signal-to-noise ratio provided by reduced distance of the coil array to the body (as compared to single volume “birdcage” coils mostly used) was mitigated by the side effect of uneven image intensity. The idea proposed independently by DK Sodickson at Harvard, USA and, in a more general form, by Klaas Paul Pruessmann and colleagues at the ETH Zurich, Switzerland was to turn the “problem” of limited spatial sensitivity of array coils into a source information that is complementary to what is provided by field gradients and allows a reduction of scanning time [21, 22]. While Sodickson’s original SMASH (simultaneous acquisition of spatial harmonics) required the array coils in a linear arrangement to mimic modulations produced by the action of field gradients, Pruessmann’s SENSE (sensitivity encoding) could work with any coil profile arrangement, as long as it represents an invertible algebraic problem. Shortly later, MA Griswold and the new generation of MRI scientists in Würzburg, Germany proposed GRAPPA (GeneRalized Autocalibrating Partially Parallel Acquisition) [23], which allowed the tricky measurement of the coil sensitivities to be avoided by a  $k$ -space data interpolation based on a few additional “autocalibration” signals, but constrains the acceleration factor to integers. What is now called parallel MRI and implemented by different vendors as SENSE, GRAPPA, or ASSET has become a standard feature of all MRI scanners, which

now contain tens of receiver channels, dedicated array coils for different parts of the body, and allow up to tenfold reduction of scan time compared to what was common in early 1990s.

The next opportunity for MR imaging—speed increase came from the rapidly evolving domain of signal compression. Its basic idea is that an image or a dynamic series of images typically contains much less information than one could judge by the number of pixels and frames. Parts of the image outside of the body are “black,” extended regions of identical tissue have similar intensity, and parts of the image do not change from frame to frame, e.g., in a heart cycle movie [24]. Consequently, a properly chosen mathematical transform of the image will have only a limited number of “sparse” signal points on a negligible background, allowing the image to be derived from a correspondingly limited amount of MRI data. This approach, known as sparse MRI or compressed-sensing MRI, initiated by M Lustig, D Donoho, and JM Pauly of Stanford University in 2007, triggered a huge wave of research, which is just making its way to clinical MRI practice [25].

Almost half a century after Lauterbur’s and Mansfield’s invention, the technology and methodology of MRI does not stop advancing. The present decade has witnessed an incredible progress in the engineering of superconducting magnets, with 23 Tesla (T) becoming available for animal and 10 T for human research [26]. Small-scale magnets for animal MRI, and, since recently, even a whole-body clinical 1.5 T system are offered with only minimum amount of cryogen (liquid helium) making MRI cheaper to install and maintain. Magnetic field gradients, the strength of which is decisive for the scanning speed and quality of diffusion MRI reach 300 mT/m on dedicated research systems and 80 mT/m on commercial scanners, while 10 mT/m was considered standard in the early days of clinical MRI. Scanner hardware is being extended by optical tracking devices allowing microscopic image resolution despite patient

motion, and by field monitoring sensors, which compensate the effects of respiration, heartbeat, and hardware instability. Tissues long considered MRI-invisible, such as bones, teeth, and lungs are being imaged with new sequences, and new quantitative methods are being proposed that provide parameter maps rather than just “weighted” images to allow absolute quantitative assessment of diseases, lesion grade, and therapy effects.

---

## 9.3 Principles of MRI

### 9.3.1 The Signal

The underlying principle of MRI is the fact, that most atomic nuclei, in particular  $^1\text{H}$  (proton; the nucleus of hydrogen atom present in high quantity of water-containing living organisms), possess a magnetic moment linked to their spin. The latter is a quantum mechanical property similar to angular momentum. Due to this linking, spins placed in the magnetic field do not simply get aligned with it by magnetic torque (as the needle of a compass within the Earth’s magnetic field). Instead, spins rotate around the field direction with an angular velocity that is proportional to the torque, and thus to the field strength. This motion, called Larmor precession, allows us to receive a signal in a conducting loop (or coil) placed close to the object. Precessing nuclear magnetization (net magnetic moment of all nuclei) generates an alternating voltage in the coil by means of electromagnetic induction, in the same way as a rotating magnet does in a dynamo. What is essential for MRI is the linear relation between the angular velocity of the nuclear precession (and the frequency of the signal) and the strength of the magnetic field ( $B_0$ ):

$$\text{Angular velocity} = 2\pi \times \text{signal frequency} = \gamma B_0$$

The constant  $\gamma$  is the gyromagnetic ratio characteristic of the nucleus. For  $^1\text{H}$ , the gyro-

magnetic ratio gives a signal frequency of 42.6 MHz/T. Thus, the resonance signals are situated in the range of radio waves in the field range available for human MRI. Frequencies of other nuclei are lower.

### 9.3.2 Excitation

Outside of the magnet, spins in the human body point in random directions and the net nuclear magnetization is zero. After the positioning in the magnet, the spins become polarized, i.e., predominantly oriented along the field in a process called longitudinal relaxation, which we will discuss again when talking about image contrast. The nuclear magnetization is created, but does not yet induce signal, since it is parallel to the magnetic field  $B_0$  (Fig. 9.1a). An external action is needed to “excite” the spins, i.e., to tip the magnetization from this “equilibrium” orientation and trigger the Larmor precession. Intuition tells us that an additional field component transverse to the main field is necessary for that. However, since only a weak field can rapidly be generated, a static transverse field would hardly change the direction of the effective magnetic field. The magnetization would start precession around this slightly tilted field but never reach a significant tip angle (Fig. 9.1b). What is needed is a transverse field that oscillates in concert with the Larmor precession. Figure 9.1c shows a simplified case, where  $B_1$  (as we call this field) jumps between two opposite directions (back and forth once per Larmor precession period). This progressively opens the angle between the magnetization vector and the effective field, and eventually brings the magnetization to a useful tilt. In practice, the  $B_1$  field is applied in a rotating manner, making the excitation most effective (shortest time to reach a desired angle with a given  $B_1$  amplitude). In that case, the end of the magnetization vector follows a spiral pathway, as shown in Fig. 9.1d. To produce the rotating field, a current pulse with a fre-

quency equal to the resonance frequency must be sent to the “transmission coil,” which may also be used to receive the signal from the whole body. Since the NMR resonance frequency is typically in the radio wave range, pulses used to tip the nuclear magnetization in MRI are called “radio-frequency (RF) pulses” and are characterized by the “tip angle” (a.k.a. flip-angle) they produce. For example, a “90° RF pulse” rotates the magnetization from the  $z$ -direction (by convention, the direction of the  $B_0$  field) to the  $x$ - $y$  plane and produces maximum induction effect and highest signal. The phase of the RF pulse determines the direction of the rotation axis.

### 9.3.3 Spatial Encoding

To obtain an image of the object emitting the resonance signal, a mechanism is needed that makes the signal dependent on the distribution of spins in space. This so-called spatial encoding of the signal is achieved in MRI by two means: gradients of the magnetic field, and local sensitivity of the receiving coils.

The magnetic field gradients in three orthogonal directions are produced by a set of three gradient coils, an additional electromagnet placed inside the main magnet bore. It is the rapid switching of strong currents in these coils and their interaction with the main field that produces vibrations and the typical intense sound during MRI examinations. The principle of using field gradients to localize a single point-like signal source is simple. With the  $x$ -gradient on, the field linearly changes with the  $x$ -position of the source and so does the resonance frequency, which can easily be measured. Two more signals with  $y$ - and  $z$ -gradients would allow a three-dimensional localization. With real objects, such as the human body, which contains a continuum of sources, the necessary number of signals and the duration of the scan depend on the required field of view and resolution of the image.



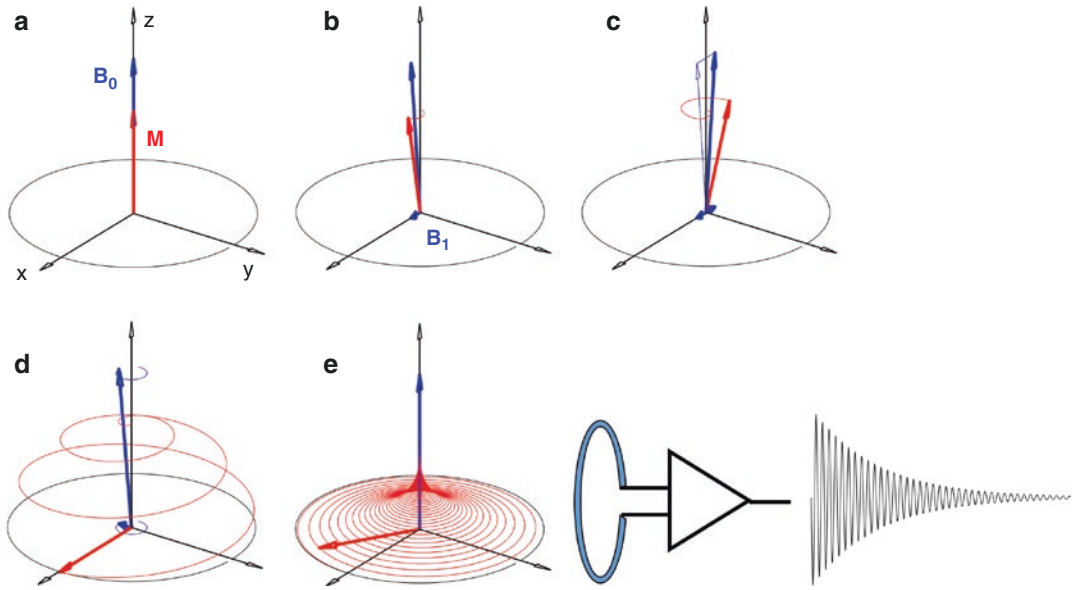


**Fig. 9.1** *Magnetic resonance.* A strong magnetic field (vector  $\mathbf{B}_0$ ) polarizes the nuclear spins and creates the nuclear magnetization ( $\mathbf{M}$ ), which is originally oriented with the field (a). An attempt to use a small static transverse field component ( $\mathbf{B}_1$ ) to tip the magnetization fails, because the precession along a slightly tilted axis has very little effect (b). Instead, a transverse field that toggles between opposite directions “in resonance” with the nuclear precession would flip the magnetization, because the angle between the effective field and the magnetization is progressively growing (c).

In practice, radio-frequency excitation pulses produced by an MRI system generate a rotating transverse field, which tips the magnetization faster, along a spiral pathway (d). After the RF pulse, the magnetization vector keeps precessing around  $\mathbf{B}_0$  and induces a radio-frequency signal in a receiving coil (e). Relaxation exponentially reduces the transverse magnetization (and the signal) while letting the longitudinal  $\mathbf{M}$  component return to the initial value. For clarity, the proportion of  $B_0$  to  $B_1$  has been reduced several thousand times with respect to a real situation

The receive coils used by an MRI system are, basically, of two types: volume coils, which gather the signal from the entire body (within the coil), and arrays of local coils. The latter provides a better signal-to-noise ratio because they may be placed closer to the patient. Array coils also provide information about the position of signal sources because signals induced in different elements depend on their distance and angular relation to the source. Parallel MRI techniques such as SENSE or GRAPPA use this information to reduce the number of gradient-encoding steps and accelerate the scan.

The way an MRI image can be derived from array signals sampled in the presence of magnetic field gradients can be seen as a linear encoding and decoding process. Each signal sample is a sum of unknown magnetization vectors of all pixels. These pixel magnetizations

contribute to the signal differently, because they may point in different directions due to the action of gradients (Fig. 9.2 left, middle), and may be differently scaled due to position-dependent sensitivity of the coils (Fig. 9.2 right). In math terms, unknown complex pixel values (with real and imaginary parts describing  $x$ - and  $y$ -components of the magnetization) are summed up after being modulated by a complex “encoding function” (with the magnitude given by coil sensitivity, and the phase by Larmor precession under the influence of gradients). Thus, each signal sample from each array coil gives us a linear equation with as many unknowns as there are pixels to reconstruct. We need at least the same number of equations with different sets of coefficients, i.e., with different encoding functions to “decode” the unknown pixels by solving a large set of linear equations.

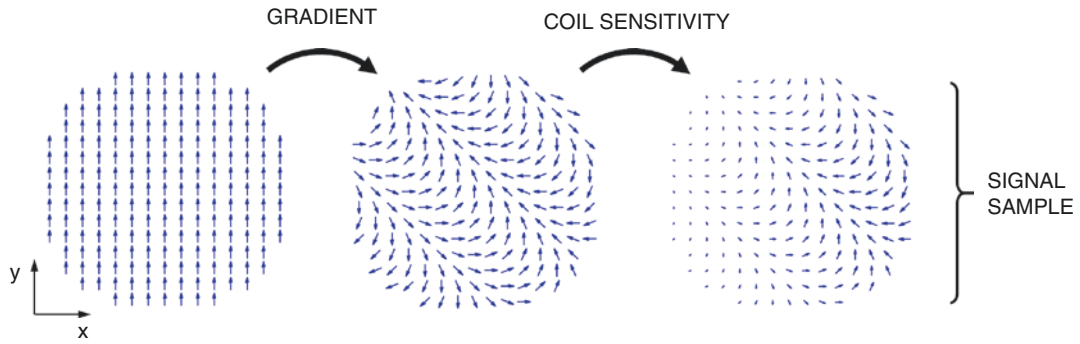


**Fig. 9.2** Spatial encoding. After the excitation, all magnetization vectors within the object point in one direction in the plane transverse to the magnetic field (left). To obtain an image of the object, we have to figure out the magnetization strength in each pixel. For that purpose, the resonance signal, which is given by the sum of all pixel magnetizations, has to be measured with different modulations of these unknown vectors, to give enough equations

to solve. Such modulations are produced with a magnetic field gradient, which leads to a position-dependent precession speed and modulates the phase (direction) of the magnetization (middle), and with local receiver coils which scale the signal contribution of magnetization vectors depending on their distance (right). In this schematic picture, the field gradient was applied towards left-up direction and the coil was placed on the right

The contribution of magnetic field gradients to the spatial encoding is quite particular and gives MRI an enlightening analogy with optics. When a gradient is switched on, the spins, originally all pointing in the same direction after being excited, start precessing with an angular speed that changes linearly in the gradient direction. After a while, the phase of the magnetization (i.e., its direction in the  $x$ - $y$  plane) is modulated by a planar wave (as we have seen in Fig. 9.2 middle). A signal sample taken at this time point represents the integral of the object modulated by a planar wave, i.e., the value of the Fourier transform of the object at the point in the Fourier domain ( $k$ -space) given by the modulation's wave vector. What an optical lens produces at the focal plane, the Fourier representation of the object, MRI provides numerically point by point by sampling the resonance signal in the presence of time-dependent gradients.

### 9.3.4 Data Sampling

MRI methods differ by the trajectory along which the Fourier space is traversed (and sampled), called  $k$ -space trajectories. A trajectory always starts in the origin of  $k$ -space, since the object is not yet modulated after the excitation.

Then, most methods sample the  $k$ -space on a set of parallel lines, with a new signal excitation needed for each line. This arrangement enables the fastest reconstruction, because the samples are arranged on a rectangular (Cartesian) grid. However, longer, non-Cartesian trajectories, like the zigzag line used in EPI, or spirals, are also used in fast MRI sequences, since they allow gathering all the necessary data with one or a few excitations only.

In so-called spin-echo MRI sequences, trajectories may also contain point-symmetric operations (jumps from  $k$  to  $-k$ ) produced by “refocusing” radiofrequency pulses, which flip the phase of the magnetization. A simple trajectory example is shown in Fig. 9.3 together with the corresponding plot of gradients amplitudes. The relation between the two is straightforward: the gradient is the speed in  $k$ -space, and the gradient slew rate—the acceleration. The range and the density of a  $k$ -space trajectory are dictated by the properties of the Fourier transformation, which are illustrated in Fig. 9.4. The range determines the resolution: the size of the smallest detail discernable in the image is proportional to the inverse of the  $k$ -space range. The density determines the field of view. Too high distances between  $k$ -space samples may lead to folding of

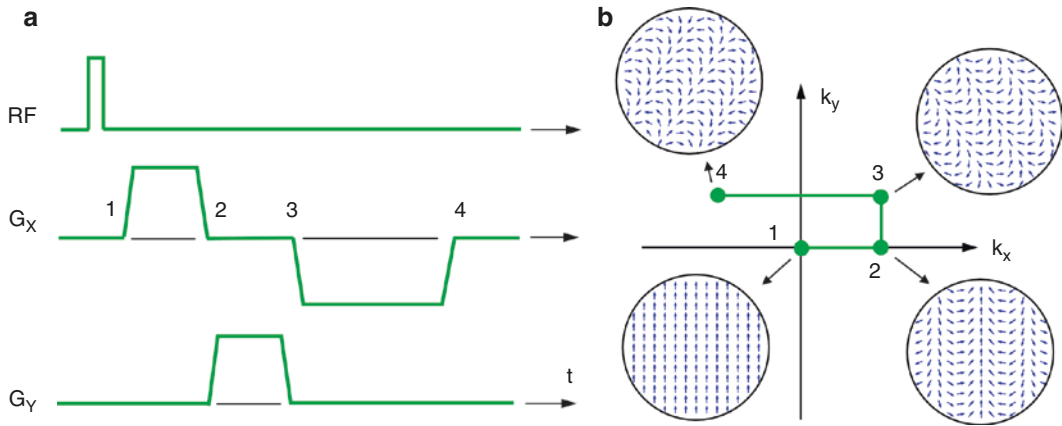


**Fig. 9.3** Scanning of the Fourier domain with gradients. During an MRI scan, the signal is excited with an RF pulse and measured in the presence of field gradients (a). Signal samples give us values of the object's Fourier transform at different points in  $k$ -space. As time evolves, the current  $k$ -space position is moving with a speed

defined by the  $x$ - and  $y$ -gradient components. Different  $k$ -space points correspond to different modulations of the nuclear magnetization (as shown for the four selected points along the trajectory) and describe the contribution of corresponding spatial frequencies to the image (b)

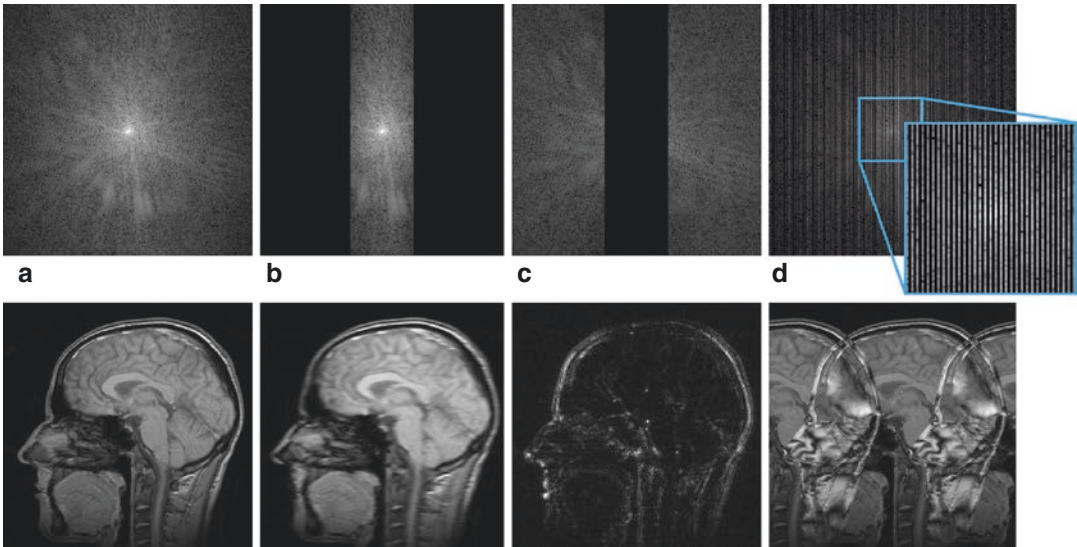


**Fig. 9.4** Properties of the  $k$ -space. The magnitude value of an MRI data matrix is shown as a " $k$ -space image" in logarithmic scale in the upper row, and "real space" images calculated from different parts of it by the two-dimensional Fourier transform are shown beneath (a). A reduction of the horizontal  $k$ -space range to central 25% results in a strong smoothing of the image in the horizontal direction (b). Reconstruction from the complementary outer  $k$ -space enhances the edges that were previously

smoothed out (c). Thus, for a higher precision (resolution) of the resulting image, a higher  $k$ -space range has to be sampled, which makes the scan time longer. An attempt to reduce the scan time by skipping every other sample (d) result in an aliasing (folding) artifact, because the sampling density becomes lower than needed for the size of the object. The purpose of parallel MRI is to avoid such artifacts (even for higher under-sampling factors) using the additional information provided by a receiver array

parts of the body into false image locations. The idea of parallel MRI is to accelerate scanning by a reduction of  $k$ -space density and to avoid the folding artifacts using the information provided by the array sensitivity in the image reconstruction procedure. In terms of linear encoding, reduction of  $k$ -space density takes away some encoding equations from our set, and the solution becomes ambiguous. Using the array information introduces new equations that compensate this information loss.

## 9.4 MRI Pulse Sequences

During a scan, the MRI system generates multiple RF and gradient pulses to excite the signal and to produce its spatial encoding. The order of these events is called an “MRI sequence.” There is a huge variety of sequences available on MRI systems from various manufacturers, but most of them can be related to the few basic examples listed here and represented together with their  $k$ -space trajectories in Figs. 9.5 and 9.6.

### 9.4.1 Gradient Echo

Gradient echo (GRE), also known as FLASH or FFE (fast field echo), uses one RF pulse and one acquisition period (repetition time) per  $k$ -space line. Gradient pulses on two channels ( $G_x$  and  $G_y$  in Fig. 9.5) are turned on for a while to bring the trajectory to the line’s start point, and then only one gradient is kept ( $G_x$  in our case) to make the line traversal while the signal is acquired. This gradient channel is usually labeled “readout” or “frequency encoding,” while the other component, which has to be incremented stepwise to reach different lines, is called “phase encoding.” This relates to the fact that the corresponding coordinates of a point source would determine the frequency and the phase of the signal, respec-

tively. An additional pulse called a “spoiler” is added on any channel after the acquisition to bring the trajectory far away from the center of  $k$ -space and make the signal vanish before the next RF excitation (otherwise interference artifacts could appear). Another post-acquisition pulse, the “rewinder,” compensates the action of the phase-encoding pulse to make the trajectory end point always the same (and to avoid another type of artifacts). The name “gradient echo” originates from the form of the signal that is seen on the central  $k$ -space line—starting from zero and reaching a peak when the  $k = 0$  point is crossed. Like in all two-dimensional sequences, the gradient channel orthogonal to the image plane (here,  $G_z$ ) is turned on during the RF pulses, which are shaped to contain a narrow and sharply delimited frequency band, to select the signal from a thin slice.

#### 9.4.1.1 Balanced Gradient Echo

Balanced gradient echo, a.k.a. true FISP (fast imaging with steady precession) or balanced SSFP (steady-state free precession) is the version of GRE where, instead of being “spoiled away,” the trajectory is purposely brought back to the center by compensation pulses on all gradient channels, and the RF pulses follow a 0–180° phase cycle to tip the magnetization back and forth. This minimizes the impact of the sequence on the spins and provides excellent signal with minimum repetition times (TR), a feature making this sequence popular in cardiac MRI. However, the balancing makes the image highly sensitive to magnetic field (in-)homogeneity. When this is insufficiently corrected by the system’s “shimming coils” (yet another electromagnet present in every MRI system), black bands appear in the image.

#### 9.4.1.2 Spoiled Gradient Echo

Spoiled gradient echo is identical with its original variant except for a special phase cycle of the RF pulses, which makes contributions from

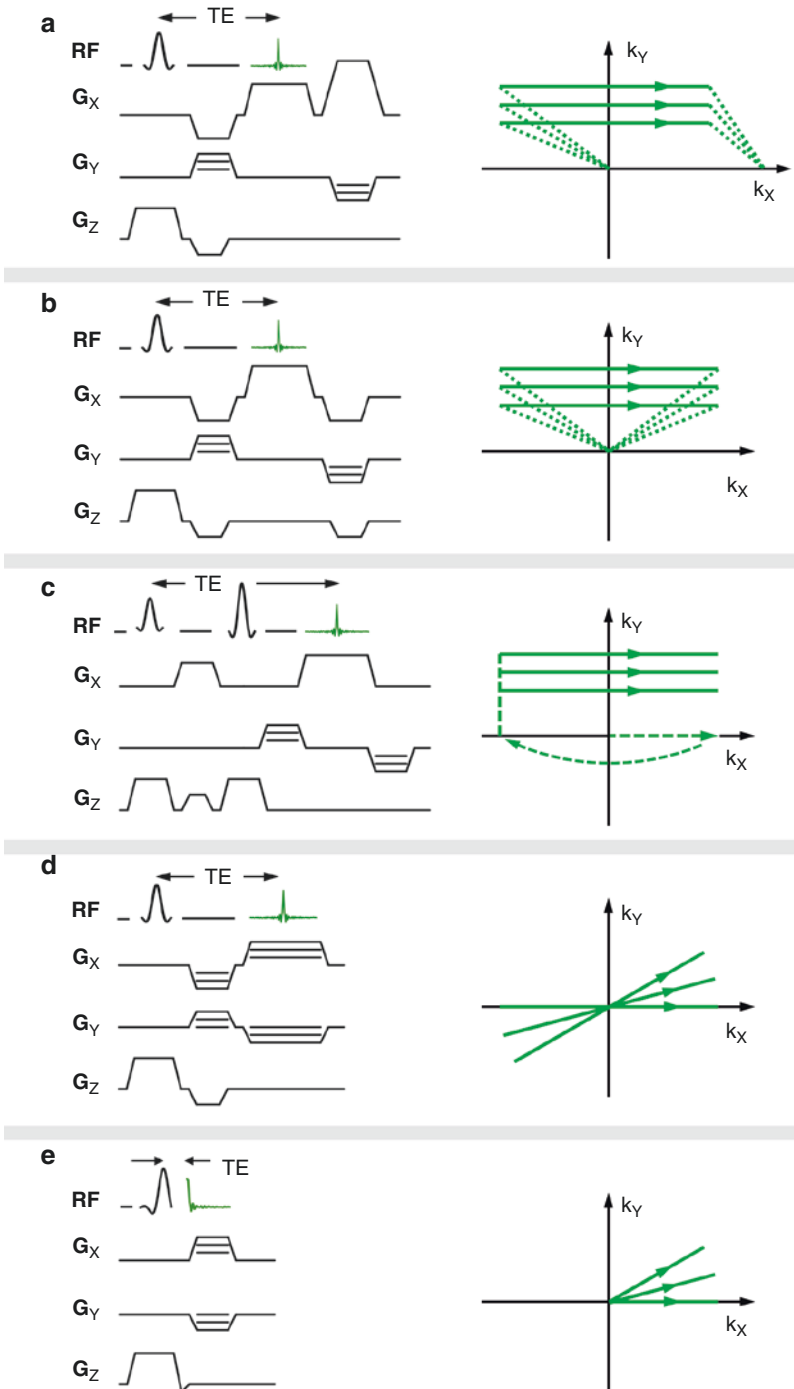
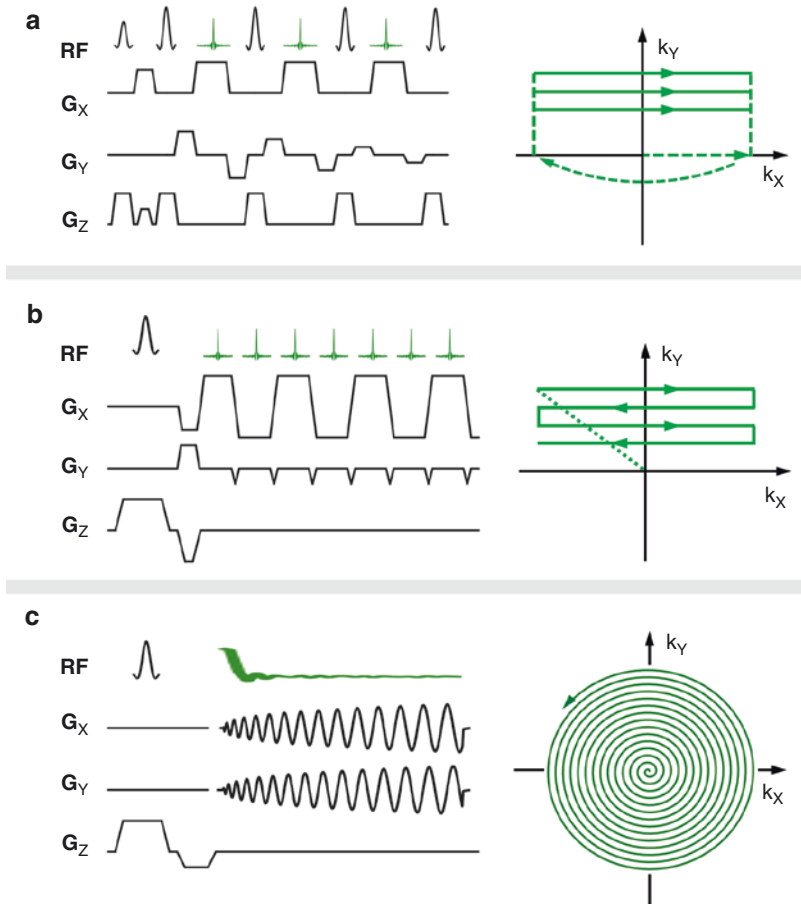


**Fig. 9.5** Basic MRI sequences and their  $k$ -space trajectories for a scan in the  $x$ - $y$  plane. GRE with all typical elements of an MRI sequence: readout gradient ( $G_x$ ) forming echo signals, a variable phase encoding pulse ( $G_y$ ) that places these echoes on different  $k$ -space lines, and the phase-encoding “rewinder” (second pulse of  $G_y$ ) together with a spoiler (last pulse of  $G_x$ ) that shift the trajectory to the same distant point after each echo (**a**); Balanced SSFP: the trajectory always ends at the origin of the  $k$ -space (**b**); Spin Echo: the second RF pulse (refocusing) inverts the  $k$ -space position (**c**), Radial

scan: phase encoding is replaced by a rotation of the readout gradient making all trajectory sections cross the  $k = 0$  point (**d**), and UTE: radial scanning with half-echo acquisitions, which provides the shortest time between the excitation and the  $k = 0$  sample (echo time, TE) (**e**). All RF pulses have a frequency-selective shape and are played out in the presence of the  $z$ -gradient to generate the signal from a slice. Additional pulses of the  $z$ -gradient are needed to compensate spin precession during the RF pulse, depending on the sequence and pulse shape

**Fig. 9.6** Fast MRI methods which are capable of acquiring the full two-dimensional data with a single excitation: Fast spin echo (FSE, **a**), Echo-planar imaging (EPI, **b**), and the spiral scan (**c**). These methods can also be used in “multi-shot” mode with interleaved trajectories



previously excited signals cancel each other and leaves only the “fresh” signal produced by tipping the relaxed longitudinal magnetization. This makes the image weighted by T<sub>1</sub>, the longitudinal relaxation time, parameter describing how rapidly the magnetization reaches the equilibrium state after tipping by an RF pulse. Maximum signal for a given TR and T<sub>1</sub> is reached when the tip angle of the RF pulse equals the Ernst angle,  $\arccos(\exp(-TR/T_1))$ , which is the best compromise between using most of the existing magnetization and leaving enough of it for the next excitation. RF spoiling is often implemented as an option of the gradient echo (called, e.g., T<sub>1</sub> enhancement) rather than an extra sequence. It should be noted that without RF spoiling, GRE with short repetition time does not provide the T<sub>1</sub> contrast despite

the “spoiler” gradient, since parts of previously excited signal are still present.

### 9.4.2 Spin Echo

Spin echo (SE), which includes an additional RF pulse to invert the spin phase and to flip the *k*-space trajectory with respect to the center. This flip also compensates the precession of the spins due to magnetic field deviations caused by the object’s magnetic susceptibility, which leads to signal “dephasing” around air-filled spaces and veins in GRE. This sequence has to run with relatively long repetition times to avoid spin saturation by the high flip angle RF pulses and requires long scan times. For this reason, it is used mostly in combination with fast sampling strategies

such as echo planar imaging and fast spin echo described below.

### 9.4.3 Fast Spin Echo

Fast spin echo (FSE), originally known as RARE (rapid acquisition with relaxation enhancement), also implemented as TSE (turbo spin echo), is an extension of the spin-echo sequence in which further echoes are generated by a train of refocusing RF pulses and each echo is used to sample another  $k$ -space line. Both spin-echo variants are sensitive to the lifetime of the transverse magnetization, which disappears due to spin interactions and cannot be refocused forever. This process is quantified by a parameter called T2—the transverse relaxation time, which is of the order of a few to hundreds of milliseconds in soft tissues. The T2 sensitivity or the T2-weighting of the image is controlled by the sequence parameter TE, the echo time, the duration between the excitation and the central echo. Since spin-echo sequences require a long repetition time to let the spins relax after high tip-angle RF pulses, FSE with its significant acceleration (one typically takes 10–20 echoes per sequence) has almost completely replaced the simple spin echo in T2-weighted imaging (Fig. 9.7).

### 9.4.4 Echo Planar Imaging

Echo planar imaging (EPI), as mentioned above, uses only one RF excitation-pulse to sample all  $k$ -space lines. It is usually implemented with gradient echo and spin echo variants, the former most prominently used for functional brain imaging (fMRI) and the latter combined with diffusion sensitizing gradients. A characteristic feature of EPI is a strong displacement of the fat signal (when it is not suppressed, see contrast modules below) and image distortions caused by magnetic field inhomogeneity. This is due to a relatively slow progression through  $k$ -space along the s-shaped trajectory, which converts

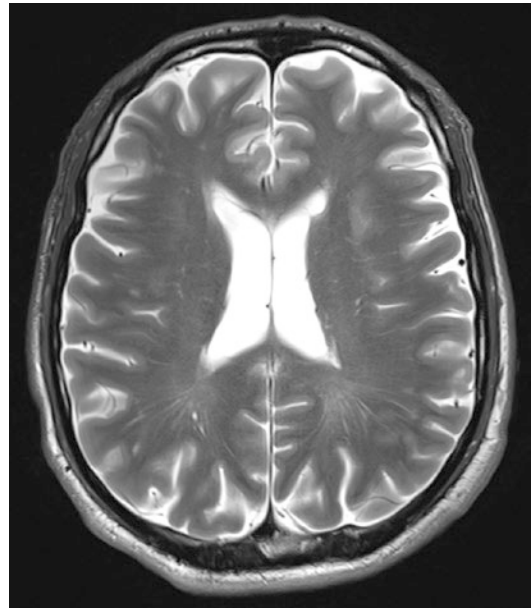


**Fig. 9.7** Example of a fast spin echo T2-weighted image with an echo train length of 16 and a repetition time of 8 s. The acquisition time is 3.43 min and would increase to 52.5 min for an equivalent spin echo acquisition

small frequency offsets to “fast”  $k$ -space modulations and big pixel shifts. This effect can be reduced by parallel imaging—skipping  $k$ -space lines, the trajectory progresses faster—and by acquisitions with interleaved or band-wise segmented trajectories—splitting the scan to a few shots. Interleaved EPI based on an “FSE” echo train is known as GRASE.

### 9.4.5 Spiral Scan

Spiral scans are ultrafast sequences following the principle of EPI (2d-information taken with one excitation), but using a more efficient trajectory. Spirals are equally sensitive to field inhomogeneity as EPI, but the related effect (blurring instead of distortions) cannot be corrected by simple post-processing of images. Due to the additional computation burden (needed also to incorporate array information), spiral MRI has still not made its way to clinical routine, although this is certainly only a matter of time.

### 9.4.6 Radial Scan

Radial acquisition is a variant of the gradient echo in which, instead of phase-encoding, the readout gradient is rotated from shot to shot leading to a  $k$ -space sampling on a bunch of lines crossing  $k = 0$ . This method is also known as projection imaging, because, mathematically, sampling the  $k$ -space on a central line is equivalent to taking a projection of the object at a corresponding angle (as used in CT imaging). The repetition of the central  $k$ -space sample in all projections allows monitoring of signal changes due to, e.g., respiration or heartbeat. For this reason, radial GRE is often used in cardiac MRI where it allows the “retrospective gating,” i.e., sorting the dynamic data along the cardiac cycle without the need of ECG recording. EPI can also be used to accelerate radial scanning. This is called PROPELLER, as the trajectory resembles an air-plane propeller turning around the  $k$ -space center.

### 9.4.7 Ultrashort Echo Time

UTE (ultrashort echo time) is a radial scan based on radii starting in the  $k$ -space center. The lack of the initial “flyback” gradient pulse allows reaching TE below a millisecond and observing signals from tissues of very short T<sub>2</sub>, such as bones and tendons.

### 9.4.8 Contrast Options

Each MRI sequence can be combined with one or more preparation modules that set the longitudinal magnetization in a particular way to determine the image contents and contrast. Combination of such “prep” modules with GRE is often made in a segmented manner (one prep sequence followed by an acquisition segment with several gradient echoes) to preserve the ability of this sequence to run with short TR. In three-dimensional scans, this strategy is known as MP-RAGE (magnetization-prepared rapid acquisition gradient echo) or TFE (turbo field echo). Most common preparation modules and other MRI contrast options are:

- **Fat suppression.** A frequency selective pulse transmitted at the resonance frequency of <sup>1</sup>H nuclei in lipids, which is lower than that of water by 3.5 ppm due to the chemical shift, tips the fat magnetization by 90° and destroys its z-component just before the excitation. This module is particularly needed for EPI where the unsuppressed fat appears with a strong displacement due to the mentioned chemical shift. Some scanners offer fat suppression by an inversion pulse (which needs more time but is more robust) and by spectral spatially selective excitation RF pulses. The DIXON method, enabling the reconstruction of water-only and fat-only images, was also introduced in clinical routine to improve the homogeneity of the fat suppression in regions with inhomogeneous magnetic fields (Fig. 9.8).
- **Saturation slabs.** A series of selective pulses applied in the presence of a gradient can suppress the magnetization (of fat and water) in a selected slab. This module typically comes with a graphic interface letting the slabs be oriented and displaced. It is used to limit the “size” of the object to the declared FOV and to avoid folding, flow, or breathing and other motion artifacts (Fig. 9.9).
- **Inversion.** The equilibrium magnetization can be inverted by a 180° RF (inversion-)pulse to enhance the T<sub>1</sub> sensitivity. The contrast strongly depends on the inversion–recovery time (delay between the inversion and the excitation, called TI or TIR). In brain imaging, TI is usually set so that the cerebrospinal fluid (which has longest T<sub>1</sub>) recovers to zero and appears black in the image, while the white and gray matter show up “white” and “gray.” The inversion module is often combined with three-dimensional segmented GRE (as MP-RAGE or MDEFT) for T<sub>1</sub>-weighted imaging, and with the T<sub>2</sub>-weighted FSE (combination called FLAIR, fluid-attenuated inversion recovery), to avoid masking of brain lesions by a strong CSF signal (Fig. 9.10).
- **Arterial spin labeling (ASL).** This module uses the sensitivity of RF excitation to motion and selectively inverts the magnetization in



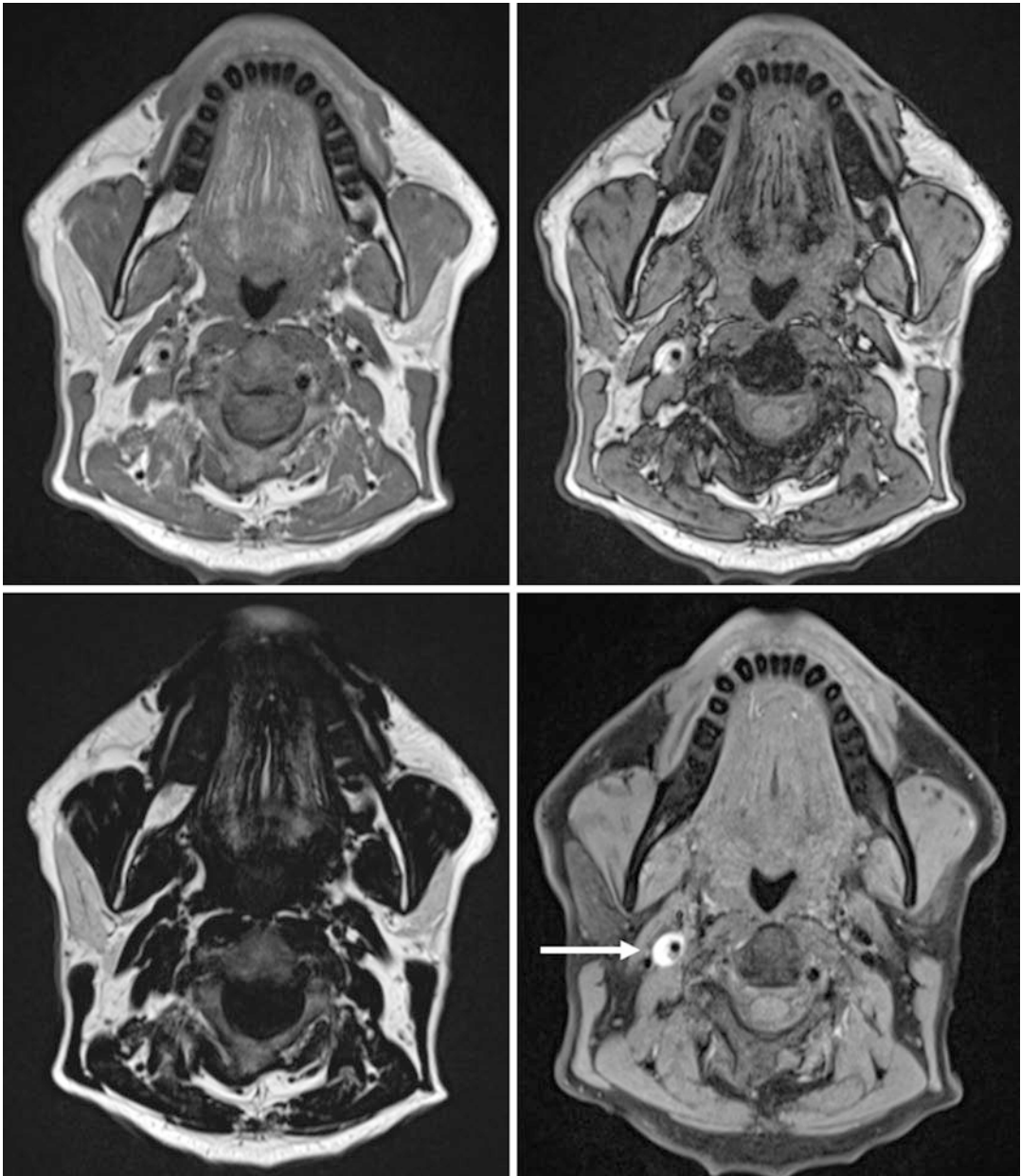


**Fig. 9.8** The Dixon method consists in calculating, from the complex in-phase (top left panel) and the out-of/ opposed-phase (top right panel) images, the fat-only (bottom left panel) and the water-only (bottom right panel) images. In this example of dissection of the right internal

carotid artery, the Dixon method allows a homogeneous fat suppression and, in the water-only image, the blood vessel hematoma is clearly visible as a hyperintense lesion with the characteristic “crescent moon” shape (arrow)



**Fig. 9.9** In this T1-weighted sagittal TSE image of the thoracic spine, the signal from the anterior thorax has been saturated using a saturation slab (in orange), to avoid breathing artifacts to fold on the spine. The phase-encoding direction is chosen, to shorten the acquisition time, as anterior–posterior

the blood flowing through the arteries to an organ in order to visualize (or quantify) its perfusion, most prominently, in the carotids to study brain perfusion. The evaluation requires comparing at least two images acquired with and without arterial blood spin inversion. The subtraction of the two contrasts is proportional to the flow. To avoid misinterpretation of ASL's cerebral blood flow estimation, a multi delay acquisition is mandatory, especially in children.

- **Flow compensation.** An option rather than a prep module, flow compensation introduces

additional gradient pulses to the sequence to make the signal phase independent on flow velocity. This reduces artifacts caused by pulsations in arteries at a price of increased TE and TR.

- **Phase-contrast angiography (PCA).** On the other hand, instead of compensating phase error due to velocity, one can use it to resolve flow speed. Based on the same notion as flow compensation (sensitizing the MRI sequence to flow using a bipolar gradient and comparing complex images with different phase sensitivity to flow), one can selectively show vessels and calculate quantitative velocity maps. From this time- (over the heartbeat) and space-resolve velocity map, flow can be tracked using streamline reconstruction or other flow visualization methods (Fig. 9.11).
- **Time-of-flight (TOF) angiography.** Flowing blood is visualized by a flow-compensated GRE sequence with short TR and high excitation flip angles (15–25°). Static spins are saturated and their signal is reduced, while “fresh” blood flowing into the imaging plane generates a much stronger signal. A good fat saturation, a homogeneous signal reconstruction (e.g., CLEAR on Philips or prescan normalize on Siemens), and a (over the slice profile) ramped flip angle are of primordial importance to have a uniform representation of the vascular tree and a good suppression of the background. Higher  $B_0$  field strength, compress sensing and sparse reconstructions, magnetization transfer contrast enhancements are some of the advanced possibilities to even further improve the resolution of TOF angiography. TOF 3D MIP reconstructions can be used for planning high-resolution 2D trough-plan phase contrast angiography and, based on a flow model, to quantify the blood flow within one particular vessel (Fig. 9.12).

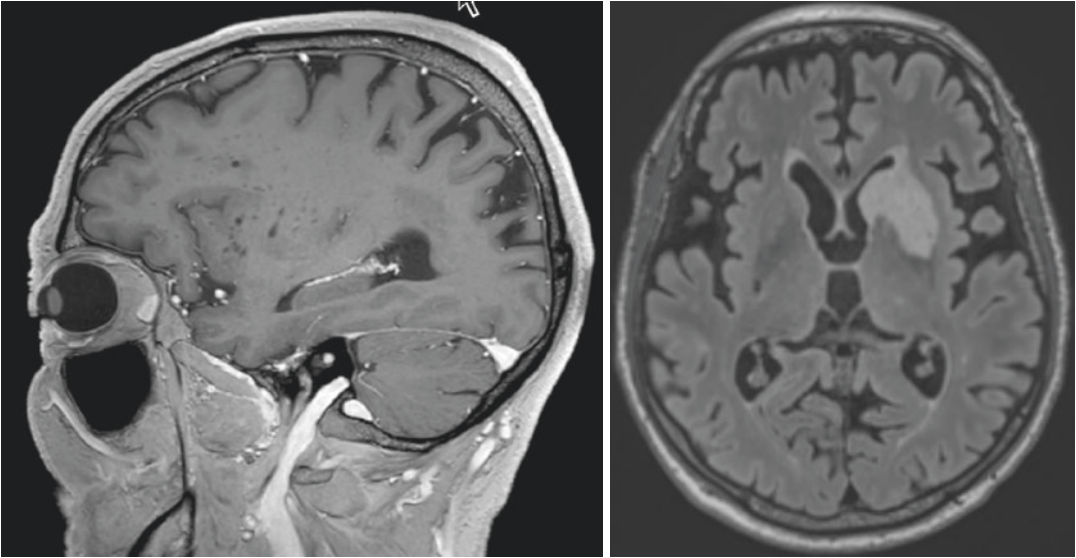


**Fig. 9.10** Inversion recovery fast gradient echo T1-weighted 3D acquisition with isotropic resolution of 0.6 mm acquired in less than 6 min. Contrast agent was

used to enhance blood signal. Right: inversion recovery T2-weighted 3D TSE (SPACE). In both images, the cerebrospinal fluid signal is suppressed

- Diffusion weighting.** More than a prep module, this is a modification of the spin-echo sequence in which two or more strong gradient pulses are applied in a manner that makes them “transparent” for static spins, but attenuates the signal when spins randomly change position due to Brownian motion. In the simplest case, these are two identical pulses on both sides of the refocusing RF pulse. By applying diffusion gradients in multiple directions, diffusion tensor imaging (DTI) can be performed to observe processes affecting tissue anisotropy. Diffusion gradients introduce an extreme sensitivity of the signal phase to patient motion, which makes this type of contrast available with single-shot sequences such as EPI and spiral. Clinically introduced for its higher resolution and the reduction of distortion due to  $B_0$  inhomogeneity, diffusion weighting multi-shot MRI is sensitive to inter-shot phase fluctuations due to patient motion. Research on field and motion monitoring shall avoid the need for

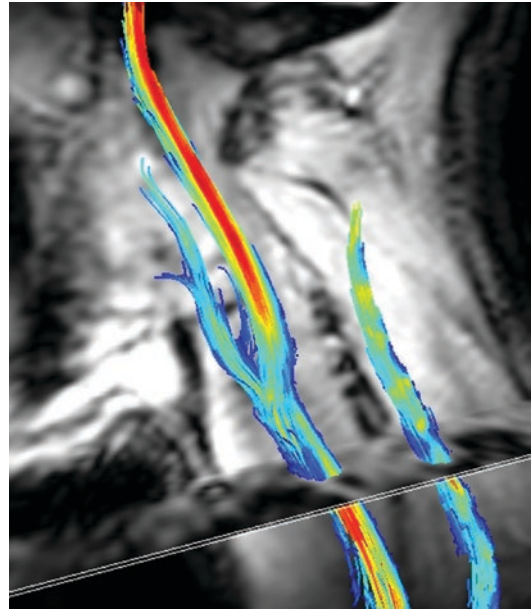


**Fig. 9.11** Streamline reconstruction (using GT Flow, Gyrotools, Zurich, Switzerland) from phase-contrast angiography of the carotid bifurcation and jugular vein obtained from a 7-T MRI with a custom-made anatomy-shaped surface coil array

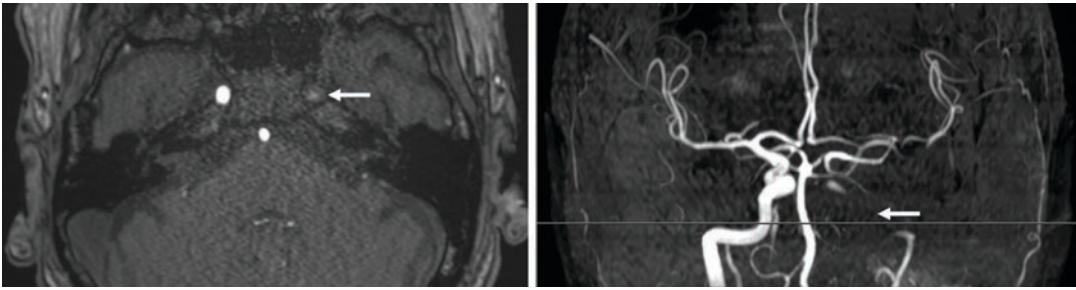


**Fig. 9.12** Clinical TOF angiography of an internal carotid artery occlusion (arrow) and its coronal MIP reconstruction, where the position of the axial slice is

shown. This 3-min acquisition is short enough to avoid motion artifacts common in stroke-patients. The protective role of the circle of Willis is clearly visible

the reacquisition of the shots compromised by motion.

- **BOLD (blood oxygenation-level dependent)** contrast is produced by setting a long TE value (usually, 30 ms at 3 T) in the gradient-echo EPI sequence, and thus does not require additional sequence modules. The resulting dependence of signal intensity on the effective transverse relaxation time ( $T2^*$ ), which varies with oxygen contents in hemoglobin, makes this sequence popular for functional imaging of the brain (fMRI) and the measurement of cerebrovascular reactivity. Multi-echo and simultaneous multi-slice acquisitions improve the quality of the data.
- **Susceptibility contrast.** Again, a processing option rather than sequence module, susceptibility contrast, or quantification is based on evaluation of the phase of GRE images with long TE, such as those used for BOLD scans. Image phase depends on local field offsets caused by magnetic susceptibility changes at tissue interfaces and reveals its structural changes, concentration of iron, hemoglobin, calcium, and others.
- **MT (magnetization transfer).** A series of long, frequency-selective RF pulses centered far away from water resonance is applied before the signal excitation. These pulses lead to saturation (nulling of the  $z$ -magnetization) of protons in macromolecules and water molecules bound to cell membranes because

their resonance lines are much broader than of those in free water. However, due to the exchange of protons with free water, partial saturation of free water may take place giving an image contrast dependent on tissue microstructure.

## 9.5 MR Safety

### 9.5.1 Overview

The MR environment poses several potential risks and hazards to patients and staff of various background sharing the responsibility to operate the MR unit in a safe way. In general, MR is very safe and several 100 Mio diagnostic studies have been performed safely up to now—but there have also been several severe incidents. The key challenges arise from the different electromagnetic fields (static magnetic field, time-varying gradient field, and RF field), the acoustic noise, and in certain cases also the contrast agents needed for MR diagnosis.

All staff working in an MR unit need a high level of knowledge about the intrinsic risks of the MR technology and their contraindications. First, the main parts of the MR scanner will be described, since those will be the source of the potential interactions. The potential interactions with the human without any implant, but also with passive and active implants will be dis-

cussed in the following section. The MR operators should understand the basic interactions with the goal to prevent any potential risks to patients and co-workers and increase the confidence in their work.

MR safety does not differ whether we do brain, heart, or lower extremity imaging. The likelihood for certain implants may be different, and cardiac imaging may need additional stress medication, but if a patient has a certain implant the same care must be taken independent the heart, the liver, or the spine is imaged.

### 9.5.2 MR System

An MR system is made up of a strong magnet, three gradient coils, and an RF transmit and receive coils. The RF transmit coil can be one coil or several independent ones. MR scanning is controlled by one or multiple computer, which controls the gradient and RF amplifiers. The signal from the RF coils will be amplified and digitized by dedicated hardware and reconstructed by a computer which sends the images to the

operator console. An overview of an MR system is given in Fig. 9.13.

The strong main magnetic field is needed to align the nuclear spins (commonly the hydrogen proton) with the magnetic field. Common clinical systems have a field strength of 1.5 T or 3 T. Worldwide, 1.5 T is still most common, but in some regions, 3 T MR systems are already more present. 3 T may also be preferred in neuro-radiology, whereas for imaging the thorax, a 1.5 T system may be favored. First 7 T MR scanners are approved for clinical use, but clinical and economic benefits have to be further proven. There exist also several MR systems with lower field strength and partly also different main magnetic field orientations.

The 3 T field is about 60,000× the earth's magnetic field (0.05 mT). Most magnets use superconductive coils to produce the magnetic field. Very low field (<0.5 T) permanent magnets and resistive electromagnets exist. Superconductive magnets are always on field and use liquid helium to keep the conductor superconductive. Removing the magnetic field in a controlled way requires a few hours and can only be done by experts from

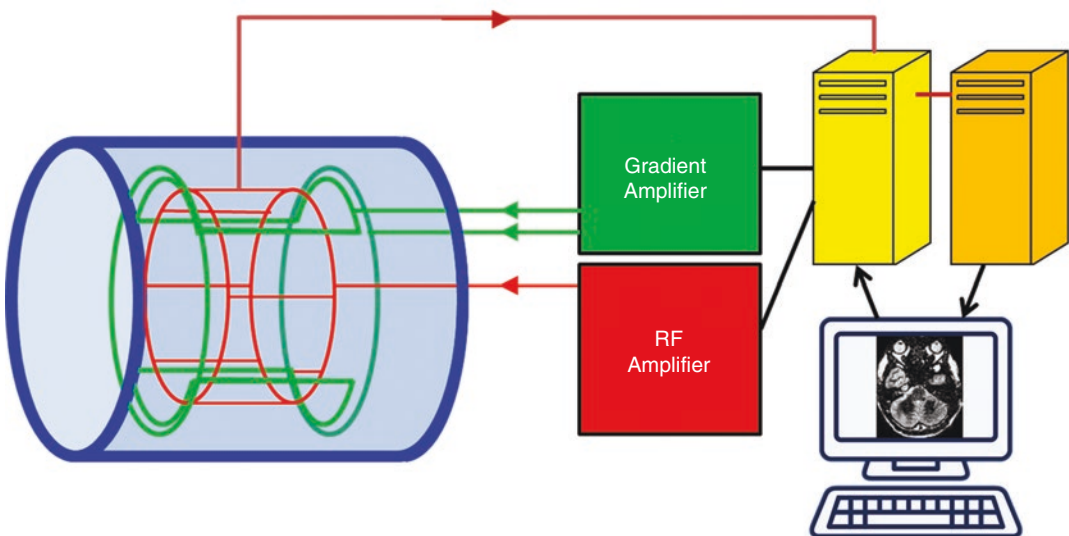


**Fig. 9.13** Schematic buildup of an MR system: Blue: Magnet for the main magnetic field, green: gradient field (only  $z$  and  $y$ -direction shown) with gradient amplifier, red: RF body coil with RF amplifier, brown: acquired sig-

nal, yellow: real-time computer performing the MR experiment and receiving the MR signal, orange: reconstruction computer, gray: host computer

the manufacturer. The fast way (emergency situations) to remove the magnetic field is quenching. The energy of the magnetic field will be converted in heat and vaporize the liquid helium. Repairing the system needs several hundred liters of liquid helium and takes a few days. In 2018, the first 1.5 T full-body magnet with less than 10 L of liquid helium was presented. This magnet will not lose any helium even in case of a quench.

The gradient fields are used for the spatial localization. The three gradient coils are assumed to modulate linearly the z-magnetization along the three space directions. The gradient will be turned on and off within less than a millisecond. The strongest gradient values are not in the center of the images, but in the periphery of the maximum FOV (typically about 30–50 cm from the isocenter of the MR system). The gradients are only on during measurements and are the source of the typical knocking noise generated during an MR scan.

The RF field is used to excite the nuclear spin. In clinical practice, only the hydrogen proton is of relevance. The resonance frequency for the hydrogen proton is 42 MHz per Tesla, e.g. for the clinical MR system, in the frequency range used for FM radio broadcasting. However, the transmitted power of the RF coils is much higher (peak power of up to 25 kW) and needs to be controlled to avoid any negative effects on the patient. For RF transmission commonly the built-in RF body coil is used. In some cases, a head or a knee transmit–receive coil may be available. The RF field pulses are only transmitted during the MR measurements. The transmit coils should not be confused with the commonly used receive-only RF coils.

The receive-only coils are used to acquire and amplify the signal and exist for various body regions. Receive-only coils cannot transmit RF energy, however if inappropriately used (not connected to the system, not closed, wrong oriented, etc.) it can concentrate RF energy from the transmit coil and lead to RF burns.

The digitized MR signal will together with its labels be sent to a computer to be reconstructed. Beside various signal corrections due to hardware limitations, Fourier transformation in all image dimensions will be performed. The final

images will be sent to the host computer for further evaluations.

### 9.5.3 Potential Safety Risks of the Electromagnetic Fields

Each of the three electromagnetic fields may pose safety risks. There are risks even for patients without implants. Additional risk may be introduced by passive implants. In case of active implants, further risk needs to be taken into account. The potential risks are summarized in Table 9.1.

**Table 9.1** The table summarizes all interactions from the three electromagnetic fields of an MR system on a patient which may have a device implanted

Electromagnetic field	Potential safety risks
<b>Main magnetic field</b> <i>Always on</i> Typical range for clinical use: 0.1–7 T Most common: 1.5 and 3 T	<ul style="list-style-type: none"> <li>• Magnetic force and torque                         <ul style="list-style-type: none"> <li>– ferromagnetic implants or objects in or on the patient</li> <li>– ferromagnetic objects/tools (e.g. bed, oxygen tank, tools, medical equipment, etc.)</li> </ul> </li> <li>• Damage or interference with active implants</li> <li>• Dynamic torque due to eddy currents</li> <li>• Damage of magnetic storage device, cards, watches etc.</li> <li>• Magnetohydrodynamic effect</li> </ul>
<b>Gradient field</b> <i>Only in use during scanning</i> Typical range for clinical use: <100 mT/m and per axis <200 mT/m/ms per axis	<ul style="list-style-type: none"> <li>• Noise</li> <li>• Peripheral nerve stimulation</li> <li>• Cardiac stimulation</li> <li>• Induced voltages in implants</li> <li>• Damage or interference with active implants</li> <li>• Heating of larger conductive surfaces (e.g., ICD cases).</li> <li>• Vibration (combined effect gradients and static magnetic field)</li> </ul>
<b>RF field</b> <i>Only in use during scanning</i> 42 MHz/T for hydrogen <25 kW peak	<ul style="list-style-type: none"> <li>• RF heating                         <ul style="list-style-type: none"> <li>– next to conductive implants</li> <li>– wires or coils on the body surface</li> <li>– bore contact</li> <li>– skin to skin contact</li> </ul> </li> <li>• Damage or interference with active implants</li> <li>• Interference with electronic devices in the magnet room</li> </ul>

### 9.5.3.1 Main Magnetic Field: Magnetic Force and Torque

As of today, three known cases of fatal accidents related to magnetic force and torque have been reported. In 1992 during preparation and moving into an MR system a patient with an aneurysm clip died. [27] Two incidents with oxygen tanks were published in newspapers: July 2001 a 6-year old boy died in New York, USA and in January 2018 a man in Mumbai, India. The forces acting on ferromagnetic materials can be over 100× larger than the gravitational force. Such a projectile can speed up to over 50 km/h within less than 2 m! Magnetic forces are highest where the field changes most (at the entrance of the magnet) whereas torque is highest at the highest magnetic fields (around the isocenter of the magnet). At a distance of 3–4 m from an active shielded 1.5 T or 3 T magnet (the commonly used magnets) magnetic forces and torque are negligible. But moving 1 m closer to the magnet and a ferromagnetic device will be strongly attracted into the magnet. Therefore, it has to be prevented that any ferromagnetic object or device enters the magnet room. Only devices (like intravenous pole, monitoring devices, etc.) which are tested by the manufacturer (or by a safety responsible person of the unit) and are labeled are allowed to enter the room. Some devices (e.g., MR conditional syringe pumps or ventilation systems) may enter the magnet room, but are requested to stay outside a certain field (e.g., 50 mT). In such cases, it is recommended that field lines are marked on the floor (e.g., the 20 mT line). Some devices have a built-in field sensor and alarm to prevent unintended movement into higher fields.

Ferromagnetic fragments in the eye, near larger nerves and blood vessels, and other critical organs should be regarded as an absolute contraindication for MRI, since magnetic force and torque could lead to injuries of those nerves, vessels, and organs.

All persons and equipment need to be screened for ferromagnetic materials. Technical devices like magnet sensors, for example as metal detec-

tor gate around the door of the magnet room, can help to detect potentially dangerous items. However, technical screening systems should not replace the screening by well-educated staff. To evaluate the potential ferromagnetic content of a device or object, a strong handheld magnet may be used. The presence of any attraction indicates the risk of magnetic forces in the magnet room. However, it has to be taken into account that a handheld magnet will only screen for material that can be approached by the magnet by less than a few centimeter, whereas the main magnetic field of the MR system will act on any ferromagnetic object!

### 9.5.3.2 Main Magnetic Field: Damage Due to the Strong Magnetic Field

Strong magnetic fields can delete data on credit cards, magnetic data storage devices, etc. Some types of magnets used to hold implants/devices in place (like used in cochlear implants or magnets to hold dental implants) can be demagnetized by the strong magnetic field of the MR system. Watches can be damaged if approached to close to the magnet. Damage of an active implant is also possible.

### 9.5.3.3 Main Magnetic Field: Interaction with Active Implants

Implants like pacemakers and [implantable cardioverter defibrillators](#) (ICDs) include sensors to measure the magnetic field. Above 1 mT (10 Gauss) they may switch to an asynchronous mode to be more robust against electromagnetic noise. However, mechanical magnet sensors do not work as intended above 0.2 T [28]. In ICDs, this may be of special concern since the transformer to generate the high voltages for a shock will not work and during charging of the ICD the battery will be shortened. Besides emptying the battery and heating and in worst case damage the device, the patient is also not protected by the device during the time in the magnet.

### 9.5.3.4 Main Magnetic Field: Dynamic Torque Due to Eddy Currents

Fast rotation of larger metallic devices will be slowed down in the magnetic field due to Eddy currents. This is pronounced in larger plates and longer rods. Faster rotation will lead to higher torque effects. Due to space restriction in the classical cylindrical MR magnets, fast rotations are very restricted. The effects were discussed for the influencing mechanical heart valve [29]. At field strength up to 3 T the effects of dynamic torque on valves are not clinically significant.

### 9.5.3.5 Main Magnetic Field: Magnetohydrodynamic Effects

Any moving conductive liquid in a magnetic field may lead to charge separation. In humans without implants, these voltages may be a limitation at very high fields (>10 T). In the currently used fields, no adverse effects are known from the magnetohydrodynamic effect. However, the voltages are visible in the surface ECG. The alteration of the measured ECG may limit the diagnostic value of the ECG, since analysis of the ST segment is potentially unreliable. The alteration of the ECG will increase with magnetic field strength.

### 9.5.3.6 Gradient Field: Noise

The noise levels of current MR system may reach 120 dB(A) [30] which can lead to rise in hearing thresholds if no sufficient hearing protections are used. Therefore, hearing protection should be mandatory for all persons laying in the MR system. Earplugs together with headphones are preferable, since earplugs can easily be placed inadequately. Ear protections are also required for unconscious patient but also for all persons staying in the magnet room during MR examinations.

### 9.5.3.7 Gradient Field: Peripheral and Cardiac Nerve Stimulation

Fast-switching gradients can stimulate nerves. Stimulation of cardiac nerves needs 5–10 times stronger gradients compared to peripheral nerves [31]. Clinical MR systems may allow peripheral

nerve stimulations, but cardiac stimulation must be prevented. In case of electrically conductive implants reaching into the heart (e.g., pacemaker leads), the likelihood of cardiac stimulation may be increased and a limitation of the gradient slew rate may be needed.

### 9.5.3.8 Gradient Field: Induced Voltages in Implants

Longer implants may theoretically increase the nerve stimulations. If an abandoned lead is not well isolated at the connector side (side where the device is located), this could lead to a stimulation of the heart. Since abandon leads are labeled as MR unsafe, mainly because high RF heating cannot be excluded, increased likelihood of cardiac stimulation would only be of importance for off-label use.

### 9.5.3.9 Gradient Field and RF Field: Damage or Interference with Active Implants

The induced currents in leads may influence the sensing of active implants. Higher voltages may theoretically destroy electronic components of the implants. Such effects must be evaluated by the device manufacturer during labeling of the active implant. In case of off-label use, dedicated monitoring of the patient prior, during, and after the intervention may be required.

### 9.5.3.10 Gradient Field: Heating of Larger Conductive Surfaces and Vibrations

Patients with larger implants (e.g., hip cups) may feel vibrations of the implants. With very gradient-intensive sequences heating of larger cases due to gradients may no longer be negligible [32].

## 9.5.4 Potential Safety Risks Due to Contrast Agents and Medication

### 9.5.4.1 Contrast Agent

Gadolinium-based contrast agents have an excellent safety profile; however, their intravenous



administration is associated with risks which the MR operators need to be familiar. The administration of linear gadolinium-based contrast agents is related to the severe nephrogenic systemic fibrosis (NSF). The risk of NSF is increased in patients with impaired renal function. Special care must be taken in infants [33] and patients with an eGFR <30 mL/min/1.73 m<sup>2</sup> and patients with an acute kidney injury. If one or more doses of gadolinium-based contrast agent of the group with the strongest association to NFS is administered to a patient with an eGFR <30 mL/min/1.73 m<sup>2</sup>, they have a 1–7% chance of developing NSF. Administer high dose >0.1 mmol/kg or multiple single doses over months to years will increase the risk. This statement and further detailed discussions on contrast media can be found online from the ACR committee on drugs and contrast media (American College of Radiology (version 10.3) 2018 [34].

In short: Gadolinium-based contrast agents are placed in three groups based on their risk to induce NSF. Group I includes the contrast agent with the highest number of cases of NSF, group II those with non or only a few unconfounded cases of NSF, and group III where only limited data are available, but for which few, if any unconfounded cases of NSF have been reported. For all risk groups for NSF contrast agents from group II are recommended and in some cases contrast agents from group I are contraindicated. In Europe, the use of the multipurpose linear GBCAs (Omniscan, OptiMark, Magnevist, MultiHance) is no longer allowed. The following linear GBCA is only allowed for special indications: Primovist and MultiHance for delayed liver imaging only and Magnevist 2 mmol/L for intra-articular use. For patients under dialysis a contrast-enhanced MR should be performed shortly before the next hemodialysis.

2015 FDA issued a safety announcement regarding the deposition of gadolinium in the globus pallidus and dentate nuclei in patients undergoing multiple contrast-enhanced MRIs even in

patients with normal renal functions [35, 36]. Gadolinium concentrations visible in MR could be found for group I contrast agents. However, in biopsy at a factor 1000 lower concentrations, also contrast agents from group II could be found. However, these depositions have up to now no known adverse clinical implications.

#### **9.5.4.2 Stress Medication, Sedation, Intensive Care Patients**

Special care has to be taken regarding application systems of other required medications. For instance, infusion poles may only enter the MR room if those are MR conditional for the intended MR system. Patients needing monitoring can only be scanned if special MR conditional monitoring systems will be used.

Medication with interaction on the thermoregulatory system may need to limit the Specific Absorption Rate (SAR) to normal operating mode to limit the power deposition in the patient.

#### **9.5.5 Other Potential Safety Risks Including Liquid Helium**

Liquid helium: current MR systems still have more than 1000 L of liquid helium around the superconductive windings of the magnet. First 1.5 T arrived with only a few liters of liquid helium. The main danger of liquid helium is the very low temperature of ~4 K or – 269 °C. Helium is nontoxic, colorless, odorless, tasteless, and inert. But it may replace oxygen and therefore, too much helium in a room may be dangerous.

Helium: In case of a quench of the magnet helium gas may get into the magnet room, visible by the mist of condensed water in the mixture of air and cold helium gas. Since helium is lighter than air, the oxygen concentration is still highest near the floor. However, during a quench most of the helium should escape through the quench pipe to the outside of the building. In

case of a blockage of the quench pipe an over-pressure inside the building may damage the building.

**High voltage:** Inside the MR system and the equipment high voltages and currents are flowing. In case of a broken or removed cover, the MR system should not be used until checked and repaired by a trained service engineer.

**Choking hazard:** Any person lying in the MR scanner must remove any removable object from the mouth to avoid choking hazard. E.g. removable dents, chewing gums, sweets, etc.

### 9.5.6 MR Safety Labels for Medical Devices





**Important:** Not only implants near the imaging region, but all implants in a patient have to be checked for MR safety.

The implant manufacturers are responsible for MR safety testing of their implantable devices. For the definition of compatibility of an implant with MR, in 1997 the FDA developed the terms “MR safe” and “MR compatible.” In 2005, the American Society for Testing and Materials International (ASTM) together with FDA developed a new set of terms: “MR safe,” “MR conditional,” and “MR unsafe” which are still valid. Implants which are tested before 2005 may still use the old labels, which were less strict. The old “MR safe” is comparable to the current “MR conditional.” However, the pictograms shown in Table 9.2 are only valid for the new definition.

### 9.5.7 Passive Implants

It is strongly recommended to find out the vendor and type of all implants in the patients. Only in this case it can be possible to search for the label of the given implants and restrict the MR

**Table 9.2** Current terminology used for labeling of implants (ASTM F2503-13)

MR safe	An item that poses no known hazards resulting from exposure to any MR environment. MR safe items are composed of materials that are electrically nonconductive, nonmetallic, and nonmagnetic	 or 
MR conditional	An item with demonstrated safety in the MR environment within defined conditions. At a minimum, address the conditions of the static magnetic field, the switched gradient magnetic field, and the radio-frequency fields. Additional conditions, including specific configurations of the item, may be required	
MR unsafe	An item which poses unacceptable risks to the patient, medical staff, or other persons within the MR environment	

sequence to the value provided in the MR conditional label.

This is the only way to avoid off-label scanning implants. However, in clinical practice, patients may not know the details of their implants or MR safety tests may not be available for the given implant. Not to scan a patient with implants with unknown MR safety labels would

exclude a larger portion of the population from the benefits of MR.

If the details of an implant are unknown, a risk to benefit evaluation may help to find out if an MR investigation should be performed. For passive implants the following points may help to find potential risks:

- Force and torque effects: most of the implants are made out of non-ferromagnetic stainless steel or titanium alloys. However, it can never be excluded that older, current but also future implants may include ferromagnetic materials. If an implant is well fixated to a bone (like most of the orthopedic implants) or other tissues (like stents), or huge forces act on the implants outside MRI (like the blood pressure on cardiac valves), the magnetic forces would be only a limited risk. On the other hand, if an implant is only fixated to a blood vessel (like in case of an aneurysm clip), ferromagnetic materials might pose a high risk and such implants should only be imaged with MR if the details on vendor, model, and MR safety status are known.
- Gradients: the risk of gradients is of less interest for passive implants. In case of long implants, ending in the heart, cardiac stimulations could not be excluded.
- RF heating: longer implants >5 cm may lead to reasonable RF heating and tissue damage cannot be excluded. Cooling from blood perfusion and blood flow may strongly reduce the risk. The risk is higher if the implant lays inside the RF transmit coil and near to the bore wall. If the implant is outside the RF transmit coil (in case of the RF body coil >40 cm out of the isocenter) the heating effects are strongly reduced. E.g. in case of a head examination, any implant in hip or lower regions are not expected to produce critical heating, whereas a long implant (e.g., a Kirschner wire) in the upper arm may still be critical. If high heating cannot be excluded but the investigation would have a high benefit, reducing SAR will also reduce the temperature increase at the endings of the implant. Reducing the SAR by a factor

of 2 will also reduce the temperature increase by a factor 2.

General guidelines for scanning certain types of implants will not be provided in this chapter. Such information is available in the guidance document on MR safe practices from the ACR [37].

One risk of such overviews is, that nobody can know if tomorrow a company brings a new device on the market, which includes a strong magnet or is ferromagnetic and would be MR unsafe. The MR staff has still to be critical during the screening of patients.

At the other side of the time line, there are historical implants that are hazardous for patients during an MR examination. There was, for example, a valve from Edwards Lifesciences (USA) with a ferromagnetic sphere as valve. It was labeled as MR unsafe, but some of those underwent MR at 1.5 T without any adverse events. Most likely there are no more patients with that valve implanted. Even a higher risk is an aneurism clip. It cannot be excluded that after 2000 still ferromagnetic aneurism clips were implanted. The percentage of ferromagnetic aneurism clips may be small, but the outcome can be fatal if a patient with such a device will be imaged. Therefore, in case of an unknown aneurism clip the risk to benefit ratio is high and should not allow such patients to enter the magnet room.

### 9.5.8 Active Implants

Over the last years, great progress with MR conditional active implants was made. However, still a large number of MR unsafe active implants are implanted. Depending on the device, the manufacturer and model name may not be sufficient enough to decide if a patient with such a device may undergo an MR investigation: the serial number of the device may be needed as well.

In addition, most of the active implants need special programming/setup, emptying of the medication tank, etc. before safe scanning is possible. Therefore, patients with active implants need special care prior to MR investigation,

which needs to be planned. Preferably the referring physician (or the specialist responsible for the active device) should fill out a form with the important information on the device and, if available, connected leads. This information will then be used to find the MR safety label and the conditions under which the patient can be scanned. If the restriction can be fulfilled, an appointment will be made for the MR investigation and, if needed, before and afterward for the reprogramming of the device. Monitoring of the patient for the time the device is switched to the MR mode might be required, since the device may no longer deliver a therapy [38]. In case the compatibility of the implant with the MR scan is unknown, the examination cannot be performed.

If MR conditional labels are followed carefully, patients with those implants may be scanned safely. Active implants which are not labeled are more demanding. For pacemaker and ICD patients, there exist guidelines and restrictions under which also unlabeled pacing systems may be scanned [38, 39]. However, MR should be limited to MR scans with a high clinical benefit, since the potential risk is higher during off-label use. Patients have to be informed that the MR investigation is off-label with their implant.

For cochlear implants, the implanted magnet may pose a problem. Some devices use magnets, which can be demagnetized in a 1.5 T or higher magnetic field. Such devices should not be scanned, since it would request a surgical procedure to replace the magnet after been placed in an MR unit. If the magnet is not destroyed by the magnetic field, the strong force and torque effects may lead to a rotation of the holding magnet. A bandage, if well placed, may reduce this risk. Current and future developments are moving in the direction of MRI-compatible devices, some of which are already available on the market.

Medication pumps may show various interactions with the MR environment. There exist pumps on the market, which may release the whole content of the reservoir to the patient due to the electromagnetic fields of the MR system. If this is a potential risk of the pump, MR is only allowed with an empty tank. Other systems may stop to function under the strong magnetic field

and some even for several hours after the MR. The administration of the medication in a different way needs to be planned and the patient has to be monitored until the device is working as intended.

It is strongly recommended to scan only active implanted systems if the device and electrodes are known and a label from the manufacturer is available. For pacemaker and ICD devices not tested for MRI, consensus papers [38, 39] are available to scan such devices off-label. However, there is additional expertise needed.

### 9.5.9 Site Planning

Site planning and site restrictions are important to prevent dangerous situations due to strong electromagnetic fields of an MR system. Well accepted is the four zones model presented in the ACR Guidance Document on MR Safe Practices [37].

Zone I is the public zone outside the MR center. It is freely accessible to the general public.

Zone II is the reception area of the MR center where patients are under supervision of the MR staff. It includes the waiting area for the unscreened patients and screening and changing of the clothes takes place in here.

Zone III includes the waiting area for the screened patients after changing clothes. Zone III should be physically restricted from general public access. Only MR personal should have free access to zone III. Other staff like cleaning, technical, or security staff should only get free access after proper education and training.

Zone IV is the magnet room and other rooms through which the 5 Gauss line goes. The door(s) of the magnet room should be continuously and directly controlled by MR personnel. Within zone IV any medical interventions are only allowed by appropriately trained and certified MR personnel. In case of an emergency situation, the patient must be moved out of the magnet room by the MR staff. External emergency personal is not allowed to enter the magnet room. Quenching the (superconductive) magnet is normally not advised in cases of medical emergency,

but the person needing care must be taken outside zone IV before emergency treatment.

Site planning should avoid any direct connection from zone I or II to zone IV.

In addition to the screening of all patients before entering zone III and IV, also staff members need to be informed that they may not be allowed to enter zone IV with active and, in some cases, also with passive implants. It is recommended that all staff members fill out a (reduced) MR safety questionnaire before getting access to the controlled area. The status must be reevaluated after any medical interventions where implants were left in the body or in case of injury with metal fragments.

Pregnant staff may in some countries be restricted to enter the magnet room by law after informing their employer (e.g., Switzerland has a static magnetic field limit of 40 mT for pregnant employees). In other countries, pregnant workers may still enter the magnet room but special attention shall be paid to pregnant workers (Directive 2013/35/EU of the European Parliament and the Council).

Inside zone IV only MR conditional devices are allowed. MR conditional monitoring devices, syringe pumps, contrast agent injector, anesthetic equipment, etc. are only allowed to be brought into the magnet room if the restrictions from the manufacturer can be followed. It is highly recommended to label such devices and mention limitations (like up to which field they are allowed) on that label.

### 9.5.10 Training

The safe operation of an MR center can only be guaranteed if all staff with access to the MR center is well trained. One person with deep knowledge in MR safety should be assigned as responsible person for MR safety.

All persons with access to the MR center should have followed a basic training to know the risks of an MR device and be able to operate safely in the MR environment. The basic training will not allow to perform any screening of other

persons nor allow other persons access to the MR environment.

Only after following an extended training MR staff is allowed to perform screening of patients or volunteers or allow any person not trained for MR safety access to the controlled area.

Depending on the local guidelines and laws, specific training may be recommended, including the documentation of the trainings.

There are various courses available from MR safety companies and organizations.

### 9.5.11 Conclusion

MR is one of the safest diagnostic procedures if staff is well trained and patients are carefully screened by experienced staff.

## References

1. Lauterbur PC. Image formation by induced local interactions: examples employing nuclear magnetic resonance. *Nature*. 1973;242:190–1.
2. Garroway AN, Grannell PK, Mansfield P. Image formation in NMR by a selective irradiative process. *J Phys C Solid State Phys*. 1974;7:L457–62.
3. Mansfield P. Multi-planar image formation using NMR spin echoes. *J Phys C: Solid State Phys*. 1977;10:L55.
4. Kumar A, Welti D, Ernst RR. Nmr Fourier Zeugmatography. *J Magn Reson*. 1975;18:69–83.
5. Edelstein WA, Hutchison JMS, Johnson G, et al. Spin warp NMR imaging and applications to human whole-body imaging. *Phys Med Biol*. 1980;25:751–6.
6. Haase A, Frahm J, Matthaei D, et al. FLASH imaging. Rapid NMR imaging using low flip-angle pulses. *J Magn Reson* (1969). 1986;67:258–66.
7. Hennig J, Nauert A, Friedburg H. RARE imaging: a fast imaging method for clinical MR. *Magn Reson Med*. 1986;3:823–33.
8. Ljunggren S. A simple graphical representation of Fourier-based imaging methods. *J Magn Reson* (1969). 1983;54:338–43.
9. Twieg DB. The k-trajectory formulation of the NMR imaging process with applications in analysis and synthesis of imaging methods. *Med Phys*. 1983;10:610–21.
10. Macovski A. Rapid NMR imaging system. Stanford, USA: Leland Stanford Junior University; 1986.
11. Meyer CH, Hu BS, Nishimura DG, et al. Fast spiral coronary artery imaging. *Magn Reson Med*. 1992;28:202–13.

12. Callaghan PT, Pinder DN. Dynamics of entangled polystyrene solutions studied by pulsed field gradient nuclear magnetic resonance. *Macromolecules*. 1980;13:1085–92.
13. Callaghan PT, Pinder DN. A pulsed field gradient NMR study of self-diffusion in a polydisperse polymer system: dextran in water. *Macromolecules*. 1983;16:968–73.
14. Bihan DL, Breton E, Lallemand D, et al. MR imaging of intravoxel incoherent motions: application to diffusion and perfusion in neurologic disorders. *Radiology*. 1986;161:401–7.
15. Callaghan PT, Eccles CD, Xia Y. NMR microscopy of dynamic displacements: k-space and q-space imaging. *J Phys E Sci Instrum*. 1988;21:820–2.
16. Basser PJ, Mattiello J, LeBihan D. MR diffusion tensor spectroscopy and imaging. *Biophys J*. 1994;66:259–67.
17. Moran PR. A flow velocity zeugmatographic interlace for NMR imaging in humans. *Magn Reson Imaging*. 1982;1:197–203.
18. Muthupillai R, Lomas DJ, Rossman PJ, et al. Magnetic resonance elastography by direct visualization of propagating acoustic strain waves. *Science*. 1995;269:1854–7.
19. Haacke EM, Xu Y, Cheng Y-CN, et al. Susceptibility weighted imaging (SWI). *Magn Reson Med*. 2004;52:612–8.
20. Roemer PB, Edelstein WA, Hayes CE, et al. The NMR phased array. *Magn Reson Med*. 1990;16:192–225.
21. Pruessmann KP, Weiger M, Scheidegger MB, et al. SENSE: sensitivity encoding for fast MRI. *Magn Reson Med*. 1999;42:952–62.
22. Sodickson DK, Manning WJ. Simultaneous acquisition of spatial harmonics (SMASH): Fast imaging with radiofrequency coil arrays. *Magn Reson Med*. 1997;38:591–603.
23. Griswold MA, Jakob PM, Heidemann RM, et al. Generalized autocalibrating partially parallel acquisitions (GRAPPA). *Magn Reson Med*. 2002;47:1202–10.
24. Tsao J, Boesiger P, Pruessmann KP. K-t BLAST and k-t SENSE: dynamic MRI with high frame rate exploiting spatiotemporal correlations. *Magn Reson Med*. 2003;50:1031–42.
25. Lustig M, Donoho D, Pauly JM. Sparse MRI: The application of compressed sensing for rapid MR imaging. *Magn Reson Med*. 2007;58:1182–95.
26. Moser E, Laistler E, Schmitt F, et al. Ultra-high field NMR and MRI—the role of magnet technology to increase sensitivity and specificity. *Front Phys*. 2017;5:33.
27. Klucznik RP, Carrier DA, Pyka R, et al. Placement of a ferromagnetic intracerebral aneurysm clip in a magnetic field with a fatal outcome. *Radiology*. 1993;187:855–6.
28. Luechinger R, Duru F, Zeijlemaker VA, et al. Pacemaker reed switch behavior in 0.5, 1.5, and 3.0 tesla magnetic resonance imaging units: are reed switches always closed in strong magnetic fields? *Pacing Clin Electrophysiol*. 2002;25:1419–23.
29. Robertson NM, Diaz-Gomez M, Condon B. Estimation of torque on mechanical heart valves due to magnetic resonance imaging including an estimation of the significance of the Lenz effect using a computational model. *Phys Med Biol*. 2000;45:3793–807.
30. Price DL, De Wilde JP, Papadaki AM, et al. Investigation of acoustic noise on 15 MRI scanners from 0.2 T to 3 T. *J Magn Reson Imaging*. 2001;13:288–93.
31. Schaefer DJ, Bourland JD, Nyenhuis JA. Review of patient safety in time-varying gradient fields. *J Magn Reson Imaging*. 2000;12:20–9.
32. Harris CT, Haw DW, Handler WB, et al. Application and experimental validation of an integral method for simulation of gradient-induced eddy currents on conducting surfaces during magnetic resonance imaging. *Phys Med Biol*. 2013;58:4367–79.
33. Sulemanji M, Vakili K. Neonatal renal physiology. *Semin Pediatr Surg*. 2013;22:195–8.
34. Media ACoDaC. *ACR Manual On Contrast Media*. 10.3 ed; 2018.
35. Kanal E, Tweedle MF. Residual or retained gadolinium: practical implications for radiologists and our patients. *Radiology*. 2015;275:630–4.
36. Kanda T, Fukusato T, Matsuda M, et al. Gadolinium-based contrast agent accumulates in the brain even in subjects without severe renal dysfunction: evaluation of autopsy brain specimens with inductively coupled plasma mass spectroscopy. *Radiology*. 2015;276:228–32.
37. Expert Panel on MRS, Kanal E, Barkovich AJ, et al. ACR guidance document on MR safe practices: 2013. *J Magn Reson Imaging*. 2013;37:501–30.
38. Sommer T, Bauer W, Fischbach K, et al. MR imaging in patients with cardiac pacemakers and implantable cardioverter defibrillators. *Rofo*. 2017;189:204–17.
39. Indik JH, Gimbel JR, Abe H, et al. 2017 HRS expert consensus statement on magnetic resonance imaging and radiation exposure in patients with cardiovascular implantable electronic devices. *Heart Rhythm*. 2017;14:e97–e153.



# Magnetic Resonance Angiography

# 10

Benjamin Peters, Sven Dekeyzer,  
Omid Nikoubashman, and Paul Marie Parizel

## Contents

10.1	<b>Introduction</b> .....	124
10.2	<b>Bright Blood Imaging</b> .....	124
10.2.1	Contrast-Enhanced MR Angiography .....	125
10.2.2	Time-of-Flight Angiography .....	125
10.2.3	Phase-Contrast Imaging .....	126
10.2.4	Arterial Spin Labelling .....	128
10.3	<b>Dark Blood Imaging</b> .....	130
10.4	<b>Clinical Applications</b> .....	130
10.4.1	Extracranial Neurovascular Imaging .....	131
10.4.2	Intracranial Neurovascular Imaging .....	131
10.5	<b>Clinical Case</b> .....	138
	<b>References</b> .....	139

## Abbreviations

ASL	Arterial spin labelling
AVM	Arteriovenous malformation
CASL	Continuous arterial spin labelling
CBF	Cerebral blood flow
CE	Contrast enhanced
CSF	Cerebrospinal fluid
3D-MPRAGE	3D-magnetization prepared rapid acquisition gradient echo
DANTE	Delay alternating with nutation for tailored excitation
dAVF	Dural arteriovenous fistula
DSC	Dynamic susceptibility contrast (MRI)
GRE	Gradient-recalled echo

---

B. Peters  
Department of Radiology, Virga Jessa Hospital,  
Hasselt, Belgium

S. Dekeyzer  
Department of Radiology, Antwerp University  
Hospital, Antwerp, Belgium

O. Nikoubashman  
Department of Neuroradiology, University Hospital  
RWTH, Aachen, Germany  
e-mail: [onikoubashman@ukaachen.de](mailto:onikoubashman@ukaachen.de)

P. M. Parizel (✉)  
David Hartley Chair of Radiology, University of  
Western Australia (UWA) & Royal Perth Hospital  
(RPH), Perth, Australia  
e-mail: [paul.parizel@health.wa.gov.au](mailto:paul.parizel@health.wa.gov.au)

MOTSA	Multiple overlapping thin slab acquisition
MRA	Magnetic resonance angiography
MT	Magnetization transfer
Non-CE	Non-contrast enhanced
PASL	Pulsed arterial spin labelling
PC	Phase contrast (angiography)
pCASL	Pseudocontinuous arterial spin labelling
PET	Positron emission tomography
PLD	Post-labelling delay
RF	Radiofrequency (pulse)
SAR	Specific absorption rate
SNR	Signal-to-noise ratio
SPECT	Single-photon emission tomography
TE	Echo time
TOF	Time-of-flight (angiography)
TONE	Tilted optimized non-saturating excitation
TR	Repetition time
TSE	Turbo spin echo
VENC	Velocity encoding (parameter)
VS-ASL	Velocity selective arterial spin labelling
VW	Vessel wall (imaging)

In dark blood imaging techniques, the signal of flowing blood is suppressed, and the signal of stationary, while the surrounding tissue is maintained, thus rendering the vessels black. Dark blood techniques are especially useful when the focus of interest is not the vessel lumen, but the vessel wall, and this technique will be discussed in the section on vessel wall imaging.

Bright blood imaging refers to MRA techniques, which enhance the signal intensity of blood, with or without suppression of the signal intensity of stationary tissue. Bright blood imaging can be further subdivided into contrast-enhanced (CE) MRA and non-contrast-enhanced (non-CE) MRA. CE-MRA relies on the paramagnetic properties of an intravenously injected gadolinium-based contrast agent, which shortens the T1-relaxation time of blood and renders the lumen of the blood vessels bright on T1-weighted sequences. Non-CE MRA on the other hand relies entirely on the intrinsic MR properties of flowing blood. Several variations are possible and only those techniques that are relevant to the field of neuroradiology will be discussed in this chapter: time-of-flight (TOF) MRA, phase-contrast (PC) MRA, arterial spin labelling (ASL) MRA and vessel wall (VW) imaging. We will conclude with an overview of clinical applications and a case [1, 2].

## 10.1 Introduction

Historically, X-ray digital subtracted angiography has long dominated vascular imaging. Due to the risks associated with ionizing radiation, catheterization and iodine contrast administration, the last 20 years have seen a shift towards MR imaging, augmented by improvements made in MR software and hardware. At present day, MR angiography (MRA) has proven to be a safe and non-invasive vascular imaging method, which provides images similar to those obtained by classical catheter angiography.

Several techniques are available for MRA. These MR methods can be divided into two broad categories, depending on whether they produce dark blood or bright blood and are hence called “dark blood imaging” and “bright blood imaging” techniques respectively.

## 10.2 Bright Blood Imaging

Bright blood imaging can be sub-divided into contrast-enhanced (CE) and non-contrast enhanced (non-CE) angiographic techniques.

Following its introduction in 1994 by Prince [3], CE-MRA was quickly adopted by the radiologic community to perform MR angiography of practically all anatomic regions. Although non-CE MRA techniques such as TOF-MRA and PCA-MRA are historically older and were already in use at the time, they were hampered by long-acquisition times, low-resolution and low signal-to-noise ratio (SNR). Hence, they were trumped by CE-MRA due to its superior imaging quality and speed.

The last decade has seen a resurgence of *non-CE MRA* techniques, however. Historically, Japan played a pivotal role in the initial development of modern non-CE MRA techniques, due to



the high cost of gadolinium-based contrast agents relative to clinical MRI reimbursement by the Japanese government. Globally, safety-related motivations, such as avoidance of gadolinium-based allergic reactions and nephrogenic systemic fibrosis, raised questions about the use of gadolinium-based contrast agents and stimulated the search for alternatives. Beyond cost-saving and safety-issues, equally important factors stimulating non-CE MRA development were technical advancements in MR hardware and software, such as the use of multichannel receiver coil arrays, the higher field strength of increasingly prevalent 3 T scanners and the application of parallel imaging techniques. The combination of these technical improvements led to a reduction in scan time and an increase in SNR and resolution of non-CE MRA techniques, making non-CE MRA feasible for routine clinical use [1, 4].

### 10.2.1 Contrast-Enhanced MR Angiography

CE-MRA is based on the T1-shortening effect of intravenous gadolinium. The signal intensity is dependent on the intraluminal concentration of gadolinium during acquisition time. This technique has long been the method of choice for vascular imaging due to its high signal-to-noise ratio, spatial resolution, and because it is less sensitive to flow-related artefacts, such as velocity, flow direction and turbulence, compared to non-CE MRA. The acquisition parameters repetition time (TR) and echo time (TE) in CE MRA should be made as short as possible to optimize the spatial and temporal resolution. Optimal MRA requires image acquisition at the peak concentration of intraluminal gadolinium in the region of interest and thus the greatest disadvantage is the restricted acquisition time, which is determined by the first passage of the peak contrast bolus. Correct timing of peak bolus arrival is of paramount importance for optimal CE-MRA. Gadolinium is usually injected in a peripheral vein through a catheter. The typical dose of injected gadolinium chelate is 0.1 mmol/kg body weight at an injection rate of 1.5–2 mL/s, by hand or by an automatic injector. An average-sized patient with normal

renal function receives 20 mL of contrast during 8–12 s. The goal is to acquire images at the time of highest bolus concentration. Several methods for adequate bolus timing are available: test bolus timing, fluoroscopic triggering and time-resolved imaging. Other disadvantages of CE MRA are the high cost of gadolinium, the possibility of adverse reactions to gadolinium, and misjudgement of peak bolus arrival. Early or late acquisition timing will result in inadequate contrast enhancement or contamination of venous structures and interfere with image interpretation. A failed acquisition timing cannot be repeated, due to the presence of contrast contamination [4, 5].

### 10.2.2 Time-of-Flight Angiography

Time-of-flight (TOF) MR angiography is the oldest and most commonly used non-CE MRA technique in intracranial vessel imaging. TOF imaging is based on the difference in magnetization between stationary and flowing protons. TOF MRA uses repetitive RF pulses to the region of interest to reduce the signal of stationary tissues, while inflowing, unsuppressed protons will result in a high signal. Repeated RF excitation of a section (slice or slab) saturates stationary spins causing their longitudinal magnetization to approach a low steady-state value, resulting in low signal intensity. Inflowing blood entering the section has not been subjected to these RF pulses, however, and arrives with full longitudinal magnetization. When these unsaturated protons are subject to a set of RF-pulse, the signal these protons generate is significantly higher than that of the stationary tissue within the slab [6].

Contrast between the stationary background tissue and inflowing blood is mainly dependent on repetition time and flip angles. The longer the repetition time, the more inflow of intraluminal protons and the higher the intraluminal signal intensity. Shorter repetition times are associated with stronger suppression of stationary tissue, but slow-flowing spins can also be suppressed. Concerning flip angles, usually moderate-to-large flip angles between 25° and 60° are used. High flip angles will lead to more suppression of stationary tissue and higher signal from inflowing

arterial protons. Intrinsic factors influencing the vascular signal are flow velocity (faster flow gives higher signal intensity), and the length and orientation of the vessel (the vascular signal will be higher if the slice is perpendicular to the axis of the vessel due to the shorter distance of travel of the spins within the slice volume). Therefore, when possible, imaging plane selection should be perpendicular to the vessel of interest.

TOF MRA is a gradient-recalled echo (GRE) sequence and can be acquired with 2D or 3D methods. In 2D acquisition, multiple thin slices are obtained in a sequential order. In 3D acquisition, an entire volume or slab is excited, and 3D TOF data can then be segmented into the desired section thickness for display. The main advantage of the 2D technique is higher sensitivity to slow flow (shorter travel of the moving spins into the slice), and the possibility to use higher flip angles, resulting in better stationary tissue saturation. The main drawback is the poor through plane spatial resolution due to the thickness of the slice. For 3D TOF imaging, flow must be maintained at a certain velocity to avoid saturation effects. To selectively visualize arterial or venous flow, presaturation bands can be applied upstream to the selected slice (arterial suppression to detect venous flow) or downstream to the selected slice (venous suppression). In our centre, we use 3D-TOF for evaluation of intracranial arteries and 2D-TOF for evaluation of intracranial veins.

Limitations of TOF MRA are signal loss due to spin dephasing, spin saturation and patient motion because of the long acquisition time (Fig. 10.1). Spin dephasing typically occurs when flow is turbulent or complex (stenoses) and can lead to overestimation of stenoses. Spin dephasing also occurs in vessels near tissues with short T1 relaxation times, such as fat and subacute haemorrhage. Spin saturation occurs when the flow is too slow and/or the vessel of interest is oriented parallel to the slice plane. A typical example of spin saturation is the so-called transverse sinus flow gaps (Fig. 10.2), absence of flow signal in the transverse sinus, which is frequently observed on venous 2D-TOF angiography.

Multiple techniques are clinically available to diminish dephasing and saturation artefacts.

Magnetization transfer (MT) pre-pulses are usually applied to further suppress signal of stationary background tissue and improve visualization of intracranial vessels. Multiple overlapping thin slab acquisition (MOTSA) will reduce spin saturation due to sequential acquisition of several overlapping 3D volumes at the cost of longer acquisition time. Tilted optimized non-saturating excitation (TONE) uses progressively higher flip angles further into the slab to counter saturation of intraluminal blood at the end of the slab, due to repetitive RF pulses to achieve background saturation [1, 4, 7, 8].

### 10.2.3 Phase-Contrast Imaging

Phase-contrast (PC) MRA has lost ground in vascular imaging due to the availability of better alternatives. The greatest disadvantage is the generally long acquisition time and therefore PC MRA is used for specific intracranial applications only such as angiograms in complex flow vascular malformations, for cerebrospinal fluid measurements and venous angiograms.

PC-MRA technique is a gradient echo technique and is based on the different effect of a bipolar phase-encoding gradient to stationary and moving spins. If a bipolar gradient is applied to a stationary spin, the net phase shift will be 0. When a bipolar gradient is applied to a moving spin, the net phase shift will be proportional to the velocity of the spin. The voxel intensity will reflect the absolute velocity of the spins in the voxel, and thus will always be positive, independent of the direction. Unfortunately, dephasing also occurs due to background field inhomogeneities and these cannot be distinguished from dephasing due to velocity. Therefore, a second toggled bipolar gradient is applied, reversing the order of the encoding gradient lobes, and the paired data are subtracted. The moving spins will cumulate dephasings in the opposite direction, while dephasing of spins due to field inhomogeneities will be identical for both acquisitions and disappear in subtraction.

To depict velocity in all spatial directions, acquisitions need to be repeated with bipolar gradients along the three different axes ( $x$ ,  $y$ ,  $z$ ).

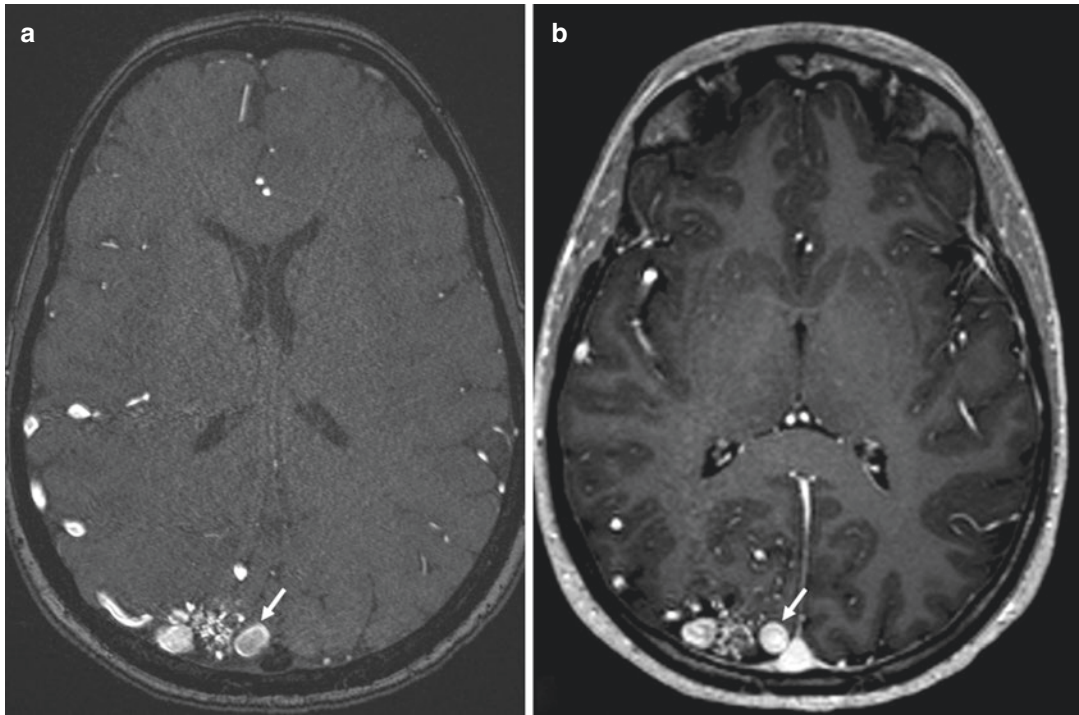


**Fig. 10.1** Axial 3D-TOF MRA (a) and axial CE T1-WI (b) in a patient with an occipital AVM. Panel (a) shows flow artefacts centrally in the draining vein and a little haziness of the inner vessel wall due to motion artefacts.

Panel (b) shows the patency of the draining vein and a sharp delineation of the vessel wall. Note the patency of the sagittal sinus in (b)

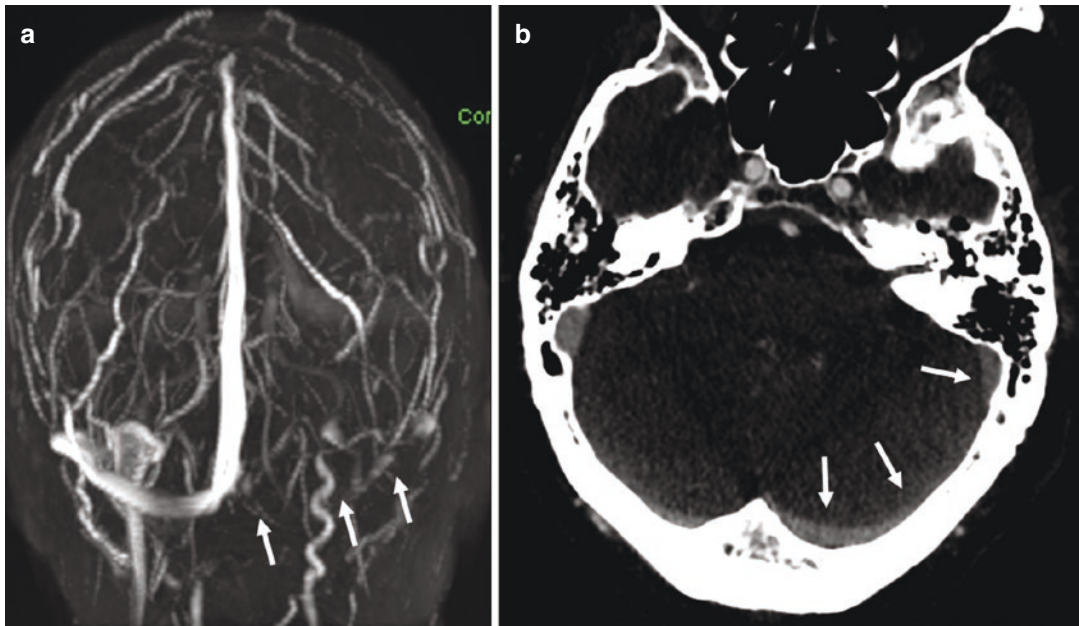


**Fig. 10.2** 2D-TOF MRA with MIP reconstruction (a) shows absent flow in the left transverse sinus (white arrows). CT venography (b), 2 days prior, shows the

patency of the left transverse sinus (white arrows). This phenomenon is called the transverse sinus flow gap

Hence, we theoretically need six different acquisitions. Methods using four acquisitions have been developed to reduce scanning time. An additional acquisition without a bipolar gradient serves as a reference. Images acquired with bipolar gradients are summed to visualize flow in all directions, and then subtracted from the reference image without bipolar gradient, so that only vessels are depicted.

A velocity-encoding (VENC) parameter should be selected before each PC-MRA. This pre-set parameter is measured in centimetre/second. As we are only interested in each acquisition in a certain velocity measurement (arterial, venous or CSF) and not in other moving spins in the same voxel, a preselected value will encompass the measurable phase shifts. A VENC of 50–80 cm/s is applicable for arterial imaging, whereas venous and sinus flow ranges around 20 cm/s. Careful selection of the VENC value is needed as velocities higher than the preselected value will not be measured or misrepresented in the image. Velocities much lower than the preselected value will not be measured and vessels will not be visible.

The advantage of PC MRA compared to an inflow-based technique, such as TOF, is the ability to directly measure flowing blood *within* the slice, as it is based on measuring velocity, whereas flow-dependent techniques require blood to flow *into* the slice to be visible (Fig. 10.3). As the imaging time of PC-MRA is usually 1.5–2 times the imaging time of TOF-MRA, the use of PC-MRA is useful in certain clinical settings such as venous angiogram, the evaluation of the direction of flow in complex arteriovenous malformations (AVM) or in subclavian steal phenomenon [4, 9–11].

#### 10.2.4 Arterial Spin Labelling

Arterial spin labelling (ASL) is an MRA technique to evaluate perfusion of the brain parenchyma based on inflowing blood, without administration of contrast. Traditional and established radiological and nuclear medicine techniques, such as



**Fig. 10.3** Phase-contrast MRA shows a small AVM in the right masseter muscle. The enlarged facial artery (white arrow) is the feeding vessel

single-photon emission tomography (SPECT), positron emission tomography (PET), perfusion-CT and dynamic susceptibility contrast (DSC)–MRI measure perfusion by dynamic imaging of the passage of an exogenous contrast, such as a radioactive isotope, or iodine- or gadolinium-based contrast agents. Conversely, ASL is based on magnetically labelled endogenous water molecules as a tracer to estimate perfusion.

The aim of ASL, in contradistinction to other perfusion techniques, is not the evaluation of macrovascular blood flow, but rather to provide a quantitative or qualitative evaluation of tissue perfusion. Tissue perfusion refers to the delivery of oxygen and nutrients to the tissue of interest by means of blood flow and takes place along the entire length of the capillary bed. The main physiological parameter that is measured with ASL is cerebral blood flow (CBF), which determines the delivery rate of oxygen and nutrients to the capillary bed and is expressed as the volume of blood per volume of tissue per minute ( $\text{mL } 100 \text{ g}^{-1} \text{ min}^{-1}$ ).

ASL starts with reference images of the region of interest. Next, upstream arterial blood

is labelled by the inversion or saturation of magnetization along the  $z$ -axis of blood water molecules in the feeding arteries. Labelling is less efficient with a saturation pulse compared to an inversion pulse. The arterial labelled spins are given time to pass the capillaries and diffuse into the brain parenchyma: the so-called post-labelling delay (PLD). The PLD is dependent on the distance of spin labelling and blood flow velocity and is chosen in such a way that imaging is performed at the time of exchange of water molecules with tissue magnetization. After the PLD, acquisitions of the region of interest are made. The tagged spins will alter the local magnetization and change the longitudinal magnetization. Perfusion images are achieved by subtracting images acquired after arterial labelling from images before labelling and thus subtract the signal of arterial labelled images from static background images. The subtracted images contain the information of local CBF. The delay between tagging and acquisition should not be too long, as longer delays result in more magnetization relaxation and thus less difference between the control images [12].

There are four main variants of proton labelling: continuous labelling (CASL), pulsed labelling (PASL), pseudocontinuous labelling (pCASL) and velocity-selective arterial spin labelling (VS-ASL).

PASL uses very *short RF* pulses (5–20 ms) over large labelling zones to invert a *thick slab* (10–15 cm) of spins proximal to the imaging plane [13].

CASL uses *long and continuous RF pulses* (2–4 s) in combination with a slice-selective gradient to invert the arterial magnetization in a *narrow slice* of spins adjacent to the imaging plane. This is done in a continuous manner while the spins flow from the tagging plane into the imaging plane. Although CASL provides higher perfusion contrast than other types of labelling, it has two major drawbacks: the long duration of the inversion pulse (1) induces magnetization transfer (MT) effects and (2) deposits large amounts of energy into the patient, resulting in a high-specific absorption rate (SAR). On the other hand, CASL

is associated with considerable MT effects. The MT effects correspond to the partial saturation of macromolecules and a reduction in the signal from the free water in the studied volume [13, 14].

In response to these limitations, pCASL was developed to mimic the tagging mechanism of CASL without the inherent drawbacks. This is accomplished by a train of discrete RF pulses together with a gradient pulse applied between two consecutive RF pulses. This way, it is possible to attain near-continuous labelling with high efficiency, but without the hardware requirements, and less RF power deposition and magnetization transfer effect of CASL [15].

PASL, CASL and pCASL are all based on the proximal labelling of the arterial magnetization followed by acquisition of images in the region of interest after a certain delay (PLD). The main problem of these techniques is the finite arterial transit time between labelling and imaging. In VS-ASL, arterial spins are labelled everywhere (including in the region of interest) based purely on flow velocity. This eliminates the effect of the transit delay time necessary for the labelled blood to reach a region of interest. A velocity-selective tag pulse saturates or inverts blood above a cut-off velocity ( $V_c$ ), and data are acquired only from spins with velocity below  $V_c$ . In this manner, only spins that decelerate through the cut-off velocity  $V_c$  during the inflow time TI will be observed and the signal will be proportional to CBF. As VS-ASL is (theoretically) inherently insensitive to transit delays, it should be the method of choice for pathologies, such as stroke, where collateral or slow flow may otherwise result in long transit delays and grossly incorrect CBF measurements. It may have more utility in the context of slow flow and/or collateral flow conditions. However, the low SNR of ASL is exacerbated in VS-ASL, since spins are labelled by saturation pulses instead of inversion pulses.

Arterial spin labelling is clinically used in patients with stroke. Recent studies show promising data on new indications of ASL MRA: dementia, tumour perfusion, arteriovenous fistula, neuropsychiatric diseases and HIV-associated neurocognitive impairment [13, 16, 17].

### 10.3 Dark Blood Imaging

The previously described MRA techniques (CE-MRA, TOF and PCA) are used to investigate abnormalities of the vessel lumen but are generally not useful for the characterization of vessel wall abnormalities and non-stenotic lesions. As a specific sequence to visualize the vessel wall (VW) has not yet been developed, VW imaging is mainly achieved by adjusting the parameters of conventional imaging techniques. To acquire diagnostic images, a high SNR and a high spatial resolution are required. Suppression of signal from flowing blood and CSF, multiplanar acquisitions in 2D or 3D and different tissue weightings are crucial for adequate VW imaging.

To achieve VW imaging with an acceptable image quality and within a reasonable scanning time, a field strength of at least 3 T is needed. As 7 T systems are mainly used for research purposes, we will further discuss parameters for 3 T systems. For optimal delineation and visualization of the vessel wall, intraluminal blood needs to be suppressed, as well as the signal of surrounding structures, mainly CSF. Most intracranial VW imaging sequences rely on the intrinsic “dark blood” properties of 3D turbo-spin echo (TSE) pulse sequences with low-flip-angle refocusing pulses. Dark blood is achieved by the intravoxel dephasing of flowing blood, which is most effective with low-flip-angle refocusing pulses. Preparation pulses, such as double inversion recovery, are a less effective alternative for flowing blood suppression. Delay alternating with nutation for tailored excitation (DANTE) is a relatively new technique, which achieves better CSF suppression and shorter acquisition time [18, 19].

Based on histopathological studies, intracranial wall thickness is known to measure between 0.2–0.4 mm for the distal internal carotid artery and between 0.2 and 0.3 mm for the middle cerebral artery and the basilar artery. This means that theoretically a 0.18-mm isotropic voxel size is necessary for adequate measurements and interpretation of the intracranial VW, which would considerably increase acquisition time and result in a time-consuming sequence if visualization of all intracranial vessels is desired. In daily

clinical practice, voxel sizes of  $0.4 \times 0.4 \text{ mm}^2$  to  $0.9 \times 0.9 \text{ mm}^2$  are used, as VW imaging in clinical practice is usually targeted at relatively large lesions in the proximal segments of the intracranial vessels. In our institution, we perform VW imaging on a 3 T system (Siemens, Magnetom Prisma, Erlangen Germany). For a 2D sequence, we use a SE with voxel size of  $2.0 \times 0.7 \times 0.7 \text{ mm}$ , with a duration of 5–7 min. For a 3D sequence, we usually use a SPACE with voxel size of  $0.9 \times 0.9 \times 0.9 \text{ mm}$  for whole brain. With these parameters, we achieve a reasonable balance between spatial resolution and SNR. As intracranial VW imaging is achieved adjusting parameters of conventional imaging techniques, all contrast weightings can be achieved. Ideally, we should use all frequently used weightings (T1, T2 and PD) to assess the vessel wall. However, this would be time-consuming and is not feasible in daily practice. We usually limit our VW images to T1–WI before and after administration of intravenous contrast. To reduce scanning time, some institutions only acquire post-contrast vessel wall images. However, this can lead to misinterpretation of intramural hematomas or dissections. Depending on the specific clinical setting, sequences with isotropic or anisotropic voxels can be used. Sequences with isotropic voxels are more appropriate for multiplanar assessment and are preferred for screening purposes. Sequences with anisotropic voxels are associated with a very high in-plane spatial resolution and detailed assessment of the VW, but have a larger through-plane voxel size, so smaller VW lesions will be subjected to partial volume effect. In daily practice, conventional MR sequences with isotropic VW-images can be used to screen for VW lesions. In patients with follow-up of a known VW lesion, SNR can be increased by using anisotropic sequences [18, 20].

---

### 10.4 Clinical Applications

In this paragraph, we will discuss the preferred imaging technique for the most frequent clinical settings. A distinction will be made between intracranial and extracranial imaging. The main

indication for imaging of the extracranial brain supplying arteries is evaluation of stenosis and dissection. Indications for intracranial vascular imaging include stroke, aneurysm, vascular malformations (arteriovenous malformations and dural arteriovenous fistulas), cerebral venous thrombosis and vasculitis.

## 10.4.1 Extracranial Neurovascular Imaging

### 10.4.1.1 Carotid Artery Stenosis

Although digital subtraction angiography is still considered the gold standard for imaging evaluation of carotid artery stenosis, this is an invasive examination and not without risks. MRA provides a safe alternative for direct stenosis evaluation. This can be done by using TOF-MRA or with CE-MRA. Contrary to CT-angiography, MRA is not hampered by the presence of calcifications and even extensive calcifications do not cause difficulties in stenosis evaluation.

Traditionally MRA of the carotids was performed by TOF MRA, both with 2D and 3D-techniques. As described previously, 2D-TOF angiography is more sensitive for the detection of slow flow, making the technique sensitive in distinguishing slow flow from occlusions. 3D-TOF on the other hand has a higher spatial resolution, a greater SNR, and a lower sensitivity for flow voids due to the smaller voxel size and shorter TE. Furthermore, the degree of stenosis can be measured according to the North American Symptomatic Carotid Endarterectomy Trial (NASCET) or the European Carotid Surgery Trial (ECST) criteria [21, 22].

After the introduction of CE-MRA, CE-MRA quickly replaced TOF MRA for carotid evaluation in many centres. Although some authors insist that TOF MRA remains the most sensitive method for carotid stenosis evaluation, the main advantage of CE-MRA is the limitation of artefacts compared to flow-based MRA techniques, such as intravoxel dephasing due to turbulent flow or saturation effects [23]. Moreover, the shorter acquisition time of CE-MRA limits the motion artefacts that cause degradation of images. In

our centre, carotid stenosis evaluation is standard performed by CE-MRA, and TOF MRA is reserved for patients with contra-indications to Gadolinium.

### 10.4.1.2 Cervical Artery Dissection

CT angiography is often the first imaging study performed for patients in whom a cervical (carotid or vertebral) artery dissection is suspected. MRI offers the additional benefit of being able to directly visualize the mural hematoma, with a sensitivity and specificity that is superior to that of CT. MRA is therefore the examination of choice if cervical artery dissection is suspected and CTA findings are equivocal. MRI has the additional benefit of being able to detect the cerebral ischemic consequences of a cervical artery dissection when present. In case MRA is performed to rule out cervical artery dissection, it is essential to include fat-saturated non-contrast enhanced T1-weighted sequences to the imaging protocol to detect a possible intramural hematoma. Caution is advised, as intramural hematomas generally are iso-intense in the acute phase and become hyperintense on T1-weighted imaging only about 7 days after the acute event. Repeat imaging is advised in case of equivocal findings.

## 10.4.2 Intracranial Neurovascular Imaging

### 10.4.2.1 Stroke

The role of MRI is limited in stroke patients in the acute setting, as most patients undergo non-contrast enhanced CT of the brain, with or without CT angiography and CT perfusion depending on the context and therapeutic implications. Exceptionally, MRI of the brain is performed in certain patients, such as patients with a wake-up stroke with inconspicuous CT findings to rule out a FLAIR-diffusion mismatch, in which case patients can be still be considered eligible for intravenous thrombolysis, or in patients with severe contra-indications to iodine contrast media. In these patients, intracranial neurovascular imaging is performed with 3D-TOF angiogra-

phy to rule out high-grade intracranial stenoses (Fig. 10.4) or occlusions. When perfusion imaging is required, DCE-MRI (Fig. 10.5) or ASL can be performed (Fig. 10.6).

#### 10.4.2.2 Cerebral Aneurysms

In patients with acute subarachnoid haemorrhage, vascular imaging is usually performed with CT angiography. Aneurysm screening, for instance in patients with autosomal dominant polycystic kidney disease, can be performed on MRI with 3D-TOF MRA. Follow-up of endovascularly treated (coiling) aneurysms is usually performed out with MRI to rule out recanalization or rest perfusion. For follow-up of endovascularly treated aneurysms we use a 3D-TOF sequence with a smaller voxel size ( $0.4 \times 0.4 \times 0.5$  mm)

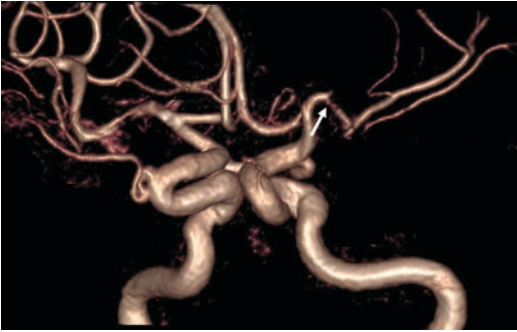


**Fig. 10.4** 3D reconstruction of a 3D-TOF shows a high-grade stenosis in M1 segment of the left middle cerebral artery (white arrow)

at our centre to improve the SNR at the cost of longer acquisition time. Sometimes additional CE MRA is needed for optimal delineation of a complex aneurysm (Fig. 10.7). VW imaging in the follow-up of aneurysms has recently gained ground in literature, as contrast enhancement of the aneurysm wall is considered a differentiation sign between stable and unstable aneurysms (Fig. 10.8). The exact role of VW imaging in the decision algorithm to decide upon elective aneurysm treatment is still unclear.

#### 10.4.2.3 Vascular Malformations

Different imaging protocols are possible in patients with vascular malformations, especially arteriovenous malformations (AVM) (Fig. 10.9) and dural arteriovenous fistulas (dAVF) (Fig. 10.10). At our centre, a 3D-TOF is included to each MRI protocol for evaluation of an AVM or dAVF. In AVMs 3D-TOF MRI nicely depicts the feeding arteries and nidus of the AVM (Fig. 10.9). Due to arteriovenous shunting, a bright signal is generally present in the enlarged draining veins (Figs. 10.10 and 10.11). PC-MRA can be considered in complex AVMs to better depict slow flow or visualize in-plane flow (Fig. 10.3). We usually add a 3D magnetization-prepared rapid gradient-echo (MPRAGE) T1 after intravenous contrast administration for optimal visualization of the draining veins and exclude complications, such as thrombosis of the draining veins (Figs. 10.1, 10.7 and 10.9).

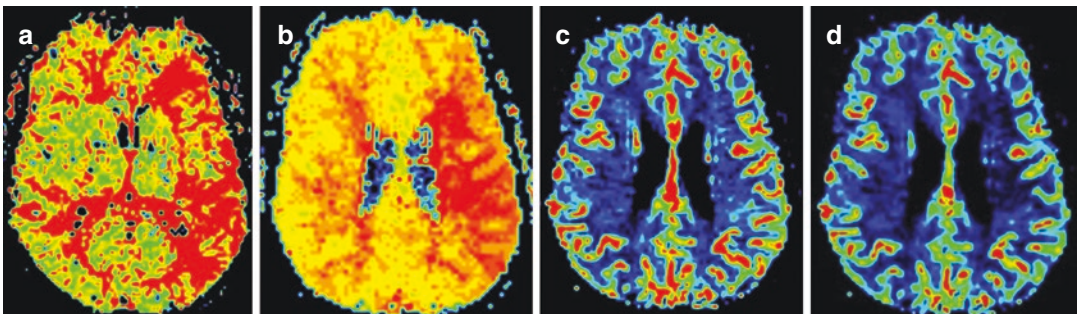


**Fig. 10.5** CE perfusion MRA, of the same patient as in Fig. 10.4, with parametric maps of MTT (a), TTP (b), CBV (c) and CBF (d). Panels (a) and (b) show a prolonged MTT and TTP in the vascular territory of the left

middle cerebral artery compared with the right side. Panels (c) and (d) show a symmetrical CBV and CBF suggestive for compensated flow due to collateral flow



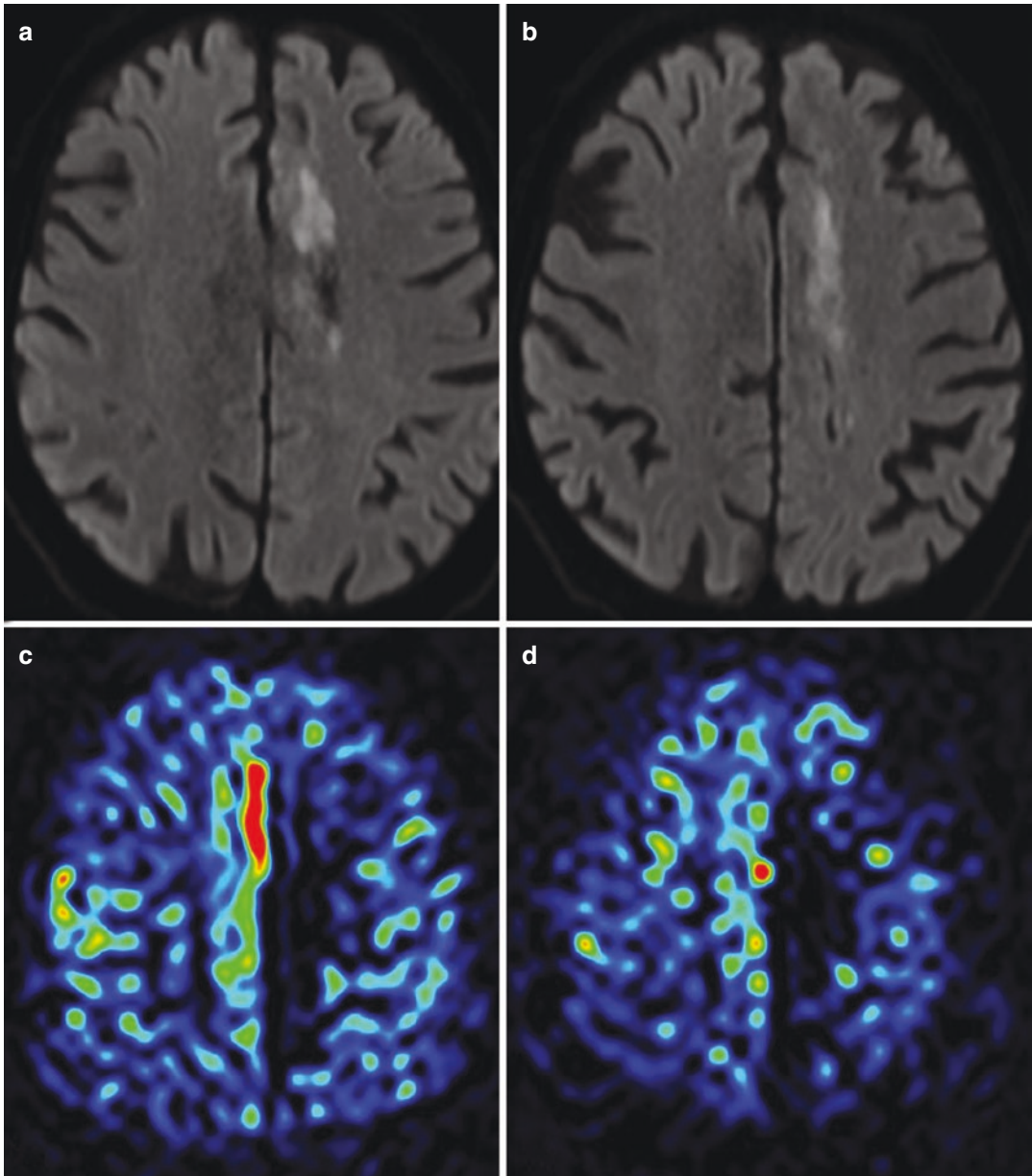


**Fig. 10.6** MRA of a patient presenting with an acute stroke with severe renal impairment. Axial diffusion-weighted imaging (DWI) (**a** and **b**) shows pathologic diffusion restriction in the vascular territory of the left anterior cerebral artery. ASL perfusion CBF maps (**c** and

**d**) shows a reduced blood flow in the vascular territory of the left anterior cerebral artery compared with right. 3D-TOF MRA (not shown) showed no proximal vessel occlusion, so the patient was treated conservatively

#### 10.4.2.4 Cerebral Venous Thrombosis

Cerebral venous thrombosis can be a difficult diagnosis, both clinically and radiologically. When MR imaging is performed, several radiological strategies are possible. First of all, a thrombus in a dural

sinus or cortical vein is often associated with signal abnormalities in the dural sinuses on standard sequences such as T1-, T2-, diffusion- and/or GRE-T2\* images. Signal characteristics vary depending on the sequence and the age of the thrombus how-

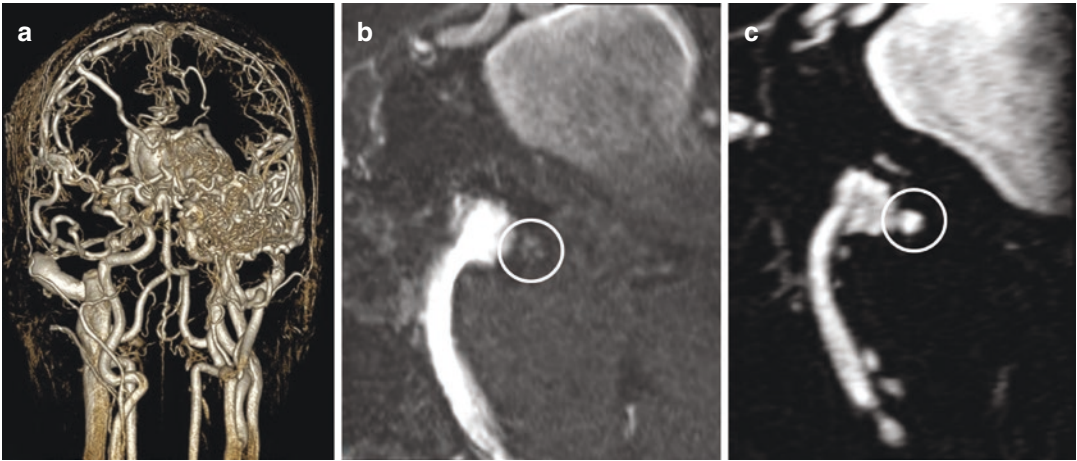


**Fig. 10.7** 3D cinematic reconstructions of a 3D MPRAGE T1 WI (a) shows an overview of a large AVM centred in the left temporal lobe. Oblique 3D TOF reconstructions (b) illustrates an endovascular treated flow

aneurysm on the tip of the basilar artery with a residual neck. In the posterior part there is a small haziness visible (circle). High-resolution CE T1-WI (c) clearly demonstrates the residual neck to be larger than shown in (b)

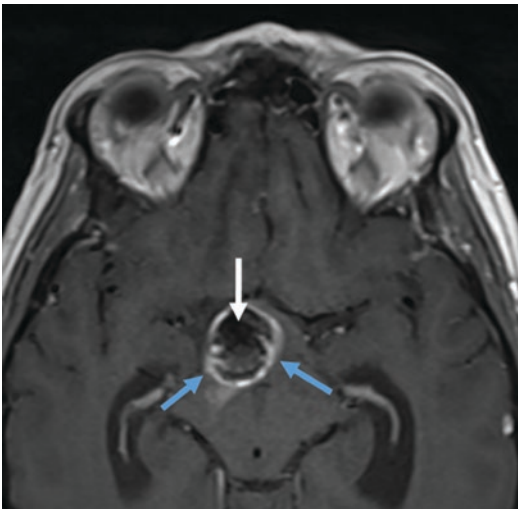


**Fig. 10.8** Axial CE T1-WI. A patient with a large, endovascular-treated aneurysm (white arrow) shows diffuse enhancement of the vessel wall (blue arrows)

ever, and the resulting imaging appearance can be confusing and not diagnostic. For adequate evaluation of the patency of the dural sinuses or cortical

veins, dedicated venous imaging is hence required. For that purpose, a 2D-TOF angiography can be performed. As 2D-TOF is susceptible to saturation artefacts, it is advised to acquire 2D-TOF images in the coronal plane, perpendicular to the superior sagittal sinus. This has the disadvantage that both transverse sinuses are visualized “in plane,” however. Hypoplasia of one or both transverse sinuses is a frequent occurrence in the general population and the combination of slow venous flow and in-plane visualization on a coronal 2D-TOF can give rise to a “transverse sinus” gap, resulting in diagnostic uncertainty (Fig. 10.2). There are several options to deal with this situation, such as inspection of the standard MRI sequences and the stack of contiguous 2D-TOF slices, on which subtle flow can often be seen, despite a “gap” being present on 3D-MIP reconstructions (Fig. 10.12). Another option is to repeat 2D-TOF in a plane perpendicular to the transverse sinuses (for instance in the sagittal plane). A third option is to perform a 3D MPRAGE T1 after intravenous contrast administration (Fig. 10.12). The conundrum here is that

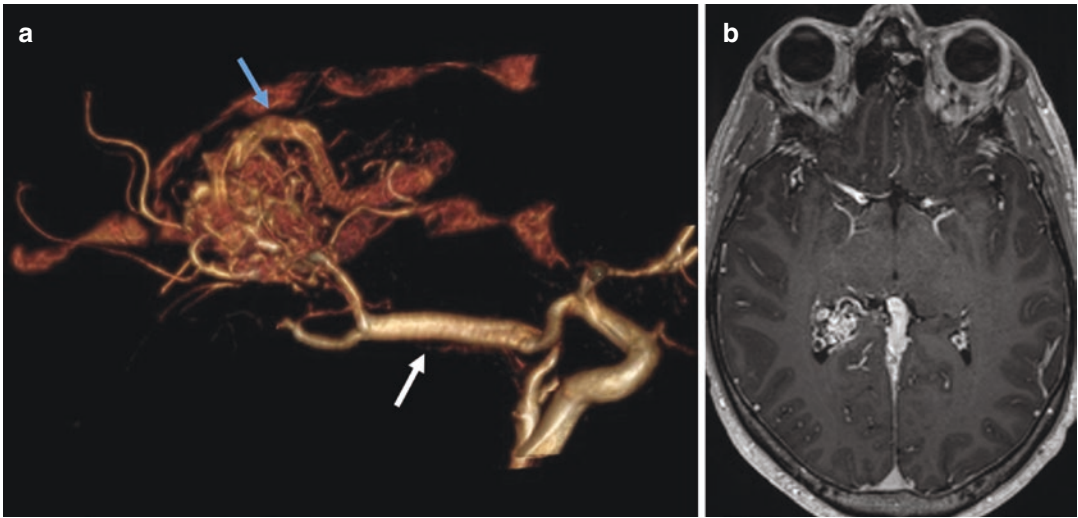


**Fig. 10.9** 3D reconstruction of a 3D TOF MRA (a) shows a hypertrophic posterior cerebral artery (white arrow) and the enlarged draining vein into the sinus rectus (blue arrow). Axial CET1-WI (b) clearly shows the intraventricular location of the AVM

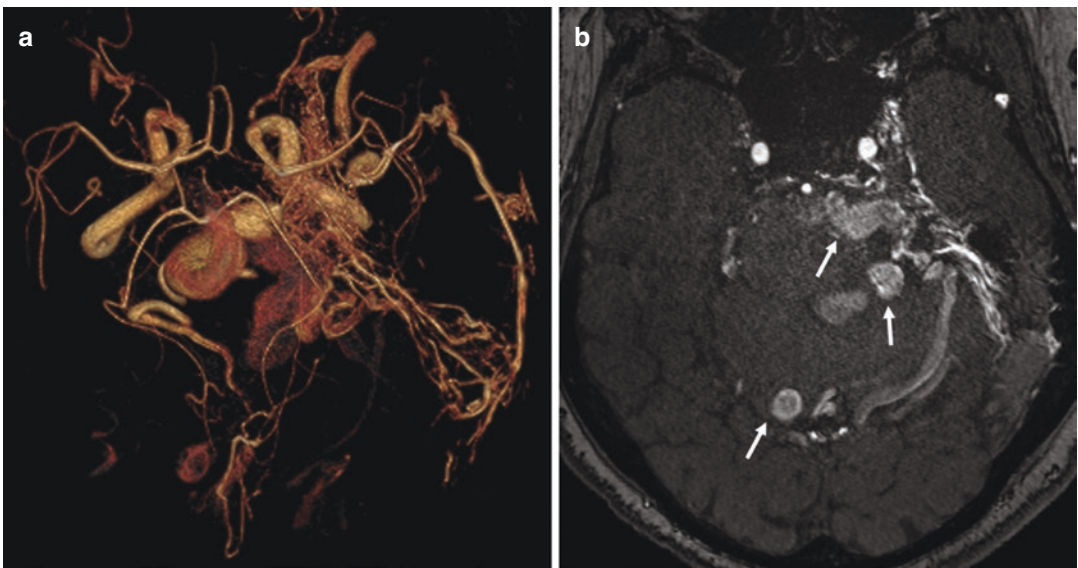


**Fig. 10.10** 3D reconstruction of a 3D TOF MRA (a) shows an overview of an extensive type IV dural fistula of the left cerebellar tentorium. (b) Axial 3D TOF MRA demonstrates the arterial flow in the enlarged tortuous draining veins (white arrows)

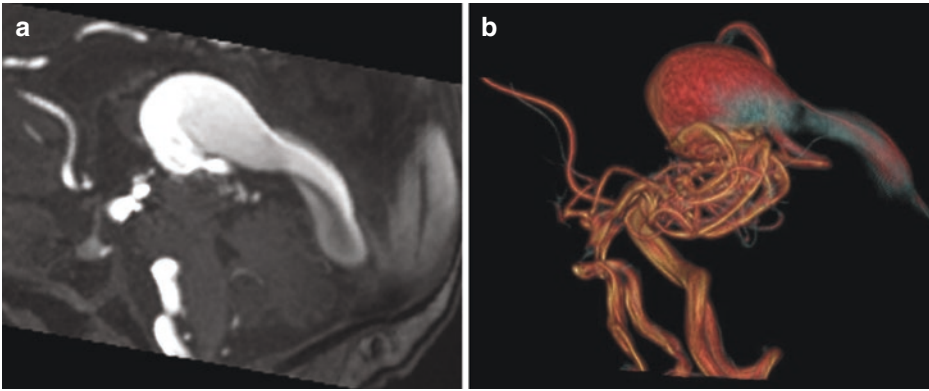


**Fig. 10.11** Sagittal (a) and 3D (b) reconstruction of a 3D TOF MRA shows a high flow vein of Galen aneurysmal malformation

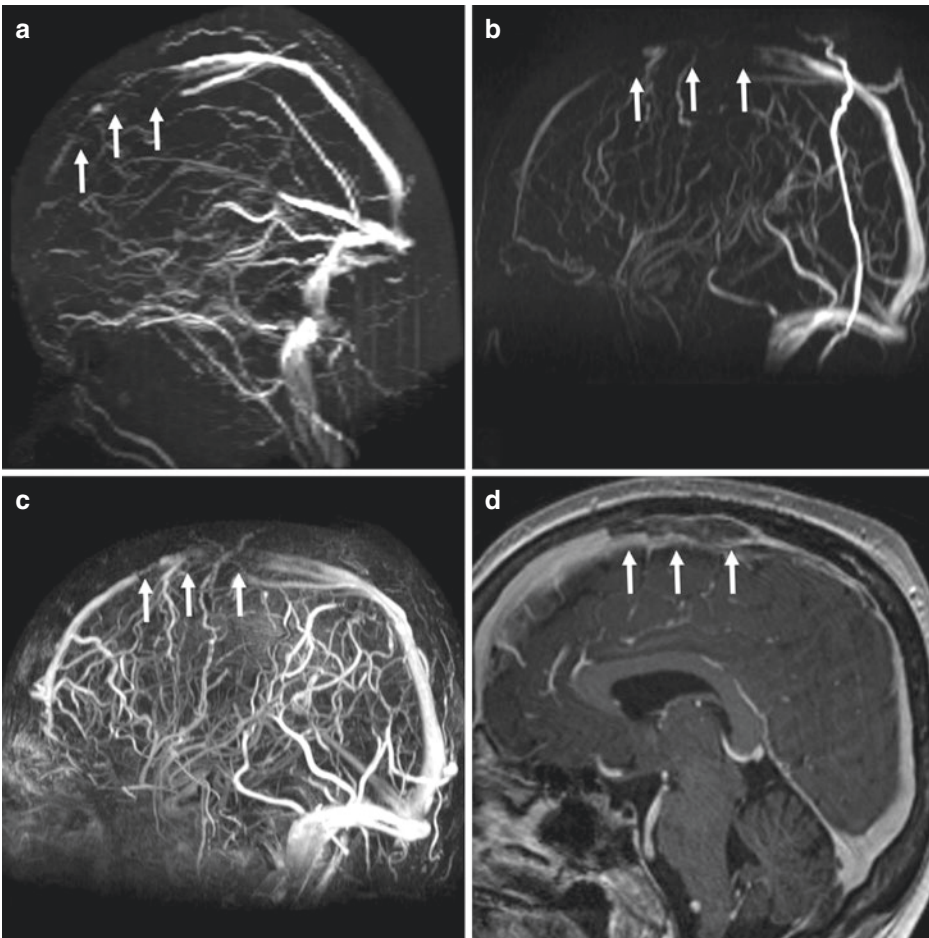


**Fig. 10.12** MIP reconstruction of 2D TOF venography (a), phase contrast venography (b), 3D MPRAGE T1-WI after administration of gadolinium (c and d). MIP reconstruction of a patient with a superior sagittal sinus thrombosis (white arrows). (b) clearly shows a better spatial resolution than (a). Note the patency of the anterior portion

of the sagittal sinus (blue arrow) in (b) and (c) whereas there is no flow visible in (a), which gives a more realistic idea of the full extent of the thrombosis in (b) and (c). Due to arterial contamination, the venous drainage overview is lost in (c). The full extent of the thrombosis (white arrows) is clearly depicted on the mid-sagittal CE T1 images in (d)

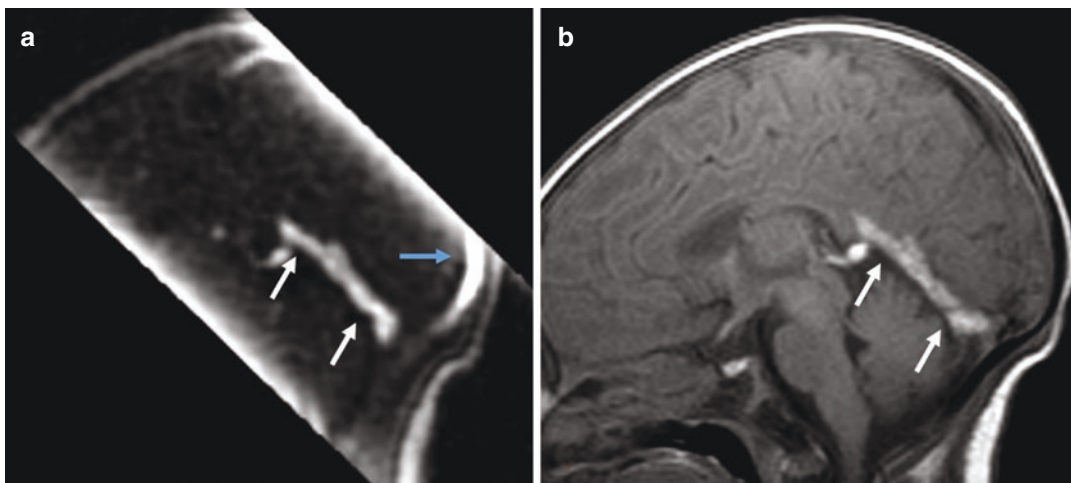


**Fig. 10.13** Sagittal reconstruction of a 3D MPRAGE T1-WI after administration of gadolinium (a) and sagittal T1-WI (b). Image with contrast (a) shows a hyperintense signal in the straight sinus (white arrows) and the superior sagittal sinus (blue arrow). Image without contrast (b) shows a spontaneous hyperintense signal in the straight

sinus and a hypointense signal in the superior sagittal sinus. This is a pitfall case: the spontaneous hyperintense aspect of the thrombosis can be misinterpreted as contrast enhancement and thus patency of the vessel. It is therefore important to compare pre- and post-contrast images carefully

subacute thrombus can be spontaneous hyperintense, so you always need T1-WI before contrast (Fig. 10.13). Another pitfall is a chronic organized dural thrombus can be contrast-enhancing and remain undetected after gadolinium administration, however, many patients undergoing MRI do so because there is a suspicion of an acute or subacute CVT. Gadolinium is contra-indicated in pregnant patients, however, a patient group in which exclusion of CVT is frequently required. PC-MRA can also be performed for evaluation of the dural sinuses (Fig. 10.12) [8].

#### 10.4.2.5 Vasculitis

Intracranial vasculitis is a rare condition and imaging appearances as well as calibre of

involved vessels varies considerably depending on the type of vasculitis. For a general evaluation of the intracranial arteries 3D-TOF angiography is performed. To cover the entire cranium, including small peripheral arteries, two slabs can be placed on the hemicranium. In case of vessel wall irregularities, it is important to differentiate vasculitis from atherosclerosis or (depending on exact appearance and clinical context) pseudovasculitis (reversible cerebral vasoconstriction syndrome). In these situations, dedicated contrast-enhanced VW imaging can be considered, as vasculitis is associated with vessel wall inflammation and contrast enhancement, while atherosclerosis and reversible cerebral vasoconstriction syndrome generally are not.

## 10.5 Clinical Case

We conclude with a case of a 58-year-old female patient with a known Moyamoya disease. She is known to have a chronic occlusion of the right middle cerebral artery (Figs. 10.14 and 10.15). She was treated with a superficial temporal artery to middle cerebral artery bypass (Figs. 10.14 and 10.15). As she is in regular follow-up, we try to minimize the contrast administration and use ASL to evaluate for perfusion (Fig. 10.16).



**Fig. 10.15** 3D reconstruction of a 3D-TOF MRA of the same patient shows a 3D overview of the chronic occlusion of the right middle cerebral artery, the puff of smoke-like appearance (white circle) and the patency of the cerebral bypass (white arrow)

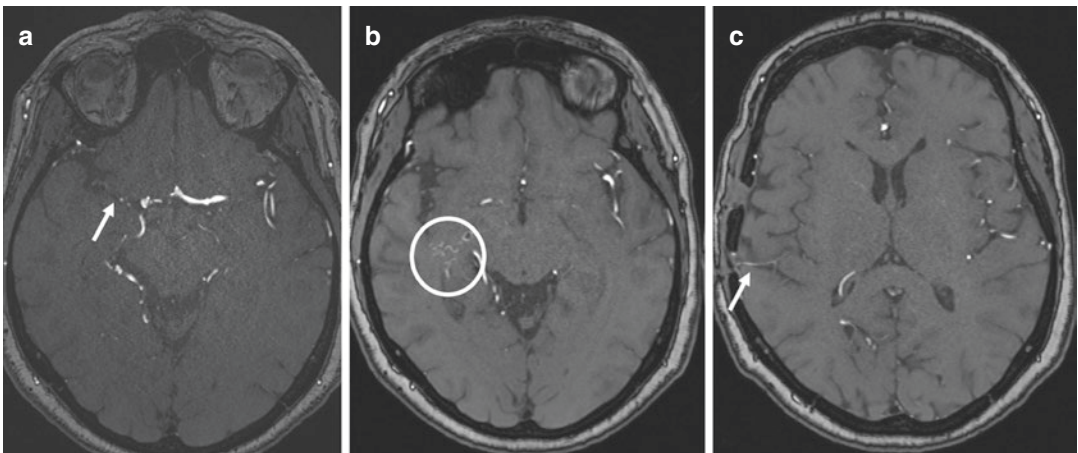


**Fig. 10.14** Axial 3D-TOF MRA of a patient with Moyamoya disease. Image (a) shows the chronic occlusion of the right cerebral artery (white arrow). Image (b) illustrates tiny abnormal intracranial collateral vessel net-

works (white circle), similar to the so-called puff of smoke on angiography. Image (c) demonstrates flow in the superficial temporal artery to middle cerebral artery bypass (white arrow)

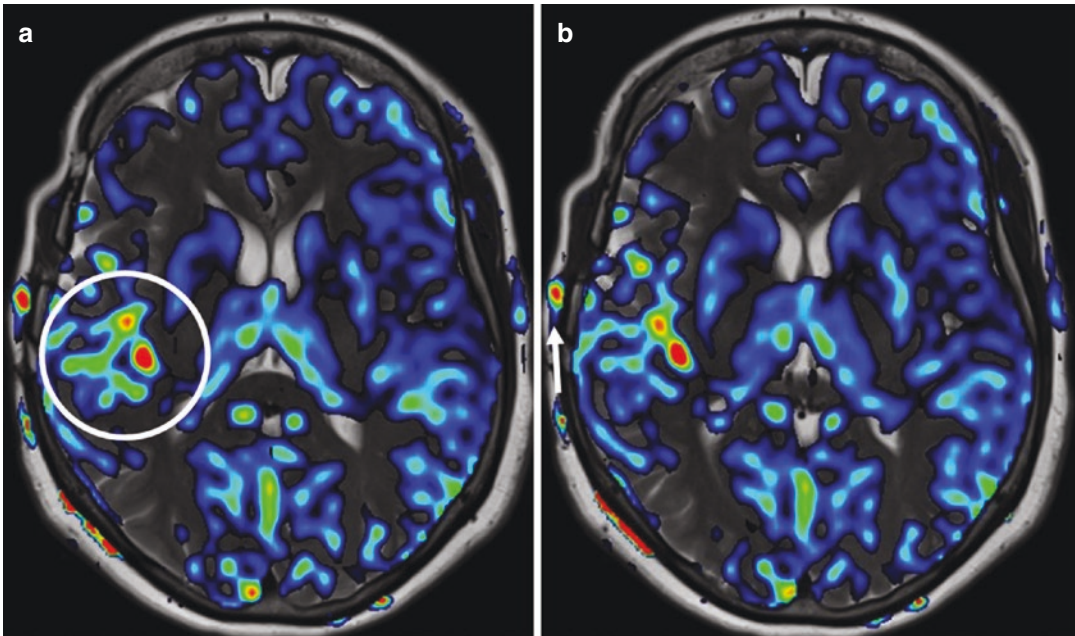


**Fig. 10.16** Fusion images of a perfusion ASL and a T2-WI (a and b). Image (a) shows an asymmetric, elevated cerebral blood flow in the vascular territory of the right

middle cerebral artery (white circle). (b) Note the higher blood flow in the right temporal artery (white arrow)

## References

- Miyazaki M, Lee VS. Nonenhanced MR angiography. *Radiology*. 2008;248(1):20–43.
- Ivančević MK, Geerts L, Weadock WJ, Chenevert TL. Technical principles of MR angiography methods. *Magn Reson Imaging Clin N Am*. 2009;17(1):1–11.
- Prince MR. Gadolinium-enhanced MR aortography. *Radiology*. 1994;191(1):155–64.
- Özsarlak Ö, Van Goethem JW, Maes M, Parizel PM. MR angiography of the intracranial vessels: technical aspects and clinical applications. *Neuroradiology*. 2004;46(12):955–72.
- Riederer SJ, Stinson EG, Weavers PT. Technical aspects of contrast-enhanced MR angiography: current status and new applications. *Magn Reson Med Sci*. 2018;17(1):3–12.
- Saloner D. The AAPM/RSNA physics tutorial for residents. An introduction to MR angiography. *Radiographics*. 1995;15(2):453–65.
- Blatter DD, Parker DL, Robison RO. Cerebral MR angiography with multiple overlapping thin slab acquisition. Part I. Quantitative analysis of vessel visibility. *Radiology*. 1991;179(3):805–11.
- Ayanzen RH, Bird CR, Keller PJ, McCully FJ, Theobald MR, Heiserman JE. Cerebral MR venography: normal anatomy and potential diagnostic pitfalls. *Am J Neuroradiol*. 2000;11(6):1107–18.
- Bakker CJ, Hoogeveen RM, Viergever MA. Construction of a protocol for measuring blood flow by two-dimensional phase-contrast MRA. *J Magn Reson Imaging*. 1999;9(1):119–27.
- Wildermuth S, Debatin JF, Huisman TA, Leung DA, McKinnon GC. 3D phase contrast EPI MR angiography of the carotid arteries. *J Comput Assist Tomogr*. 1995;19(6):871–8.
- Dumoulin CL. Phase contrast MR angiography techniques. *Magn Reson Imaging Clin N Am*. 1995;3(3):399–411.
- Alsop DC, Detre JA. Multisection cerebral blood flow MR imaging with continuous arterial spin labeling. *Radiology*. 1998;208(2):410–6.

13. Petcharunpaisan S, Ramalho J, Castillo M. Arterial spin labeling in neuroimaging. *World J Radiol.* 2010;2(10):384–98.
14. Wang J, Alsop DC, Li L, Listerud J, Gonzalez-At JB, Schnall MD, et al. Comparison of quantitative perfusion imaging using arterial spin labeling at 1.5 and 4.0 tesla. *Magn Reson Med.* 2002;48(2): 242–54.
15. Alsop DC, Detre JA, Golay X, Günther M, Hendrikse J, Hernandez-Garcia L, et al. Recommended implementation of arterial spin-labeled perfusion MRI for clinical applications: a consensus of the ISMRM perfusion study group and the European consortium for ASL in dementia. *Magn Reson Med.* 2015;73(1):102–16.
16. Haller S, Zaharchuk G, Thomas DL, Lovblad K-O, Barkhof F, Golay X. Arterial spin labeling perfusion of the brain: emerging clinical applications. *Radiology.* 2016;281(2):337–56.
17. Brown GG, Clark C, Liu TT. Measurement of cerebral perfusion with arterial spin labeling: part 2. Applications. *J Int Neuropsychol Soc.* 2007;13(03):526–38.
18. Mandell DM, Mossa-Basha M, Qiao Y, Hess CP, Hui F, Matouk C, et al. Intracranial vessel wall MRI: principles and expert consensus recommendations of the American Society of Neuroradiology. *Am J Neuroradiol.* 2017;38(2):218–29.
19. Viessmann O, Li L, Benjamin P, Jezzard P. T2-weighted intracranial vessel wall imaging at 7 tesla using a DANTE-prepared variable flip angle turbo spin echo readout (DANTE-SPACE). *Magn Reson Med.* 2017;77(2):655–63.
20. Lindenholtz A, van der Kolk AG, Zwanenburg JJM, Hendrikse J. The use and pitfalls of intracranial vessel wall imaging: how we do it. *Radiology.* 2018;286(1):12–28.
21. Barnett HJM, Taylor DW, Eliasziw M, Fox AJ, Ferguson GG, Haynes RB, et al. Benefit of carotid endarterectomy in patients with symptomatic moderate or severe stenosis. *N Engl J Med.* 1998;339(20):1415–25.
22. Randomised trial of endarterectomy for recently symptomatic carotid stenosis: final results of the MRC European Carotid Surgery Trial (ECST). *Lancet.* 1998;351(9113):1379–87.
23. Townsend TC, Saloner D, Pan XM, Rapp JH. Contrast material-enhanced MRA overestimates severity of carotid stenosis, compared with 3D time-of-flight MRA. *J Vasc Surg.* 2003;38(1):36–40.





# MRI Perfusion Techniques

# 11

Kyrre E. Emblem, Christopher Larsson,  
Inge R. Groote, and Atle Bjørnerud

## Contents

11.1	<b>Introduction</b> .....	142
11.2	<b>Technical Background</b> .....	143
11.2.1	Physical Principles of DSC and DCE .....	143
11.2.2	From MR Signal to Tracer Concentration .....	144
11.2.3	Physical Principles of ASL .....	145
11.2.4	Tracer Kinetic Modeling .....	146
11.2.5	Model-Free Analysis .....	147
11.2.6	Model-Based Analysis .....	148
11.2.7	Freely Diffusible Tracer Analysis .....	149
11.2.8	Descriptive Analysis .....	150
11.3	<b>Current Clinical Applications</b> .....	150
11.4	<b>CNS Cancers</b> .....	151
11.4.1	Presurgical Characterization of Gliomas .....	151
11.4.2	Differential Diagnoses and Non-Gliomas .....	152
11.4.3	Targeted Therapies .....	153
11.5	<b>Cerebrovascular Disease</b> .....	154
11.5.1	Stroke .....	154
11.5.2	Neurodegenerative Disease .....	156
11.5.3	Demyelinating Disease .....	156
11.6	<b>Future Directions</b> .....	157
11.7	<b>Clinical Case</b> .....	158
	<b>References</b> .....	159

K. E. Emblem  
Department of Diagnostic Physics, Oslo University  
Hospital, Oslo, Norway  
e-mail: [kyrre.eeg.emblem@rr-research.no](mailto:kyrre.eeg.emblem@rr-research.no)

C. Larsson  
Department of Neurosurgery, Oslo University  
Hospital, Oslo, Norway

I. R. Groote  
Computational Radiology and Artificial Intelligence  
(CRAI) Unit, Division of Radiology and Nuclear  
Medicine, Oslo University Hospital, Oslo, Norway

A. Bjørnerud (✉)  
Computational Radiology and Artificial Intelligence  
(CRAI) Unit, Division of Radiology and Nuclear  
Medicine, Oslo University Hospital, Oslo, Norway

Department of Physics, University of Oslo, Oslo, Norway  
e-mail: [atlebjo@fys.uio.no](mailto:atlebjo@fys.uio.no)

### 11.1 Introduction

The role of the biologic process known as perfusion, or blood flow, in the human body is to maintain sufficient delivery of vital nutrients, such as oxygen, to most organs. Moreover, perfusion is an effective regulator of body temperature and plays a part in the removal of metabolic waste. Cerebrovascular disease and a wide range of central nervous system (CNS) pathologies are recognized by irregular or insufficient blood flow or vascularization, making perfusion an essential target for MR-based diagnostic monitoring. Some pathological processes of the CNS such as inflammation and neoplasms are also characterized by increased capillary permeability and the possibility of quantifying the degree of pathology-induced transcapillary “leakiness” to a given tracer is an additional and important opportunity for MRI. To this end, MRI techniques to measure

perfusion and permeability-related metrics will be the focus of this chapter.

The term “perfusion-weighted” MRI (pMRI) is commonly used to collectively describe MRI techniques that measure both perfusion- and permeability-related parameters, in spite of the fact that tissue perfusion and transcapillary permeability are separate physiological processes that may or may not be interdependent. Figure 11.1 gives a schematic overview of the three different MRI perfusion techniques covered in this chapter; dynamic susceptibility contrast (DSC)-MRI, dynamic contrast-enhanced (DCE)-MRI, and arterial spin labeling (ASL)-MRI. Whereas, DSC and DCE are based on the use of an exogenous (externally administered) contrast agent (CA), ASL makes use of magnetically labeled blood as an endogenous tracer. The general tracer kinetic model valid for all three techniques is shown in Fig. 11.2. Here, a bolus of

**Fig. 11.1** Schematic overview of the three perfusion MRI techniques; dynamic susceptibility contrast (DSC)-MRI, dynamic contrast-enhanced (DCE)-MRI and arterial spin labeling (ASL). See text for details of the different techniques and the parameters that are accessible for each method

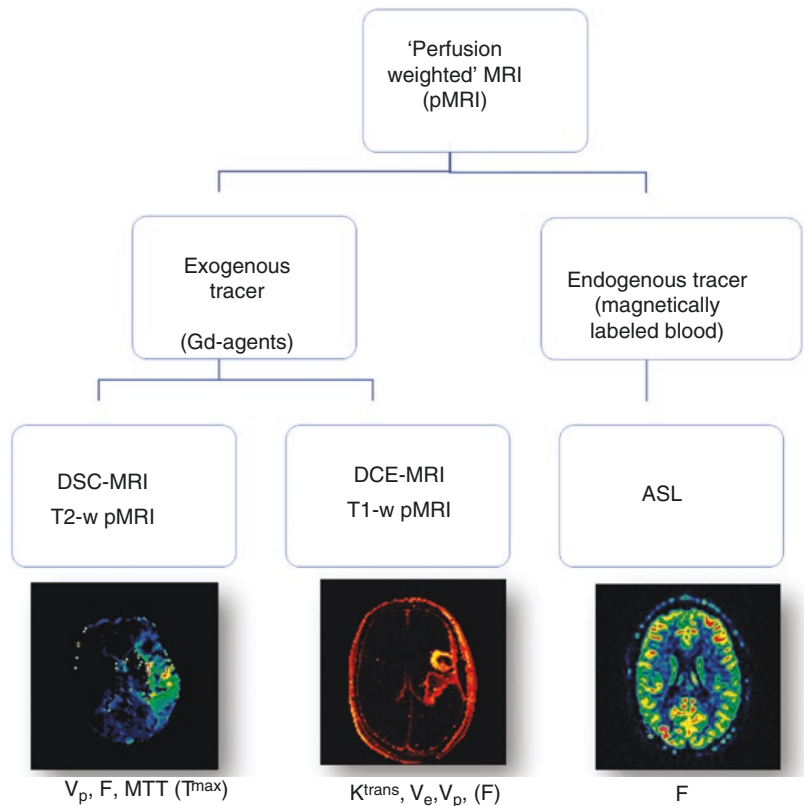
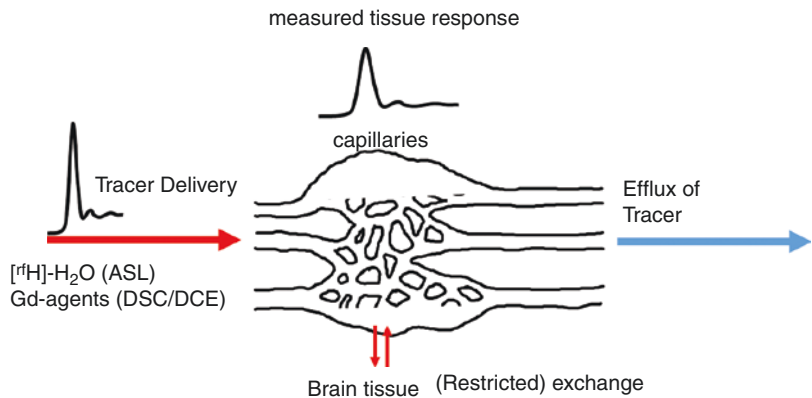


**Fig. 11.2** General tracer kinetic model valid for all three modalities, DCS-MRI, DCE-MRI, and ASL



tracer<sup>1</sup> arrives (and is possibly measured) on the arterial side of the tissue. The measured signal intensity will change in response to the transient presence of the tracer in tissue and the objective of pMRI is to relate the measurable tracer induced signal response to relevant hemodynamic properties of tissue.

## 11.2 Technical Background

### 11.2.1 Physical Principles of DSC and DCE

As seen from Fig. 11.2, both DSC and DCE are “dynamic contrast-enhanced” MRI procedures in that the change in tissue signal is measured in response to a (rapid) injection of a CA bolus. The difference between the two techniques is determined by which contrast mechanism is utilized. As the name indicates, DSC-based MRI techniques exploit the magnetic susceptibility effect of tissue, which is a particularly striking phenomenon observed in  $T_2^*/T_2$ -weighted imaging techniques [1]. When exposed to a magnetic field, susceptibility is a dimensionless constant for a given medium describing the level of magnetization induced in the tissue and local variations in

tissue susceptibility is a major contributor to in vivo  $T_2/T_2^*$ -relaxation.<sup>2</sup> Injected as a rapid bolus, paramagnetic gadolinium (Gd)-based agents in current clinical use can dramatically modify the local magnetization, thereby increasing the  $T_2$ -relaxation rate of the tissue, resulting in a temporal loss of MR signal [2]. The susceptibility effect induced by paramagnetic agents is “long range,” meaning that it also induces  $T_2$ -relaxation in tissues outside the compartment where the agent is present, which is usually the intravascular compartment in the CNS. Contrary to the susceptibility effect,  $T_1$ -relaxation is induced by the interaction between free water and the paramagnetic center of Gd agents are “short range” and will thus mainly affect intravascular protons in regions with intact blood–brain barrier (BBB). If the BBB is intact, the  $T_1$  effect is therefore much weaker in the brain compared to the susceptibility-induced relaxation effect [3]. The situation is, however, dramatically changed in areas of BBB breakdown. Once the CA extravasates, a much larger proportion of tissue water will have direct access to the Gd agent, causing a sharp increase in  $T_1$ -relaxation enhancement.

<sup>1</sup>“Tracer” will be used here as the general term for any agent used to induce a temporal MRI signal change in tissue.

<sup>2</sup>The term ‘ $T_2^*$ -relaxation’ here refers to the effective transverse relaxation rate in a gradient echo sequence where static inhomogeneities are not refocused; in contrast to  $T_2$ -relaxation where static dephasing is eliminated by use of refocusing RF-pulses. For simplicity, the term ‘ $T_2$ -relaxation’ will be used to describe both effects, unless the difference between the two effects is explicitly addressed.

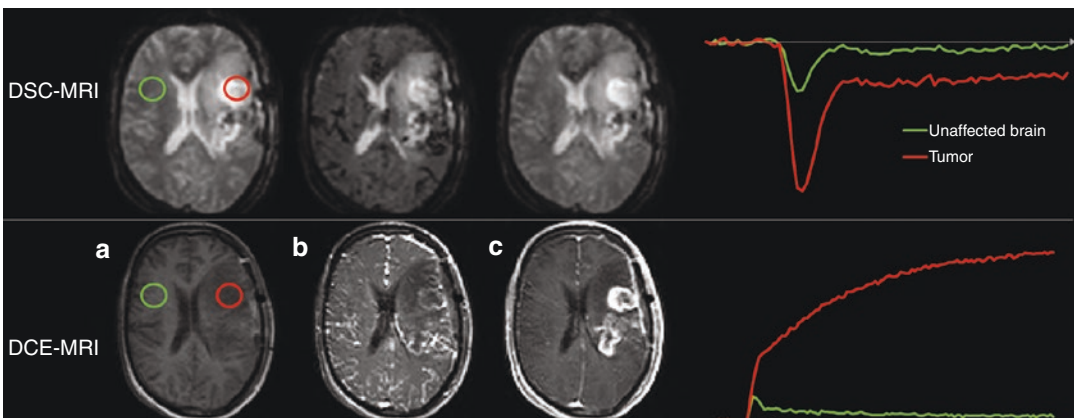
$T_1$ -based MRI is therefore very sensitive to detecting areas of disrupted BBB, and is thus also well established as a “static” contrast-enhanced MRI technique. Mainly for historical reasons,  $T_1$ -weighted pMRI is referred to as “dynamic contrast-enhanced” MRI, although the term is equally valid for DSC-MRI. Interestingly,  $T_2$ -relaxation may be proportionally reduced once the agent extravasates due to more homogeneous CA distribution within a given voxel, reducing local susceptibility-induced field variations. DSC therefore has a less well-defined CA dose–response in areas of disrupted BBB, which may result in ambiguous dose–response once CA extravasation takes place. In DSC, the unwanted effects of CA extravasation therefore need to be corrected for, and different methods are available for this purpose [4].

Figure 11.3 shows a sample case where both DSC and DCE were acquired in the same glioblastoma patient. Note the striking difference in DCE signal response in unaffected brain versus tumor, reflecting the dramatic increase in CA induced  $T_1$ -relaxation once the agent extravasates. The difference in DSC response between the two regions is less dramatic; mainly reflecting increased blood volume in tumor versus unaffected tissue.

### 11.2.2 From MR Signal to Tracer Concentration

Kinetic modeling refers to the process of fitting the measured tracer induced signal response to a mathematical model thought to represent the pharmacokinetic distribution of the tracer in tissue. The kinetic models rely on the dynamic tracer concentrations in tissue and blood to be known, which pose challenges in MRI as this is inherently not a quantitative imaging technique. This is particularly challenging in DSC and DCE where a Gd–chelate is used, affecting both  $T_1$  and  $T_2$ -relaxation to varying degrees. Therefore, to convert the measured signal response to Gd concentration, several assumptions must be made regarding the relative contribution of the different relaxation mechanisms and how they affect the measured signal response.

In DSC, heavily  $T_2$ - or  $T_2^*$ -weighted echo-planar imaging (EPI) sequences are used, assumed to be insensitive to the concurrent  $T_1$ -relaxation effect of the CA [5]. By further assuming a mono-exponential relationship between measured signal and  $T_2$ -relaxation it can be shown that the relationship between measured signal change and corresponding change in tracer concentration  $C(t)$  is given by:



**Fig. 11.3** DSC-MRI (top) and DCE-MRI sample case from a patient with glioblastoma with pre-contrast (a) peak response (b) and late response (c) for the respective sequences. The green curves show the signal response in

apparent normal brain tissue contralateral to the tumor and the red curves show the response in tumor. Note the striking difference in signal response in normal tissue versus tumor for the DCE-MRI sequence

$$\Delta R_2(t) = \frac{-k}{TE} \log_e \left( \frac{S(t)}{S(0)} \right) \propto C(t) \quad (11.1)$$

where  $\log_e$  is the natural logarithm,  $S(t)$  is the measured dynamic signal response,  $S(0)$  represents the initial MR signal before the CA bolus arrives in the tissue of interest.  $\Delta R_2(t)$  is the time-dependent change transverse relaxation rate ( $1/T_2$ ) due to the tracer,  $TE$  is the echo time, and  $k$  is an unknown proportionality constant which is usually assumed to be unity and independent of tissue structure. Of note,  $T_2$ - and  $T_2^*$ -weighted EPI sequences have distinctly different dose-response to microvascular structure and by simultaneous acquisition of both SE- and GRE-EPI images by use of double echo techniques, novel information about microvascular structure and function can be obtained [6, 7].

In DCE,  $T_2$ -relaxation is assumed to be negligible so that the dynamic signal change is only due to tracer induced  $T_1$ -relaxation. Spoiled gradient-echo (SPGR) sequences are most commonly used, enabling combination of strong  $T_1$ -weighting, 2D or 3D acquisition, and relatively high temporal and spatial resolution. Assuming negligible  $T_2$  effects, the signal behavior of SPGR sequences is given by [8]:

$$SI(t) = M \frac{\sin(\alpha)(1 - \exp(-TR \cdot R_1(t)))}{1 - \cos(\alpha)\exp(-TR \cdot R_1(t))} \quad (11.2)$$

where  $M$  is a factor depending on proton density and system-specific scaling factors,  $\alpha$  is the flip angle,  $TR$  is the repetition time, and  $R_1(t)$  is the time-dependent  $T_1$ -relaxation rate. It can be shown that the  $T_1$ -relaxation rate can then be obtained from the ratio of measured  $S(t)$  to the pre-contrast  $S(0)$  according to the expression [9]:

$$\Delta R_1(t) = -\frac{1}{TR} \log_e \left[ \frac{Y - 1}{Y \cos(\alpha) - 1} \right] - R_1(0) \propto C(t) \quad (11.3)$$

and  $Y = \frac{S(t)}{S(0)} SI(0)$

where  $S(t)$  and  $S(0)$  are the measured signal intensities at time  $t$  and pre-contrast, respectively and  $SI(0)$  is the calculated pre-contrast intensity obtained from Eq. (11.2) using the baseline relaxation rate  $R_1(0)$ . Contrary to the situation in DSC, the pre-contrast relaxation rate is therefore needed in DCE to convert the measured  $SI$  to corresponding  $R_1$ -relaxation rate. Pixel-wise estimation of  $R_1(0)$  requires a separate acquisition, and different sequences are available for quantitative  $T_1$ -mapping [10, 11]. The need for  $T_1$ -mapping adds extra complexity to the DCE experiment and some studies advocate that a fixed  $R_1(0)$  value may be used without significant loss of accuracy in parameter estimation [12]. Another simplification used is to assume a linear dose-response, which theoretically is the limiting condition for the SPGR sequence when  $TR \ll T_1$  combined with a  $90^\circ$  flip angle. When these conditions are violated, a linear approximation will tend to underestimate high CA concentrations.

### 11.2.3 Physical Principles of ASL

Contrary to DSC and DCE, ASL is a completely noninvasive and infinitely repeatable method where magnetically labeled blood water protons act as an endogenous, freely diffusable tracer. ASL is performed by labeling inflowing arterial blood water protons with radiofrequency (RF) irradiation immediately prior to entering the tissue of interest. For brain ASL, blood water protons are labeled by applying RF pulses to the precerebral arteries of the neck, thereby inverting the magnetization of the inflowing blood water protons. After labeling for a certain period of time—the *labeling duration* (LD)—there is a critical short period of waiting time—the *postlabeling delay* (PLD)—the inflow time before the labeled protons reach the brain parenchyma and the brain is imaged. The resulting images contain signal from static water protons in the imaging region as well as magnetically labeled water protons from the labeling procedure in the neck. In

addition to images that have been prepared with ASL, unlabeled images are acquired as well. The signal difference between labeled and control images is proportional to the amount of magnetization inverted and delivered to the tissue and hence scales directly with tissue perfusion. The signal difference between a label- and control image is very small—of the order of 1–2%—and the labeling process must therefore be repeated many times to obtain sufficient signal-to-noise (SNR) to enable robust estimation of regional brain perfusion from the ASL signal (Fig. 11.4). The ASL procedure can be divided into two distinct phases; (1) the labeling procedure, generating the label–control conditions and (2) the readout procedure whereby images are created where subtle intensity differences between label and control images reflect perfusion. Many different labeling and readout approaches have been proposed and used but a recent white (consensus) paper recommends that the labeling technique referred to as pseudo-continuous ASL (PCASL) should be the preferred method, combined with a volumetric (3D) readout sequence [13]. Alternatively, a faster multi-slice 2D EPI-based

readout can be used. Since ASL is a subtraction technique, it is inherently very sensitive to motion, and the motion sensitivity can be reduced by suppression of static background signal using additional inversion pulses during the preparation phase. More homogeneous background suppression can be obtained with a 3D readout compared to multi-slice readout. Also, 3D sequences generally give higher SNR combined with less sensitivity to susceptibility artifacts compared to the alternative 2D EPI readout scheme.

### 11.2.4 Tracer Kinetic Modeling

Tracer kinetic modeling here refers to the concept of fitting measured dose–response data to a given mathematical model assumed to describe the kinetic behavior of the tracer in tissue and blood. A correct choice and implementation of kinetic model are therefore a critical step to convert the measured pixel-wise dose–response to physiologically meaningful parameters. The general tracer kinetic principle depicted in Fig. 11.2 can be subdivided into three main models used in

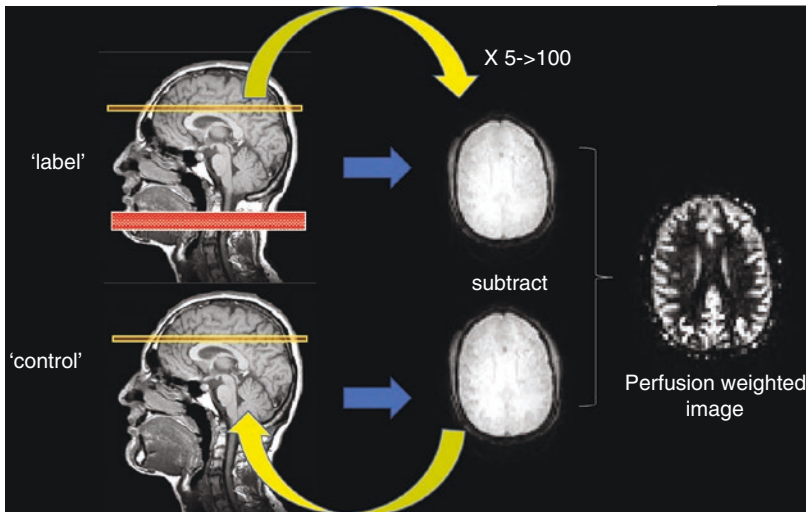


**Fig. 11.4** The generic ASL perfusion image generation process. A magnetization “labeled” image is created by selective inversion of blood water in the feeding arteries, which will affect the signal in the “readout” images acquired in the brain. A control image is needed with

identical readout to the labeled image but with no RF inversion. The label and control images are subtracted and the procedure is repeated multiple times to obtain sufficient signal-to-noise ratio in the resulting perfusion-weighted image

MRI (Fig. 11.5) where the choice of model depends on the property of the tracer used and the objectives of the analysis.

### 11.2.5 Model-Free Analysis

The term “model-free” reflects the fact that the model makes no explicit assumptions about the internal structure of the tissue compartments where the tracer response is measured. This may appear to be a dubious assumption, but in tissues with intact BBB one can assume current Gd-agents to be purely intravascular so that the dose–response reflects only the intravascular properties of tissue. As shown in Fig. 11.5 top, tissue hemodynamics can then be described in terms of plasma flow ( $F_p$ ), the intravascular volume fraction of tracer distribution in tissue ( $v_p$ ), and the average time it takes the tracer molecules to traverse the tissue from the arterial inlet to the venous outlet; referred to as the mean transit time, MTT. The central volume principle [14] then describes the following relationship:

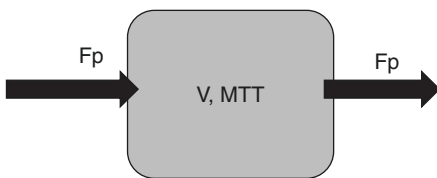
$$v_p = F_p \cdot \text{MTT} \tag{11.4}$$

In terms of the measured dynamic dose–response it can be shown that  $v_p$  is also given by the area under the tissue concentration–time curve,  $C(t)$ , normalized to the area under the arterial curve:

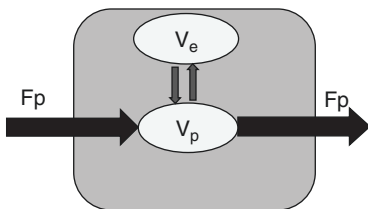
$$v_p = K \frac{\int C(t) dt}{\int C_a(t) dt} \tag{11.5}$$

where  $K$  is a scaling factor depending on tissue density and blood hematocrit [15] and  $C_a(t)$  is the concentration–time curve in a feeding artery; referred to as the arterial input function (AIF). In the neuro pMRI literature, the terms cerebral blood volume (CBV) and cerebral blood flow (CBF) are commonly used for  $v_p$  and  $F_p$ , respectively.

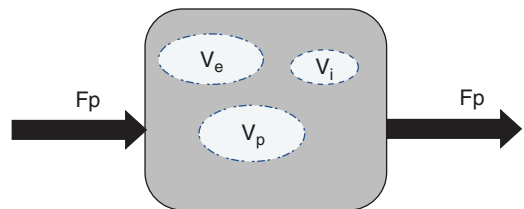
Estimation of CBF and MTT requires more complex analysis involving the concept of the *tissue residue function*,  $R(t)$ . The tissue residue function can be thought of as a probability function describing the amount of tracer instantaneously present at the tissue arterial input at time



DSC = ‘model-free’ analysis:  
No modelling of internal tissue structure



DCE = ‘model-based’ analysis:  
Assume separate internal compartments and restricted inter-compartmental tracer exchange



ASL = ‘model-free’ analysis:  
Assume ‘freely diffusible’ tracer with no restriction between compartments

**Fig. 11.5** Models as assumptions for kinetic analysis of the respective pMRI techniques. See text for details

zero ( $R(0) = 1$ ) still present in tissue at time  $t$  [16]. The residue function reflects the underlying tissue hemodynamic properties without being influenced by procedure specific parameters like tracer injection speed/dose and tracer dispersion from injection site to tissue of interest. As such, it provides a more objective, and potentially quantitative estimate of tissue hemodynamic properties. To estimate  $R(t)$  from the measured dynamic concentration–time signal, a mathematical operation referred to as *deconvolution* is required, and it can be shown that the relationship between  $F_p$  and  $R(t)$  is given by:

$$\begin{aligned} C(t) &= K \cdot F_p \otimes C_a(t) \\ &= K \cdot F_p \int_0^t C_a(t-\tau) \cdot R(t) d\tau \end{aligned} \quad (11.6)$$

where  $\otimes$  is the convolution operator and  $K$  is the constant from Eq. (11.5).

From Eq. (11.6) it is then possible to estimate  $R(t)$  and  $F_p$  from measured  $C(t)$  and  $C_a(t)$  using established deconvolution methods [16]. In practice, deconvolution provides estimates of the scaled residue function  $H(t) = K \cdot F_p \cdot R(t)$  so that  $F_p$  is obtained from the peak height of  $H(t)$ . Of importance is that the peak value of  $H(t)$  ( $H^{\max}$ ) does not need to occur at  $t = 0$  and the time at  $H^{\max}$ , commonly referred to as  $T^{\max}$ , is an important clinical parameter in that elevated  $T^{\max}$  values are associated with cerebrovascular pathology [17]. The residue function has the same number of time points as the acquired dynamic data and is estimated without any assumptions about its shape, beyond the fact that it must be monotonously decreasing function of time (at  $t > T^{\max}$ ). Regardless of shape, provided the tracer remains in the intravascular space, the mean transit time is given by:

$$\text{MTT} = \int R(t) dt \quad (11.7)$$

MTT, being the transit time of the tracer through the tissue vascular space, is also a sensitive marker for cerebrovascular pathology [17]. It should be noted that MTT can be estimated either from the ratio  $v_p/F_p$  [Eqs. (11.5) and (11.6)] or from the area under the  $R(t)$  curve [Eq. (11.7)].

Similarly,  $v_p$  can be determined either from Eq. (11.5) or from the central volume theorem  $v_p = F_p \cdot \text{MTT}$ , obtained directly from the area under the scaled residue function.

It should finally be stressed that the above analysis explicitly assumes that the tracer remains in the intravascular tissue compartment for the duration of the measurement period. Tracer extravasation will affect the shape as well as the physiological interpretation of the residue function; and a model-based analysis will then be required for correct interpretation, as discussed in the next section.

## 11.2.6 Model-Based Analysis

A model-free analysis approach becomes harder to interpret in situations where the tracer extravasates from the plasma compartment to the extravascular extracellular space (EES). In this situation, the residue function reflects a combination of two kinetic processes; both the capillary transit time and the transit time associated with the transfer of tracer between the two compartments. Under these conditions, a model-based analysis approach is more appropriate where explicit assumptions are made about the internal structure of the tissue and about the rate at which the tracer is transferred between the different tissue compartments. All existing CAs in clinical use for neuroimaging are water-soluble low-molecular weight Gd agents which are distributed in plasma or in the EES in areas of BBB breakdown. A two-compartment model, as shown in Fig. 11.5 bottom left is therefore the most appropriate kinetic model to use to describe the general tissue distribution of these agents in the brain; not limited to the intact BBB condition [18]. The two-compartment exchange model then has four model parameters;  $F_p$ ,  $v_p$ , the volume fraction ( $v_e$ ) of the EES, and the rate of tracer flux from the plasma- to the interstitial compartment,  $K^{\text{trans}}$ . The reflux rate constant  $k_{ep}$  is by mass balance given by  $k_{ep} = K^{\text{trans}}/v_e$ . Although a full two-compartment analysis is technically possible, stable four-parameter estimations are generally



challenging given the typical image quality and temporal resolution obtainable with current DCE-MRI methods [18]. Simplified models are thus commonly used, aiming at obtaining more stable estimates of the main parameter of interest. The extended Tofts models (ETM) are currently the most commonly used model in DCE-MRI. The ETM results from the assumption of weakly vascularized (low  $v_p$ ) and highly perfused (high  $F_p$ ) tissues, which can be shown to lead to the following expression [18]:

$$C(t) = K^{\text{trans}} e^{-\frac{K^{\text{trans}}}{v_e} t} \otimes C_a(t) + v_p C_a(t) \quad (11.8)$$

It follows that  $F_p$  cannot be estimated from the ETM, but it generally provides more stable estimates of the other kinetic parameters compared to the full four-parameter model. A further simplification can be obtained by assuming tracer reflux to negligible during the observation period

so that  $k_{\text{ep}} = \frac{K^{\text{trans}}}{v_e} \approx 0$ . This assumption enables

Eq. (11.8) to be reformulated to a linear form, also referred to as a Patlak plot, and  $K^{\text{trans}}$  and  $v_p$  can then be estimated from robust linear regression analysis. The Patlak model is particularly useful when attempting estimation of very low  $K^{\text{trans}}$  values; for instance, in multiple sclerosis or neurodegenerative disease [19].

### 11.2.7 Freely Diffusible Tracer Analysis

In ASL, magnetically labeled blood water protons are used as the tracer, which is well approximated as a freely diffusible tracer (Fig. 11.5 bottom right) with rapid distribution to all tissue compartments in the brain. Kinetic modeling of the ASL signal follows the same theory as that of DSC-MRI, but with the important difference that most current ASL approaches only measures the effect of the tracer in the brain at a single point in time, given by the PLD parameter [13]. It can then be shown that, for the recommended PCASL approach [13], perfusion is given by the following expression [20]:

$$\text{CBF} = \frac{6000 \cdot \lambda \cdot (\text{SI}_{\text{control}} - \text{SI}_{\text{label}}) \cdot \exp\left(\frac{\text{PLD}}{T_{1\text{blood}}}\right)}{2 \cdot \alpha \cdot T_{1\text{blood}} \cdot \text{SI}_{\text{PD}} \cdot \left(1 - \exp\left(\frac{-\text{LD}}{T_{1\text{blood}}}\right)\right)} \quad (11.9)$$

where CBF is perfusion in units of mL/100 g/min,  $\lambda$  is the blood/brain partition coefficient in mL/g,  $\text{SI}_{\text{control}}$  and  $\text{SI}_{\text{label}}$  are the voxel-wise signal intensities in the control- and label image, respectively.  $T_{1\text{blood}}$  is the longitudinal relaxation time of blood,  $\alpha$  is the labeling efficiency,  $\text{SI}_{\text{PD}}$  is the voxel-wise proton density (fully relaxed signal). PLD and LD are the post labeling delay and labeling duration, as previously described. A similar expression can be derived for pulsed ASL [13].

It should be noted that standard ASL in current use is not “time-resolved” in the sense that we are able to dynamically measure the effect of the labeled water in tissue. The choice of PLD is therefore critical. It needs to be long enough for the labeled blood to reach the brain parenchyma but not so long that the labeling effect has decayed due to  $T_1$ -relaxation of the inverted spins. The population-averaged optimal PLD increases with age, and the recommended PLD for pediatric and adult clinical populations is 1.5–2 s [13]. If the true PLD is outside the normal range—as can be the case in many cervical and intracranial vascular conditions as well as in states of reduced cardiac output—using a “recommended PLD value” may give images that appear underperfused and false diagnosis may ensue [21]. Alternative multi-PLD ASL approaches exist, enabling time-resolved analysis of the tissue transit of the labeled magnetization, providing improved perfusion quantification independent of arterial arrival time (AAT) [13].

The single time-point assessment of ASL further limits the number of hemodynamic parameters which can be assessed, and CBV and MTT cannot be estimated from single time-point ASL techniques. The major strength of ASL is, however, that the method has a greater potential for quantification since the difference between the

label and control signal can be directly related to CBF without the need for complex mathematical deconvolution with an arterial input function. The accuracy of the CBF estimates obtained with ASL is still dependent on several parameters which are not always easily measurable.

### 11.2.8 Descriptive Analysis

In both DSC- and DCE-MRI estimation of the AIF is required for (semi-) quantitative analysis of perfusion and permeability related metrics. For both modalities, AIF determination is a major challenge due to limited spatial resolution and, in the case of DSC, susceptibility-induced temporal and spatial distortions of the vessels as well as nonlinear intravascular dose–response [22, 23]. Lack of inter- and intra-patient reproducibility of AIF is currently a major limitation for clinical acceptance of both DSC- and DCE-derive quantitative metrics, and consequently the use of descriptive parameters not requiring AIF determination is commonly used in clinical practice. In DSC-MRI, relative CBV (rCBV) is often estimated from the area under the tissue response curve without normalizing to the AIF. The resulting rCBV can then be used to assess regional differences in the same image, or for relative intra- and inter-patient comparisons by normalizing rCBV maps to a standardized mean rCBV value of selected tissue, such as white matter. This is a particularly widespread practice in brain tumor diagnostics [24]. Further, time from bolus arrival to peak enhancement measured from the tissue response curve (TTP) has value in predicting infarct growth in acute stroke patients with comparable diagnostic accuracy to the AIF-dependent parameter  $T^{\max}$  [17]. In DCE, the initial area under the tissue response curve (iAUC), typically measured for the initial 120 s has reported clinical value e.g. in glioma treatment response assessment [25]. In ASL, percent or absolute difference between label and control images can be used as a measure of relative perfusion in cases where the different parameters needed for quantification cannot be obtained [Eq. (11.9)].

Despite the reported diagnostic value of certain descriptive parameters, these methods have obvious shortcomings in terms of biological interpretation, inter-patient reproducibility, and variability. There is therefore a continuing effort to develop better methods for robust and reproducible estimates of quantitative perfusion and permeability-related biomarkers. Initiatives such as the Quantitative Imaging Biomarker Alliance ([www.rsna.org/QIBA/](http://www.rsna.org/QIBA/)) aim at providing guidelines and standardized test procedures for quantitative imaging biomarker performance studies so results between studies and institutions can be compared, contrasted, or combined [26].

## 11.3 Current Clinical Applications

Unlike non-imaging modalities, radiographic biomarkers can capture the formidable spatial heterogeneity of a CNS lesion noninvasively and thereby identify aggressive regions that drive disease progression and resist treatment [27]. Alternative approaches such as tissue sampling require invasive surgery to collect biologic material and is therefore not an acceptable option in many conditions, and not compatible with repeated measurements in humans. Moreover, blood sampling, liquid biopsies that detect circulating pathologic cells, does not reveal their spatial origin [28]. In contrast, imaging allows for repeated assessments with minimal side effects. This is especially true for MRI that, with its high spatial resolution and sensitivity, and nonionizing nature, is the modality of choice for in vivo assessment of status and progression in most CNS diseases.

In this chapter, we discuss some of the recent advances in perfusion imaging for clinical use, with focus on its current main target, CNS cancers, but also cerebrovascular and neurodegenerative disease. With some historical background, extensively documented in previous reviews, this chapter will rather shed light on recent reports. The large body of work available reflects the technique's clinical utility, ranging from the small sample, explorative studies forming a platform for further research, to the large cohort,

multicenter trials using proven biomarkers to monitor therapy response.

## 11.4 CNS Cancers

### 11.4.1 Presurgical Characterization of Gliomas

Presurgical characterization of gliomas was early defined as a target of DSC-MRI [29]. Because of the increase in capillary density associated with tumor angiogenesis, CBV is well established as a parameter to grade CNS tumors according to their level of micro-vascularity and thus malignancy [30]. In general, increased and heterogeneous levels of CBV, often attributed to abnormal signal recovery following the bolus passage, correspond to aggressive tumors of higher grades per the World Health Organization (WHO) classification standard (grades I–IV) [31, 32]. Used with caution [33], the technique may also help form treatment decision-making by prognostic estimates of survival. Similar to grading, patients with shorter survival are identified by higher microvascular density (represented by CBV) and abnormal and heterogeneous hemodynamic profile [34–36].

Moreover, with the advent of available and affordable tools for genomic mapping of sampled tissue, efforts now also focus on the added value of perfusion for stratifying genetic signatures. For example, reports now suggest glioblastoma patients with elevated levels of CBV are associated with epidermal growth factor receptor (EGFR) gene amplification and unmethylated 6-methylguanine-DNA methyltransferase (MGMT) status [37].

With these advances of potential clinical value, the question rather becomes whether DSC-MRI may also have discriminative power to identify presurgical vascular features that are unique for glioma types, grades, or genetic profiles. While accelerated DSC-MRI acquisitions show promise, still, available tools for clinical use today are limited in terms of spatial resolution and by its  $T_2$ -dominance, as well as for reliable measures of vessel permeability. To this end, a

reasonable alternative is to take advantage of the full potential of a clinical MRI exam. Multi-parametric MRI, combining complementary information from anatomical data and functional measures of diffusion, permeability (by DCE-MRI) and perfusion (by DSC-MRI), may better identify tumor types [38–40] and quantify tissue compartments both within- and outside the tumor bed [41]. The argument for a multi-parametric approach is further strengthened by the advent of automatic and computer-aided segmentation and classification tools [42, 43].

Compared to DSC-MRI, considerable fewer clinical studies have been performed using DCE-MRI in brain tumors. However, existing results both confirm and supplement the results from DSC-MRI. The volume transfer constant,  $K^{\text{trans}}$  is the DCE-derived parameter most often reported in the literature. Although elevated CBV measured by DCE ( $v_p$ ) is associated with glioma malignancy, elevated  $K^{\text{trans}}$  is the parameter most consistently associated with high-grade gliomas [44, 45]. A challenge when using DCE in glioma grading is that BBB damage is needed for measurement of meaningful  $K^{\text{trans}}$  values [46]. However, histogram analysis from whole tumor regions of interest defined from FLAIR and  $T_2$ -weighted images have shown increasing values of  $K^{\text{trans}}$ , as well as  $v_p$  and  $v_e$  with increasing glioma grade [45]. DCE has also shown promise as a preoperative prognostic marker in gliomas whereby elevated  $K^{\text{trans}}$  and  $v_p$  values have been associated with reduced overall survival [47, 48]. Further, the value of  $K^{\text{trans}}$  in non-enhancing lesions with high  $T_2$ -weighted signal in preoperative MRI of glioblastoma patients has shown promise to predict progression 2 months after treatment [49].

The role of ASL in glioma characterization is currently less clear, but some studies suggest similar performance of ASL and DSC-MRI in glioma grading [50, 51], with the potential advantage of ASL of being less sensitive to susceptibility-induced distortions [52]. Although the noninvasive nature of ASL is a clear general advantage of this technique, most tumor imaging protocols rely on CA-enhanced structural imaging to assess structural pathoanatomy and tumor

growth. The addition of a DSC-MRI acquisition during CA administration is therefore less of an issue in this patient group. ASL may be an important alternative to DSC-MRI in cases where the use of Gd-based CAs should be limited, such as in patients with reduced kidney function, pediatric populations, and in patients where repeated imaging procedures are expected or warranted.

### 11.4.2 Differential Diagnoses and Non-Gliomas

The limitations of MRI-based contrast enhancement as a biomarker for CNS tumor characterization are easily recognized in malignant lesions. The majority of aggressive and rapidly proliferating tumors are identified by tortuous and permeable vessel structures with substantial enhancement on anatomical  $T_1$ -weighted MRIs. pMRI therefore sheds new light on the vascular features of a range of tumors *in vivo*. For example, explorative analyses of DSC in adult medulloblastoma show CBV levels similar to that of normal-appearing tissue and with considerable vessel permeability. Additionally, DSC shows its value as a tool in differentiation of both diffuse and high-grade gliomas from primary CNS lymphomas (PCNSLs) [53, 54]. With proper CA leakage correction methods (accounting for both  $T_1$  and  $T_2^*$  effects), the perfusion signature and blood volume level of PCNSL are generally lower, while the vessel permeability is reported higher, compared to that of high-grade diffuse gliomas [55, 56]. In a recent meta-analysis, DSC-MRI showed higher discriminative power than alternative approaches by DCE-MRI or ASL [53]. Interestingly, DSC-MRI can also be used to separate PCNSL from CNS infections and malignant tumors that may present similar enhancement patterns [57]. Toxoplasmosis lesions are identified by very similar blood volume levels to that of reference tissue, PCNSL is generally twice as high, while the levels of glioblastomas and metastatic lesions are usually several times higher [58, 59].

The vascular properties of a metastasis in the CNS can be quite different from that of a primary

brain tumor. While a solitary metastasis may resemble a glioblastoma by contrast enhancement alone, studies using DSC-MRI of the peritumoral zone suggest that the microvascular densities (as represented by CBV) of both high- and low-grade diffuse gliomas are several times higher than that of metastases, while the mean diffusivity is lower [60, 61].

Earlier work has shown increased permeability in PCNSL compared to gliomas and brain metastasis [62]. This has been reproduced using DCE-MRI in differentiation of PCNSL, glioblastoma, and metastasis [63, 64]. Here  $K^{\text{trans}}$  was twice as high in PCNSL compared to both glioblastoma and metastasis. No difference was seen between the latter tumor types. Similar results were seen in  $v_e$ . Differentiation of gliomas and metastasis seems more elusive using DCE-MRI [65]. Additionally, DCE-MRI might be helpful when trying to separate infective from neoplastic brain lesions. In a study with both DSC-MRI and DCE-MRI,  $K^{\text{trans}}$  and  $v_e$  were increased in infective disease and found to be superior to rCBV and rCBF from DSC-MRI for differentiation of pathologies [66].

The use of ASL in brain tumor imaging for differential diagnosis indicates a high correlation between areas of increased CBF as measured with ASL and increased CBV as measured with DSC perfusion imaging in a range of conditions [52, 67].

#### 11.4.2.1 Radiation Therapy Monitoring

Identifying the imaging characteristics of a growing CNS tumor from those caused by treatment-related changes is a formidable and daunting task for any physician. With the dismal survival prognosis of most CNS cancers, biomarkers of early response are critical to differentiate patients responding to therapy from those patients who only suffer the side effects. Based primarily on CA enhancement on anatomical MRI, radiation therapy in CNS disease is monitored using consensus guidelines formulated by the Response Assessment in Neuro-Oncology (RANO) working group [68–70].

Unfortunately, as accepted by the RANO authors, all image-based cancer diagnosis criteria

are challenged by high heterogeneity within-, and between, disease subtypes for both treatment response and time to progression [68, 71]. Treatment-induced contrast enhancement, termed *pseudoprogession*, often mimics *true* tumor progression [72]. Unlike *true* tumor progression, however, CA enhancement changes from radiotherapy typically reverse after a few weeks or months without any change in therapy. Pseudoprogession appears in as much as 30% of patients with intra-axial brain tumors [68, 72], and up to a year of follow-up examinations may be required to confirm radionecrosis on conventional MRI [73].

DSC-MRI may potentially identify certain glioblastoma patients with sufficient perfusion and vascular efficacy to respond to, and sustain radiation therapy and hence observe prolonged progression-free survival [74]. A large body of evidence now also shows that DSC-MRI is an early identifier of tumor recurrence by levels of elevated perfusion and CBV compared to the transient enhancement patterns in lesions of radiation-related nature [75–78]. Interestingly, in contrast, a recent study showed that increased levels of rCBV were a positive indicator of progression-free survival in children with diffuse infiltrating pontine gliomas and that the apparent increase in blood volume following radiation should therefore not be mistaken for tumor progression in this patient group [79]. Furthermore, perfusion changes are not just observed in the lesion area, but a recent study also suggests both rCBV and rCBF increase in healthy tissue, with a maximum response in gray matter at doses of 5–10 Gy following stereotactic radiosurgery of brain metastases [80]. This type of observation is important as it may help develop measures to limit neurologic deficits and other complications following radiation therapy.

Still, use of DSC-MRI for clinical radiation therapy monitoring is in its infancy and currently limited by a lack of consensus guidelines across imaging platforms and institutions [100, 109].

In DCE-MRI,  $K^{\text{trans}}$  and  $v_p$  have been shown to be elevated in patients with progressive glioblastoma compared to those with pseudoprogession [81]. Similar results were seen in a prospective

study, where  $K^{\text{trans}}$  and  $v_e$  were significantly elevated in progressive disease compared to pseudoprogession in glioblastoma patients [82]. This indicates that the BBB damage in tumor progression is different than the inflammatory change in pseudoprogession. This difference is sometimes distinguishable using contrast-enhanced  $T_1$ -weighted imaging but sensitivity and specificity are low [83]. In a recent meta-analysis study including 28 studies, it was concluded that both DCE- and DSC-MRI show good differentiation power between viable tumor and treatment-induced changes in individual studies. However, the relevant threshold values varied significantly between studies and better sequence and protocol standardization is needed before data can be reliably compared between studies and institutions [84]. The provided clinical case shows a sample case from a chemoradiotherapy treatment monitoring study where both DSC- and DCE-MRI were acquired, indicating the value of obtaining both rCBV and  $K^{\text{trans}}$  information in distinguishing tumor progression from treatment-induced pseudoprogession.

Concerning ASL, it may also be used as an alternative approach for distinguishing tumor recurrence from treatment effects [85, 86]. With the recent increased focus on limiting the use of Gd-based CAs in repeated measurements and monitoring, ASL may well receive a more prominent role in serial follow-up MRI of treatment response.

### 11.4.3 Targeted Therapies

The growing range of targeted therapeutic options also effectively makes response assessments by RANO challenging, either by the *decrease* in MRI-based contrast enhancement from remodeling of the vessel wall after antiangiogenic therapy, or contradistinctively, the *increase* in contrast enhancement associated with the apparent inflammatory response of immunotherapy [87–89]. With bevacizumab in particular, a humanized monoclonal antibody that targets vascular endothelial-derived growth factor (VEGF), DSC-MRI already has a long history of use.

Collectively, results indicate a reduction, or a gradient towards normalization, of abnormal blood volume levels (by rCBV) in malignant gliomas on follow-up MRIs after treatment with antiangiogenic drugs [6, 90, 91]. Vascular normalization by DSC-MRI is also shown using other immunotherapeutic drugs [92, 93].

$K^{\text{trans}}$  has also been used to monitor the effect of antiangiogenic therapy. In metastatic brain tumors from breast cancer a significant reduction in  $K^{\text{trans}}$  already 1 h after complete administration of bevacizumab was observed; increasing further at 24 h and 21 days after administration [94]. The observed reduction in  $K^{\text{trans}}$  is thought to reflect vascular normalization and has been proposed to enhance the efficacy of chemotherapy. A similar vascular normalization was observed in recurrent glioblastoma patients receiving antiangiogenic therapy and a greater reduction in  $K^{\text{trans}}$  1 day after treatment was seen in patients with increased overall survival and progression-free survival [90].

What qualifies as the optimal response measure by DSC-MRI or DCE-MRI in antiangiogenic and anti-vascular therapy remains a topic of much research and debate, probably in large owing to a lack of standardization of image acquisition, analysis, and interpretation [95–97]. Ongoing efforts now focus on incorporating immune-related mechanisms in the updated immunotherapy Response Assessment for Neuro-Oncology (iRANO) criteria [98]. The iRANO criteria put more weight to neurologic status and effectively prolong the time needed to identify disease progression, allowing patients who experience image-based, but not neurologic decline, to continue treatment [99]. Here, DSC-MRI and DCE-MRI may add value by distinguishing immune-related changes from true tumor progression based on the vascular biology driving the two processes.

## 11.5 Cerebrovascular Disease

### 11.5.1 Stroke

MRI is a well-established modality for stroke imaging and diagnosis. While currently lacking

the speed and accessibility of a CT exam, MRI is an important supplement due to its sensitivity [100]. Because of its long history of use, consensus guidelines for MRI-based research, and thus subsequent clinical use, are now available owing to a series of dedicated imaging roadmaps [101–103]. The underlying philosophy of this approach is that only patients with reversible ischemia will benefit from reperfusion therapy, and that imaging may identify these patients. Ideally, diagnosis of acute stroke and therapy response should include multiple MRI time points [102]. For all time points, the MRI examination should include MR diffusion, an MR angiogram of intracranial arteries, gradient-echo based DSC-MRI, and anatomical T<sub>2</sub>-fluid attenuated inversion recovery (FLAIR) [104]. Recently, thrombectomy up to 24 h after onset of stroke has been proved safe in selected patients based on perfusion imaging or small infarction core compared to the neurological deficit [105]. Two methods to assess the area for potential salvage therapy in MRI exist. A diffusion/FLAIR mismatch has been proposed as a marker for potential salvage tissue due to delay of FLAIR changes in acute stroke. Perfusion imaging offers a more advanced method to predict potential saveable tissue. This area, denoted the penumbra, was originally set as a probabilistic measure of the mismatch between the region of impaired perfusion (usually by MTT or TTP) and the ischemic core [106, 107]. The definitions and interpretations of the terms *mismatch* and *penumbra*, however, have since been revised repeatedly [103, 108], in part because alternative measures by PET indicate that MRI-based measures of perfusion may miscalculate or overestimate the area at risk, while diffusion may underestimate the corresponding ischemic core [109, 110]. Therefore, rather than chasing the exact volume of the penumbra, focus is turned toward so-called non-favorable perfusion patterns on the baseline MRIs (Fig. 11.6). Here, an impaired tissue volume of more than 100 mL with prolonged  $T^{\text{max}}$  values (usually above 6–8 s) is indicative of patients likely to observe parenchymal hemorrhages and poor response to reperfusion therapy [108, 109, 111]. Another interesting parameter for the tissue at risk is asso-

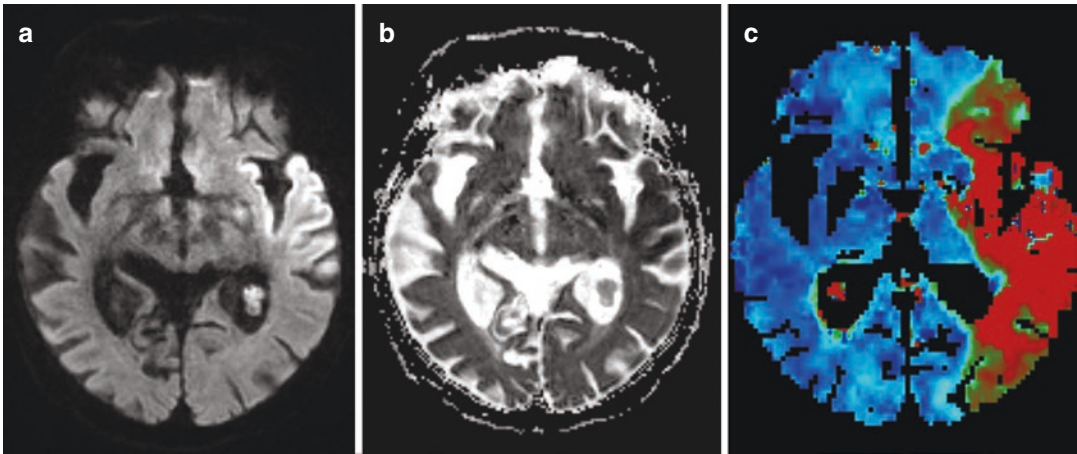


**Fig. 11.6** Acute ischemic stroke in an elderly patient in the territory of the left middle cerebral artery. Diffusion-weighted imaging (**a**, **b**) with the b1000 image (**a**) and the corresponding ADC map (**b**) demonstrates areas of restricted diffusion in the left insular region and in the left temporal lobe. DSC-MRI perfusion shows a markedly

larger area of prolonged time to peak (TTP) (**c**) affecting almost the whole vascular territory of the left middle cerebral artery. This case reveals a mismatch between DWI with the ischemic core of the infarct and the tissue at risk shown in the TTP. These findings suggest that this patient may benefit from further reperfusion therapy

ciated with metabolic consumption of oxygen. Here, rCBV is used in combination with multi-echo quantitative  $T_2$  and  $T_2^*$ -mapping to derive measures of the cerebral metabolic rate of oxygen ( $CMRO_2$ ) based on differences in deoxyhemoglobin concentrations in blood [112]. For stroke,  $CMRO_2$  is reported decreased in diffusion-restricted tissue, while normal in perfusion-impaired tissue, suggesting a shoulder-like pattern where suddenly the feeding vasculature following a stroke becomes incapable of delivering sufficient nutrients to central tissue regions [112]. Similar approaches suggest a carefully selected threshold for metabolic oxygen consumption may further help delineate the ischemic penumbra [113].

While the real added value of MRI on patient management and outcome is still in question [108, 114], clinical imaging of acute stroke by DSC continues to show promise and is integral in the imperative transfer from research-based method development to user-friendly clinical routine [115].

DCE-MRI is considerably less used in stroke imaging compared to DSC-MRI due to generally lower temporal resolution and lower intravascular CA sensitivity, as discussed in Sect. 11.1.

DCE does, however, have a role in the assessment of stroke-induced changes in BBB integrity. A gradual increase in BBB permeability has been observed in ischemic stroke patients with a peak at 6–48 h after stroke onset and a detectable BBB leakage at 90 h [116]. Further studies are warranted for evaluation of  $K^{trans}$  as a predictor for type of future cerebrovascular events. DCE in established atherosclerotic disease looks to be an important tool to evaluate therapy effect and as a marker of plaque vulnerability.

In the evaluation of ischemic stroke, ASL again has the reserve role compared to DSC, called upon when contrast agent injections are contraindicated. ASL in acute stroke shows decreased perfusion in tissue distal to an arterial occlusion and increased signal within cortical vessels before the occlusion due to sluggish or collateral blood flow. When opting for ASL, it can be used to identify the penumbra in acute stroke and regions with low poststroke CBF values have been shown to be consistent with regions of DSC hypoperfusion [117–120]. If opting for ASL in stroke imaging, it must be borne in mind that using a single-PLD approach carries the risk of quantification errors due to prolonged  $T^{max}$  often seen in stroke. From this reason, a multi-

PLD (time-resolved) approach may be a better technique, which will result in prolonged scan times and inherent trade-off against signal-to-noise [121].

### 11.5.2 Neurodegenerative Disease

Neurovascular dysfunction from unbalance in cerebral perfusion, abnormal capillary morphology, impaired oxygen delivery, and reduced neuronal activity constitute the early stages of neurodegenerative disease [122]. The complex vascular profiles associated with Alzheimer's disease (AD) makes perfusion-based MRI a promising vehicle for diagnosis and detection of early signs of disease. Clinical use of both DSC- and DCE-MRI in the diagnostic workup in neurodegenerative disease is however limited at present and positron emission tomography (PET) is currently the preferred modality both for assessment of dysmetabolism and accumulation of amyloid plaques. As a research tool, DSC-MRI shows promise as a tool supporting the capillary dysfunction hypothesis of AD [123]. Here, compared to healthy controls, patients with AD and mild cognitive impairment show impaired perfusion patterns in large parts of the cerebral cortex, including temporal, parietal, and frontal lobes [124, 125]. Moreover, DSC is used to identify increased relative capillary transit time heterogeneity in patients, a measure coupled to the apparent oxygen extraction fraction [126].

Beyond perfusion-related analysis, measurements of subtle alterations in BBB permeability in neurodegenerative disease have also gained momentum over the last 10 years due to better DCE-MRI methods. In early AD, increased permeability has been reported in gray matter compared to healthy controls, with a correlation between increase in permeability and reduction in cognitive performance [127]. Similar associations have been observed in vascular cognitive impairment [128].

ASL has been proposed as an alternative to DSC-MRI and fluorodeoxyglucose (FDG)-PET to assess characteristic hypoperfusion patterns in

the cerebral cortices. The main benefit of this is that ASL may easily be added to the structural MRI examination—the cornerstone in dementia evaluations—at a low incremental cost and without the addition of a CA injection. In patients with dementia spectrum disorders, ASL exhibits hypoperfusion patterns that are similar to hypometabolism patterns seen with FDG-PET [129], but the change toward using ASL as the preferred method for measuring this hypoperfusion has yet to come.

### 11.5.3 Demyelinating Disease

Early signs of multiple sclerosis (MS) include increased BBB leakage and reduced perfusion anomalies [130]. In MS and other demyelination diseases contrast-enhanced MRI and contrast enhancement are used to support or supplement clinical diagnosis [131]. Repeated MRI studies in the early 1990s showed that contrast-enhancing lesions were associated with acute inflammation in autopsy materials, and non-enhancing  $T_2$ -weighted lesions associated with chronic changes [132]. MS was one of the very early target applications of DCE-MRI where the concept of quantitative assessment of BBB permeability and leakage space was formalized by Tofts and Kermode [133] and independently by Larsson and coworkers [134] in the early 1990s. Today, characterization of contrast-enhancing lesions is a cornerstone in the evaluation of active MS disease. Different enhancing patterns can be observed and DCE enables investigation beyond the binary (enhancing non-enhancing) evaluation. Recently it was shown by DCE that ring-enhancing lesions enhance centrifugally and become nodular in more than 80% and nearly nodular in the remaining cases [135]. This suggests that a single post-contrast-enhancing  $T_1$ -weighted image only yields a crude characterization of active MS plaques.

Using more complex compartmental modeling in DCE-MRI; both CBV and CBF and permeability was shown to be increased in enhancing lesions compared to non-enhancing lesions,



attributed to active inflammation [136]. Perfusion-related changes in MS have also been reported using DSC-based methods. Several studies using DSC suggest consistent reduction in rCBF in both cortical and white matter lesions in patients with relapsing–remitting and newly diagnosed MS, respectively [137, 138]. The picture for rCBV and MTT however, is not as clear, and may indicate that perfusion patterns are dependent on disease heterogeneity and activity [139]. This finding is corroborated by work suggesting patients with highly active and rapidly progressive cerebral inflammatory lesions depict higher rCBF and rCBV [140], as well as increased capillary flow heterogeneity [141], compared to low-inflammatory, stable patients. Moreover, rCBV in cerebral inflammation is also associated with reduced working and secondary verbal memory [142].

Increased permeability by DCE-MRI has also been measured in normal-appearing white matter (NAWM) and thalamic gray matter in MS patients compared to healthy controls [143]. Here, immunomodulatory treatment and recent relapse were also found to be significant predictors of permeability in MS lesions and periventricular NAWM. The observed alterations in perfusion and permeability in normal-appearing tissue in MS patients are, however, subtle and at the limit of detection with current DCE-based methods as reflected in the absence of detectable change in other studies [144].

## 11.6 Future Directions

MRI development is historically technology driven. For advanced techniques like pMRI, standardization, rather than available technology is likely to be the limiting factor for widespread clinical utility. To this end, standardization initiatives like those initiated by QIBA ([www.rsna.org/QIBA](http://www.rsna.org/QIBA)) and ASFNR ([www.asfnr.org](http://www.asfnr.org)) will be important drivers for widespread clinical acceptance of new quantitative neuroimaging biomarkers. In addition to protocol and acquisition

standardization, there is a strong need for better standardization of image processing and analysis tools.

Still, we observe some important technological developments that may have a big impact on potential applications in the near future. The rapid advance seen in acquisition parallelization [145] and sparse sampling techniques [146] will enable improved kinetic modeling of pathophysiology with higher spatial–temporal resolution combined with whole-brain coverage. We predict more use of contrast-enhanced acquisition techniques, combining multiple contrasts ( $T_1$ ,  $T_2$ ,  $T_2^*$ ) in a single acquisition thereby significantly increasing the range of microvascular properties accessible by MRI.

As shown in Table 11.1, ASL is currently the least established perfusion MRI technique, based on published clinical results. We believe that ASL will gain more widespread clinical acceptance because of better standardization between vendors. We will likely see better time-resolved approaches overcoming the current limitation of single PLD methods where variations in arterial transit times introduce significant uncertainty in the resulting perfusion values. More efficient labeling techniques will also move the ASL technique forward by reducing scan time without sacrificing image quality.

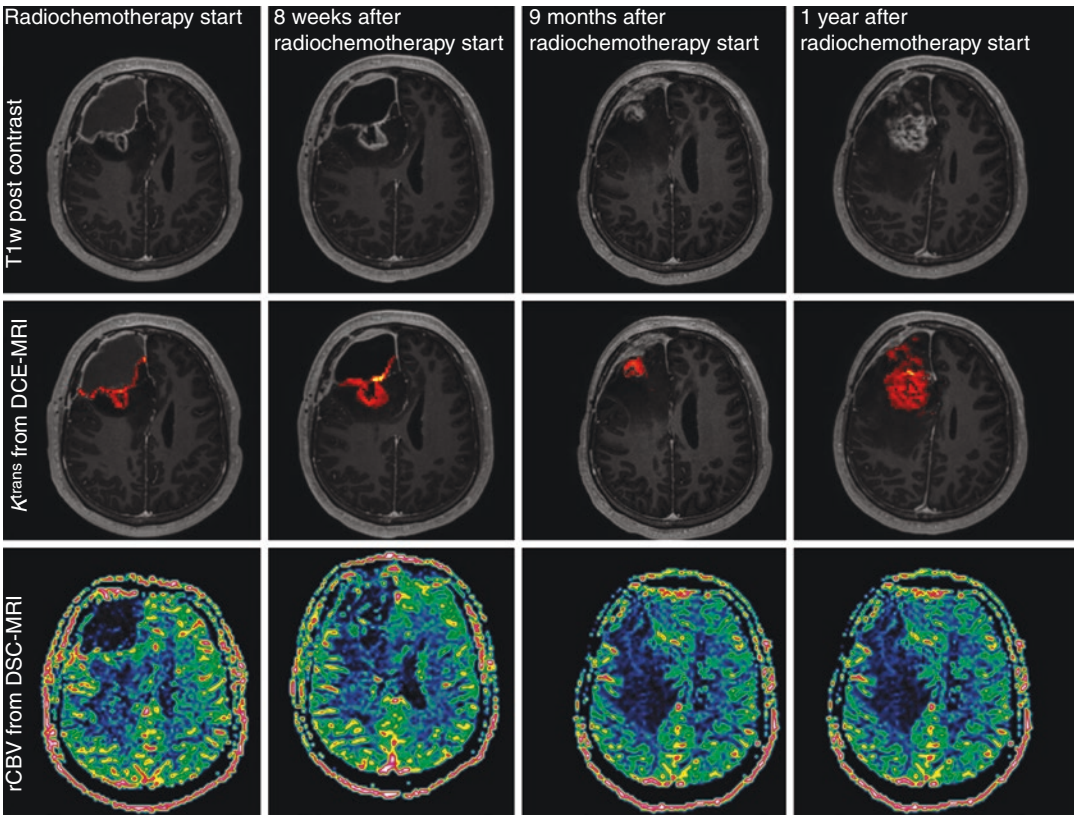
These technical advances, combined with improved standardization, hold promise for better pMRI-based diagnostic tools for clinical use across all the different indications discussed in this chapter and beyond.

**Table 11.1** Overview of the clinical use of the different pMRI techniques based upon amount of published material and current clinical utility

	DSC-MRI	DCE-MRI	ASL
Tumor	↑↑↑	↑↑↑	↑
Stroke	↑↑	↑ <sup>a</sup>	↑
Neurodegenerative disease	↑	↑	↑↑
Demyelinating disease	↑	↑↑	

<sup>a</sup>Atherosclerotic imaging

## 11.7 Clinical Case



Images obtained in a 58-year-old male included in a prospective study of MRI imaging markers during standard radiochemotherapy (RCT) treatment in patients with high-grade gliomas. Relative cerebral volume (rCBV) maps from DSC-MRI and volume transfer constant ( $K^{\text{trans}}$ ) maps from DCE-MRI were generated. The images to the left were taken the day before the RCT start. The  $T_{1w}$  post-contrast series show some contrast enhancement with surrounding edema.  $K^{\text{trans}}$  in the contrast-enhancing area shows homogenous leakage in tumor rim. rCBV in tumor is similar to that of gray matter. Images taken 2 weeks after radiation therapy (RT) end (8 weeks after pretreatment scans) show an increase in the contrast-enhancing area. The  $K^{\text{trans}}$  values in tumor are mostly unchanged from baseline but a small area of increased leakage is noted toward the midline. rCBV is not elevated. At

6 months post-RT, a small contrast-enhancing nodule is still present.  $K^{\text{trans}}$  in the nodule is unchanged and there is still no increased rCBV. At the 1-year control after start of RCT, a large increase in contrast enhancement is seen. There are increased edema and a midline shift. The patient reported slight fatigue but no clear clinical deterioration. Interestingly, the  $K^{\text{trans}}$  values are still not increased compared to the values from the first examination. Similarly, no increase in rCBV is seen. However, due to the increase in contrast enhancement, midline shift, and late onset of these changes, a new surgery was scheduled. The biopsy from the surgery showed changes from radiation necrosis. No signs of tumor recurrence were seen. This shows the possible utility of perfusion imaging for differentiation of treatment-induced pseudoprogression from recurrent tumor.

## References

- Barbier EL, Lamalle L, Decors M. Methodology of brain perfusion imaging. *J Magn Reson Imaging*. 2001;13(4):496–520.
- Weisskoff RM, Zuo CS, Boxerman JL, Rosen BR. Microscopic susceptibility variation and transverse relaxation: theory and experiment. *Magn Reson Med*. 1994;31(6):601–10.
- Larsson HB, Hansen AE, Berg HK, Rostrup E, Haraldseth O. Dynamic contrast-enhanced quantitative perfusion measurement of the brain using T1-weighted MRI at 3T. *J Magn Reson Imaging*. 2008;27(4):754–62.
- Bjornerud A, Sorensen AG, Mouridsen K, Emblem KE. T(1)- and T(2)(\*)-dominant extravasation correction in DSC-MRI: part I-theoretical considerations and implications for assessment of tumor hemodynamic properties. *J Cereb Blood Flow Metab*. 2011;31:2041.
- Ostergaard L. Principles of cerebral perfusion imaging by bolus tracking. *J Magn Reson Imaging*. 2005;22(6):710–7.
- Emblem KE, Mouridsen K, Bjornerud A, Farrar CT, Jennings DL, Borra RJ, et al. Vessel architectural imaging identifies cancer patient responders to anti-angiogenic therapy. *Proc American Association for Cancer Research (AACR) Annual Meeting*. 2013;LB-297: Minisymposium—Biomarkers of Clinical Response.
- Kiselev VG, Strecker R, Ziyeh S, Speck O, Hennig J. Vessel size imaging in humans. *Magn Reson Med*. 2005;53(3):553–63.
- Haacke EM, Filletti CL, Gattu R, Ciulla C, Al-Bashir A, Suryanarayanan K, et al. New algorithm for quantifying vascular changes in dynamic contrast-enhanced MRI independent of absolute T1 values. *Magn Reson Med*. 2007;58(3):463–72.
- Morell A, Lennmyr F, Jonsson O, Tovedal T, Pettersson J, Bergquist J, et al. Influence of blood/tissue differences in contrast agent relaxivity on tracer-based MR perfusion measurements. *MAGMA*. 2015;28(2):135–47.
- Fram EK, Herfkens RJ, Johnson GA, Glover GH, Karis JP, Shimakawa A, et al. Rapid calculation of T1 using variable flip angle gradient refocused imaging. *Magn Reson Imaging*. 1987;5(3):201–8.
- Henderson E, McKinnon G, Lee TY, Rutt BK. A fast 3D look-locker method for volumetric T1 mapping. *Magn Reson Imaging*. 1999;17(8):1163–71.
- Larsson C, Kleppetto M, Grothe I, Vardal J, Bjornerud A. T1 in high-grade glioma and the influence of different measurement strategies on parameter estimations in DCE-MRI. *J Magn Reson Imaging*. 2015;42(1):97–104.
- Alsop DC, Detre JA, Golay X, Gunther M, Hendrikse J, Hernandez-Garcia L, et al. Recommended implementation of arterial spin-labeled perfusion MRI for clinical applications: a consensus of the ISMRM perfusion study group and the European consortium for ASL in dementia. *Magn Reson Med*. 2015;73(1):102–16.
- Meier P, Zierler KL. On the theory of the indicator-dilution method for measurement of blood flow and volume. *J Appl Physiol*. 1954;6(12):731–44.
- Bjornerud A, Emblem KE. A fully automated method for quantitative cerebral hemodynamic analysis using DSC-MRI. *J Cereb Blood Flow Metab*. 2010;30(5):1066–78.
- Ostergaard L, Weisskoff RM, Chesler DA, Gyldensted C, Rosen BR. High resolution measurement of cerebral blood flow using intravascular tracer bolus passages. Part I: mathematical approach and statistical analysis. *Magn Reson Med*. 1996;36(5):715–25.
- Christensen S, Mouridsen K, Wu O, Hjort N, Karstoft H, Thomalla G, et al. Comparison of 10 perfusion MRI parameters in 97 sub-6-hour stroke patients using voxel-based receiver operating characteristics analysis. *Stroke*. 2009;40(6):2055–61.
- Sourbron SP, Buckley DL. Tracer kinetic modelling in MRI: estimating perfusion and capillary permeability. *Phys Med Biol*. 2012;57(2):R1–33.
- Cramer SP, Larsson HB. Accurate determination of blood-brain barrier permeability using dynamic contrast-enhanced T1-weighted MRI: a simulation and in vivo study on healthy subjects and multiple sclerosis patients. *J Cereb Blood Flow Metab*. 2014;34(10):1655–65.
- Buxton RB, Frank LR, Wong EC, Siewert B, Warach S, Edelman RR. A general kinetic model for quantitative perfusion imaging with arterial spin labeling. *Magn Reson Med*. 1998;40(3):383–96.
- MacIntosh BJ, Lindsay AC, Kyliantiras I, Kuker W, Gunther M, Robson MD, et al. Multiple inflow pulsed arterial spin-labeling reveals delays in the arterial arrival time in minor stroke and transient ischemic attack. *AJNR Am J Neuroradiol*. 2010;31(10):1892–4.
- Keil VC, Madler B, Gieseke J, Fimmers R, Hattingen E, Schild HH, et al. Effects of arterial input function selection on kinetic parameters in brain dynamic contrast-enhanced MRI. *Magn Reson Imaging*. 2017;40:83–90.
- Mouridsen K, Christensen S, Gyldensted L, Ostergaard L. Automatic selection of arterial input function using cluster analysis. *Magn Reson Med*. 2006;55(3):524–31.
- Caseiras GB, Chheang S, Babb J, Rees JH, Pecorelli N, Tozer DJ, et al. Relative cerebral blood volume measurements of low-grade gliomas predict patient outcome in a multi-institution setting. *Eur J Radiol*. 2010;73(2):215–20.
- Kim HS, Goh MJ, Kim N, Choi CG, Kim SJ, Kim JH. Which combination of MR imaging modalities is best for predicting recurrent glioblastoma? Study of diagnostic accuracy and reproducibility. *Radiology*. 2014;273(3):831–43.

26. Raunig DL, McShane LM, Pennello G, Gatsonis C, Carson PL, Voyvodic JT, et al. Quantitative imaging biomarkers: a review of statistical methods for technical performance assessment. *Stat Methods Med Res.* 2015;24(1):27–67.
27. Yang X, Knopp MV. Quantifying tumor vascular heterogeneity with dynamic contrast-enhanced magnetic resonance imaging: a review. *J Biomed Biotechnol.* 2011;2011:732848.
28. Patel AP, Tirosh I, Trombetta JJ, Shalek AK, Gillespie SM, Wakimoto H, et al. Single-cell RNA-seq highlights intratumoral heterogeneity in primary glioblastoma. *Science.* 2014;344(6190):1396–401.
29. Rosen BR, Belliveau JW, Buchbinder BR, McKinstry RC, Porkka LM, Kennedy DN, et al. Contrast agents and cerebral hemodynamics. *Magn Reson Med.* 1991;19(2):285–92.
30. Kalpathy-Cramer J, Gerstner ER, Emblem KE, Andronesi O, Rosen B. Advanced magnetic resonance imaging of the physical processes in human glioblastoma. *Cancer Res.* 2014;74(17):4622–37.
31. Smitha KA, Gupta AK, Jayasree RS. Relative percentage signal intensity recovery of perfusion metrics—an efficient tool for differentiating grades of glioma. *Br J Radiol.* 2015;88(1052):20140784.
32. Arisawa A, Watanabe Y, Tanaka H, Takahashi H, Matsuo C, Fujiwara T, et al. Vessel-masked perfusion magnetic resonance imaging with histogram analysis improves diagnostic accuracy for the grading of glioma. *J Comput Assist Tomogr.* 2017;41(6):910–5.
33. Burth S, Kickingereder P, Eidel O, Tichy D, Bonekamp D, Weberling L, et al. Clinical parameters outweigh diffusion- and perfusion-derived MRI parameters in predicting survival in newly diagnosed glioblastoma. *Neuro Oncol.* 2016;18(12):1673–9.
34. Lee J, Jain R, Khalil K, Griffith B, Bosca R, Rao G, et al. Texture feature ratios from relative CBV maps of perfusion MRI are associated with patient survival in glioblastoma. *AJNR Am J Neuroradiol.* 2016;37(1):37–43.
35. Emblem KE, Due-Tonnessen P, Hald JK, Bjornerud A, Pinho MC, Scheie D, et al. Machine learning in preoperative glioma MRI: survival associations by perfusion-based support vector machine outperforms traditional MRI. *J Magn Reson Imaging.* 2014;40(1):47–54.
36. Coban G, Mohan S, Kural F, Wang S, O'Rourke DM, Poptani H. Prognostic value of dynamic susceptibility contrast-enhanced and diffusion-weighted MR imaging in patients with glioblastomas. *AJNR Am J Neuroradiol.* 2015;36(7):1247–52.
37. Ryoo I, Choi SH, Kim JH, Sohn CH, Kim SC, Shin HS, et al. Cerebral blood volume calculated by dynamic susceptibility contrast-enhanced perfusion MR imaging: preliminary correlation study with glioblastoma genetic profiles. *PLoS One.* 2013;8(8):e71704.
38. Santarosa C, Castellano A, Conte GM, Cadioli M, Iadanza A, Terreni MR, et al. Dynamic contrast-enhanced and dynamic susceptibility contrast perfusion MR imaging for glioma grading: preliminary comparison of vessel compartment and permeability parameters using hotspot and histogram analysis. *Eur J Radiol.* 2016;85(6):1147–56.
39. Lee S, Yun TJ, Kang KM, Rhim JH, Park CK, Kim TM, et al. Application of diffusion-weighted imaging and dynamic susceptibility contrast perfusion-weighted imaging for ganglioglioma in adults: comparison study with oligodendroglioma. *J Neuroradiol.* 2016;43(5):331–8.
40. Lee S, Choi SH, Ryoo I, Yoon TJ, Kim TM, Lee SH, et al. Evaluation of the microenvironmental heterogeneity in high-grade gliomas with IDH1/2 gene mutation using histogram analysis of diffusion-weighted imaging and dynamic-susceptibility contrast perfusion imaging. *J Neurooncol.* 2015;121(1):141–50.
41. Nguyen TB, Cron GO, Bezzina K, Perdrizet K, Torres CH, Chakraborty S, et al. Correlation of tumor immunohistochemistry with dynamic contrast-enhanced and DSC-MRI parameters in patients with gliomas. *AJNR Am J Neuroradiol.* 2016;37(12):2217–23.
42. Sauwen N, Acou M, Van CS, Sima DM, Veraart J, Maes F, et al. Comparison of unsupervised classification methods for brain tumor segmentation using multi-parametric MRI. *Neuroimage Clin.* 2016;12:753–64.
43. Juan-Albarracin J, Fuster-Garcia E, Perez-Girbes A, Aparici-Robles F, Alberich-Bayarri A, Revert-Ventura A, et al. Glioblastoma: vascular habitats detected at preoperative dynamic susceptibility-weighted contrast-enhanced perfusion MR imaging predict survival. *Radiology.* 2018;287:944–54.
44. Roberts HC, Roberts TP, Brasch RC, Dillon WP. Quantitative measurement of microvascular permeability in human brain tumors achieved using dynamic contrast-enhanced MR imaging: correlation with histologic grade. *AJNR Am J Neuroradiol.* 2000;21(5):891–9.
45. Jung SC, Yeom JA, Kim JH, Ryoo I, Kim SC, Shin H, et al. Glioma: application of histogram analysis of pharmacokinetic parameters from T1-weighted dynamic contrast-enhanced MR imaging to tumor grading. *AJNR Am J Neuroradiol.* 2014;35(6):1103–10.
46. Sourbron SP, Buckley DL. On the scope and interpretation of the Tofts models for DCE-MRI. *Magn Reson Med.* 2011;66(3):735–45.
47. Nguyen TB, Cron GO, Mercier JF, Footitt C, Torres CH, Chakraborty S, et al. Preoperative prognostic value of dynamic contrast-enhanced MRI-derived contrast transfer coefficient and plasma volume in patients with cerebral gliomas. *AJNR Am J Neuroradiol.* 2015;36(1):63–9.
48. Bonekamp D, Deike K, Wiestler B, Wick W, Bendszus M, Radbruch A, et al. Association of overall survival in patients with newly diagnosed glioblastoma with contrast-enhanced perfusion MRI: comparison of intraindividually matched T1- and T2 (\*)-based bolus techniques. *J Magn Reson Imaging.* 2015;42(1):87–96.

49. Kim R, Choi SH, Yun TJ, Lee ST, Park CK, Kim TM, et al. Prognosis prediction of non-enhancing T2 high signal intensity lesions in glioblastoma patients after standard treatment: application of dynamic contrast-enhanced MR imaging. *Eur Radiol.* 2017;27(3):1176–85.
50. Lehmann P, Monet P, de Marco G, Saliou G, Perrin M, Stoquart-Elsankari S, et al. A comparative study of perfusion measurement in brain tumours at 3 tesla MR: arterial spin labeling versus dynamic susceptibility contrast-enhanced MRI. *Eur Neurol.* 2010;64(1):21–6.
51. Kong L, Chen H, Yang Y, Chen L. A meta-analysis of arterial spin labelling perfusion values for the prediction of glioma grade. *Clin Radiol.* 2017;72(3):255–61.
52. Järnum H, Steffensen EG, Knutsson L, Fründ E-T, Simonsen CW, Lundbye-Christensen S, et al. Perfusion MRI of brain tumours: a comparative study of pseudo-continuous arterial spin labelling and dynamic susceptibility contrast imaging. *Neuroradiology.* 2009;52(4):307–17.
53. Xu W, Wang Q, Shao A, Xu B, Zhang J. The performance of MR perfusion-weighted imaging for the differentiation of high-grade glioma from primary central nervous system lymphoma: a systematic review and meta-analysis. *PLoS One.* 2017;12(3):e0173430.
54. Nakajima S, Okada T, Yamamoto A, Kanagaki M, Fushimi Y, Okada T, et al. Primary central nervous system lymphoma and glioblastoma: differentiation using dynamic susceptibility-contrast perfusion-weighted imaging, diffusion-weighted imaging, and (18)F-fluorodeoxyglucose positron emission tomography. *Clin Imaging.* 2015;39(3):390–5.
55. Nakajima S, Okada T, Yamamoto A, Kanagaki M, Fushimi Y, Okada T, et al. Differentiation between primary central nervous system lymphoma and glioblastoma: a comparative study of parameters derived from dynamic susceptibility contrast-enhanced perfusion-weighted MRI. *Clin Radiol.* 2015;70(12):1393–9.
56. Blasel S, Jurcoane A, Bahr O, Weise L, Harter PN, Hattingen E. MR perfusion in and around the contrast-enhancement of primary CNS lymphomas. *J Neurooncol.* 2013;114(1):127–34.
57. Dibble EH, Boxerman JL, Baird GL, Donahue JE, Rogg JM. Toxoplasmosis versus lymphoma: cerebral lesion characterization using DSC-MRI revisited. *Clin Neurol Neurosurg.* 2017;152:84–9.
58. Toh CH, Wei KC, Chang CN, Ng SH, Wong HF, Lin CP. Differentiation of brain abscesses from glioblastomas and metastatic brain tumors: comparisons of diagnostic performance of dynamic susceptibility contrast-enhanced perfusion MR imaging before and after mathematic contrast leakage correction. *PLoS One.* 2014;9(10):e109172.
59. Floriano VH, Torres US, Spotti AR, Ferraz-Filho JR, Tognola WA. The role of dynamic susceptibility contrast-enhanced perfusion MR imaging in differentiating between infectious and neoplastic focal brain lesions: results from a cohort of 100 consecutive patients. *PLoS One.* 2013;8(12):e81509.
60. Sparacia G, Gadde JA, Iaia A, Sparacia B, Midiri M. Usefulness of quantitative peritumoural perfusion and proton spectroscopic magnetic resonance imaging evaluation in differentiating brain gliomas from solitary brain metastases. *Neuroradiol J.* 2016;29(3):160–7.
61. Bauer AH, Erly W, Moser FG, Maya M, Nael K. Differentiation of solitary brain metastasis from glioblastoma multiforme: a predictive multiparametric approach using combined MR diffusion and perfusion. *Neuroradiology.* 2015;57(7):697–703.
62. Warnke PC, Timmer J, Ostertag CB, Kopitzki K. Capillary physiology and drug delivery in central nervous system lymphomas. *Ann Neurol.* 2005;57(1):136–9.
63. Lu S, Gao Q, Yu J, Li Y, Cao P, Shi H, et al. Utility of dynamic contrast-enhanced magnetic resonance imaging for differentiating glioblastoma, primary central nervous system lymphoma and brain metastatic tumor. *Eur J Radiol.* 2016;85(10):1722–7.
64. Kickingereder P, Sahn F, Wiestler B, Roethke M, Heiland S, Schlemmer HP, et al. Evaluation of microvascular permeability with dynamic contrast-enhanced MRI for the differentiation of primary CNS lymphoma and glioblastoma: radiologic-pathologic correlation. *AJNR Am J Neuroradiol.* 2014;35(8):1503–8.
65. Ludemann L, Grieger W, Wurm R, Wust P, Zimmer C. Quantitative measurement of leakage volume and permeability in gliomas, meningiomas and brain metastases with dynamic contrast-enhanced MRI. *Magn Reson Imaging.* 2005;23(8):833–41.
66. Haris M, Gupta RK, Singh A, Husain N, Husain M, Pandey CM, et al. Differentiation of infective from neoplastic brain lesions by dynamic contrast-enhanced MRI. *Neuroradiology.* 2008;50(6):531–40.
67. Hirai T, Kitajima M, Nakamura H, Okuda T, Sasao A, Shigematsu Y, et al. Quantitative blood flow measurements in gliomas using arterial spin-labeling at 3T: intermodality agreement and inter- and intraobserver reproducibility study. *Am J Neuroradiol.* 2011;32(11):2073–9.
68. Wen PY, Macdonald DR, Reardon DA, Cloughesy TF, Sorensen AG, Galanis E, et al. Updated response assessment criteria for high-grade gliomas: response assessment in neuro-oncology working group. *J Clin Oncol.* 2010;28(11):1963–72.
69. Lin NU, Wefel JS, Lee EQ, Schiff D, van den Bent MJ, Soffiotti R, et al. Challenges relating to solid tumour brain metastases in clinical trials, part 2: neurocognitive, neurological, and quality-of-life outcomes. A report from the RANO group. *Lancet Oncol.* 2013;14(10):e407–e16.
70. Lin NU, Lee EQ, Aoyama H, Barani IJ, Barboriak DP, Baumert BG, et al. Response assessment criteria for brain metastases: proposal from the RANO group. *Lancet Oncol.* 2015;16(6):e270–e8.

71. Oxnard GR, Morris MJ, Hodi FS, Baker LH, Kris MG, Venook AP, et al. When progressive disease does not mean treatment failure: reconsidering the criteria for progression. *J Natl Cancer Inst.* 2012;104(20):1534–41.
72. Brandsma D, Stalpers L, Taal W, Sminia P, van den Bent MJ. Clinical features, mechanisms, and management of pseudoprogression in malignant gliomas. *Lancet Oncol.* 2008;9(5):453–61.
73. Hoefnagels FW, Lagerwaard FJ, Sanchez E, Haasbeek CJ, Knol DL, Slotman BJ, et al. Radiological progression of cerebral metastases after radiosurgery: assessment of perfusion MRI for differentiating between necrosis and recurrence. *J Neurol.* 2009;256(6):878–87.
74. Kim JH, Choi SH, Ryoo I, Yun TJ, Kim TM, Lee SH, et al. Prognosis prediction of measurable enhancing lesion after completion of standard concomitant chemoradiotherapy and adjuvant temozolomide in glioblastoma patients: application of dynamic susceptibility contrast perfusion and diffusion-weighted imaging. *PLoS One.* 2014;9(11):e113587.
75. Boxerman JL, Ellingson BM, Jeyapalan S, Elinzano H, Harris RJ, Rogg JM, et al. Longitudinal DSC-MRI for distinguishing tumor recurrence from pseudoprogression in patients with a high-grade glioma. *Am J Clin Oncol.* 2017;40(3):228–34.
76. Kim TH, Yun TJ, Park CK, Kim TM, Kim JH, Sohn CH, et al. Combined use of susceptibility weighted magnetic resonance imaging sequences and dynamic susceptibility contrast perfusion weighted imaging to improve the accuracy of the differential diagnosis of recurrence and radionecrosis in high-grade glioma patients. *Oncotarget.* 2017;8(12):20340–53.
77. Shin KE, Ahn KJ, Choi HS, Jung SL, Kim BS, Jeon SS, et al. DCE and DSC MR perfusion imaging in the differentiation of recurrent tumour from treatment-related changes in patients with glioma. *Clin Radiol.* 2014;69(6):e264–e72.
78. van Dijken BRJ, van Laar PJ, Holtman GA, van der Hoorn A. Diagnostic accuracy of magnetic resonance imaging techniques for treatment response evaluation in patients with high-grade glioma, a systematic review and meta-analysis. *Eur Radiol.* 2017;27(10):4129–44.
79. Calmon R, Puget S, Varlet P, Beccaria K, Blauwblomme T, Grevent D, et al. Multimodal magnetic resonance imaging of treatment-induced changes to diffuse infiltrating pontine gliomas in children and correlation to patient progression-free survival. *Int J Radiat Oncol Biol Phys.* 2017;99(2):476–85.
80. Jakubovic R, Sahgal A, Ruschin M, Pejovic-Milic A, Milwid R, Aviv RI. Non tumor perfusion changes following stereotactic radiosurgery to brain metastases. *Technol Cancer Res Treat.* 2015;14(4):497–503.
81. Thomas AA, Arevalo-Perez J, Kaley T, Lyo J, Peck KK, Shi W, et al. Dynamic contrast enhanced T1 MRI perfusion differentiates pseudoprogression from recurrent glioblastoma. *J Neurooncol.* 2015;125(1):183–90.
82. Yun TJ, Park CK, Kim TM, Lee SH, Kim JH, Sohn CH, et al. Glioblastoma treated with concurrent radiation therapy and temozolomide chemotherapy: differentiation of true progression from pseudoprogression with quantitative dynamic contrast-enhanced MR imaging. *Radiology.* 2015;274(3):830–40.
83. Young RJ, Gupta A, Shah AD, Graber JJ, Zhang Z, Shi W, et al. Potential utility of conventional MRI signs in diagnosing pseudoprogression in glioblastoma. *Neurology.* 2011;76(22):1918–24.
84. Patel P, Baradaran H, Delgado D, Askin G, Christos P, John Tsiouris A, et al. MR perfusion-weighted imaging in the evaluation of high-grade gliomas after treatment: a systematic review and meta-analysis. *Neuro Oncol.* 2017;19(1):118–27.
85. Ye J, Bhagat SK, Li H, Luo X, Wang B, Liu L, et al. Differentiation between recurrent gliomas and radiation necrosis using arterial spin labeling perfusion imaging. *Exp Ther Med.* 2016;11(6):2432–6.
86. Jovanovic M, Radenkovic S, Stosic-Opincal T, Lavrnica S, Gavrilovic S, Lazovic-Popovic B, et al. Differentiation between progression and pseudoprogression by arterial spin labeling MRI in patients with glioblastoma multiforme. *J BUON.* 2017;22(4):1061–7.
87. Lu-Emerson C, Duda DG, Emblem KE, Taylor JW, Gerstner ER, Loeffler JS, et al. Lessons from anti-vascular endothelial growth factor and anti-vascular endothelial growth factor receptor trials in patients with glioblastoma. *J Clin Oncol.* 2015;33(10):1197–213.
88. Huang RY, Neagu MR, Reardon DA, Wen PY. Pitfalls in the neuroimaging of glioblastoma in the era of antiangiogenic and immuno/targeted therapy—detecting illusive disease, defining response. *Front Neurol.* 2015;6:33.
89. Boxerman JL, Ellingson BM. Response assessment and magnetic resonance imaging issues for clinical trials involving high-grade Gliomas. *Top Magn Reson Imaging.* 2015;24(3):127–36.
90. Sorensen AG, Emblem KE, Polaskova P, Jennings D, Kim H, Ancukiewicz M, et al. Increased survival of Glioblastoma patients who respond to antiangiogenic therapy with elevated blood perfusion. *Cancer Res.* 2012;72(2):402–7.
91. Batchelor TT, Gerstner ER, Emblem KE, Duda DG, Kalpathy-Cramer J, Snuderl M, et al. Improved tumor oxygenation and survival in glioblastoma patients who show increased blood perfusion after cediranib and chemoradiation. *Proc Natl Acad Sci U S A.* 2013;110(47):19,059–64.
92. Ken S, Deviers A, Filleron T, Catalaa I, Lotterie JA, Khalifa J, et al. Voxel-based evidence of perfusion normalization in glioblastoma patients included in a phase I-II trial of radiotherapy/tipifarnib combination. *J Neurooncol.* 2015;124(3):465–73.
93. Kalpathy-Cramer J, Chandra V, Da X, Ou Y, Emblem KE, Muzikansky A, et al. Phase II study of tivozanib, an oral VEGFR inhibitor, in patients with recurrent glioblastoma. *J Neurooncol.* 2017;131(3):603–10.

94. Chen BB, Lu YS, Lin CH, Chen WW, Wu PF, Hsu CY, et al. A pilot study to determine the timing and effect of bevacizumab on vascular normalization of metastatic brain tumors in breast cancer. *BMC Cancer*. 2016;16:466.
95. Leu K, Enzmann DR, Woodworth DC, Harris RJ, Tran AN, Lai A, et al. Hypervascular tumor volume estimated by comparison to a large-scale cerebral blood volume radiographic atlas predicts survival in recurrent glioblastoma treated with bevacizumab. *Cancer Imaging*. 2014;14:31.
96. Gerstner ER, Emblem KE, Sorensen GA. Vascular magnetic resonance imaging in brain tumors during antiangiogenic therapy—are we there yet? *Cancer J*. 2015;21(4):337–42.
97. Boxerman JL, Schmainda KM, Zhang Z, Barboriak DP. Dynamic susceptibility contrast MRI measures of relative cerebral blood volume continue to show promise as an early response marker in the setting of bevacizumab treatment. *Neuro Oncol*. 2015;17(11):1538–9.
98. Okada H, Weller M, Huang R, Finocchiaro G, Gilbert MR, Wick W, et al. Immunotherapy response assessment in neuro-oncology: a report of the RANO working group. *Lancet Oncol*. 2015;16(15):e534–e42.
99. Aquino D, Gioppo A, Finocchiaro G, Bruzzzone MG, Cuccarini V. MRI in Glioma immunotherapy: evidence, pitfalls, and perspectives. *J Immunol Res*. 2017;2017:5813951.
100. Chalela JA, Kidwell CS, Nentwich LM, Luby M, Butman JA, Demchuk AM, et al. Magnetic resonance imaging and computed tomography in emergency assessment of patients with suspected acute stroke: a prospective comparison. *Lancet*. 2007;369(9558):293–8.
101. Wintermark M, Albers GW, Broderick JP, Demchuk AM, Fiebach JB, Fiehler J, et al. Acute stroke imaging research roadmap II. *Stroke*. 2013;44(9):2628–39.
102. Wintermark M, Albers GW, Alexandrov AV, Alger JR, Bammer R, Baron JC, et al. Acute stroke imaging research roadmap. *Stroke*. 2008;39(5):1621–8.
103. Warach SJ, Luby M, Albers GW, Bammer R, Bivard A, Campbell BC, et al. Acute stroke imaging research roadmap III imaging selection and outcomes in acute stroke reperfusion clinical trials: consensus recommendations and further research priorities. *Stroke*. 2016;47(5):1389–98.
104. Nael K, Khan R, Choudhary G, Meshksar A, Villablanca P, Tay J, et al. Six-minute magnetic resonance imaging protocol for evaluation of acute ischemic stroke: pushing the boundaries. *Stroke*. 2014;45(7):1985–91.
105. Powers WJ, Rabinstein AA, Ackerson T, Adeoye OM, Bambakidis NC, Becker K, et al. 2018 guidelines for the early management of patients with acute ischemic stroke: a guideline for healthcare professionals from the American Heart Association/American Stroke Association. *Stroke*. 2018;49(3):e46–e110.
106. Astrup J. Energy-requiring cell functions in the ischemic brain. Their critical supply and possible inhibition in protective therapy. *J Neurosurg*. 1982;56(4):482–97.
107. Albers GW, Thijs VN, Wechsler L, Kemp S, Schlaug G, Skalabrin E, et al. Magnetic resonance imaging profiles predict clinical response to early reperfusion: the diffusion and perfusion imaging evaluation for understanding stroke evolution (DEFUSE) study. *Ann Neurol*. 2006;60(5):508–17.
108. Campbell BC, Macrae IM. Translational perspectives on perfusion-diffusion mismatch in ischemic stroke. *Int J Stroke*. 2015;10(2):153–62.
109. Zaro-Weber O, Livne M, Martin SZ, von Samson-Himmelstjerna FC, Moeller-Hartmann W, Schuster A, et al. Comparison of the 2 most popular deconvolution techniques for the detection of penumbral flow in acute stroke. *Stroke*. 2015;46(10):2795–9.
110. Sobesky J, Zaro WO, Lehnhardt FG, Hesselmann V, Neveling M, Jacobs A, et al. Does the mismatch match the penumbra? Magnetic resonance imaging and positron emission tomography in early ischemic stroke. *Stroke*. 2005;36(5):980–5.
111. Mlynash M, Lansberg MG, De Silva DA, Lee J, Christensen S, Straka M, et al. Refining the definition of the malignant profile: insights from the DEFUSE-EPITHET pooled data set. *Stroke*. 2011;42(5):1270–5.
112. Hirsch NM, Toth V, Forschler A, Kooijman H, Zimmer C, Preibisch C. Technical considerations on the validity of blood oxygenation level-dependent-based MR assessment of vascular deoxygenation. *NMR Biomed*. 2014;27(7):853–62.
113. An H, Ford AL, Chen Y, Zhu H, Ponisio R, Kumar G, et al. Defining the ischemic penumbra using magnetic resonance oxygen metabolic index. *Stroke*. 2015;46(4):982–8.
114. Burke JF, Gelb DJ, Quint DJ, Morgenstern LB, Kerber KA. The impact of MRI on stroke management and outcomes: a systematic review. *J Eval Clin Pract*. 2013;19(6):987–93.
115. Iadecola C, Yaffe K, Biller J, Bratzke LC, Faraci FM, Gorelick PB, et al. Impact of hypertension on cognitive function: a scientific statement from the American Heart Association. *Hypertension*. 2016;68(6):e67–94.
116. Merali Z, Huang K, Mikulis D, Silver F, Kassner A. Evolution of blood-brain-barrier permeability after acute ischemic stroke. *PLoS One*. 2017;12(2):e0171558.
117. Zaharchuk G, El Mogy IS, Fischbein NJ, Albers GW. Comparison of arterial spin labeling and bolus perfusion-weighted imaging for detecting mismatch in acute stroke. *Stroke*. 2012;43(7):1843–8.
118. Wang DJJ, Alger JR, Qiao JX, Hao Q, Hou S, Fiaz R, et al. The value of arterial spin-labeled perfusion imaging in acute ischemic stroke: comparison with dynamic susceptibility contrast-enhanced MRI. *Stroke*. 2012;43(4):1018–24.
119. Bokkers RP, Bremmer JP, van Berckel BN, Lammertsma AA, Hendrikse J, Pluim JP, et al. Arterial spin labeling perfusion MRI at multiple delay times: a correlative study with H215O positron emission tomography in patients with symptomatic carotid artery occlusion. *J Cereb Blood Flow Metab*. 2009;30(1):222–9.

120. Bivard A, Krishnamurthy V, Stanwell P, Levi C, Spratt NJ, Davis S, et al. Arterial spin labeling versus bolus-tracking perfusion in hyperacute stroke. *Stroke*. 2014;45(1):127–33.
121. Alsop DC, Detre JA. Reduced transit-time sensitivity in noninvasive magnetic resonance imaging of human cerebral blood flow. *J Cereb Blood Flow Metab*. 1996;16(6):1236–49.
122. Kisler K, Nelson AR, Montagne A, Zlokovic BV. Cerebral blood flow regulation and neurovascular dysfunction in Alzheimer disease. *Nat Rev Neurosci*. 2017;18(7):419–34.
123. Ostergaard L, Aamand R, Gutierrez-Jimenez E, Ho YC, Blicher JU, Madsen SM, et al. The capillary dysfunction hypothesis of Alzheimer's disease. *Neurobiol Aging*. 2013;34(4):1018–31.
124. Hauser T, Schonknecht P, Thomann PA, Gerigk L, Schroder J, Henze R, et al. Regional cerebral perfusion alterations in patients with mild cognitive impairment and Alzheimer disease using dynamic susceptibility contrast MRI. *Acad Radiol*. 2013;20(6):705–11.
125. Eskildsen SF, Gyldensted L, Nagenthiraja K, Nielsen RB, Hansen MB, Dalby RB, et al. Increased cortical capillary transit time heterogeneity in Alzheimer's disease: a DSC-MRI perfusion study. *Neurobiol Aging*. 2017;50:107–18.
126. Jespersen SN, Ostergaard L. The roles of cerebral blood flow, capillary transit time heterogeneity, and oxygen tension in brain oxygenation and metabolism. *J Cereb Blood Flow Metab*. 2012;32(2):264–77.
127. van de Haar HJ, Burgmans S, Jansen JF, van Osch MJ, van Buchem MA, Muller M, et al. Blood-brain barrier leakage in patients with early Alzheimer disease. *Radiology*. 2016;281(2):527–35.
128. Taheri S, Gasparovic C, Huisa BN, Adair JC, Edmonds E, Prestopnik J, et al. Blood-brain barrier permeability abnormalities in vascular cognitive impairment. *Stroke*. 2011;42(8):2158–63.
129. Tosun D, Schuff N, Jagust W, Weiner MW. Alzheimer's disease neuroimaging I. discriminative power of arterial spin labeling magnetic resonance imaging and 18F-fluorodeoxyglucose positron emission tomography changes for amyloid-beta-positive subjects in the Alzheimer's disease continuum. *Neurodegener Dis*. 2016;16(1–2):87–94.
130. Law M, Saindane AM, Ge Y, Babb JS, Johnson G, Mannon LJ, et al. Microvascular abnormality in relapsing-remitting multiple sclerosis: perfusion MR imaging findings in normal-appearing white matter. *Radiology*. 2004;231(3):645–52.
131. Polman CH, Reingold SC, Banwell B, Clanet M, Cohen JA, Filippi M, et al. Diagnostic criteria for multiple sclerosis: 2010 revisions to the McDonald criteria. *Ann Neurol*. 2011;69(2):292–302.
132. Lassmann H. The pathologic substrate of magnetic resonance alterations in multiple sclerosis. *Neuroimaging Clin N Am*. 2008;18(4):563–76, ix.
133. Tofts PS, Kermode AG. Measurement of the blood-brain barrier permeability and leakage space using dynamic MR imaging. 1. Fundamental concepts. *Magn Reson Med*. 1991;17(2):357–67.
134. Larsson HB, Stubgaard M, Frederiksen JL, Jensen M, Henriksen O, Paulson OB. Quantitation of blood-brain barrier defect by magnetic resonance imaging and gadolinium-DTPA in patients with multiple sclerosis and brain tumors. *Magn Reson Med*. 1990;16(1):117–31.
135. Gaitan MI, Shea CD, Evangelou IE, Stone RD, Fenton KM, Bielekova B, et al. Evolution of the blood-brain barrier in newly forming multiple sclerosis lesions. *Ann Neurol*. 2011;70(1):22–9.
136. Ingrisch M, Sourbron S, Morhard D, Ertl-Wagner B, Kumpfel T, Hohlfeld R, et al. Quantification of perfusion and permeability in multiple sclerosis: dynamic contrast-enhanced MRI in 3D at 3T. *Invest Radiol*. 2012;47(4):252–8.
137. Sowa P, Bjornerud A, Nygaard GO, Damangir S, Spulber G, Celius EG, et al. Reduced perfusion in white matter lesions in multiple sclerosis. *Eur J Radiol*. 2015;84(12):2605–12.
138. Peruzzo D, Castellaro M, Calabrese M, Veronese E, Rinaldi F, Bernardi V, et al. Heterogeneity of cortical lesions in multiple sclerosis: an MRI perfusion study. *J Cereb Blood Flow Metab*. 2013;33(3):457–63.
139. Sowa P, Nygaard GO, Bjornerud A, Celius EG, Harbo HF, Beyer MK. Magnetic resonance imaging perfusion is associated with disease severity and activity in multiple sclerosis. *Neuroradiology*. 2017;59(7):655–64.
140. Bester M, Forkert ND, Stellmann JP, Aly L, Drabik A, Young KL, et al. Increased perfusion in normal appearing white matter in high inflammatory multiple sclerosis patients. *PLoS One*. 2015;10(3):e0119356.
141. Lauer A, Da X, Hansen MB, Boulouis G, Ou Y, Cai X, et al. ABCD1 dysfunction alters white matter microvascular perfusion. *Brain*. 2017;140(12):3139–52.
142. Papadaki EZ, Simos PG, Panou T, Mastorodemos VC, Maris TG, Karantanis AH, et al. Hemodynamic evidence linking cognitive deficits in clinically isolated syndrome to regional brain inflammation. *Eur J Neurol*. 2014;21(3):499–505.
143. Cramer SP, Simonsen H, Frederiksen JL, Rostrup E, Larsson HB. Abnormal blood-brain barrier permeability in normal appearing white matter in multiple sclerosis investigated by MRI. *Neuroimage Clin*. 2014;4:182–9.
144. Ingrisch M, Sourbron S, Herberich S, Schneider MJ, Kumpfel T, Hohlfeld R, et al. Dynamic contrast-enhanced magnetic resonance imaging suggests normal perfusion in normal-appearing white matter in multiple sclerosis. *Invest Radiol*. 2017;52(3):135–41.
145. Feinberg DA, Setsompop K. Ultra-fast MRI of the human brain with simultaneous multi-slice imaging. *J Magn Reson*. 2013;229:90–100.
146. Jaspán ON, Fleysher R, Lipton ML. Compressed sensing MRI: a review of the clinical literature. *Br J Radiol*. 2015;88(1056):20150487.





# Susceptibility Weighted Imaging

# 12

Jürgen R. Reichenbach

## Contents

12.1	<b>Introduction</b> .....	165
12.2	<b>Physical and Technical Background</b> .....	166
12.2.1	Data Acquisition.....	167
12.2.2	Data Processing.....	169
12.2.3	Field Strength.....	170
12.3	<b>Clinical Applications</b> .....	171
12.3.1	Stroke Imaging.....	171
12.3.2	Tumor Imaging.....	171
12.3.3	Traumatic Brain Injury (TBI).....	173
12.3.4	Vascular Malformation.....	174
12.3.5	Multiple Sclerosis (MS).....	174
12.3.6	Neurodegenerative Disorders.....	175
12.3.7	Calcifications.....	175
12.4	<b>Practical Considerations and Limitations</b> .....	175
12.5	<b>Future Directions and Summary</b> .....	177
12.6	<b>Clinical Case</b> .....	179
	<b>References</b> .....	180

## 12.1 Introduction

Susceptibility-weighted imaging (SWI) is a magnetic resonance imaging (MRI) technique that utilizes the intrinsic differences of mag-

netic susceptibility between various tissues to produce a specific contrast on MR images [1–4]. Since the inception of magnetic resonance imaging, creation of contrast on MR images has been one of its cornerstones by exploiting the influence of different physical quantities on signal formation. Physical quantities or parameters typically used for contrast generation in MRI include, among others, spin density, longitudinal and transverse relaxation time constants, diffusion, perfusion, flow, chemical shift, or spin exchange. Magnetic susceptibility,

J. R. Reichenbach (✉)

Medical Physics Group, Department of Diagnostic and Interventional Radiology, University Hospital Jena—Friedrich-Schiller-University, Jena, Germany  
e-mail: [juergen.reichenbach@med.uni-jena.de](mailto:juergen.reichenbach@med.uni-jena.de)

which can be considered a “response quantity,” characterizes the degree of a substance or tissue to become magnetized when exposed to an external magnetic field. Often perceived to be a nuisance due to signal loss and image distortions it can induce on MR images [5], magnetic susceptibility has only relatively lately been transformed into a useful source of intrinsic tissue image contrast. SWI, as a particular form of susceptibility-based imaging, uses local phase or MR frequency information derived from gradient-echo imaging with typically relatively long echo times to enhance contrast of various susceptibility sources in combination with the corresponding magnitude information, thus facilitating diagnostic interpretation. Due to its fast-growing applications with respect to highlighting tissue structures and compounds, which otherwise may be difficult to detect by conventional MRI methods, it has meanwhile become an integral part of MR neuroimaging protocols [6–9]. Since the first description of the method in 1997 [10], SWI has proven useful in a variety of clinical applications, including high-resolution MR venography, imaging hemorrhages from trauma, visualization of blood products (e.g., hemosiderin, ferritin) and vascularization of tumors, or assessment of iron deposits and calcifications in the brain—to name but a few [3, 11–14]. Today, all major providers of MRI scanners have susceptibility-based sequences in their portfolio that run under their own brand names. While Siemens Healthineers and GE Healthcare call it SWI and SWAN (susceptibility-weighted angiography), respectively, Philips offers it under the acronym SWIp (SWI phase), Hitachi Healthcare under BSI (Blood Sensitive Imaging), and Canon Medical Systems under the name FIBB (flow-insensitive black blood).

The aim of this chapter is to provide a background of the SWI method, to review the current research and clinical applications, and to describe some of the limitations and potential future directions of the technique.

## 12.2 Physical and Technical Background

Placing a material sample into an external magnetic field will magnetize it, i.e. the sample acquires a macroscopic magnetic dipole moment  $\mathbf{m}$  that can be represented as an integral over a microscopic magnetization density  $\mathbf{M}(\mathbf{r})$ , which may vary spatially in the sample. Often the relationship between the magnetization  $\mathbf{M}$  and the external magnetic field is linear (as for isotropic, non-ferromagnetic materials), and the dimensionless proportionality factor is referred to as the magnetic susceptibility  $\chi$  of the material:

$$\mathbf{M} = \chi \cdot \mathbf{H} \quad (12.1)$$

The induced magnetization produces an additional magnetic field that affects the evolution of the magnetic resonance signals. Figure 12.1 illustrates the impressive range of magnetic susceptibilities for the different material classes, classified as diamagnetic (negative susceptibilities), paramagnetic (small positive susceptibilities), and ferromagnetic (large positive susceptibilities) materials, together with a depiction of the much smaller range of susceptibilities encompassing mainly biological soft tissues. Susceptibility values of most human tissues are diamagnetic ranging from about  $-7$  to  $-11$  ppm (1 ppm (parts per million) =  $10^{-6}$ ) [15, 16].

Putting a sample with a finite magnetic susceptibility into an external magnetic field generally modifies the field, both inside and outside the sample, where this modification is in addition a function of the geometry of the object [17]. It is these changes of the field induced by the tissues due to their underlying associated magnetic susceptibility distributions and the local susceptibility differences between them that are then picked up by the phase images of gradient echo-based sequences in MRI and utilized in SWI to obtain important anatomical and physiological information about vessels and tissues or anatomical structures. The phase shift  $\Delta\phi$  induced at location  $\mathbf{r}$  at echo time TE can be written as

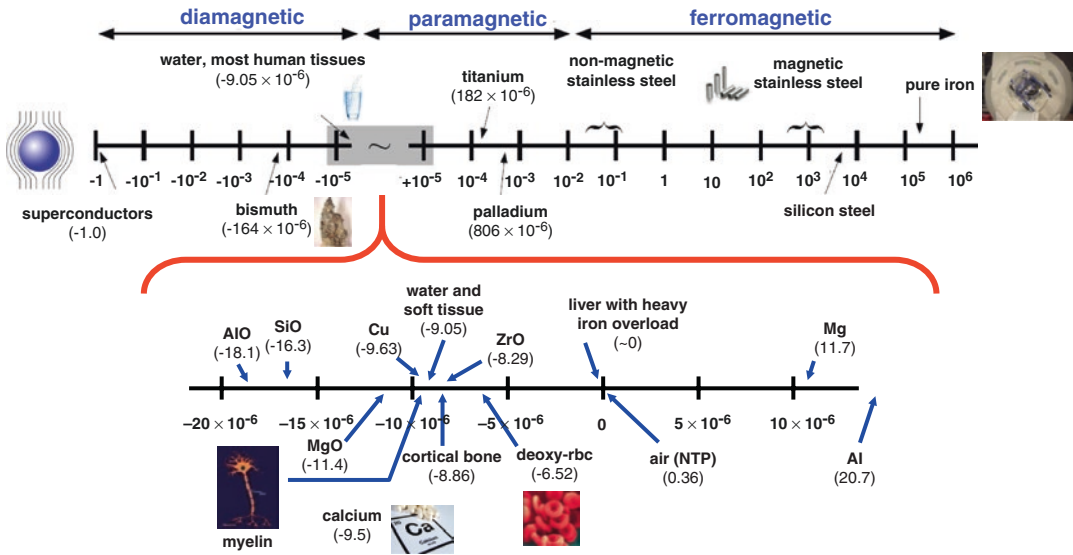


**Fig. 12.1** Diagram of magnetic susceptibilities (susceptibility spectrum). The upper logarithmic scale displays the full range of susceptibility values, extending from superconductors ( $\chi = -1$ ) to ferromagnetic materials ( $\chi = 10^6$  and larger). The lower scale is a linear scale

encompassing the substantially narrowed range of magnetic susceptibilities for biological soft tissues and other substances. (Adapted from Schenck [15] with permission by the publisher)

$$\begin{aligned} \Delta\phi(\mathbf{r}) &= \gamma \cdot \Delta B(\mathbf{r}) \cdot TE \\ &= \gamma \cdot g \cdot \Delta\chi(\mathbf{r}) \cdot B_0 \cdot TE \end{aligned} \quad (12.2)$$

where  $\gamma$  is the gyromagnetic ratio (for protons),  $\Delta B$  represents the local field deviation,  $\Delta\chi$  is the difference of the local magnetic susceptibility of the tissue of interest from its surroundings,  $B_0$  is the field strength, and  $g$  is a geometric factor characterizing the object.

Diamagnetic materials, such as water or calcifications, tend to weaken the external magnetic field resulting in a negative phase shift for a left-handed coordinate system, whereas paramagnetic substances, such as deoxygenated hemoglobin in the blood, hemorrhagic degradation products or ferritin, which is the storage form of iron, slightly amplify the external magnetic field and produce a positive phase shift in case of said coordinate system. Indeed, and besides the geometry and orientation of the object with respect to the main static magnetic field and the size of the object relative to the imaging voxel, the actual sign of the phase shift for a given MRI system and a given material or tissue

(i.e., diamagnetic or paramagnetic) may be vendor dependent and can be affected by technical details of the hardware or the gradient polarity during readout as well as possible sign modifications occurring during processing of the sampled MR signals [18]. It is thus advisable to check the sign convention of one's own scanner when interpreting the phase information [6]. Apart from these rather technical remarks, Fig. 12.2 illustrates the impressive wealth of information associated with the small local susceptibility differences between brain tissues that can be brought to light on an in vivo high-resolution phase image of a gradient-echo sequence, as compared to a stained brain slice with similar anatomical position.

### 12.2.1 Data Acquisition

Most commonly, SWI employs a three-dimensional fully velocity compensated gradient echo sequence with high spatial resolution on the order of 1 mm and higher, i.e. with submillimeter

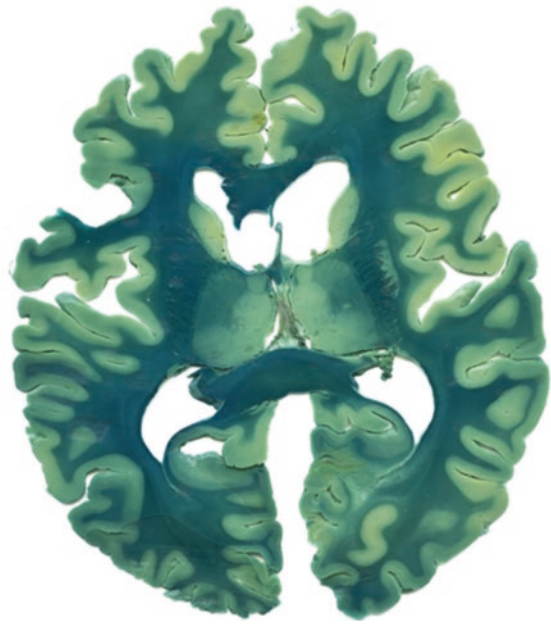
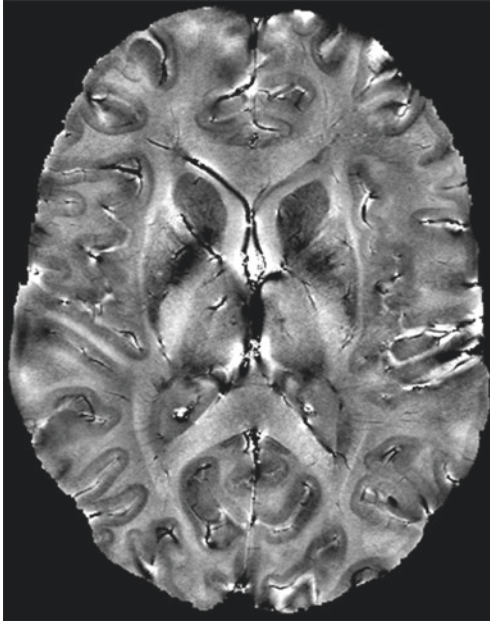


**Fig. 12.2** (Left) In vivo phase image of a gradient echo sequence (7 T, spatial resolution  $360\ \mu\text{m} \times 360\ \mu\text{m} \times 600\ \mu\text{m}$ ) reflecting anatomical details in the brain due to susceptibil-

ity differences between the tissues. (Right) Stained brain tissue slice. (Courtesy of Prof. C. Redies, Institute of Anatomy I, University Hospital Jena)

voxel dimensions [1, 2, 4, 10, 19]. Data can be captured with single-echo or multi-echo sequences [20, 21], the former being well-suited to visualize veins, while the latter provides more flexibility in the choice of echo time and are superior for imaging stroke, cerebral microbleeds, or other structures that may include a range of magnetic susceptibilities values. Longer echo times increase the sensitivity to resolve smaller susceptibilities differences between tissues, but at the same time induce more phase aliasing and signal loss due to increased  $T_2^*$ -weighting, while shorter echo times are recommended for higher susceptibilities, such as tissues or structures with high iron content or veins containing deoxyhemoglobin. Other sequence parameters, e.g., echo time, flip angle, spatial resolution or readout bandwidth, can be tuned to the specific imaging application or adjusted to optimize signal-to-noise ratio (SNR) or phase dispersion across a voxel. For instance, non-isotropic resolution is beneficial for SWI, espe-

cially to obtain good vessel contrast [22, 23]. A detailed overview of suitable imaging parameters for SWI at different field strengths can be found in [4, 24, 25].

Acquiring more than one gradient echo with the same sequence not only allows adjustment of the image contrast due to susceptibility effects but also the collection of complete MR angiographic data (i.e., arterial information) together with SWI data (i.e., venous information) simultaneously in a single scan [22, 26, 27]. Figure 12.3 shows intensity projections of such a dual-echo ToF-SWI scan, where the first echo (time-of-flight (ToF) echo) utilizes the inflow of unsaturated (arterial) spins into the acquisition volume and the second echo is tailored for displaying the venous vasculature [28]. Advantages of such dual- or multi-echo data acquisitions include no time penalty for the short echo data set, intrinsic co-registration of the data sets, and improved differentiation between veins and thrombi on the SWI and arterial angiograms, respectively.

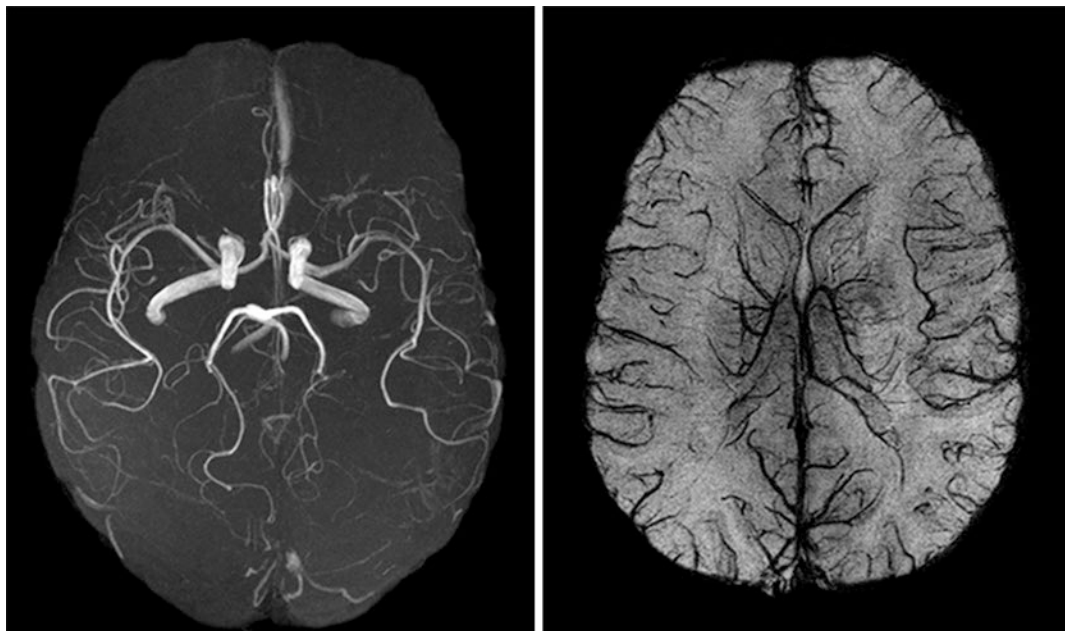


**Fig. 12.3** Dual-echo ToF-SWI at 3 T with the following sequence parameters:  $TE_1/TE_2/TR/\alpha/BW_1/BW_2 = 3.42 \text{ ms}/25 \text{ ms}/42 \text{ ms}/20^\circ/\text{TONE-pulse}/271 \text{ Hz}/\text{px}/78 \text{ Hz}/\text{px}$ ; acquisition time 24:23 min:s; voxel size  $0.43 \text{ mm} \times 0.43 \text{ mm} \times 1.2 \text{ mm}$ ; matrix  $512 \times 352 \times 44$ ; three slabs with an overlapping factor of 20.45%; 75% partial Fourier acquisition in phase and slice-encoding

direction. (Left) Maximum intensity projection (MIP) across the whole volume of the first echo in transverse view. (Right) Minimum intensity projection (mIP) of transverse susceptibility-weighted images over 13.2 mm of the same volume obtained from the second echo of the TOF-SWI sequence. (Adapted from Deistung [28])

### 12.2.2 Data Processing

The standard post-processing pipeline for SWI is schematically summarized in Fig. 12.4. After coil combination and background phase removal by applying, e.g., a homodyne high-pass filter to the initial raw phase image, phase data are converted to a phase mask using a special weighting function, which is then multi-

plied with the corresponding magnitude data to improve the contrast between the tissue structures. Conventionally, this weighting function either scales negative phase values linearly between 1 and 0 and sets positive values to unity (right-handed coordinate system) or scales positive phase values linearly between 1 and 0 and sets negative values to unity (left-handed coordinate-system):

---


$$\begin{aligned}
 &\text{right handed system } f(x,y) = \begin{cases} (\pi + \varphi(x,y)) / \pi & \text{for } -\pi \leq \varphi(x,y) < 0 \\ = 1 & \text{otherwise} \end{cases} \\
 &\text{left handed system } f(x,y) = \begin{cases} (\pi - \varphi(x,y)) / \pi & \text{for } 0 \leq \varphi(x,y) < \pi \\ = 1 & \text{otherwise} \end{cases}
 \end{aligned} \tag{12.3}$$


---

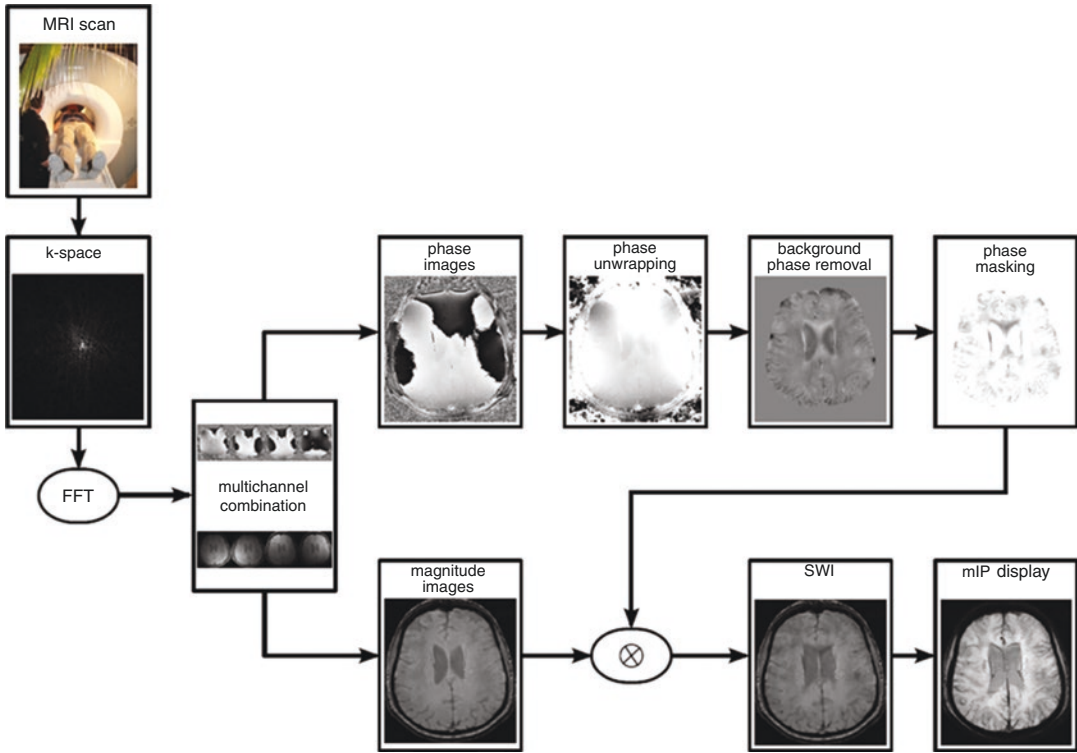


**Fig. 12.4** Flow chart of the post-processing steps applied in SWI. In the standard SWI-processing scheme, phase unwrapping and background field removal are performed

simultaneously by using homodyne filtering. (Adapted from Deistung [28])

The first set of equations accentuates voxels with a negative phase, whereas the second set of equations accentuates voxels with a positive phase. Multiplying the phase mask with the magnitude image will thus create lower values for negative phase voxels and increase the contrast relative to voxels with nonnegative phase values in the first case, whereas in the second case lower magnitude signal values will be created for positive phase voxels with the resulting contrast increase relative to voxels with negative phase values. In addition to such linear scaling, further phase masks have been proposed, including sigmoid masks [29], triangular masks [30], exponential masks [31], or other nonlinear masks [32].

Typically, fourfold multiplication of the phase mask with the corresponding magnitude image is applied to produce a novel type of hybrid contrast and to yield good contrast-to-noise ratio (CNR) for, e.g., venous vessels [1, 33]. A minimum

intensity projection (mIP) over adjacent contiguous slices further improves contrast and may facilitate detection of pathologies or continuity of the venous system.

### 12.2.3 Field Strength

SWI greatly benefits from field strength as the induced phase or frequency shifts not only depend on the susceptibility differences  $\Delta\chi$  between tissues but also on the static magnetic field  $B_0$  [34–36]. In addition to the gain in SNR and susceptibility related  $T_2^*$  contrast at higher magnetic field strength, frequency shifts increase linearly with field strength (Eq. 12.2) which, when taken all together, dramatically improves CNR (see Fig. 12.2). Due to larger phase shifts and faster dephasing (shorter  $T_2^*$  relaxation times compared to lower field strengths), high or ultra-

high field (UHF) allows for the use of shorter echo times and in turn shorter repetition times, resulting in shorter scan times [37]. This saving in scan time can be used to acquire images with higher spatial resolution. Specifically, excellent vascular mapping can be performed at 7 T [34, 38–41], when compared with 1.5 or 3 T [36], and the concept of SWI gives rise to completely new contrast possibilities at 7 T [42].

---

## 12.3 Clinical Applications

The areas of clinical application for SWI have grown over the years and include, among others, the imaging of venous blood in acute or chronic ischemia, the visualization of the vascularization, hemorrhage and calcification of tumors, or the identification of iron deposition in neurodegenerative diseases. SWI has been shown to be particularly useful in imaging trauma, but is also of great value in the characterization of low flow occult, vascular malformations, cerebral micro-bleeds, or intracranial calcifications. In the following, some of these applications are discussed and summarized. For a comprehensive overview, see [3].

### 12.3.1 Stroke Imaging

SWI complements the imaging management of stroke patients [43], and is used to detect arterial thrombi [44, 45] or hemorrhages in the infarct area. It also serves to identify brain areas with impaired perfusion due to the presence of asymmetric hypointense cortical veins in the ischemic territory [12, 46–48], to visualize older micro-bleeds as an indicator of the vulnerability of the vascular system [49], or to assess the likelihood of a hemorrhagic transformation [50, 51]. Consequently, SWI has been recommended for inclusion in protocols for the evaluation of acute stroke [52, 53].

In addition to the extent of the diffusion–perfusion mismatch, the exact location of the thrombus is prognostically and therapeutically relevant. Diffusion and perfusion imaging is routinely applied to identify the area affected by ischemic

stroke, whereas for an exact localization of the intravascular thromboembolus, a time-of-flight (TOF) MR angiography is performed. In some cases, however, it may be challenging to identify the thrombus, particularly in downstream distal vascular branches. In this regard, SWI has been shown to be superior to TOF MR angiography in determining the location of the thromboembolus in form of hypo-intense signals within occluded arteries [44, 54, 55], which is also known as the susceptibility vessel sign (SVS) [43, 56].

Furthermore, SWI is a useful MRI sequence for the diagnosis of cerebral amyloid angiopathy (CAA) [57]. This disorder is characterized by an accumulation of amyloid deposits in the wall of intracranial vessels, which might result in numerous tiny cerebral microhemorrhages and eventually in lobar intracerebral hemorrhage. Microhemorrhages in CAA are particularly found in the cortico-subcortical region of the brain and are typically sparing the centrally located basal ganglia and the pons [58, 59]. This periphery dominated topographical distribution of microhemorrhages is in contrast to the more centrally located microhemorrhages which is described as a typical pattern in patients with hypertensive microangiopathy due to an elevated systemic blood pressure. Predominant locations of hypertension-associated microhemorrhages are the basal ganglia, the pons, and the cerebellar hemispheres [60, 61].

### 12.3.2 Tumor Imaging

Regarding tumor imaging, SWI plays an important role in the detection, grading, and staging of cerebral tumors [62–65]. Its sensitivity in delineating tumor vessels, the internal architecture of the tumors, or the detection of hemorrhage has been shown to be superior compared to conventional MRI sequences, including  $T_1$ , contrast-enhanced  $T_1$ ,  $T_2$ ,  $T_2^*$ , FLAIR, PD-weighted, and diffusion-weighted imaging (DWI) [9, 66–68] (Figs. 12.5 and 12.6). High-pass-filtered phase images, for instance, can better depict intratumoral calcification in oligodendrogliomas than conventional MR images [69].

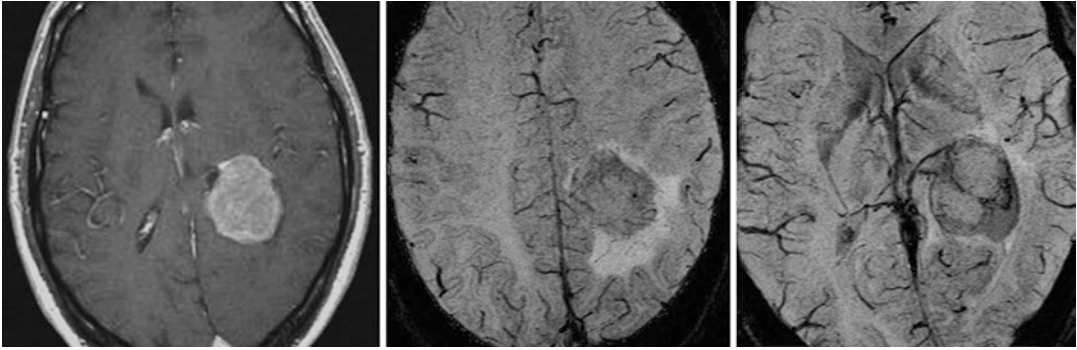


**Fig. 12.5** Glioblastoma multiforme. Contrast-enhanced T<sub>1</sub>-weighted image (*left*) and SWI images of the tumor (*middle and right*). Whereas the T<sub>1</sub>-weighted, contrast-enhanced image only shows some peripheral enhancement, the SWI images clearly show large veins at the periphery of the tumor as well as interior vessels. In addition,

they also show the edema surrounding the tumor. (Adapted from Reichenbach JR and Haacke EM. High-resolution BOLD venographic imaging: a window into brain function. *NMR in Biomedicine* 2001;14:452–467, reproduced with permission)

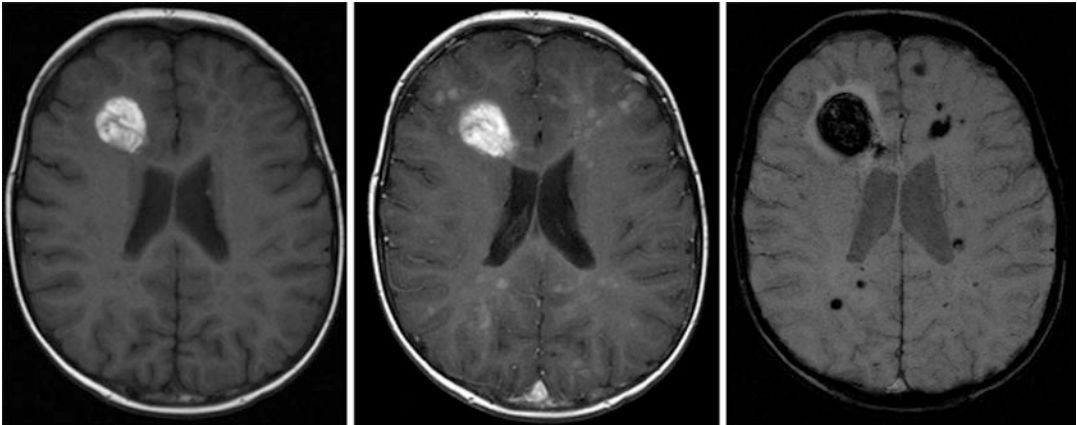


**Fig. 12.6** Metastatic CNS neuroblastoma. 4-year-old patient with neuroblastoma stage 4 and metastases in liver, lung, and bone. T<sub>1</sub>-weighted spin-echo image (*left*) shows a prominent lesion frontal right. After administra-

tion of contrast agent, demarcation of multiple, disseminated lesions (*middle*). The SWI image shows pronounced susceptibility effects due to multiple hemorrhages

Due to the pronounced heterogeneity of some brain tumors, histopathology may not always bring forth a definite diagnosis. In such cases, a complementary SWI can provide further valuable information on tumor grading [70, 71]. Particularly, the so-called intra-tumoral susceptibility signal (ITSS), which refers to linear or dot-like areas of low signal within the tumor, with or without conglomeration, seen on non-contrast enhanced SWI, appears to be a promising marker for the grading of gliomas [72] or the differentia-

tion between glioblastoma and primary CNS lymphoma [73]. Since the morphological patterns of ITSS have been shown to correlate with the degree of neo-angiogenesis, necrosis, and CBV, ITSS supports assessment of tumor grade and is an important indicator during surveillance of tumor progression or malignant transformation [64, 72]. Contrast-enhanced SWI (CE-SWI) has shown improved delineation of the highly vascularized peripheral tumoral invasion zone in high-grade glioma, offering more information by



delineating additional contrast-induced phase shifts [63, 74].

Furthermore, SWI has relevance in the distinction between brain abscesses and necrotic glioblastomas [75] and the classification of different types of brain metastases [76].

### 12.3.3 Traumatic Brain Injury (TBI)

Traumatic brain injury (TBI) is a heterogeneous pathology that usually results from a violent blow or jolt to the head. Often it is associated with (micro)hemorrhages that result from injuries of small vessels, particularly in patients with diffuse axonal injury (DAI) of major white matter tracts, at the junction of gray and white matter [77]. Characteristic for DAI is punctuate hemorrhages in the deep subcortical white matter, which are not routinely visible on CT or on the images of conventional MRI sequences, and whose presence and location appear to correlate with specific neuropsychological deficits [78–81].

SWI has demonstrated greater sensitivity than CT and conventional MRI techniques in the detection of such trauma-related (micro)hemorrhages (Fig. 12.7) [82–84]. Furthermore, as shown by a recent study in mild TBI patients, the presence of microbleeds detected by SWI was associated with worse cognitive outcome and persistent post-concussion syndrome, while DTI was not predictive of neuropsychological outcome in the acute phase [85]. SWI has particularly helped to better understand the different kinds of distribution of hemorrhages in trauma as well as to assess their persistence during follow-up. It also facilitates detection of otherwise invisible brain injuries that may help to explain the impairment of the patient and potentially predict outcome. This is of particular interest in comatose patients for whom it may sometimes be challenging to understand their acute condition based on conventional imaging findings, while SWI is able to identify the location of the hemorrhages (e.g., brain stem) that might then explain why the patient remains in a coma.

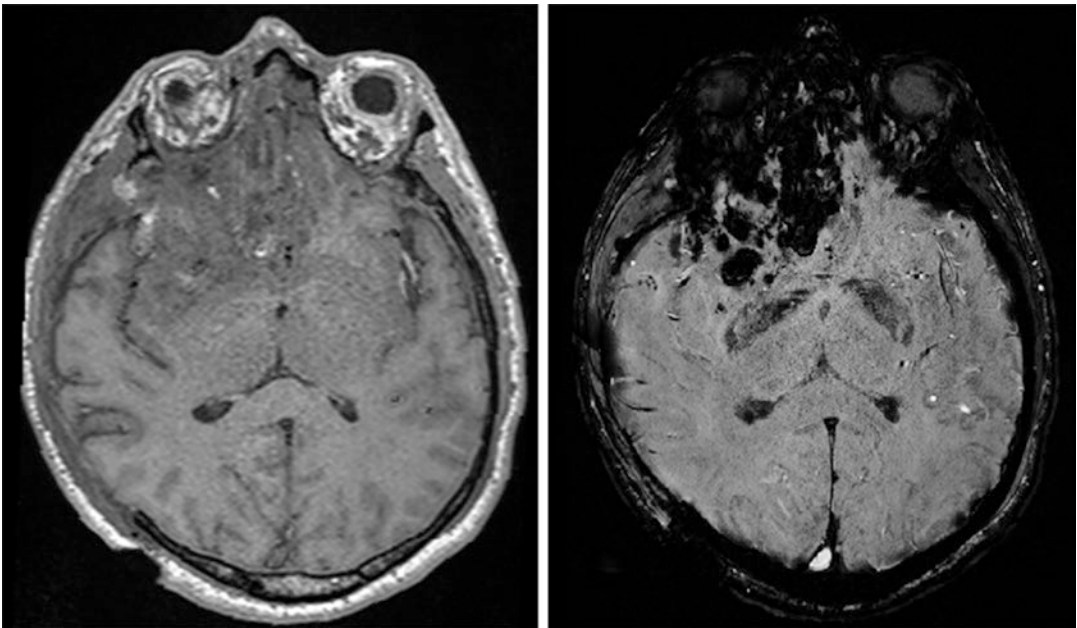


**Fig. 12.7** Traumatic brain injury (TBI). A 62-year-old patient with severe contusion. Due to its high sensitivity against paramagnetic blood breakdown products, the

extent of the hemorrhage can be better assessed with SWI (*right*) compared to images of a conventional gradient-echo sequence (*left*)

### 12.3.4 Vascular Malformation

The sensitivity of SWI for deoxyhemoglobin makes it superior for detecting and monitoring many slow-flow vascular malformations [86, 87], such as venous anomalies, cavernous malformations, telangiectasias, or the subtle changes in the brain associated with the Sturge–Weber syndrome [88].

The potential of SWI for improved detection of small vein abnormalities in Sturge–Weber syndrome, which is a rare congenital neurocutaneous disorder, typically manifested in children and eventually causing atrophy and calcifications, was demonstrated first in an infant whose initial conventional MRI, including contrast agent administration, revealed no definite abnormalities, whereas SWI detected abnormal transmedullary veins [89]. Characteristic features of the disease include abnormal gyral calcifications, abnormal deep venous collateral, and impaired venous outflow as well as unilateral hemispheric involvement.

Developmental venous anomalies (DVA), also known as cerebral venous angiomas or cerebral venous malformations, are the most common cerebral vascular malformation found on autopsy studies, and they are often encountered as incidental findings on neuroimaging studies [90]. Often invisible with conventional imaging, although sometimes better seen with contrast agent administration, they are very pronounced on SWI, thus obviating the need for contrast-enhanced MRI sequences [91].

As regards cerebral cavernous malformations (CCM), which are low-flow focal vascular abnormalities, histologically characterized as closely packed thin-walled vessels filled with blood at different stages of thrombosis, recent work demonstrated superior sensitivity of SWI in detecting the familial form of the disease, compared to conventional  $T_2$ -weighted spin-echo and  $T_2^*$ -weighted gradient-echo MR sequences [92, 93]. More specifically, SWI was able to identify two different SWI patterns in the CCM-associated cerebral venous angioarchitec-

ture that occur in the sporadic or familial form of the disease [94]. Image characteristics of cortical cavernous malformations include their popcorn-like appearance due to calcification and bleeding as well as their hypointense rim caused by the presence of hemosiderin.

### 12.3.5 Multiple Sclerosis (MS)

Multiple sclerosis (MS) is the most common inflammatory demyelinating disease of the central nervous system (CNS). Its radiological hallmarks are focal demyelinated hyperintense white matter (WM) lesions on  $T_2$ -weighted MRI; however, diffuse changes of the non-lesional WM have been reported as well, as detected by proton MR spectroscopy [95], magnetization transfer ratio, myelin water imaging [96], or  $R_2^*$ -mapping in combination with diffusion tensor imaging (DTI). Susceptibility-weighted imaging (SWI) has demonstrated high sensitivity for detecting iron-containing tissue and small veins due to their paramagnetic properties. With respect to the latter, SWI has gained in importance in MS due to its ability to visualize small veins within MS lesions [97–99]. Several studies showed that a substantial proportion (>40%) of MS lesions contain a central vein [100–102].

Application of contrast-enhanced SWI with gadolinium-based agents may facilitate the detection of central veins that may otherwise not be visible with the same SWI sequence acquired before CM injection [103], but may be also beneficial in detecting blood–brain barrier dysfunction in MS plaques, as demonstrated in a recent study [104].

Investigation of the iron content in the basal ganglia, pulvinar, and thalamus in patients with MS revealed a clear separation between healthy subjects and patients based on phase analyses of SWI data [105, 106]. In a group of 122 healthy volunteers 13% and in 52 patients with MS 65% showed an iron-weighting factor larger than three standard deviations from the normal mean. The results for patients under 40 years were even

more impressive. In these groups, only 1% of healthy volunteers, but 67% of patients with relapsing-remitting MS (RRMS) showed abnormally high levels of iron.

Ultrahigh field (7 T) SWI appears quite promising for assessing multiple sclerosis due to the increased signal intensity and enhanced susceptibility effects [107] and has gained increasing attention in recent years [108–111].

### 12.3.6 Neurodegenerative Disorders

Increased iron levels in the CNS beyond deposition with normal aging are encountered in a variety of neurodegenerative diseases [112], such as Alzheimer's disease (AD) [113–116], Parkinson's disease (PD) [117–119], multiple sclerosis (MS) [120], amyotrophic lateral sclerosis (ALS) [121, 122], Huntington's disease [123], and Friedreich's ataxia [124]. Iron accumulation affects mainly the basal ganglia regions, such as globus pallidus (GP) and substantia nigra (SN), but can also occur in other regions such as the cortex and cerebellum.

Due to its exquisite sensitivity to iron-containing paramagnetic compounds, SWI is well suited for in vivo detection and analysis and may help to predict disease progression and treatment outcome [125–129]. More recently, the loss of the so-called swallow-tail sign in the substantia nigra has been proposed as a diagnostic marker of Parkinson's disease, which raised the question whether this sign can be reliably detected with SWI [130]. Subsequent work revealed that the work-up of early-stage parkinsonism based on the swallow-tail sign requires an optimized high-resolution SWI protocol [131] and that ultrahigh field investigations are advantageous in terms of reliability [132–134].

### 12.3.7 Calcifications

Diamagnetic compounds, such as bone minerals or dystrophic calcifications, lead to signal drop-out on magnitude images of SWI. However, these

compounds can be differentiated by their opposite appearance on phase images when compared to paramagnetic compounds [135]. As stated before, it is thus advisable to set a reference for interpreting the phase image by comparing an area of known calcification, such as the pineal gland or the choroid plexus, with the diamagnetic lesion in question.

Several studies indicated that SWI can play a pivotal role in the detection of intracranial calcifications and chronic microbleeds as well as in resolving ambiguity in their diagnosis [136–139]. In the assessment of brain tumors, calcification is considered to be a very important indicator [140, 141], as the differential diagnosis may be confined to those lesions that often have intratumoral calcification, such as oligodendrogliomas, craniopharyngiomas, meningiomas, pineal gland tumors, and ependymomas [69, 142].

Extensive calcifications of the basal ganglia, as observed, for example, in the case of Fahr's disease, a well-defined rare neurodegenerative disease characterized by idiopathic bilateral symmetric extensive striopallidodentate calcifications, are well recognized on SWI images [143–145].

The results of a recent meta-analysis [146] on the diagnostic performance of susceptibility-based MRI for the detection of calcifications in brain and body soft tissues suggest that SWI is a reliable method for detecting calcifications with an accuracy close to CT.

## 12.4 Practical Considerations and Limitations

Despite its technical robustness, there are a few issues that should be kept in mind when applying SWI. Because the phase information is essential, it is important to reconstruct phase properly from the complex MRI data. Since the phase of MR data is only defined within a  $2\pi$ -range, aliasing occurs when phase exceeds  $2\pi$ , which produces so-called phase wraps. Since the original phase is corrected by removing spatially slowly varying

phase effects during the SWI processing, the resulting phase information may incorrectly reflect the susceptibility of the material or lesion, and the processing may even remove some of the physiologically or pathophysiologically relevant phase information from larger anatomic structures. In such cases, it may be helpful to examine the phase in the periphery of the lesion to draw corresponding conclusions about the sign of the susceptibility.

In standard SWI processing, the low spatial frequencies of the bulk phase shifts are removed by applying a homodyne high-pass filter, which works by dividing the original complex image by a low-pass Fourier-filtered image at a specific cutoff frequency of a fixed size Hamming or Hann window. The kernel size of the homodyne filter is typically restricted to  $64 \times 64$  (in case of a  $512 \times 512$  matrix acquired) to avoid adverse effects.

Unwanted or confounding artifacts on SWI images may be associated with air/bone-tissue interfaces, such as areas adjacent to the temporal bone and sinuses [147], as well as uncompensated blood flow, which may cause remnant flow-induced phase components [22]. In addition, the blooming artifact, a useful sign for detecting sources of field inhomogeneity, may sometimes lead to extreme tissue signal cancellation and loss of anatomical borders. Moreover, it should also be considered that the nonlocal phase effects in SWI and phase images depend on the geometry of the susceptibility source. Comparison of phase between subjects can thus be problematic due to this dependency, which may become particularly troublesome when trying, for instance, to relate the phase directly to the iron content. Inferring nonheme iron content from an assignment of a given phase change in a specific tissue may be misleading as it neglects, besides geometry, the possibility that

part of this phase shift may also stem from heme iron. Parts of these problems are overcome by quantitative susceptibility mapping (see below).

Another issue regarding the venous contrast associated with SWI scans is anesthesia. Initial evidence of poor visualization of venous anatomy was reported in pediatric patients under anesthesia (2–3% sevoflurane in oxygen) [148], which was attributed to slight decreases of the regional oxygen extraction fraction (rOEF) induced by the anesthetic compared to awake patients. In a subsequent study encompassing 108 SWI pediatric examinations with different depth of anesthesia (propofol, 150–300  $\mu\text{g}/\text{kg}/\text{min}$ ) [149], it was concluded that the source for the venous contrast variations were most likely CBF changes induced by the anesthesia. Apart from this and along more general lines, exceptional flow conditions should thus be kept in mind when interpreting SW images in patients with unusual findings [150].

In clinical applications of SWI it is often tacitly assumed that blood products of all ages show a hypointense image signal due to the presence of paramagnetic deoxyhemoglobin and hemoglobin degradation products, such as hemosiderin. As pointed out recently [151], a commonly encountered example of a “ $T_1$  shine through” effect on SWI is a central hyperintense signal in late subacute intracerebral hematoma [152] due to the presence of a high concentration of methemoglobin at the center of the hematoma. This may indeed result in a remarkable SWI hyperintensity due to  $T_1$ -relaxivity effects which, if properly taken into account, may, however, be also used to advantage in diagnoses.

One significant limitation of SWI is, as already mentioned, the fact that the magnetic field patterns reflected in phase images and caused by the local susceptibility distributions

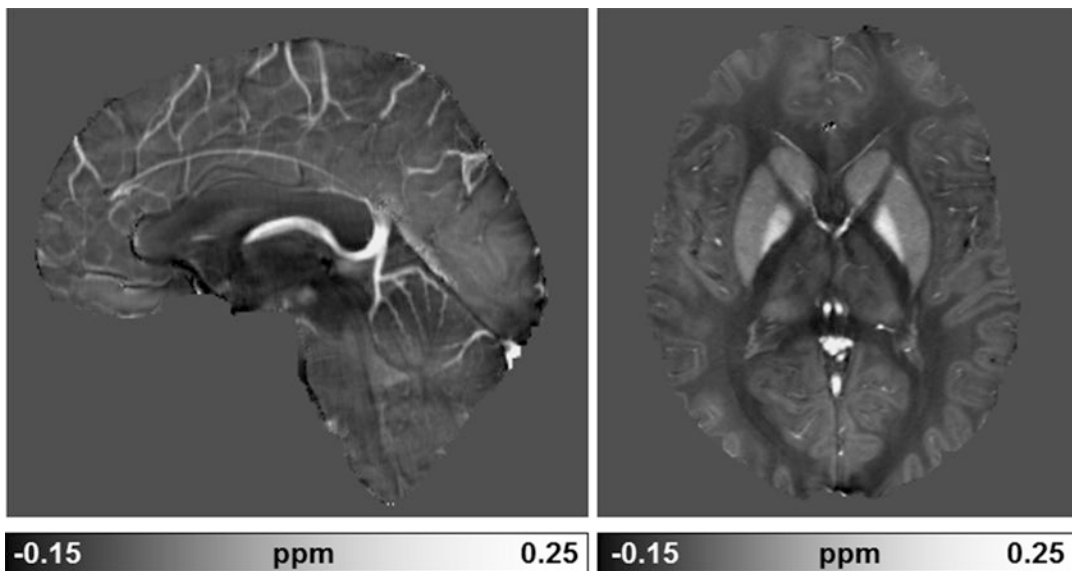


**Fig. 12.8** Quantitative susceptibility mapping (QSM). Maps of the susceptibility distribution in the human brain in sagittal (*left*) and transverse view (*right*). The maps were calculated by solving the intricate inverse problem of deriving the magnetic susceptibility of brain tissue from the measured phase distribution acquired with

gradient-echo-based sequences. Bright areas and structures on these maps correspond to more paramagnetic brain areas, such as venous vessels or iron-laden parts of the basal ganglia, whereas more hypodense areas indicate more diamagnetic tissues, such as white matter structures

are nonlocal in nature. Consequently, phase patterns do not necessarily reflect the local anatomical structures correctly, and the resulting contrast seen on the phase images may furthermore depend on the orientation of the object or anatomic structure in relation to the main magnetic field. Caution should therefore be exercised when relating phase contrast to brain anatomy or assessment of lesions. A more recently developed method to overcome this limitation is quantitative susceptibility mapping (QSM), which also utilizes phase information, but additionally solves the magnetic field to susceptibility source inverse problem and generates a three-dimensional susceptibility distribution (Fig. 12.8) [153].

## 12.5 Future Directions and Summary

Quantitative susceptibility mapping (QSM) is certainly the most important and promising development that evolved more recently from SWI. As stated, QSM aims to recover the susceptibility distribution of human tissue from the measured local field that can mathematically be described by a convolution of the susceptibility distribution with the magnetic field generated by a magnetic unit dipole. This inverse problem, however, is ill-posed due to the presence of zeros on a cone in the Fourier representation of the unit dipole kernel. Several methods have been developed over the years to overcome this prob-

lem and to mitigate the associated artifacts in the reconstructed susceptibility maps, which rely either on repeated measurements of the object after having been rotated with respect to the magnetic field and combining data [154] or, in case of single orientation imaging, on direct and fast  $k$ -space thresholding [155–157], or iterative image-space based regularization methods [158–163]. With regularization one seeks to incorporate a priori knowledge into the solution process, such as, e.g., amount or type of noise, smoothness or sparsity of the solution, or restrictions on the values the solution may take on, which requires the choice of one or more regularization parameters. For recent reviews of QSM, see [21, 24, 164–166].

QSM was rapidly adopted by the MRI research community and consistently applied to the same clinical fields of application as SWI and beyond. This transition from qualitative SWI to quantitative susceptibility mapping appeared more or less seamless since the input data of SWI and QSM are both based on gradient-echo acquisitions and can be used in both reconstructions. In this context, interesting approaches have been proposed to use susceptibility maps to generate masks that are used to create so-called true susceptibility-weighted images (tSWI) that overcome the problems of the phase dependence on the orientation and geometry or shape of the object [167–169], and at the same time allow, for example, quantitative analysis of iron content or oxygen saturation in venous vessels. Efforts have now been made to integrate QSM into the clinical setting for clinical and neurosurgical purposes on a larger scale in a wide range of pathophysiological conditions, including glioma, ischemic stroke, and multiple sclerosis [170–172].

One of the newest and most dynamic developments is the application of deep learning algorithms to replace conventional iterative methods for solving the inverse problem of QSM and directly invert the magnetic dipole kernel convolution by training a deep convolutional neural network [173–175]. The use of deep learning approaches has also been proposed in the case of SWI in connection with the detection of cerebral microbleeds [176] as well as vein segmentation [177].

Since SWI and QSM require relatively long echo times to accrue sufficient phase contrast, the acquisition times of the 3D gradient echo acquisition are typically also long. This, in turn, may lead to major motion artifacts, less patient compliance, or even patient anxiety. Recent research work indicates that highly accelerated 3D imaging with wave-CAIPI sequences (controlled aliasing in parallel imaging) [178] or simultaneous time-interleaved multislice (STIMS) echo-shift techniques [179] may lift this limitation while providing comparable performance in diagnosing clinical pathologies [180].

In summary, susceptibility-weighted imaging (SWI) has matured into an indispensable neuroimaging technique that has become well-established and provides clinically useful and unique information that is complementary to conventional MRI sequences. Through post-processed quantitative susceptibility mapping (QSM), SWI sequences allow the quantification of magnetic susceptibilities and overcome intrinsic limitations of SWI. Thus, magnetic susceptibility has gained an important place in neuroimaging, providing substantial and unique insight into normal brain tissue and its diseased conditions by allowing to evaluate compounds that alter the magnetic field in the brain.

## 12.6 Clinical Case (Fig. 12.9)

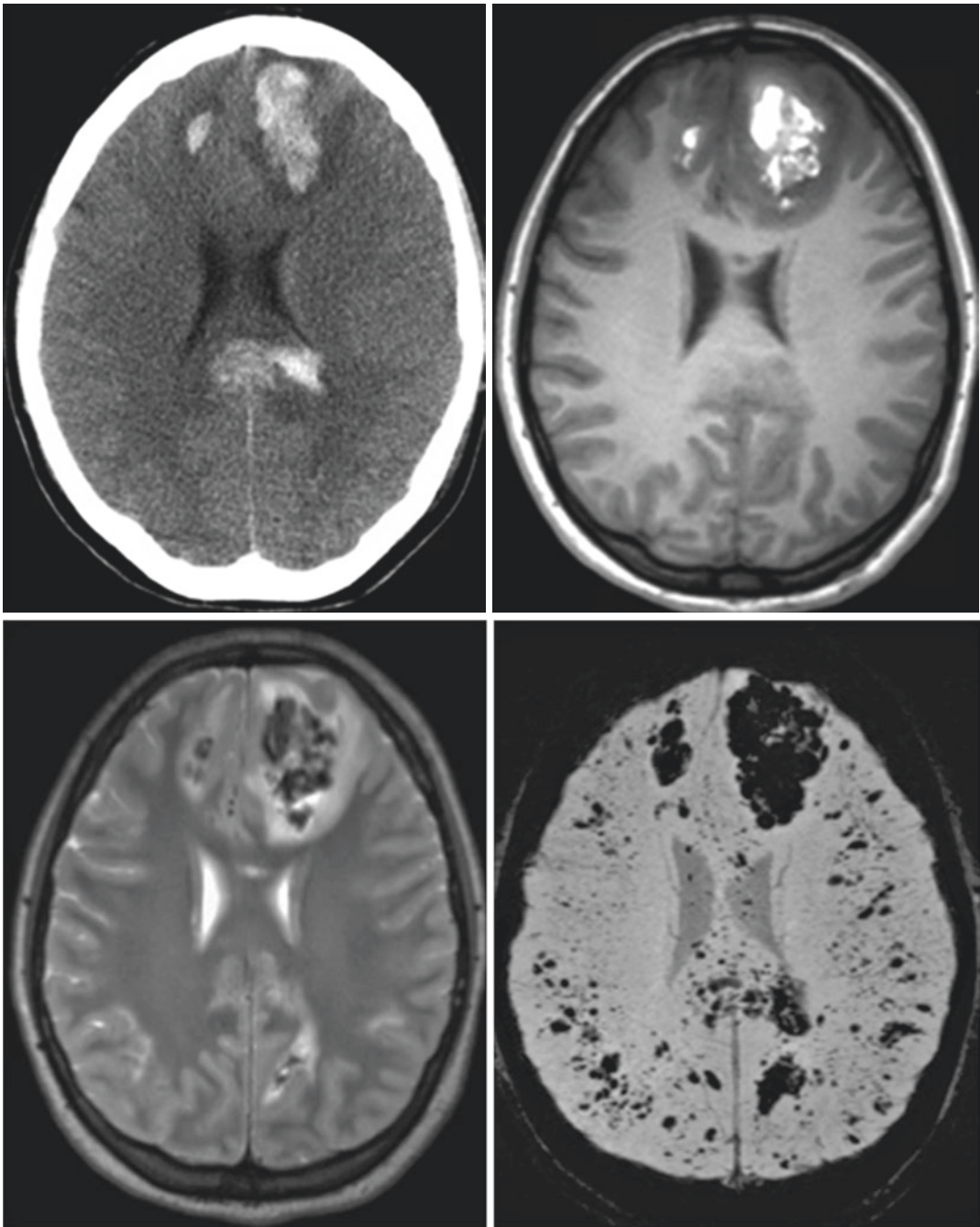


**Fig. 12.9** Traumatic brain injury (TBI). Images from a 16-year-old patient involved in a motor vehicle accident show large hemorrhagic contusions in the frontal lobes on CT (*upper left*), T<sub>1</sub>-weighted image (*upper right*), T<sub>2</sub>-weighted image (*lower left*), and SWI (*lower right*).

Widespread traumatic micro-hemorrhages throughout the gray–white matter junction and corpus callosum are only visible on SWI. (Courtesy of Dr. Karen A. Tong, Loma Linda University Health, Loma Linda, CA 92354, USA)

## References

- Haacke EM, Xu Y, Cheng YC, Reichenbach JR. Susceptibility weighted imaging (SWI). *Magn Reson Med*. 2004;52(3):612–8.
- Haacke EM, Mittal S, Wu Z, Neelavalli J, Cheng YC. Susceptibility-weighted imaging: technical aspects and clinical applications, part 1. *AJNR Am J Neuroradiol*. 2009;30:19–30.
- Haacke EM, Reichenbach JR, editors. *Susceptibility weighted imaging in MRI. Basic concepts and clinical applications*. Hoboken, NJ: Wiley-Blackwell; 2011, 743 pp.
- Liu S, Buch S, Chen Y, Choi HS, Dai Y, Habib C, Hu J, Jung JY, Luo Y, Utraiainen D, Wang M, Wu D, Xia S, Haacke EM. Susceptibility-weighted imaging: current status and future directions. *NMR Biomed*. 2017;30(4):e3552. <https://doi.org/10.1002/nbm.3552>.
- Reichenbach JR, Venkatesan R, Yablonskiy DA, Thompson MR, Lai S, Haacke EM. Theory and application of static field inhomogeneity effects in gradient-echo imaging. *J Magn Reson Imaging*. 1997;7(2):266–79.
- Heyn C, Alcaide-Leon P, Bharatha A, Sussman MS, Kucharczyk W, Mandell DM. Susceptibility-weighted imaging in neurovascular disease. *Top Magn Reson Imaging*. 2016;25(2):63–71.
- Robinson RJ, Bhuta S. Susceptibility-weighted imaging of the brain: current utility and potential applications. *J Neuroimaging*. 2011;21(4):e189–204.
- Sehgal V, Delproposito Z, Haacke EM, Tong KA, Wycliffe N, Kido DK, Xu Y, Neelavalli J, Haddar D, Reichenbach JR. Clinical applications of neuroimaging with susceptibility-weighted imaging. *J Magn Reson Imaging*. 2005;22(4):439–50.
- Sehgal V, Delproposito Z, Haddar D, Haacke EM, Sloan AE, Zamorano LJ, Barger G, Hu J, Xu Y, Prabhakaran KP, Elangovan IR, Neelavalli J, Reichenbach JR. Susceptibility-weighted imaging to visualize blood products and improve tumor contrast in the study of brain masses. *J Magn Reson Imaging*. 2006;24(1):41–51.
- Reichenbach JR, Venkatesan R, Schillinger DJ, Kido DK, Haacke EM. Small vessels in the human brain: MR venography with deoxyhemoglobin as an intrinsic contrast agent. *Radiology*. 1997;204(1):272–7.
- Krishnan AS, Lansley JA, Jäger HR, Mankad K. New vistas in clinical practice: susceptibility-weighted imaging. *Quant Imaging Med Surg*. 2015;5(3):448–52.
- Mittal S, Wu Z, Neelavalli J, Haacke EM. Susceptibility-weighted imaging: technical aspects and clinical applications, part 2. *AJNR Am J Neuroradiol*. 2009;30:232–52.
- Skalski KA, Kessler AT, Bhatt AA. Hemorrhagic and non-hemorrhagic causes of signal loss on susceptibility-weighted imaging. *Emerg Radiol*. 2018;25(6):691–701.
- Thomas B, Somasundaram S, Thamburaj K, Kesavadas C, Gupta AK, Bodhey NK, Kapilamoorthy TR. Clinical applications of susceptibility weighted MR imaging of the brain—a pictorial review. *Neuroradiology*. 2008;50(2):105–16.
- Schenck JF. The role of magnetic susceptibility in magnetic resonance imaging: MRI magnetic compatibility of the first and second kinds. *Med Phys*. 1996;23(6):815–50.
- Duyn JH, Schenck J. Contributions to magnetic susceptibility of brain tissue. *NMR Biomed*. 2017;30(4):e3546. <https://doi.org/10.1002/nbm.3546>.
- Chu SC, Xu Y, Balschi JA, Springer CS Jr. Bulk magnetic susceptibility shifts in NMR studies of compartmentalized samples: use of paramagnetic reagents. *Magn Reson Med*. 1990;13(2):239–62.
- Hagberg GE, Welch EB, Greiser A. The sign convention for phase values on different vendor systems: definition and implications for susceptibility-weighted imaging. *Magn Reson Imaging*. 2010;28(2):297–300.
- Rauscher A, Sedlacik J, Deistung A, Mentzel HJ, Reichenbach JR. Susceptibility weighted imaging: data acquisition, image reconstruction and clinical applications. *Z Med Phys*. 2006;16:240–50.
- Denk C, Rauscher A. Susceptibility weighted imaging with multiple echoes. *J Magn Reson Imaging*. 2010;31(1):185–91.
- Liu C, Li W, Tong KA, Yeom KW, Kuzminski S. Susceptibility-weighted imaging and quantitative susceptibility mapping in the brain. *J Magn Reson Imaging*. 2015;42(1):23–41.
- Deistung A, Dittrich E, Sedlacik J, Rauscher A, Reichenbach JR. ToF-SWI: simultaneous time of flight and fully flow compensated susceptibility weighted imaging. *J Magn Reson Imaging*. 2009;29(6):1478–84.
- Xu Y, Haacke EM. The role of voxel aspect ratio in determining apparent vascular phase behavior in susceptibility weighted imaging. *Magn Reson Imaging*. 2006;24(2):155–60.
- Haacke EM, Liu S, Buch S, Zheng W, Wu D, Ye Y. Quantitative susceptibility mapping: current status and future directions. *Magn Reson Imaging*. 2015;33(1):1–25.
- Halefoglu AM, Yousem DM. Susceptibility weighted imaging: clinical applications and future directions. *World J Radiol*. 2018;10(4):30–45.
- Du YP, Jin Z. Simultaneous acquisition of MR angiography and venography (MRV). *Magn Reson Med*. 2008;59(5):954–8.
- Ye H, Hu J, Wu D, Haacke EM. Noncontrast-enhanced magnetic resonance angiography and venography imaging with enhanced angiography. *J Magn Reson Imaging*. 2013;38(6):1539–48.
- Deistung A. Susceptibility weighted imaging and quantitative susceptibility mapping at 3 Tesla and beyond. PhD Thesis, Technical University Ilmenau. 2013.
- Martínez-Santesteban FM, Swanson SD, Noll DC, Anderson DJ. Object orientation independence of susceptibility weighted imaging by using a sigmoid-type phase window. *Proc Int Soc Mag Reson Med*. 2006;14:2399.



30. Brainovich V, Sabatini U, Hagberg GE. Advantages of using multiple-echo image combination and asymmetric triangular phase masking in magnetic resonance venography at 3 T. *Magn Reson Imaging*. 2009;27(1):23–37.
31. Casciaro S, Bianco R, Franchini R, Casciaro E, Conversano F. A new automatic phase mask filter for high-resolution brain venography at 3 T: theoretical background and experimental validation. *Magn Reson Imaging*. 2010;28(4):511–9.
32. Quinn MP, Gati JS, Klassen LM, Lin AW, Bird JR, Leung SE, Menon RS. Comparison of multiecho post-processing schemes for SWI with use of linear and nonlinear mask functions. *AJNR Am J Neuroradiol*. 2014;35(1):38–44.
33. Reichenbach JR, Essig M, Haacke EM, Lee BC, Przetak C, Kaiser WA, Schad LR. High-resolution venography of the brain using magnetic resonance imaging. *MAGMA*. 1998;6(1):62–9.
34. Deistung A, Rauscher A, Sedlacik J, Stadler J, Witoszynskij S, Reichenbach JR. Susceptibility weighted imaging at ultrahigh magnetic field strengths: theoretical considerations and experimental results. *Magn Reson Med*. 2008;60(5):1155–68.
35. Duyn JH. MR susceptibility imaging. *J Magn Reson*. 2013;229:198–207.
36. Reichenbach JR, Barth M, Haacke EM, Klarhöfer M, Kaiser WA, Moser E. High-resolution MR venography at 3.0 Tesla. *J Comput Assist Tomogr*. 2000;24(6):949–57.
37. Ladd ME, Bachert P, Meyerspeer M, Moser E, Nagel AM, Norris DG, Schmitter S, Speck O, Straub S, Zaiss M. Pros and cons of ultra-high-field MRI/MRS for human application. *Prog Nucl Magn Reson Spectrosc*. 2018;109:1–50.
38. Ge Y, Barnes S, Heller S, Sodickson DK, Tang L, Haacke EM, Dai J, Grossman RI. Three-dimensional high resolution venography using susceptibility weighted imaging at 7 T. *Chin J Magn Reson Imaging*. 2010;1(2):83–93.
39. Geißler A, Fischmeister FP, Grabner G, Wurnig M, Rath J, Foki T, Matt E, Trattnig S, Beisteiner R, Robinson SD. Comparing the microvascular specificity of the 3- and 7-T BOLD response using ICA and susceptibility-weighted imaging. *Front Hum Neurosci*. 2013;7:474.
40. Koopmans PJ, Manniesing R, Niessen WJ, Viergever MA, Barth M. MR venography of the human brain using susceptibility weighted imaging at very high field strength. *MAGMA*. 2008;21(1–2):149–58.
41. Liu S, Brisset JC, Hu J, Haacke EM, Ge Y. Susceptibility weighted imaging and quantitative susceptibility mapping of the cerebral vasculature using ferumoxytol. *J Magn Reson Imaging*. 2018;47(3):621–33.
42. Moser E, Stahlberg F, Ladd ME, Trattnig S. 7-T MR— from research to clinical applications? *NMR Biomed*. 2012;25(5):695–716.
43. Hsu CC, Kwan GNC, Hapugoda S, Craigie M, Watkins TW, Haacke EM. Susceptibility weighted imaging in acute cerebral ischemia: review of emerging technical concepts and clinical applications. *Neuroradiol J*. 2017;30(2):109–19.
44. Radbruch A, Mucke J, Schweser F, Deistung A, Ringleb PA, Ziener CH, Roethke M, Schlemmer HP, Heiland S, Reichenbach JR, Bendszus M, Rohde S. Comparison of susceptibility weighted imaging and TOF-angiography for the detection of thrombi in acute stroke. *PLoS One*. 2013;8(5):e63459.
45. Weisstanner C, Gratz PP, Schroth G, Verma RK, Köchl A, Jung S, Arnold M, Gralla J, Zubler C, Hsieh K, Mordasini P, El-Koussy M. Thrombus imaging in acute stroke: correlation of thrombus length on susceptibility-weighted imaging with endovascular reperfusion success. *Eur Radiol*. 2014;24(8):1735–41.
46. Chen CY, Chen CI, Tsai FY, Tsai PH, Chan WP. Prominent vessel sign on susceptibility-weighted imaging in acute stroke: prediction of infarct growth and clinical outcome. *PLoS One*. 2015;10(6):e0131118.
47. Xia S, Utraiainen D, Tang J, Kou Z, Zheng G, Wang X, Shen W, Haacke EM, Lu G. Decreased oxygen saturation in asymmetrically prominent cortical veins in patients with cerebral ischemic stroke. *Magn Reson Imaging*. 2014;32(10):1272–6.
48. Yuan T, Ren G, Quan G, Gao D. Fewer peripheral asymmetrical cortical veins is a predictor of favorable outcome in MCA infarctions with SWI-DWI mismatch. *J Magn Reson Imaging*. 2018;48(4):964–70.
49. Nighoghossian N, Hermier M, Adeleine P, Blanc-Lasserre K, Derex L, Honnorat J, Philippeau F, Dugor JF, Froment JC, Trouillas P. Old microbleeds are a potential risk factor for cerebral bleeding after ischemic stroke: a gradient-echo T2\*-weighted brain MRI study. *Stroke*. 2002;33(3):735–42.
50. Annan M, Gaudron M, Cottier JP, Cazals X, Dejobert M, Corcia P, Bertrand P, Mondon K, de Toffol B, Debais S. Functional outcome of hemorrhagic transformation after thrombolysis for ischemic stroke: a prospective study. *Cerebrovasc Dis Extra*. 2015;5(3):103–6.
51. Lu J, Li YH, Li YD, Li MH, Zhao JG, Chen SW. The clinical value of antiplatelet therapy for patients with hemorrhage after thrombolysis based on susceptibility-weighted imaging: a prospective pilot study. *Eur J Radiol*. 2012;81(12):4094–8.
52. Mane RS, Gowda AK, Kamte SG, Mohan B, Hedna V, Zohra F, Krishnamurthy U, Kumar AA. Should susceptibility-weighted imaging be included in the protocol for evaluation of acute ischemic stroke patients? *West Afr J Radiol*. 2016;23:59–63.
53. Vercluyte S, Fisch O, Colas L, Vanaerde O, Toledano M, Budzik JF. ASL and susceptibility-weighted imaging contribution to the management of acute ischaemic stroke. *Insights Imaging*. 2017;8(1):91–100.
54. Park MG, Yoon CH, Baik SK, Park KP. Susceptibility vessel sign for intra-arterial thrombus in acute posterior cerebral artery infarction. *J Stroke Cerebrovasc Dis*. 2015;24(6):1229–34.

55. Park MG, Oh SJ, Baik SK, Jung DS, Park KP. Susceptibility-weighted imaging for detection of thrombus in acute cardioembolic stroke. *J Stroke*. 2016;18(1):73–9.
56. Payabvash S, Benson JC, Taleb S, Rykken JB, Hoffman B, McKinney AM, Oswood MC. Susceptible vessel sign: identification of arterial occlusion and clinical implications in acute ischaemic stroke. *Clin Radiol*. 2017;72(2):116–22.
57. Haacke EM, DelProposto ZS, Chaturvedi S, Sehgal V, Tenzer M, Neelavalli J, Kido D. Imaging cerebral amyloid angiopathy with susceptibility-weighted imaging. *AJNR Am J Neuroradiol*. 2007;28(2):316–7.
58. Dierksen GA, Skehan ME, Khan MA, Jeng J, Nandigam RN, Becker JA, Kumar A, Neal KL, Betensky RA, Frosch MP, Rosand J, Johnson KA, Viswanathan A, Salat DH, Greenberg SM. Spatial relation between microbleeds and amyloid deposits in amyloid angiopathy. *Ann Neurol*. 2010;68(4):545–8.
59. Samarasekera N, Smith C, Al-Shahi Salman R. The association between cerebral amyloid angiopathy and intracerebral haemorrhage: systematic review and meta-analysis. *J Neurol Neurosurg Psychiatry*. 2012;83(3):275–81.
60. Fisher CM. Hypertensive cerebral hemorrhage. Demonstration of the source of bleeding. *J Neuropathol Exp Neurol*. 2003;62(1):104–7.
61. Pantoni L. Cerebral small vessel disease: from pathogenesis and clinical characteristics to therapeutic challenges. *Lancet Neurol*. 2010;9(7):689–701.
62. Baig MA, Klein JP, Mechtler LL. Imaging of brain tumors. *Continuum (Minneapolis)*. 2016;22(5, Neuroimaging):1529–52.
63. Hsu CC, Watkins TW, Kwan GN, Haacke EM. Susceptibility-weighted imaging of glioma: update on current imaging status and future directions. *J Neuroimaging*. 2016;26(4):383–90.
64. Li X, Zhu Y, Kang H, Zhang Y, Liang H, Wang S, Zhang W. Glioma grading by microvascular permeability parameters derived from dynamic contrast-enhanced MRI and intratumoral susceptibility signal on susceptibility weighted imaging. *Cancer Imaging*. 2015;15:4.
65. Mohammed W, Xunning H, Haibin S, Jingzhi M. Clinical applications of susceptibility-weighted imaging in detecting and grading intracranial gliomas: a review. *Cancer Imaging*. 2013;13:186–95.
66. Barth M, Nöbauer-Huhmann IM, Reichenbach JR, Mlynárik V, Schögl A, Matula C, Trattnig S. High-resolution three-dimensional contrast-enhanced blood oxygenation level-dependent magnetic resonance venography of brain tumors at 3 Tesla: first clinical experience and comparison with 1.5 Tesla. *Investig Radiol*. 2003;38(7):409–14.
67. Di Ieva A, Lam T, Alcaide-Leon P, Bharatha A, Montanera W, Cusimano MD. Magnetic resonance susceptibility weighted imaging in neurosurgery: current applications and future perspectives. *J Neurosurg*. 2015;123(6):1463–75.
68. Li C, Ai B, Li Y, Qi H, Wu L. Susceptibility-weighted imaging in grading brain astrocytomas. *Eur J Radiol*. 2010;75:e81–5.
69. Wu Z, Mittal S, Kish K, Yu Y, Hu J, Haacke EM. Identification of calcification with MRI using susceptibility-weighted imaging: a case study. *J Magn Reson Imaging*. 2009;29(1):177–82.
70. Di Ieva A, Göd S, Grabner G, Grizzi F, Sherif C, Matula C, Tschabitscher M, Trattnig S. Three-dimensional susceptibility-weighted imaging at 7T using fractal-based quantitative analysis to grade gliomas. *Neuroradiology*. 2013;55:35–40.
71. Saini J, Gupta PK, Sahoo P, Singh A, Patir R, Ahlawat S, Beniwal M, Thenarasu K, Santosh V, Gupta RK. Differentiation of grade II/III and grade IV glioma by combining “T1 contrast-enhanced brain perfusion imaging” and susceptibility-weighted quantitative imaging. *Neuroradiology*. 2018;60(1):43–50.
72. Park MJ, Kim HS, Jahng GH, Ryu CW, Park SM, Kim SY. Semiquantitative assessment of intratumoral susceptibility signals using non-contrast-enhanced high-field high-resolution susceptibility-weighted imaging in patients with gliomas: comparison with MR perfusion imaging. *AJNR Am J Neuroradiol*. 2009;30:1402–8.
73. Radbruch A, Wiestler B, Kramp L, Lutz K, Bäumer P, Weiler M, Roethke M, Sahn F, Schlemmer HP, Wick W, Heiland S, Bendszus M. Differentiation of glioblastoma and primary CNS lymphomas using susceptibility weighted imaging. *Eur J Radiol*. 2013;82(3):552–6.
74. Fahrendorf D, Schwindt W, Wölfer J, Jeibmann A, Kooijman H, Kugel H, Grauer O, Heindel W, Hesselmann V, Bink A. Benefits of contrast-enhanced SWI in patients with glioblastoma multiforme. *Eur Radiol*. 2013;23(10):2868–79.
75. Toh CH, Wei KC, Chang CN, Hsu PW, Wong HF, Ng SH, Castillo M, Lin CP. Differentiation of pyogenic brain abscesses from necrotic glioblastomas with use of susceptibility-weighted imaging. *AJNR Am J Neuroradiol*. 2012;33(8):1534–8.
76. Radbruch A, Graf M, Kramp L, Wiestler B, Floca R, Bäumer P, Roethke M, Stieltjes B, Schlemmer HP, Heiland S, Bendszus M. Differentiation of brain metastases by percentagewise quantification of intratumoral-susceptibility-signals at 3Tesla. *Eur J Radiol*. 2012;81(12):4064–8.
77. Liu J, Xia S, Hanks R, Wiseman N, Peng C, Zhou S, Haacke EM, Kou Z. Susceptibility weighted imaging and mapping of micro-hemorrhages and major deep veins after traumatic brain injury. *J Neurotrauma*. 2016;33(1):10–21.
78. Babikian T, Freier MC, Tong KA, Nickerson JP, Wall CJ, Holshouser BA, Burley T, Riggs ML, Ashwal S. Susceptibility weighted imaging: neuropsychologic outcome and pediatric head injury. *Pediatr Neurol*. 2005;33(3):184–94.
79. Huang YL, Kuo YS, Tseng YC, Chen DY, Chiu WT, Chen CJ. Susceptibility-weighted MRI in mild traumatic brain injury. *Neurology*. 2015;84(6):580–5.

80. Kou Z, Wu Z, Tong KA, Holshouser B, Benson RR, Hu J, Haacke EM. The role of advanced MR imaging findings as biomarkers of traumatic brain injury. *J Head Trauma Rehabil.* 2010;25(4):267–82.
81. Pavlovic D, Pekic S, Stojanovic M, Popovic V. Traumatic brain injury: neuropathological, neurocognitive and neurobehavioral sequelae. *Pituitary.* 2019;22(3):270–82.
82. Hunter JV, Wilde EA, Tong KA, Holshouser BA. Emerging imaging tools for use with traumatic brain injury research. *J Neurotrauma.* 2012;29(4):654–71.
83. Tong KA, Ashwal S, Holshouser BA, Shutter LA, Herigault G, Haacke EM, Kido DK. Hemorrhagic shearing lesions in children and adolescents with post-traumatic diffuse axonal injury: improved detection and initial results. *Radiology.* 2003;227:332–9.
84. Tong KA, Ashwal S, Holshouser BA, Nickerson JP, Wall CJ, Shutter LA, Osterdock RJ, Haacke EM, Kido D. Diffuse axonal injury in children: clinical correlation with hemorrhagic lesions. *Ann Neurol.* 2004;56(1):36–50.
85. Studerus-Germann AM, Gautschi OP, Bontempi P, Thiran JP, Daducci A, Romascano D, von Ow D, Hildebrandt G, von Hessling A, Engel DC. Central nervous system microbleeds in the acute phase are associated with structural integrity by DTI one year after mild traumatic brain injury: a longitudinal study. *Neurol Neurochir Pol.* 2018;52(6):710–9.
86. Gasparotti R, Pinelli L, Liserre R. New MR sequences in daily practice: susceptibility weighted imaging. A pictorial essay. *Insights Imaging.* 2011;2(3):335–47.
87. Lee BC, Vo KD, Kido DK, Mukherjee P, Reichenbach J, Lin W, Yoon MS, Haacke M. MR high-resolution blood oxygenation level-dependent venography of occult (low-flow) vascular lesions. *AJNR Am J Neuroradiol.* 1999;20(7):1239–42.
88. Hu J, Yu Y, Juhasz C, Kou Z, Xuan Y, Latif Z, Kudo K, Chugani HT, Haacke EM. MR susceptibility weighted imaging (SWI) complements conventional contrast enhanced T1 weighted MRI in characterizing brain abnormalities of Sturge-Weber Syndrome. *J Magn Reson Imaging.* 2008;28(2):300–7.
89. Mentzel HJ, Dieckmann A, Fitzek C, Brandl U, Reichenbach JR, Kaiser WA. Early diagnosis of cerebral involvement in Sturge-Weber syndrome using high-resolution BOLD MR venography. *Pediatr Radiol.* 2005;35:85–90.
90. Mooney MA, Zabramski JM. Developmental venous anomalies. *Handb Clin Neurol.* 2017;143:279–82.
91. Young A, Poretti A, Bosemani T, Goel R, Huisman TAGM. Sensitivity of susceptibility-weighted imaging in detecting developmental venous anomalies and associated cavernomas and microhemorrhages in children. *Neuroradiology.* 2017;59(8):797–802.
92. Dammann P, Barth ME, Zhu Y, Maderwald S, Schlamann M, Ladd ME, Sure U. Susceptibility weighted magnetic resonance imaging of cerebral cavernous malformations: prospects, drawbacks, and first experience at ultra-high field strength (7-Tesla) magnetic resonance imaging. *Neurosurg Focus.* 2010;29(3):E5.
93. Sparacia G, Speciale C, Banco A, Bencivinni F, Midiri M. Accuracy of SWI sequences compared to T2\*-weighted gradient echo sequences in the detection of cerebral cavernous malformations in the familial form. *Neuroradiol J.* 2016;29(5):326–35.
94. Dammann P, Wrede K, Zhu Y, Matsushige T, Maderwald S, Umutlu L, Quick HH, Hehr U, Rath M, Ladd ME, Felbor U, Sure U. Correlation of the venous angioarchitecture of multiple cerebral cavernous malformations with familial or sporadic disease: a susceptibility-weighted imaging study with 7-Tesla MRI. *J Neurosurg.* 2017;126(2):570–7.
95. Tisell A, Leinhard OD, Wärntjes JB, Aalto A, Smedby Ö, Landtblom AM, Lundberg P. Increased concentrations of glutamate and glutamine in normal-appearing white matter of patients with multiple sclerosis and normal MR imaging brain scans. *PLoS One.* 2013;8(4):e61817.
96. Laule C, Vavasour IM, Moore GR, Oger J, Li DK, Paty DW, MacKay AL. Water content and myelin water fraction in multiple sclerosis. A T2 relaxation study. *J Neurol.* 2004;251(3):284–93.
97. Maggi P, Absinta M, Grammatico M, Vuolo L, Emmi G, Carlucci G, Spagni G, Barilaro A, Repice AM, Emmi L, Prisco D, Martinelli V, Scotti R, Sadeghi N, Perrotta G, Sati P, Dachy B, Reich DS, Filippi M, Massacesi L. Central vein sign differentiates multiple sclerosis from central nervous system inflammatory vasculopathies. *Ann Neurol.* 2018;83(2):283–94.
98. Sati P, Oh J, Constable RT, Evangelou N, Guttmann CR, Henry RG, Klawiter EC, Mainero C, Massacesi L, McFarland H, Nelson F, Ontaneda D, Rauscher A, Rooney WD, Samaraweera AP, Shinohara RT, Sobel RA, Solomon AJ, Treaba CA, Wuerfel J, Zivadinov R, Sicotte NL, Pelletier D, Reich DS, NAIMS Cooperative. The central vein sign and its clinical evaluation for the diagnosis of multiple sclerosis: a consensus statement from the North American Imaging in Multiple Sclerosis Cooperative. *Nat Rev Neurol.* 2016;12:714–22.
99. Tan IL, van Schijndel RA, Pouwels PJ, van Walderveen MA, Reichenbach JR, Manoliu RA, Barkhof F. MR venography of multiple sclerosis. *AJNR Am J Neuroradiol.* 2000;21(6):1039–42.
100. Kau T, Taschwer M, Deutschmann H, Schönfelder M, Weber JR, Hausegger KA. The “central vein sign”: is there a place for susceptibility weighted imaging in possible multiple sclerosis? *Eur Radiol.* 2013;23(7):1956–62.
101. Luo J, Yablonskiy DA, Hildebolt CF, Lancia S, Cross AH. Gradient echo magnetic resonance imaging correlates with clinical measures and allows visualization of veins within multiple sclerosis lesions. *Mult Scler.* 2014;20(3):349–55.

102. Sparacia G, Agnello F, Gambino A, Sciortino M, Midiri M. Multiple sclerosis: high prevalence of the 'central vein' sign in white matter lesions on susceptibility-weighted images. *Neuroradiol J*. 2018;31(4):356–61.
103. Maggi P, Mazzoni LN, Moretti M, Grammatico M, Chiti S, Massacesi L. SWI enhances vein detection using gadolinium in multiple sclerosis. *Acta Radiol Open*. 2015;4(3):2047981614560938.
104. do Amaral LLF, Fragoso DC, Nunes RH, Littig IA, da Rocha AJ. Gadolinium-enhanced susceptibility-weighted imaging in multiple sclerosis: optimizing the recognition of active plaques for different MR imaging sequences. *AJNR Am J Neuroradiol*. 2019;40(4):614–9.
105. Haacke EM, Makki M, Ge Y, Maheshwari M, Sehgal V, Hu J, Selvan M, Wu Z, Latif Z, Xuan Y, Khan O, Garbern J, Grossman RI. Characterizing iron deposition in multiple sclerosis lesions using susceptibility weighted imaging. *J Magn Reson Imaging*. 2009;29(3):537–44.
106. Habib CA, Liu M, Bawany N, Garbern J, Krumbein I, Mentzel HJ, Reichenbach J, Magnano C, Zivadinov R, Haacke EM. Assessing abnormal iron content in the deep gray matter of patients with multiple sclerosis versus healthy controls. *AJNR Am J Neuroradiol*. 2012;33(2):252–8.
107. Rauscher A, Barth M, Herrmann KH, Witoszynskij S, Deistung A, Reichenbach JR. Improved elimination of phase effects from background field inhomogeneities for susceptibility weighted imaging at high magnetic field strengths. *Magn Reson Imaging*. 2008;26(8):1145–51.
108. Chawla S, Kister I, Wuerfel J, Brisset JC, Liu S, Sinnecker T, Dusek P, Haacke EM, Paul F, Ge Y. Iron and non-iron-related characteristics of multiple sclerosis and neuromyelitis optica lesions at 7T MRI. *AJNR Am J Neuroradiol*. 2016;37(7):1223–30.
109. Chawla S, Kister I, Sinnecker T, Wuerfel J, Brisset JC, Paul F, Ge Y. Longitudinal study of multiple sclerosis lesions using ultra-high field (7T) multiparametric MR imaging. *PLoS One*. 2018;13(9):e0202918.
110. Dal-Bianco A, Grabner G, Kronnerwetter C, Weber M, Höftberger R, Berger T, Auff E, Leutmezer F, Trattnig S, Lassmann H, Bagnato F, Hametner S. Slow expansion of multiple sclerosis iron rim lesions: pathology and 7 T magnetic resonance imaging. *Acta Neuropathol*. 2017;133(1):25–42.
111. Hosseini Z, Matusinec J, Rudko DA, Liu J, Kwan BYM, Salehi F, Sharma M, Kremenchutzky M, Menon RS, Drangova M. Morphology-specific discrimination between MS white matter lesions and benign white matter hyperintensities using ultra-high-field MRI. *AJNR Am J Neuroradiol*. 2018;39(8):1473–9.
112. Ndayisaba A, Kaindlstorfer C, Wenning GK. Iron in neurodegeneration—cause or consequence? *Front Neurosci*. 2019;13:180.
113. Hare DJ, Raven EP, Roberts BR, Bogeski M, Portbury SD, McLean CA, Masters CL, Connor JR, Bush AI, Crouch PJ, Doble PA. Laser ablation-inductively coupled plasma-mass spectrometry imaging of white and gray matter iron distribution in Alzheimer's disease frontal cortex. *NeuroImage*. 2016;137:124–31.
114. Smith MA, Harris PL, Sayre LM, Perry G. Iron accumulation in Alzheimer disease is a source of redox-generated free radicals. *Proc Natl Acad Sci U S A*. 1997;94:9866–8.
115. Wang D, Zhu D, Wei XE, Li YH, Li WB. Using susceptibility-weighted images to quantify iron deposition differences in amnesic mild cognitive impairment and Alzheimer's disease. *Neurol India*. 2013;61(1):26–34.
116. Ward RJ, Zucca FA, Duyn JH, Crichton RR, Zecca L. The role of iron in brain ageing and neurodegenerative disorders. *Lancet Neurol*. 2014;13:1045–60.
117. Barbosa JH, Santos AC, Tumas V, Liu M, Zheng W, Haacke EM, Salmon CE. Quantifying brain iron deposition in patients with Parkinson's disease using quantitative susceptibility mapping, R2 and R2\*. *Magn Reson Imaging*. 2015;33:559–65.
118. Griffiths PD, Dobson BR, Jones GR, Clarke DT. Iron in the basal ganglia in Parkinson's disease: an in vitro study using extended X-ray absorption fine structure and cryo-electron microscopy. *Brain*. 1999;122:667–73.
119. Liu Z, Shen HC, Lian TH, Mao L, Tang SX, Sun L, Huang XY, Guo P, Cao CJ, Yu SY, Zuo LJ, Wang XM, Chen SD, Chan P, Zhang W. Iron deposition in substantia nigra: abnormal iron metabolism, neuro-inflammatory mechanism and clinical relevance. *Sci Rep*. 2017;7(1):14973.
120. Bergsland N, Tavazzi E, Laganà MM, Baglio F, Cecconi P, Viotti S, Zivadinov R, Baselli G, Rovaris M. White matter tract injury is associated with deep gray matter iron deposition in multiple sclerosis. *J Neuroimaging*. 2017;27:107–13.
121. Oshiro S, Morioka MS, Kikuchi M. Dysregulation of iron metabolism in Alzheimer's disease, Parkinson's disease, and amyotrophic lateral sclerosis. *Adv Pharmacol Sci*. 2011;2011:378278.
122. Prell T, Hartung V, Tietz F, Penzlin S, Ilse B, Schweser F, Deistung A, Bokemeyer M, Reichenbach JR, Witte OW, Grosskreutz J. Susceptibility-weighted imaging provides insight into white matter damage in amyotrophic lateral sclerosis. *PLoS One*. 2015;10(6):e0131114.
123. Agrawal S, Fox J, Thyagarajan B, Fox JH. Brain mitochondrial iron accumulates in Huntington's disease, mediates mitochondrial dysfunction, and can be removed pharmacologically. *Free Radic Biol Med*. 2018;120:317–29.
124. Martelli A, Puccio H. Dysregulation of cellular iron metabolism in Friedreich ataxia: from primary iron-sulfur cluster deficit to mitochondrial iron accumulation. *Front Pharmacol*. 2014;5:130.
125. Donatelli G, Ceravolo R, Frosini D, Tosetti M, Bonuccelli U, Cosottini M. Present and future of

- ultra-high field MRI in neurodegenerative disorders. *Curr Neurol Neurosci Rep.* 2018;18(6):31.
126. Johns SLM, Ishaque A, Khan M, Yang YH, Wilman AH, Kalra S. Quantifying changes on susceptibility weighted images in amyotrophic lateral sclerosis using MRI texture analysis. *Amyotroph Lateral Scler Frontotemporal Degener.* 2019;20(5-6):396–403.
  127. Macerollo A, Perry R, Stamelou M, Batla A, Mazumder AA, Adams ME, Bhatia KP. Susceptibility-weighted imaging changes suggesting brain iron accumulation in Huntington's disease: an epiphenomenon which causes diagnostic difficulty. *Eur J Neurol.* 2014;21(2):e16–7.
  128. Park M, Moon Y, Han SH, Moon WJ. Motor cortex hypointensity on susceptibility-weighted imaging: a potential imaging marker of iron accumulation in patients with cognitive impairment. *Neuroradiology.* 2019;61(6):675–83.
  129. Solbach K, Kraff O, Minnerop M, Beck A, Schöls L, Gizewski ER, Ladd ME, Timmann D. Cerebellar pathology in Friedreich's ataxia: atrophied dentate nuclei with normal iron content. *NeuroImage Clin.* 2014;6:93–9.
  130. Schwarz ST, Afzal M, Morgan PS, Bajaj N, Gowland PA, Auer DP. The 'swallow tail' appearance of the healthy nigrosome—a new accurate test of Parkinson's disease: a case-control and retrospective cross-sectional MRI study at 3T. *PLoS One.* 2014;9(4):e93814.
  131. Meijer FJ, Steens SC, van Rumund A, van Cappellen van Walsum AM, Küsters B, Esselink RA, Verbeek MM, Bloem BR, Goraj B. Nigrosome-1 on susceptibility weighted imaging to differentiate Parkinson's disease from atypical parkinsonism: an in vivo and ex vivo pilot study. *Pol J Radiol.* 2016;81:363–9.
  132. Gramsch C, Reuter I, Kraff O, Quick HH, Tanislav C, Roessler F, Deuschl C, Forsting M, Schlamann M. Nigrosome 1 visibility at susceptibility weighted 7T MRI - A dependable diagnostic marker for Parkinson's disease or merely an inconsistent, age-dependent imaging finding? *PLoS One.* 2017;12(10):e0185489.
  133. Kau T, Hametner S, Endmayr V, Deistung A, Prihoda M, Haimburger E, Menard C, Haider T, Höftberger R, Robinson S, Reichenbach JR, Lassmann H, Traxler H, Trattnig S, Grabner G. Microvessels may confound the "Swallow Tail Sign" in normal aged midbrains: a postmortem 7 T SW-MRI study. *J Neuroimaging.* 2019;29(1):65–9.
  134. Schmidt MA, Engelhorn T, Marxreiter F, Winkler J, Lang S, Kloska S, Goelitz P, Doerfler A. Ultra high-field SWI of the substantia nigra at 7T: reliability and consistency of the swallow-tail sign. *BMC Neurol.* 2017;17(1):194.
  135. Deistung A, Mentzel HJ, Rauscher A, Witoszynskij S, Kaiser WA, Reichenbach JR. Demonstration of paramagnetic and diamagnetic cerebral lesions by using susceptibility weighted phase imaging (SWI). *Z Med Phys.* 2006;16(4):261–7.
  136. Azad R, Mittal P, Malhotra A, Gangrade S. Detection and differentiation of focal intracranial calcifications and chronic microbleeds using MRI. *J Clin Diagn Res.* 2017;11(5):TC19–23.
  137. Ciraci S, Gumus K, Doganay S, Dundar MS, Kaya Ozcora GD, Gorkem SB, Per H, Coskun A. Diagnosis of intracranial calcification and hemorrhage in pediatric patients: comparison of quantitative susceptibility mapping and phase images of susceptibility-weighted imaging. *Diagn Interv Imaging.* 2017;98(10):707–14.
  138. Gumus K, Koc G, Doganay S, Gorkem SB, Dogan MS, Canpolat M, Coskun A, Bilgen M. Susceptibility-based differentiation of intracranial calcification and hemorrhage in pediatric patients. *J Child Neurol.* 2015;30(8):1029–36.
  139. Zhu WZ, Qi JP, Zhan CJ, Shu HG, Zhang L, Wang CY, Xia LM, Hu JW, Feng DY. Magnetic resonance susceptibility weighted imaging in detecting intracranial calcification and hemorrhage. *Chin Med J (Engl).* 2008;121(20):2021–5.
  140. Berberat J, Grobholz R, Boxheimer L, Rogers S, Remonda L, Roelcke U. Differentiation between calcification and hemorrhage in brain tumors using susceptibility-weighted imaging: a pilot study. *AJR Am J Roentgenol.* 2014;202(4):847–50.
  141. Zulfikar M, Dumrongpisutikul N, Intrapiomkul J, Yousem DM. Detection of intratumoral calcification in oligodendrogliomas by susceptibility-weighted MR imaging. *AJNR Am J Neuroradiol.* 2012;33:858–64.
  142. Adams LC, Böker SM, Bender YY, Fallenberg EM, Wagner M, Buchert R, Hamm B, Makowski MR. Assessment of intracranial meningioma-associated calcifications using susceptibility-weighted MRI. *J Magn Reson Imaging.* 2017;46(4):1177–86.
  143. Bekiesinska-Figatowska M, Mierzewska H, Jurkiewicz E. Basal ganglia lesions in children and adults. *Eur J Radiol.* 2013;82(5):837–49.
  144. Böttcher J, Sauner D, Jentsch A, Mentzel HJ, Becker H, Reichenbach JR, Kaiser WA. [Visualization of symmetric striopallidodentate calcinosis by using high-resolution susceptibility-weighted MR imaging. An account of the impact of different diagnostic methods of M. Fahr]. *Nervenarzt.* 2004;75(4):355–61.
  145. Sahin N, Solak A, Genc B, Kulu U. Fahr disease: use of susceptibility-weighted imaging for diagnostic dilemma with magnetic resonance imaging. *Quant Imaging Med Surg.* 2015;5(4):628–32.
  146. Adams LC, Bressemer K, Böker SM, Bender YN, Nörenberg D, Hamm B, Makowski MR. Diagnostic performance of susceptibility-weighted magnetic resonance imaging for the detection of calcifications: a systematic review and meta-analysis. *Sci Rep.* 2017;7(1):15506.
  147. Neelavalli J, Cheng YC, Jiang J, Haacke EM. Removing background phase variations in susceptibility-weighted imaging using a fast, forward-field calculation. *J Magn Reson Imaging.* 2009;29(4):937–48.

148. Kesavadas C, Thomas B, Misra S, Saini J. Attenuation of cerebral veins in susceptibility-weighted MR imaging performed with the patient under general anesthesia. *AJNR Am J Neuroradiol.* 2008;29:e71.
149. Sedlacik J, Löbel U, Kocak M, Loeffler RB, Reichenbach JR, Broniscer A, Patay Z, Hillenbrand CM. Attenuation of cerebral venous contrast in susceptibility-weighted imaging of spontaneously breathing pediatric patients sedated with propofol. *AJNR Am J Neuroradiol.* 2010;31(5):901–6.
150. Fushimi Y, Miki Y, Togashi K, Kikuta K, Hashimoto N, Fukuyama H. A developmental venous anomaly presenting atypical findings on susceptibility-weighted imaging. *AJNR Am J Neuroradiol.* 2008;29:e56.
151. Hsu CC, Haacke EM, Heyn CC, Watkins TW, Krings T. The T1 shine through effect on susceptibility weighted imaging: an under recognized phenomenon. *Neuroradiology.* 2018;60(3):235–7.
152. Salmela MB, Krishna SH, Martin DJ, Roshan SK, McKinney AM, Tore HG, Knaeble B, Rykken JB, Cayci Z, Jagadeesan BD. All that bleeds is not black: susceptibility weighted imaging of intracranial hemorrhage and the effect of T1 signal. *Clin Imaging.* 2017;41:69–72.
153. Reichenbach JR, Schweser F, Serres B, Deistung A. Quantitative susceptibility mapping: concepts and applications. *Clin Neuroradiol.* 2015;25(Suppl 2):225–30.
154. Liu T, Spincemaille P, de Rochefort L, Kressler B, Wang Y. Calculation of susceptibility through multiple orientation sampling (COSMOS): a method for conditioning the inverse problem from measured magnetic field map to susceptibility source image in MRI. *Magn Reson Med.* 2009;61(1):196–204.
155. Shmueli K, de Zwart JA, van Gelderen P, Li TQ, Dodd SJ, Duyn JH. Magnetic susceptibility mapping of brain tissue in vivo using MRI phase data. *Magn Reson Med.* 2009;62(6):1510–22.
156. Tang J, Liu S, Neelavalli J, Cheng YC, Buch S, Haacke EM. Improving susceptibility mapping using a threshold-based k-space/image domain iterative reconstruction approach. *Magn Reson Med.* 2013;69(5):1396–407.
157. Wharton S, Schäfer A, Bowtell R. Susceptibility mapping in the human brain using threshold-based k-space division. *Magn Reson Med.* 2010;63(5):1292–304.
158. Bao L, Li X, Cai C, Chen Z, van Zijl PC. Quantitative susceptibility mapping using structural feature based collaborative reconstruction (SFCR) in the human brain. *IEEE Trans Med Imaging.* 2016;35(9):2040–50.
159. de Rochefort L, Liu T, Kressler B, Liu J, Spincemaille P, Lebon V, Wu J, Wang Y. Quantitative susceptibility map reconstruction from MR phase data using Bayesian regularization: validation and application to brain imaging. *Magn Reson Med.* 2010;63(1):194–206.
160. Khabipova D, Wiaux Y, Gruetter R, Marques JP. A modulated closed form solution for quantitative susceptibility mapping—a thorough evaluation and comparison to iterative methods based on edge prior knowledge. *NeuroImage.* 2015;107:163–74.
161. Li W, Wang N, Yu F, Han H, Cao W, Romero R, Tantiwongkosi B, Duong TQ, Liu C. A method for estimating and removing streaking artifacts in quantitative susceptibility mapping. *NeuroImage.* 2015;108:111–22.
162. Liu T, Liu J, de Rochefort L, Spincemaille P, Khalidov I, Ledoux JR, Wang Y. Morphology enabled dipole inversion (MEDI) from a single-angle acquisition: comparison with COSMOS in human brain imaging. *Magn Reson Med.* 2011;66(3):777–83.
163. Schweser F, Sommer K, Deistung A, Reichenbach JR. Quantitative susceptibility mapping for investigating subtle susceptibility variations in the human brain. *NeuroImage.* 2012;62(3):2083–100.
164. Deistung A, Schweser F, Reichenbach JR. Overview of quantitative susceptibility mapping. *NMR Biomed.* 2017;30(4):e3569. <https://doi.org/10.1002/nbm.3569>.
165. Schweser F, Deistung A, Reichenbach JR. Foundations of MRI phase imaging and processing for quantitative susceptibility mapping (QSM). *Z Med Phys.* 2016;26(1):6–34.
166. Wang Y, Liu T. Quantitative susceptibility mapping (QSM): decoding MRI data for a tissue magnetic biomarker. *Magn Reson Med.* 2015;73(1):82–101.
167. Chen Y, Liu S, Buch S, Hu J, Kang Y, Haacke EM. An interleaved sequence for simultaneous magnetic resonance angiography (MRA), susceptibility weighted imaging (SWI) and quantitative susceptibility mapping (QSM). *Magn Reson Imaging.* 2018;47:1–6.
168. Gho SM, Liu C, Li W, Jang U, Kim EY, Hwang D, Kim DH. Susceptibility map-weighted imaging (SMWI) for neuroimaging. *Magn Reson Med.* 2014;72(2):337–46.
169. Liu S, Mok K, Neelavalli J, Cheng YC, Tang J, Ye Y, Haacke EM. Improved MR venography using quantitative susceptibility-weighted imaging. *J Magn Reson Imaging.* 2014;40(3):698–708.
170. Bandt SK, de Rochefort L, Chen W, Dimov AV, Spincemaille P, Kopell BH, Gupta A, Wang Y. Clinical integration of quantitative susceptibility mapping magnetic resonance imaging into neurosurgical practice. *World Neurosurg.* 2019;122:e10–1.
171. Eskreis-Winkler S, Zhang Y, Zhang J, Liu Z, Dimov A, Gupta A, Wang Y. The clinical utility of QSM: disease diagnosis, medical management, and surgical planning. *NMR Biomed.* 2017;30(4):e3668. <https://doi.org/10.1002/nbm.3668>.

172. Zhang S, Liu Z, Nguyen TD, Yao Y, Gillen KM, Spincemaille P, Kovanlikaya I, Gupta A, Wang Y. Clinical feasibility of brain quantitative susceptibility mapping. *Magn Reson Imaging*. 2019;60:44–51.
173. Bollmann S, Kristensen MH, Larsen MS, Olsen MV, Pedersen MJ, Østergaard LR, O'Brien K, Langkammer C, Fazlollahi A, Barth M. SHARQnet—sophisticated harmonic artifact reduction in quantitative susceptibility mapping using a deep convolutional neural network. *Z Med Phys*. 2019;29(2):139–49.
174. Bollmann S, Rasmussen KGB, Kristensen M, Blendal RG, Østergaard LR, Plochanski M, O'Brien K, Langkammer C, Janke A, Barth M. DeepQSM—using deep learning to solve the dipole inversion for quantitative susceptibility mapping. *NeuroImage*. 2019;195:373–83.
175. Yoon J, Gong E, Chatnuntaweck I, Bilgic B, Lee J, Jung W, Ko J, Jung H, Setsompop K, Zaharchuk G, Kim EY, Pauly J, Lee J. Quantitative susceptibility mapping using deep neural network: QSMnet. *NeuroImage*. 2018;179:199–206.
176. Liu S, Utraiainen D, Chai C, Chen Y, Wang L, Sethi SK, Xia S, Haacke EM. Cerebral microbleed detection using susceptibility weighted imaging and deep learning. *NeuroImage*. 2019;198:271–82.
177. Zhang X, Zhang Y, Hu Q. Deep learning based vein segmentation from susceptibility-weighted images. *Computing*. 2019;101:637–52.
178. Bilgic B, Gagoski BA, Cauley SF, Fan AP, Polimeni JR, Grant PE, Wald LL, Setsompop K. Wave-CAIPI for highly accelerated 3D imaging. *Magn Reson Med*. 2015;73(6):2152–62.
179. Bilgic B, Ye H, Wald LL, Setsompop K. Simultaneous Time Interleaved MultiSlice (STIMS) for rapid susceptibility weighted acquisition. *NeuroImage*. 2017;155:577–86.
180. Conklin J, Longo MG, Cauley S, Setsompop K, Kirsch J, Liu W, Ahn S, Beck T, Gonzalez R, Schaefer P, Rapalino O, Huang S. Prospective evaluation of wave-CAIPI susceptibility-weighted imaging (SWI) compared to conventional 3D SWI in a clinical setting. *Proc Int Soc Mag Reson Med*. 2019;27:3092.



Tarini Ratneswaren and Tomasz Matys

## Contents

13.1	<b>Introduction</b> .....	189
13.2	<b>Background</b> .....	190
13.2.1	Diffusion and Brownian Motion .....	190
13.2.2	Imaging Diffusion In Vivo with MRI .....	190
13.2.3	Pulsed Gradient Spin Echo .....	191
13.2.4	<i>b</i> Values .....	192
13.2.5	T2 Shine Through and T2 Blackout .....	192
13.2.6	ADC Maps .....	192
13.2.7	Signal Readout .....	192
13.3	<b>Clinical Applications</b> .....	194
13.3.1	Ischaemic Stroke .....	194
13.3.2	Brain Abscess/Infection Imaging .....	196
13.3.3	Brain Tumour Imaging .....	197
13.3.4	Epidermoid Cyst and Cholesteatoma .....	197
13.4	<b>Clinical Case</b> .....	200
13.4.1	History .....	200
13.4.2	Examination .....	200
13.4.3	Imaging .....	200
13.4.4	Discussion .....	200
	<b>References</b> .....	201

## 13.1 Introduction

Diffusion-weighted imaging (DWI) has revolutionized neuroimaging in the last two decades, as the first neuroimaging technique introduced into clinical practice that offers insight into physiological properties of tissue. In particular, DWI provided significant practical advantage in neuroimaging of ischaemic stroke, intracranial infections, as well as certain brain and head and neck tumours. In this chapter, we briefly consider the

---

T. Ratneswaren (✉)

Department of Radiology, Addenbrooke's Hospital,  
Cambridge University Hospitals NHS Foundation Trust,  
Cambridge, UK

e-mail: [tratneswaren@nhs.net](mailto:tratneswaren@nhs.net)

T. Matys

Department of Radiology, Addenbrooke's Hospital,  
Cambridge University Hospitals NHS Foundation Trust,  
Cambridge, UK

Department of Radiology, University of Cambridge,  
Cambridge, UK



technical background to DWI, the current clinical applications of basic DWI techniques and the common pitfalls seen in clinical practice. Advanced DWI techniques and diffusion tensor imaging are discussed separately.

## 13.2 Background

### 13.2.1 Diffusion and Brownian Motion

Diffusion is the process by which particles move from an area of high concentration to an area of low concentration without bulk mixing. In 1855, Adolf Fick, a German physician and physiologist, demonstrated that the movement of particles was proportional to the concentration gradient and a diffusion gradient. Fick suggested that when the concentration gradient was removed there should be no further diffusion.

Earlier, in 1827, Scottish Botanist Robert Brown investigated the fertilization of pollen grains suspended in water with microscopy. Brown observed that the pollen particles moved in a random zigzag path (Fig. 13.1), a phenomenon which became known as Brownian motion.

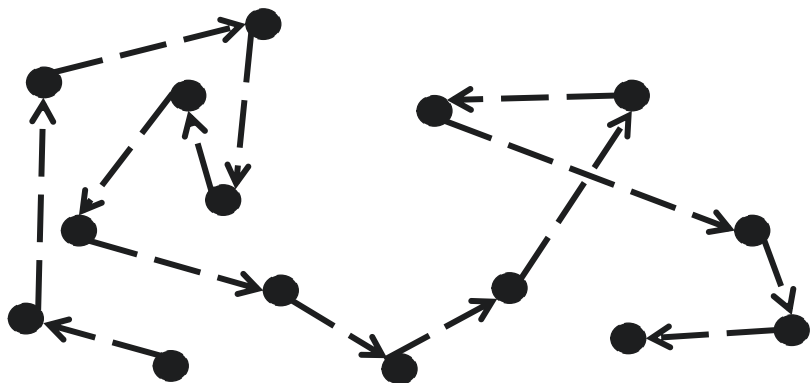
Almost a century later, Albert Einstein, in his PhD thesis in 1905, quantitatively linked Brownian motion, the random motion of particles, with the process of diffusion. Brownian motion varies with the kinetic energy of the particle, dependent on the mass and temperature of the diffusing particles, as well as the viscosity of

the surrounding material. The random path is caused by collision with other molecules. At higher temperatures and in more viscous environments particles diffuse faster. Einstein quantified this as a linear relationship related to time and the diffusion coefficient and successfully demonstrated that, contrary to Fick's model, even if there is no concentration gradient, particles continue to display this random walk due to self-diffusivity.

### 13.2.2 Imaging Diffusion In Vivo with MRI

Measurement of diffusion in vivo relies on measuring movement of water molecules. The majority of body mass is attributable to water, which constitutes around three-quarters of body weight at birth to 60% of total body weight in an adult. The total body water is distributed in different compartments—65% of body water is intracellular and 35% is extracellular in (1) interstitial spaces (between cells), (2) transcellular spaces (epithelial lined spaces, e.g. ventricles) and (3) intravascular spaces (blood and lymph vessels). Water molecules are prevented from diffusing freely between intracellular and extracellular compartments by the cell membrane, and intracellularly by cytoplasm and organelles. Pathological processes in the brain can alter the cellular architecture, cellular density or water content in localized areas causing changes in water diffusion. So how do we image diffusion in vivo with MR?

**Fig. 13.1** Brownian motion—the random path of a particle



### 13.2.3 Pulsed Gradient Spin Echo

Measurement of diffusion of water molecules relies on attenuation of MRI signal in moving spins due to dephasing, first described by Erwin Hahn in the 1950s. In early experiments on measuring diffusion, Carr and Purcell used constant gradient applied throughout the spin-echo sequence [1]. In 1965 Stejskal and Tanner introduced pulsed gradient spin echo (PGSE) sequence in which constant field gradient was replaced by two matched pulses applied on each side of the refocusing pulse [2]. The significant advantage of this approach is that diffusion encoding gradients are only applied for a short time, and do not interfere with slice selection or readout process. Stejskal and Tanner sequence remains the most widely used method today. The PGSE sequence is demonstrated in Fig. 13.2. The stages of a PGSE sequence are:

1. An initial diffusion gradient ( $G1$ ) is applied between the initial  $90^\circ$  pulse and the  $180^\circ$  refocusing pulse which induces spin dephas-

ing and results in phase shift dependent on the position of the spin along the gradient.

2. A second diffusion gradient ( $G2$ ) is applied after the  $180^\circ$  refocusing pulse. The gradient is of the same strength and direction as  $G1$  but since the spins have been flipped by the  $180^\circ$  refocusing pulse, it acts to reverse the dephasing effect of  $G1$ . In a stationary molecule, the dephasing caused by  $G1$  is fully countered by  $G2$  and the net dephasing is zero. A diffusing molecule will move between the application of  $G1$  and  $G2$  and will be subject to different gradient strengths. As a result, the phase changes caused by  $G1$  and  $G2$  will be different and will not cancel each other, resulting in a net phase change and signal loss. Maximum phase changes will be seen in molecules moving along the direction of the gradients, while molecules moving perpendicular to the gradients will not experience a net phase change. It is important to note that as the diffusion process happens universally in all water-containing tissues, most areas in the image will show diffusion-related signal

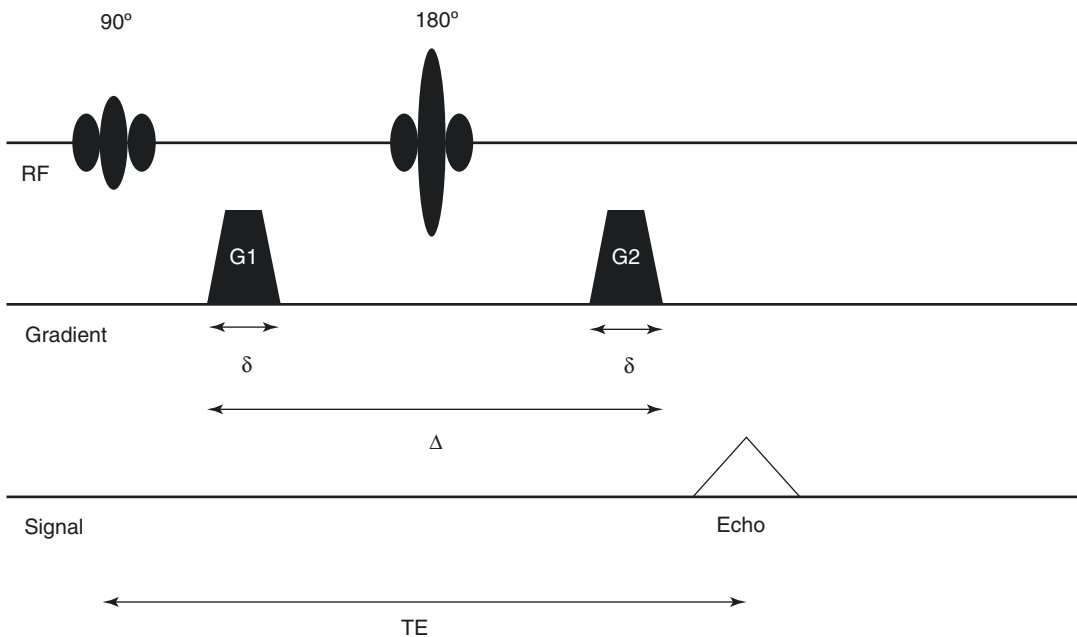


**Fig. 13.2** PGSE pulse sequence. *RF* radiofrequency pulse, *G* diffusion weighting gradient,  $\delta$  gradient pulse width,  $\Delta$  gradient pulse separation, *TE* echo time

drop out; on this background, structures with restricted diffusion will demonstrate relative high signal.

### 13.2.4 *b* Values

The degree of diffusion weighting in a PGSE sequence is characterized quantitatively with a *b* value, which is dependent on *G*—diffusion gradient strength,  $\delta$ —diffusion gradient pulse width and  $\Delta$ —gradient pulse separation. Higher *b* values result in higher diffusion weighting. Images are acquired after the application of gradients with one or more different *b* values, and a *b*<sub>0</sub> map obtained without the gradient, which provides a T2 weighted image used for comparison with the diffusion images.

As mentioned above, PGSE sequence is sensitive to movement of water occurring along the direction of the gradient. To accurately measure diffusion in space, images are acquired for each *b* value in at least three perpendicular directions (often referred to as ‘source’ images) and the data are averaged for each voxel (to produce a ‘trace’ or ‘isotropic’ image). Routine DWI images are usually obtained using one *b* value (typically 1000 or 1500 s mm<sup>-2</sup>) and three encoding gradient directions. Multiple *b* values and multiple directions can be used in DTI and advanced diffusion methods.

### 13.2.5 T2 Shine Through and T2 Blackout

The PGSE sequence is very useful for imaging diffusion in vivo, although care must be taken when interpreting images, as the signal is not only diffusion weighted but also T2 weighted. To achieve a typical *b* value of 1000 s mm<sup>-2</sup>, relatively long gradient pulse durations are required, forcing a relatively long TE (which is at least double the gradient pulse duration) resulting in T2 weighting to DWI images. This T2 weighting can lead to false positives due to T2 shine through, where tissues with a long T2 appear bright on DWI (Fig. 13.3) even though diffusion may not

be restricted. Conversely, tissues with very short T2 may show dark signal on DWI (T2 blackout), which does not reflect increased diffusivity (Fig. 13.3).

### 13.2.6 ADC Maps

In order to distinguish restricted diffusion from T2 shine through, a quantitative measurement of the apparent diffusion coefficient (ADC) can be made. Using source images with different *b* values the diffusivity or ADC can be calculated for each voxel independent of T2 and the values displayed as a parametric ADC map. The measurement is described as the ‘apparent’ diffusion coefficient because in addition to intrinsic properties of the diffusing particles, it takes into account restrictions to free movement resulting from the presence of cell membranes and other intracellular structures, bulk flow, patient motion and averaging of diffusivity measurement over a whole voxel.

Tissue with true restricted diffusion will have high signal on DWI and low signal on ADC map confirming the low diffusion coefficient (Fig. 13.3a). T2 shine through due to high intrinsic T2 will appear as high signal on DWI but normal or increased signal on ADC map (Fig. 13.3b). Similarly, in T2 blackout, regions may appear normal or darker than normal parenchyma on DWI imaging due to very low T2 (Fig. 13.3c). The ADC values may be inaccurate in this situation.

### 13.2.7 Signal Readout

The high sensitivity of DWI to small movements of water molecules also means that DWI is sensitive to artefact from patient motion and the acquisition needs to be fast enough to minimize this effect. The most commonly used technique for signal readout in DWI is echo-planar imaging (EPI)—a rapid spin-echo technique, which after the initial 180° refocussing radiofrequency pulse uses rapid oscillations of the frequency gradient to acquire multiple echoes. The entire image can

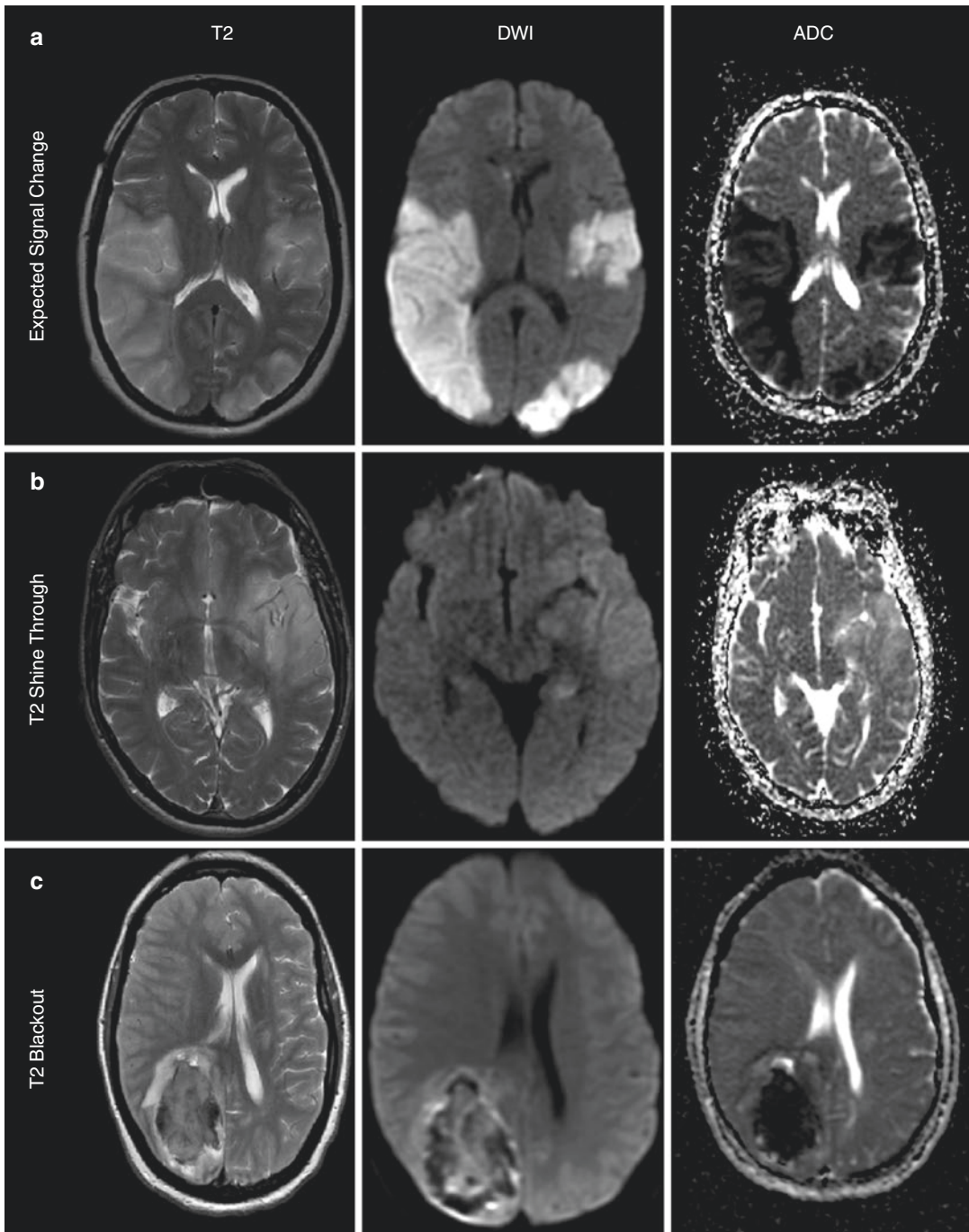


**Fig. 13.3** T2, DWI and ADC maps in (a) true restricted diffusion, (b) T2 shine through and (c) T2 blackout. (a) An example of bilateral large vessel territory infarcts with restricted diffusion—the abnormal regions demonstrate high T2, high DWI, and low ADC signal (confirming restricted diffusion). (b) An example of shine through phenomenon in low-grade glioma in the left anterior tem-

poral lobe with high T2 and slightly elevated DWI signal; ADC is also elevated indicating that this is not true restricted diffusion but T2 shine through. (c) An example of T2 blackout phenomenon in a large parietal intracerebral haematoma; note low DWI signal with corresponding low T2 and ADC

be obtained after a single radiofrequency excitation (single-shot EPI) or several excitations (multi-shot EPI). The speed of EPI comes at the expense of increased susceptibility to field inhomogeneities and resulting artefacts [3]. Such inhomogeneities occur in particular at air–bone interfaces, e.g. paranasal sinuses and mastoid air cells, leading to image distortion and linear areas of apparently increased DWI. There are certain clinical situations where the clinical region of interest is contained within susceptible areas (e.g. imaging of cholesteatoma within the temporal bone close to the mastoid air cells). In order to overcome these susceptibility effects, alternative non-EPI acquisition methods can be utilized [4], e.g. fast spin-echo (where refocusing RF pulses are repeated during the echo train within a single TR). The trade-off of reduced susceptibility to field inhomogeneities is a longer scan time and hence increased susceptibility to motion artefact.

### 13.3 Clinical Applications

#### 13.3.1 Ischaemic Stroke

##### 13.3.1.1 Diagnosis

Stroke is the second most common cause of death worldwide and the third most common cause of disability [5]. Eighty percent of strokes are ischemic in origin. The sensitivity of DWI in diagnosing acute ischemic stroke is superior to CT (100% vs. 55% in the first 6 h [6]) and it can be

helpful in assessing timing of the infarct (Table 13.1) [7].

In the acute setting (day 0–7), cerebral ischaemia causes restricted diffusion and a corresponding increase in DWI signal and decrease in ADC values, which occurs as early as 30 min post ictus [8] (Figs. 13.3a and 13.4).

There are multiple mechanisms underlying these changes. Several theories suggest that there is a relative shift of water molecules from the extracellular space to the intracellular space (where diffusion is restricted due to organelles), e.g. due to a decrease in intracellular ATP leading to failure of Na–K–ATPase and hence a loss of the ionic gradients driving water out of cells [9]. There is also an increase in cell volume with resulting reduction of extracellular space [10] (Fig. 13.5b). In the subacute period, the ADC values return to normal (ADC pseudonormalization) (around day 5–7), likely due to a relative shift of fluid from the intracellular to extracellular compartment secondary to increasing vasogenic oedema mediated by inflammatory mediators. The DWI remains hyperintense, despite the normalization of ADC, as T2 effects predominate with high T2 signal due to oedema [11]. In the chronic stages, neuronal death and encephalomalacia allow enhanced diffusion relative to healthy brain tissue and the ADC values increase. The resulting DWI signal is a combination of ADC and T2 contributions and may be low or normal depending on their relative effects.

**Table 13.1** Timing of DWI and ADC changes in stroke

	<b>Acute (0-7 days)</b>	<b>Subacute (1-3 weeks)</b>	<b>Chronic (&gt;3 weeks)</b>
<b>DWI</b>	↑	↑	↔/↓
<b>ADC</b>	↓	↔	↑

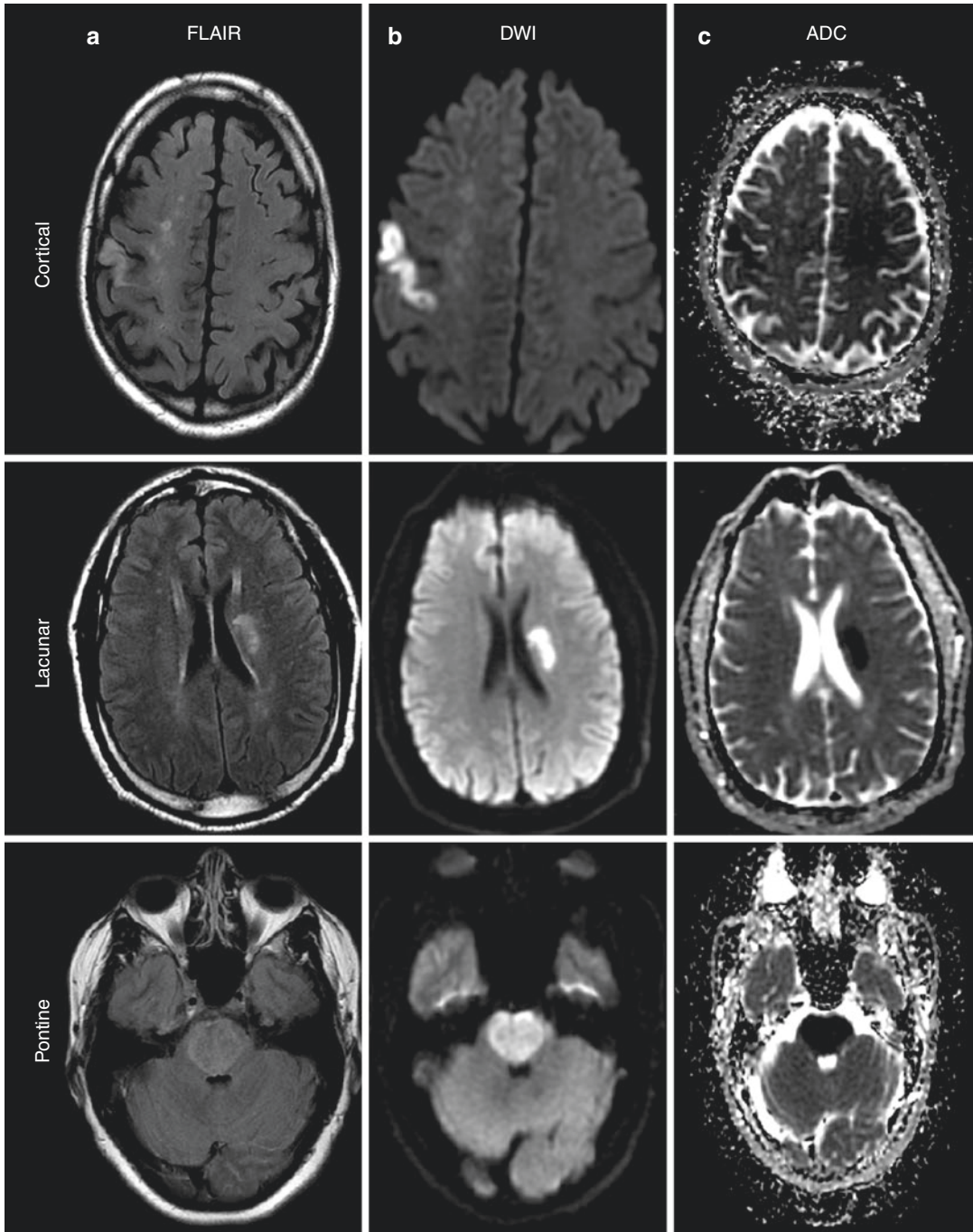


**Fig. 13.4** Examples of (a) cortical, (b) lacunar and (c) pontine infarcts. Note typical hyperintensity on FLAIR (T2 with fluid attenuation) with high signal on DWI and low ADC values in the (a) right precentral gyrus, (b) left corona radiata and (c) pons

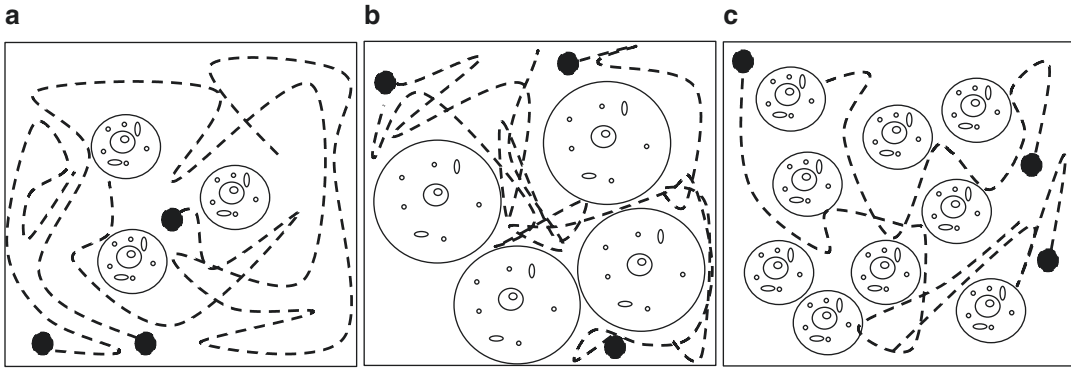


**Fig. 13.5** (a) Normal and restricted diffusion due to (b) cellular swelling, e.g. in ischaemic stroke and (c) increased cellularity, e.g. in tumour

### 13.3.1.2 Guiding Treatment with DWI

Treatment of acute ischaemic stroke improved dramatically when it was demonstrated that reperfusion therapy (thrombolysis or mechanical thrombectomy) within the initial hours of symptom onset could reduce morbidity and mortality [12]. The principle underlying current reperfusion therapy is to salvage the ischaemic penumbra of potentially viable tissue surrounding the central core of irreversibly damaged necrotic tissue [13]. DWI estimates the size of the central core of necrosis and there is evidence to suggest that a larger initial area of DWI change correlates with worse outcomes [14, 15], which can however be improved by intravenous thrombolysis [16] or mechanical thrombectomy [17].

Comparison of DWI volume with area of reduced perfusion estimates the size of ischaemic penumbra (ischaemic but not infarcted tissue at risk which can be salvaged by reperfusion). The degree of perfusion—diffusion mismatch can help decide which patients should receive therapy (the greater the mismatch, the greater the potential gain from reperfusion) [18].

### 13.3.2 Brain Abscess/Infection Imaging

Pyogenic brain abscesses usually manifest as ring-enhancing lesions with surrounding oedema, a radiological picture similar to high-grade primary neoplasm or metastasis. Characteristically,

abscesses demonstrate a central region of restricted diffusion with high DWI and low ADC signal intensity [19] due to pus containing cellular components, debris and fibrinogen (Fig. 13.6). DWI is invaluable in differentiating abscess from necrotic tumour with a high specificity (91%) and sensitivity (93%) [19]. Furthermore, treatment response can be monitored using DWI, as with successful treatment the DWI signal intensity becomes low and the ADC becomes high. Areas with sustained high DWI signal and low ADC correspond accurately to re-accumulation of pus within the abscess [20]. Variable DWI signal is seen in fungal, toxoplasmosis [21] and tuberculosis [22] abscesses and careful correlation with clinical findings and additional neuro-imaging findings are required.

Subdural empyemas are collections of pus in the subdural space and are rare, serious complications of meningitis, otitis media or sinusitis, typically affecting children [23]. The differential for subdural collection in these patients is subdural empyema and reactive subdural hygroma, where damage to the arachnoid layer allows CSF leak into the subdural space. DWI can be helpful in differentiating these pathologies as empyema demonstrates restricted diffusion with high DWI and low ADC compared with reactive hygroma, which has low DWI and high ADC [24]. This is important clinically as management of reactive hygroma is often conservative whilst empyema requires aggressive medical and/or surgical management [25].

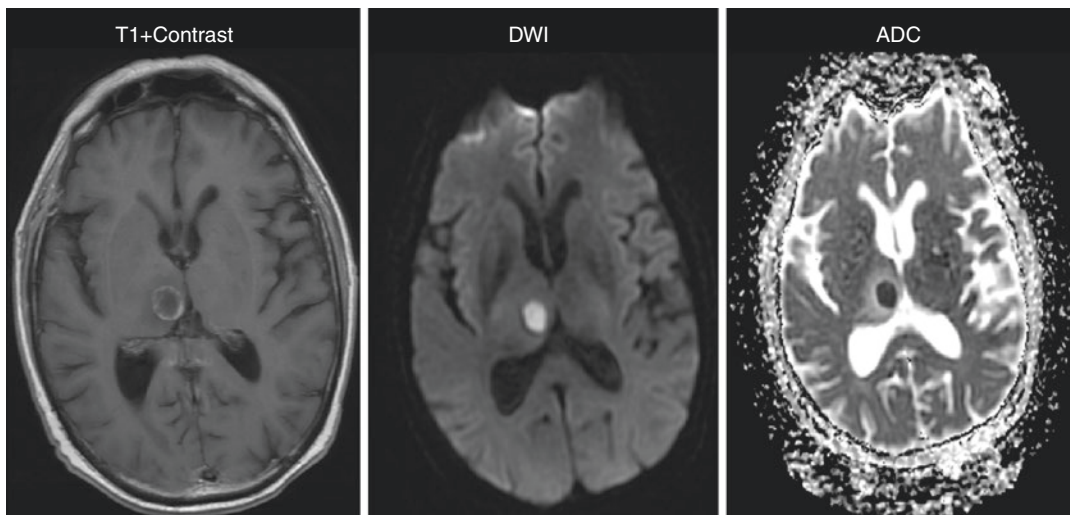


**Fig. 13.6** An example of a right thalamic abscess. The central core of the ring-enhancing lesion demonstrates high DWI and low ADC in keeping with restricted diffusion due to pus content

### 13.3.3 Brain Tumour Imaging

Despite advances in neuroimaging, brain tumours can be difficult to accurately diagnose on imaging—both in staging and differentiation from other pathologies.

We have discussed above how abscess can be differentiated from tumour based on the centre demonstrating restricted diffusion. Some tumours may demonstrate restricted diffusion in the solid component (e.g. in the wall of the cyst) due to high cellularity (see below) but usually lack restricted diffusion in the centre of the cystic component (Fig. 13.7).

High tumour cellularity causes restricted diffusion through a relative reduction in extracellular space due to increased cell density and higher nuclear to cytoplasmic ratio (see Fig. 13.5c). Thus, solid lesions with a high cellular density demonstrate increased restricted diffusion [26]. This may be clinically useful, e.g. in characterizing meningiomas, where higher grade atypical meningiomas have greater restricted diffusion [27] aiding in planning the extent of surgery and adjuvant therapies. In other solid highly cellular tumours such as lymphoma (Fig. 13.7) or medulloblastoma, ADC measure-

ments can aid diagnosis and monitoring treatment response [28–30].

Similarly, differences in DWI signal due to degree of cellularity can help characterize the type of metastasis. Highly cellular neuroendocrine tumours and poorly differentiated adenocarcinomas tend to be hyperintense on DWI (with low ADC value) compared with well-differentiated adenocarcinomas, which are hypointense on DWI with high ADC values [31].

In serial monitoring of patients with high-grade primary tumours or metastases treated with radiotherapy DWI can assist in differentiating recurrent tumour from radiation necrosis, which both appear as a new ring-enhancing lesions with mass effect, and are undistinguishable on conventional imaging. Lower ADC ratios favour the diagnosis of tumour recurrence rather than radiation necrosis [32].

### 13.3.4 Epidermoid Cyst and Cholesteatoma

Some lesions characteristically demonstrate restricted diffusion due to the content of keratin and stratified epithelial cells. These include



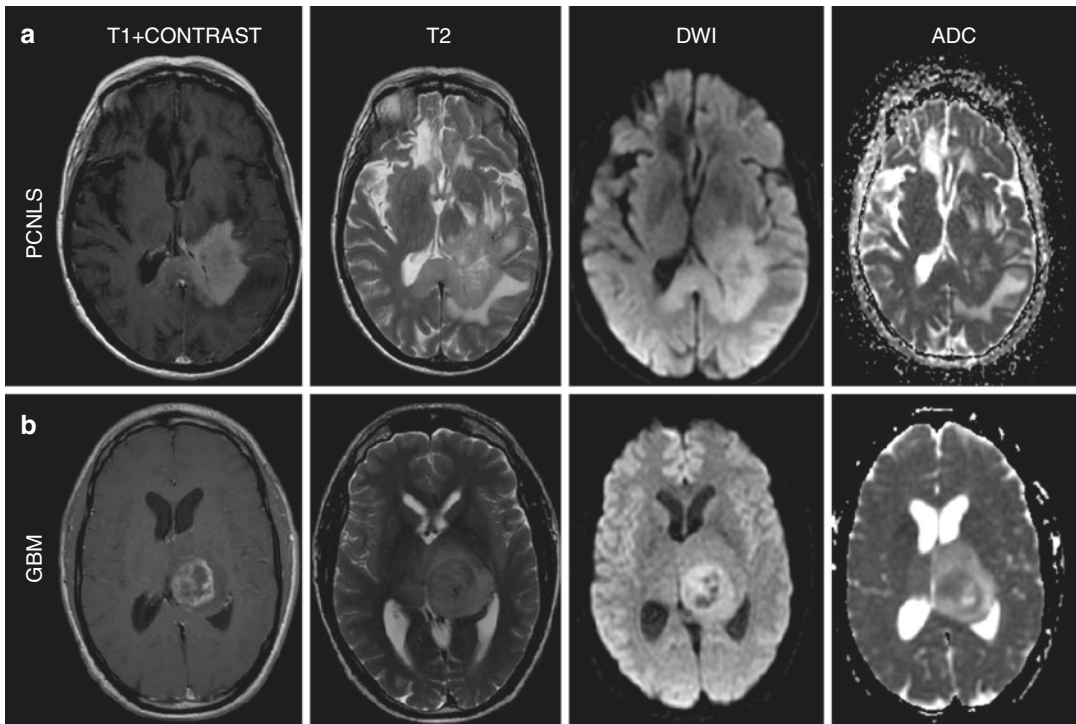


**Fig. 13.7** Examples of restricted diffusion in brain tumours—(a) primary central nervous system lymphoma (PCNSL) and (b) glioblastoma multiforme (GBM). (a) Homogenously enhancing lesion involving the splenium of the corpus callosum histologically confirmed as PCNSL; restricted diffusion is a typical imaging feature

of these tumours due to high cellularity. (b) GBM usually appears as a ring-enhancing lesion which may be similar to abscess; it may display restricted diffusion in the peripheral solid component—this should not be confused with restricted diffusion in an abscess, in which high DWI signal is seen in the pus-filled central cavity (Fig. 13.6)

epidermoid cysts (intracranial, extra-axial) and cholesteatomas (extracranial), which are histologically identical but differentiated according to their location [33].

Epidermoid cysts are benign ectodermal lesions, most often seen in the cerebellopontine angle, and may appear similar on conventional imaging to an arachnoid cyst, with high signal on T2 and lack of enhancement. Presence of restricted diffusion can accurately distinguish epidermoid cyst from arachnoid cyst with a sensitivity and specificity of 100% [34] (Fig. 13.8).

Cholesteatomas are enlarging cystic masses of keratinizing stratified squamous epithelium surrounding keratin/cholesterol debris. Ninety-eight percent are acquired and occur in the middle ear or

temporal bone—particularly the mastoid and petrous apex, 2% are congenital. As cholesteatomas are histologically similar to epidermoid tumours, they demonstrate restricted diffusion. If left untreated, middle ear cholesteatoma can lead to destruction of the ossicles resulting in an acquired conductive hearing loss. Diagnosis is generally made with examination of the eardrum with otoscopy and high-resolution CT of the petrous-temporal bone to demonstrate bone involvement. However, in situations where there is diagnostic uncertainty (e.g. with cholesteatoma that cannot be visualized clinically), MRI can be used to detect these lesions with high specificity and sensitivity [35]. MRI is also very useful in suspected recurrence after surgery (Fig. 13.9). As mentioned

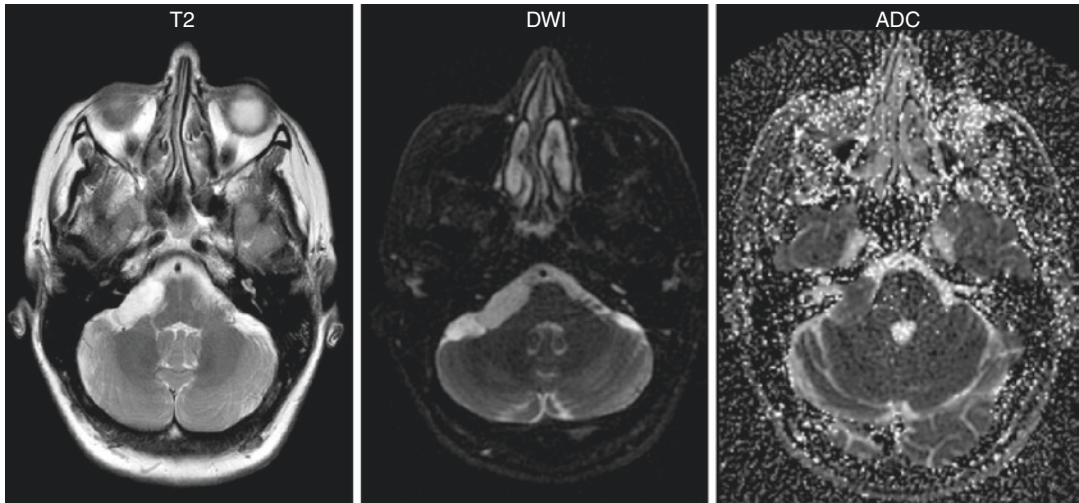


**Fig. 13.8** Right cerebellopontine angle epidermoid cyst showing high signal on T2 and restricted diffusion (high DWI and low ADC)

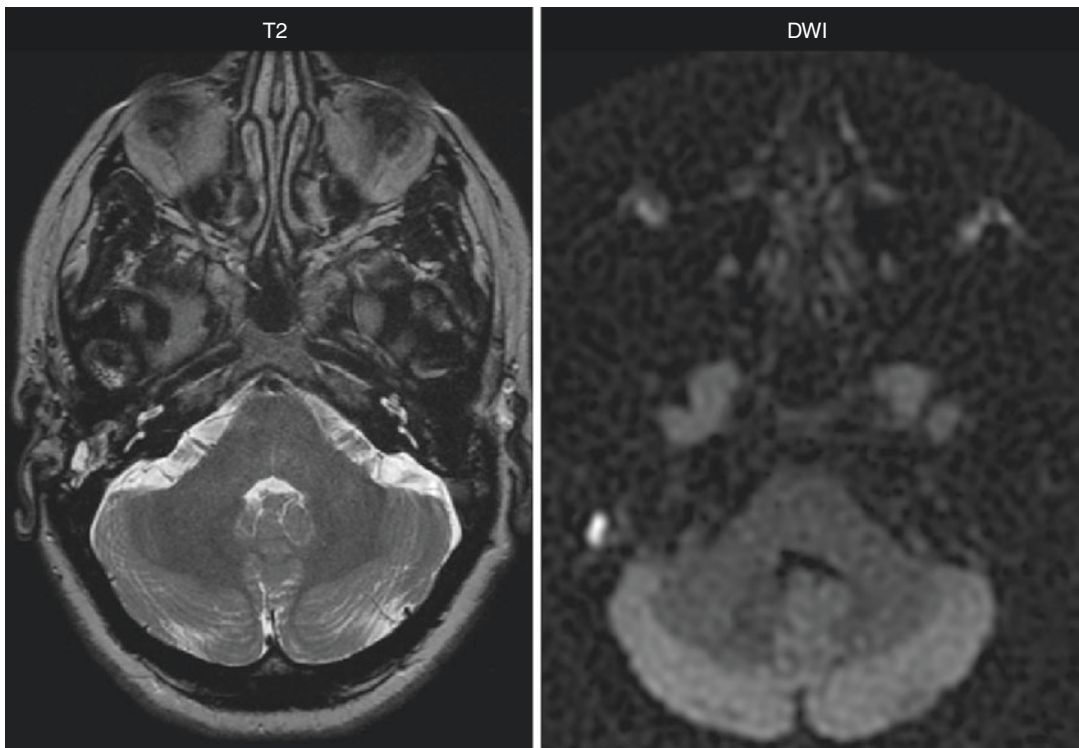


**Fig. 13.9** Recurrent right middle ear cholesteatoma in a patient with previous mastoidectomy. There is a focus of high DWI signal within the right mastoidectomy cavity demonstrating recurrent disease

above, imaging of the petrous bone is best performed with non-EPI DWI methods which are less prone to geometric distortion and artefacts [4].

## 13.4 Clinical Case

### 13.4.1 History

Fifty-two-year-old woman presented to ED with rapidly progressing confusion and twitching movements. This was on a background of a fourth-month history of sensation of disequilibrium, diplopia, blurring of vision, slow speech and disorientation. There was no past medical, social or family history of note.

### 13.4.2 Examination

Examination revealed wide-based ataxic gait, past pointing, diplopia looking to the extreme left, as well as cognitive impairment with word-finding difficulty.

### 13.4.3 Imaging

Imaging findings are shown in (Fig. 13.10).

### 13.4.4 Discussion

CJD is a spongiform encephalopathy where prion proteins accumulate within the brain and cause early neurodegenerative disease, which manifests with rapidly progressive dementia, psychiatric symptoms and cerebellar symptoms. There are four main subtypes of CJD sporadic (the most common affecting 85%), variant, familial and iatrogenic [36]. Although there is some overlap between MRI imaging patterns of different subtypes of the disease, the pattern shown here is suggestive of variant CJD [37]. DWI is very useful in diagnosis as DWI signal change is fairly sensitive in CJD [38] and can precede the onset of clinical symptoms [39]. Furthermore, the most likely differential diagnosis for CJD is autoimmune encephalitis, which does not cause significant restricted diffusion [40].

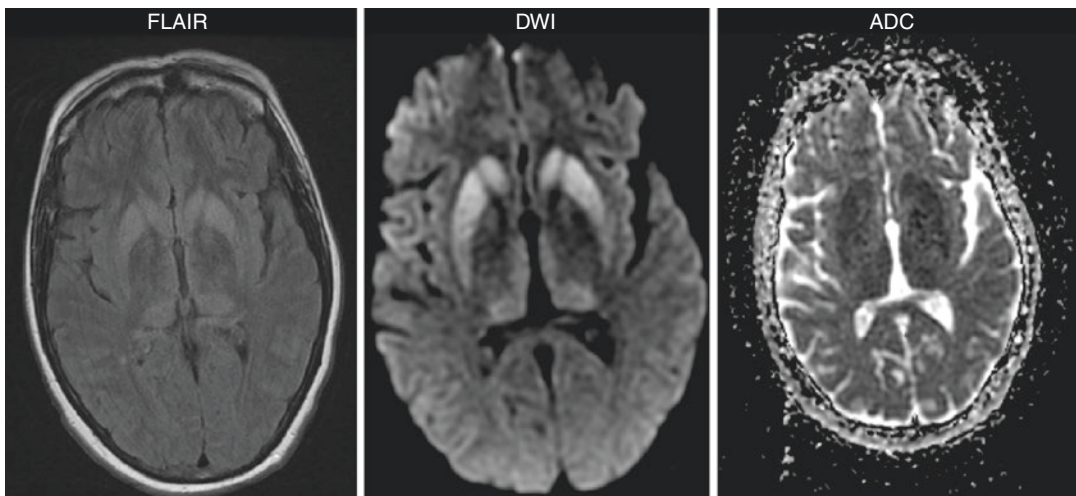


**Fig. 13.10** MRI of the patient demonstrates symmetrical bilateral increased FLAIR, increased DWI and reduced ADC (restricted diffusion) within the caudate, lentiform nucleus and bilateral thalami suggestive of Creutzfeldt–

Jakob disease (CJD). The FLAIR and DWI demonstrate the ‘double hockey stick sign’ with hyperintense signal involving bilateral pulvinar and dorsomedial thalamic nuclei

## References

- Carr HY, Purcell EM. Effects of diffusion on free precession in nuclear magnetic resonance experiments. *Phys Rev.* 1954;94:630.
- Stejskal EO, Tanner JE. Spin diffusion measurements: spin echoes in the presence of a time-dependent field gradient. *J Chem Phys.* 1965;42:288–92.
- Bammer R. Basic principles of diffusion-weighted imaging. *Eur J Radiol.* 2003;45:169–84.
- Más-Estellés F, et al. Contemporary non-echo-planar diffusion-weighted imaging of middle ear cholesteatomas. *Radiographics.* 2012;32:1197–213.
- Feigin VL, et al. Update on the global burden of ischemic and hemorrhagic stroke in 1990–2013: the GBD 2013 study. *Neuroepidemiology.* 2015;45:161–76. <https://doi.org/10.1159/000441085>.
- Urbach H, et al. Detectability and detection rate of acute cerebral hemisphere infarcts on CT and diffusion-weighted MRI. *Neuroradiology.* 2000;42:722–7.
- Eastwood JD, Engelter ST, MacFall JF, DeLong DM, Provenzale JM. Quantitative assessment of the time course of infarct signal intensity on diffusion-weighted images. *AJNR Am J Neuroradiol.* 2003;24:680–7.
- Srinivasan A, Goyal M, Azri FA, Lum C. State-of-the-art imaging of acute stroke. *Radiographics.* 2006;26:S75–95.
- Qiao M, Maliszka KL, Del Bigio MR, Tuor UI. Transient hypoxia-ischemia in rats: changes in diffusion-sensitive MR imaging findings, extracellular space, and Na<sup>+</sup>-K<sup>+</sup>-adenosine triphosphatase and cytochrome oxidase activity. *Radiology.* 2002;223:65–75. <https://doi.org/10.1148/radiol.2231010736>.
- Liu KF, et al. Regional variations in the apparent diffusion coefficient and the intracellular distribution of water in rat brain during acute focal ischemia. *Stroke.* 2001;32:1897–905.
- Welch KM, et al. A model to predict the histopathology of human stroke using diffusion and T2-weighted magnetic resonance imaging. *Stroke.* 1995;26:1983–9.
- Evans M, White P, Cowley P, Werring D. Revolution in acute ischaemic stroke care: a practical guide to mechanical thrombectomy. *Pract Neurol.* 2017;17:252–65. <https://doi.org/10.1136/practneurol-2017-001685>.
- Prabhakaran S, Ruff I, Bernstein RA. Acute stroke intervention: a systematic review. *JAMA.* 2015;313:1451–62. <https://doi.org/10.1001/jama.2015.3058>.
- Derex L, et al. Influence of pretreatment MRI parameters on clinical outcome, recanalization and infarct size in 49 stroke patients treated by intravenous tissue plasminogen activator. *J Neurol Sci.* 2004;225:3–9. <https://doi.org/10.1016/j.jns.2004.05.020>.
- Yoo AJ, et al. MRI-based selection for intra-arterial stroke therapy: value of pretreatment diffusion-weighted imaging lesion volume in selecting patients with acute stroke who will benefit from early recanalization. *Stroke.* 2009;40:2046–54. <https://doi.org/10.1161/strokeaha.108.541656>.
- Tisserand M, et al. Does diffusion lesion volume above 70 mL preclude favorable outcome despite post-thrombolysis recanalization? *Stroke.* 2016;47:1005–11. <https://doi.org/10.1161/strokeaha.115.012518>.
- Gilgen MD, et al. Younger stroke patients with large pretreatment diffusion-weighted imaging lesions may benefit from endovascular treatment. *Stroke.* 2015;46:2510–6. <https://doi.org/10.1161/strokeaha.115.010250>.
- Chen F, Ni Y-C. Magnetic resonance diffusion-perfusion mismatch in acute ischemic stroke: an update. *World J Radiol.* 2012;4:63.
- Chang SC, et al. Diffusion-weighted MRI features of brain abscess and cystic or necrotic brain tumors: comparison with conventional MRI. *Clin Imaging.* 2002;26:227–36.
- Cartes-Zumelzu FW, et al. Diffusion-weighted imaging in the assessment of brain abscesses therapy. *AJNR Am J Neuroradiol.* 2004;25:1310–7.
- Batra A, Tripathi R, Gorthi S. Magnetic resonance evaluation of cerebral toxoplasmosis in patients with the acquired immunodeficiency syndrome. *Acta Radiol.* 2004;45:212–21.
- Batra A, Tripathi R. Diffusion-weighted magnetic resonance imaging and magnetic resonance spectroscopy in the evaluation of focal cerebral tubercular lesions. *Acta Radiol.* 2004;45:679–88.
- Greenlee JE. Subdural empyema. *Curr Treat Options Neurol.* 2003;5:13–22.
- Wong AM, Zimmerman RA, Simon EM, Pollock AN, Bilaniuk LT. Diffusion-weighted MR imaging of subdural empyemas in children. *AJNR Am J Neuroradiol.* 2004;25:1016–21.
- Liu Z-H, Chen N-Y, Tu P-H, Lee S-T, Wu C-T. The treatment and outcome of postmeningitic subdural empyema in infants. *J Neurosurg Pediatr.* 2010;6:38–42. <https://doi.org/10.3171/2010.4.peds09433>.
- Yang D, et al. Cerebral gliomas: prospective comparison of multivoxel 2D chemical-shift imaging proton MR spectroscopy, echoplanar perfusion and diffusion-weighted MRI. *Neuroradiology.* 2002;44:656–66. <https://doi.org/10.1007/s00234-002-0816-9>.
- Filippi CG, et al. Appearance of meningiomas on diffusion-weighted images: correlating diffusion constants with histopathologic findings. *AJNR Am J Neuroradiol.* 2001;22:65–72.
- Barajas R, Rubenstein J, Chang J, Hwang J, Cha S. Diffusion-weighted MR imaging derived apparent diffusion coefficient is predictive of clinical outcome in primary central nervous system lymphoma. *Am J Neuroradiol.* 2010;31:60–6.

29. Huang W-Y, et al. Diffusion-weighted imaging for predicting and monitoring primary central nervous system lymphoma treatment response. *Am J Neuroradiol.* 2016;37:2010–8.
30. Schubert M, Wilke M, Müller-Wehrich S, Auer D. Diffusion-weighted magnetic resonance imaging of treatment-associated changes in recurrent and residual medulloblastoma: preliminary observations in three children. *Acta Radiol.* 2006;47:1100–4.
31. Hayashida Y, et al. Diffusion-weighted imaging of metastatic brain tumors: comparison with histologic type and tumor cellularity. *AJNR Am J Neuroradiol.* 2006;27:1419–25.
32. Hein PA, Eskey CJ, Dunn JF, Hug EB. Diffusion-weighted imaging in the follow-up of treated high-grade gliomas: tumor recurrence versus radiation injury. *AJNR Am J Neuroradiol.* 2004;25:201–9.
33. Barath K, Huber AM, Stampfli P, Varga Z, Kollias S. Neuroradiology of cholesteatomas. *AJNR Am J Neuroradiol.* 2011;32:221–9. <https://doi.org/10.3174/ajnr.A2052>.
34. Yousef AF, Elkhartbotly A, Settin M, Mousa Y. Role of diffusion-weighted MR imaging in discrimination between the intracranial cystic masses. *Egypt J Radiol Nucl Med.* 2014;45:869–75.
35. Li PM, Linos E, Gurgel RK, Fischbein NJ, Blevins NH. Evaluating the utility of non-echo-planar diffusion-weighted imaging in the preoperative evaluation of cholesteatoma: a meta-analysis. *Laryngoscope.* 2013;123:1247–50. <https://doi.org/10.1002/lary.23759>.
36. Johnson RT. Prion diseases. *Lancet Neurol.* 2005;4:635–42. [https://doi.org/10.1016/S1474-4422\(05\)70192-7](https://doi.org/10.1016/S1474-4422(05)70192-7).
37. Fragoso DC, et al. Imaging of Creutzfeldt-Jakob disease: imaging patterns and their differential diagnosis. *Radiographics.* 2017;37:234–57. <https://doi.org/10.1148/rg.2017160075>.
38. Kallenberg K, et al. Creutzfeldt-Jakob disease: comparative analysis of MR imaging sequences. *Am J Neuroradiol.* 2006;27:1459–62.
39. Suzuki K, Kawasaki A, Nagashima T, Hirata K. Diffusion-weighted MRI abnormalities antedate the onset of sporadic Creutzfeldt-Jakob disease. *Neurology.* 2016;87:843–5.
40. Kelley BP, et al. Autoimmune encephalitis: pathophysiology and imaging review of an overlooked diagnosis. *Am J Neuroradiol.* 2017;38:1070–8. <https://doi.org/10.3174/ajnr.A5086>.



Samira N. Kashefi and Gavin P. Winston

## Contents

14.1	<b>Diffusion Tensor Imaging (DTI)</b> .....	203
14.1.1	Principles of DTI.....	203
14.1.2	How DTI Images are Acquired.....	204
14.1.3	How DTI Imaging Is Displayed.....	205
14.1.4	How DTI Images are Analysed.....	206
14.1.5	DTI Limitations.....	206
14.2	<b>Clinical Applications</b> .....	207
14.2.1	DTI in the Developing Brain.....	207
14.2.2	Multiple Sclerosis (MS).....	208
14.2.3	Neurosurgical Planning.....	209
14.3	<b>Conclusions</b> .....	211
14.4	<b>Clinical Case</b> .....	212
	<b>References</b> .....	212

---

## 14.1 Diffusion Tensor Imaging (DTI)

### 14.1.1 Principles of DTI

Diffusion tensor imaging (DTI) has been extensively used in human brain research since the 1990s [1]. DTI explores the random micro-movements of water molecules inside the tissue. The diffusion of water in biological tissues is restricted by a multitude of microscopic structural features such as cell membranes and macromolecules. By measuring the degree of water diffusion in multiple directions and mathematical modelling as a tensor, DTI can be used to probe

---

S. N. Kashefi  
UCL Queen Square Institute of Neurology,  
London, UK

G. P. Winston (✉)  
UCL Queen Square Institute of Neurology,  
London, UK

Epilepsy Society MRI Unit,  
Chalfont St Peter, UK

Division of Neurology, Department of Medicine,  
Queen's University, Kingston, ON, Canada  
e-mail: [g.winston@ucl.ac.uk](mailto:g.winston@ucl.ac.uk)

tissue microstructure *in vivo* and demonstrate neuronal alterations, primarily in white matter (WM), which may not be visible with conventional imaging [2].

DTI models the diffusional displacement of water molecules with a three-dimensional Gaussian distribution to provide insight into the microscopic environment of the water molecules within a tissue [2, 3]. The mathematical model of the tensor that describes the diffusion process can be visually represented by an ellipsoid with three axes determined by the eigenvectors (Fig. 14.1). The long axis represents the predominant direction of diffusion in each voxel (with a corresponding magnitude given by the eigenvalue  $\lambda_1$ ) and the two short axes represent directions with more restricted diffusion (eigenvalues  $\lambda_2$  and  $\lambda_3$ ).

The eigenvalues can yield many quantitative measurements that can be used to evaluate certain tissue physiological states [2, 4]. Fractional anisotropy (FA) is the most widely used measure of anisotropy and indicates the degree of directionality of diffusion within a voxel. FA values vary from 0, indicating fully isotropic diffusion (e.g. cerebrospinal fluid, CSF), to 1 in a completely anisotropic condition. FA can be considered a normalised variance of the eigenvalues. It is a summary measure of microstructural integrity that is extremely sensitive to microstructural changes but less specific to the type of change, so the use of additional DTI parameters is highly recommended [3, 5].

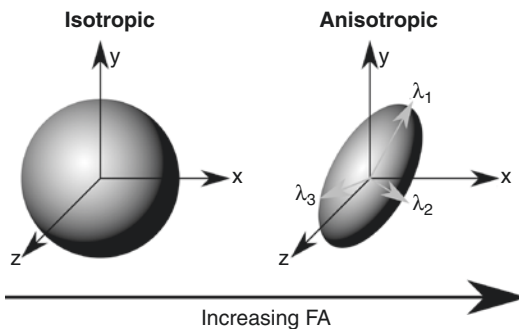


**Fig. 14.1** In CSF, water diffusion is isotropic whereas in WM it is anisotropic and can be represented by an ellipsoid. FA ranges from 0, when diffusion is isotropic, to 1, representing completely anisotropic diffusion. Typical values in WM are  $\sim 0.7$

The average of the three eigenvalues yields mean diffusivity (MD) and corresponds to the directionally averaged magnitude of water diffusion that tends to increase in WM disruption. For example, the MD increases and FA decreases in the presence of extracellular oedema, whereas the MD decreases and FA increases when there are high-grade tumours [6]. In the case of axonal fibre degeneration and myelin breakdown, the MD increases, and FA decreases [7]. Any other disruption of parallel water motion along the WM tracts from other causes such as trauma, infection and inflammation can result in increased MD and decreased FA. The utility of DTI is however limited because it has been shown these parameters can be affected by many other pathophysiological changes [2].

The mean diffusivity can be decomposed into axial diffusivity (AD), the eigenvalue corresponding to the long axis, and radial diffusivity (RD), the average of the other two eigenvalues. AD and RD measure the rate of water motion parallel and perpendicular, respectively, to the predominant direction of diffusion within a voxel. RD has been considered to be a myelin marker as it may increase when there is damage to or loss of myelin while AD has been considered a marker of axonal injury and may decrease when there is axonal injury [2, 5]. However, this is an overly simplistic representation that may not hold depending on the tissue microstructure [8].

### 14.1.2 How DTI Images are Acquired

Diffusion-weighting is achieved by applying diffusion-sensitising gradients during the MR pulse sequence that results in a signal loss whose magnitude depends on the degree of water diffusion in the direction of the applied gradient. When these gradients are applied with numerous different directions, the three-dimensional directional dependence of the rate of diffusion in tissues can be sampled [3].

One of the most important factors is the number of diffusion-encoding gradient directions

used. As the symmetric diffusion tensor has six unique elements, a minimum of six diffusion-weighted images with diffusion determined along non-collinear axes and one image without diffusion weighting is needed. Initial studies, therefore, used few directions (to minimise scan time) but it was subsequently shown that a larger number of acquisitions is necessary to obtain reliable unbiased estimates of DTI parameters that are robust to noise [9].

Typical voxel dimensions are 2.0–2.5 mm isotropic at 1.5 and 3 T with a scan duration that varies according to the acquisition scheme and sequence. The echo-planar imaging sequences used to acquire DTI can distort air–bone interfaces, such as the orbitofrontal cortex, temporal pole and brain stem and therefore it is important to remember these limitations when interpreting DTI data [4, 10].

### 14.1.3 How DTI Imaging Is Displayed

DTI can be visualised by displaying a scalar quantity, such as FA or MD (Fig. 14.2), or by displaying the main eigenvector direction using a colour-coding scheme known as directional encoding colour (DEC) [11]. DEC represents the orientation of the major eigenvector using the following colour scheme: red for left–right, green for anterior–posterior and blue for superior–inferior. For example, if the main eigenvector points mostly left/right, then the colour will be primarily red but otherwise, the colour will be a mixture of red, green and blue depending on the magnitudes of the components in each direction. FA can be used to modulate the brightness of the colours and enhance information from the WM and suppress visualisation from outside (Fig. 14.2, top middle).

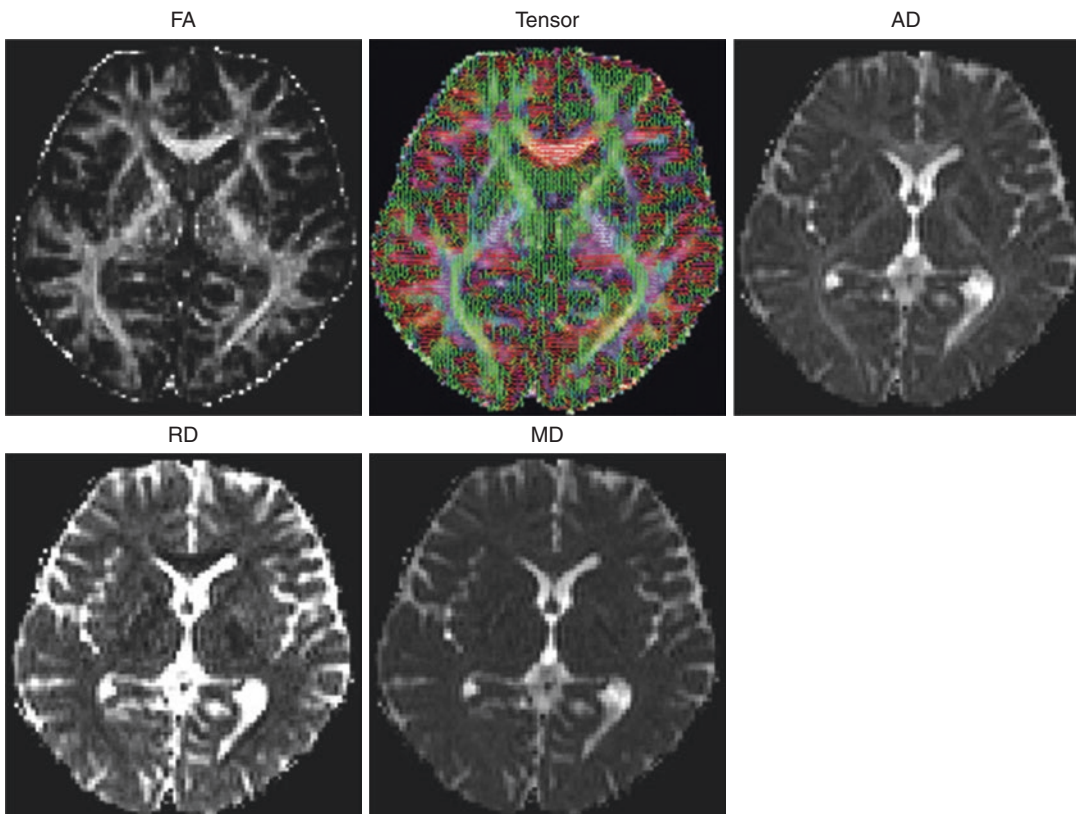


**Fig. 14.2** Representation of scalar parameters derived from a DTI acquisition (FA, AD, RD, MD) and DEC of the direction of the predominant eigenvector. (Adapted from [3] under CC BY-NC 4.0 licence)



#### 14.1.4 How DTI Images are Analysed

In clinical practice and research, it might be important to assess the integrity of WM tracts at a specific location or globally within the whole brain. There are various approaches to the statistical quantification of DTI parameters. The most common methods are region of interest (ROI)-based analysis, tract-based spatial statistics (TBSS) and voxel-based morphometry (VBM), each with their respective advantages and disadvantages [2]. It is very important to understand that significant variation may exist between study findings obtained using different analysis techniques. Even when data acquisition methods are the same, significantly different values have been obtained following the use of different analysis techniques.

ROI-based approaches analyse voxels within selected anatomically defined structures. They may find small differences not apparent on whole-brain analyses. ROIs are typically manually delineated, which is time-consuming and ineffective as the sample size increases. ROIs can also be achieved by semi-automated segmentation, which is less subjective and time-consuming but may be subject to errors depending on the methods employed [12].

TBSS and VBM are whole-brain analysis techniques for comparing DTI parameters between different groups or their correlation with clinical variables. VBM uses spatial normalisation to align each brain to a group template and smoothing to minimise the effects of registration errors and allow statistical assumptions about the distribution of data. Group comparisons are made on a voxel-wise basis and then corrected for multiple comparisons [13].

TBSS was developed to study the core of WM tracts by projecting each subject's diffusion data onto a common skeleton and minimises any registration inaccuracies [14]. The resulting maps require no smoothing and group-wise analyses are performed similarly to VBM. The major limitation of TBSS is that it cannot detect variation in the periphery of WM fibres (or indeed grey matter [GM]), as it is not included in the analysis.

Information from the diffusion tensor can also be used to reconstruct fibre pathways and this

technique is known as tractography. Tractography non-invasively maps neuronal fibres by successively piecing together estimates of fibre pathways using the direction of maximum diffusion within each voxel. Both deterministic and probabilistic tractography algorithms are available that start from a point or region in the brain (seed) and trace connections [12, 15].

Deterministic approaches generate streamlines from the seed region using the estimated fibre orientation step-by-step in each voxel and terminate at pre-specified criteria such as a large change in direction or low FA. Using prior anatomical knowledge of WM tracts, inclusion and exclusion regions can be specified to improve the results. However, factors such as crossing or branching fibres, acquisition noise, artefacts and patient movement can create uncertainty in the estimated direction. Probabilistic algorithms aim to compensate for these problems by generating multiple possible streamlines from each voxel in the seed region that incorporate this uncertainty [15].

#### 14.1.5 DTI Limitations

It is important to understand that DTI measurements are not direct representations of brain anatomy or axons but a model that may be improved to more accurately represent complex tissue architecture. Therefore, this factor must be considered when using DTI in clinical practice [12].

DTI limitations derived from acquisition include poor spatial resolution, inaccuracies introduced by low signal-to-noise ratio and distortions from magnetic susceptibility that can cause misregistration with anatomical images [3, 4, 12]. New techniques have been developed to improve the quality of DTI images [5], including reduction of field of view (FOV), smaller slice thickness and acquisition in the axial plane.

DTI assumes a single diffusion process following a Gaussian distribution within each voxel and represents an overly simplistic view of tissue microstructure [2, 3]. In biological tissue, the environments are not homogenous due to the presence of complex cellular microstructure and DTI cannot resolve multiple crossing fibres or geometries such as fanning fibres as only a single

fibre population is modelled in each voxel. More advanced models of diffusion such as high angular resolution diffusion imaging (HARDI), diffusion kurtosis imaging [16] and diffusion spectrum imaging (DSI) have been developed to address these problems [17].

## 14.2 Clinical Applications

DTI has been used to demonstrate abnormalities in a variety of brain disorders, including stroke, multiple sclerosis, dyslexia and epilepsy, and is becoming a part of many routine clinical protocols. Owing to the technical challenges of the small cross-sectional area and relatively large voxel dimensions, DTI is used much less commonly in the clinical assessment of the spinal cord [18]. Diffusion anisotropy is not a unique property of neural tissue and has been observed in other tissues; however, in this chapter, we concentrate on brain tissue.

### 14.2.1 DTI in the Developing Brain

Brain development is a dynamic and evolving process particularly during the prenatal period and the first two years after birth. During these stages, cognitive and motor function develops, as well as many neurodevelopmental disorders. Asynchronous myelin maturation starts late in embryonic development, peaks during the first year of life and continues through to the end of adolescence. DTI has been used for anatomical studies, to investigate changes in WM at different

stages of brain development and to understand neurocognitive development and brain abnormalities in early life [19].

DTI can track the maturation of WM tracts as the brain develops. In normal growth and development, the brain water content decreases with maturation as axonal membranes become more densely packed, and restriction of water motion increases. The WM of the neonate's brain has an MD value almost twice that of the fully myelinated brain, which decreases with maturation, while FA is relatively low and increases steadily with maturation [20]. The whole-brain volume nearly quadruples between birth and 5 years of age.

DTI studies have enabled the visualisation of subtle structures of the foetal brain from 18 weeks' gestational age. WM maturation appears to evolve from the inner to outer layers and from anterior to posterior. It is also non-linear, with the maximum degrees of change detected in the majority of tracts by 5 years of age. Many of the major WM fibres such as peduncles, internal capsules, corticospinal tract and the composite dorsal brainstem tract are visible on the DEC maps of new-borns. Major tracts such as the inferior longitudinal fasciculi become apparent around 3 months of age. DTI tractography can demonstrate the absence of right–left commissural crossing fibres, as well as the presence of large heterotopic intra-hemispheric fibres along the medial and superior walls of the lateral ventricles, which are oriented in the anterior–posterior direction (Fig. 14.3) [5].

The development of WM can be divided into three stages using DTI parameters [21]. In the

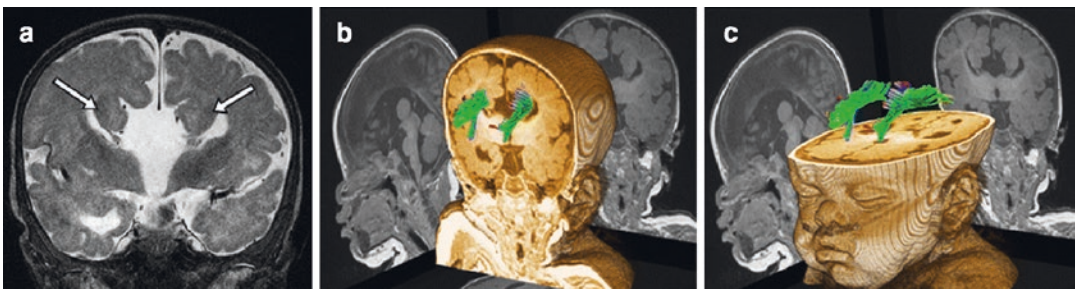


**Fig. 14.3** (a) Coronal T2-weighted image demonstrates third ventricle communicating superiorly with the interhemispheric cistern, and the presence of Probst bundles (arrows), (b) and (c) Probst bundles, white matter fibres that would normally cross the corpus callosum and instead run parallel can be reconstructed using DTI tractography

first stage, progressive fibre organisation occurs, high FA is observed, and it can be due to an increase in AD and a decrease in RD. In the second stage, membrane density increases due to the proliferation of glial cells and oligodendrocytes, but WM development is isotropic. Therefore, a reduction in MD but no effect on FA is observed. In the last stage, the maturation of WM results in an increase in FA and a decrease in RD and MD [22]. Cortical development is not homogeneous throughout the brain and shows considerable regional differences, with anisotropy decreasing first in the pre-central cortex, followed by the occipital and frontal cortices.

DTI is also useful for assessing perinatal brain injuries such as perinatal arterial stroke and hypoxic-ischaemic encephalopathy in the term-born infant. The pre-term brain is susceptible to injury from ischaemic, haemorrhagic, inflammatory and infective insults. DTI studies have observed lower FA in the centrum semiovale, frontal WM and genu of the corpus callosum compared to age- and sex-matched term-born controls [20, 22]. The most immature infants, born before 28 weeks post-menstrual age (PMA), displayed further reductions in FA at term and suggests that cortical microstructure in the pre-term brain differs from that of healthy term controls. Studies have shown that DTI can successfully predict hemiparesis in ex-preterm infants by detecting asymmetric corticospinal tract disruption at the level of the periventricular WM that is not apparent on conventional MRI. In addition, tractography has also demonstrated disrupted thalamocortical connectivity at sites distant from the initial infarct in unilateral periventricular haemorrhagic infarction [22].

In summary, DTI can provide valuable information on alterations in the underlying tissue microstructure during brain development and in perinatal brain injury. It can be used as an imaging biomarker to assess the efficacy of treatment and as a surrogate measure of subsequent performance. More advanced DTI techniques are beginning to be employed to assess the infant brain and may improve our understanding of the impact of prematurity or perinatal brain injury on subsequent axonal and neuronal development

and thereby help inform decisions about future therapeutic targets.

### 14.2.2 Multiple Sclerosis (MS)

MS is an inflammatory disease of the central nervous system (CNS), consisting of the brain and the spinal cord. It causes gradual destruction of the myelin sheath, leading to axonal injury and neuronal cell death. The clinical course and neuropathology of MS vary between individuals, so diagnosis and complete understanding of the disease remains challenging. Conventional MRI provides little information on tissue integrity, the severity of the injury and its later recovery [23]. DTI provides a greater dynamic range of information on WM microarchitecture and disorganisation both within lesions as well as within the WM that appears normal on conventional MRI scans. MS lesions typically show increased MD and decreased FA that correlate with axonal structural and myelin destruction [7, 23].

DTI parameters have been used to differentiate acute and chronic lesions [23]. In chronic lesions where diffusion is least restricted, MD is very high and FA very low. FA values are relatively low in enhancing lesions compared with non-enhancing lesions, but the MD does not show any correlation with the presence of enhancement. Increased RD values have been detected in focal T2-weighted lesions and normal-appearing WM (NAWM). A relative increase in AD values has also been detected in lesional fibres and this is consistent with Wallerian degeneration [7, 24].

DTI changes have been detected in the NAWM prior to the appearance of new lesions. Many studies have shown significant DTI changes in the NAWM of patients with MS compared to control subjects [22]. Patients who were early in the course of MS had significant DTI abnormalities in the corpus callosum, basal ganglia and other regions that appeared normal on conventional MRI [24]. Another study has shown the relationship between increased FA in normal-appearing grey matter, decreased GM volume and clinical disability in patients with MS [7].

Several studies have shown that DTI parameters are significantly different in the optic nerve of patients with MS compared to healthy controls [25]. This may indicate optic nerve damage in terms of demyelination and axonal degradation after optic neuritis in MS. Longitudinal follow-up of up to one year after acute optic neuritis showed reduced AD at the beginning, which increased to normal levels over time. FA values were normal at the onset but decreased over time. It was suggested that these findings may show demyelination and axonal loss at the onset but possible reorganisation processes over time. DTI, at least to a certain extent, can detect and quantify these processes and could be used as a marker of the degenerative changes in the chronic state after optic neuritis. However, it is essential to recognise that DTI is not reliable in regions of fibre crossings and may show very low FA values in these regions. In addition, DTI parameters cannot differentiate axonal disruption from demyelination or focal tissue oedema, as frequently seen in MS [23]. Therefore, any given voxel might contain varying amounts of cells that could be normal and damaged axons and free space due to vasogenic oedema.

Fibre tractography may also be helpful to assess changes in WM tract course and integrity in MS. Fewer fibre tracts are generated in locations with lesions than contralateral NAWM [26]. However, it is vital to understand that the number of fibres created also depends on the selected FA and angle of trajectory thresholds. Furthermore, tractography is susceptible to artefacts and may lack anatomical accuracy especially when anatomical changes occur due to disease such as atrophy of the ventricles.

DTI represents a very sensitive and potentially useful marker of tissue integrity in the clinical evaluation of MS, but several limitations still hinder its use in routine clinical diagnostics of MS. In addition, the heterogeneity of MS lesions and partial volume contamination of adjacent structures renders it technically difficult to obtain high-quality images. Therefore, a more accurate method that reflects the complexities of MS pathology has to be developed. Nonetheless, recent technical developments in image post-

processing have increased the reliability of DTI tractography in evaluating neural fibre integrity and acute inflammatory injury in relapsing-remitting MS to chronic degeneration in primary and secondary progressive MS. However, further studies are needed to validate these findings and to fully understand the clinical potential and implications of DTI in MS.

### 14.2.3 Neurosurgical Planning

DTI is a powerful tool for neurosurgical use and has made the most profound impact by providing valuable anatomic information for surgical planning. DTI fibre tractography combined with structural MRI is used for pre-surgical planning and intra-operative guidance. DTI allows the visualisation of structures such as the corticospinal tract, optic radiations and arcuate fasciculus to permit maximum surgical resection while minimising damage to these critical white matter tracts connecting eloquent cortex [27–29].

DTI has been used in the resection of both low- and high-grade gliomas [30]. The first study that introduced the possible neurosurgical use of DTI was in 2001 [27]. A year later, another study suggested DTI as a possible avenue of research after analysing 103 patients with gliomas treated with resection guided by direct stimulation [30]. Within the following 2 years, several groups began investigating the integrity of DTI and subsequently its use in tumour resection.

A randomised study showed a significantly decreased incidence of postoperative motor deficits (from 33% to 15%) in patients with brain tumour with motor tract involvement when preoperative DTI scans were utilised in the intra-operative navigational system [31]. In the high-grade tumour subgroup, median survival increased significantly from 14 months to 21 months with the intraoperative use of preoperative DTI. Many studies and experimental data have suggested that preoperative DTI improves surgical outcomes for patients with a brain tumour, but that DTI should be used with caution because it only suggests where large-bundle WM tracts are likely to be located (Fig. 14.4) [28].

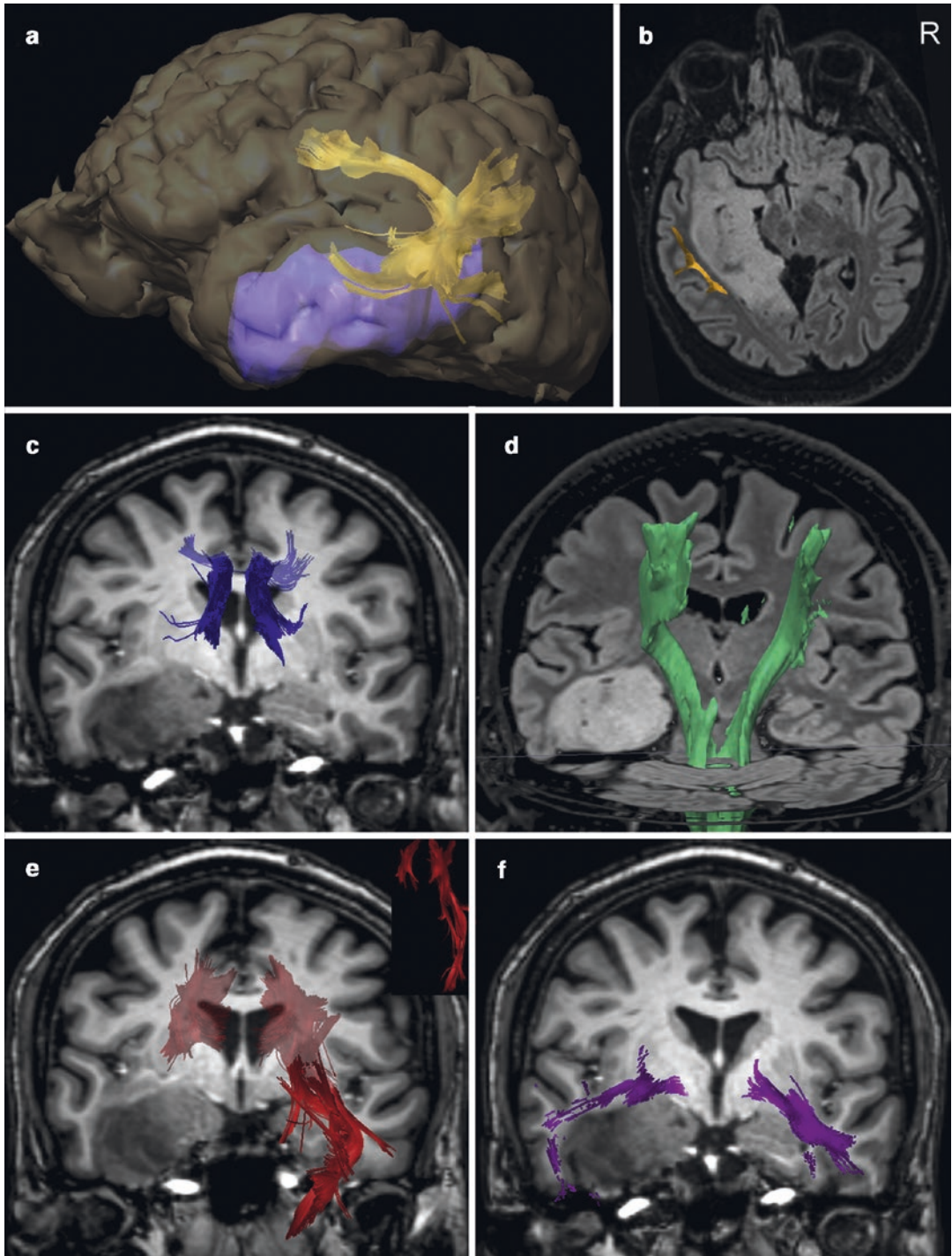


**Fig. 14.4** Preoperative DTI images show a close relationship of deep structures with the tumour in a 40-year-old patient with left-sided diffuse astrocytoma and focal seizures. (a) 3D view of tumour (blue/purple) and arcuate fasciculus (yellow) projected on cerebral cortex, (b) the same shown on T2-weighted FLAIR MRI, (c) the cingu-

late fasciculi projected on a coronal T1-weighted MRI, (d) the pyramidal tracts projected on a coronal T2-weighted FLAIR MRI, (e) the left inferior fronto-occipital fasciculus is disrupted by the tumour, (f) the left uncinate fasciculus is displaced by the tumour. (Reproduced from [38] with permission)

Another important problem is that brain shift may occur during surgery, especially when peritumoural oedema is present [28]. One possible approach to overcoming this problem is to make full use of the neuroimaging data by continuously comparing pre and updated intraoperative images acquired during surgery [32].

Tractography is also valuable for epilepsy surgery. Anterior temporal lobe resection (ATLR) is a well-established treatment for patients with drug-resistant epilepsy but 50% to 90% of patients who undergo ATLR develop a postoperative visual field defect due to injury to the most anterior part of the optic radiation, Meyer's loop (ML) [33]. ML is located in the anterior temporal lobe, adjacent to other WM pathways, and it cannot be visually identified by the human eye or by conventional imaging techniques. DTI is helpful in delineating the optic radiation before ATLR to assess the risk of developing a visual field defect [29, 33, 34] as well as for intraoperative use to avoid injury to ML [35, 36] where correction for brain shift can be made.

Tractography can evaluate other functional pathways pre-surgically including language tracts in patients undergoing ATLR for predicting language deficits [19, 30]. The use of pre- and post-operative tractography for language function improves the preservation of language tracts in patients and prevents post-operative language deficits [37]. In patients with high-grade glioma, it was possible to attain satisfactory resection while conserving or improving the preoperative neurologic status [30, 37].

In summary, DTI methods have the potential to be integrated effectively with other neuroimaging modalities in the planning of neurosurgery. It may be employed to avoid injury to the WM

tracts connecting eloquent cortical regions. However, only small trials have examined the potential benefit of DTI guidance in addition to conventional imaging. Therefore, further research is required to demonstrate the effectiveness of DTI techniques.

---

### 14.3 Conclusions

DTI is an increasingly studied imaging modality that enables the quantitative evaluation of the human brain structure and the visualisation of WM anatomy *in vivo*. Owing to the complex anatomy of the human brain, DTI has found many uses in brain research and treatments. DTI is a promising modality for the study and analysis of brain development, the evaluation and understanding of MS and effective planning for neurosurgery. DTI can be acquired easily and quickly on most scanners so is clinically applicable. However, it employs a simplistic model of tissue microstructure with assumptions that may not be valid in biological systems.

More advanced models of diffusion such as diffusion kurtosis imaging (DKI) and diffusion spectrum imaging (DSI) have been developed. DKI is an extension of DTI that quantifies deviations from Gaussian diffusion. It is proposed as being highly sensitive to microstructural changes in tissues with the potential for early diagnosis of diseases such as Alzheimer's and epilepsy. Nevertheless, it is clear that DTI provides important information about the biological property of various WM pathways, and the end-user should appreciate the sources of error from DTI to derive the most useful conclusions.

## 14.4 Clinical Case (Fig. 14.5)

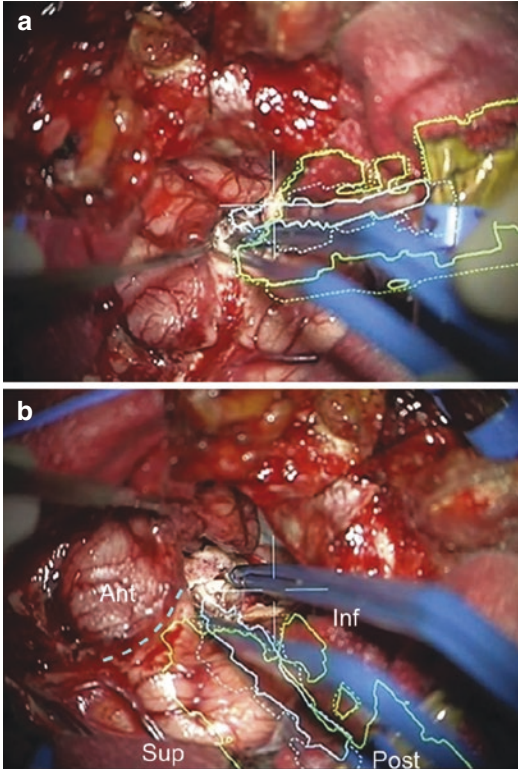


**Fig. 14.5** Operating microscope display of a patient undergoing right anterior temporal lobe resection. The head is rotated in the operating position as indicated in the lower panel. The superimposed outlines are the optic radiation (yellow-green) and the ventricle (blue). Solid outlines refer to the structure in the focal plane and dashed outlines refer to the maximum extent below this. (a) The surgeon approaching the tip of the temporal horn of the lateral ventricle from the middle cranial fossa while remaining inferior to the optic radiation. (b) The point of entry into the lateral ventricle exposing the hippocampus. The next step of the operation is to transect the temporal stem along the dotted blue line remaining anterior to the maximal projection of the optic radiation. (Reproduced from [36] under Creative Commons Attribution License)

**Acknowledgements** Dr. Winston was funded by an MRC Clinician Scientist Fellowship (MR/M00841X/1).

## References

1. Bassar PJ, Mattiello J, LeBihan D. Estimation of the effective self-diffusion tensor from the NMR spin echo. *J Magn Reson B*. 1994;103(3):247–54.
2. Winston GP. The physical and biological basis of quantitative parameters derived from diffusion MRI. *Quant Imaging Med Surg*. 2012;2(4):254–65.
3. Tae WS, Ham BJ, Pyun SB, Kang SH, Kim BJ. Current clinical applications of diffusion-tensor imaging in neurological disorders. *J Clin Neurol*. 2018;14(2):129–40.
4. Huston JM, Field AS. Clinical applications of diffusion tensor imaging. *Magn Reson Imaging Clin N Am*. 2013;21(2):279–98.
5. Vorona GA, Berman JI. Review of diffusion tensor imaging and its application in children. *Pediatr Radiol*. 2015;45(Suppl 3):S375–81.
6. Tsolaki E, Kousi E, Svolos P, Kapsalaki E, Theodorou K, Kappas C, et al. Clinical decision support systems for brain tumor characterization using advanced magnetic resonance imaging techniques. *World J Radiol*. 2014;6(4):72–81.
7. Calabrese M, Rinaldi F, Seppi D, Favaretto A, Squarcina L, Mattisi I, et al. Cortical diffusion-tensor imaging abnormalities in multiple sclerosis: a 3-year longitudinal study. *Radiology*. 2011;261(3):891–8.
8. Wheeler-Kingshott CA, Cercignani M. About “axial” and “radial” diffusivities. *Magn Reson Med*. 2009;61(5):1255–60.
9. Jones DK. The effect of gradient sampling schemes on measures derived from diffusion tensor MRI: a Monte Carlo study. *Magn Reson Med*. 2004;51(4):807–15.
10. Ni H, Kavcic V, Zhu T, Ekholm S, Zhong J. Effects of number of diffusion gradient directions on derived diffusion tensor imaging indices in human brain. *AJNR Am J Neuroradiol*. 2006;27(8):1776–81.
11. Pajevic S, Pierpaoli C. Color schemes to represent the orientation of anisotropic tissues from diffusion tensor data: application to white matter fiber tract mapping in the human brain. *Magn Reson Med*. 1999;42(3):526–40.
12. Lerner A, Mogensen MA, Kim PE, Shiroishi MS, Hwang DH, Law M. Clinical applications of diffusion tensor imaging. *World Neurosurg*. 2014;82(1–2):96–109.
13. Ashburner J. Computational anatomy with the SPM software. *Magn Reson Imaging*. 2009;27(8):1163–74.
14. Smith SM, Jenkinson M, Johansen-Berg H, Rueckert D, Nichols TE, Mackay CE, et al. Tract-based spatial statistics: voxelwise analysis of multi-subject diffusion data. *NeuroImage*. 2006;31(4):1487–505.
15. Lilja Y, Ljungberg M, Starck G, Malmgren K, Rydenhag B, Nilsson DT. Visualizing Meyer’s loop: a comparison of deterministic and probabilistic tractography. *Epilepsy Res*. 2014;108(3):481–90.
16. Winston GP. The potential role of novel diffusion imaging techniques in the understanding and treatment of epilepsy. *Quant Imaging Med Surg*. 2015;5(2):279–87.
17. Wedeen VJ, Wang RP, Schmahmann JD, Benner T, Tseng WY, Dai G, et al. Diffusion spectrum magnetic resonance imaging (DSI) tractography of crossing fibers. *NeuroImage*. 2008;41(4):1267–77.
18. Rutman AM, Peterson DJ, Cohen WA, Mossa-Basha M. Diffusion tensor imaging of the spinal cord: clinical

- cal value, investigational applications, and technical limitations. *Curr Probl Diagn Radiol.* 2018;47(4):257–69.
19. Ashwal S, Tong KA, Ghosh N, Bartnik-Olson B, Holshouser BA. Application of advanced neuroimaging modalities in pediatric traumatic brain injury. *J Child Neurol.* 2014;29(12):1704–17.
  20. Deshpande R, Chang L, Oishi K. Construction and application of human neonatal DTI atlases. *Front Neuroanat.* 2015;9:138.
  21. Dubois J, Dehaene-Lambertz G, Perrin M, Mangin JF, Cointepas Y, Duchesnay E, et al. Asynchrony of the early maturation of white matter bundles in healthy infants: quantitative landmarks revealed noninvasively by diffusion tensor imaging. *Hum Brain Mapp.* 2008;29(1):14–27.
  22. Qiu A, Mori S, Miller MI. Diffusion tensor imaging for understanding brain development in early life. *Annu Rev Psychol.* 2015;66:853–76.
  23. Fox RJ. Picturing multiple sclerosis: conventional and diffusion tensor imaging. *Semin Neurol.* 2008;28(4):453–66.
  24. Ge Y, Law M, Johnson G, Herbert J, Babb JS, Mannon LJ, et al. Preferential occult injury of corpus callosum in multiple sclerosis measured by diffusion tensor imaging. *J Magn Reson Imaging.* 2004;20(1):1–7.
  25. Kuchling J, Brandt AU, Paul F, Scheel M. Diffusion tensor imaging for multilevel assessment of the visual pathway: possibilities for personalized outcome prediction in autoimmune disorders of the central nervous system. *EPMA J.* 2017;8(3):279–94.
  26. Ge Y. Multiple sclerosis: the role of MR imaging. *AJNR Am J Neuroradiol.* 2006;27(6):1165–76.
  27. Coenen VA, Krings T, Mayfrank L, Polin RS, Reinges MH, Thron A, et al. Three-dimensional visualization of the pyramidal tract in a neuronavigation system during brain tumor surgery: first experiences and technical note. *Neurosurgery.* 2001;49(1):86–92; discussion 92–3.
  28. Ulmer JL, Klein AP, Mueller WM, DeYoe EA, Mark LP. Preoperative diffusion tensor imaging: improving neurosurgical outcomes in brain tumor patients. *Neuroimaging Clin N Am.* 2014;24(4):599–617.
  29. Winston GP, Yogarajah M, Symms MR, McEvoy AW, Micallef C, Duncan JS. Diffusion tensor imaging tractography to visualize the relationship of the optic radiation to epileptogenic lesions prior to neurosurgery. *Epilepsia.* 2011;52(8):1430–8.
  30. Abdullah KG, Lubelski D, Nucifora PG, Brem S. Use of diffusion tensor imaging in glioma resection. *Neurosurg Focus.* 2013;34(4):E1.
  31. Wu JS, Zhou LF, Tang WJ, Mao Y, Hu J, Song YY, et al. Clinical evaluation and follow-up outcome of diffusion tensor imaging-based functional neuronavigation: a prospective, controlled study in patients with gliomas involving pyramidal tracts. *Neurosurgery.* 2007;61(5):935–48; discussion 48–9.
  32. Bayer S, Maier A, Ostermeier M, Fahrig R. Intraoperative imaging modalities and compensation for brain shift in tumor resection surgery. *Int J Biomed Imaging.* 2017;2017:6028645.
  33. Winston GP. Epilepsy surgery, vision, and driving: what has surgery taught us and could modern imaging reduce the risk of visual deficits? *Epilepsia.* 2013;54(11):1877–88.
  34. Lilja Y, Nilsson DT. Strengths and limitations of tractography methods to identify the optic radiation for epilepsy surgery. *Quant Imaging Med Surg.* 2015;5(2):288–99.
  35. Cui Z, Ling Z, Pan L, Song H, Chen X, Shi W, et al. Optic radiation mapping reduces the risk of visual field deficits in anterior temporal lobe resection. *Int J Clin Exp Med.* 2015;8(8):14283–95.
  36. Winston GP, Daga P, White MJ, Micallef C, Misericchi A, Mancini L, et al. Preventing visual field deficits from neurosurgery. *Neurology.* 2014;83(7):604–11.
  37. Bello L, Castellano A, Fava E, Casaceli G, Riva M, Scotti G, et al. Intraoperative use of diffusion tensor imaging fiber tractography and subcortical mapping for resection of gliomas: technical considerations. *Neurosurg Focus.* 2010;28(2):E6.
  38. Potgieser AR, Wagemakers M, van Hulzen AL, de Jong BM, Hoving EW, Groen RJ. The role of diffusion tensor imaging in brain tumor surgery: a review of the literature. *Clin Neurol Neurosurg.* 2014;124:51–8.





Jiachen Zhuo and Rao P. Gullapalli

## Contents

15.1	<b>Introduction</b> .....	215
15.2	<b>Technical Background</b> .....	216
15.2.1	Model.....	216
15.2.2	Diffusion Kurtosis Imaging Parameters.....	217
15.2.3	DKI Reconstruction.....	219
15.2.4	Fiber Tracking Using DKI.....	219
15.3	<b>Clinical Applications</b> .....	221
15.3.1	Ischemia and Stroke.....	221
15.3.2	Glioma Grading.....	221
15.3.3	Traumatic Brain Injury (TBI).....	222
15.3.4	Multiple Sclerosis (MS).....	223
15.3.5	Other Neurodegenerative Disorders (Alzheimer's Disease, Parkinson Disease).....	224
15.4	<b>Practical Considerations and Limitations</b> .....	225
15.5	<b>Summary and Future Directions</b> .....	225
15.6	<b>Clinical Case</b> .....	226
	<b>References</b> .....	226

## 15.1 Introduction

Diffusion-weighted imaging (DWI) signal intensity relies on the Brownian motion of water molecules within the brain tissue. Diffusion Tensor Imaging (DTI) is an extension of the DWI technique and measures not only the average diffusion coefficient within the tissue, but also the

directionality of water diffusion. Despite the wide-spread adoption of DWI and DTI for clinical use, the underlying diffusion model is limited as it assumes a simplified Gaussian model for water diffusion distribution. More advanced diffusion imaging models are being put forward to better represent the underlying nature of the tissue microstructure.

In probability theory, the Gaussian distribution is a normative distribution of a given population that takes the form of a bell curve. DWI and DTI assume that the probability for a water

---

J. Zhuo · R. P. Gullapalli (✉)  
University of Maryland School of Medicine,  
Baltimore, MD, USA  
e-mail: [rgullapalli@som.umaryland.edu](mailto:rgullapalli@som.umaryland.edu)

molecule to travel a certain distance over time follows a Gaussian distribution, which is really only true if water molecules diffuse uniformly in an isotropic fashion, as in the case of a bucket of water (Fig. 15.1). In real tissue with complex cellular structures, water molecules are more likely to move through a highly heterogeneous environment leading to a deviation from the assumed Gaussian model (Fig. 15.1). Diffusion Kurtosis Imaging (DKI) is a recently developed diffusion technique that attempts to address this property of water diffusion by modeling the deviation from the Gaussian distribution to more appropriately capture the true nature of the tissue micro-environment. In probability theory and statistics, kurtosis is a measure of skewness of the shape of a probability distribution, which reflects the deviation of a given distribution from the normal Gaussian distribution. With the extra kurtosis term in the model, DKI can better capture the non-Gaussian diffusion behavior, which has been shown to reflect tissue microstructure and may be an important imaging marker for tissue heterogeneity [1]. A classic example is offered by the original inventor of the DKI method [2], who provides a contrasting example between the apparent diffusion coefficient and apparent diffusion kurtosis maps of phantoms with sucrose solutions (sucrose concentrations ranging from 5% to 25%) in comparison to pureed asparagus.

While the diffusion coefficients are similar in pureed asparagus versus sucrose solutions, the diffusion kurtosis parameter is able to capture the unique and independent feature associated with pureed asparagus that is reflective of a higher degree of structural complexity.

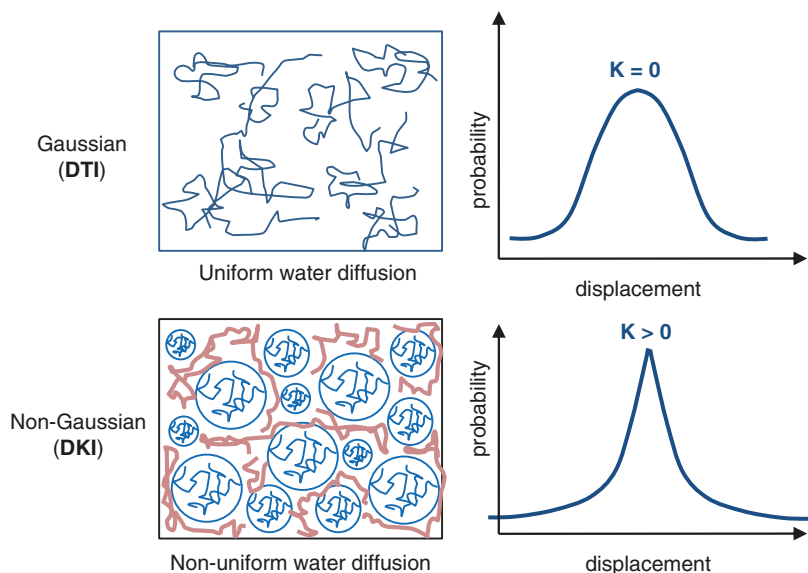
DKI has advantages over DTI because of its higher sensitivity to tissue heterogeneity, not only in white matter regions but also in regions with isotropic diffusion (e.g. gray matter, tumor) where DTI lacks sensitivity. In diseased brain tissue, diffusion kurtosis could change due to cytotoxic edema, reactive gliosis, alterations in cell packing geometry, changes in cell membranes, or change in cell size distribution resulting from cell necrosis [3–5]. Since there is a growing interest in using DKI in various clinical applications, the goal of this chapter is to give the readers a physics background of the DKI method, review the current research and clinical applications, and describe the limitation and potential future directions of the technique.

## 15.2 Technical Background

### 15.2.1 Model

In typical diffusion models (e.g. DWI or DTI), the diffusion-weighted signal decay follows a mono-exponential function (Eq. 15.1). With  $S(b)$

**Fig. 15.1** Diagram shows Gaussian and non-Gaussian diffusion environment and corresponding diffusion displacement distribution. Non-Gaussian diffusion is represented with a kurtosis  $K > 0$ , with more peakedness. *DTI* diffusion tensor imaging, *DKI* diffusion kurtosis imaging



being the diffusion-weighted signal along a certain direction with certain  $b$ -value, and  $S_0$  the non-diffusion weighted signal, the natural log of the signal attenuation  $\ln(S(b)/S_0)$  is related to the diffusion-weighting factor  $b$  in a manner that is related to the apparent diffusion coefficient,  $D$ . In the DKI model, this relationship is extended by including a higher-order  $b^2$  term, where the diffusion kurtosis,  $K$ , describes the deviation of the model from the original Gaussian model (Eq. 15.2).

$$\text{DWI or DTI: } \ln\left(\frac{S(b)}{S_0}\right) = -bD \quad (15.1)$$

$$\text{DKI: } \ln\left(\frac{S(b)}{S_0}\right) = -bD + \frac{1}{6}b^2D^2K^2 \quad (15.2)$$

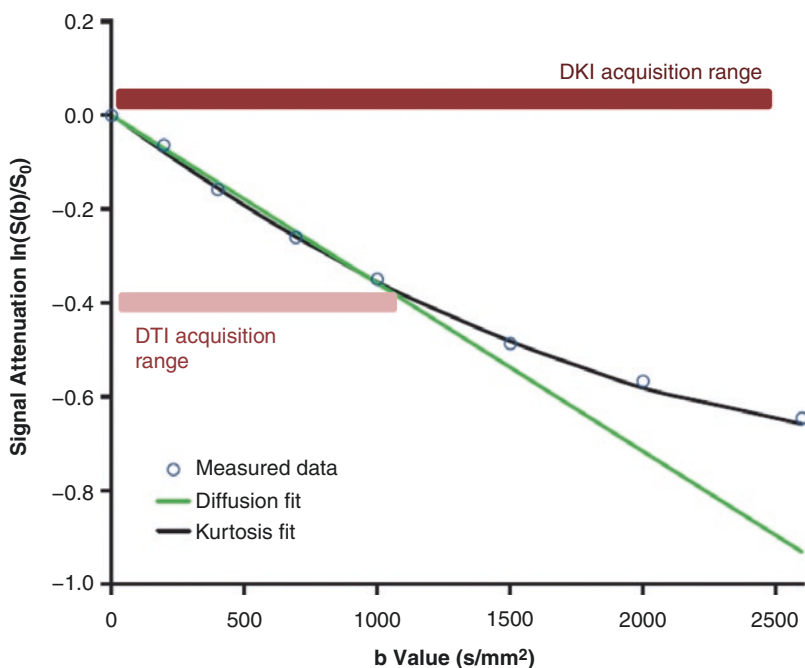
Figure 15.2 shows the measured diffusion-weighted signal in the corpus callosum using a  $b$ -value from 0 to 2600  $\text{s/mm}^2$  fitted with the diffusion model (green line) and the kurtosis model (black line). Clinically, a  $b$ -value of 800–1200  $\text{s/mm}^2$  is routinely used to obtain diffusion-weighted images. In this range (DTI acquisition range) water diffusion still largely approximates Gaussian diffusion and therefore is well modeled

by the classic model (Eq. 15.1). When stronger  $b$ -values are used ( $b$  of 2000–2500  $\text{s/mm}^2$ ) the diffusion-weighted signal deviates from the Gaussian model as the imaging technique becomes increasingly sensitive to shorter molecular distances and hence becomes more and more sensitive to heterogeneous water diffusion barriers from various cellular structures. The DKI model compared to the standard Gaussian model better captures such signal behavior. Although mathematically kurtosis can be either positive or negative, multi-compartment diffusion models and empirical evidence indicate that kurtosis is always non-negative ( $K \geq 0$ ) [6]. Higher kurtosis values reflect increased deviation from Gaussian distribution implying that water diffusion has to navigate through tissue microenvironment that is more and more complex.

### 15.2.2 Diffusion Kurtosis Imaging Parameters

The diffusion model presented in Eqs. (15.1) and (15.2) describes the DW signal when diffusion weighting is applied in a certain direction.

**Fig. 15.2** Diffusion-weighted signal attenuation  $\ln(S(b)/S_0)$  measured in the corpus callosum (blue circles) clearly shows deviation from the linear diffusion fitting (green line) beyond  $b$ -value of 1000  $\text{s/mm}^2$  and is well fitted with the kurtosis model (black line). DKI acquisition ranges need to extend the maximum  $b$ -value to 2000–2500  $\text{s/mm}^2$ . DKI diffusion kurtosis imaging



As diffusion is directional, the diffusion kurtosis also varies across different directions of diffusion and is dependent on the direction the diffusion weighting is applied. In DTI, which uses the Gaussian model, the directional diffusion profile is captured by a diffusion tensor (a second order tensor) and is often presented as a diffusion ellipsoid, with the principle axis pointing along the direction where diffusion is least restricted, and other two directions aligning within a plane radial to the principle diffusion axis. Similarly, the directional kurtosis is captured by a diffusion kurtosis tensor (a fourth order tensor) and has a far more complex profile. While the characteristics of a full kurtosis tensor is a topic of research exploration, the most commonly used DKI parameters are those related to the diffusion tensor. Analogous to the DTI parameters that include mean diffusivity (MD or ADC), fractional anisotropy (FA), axial diffusivity (AD) and radial diffusivity (RD), the commonly used DKI parameters include the unit less quantities of mean kurtosis (MK), kur-

tosis fractional anisotropy (FAK), axial kurtosis (AK) and radial kurtosis (RK). Figure 15.3 shows a simplified visual depiction diffusion kurtosis distribution, where it is shaped like a pancake, in relation to the diffusion ellipsoid. Figure 15.3 also shows various parametric maps using the DKI reconstruction (see next section) in a coronal brain section. Kurtosis increases as water diffusion deviates more and more from the Gaussian distribution, and typically this is the case when the underlying complexity of the tissue microstructure increases. White matter has higher kurtosis than gray matter due to the more complex axonal and myelin structure. Lower kurtosis along the axial direction (AK) is reflective of increased water diffusion along the principle diffusion direction and the least deviation from Gaussian distribution. High RK corresponds to highly restricted diffusion along the radial direction of the axon, where also the most tissue complexity comes into play. FAK is similar to FA, which measures the degree of anisotropy in the kurtosis distribution.

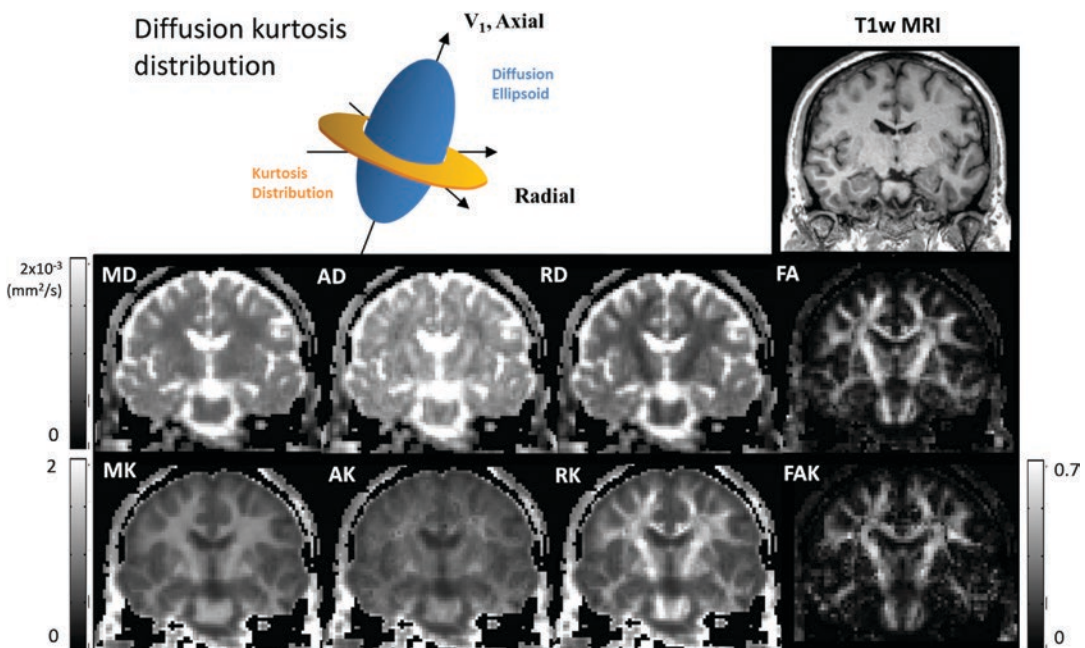


**Fig. 15.3** Simplified diffusion kurtosis distribution corresponds to the diffusion ellipsoid, and typical DKI maps in a coronal slice of brain along with the T1w MRI image. Gray bar shows range of diffusion coefficient (MD, AD, RD) from 0 to  $2 \times 10^{-3}$  mm<sup>2</sup>/s, range of kurtosis (MK, AK,

RK) from 0 to 2, and range of FA and FAK from 0 to 0.7. MD mean diffusivity, AD axial diffusivity, RD radial diffusivity, MK mean kurtosis, AK axial kurtosis, RK radial kurtosis, FA fractional anisotropy, FAK kurtosis fractional anisotropy

### 15.2.3 DKI Reconstruction

DKI reconstruction involves estimating both the diffusion tensor (DT) and the kurtosis tensor (KT) [7]. The full DKI equation as compared to the full DTI equation is the addition of the second term with  $b^2$ .

$$\ln \frac{S(\mathbf{g}, b)}{S_0} = -b \sum_{i=1}^3 \sum_{j=1}^3 g_i g_j D_{ij} + \frac{1}{6} b^2 \cdot \text{MD}^2 \cdot \sum_{i=1}^3 \sum_{j=1}^3 \sum_{k=1}^3 \sum_{l=1}^3 g_i g_j g_k g_l W_{ijkl} \quad (15.3)$$

where  $D_{ij}$  is an element of the second order DT  $\mathbf{D}$ ,  $K_{ijkl}$  is an element of the fourth order KT  $\mathbf{W}$ . MD is the mean diffusivity  $\text{MD} = \text{Trace}(\mathbf{D})/3$ .  $\mathbf{g} = (g_1, g_2, g_3)$  is the unit-vector direction of the diffusion gradient.  $S(\mathbf{g}, b)$  is the diffusion-weighted signal at a particular  $b$  value with direction  $\mathbf{g}$ . The apparent diffusion coefficient  $D_{\text{app}}(\mathbf{g})$  and apparent kurtosis  $K_{\text{app}}(\mathbf{g})$  for any direction  $\mathbf{g}$  can then be calculated from:

$$D_{\text{app}}(\mathbf{g}) = \sum_{i=1}^3 \sum_{j=1}^3 g_i g_j D_{ij} \quad (15.4)$$

$$K_{\text{app}}(\mathbf{g}) = \frac{\text{MD}^2}{D_{\text{app}}(\mathbf{g})^2} \sum_{i=1}^3 \sum_{j=1}^3 \sum_{k=1}^3 \sum_{l=1}^3 g_i g_j g_k g_l W_{ijkl} \quad (15.5)$$

Following data fitting for both DT and KT, all DTI related parameters (MD, FA, AD, RD, etc.) can be generated by the standard DTI equations from the estimated diffusion tensor, with the principle axes defined by the eigenvectors of the DT ( $\mathbf{v}_1, \mathbf{v}_2, \mathbf{v}_3$ ) (Fig. 15.3). Kurtosis values along ( $\mathbf{v}_1, \mathbf{v}_2, \mathbf{v}_3$ ) and kurtosis parameters can be calculated based on Eq. (15.5) analogous to DTI parameters using the following equations:

$$K_1 = K_{\text{app}}(\mathbf{v}_1); K_2 = K_{\text{app}}(\mathbf{v}_2); K_3 = K_{\text{app}}(\mathbf{v}_3); \quad (15.6)$$

$$\text{MK} = \frac{K_1 + K_2 + K_3}{3}, \quad \text{AK} = K_1, \text{RK} = \frac{K_2 + K_3}{2} \quad (15.7)$$

$$\text{FA}_k = \frac{\sqrt{3 \left[ (K_1 - \text{MK})^2 + (K_2 - \text{MK})^2 + (K_3 - \text{MK})^2 \right]}}{\sqrt{2(K_1^2 + K_2^2 + K_3^2)}} \quad (15.8)$$

It should be noted that the KT, unlike DT, is not defined just by an ellipsoidal profile. Even though DWI with only three arbitrary orthogonal diffusion directions can fully define the MD ( $\text{Trace}(\mathbf{D})$  is rotationally invariant, and so is MD), the mean kurtosis is not uniquely determined by simply averaging  $K$ 's along only three orthogonal directions. An example of tensor shapes for KT and DT is shown in Fig. 15.4. More accurate estimate for MK and RK are only available when the full KT is available, and are estimated by averaging the  $K_{\text{app}}$ 's on the whole sphere (for MK), and  $K_{\text{app}}$ 's on all radial directions to the DT (for RK). Explicit formulas through surface integral can be found in Jensen and Helpern [9].

### 15.2.4 Fiber Tracking Using DKI

DKI addresses another limitation of the DTI in that DTI only assumes a single tensor structure within an imaging voxel, which fails when there is fiber crossing or fiber kissing within a given voxel. Typically, DTI imaging voxel is 2–3 mm isotropic. Given this, the  $3 \times 3$  diffusion tensor is only able to model the diffusion distribution within the voxel as a single ellipsoid. The diffusion kurtosis tensor, being a fourth-order tensor of dimension  $3 \times 3 \times 3 \times 3$ , is able to model more complex diffusion distribution [10]. Figure 15.4 shows an example of diffusion tensor (DT) and kurtosis tensor (KT), as well as the Orientation Distribution Function based on DKI (DKI-ODF) geometries from four real brain voxels [8]. In these cases, the first two rows represent a region with a single fiber direction (corpus callosum and internal capsule), where the DT and KT geometry corresponds to the diagram in Fig. 15.4. The third and fourth row shows region (corpus callosum and pontocerebellar) with at least two fibers crossing. In these cases, DT fails to provide correct fiber direction, while the KT provides an

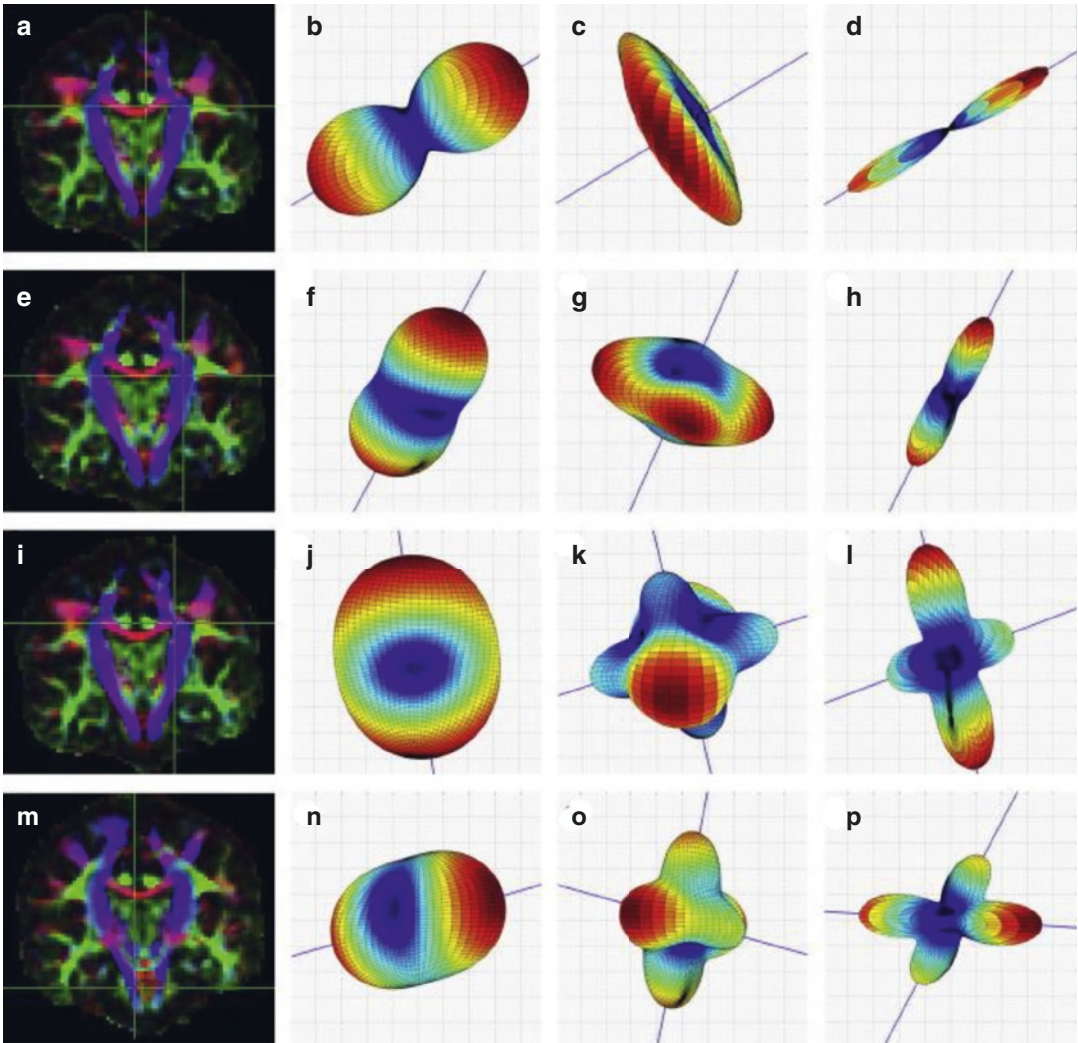


**Fig. 15.4** Geometries of DT (panels **b**, **f**, **j**, and **n**), KT (panels **c**, **g**, **k**, and **o**) and DKI-ODF (panels **d**, **h**, **l**, and **p**) extracted from real data of a representative subject. Geometries are extracted from four regions of interest defined on the FA map (panel **a**, **e**, **i** and **m**), which is color-coded according to the direction of the larger principal DT eigenvector (red, blue and green correspond to right-left, inferior-superior and posterior-anterior, respectively). Top panels show the geometries extracted from voxels corresponding to well-aligned corpus callo-

sum fibers (panels **b**, **c**, and **d**) and ascending fibers (**f**, **g**, and **h**), while the bottom panels display the geometries for voxels where ascending fibers are known to cross with corpus callosum (panels **j**, **k**, and **l**) and pontocerebellar fibers (panels **n**, **o**, and **p**). Blue lines on each panel represent the fiber direction estimates obtained from each geometry. *DT* diffusion tensor, *DKI-ODF* diffusion kurtosis imaging—orientation distribution function. (Figure adapted from Neto Henriques et al. [8])

indication of the more complex geometry, and DKI allows profiling of crossing fibers (DKI-ODF). Nevertheless, it should be noted that if the sole purpose of diffusion imaging is for fiber tracking, then Higher Angular Resolution

Diffusion Imaging (HARDI) type of acquisition should be performed with more diffusion directions, and Q-Ball reconstruction [11, 12] or even Diffusion Spectrum Imaging (DSI) methods [13, 14] should be considered.

## 15.3 Clinical Applications

### 15.3.1 Ischemia and Stroke

Diffusion MRI has been the most reliable neuroimaging technique to assess acute and subacute ischemic stroke. Restricted diffusion is often used to identify severely damaged infarction core and the surrounding ischemic region. However, the extent of the tissue damage within the DWI lesion can be quite heterogeneous, leading to an investigation into more advanced identification of potentially salvageable ischemic brain tissue, especially after reperfusion. Using a rodent model of transient middle cerebral artery occlusion (MCAO), Hui et al. [3] and Cheung et al. [15] both reported a mismatch in the MD determined lesion and the MK determined lesion, where the hypo-intense region in MD determined lesion is larger than the hyper-intensity seen in the MK determined lesion. It should be noted that the common areas determined by MD and MK deficits did not show any recovery while the mismatch areas for the two parameters demonstrated recovery after reperfusion. Cheung et al. contribute the MD decrease following the acute stroke to cytotoxic edema, while the MK increases to the “intracellular tortuosity and viscosity changes subsequent to breakdown of cytoskeletal structures and swelling of mitochondria, likely indicating more severe tissue damage”. The notion that MD lesion is always larger than MK lesion, and MK is able to better define salvageable tissue compared to MD has been further validated by Wang et al. [16] and Lu et al. [17] through experimental acute stroke model, where they found significantly lower pH value in the MK lesion compared to the MD/MK mismatch area, indicating that MK lesion may be more specific to infarction core. Differentiation between the kurtosis vs. DWI determined lesions have also been reported in acute infarction in patients, wherein a study of 37 patients imaged within 24 h and 1 month after symptom onset, a better correlation of acute stage kurtosis lesion size with 1-month T2-weighted images was observed [18]. Furthermore, the study reported the detection of a larger number of acute small kurtosis lesions than

DWI lesions. While animal models suggest that the MD/MK mismatch disappears within 48 h after stroke onset [15], Guo et al. [19] reported persisting MD/MK mismatch in subacute ischemic stroke, where a significantly larger MD/MK mismatched area was found in stroke patients with neurological deterioration than those without, indicating the sensitivity of MK to the heterogeneity presumably from inflammation in ischemic lesions.

### 15.3.2 Glioma Grading

Gliomas are the most common type of intra-axial brain tumors. They are heterogeneous in nature, and the grading of gliomas is based on tumor cellularity, mitosis, neovascularity, and necrosis. Adequate grading of gliomas prior to treatment is considered the most important task in predicting treatment response and outcome. DWI and DTI have been applied to better characterize gliomas and to identify the infiltration zones, but common DTI parameters such as MD or FA have offered inconclusive results among glioma grades. Generally speaking, water diffusion inversely correlates with tumor cellularity, with restricted diffusion reflective of tightly packed tumor cells [20]. FA is less useful in characterizing gliomas due to the relatively low anisotropic diffusion profile within the tumor [21]. Raab et al. [22] and Van Cauter et al. [23] first reported the utility of using DKI to aid in the grading of gliomas where high MK is associated with high-grade tumors. High kurtosis value in tumors is thought to be associated with the intra-voxel heterogeneity resulting from tumor invasion, increased tumor cellularity, necrosis, hemorrhage, and endothelial proliferation. Figure 15.5 shows example MD and MK maps in three representative subjects with Grades II–IV gliomas, where one can appreciate the additional contrast offered in the MK map, differentiating gliomas grades [24]. In a study of 74 consecutive patients with histopathology confirmed gliomas of grade II, III, IV, Jiang et al. [25] showed that kurtosis metrics were most strongly correlated with cellular proliferation of gliomas through Ki-67 labeling

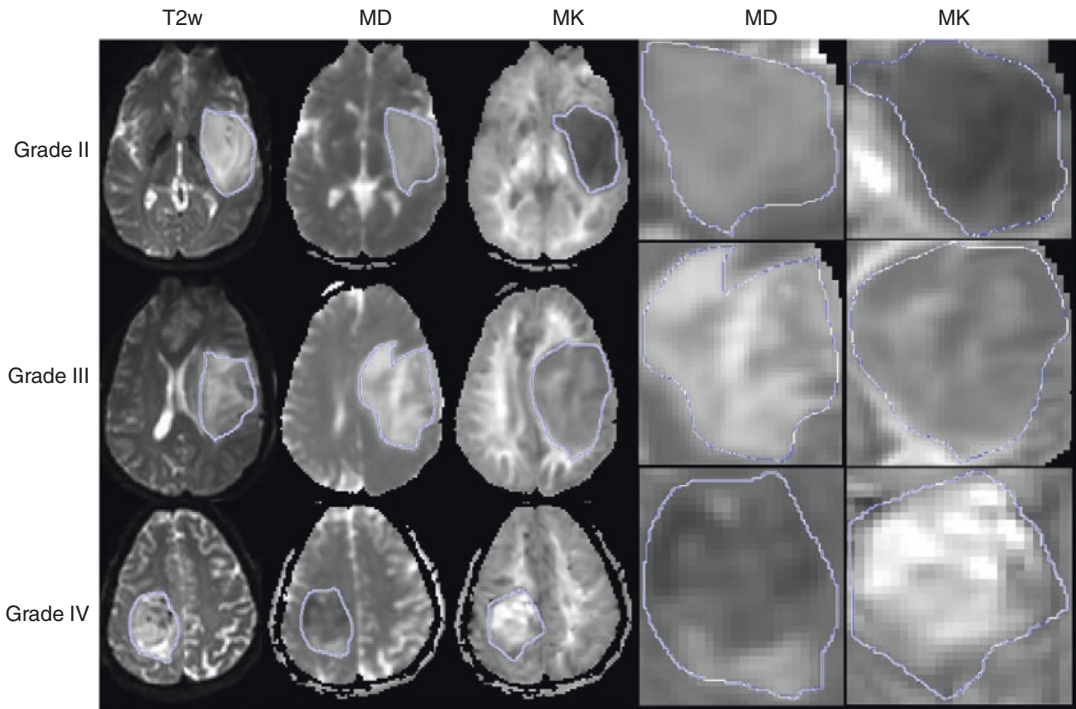


**Fig. 15.5** MD and MK parametric maps shown for representative subjects from grades II, III, and IV. Tumor regions are hand marked. Row-wise: Grade II (30-year-old male subject having astrocytoma); Grade III (25-year-old male subject having anaplastic astrocytoma); Grade IV (21-year-old male subject having glioblastoma).

Column-wise a T2-weighted images for a single slice and corresponding MD, MK maps; zoomed tumor region of MD and MK maps (tumor regions marked were zoomed to show the visual heterogeneity differences between grades). *MD* mean diffusivity, *MK* mean kurtosis. (Figure adapted from Raja et al. [24])

index (Ki-67 LI). Meta-analysis of the diagnostic accuracy of DKI in glioma grade discrimination (high vs. low grade) reported 0.85 (95% CI: 0.74, 0.92) sensitivity and 0.92 (95% CI: 0.82, 0.96) specificity [26]. Given the high sensitivity and specificity afforded by DKI it is quite likely that this technique will find applications in determining lower-grade gliomas, and also may play a significant role in characterizing other types of tumors.

### 15.3.3 Traumatic Brain Injury (TBI)

Traumatic brain injury (TBI) is a leading cause of death and also leads to lifelong disability throughout developed nations. The primary injury is typically the sudden acceleration, deceleration, and/or rotational forces, yet the secondary injury could

be widespread degeneration of neurons and glial cells in the months or years following the initial impact. A big challenge in TBI management is the lack of diagnostic sensitivity in conventional imaging tools (CT or conventional MRI) in detecting subtle changes in structural and functional integrity within the brain. DTI has been a popular tool in probing the diffuse axonal injury following TBI. Reduced FA, indicative of disrupted white matter where conventional MR methods have found to be occult, has been shown to be a sensitive parameter associated with the cognitive outcome even in mild TBI [27–29]. DKI has been shown to be effective in detecting microstructure changes not only in white matter but also in gray matter regions. In a rodent model of CCI (controlled cortical impact) method of experimental injury, increased MK was found in the normal-appearing contra-lateral cortex associated with



increased glial activity and possibly inflammation sub-acutely following TBI [5]. Similar findings of increased MK were observed in the hippocampus in a rodent model of blast TBI [30], along with increased choline level (measured by MR spectroscopy), indicating membrane break down, and significant microglial activation and neurodegeneration. What makes this more relevant is that conventional MR was unable to detect such tissue damage. In both studies, although changes in MD and FA were observed, they were non-significant, indicating DKI may offer additional sensitivity to detect the subtle injury from TBI.

Reduced MK values are more often reported in human TBI studies at a delayed phase post-injury, suggesting loss of cellular structures, axonal breakdown, membrane leakage, and perhaps even persistent inflammation. Grossman et al. found reduced MK in the thalamus in mild TBI patients to be associated with cognitive impairment on 1-year post-TBI. Longitudinal studies in mild TBI in patients indicate that increase in MK and the kurtosis along the radial direction (RK) from 1 month to 6 months post-injury correlates with cognitive recovery in the thalamus, internal capsule, and corpus callosum [31]. Figure 15.6 shows DKI maps of two representative severe TBI patients, where one can appreciate different contrast offered by the MK map, as opposed to MD and FA maps. It should be noted that the utility of DTI is limited to the white matter, whereas DKI extends the use of diffusion-based techniques to probe both white matter and gray matter as well. Together these techniques are likely to provide insights into the complex changes in brain tissue following brain injury and may prove to be useful imaging markers for both the diagnosis and long-term prognosis following TBI.

### 15.3.4 Multiple Sclerosis (MS)

MS is the most common cause of non-traumatic disability in young adults. A hallmark of MS is the white matter degeneration that involves inflammation, demyelination, axonal loss, edema, and demyelination. DTI has been popu-

lar in evaluating MS due to its sensitivity in detecting white matter integrity changes where decreased FA and increased MD are commonly associated with white matter deterioration. More specifically, the radial diffusivity (RD, the diffusion perpendicular to the axon direction) is thought to directly link to myelin integrity where RD increases during myelin break down [32]. Multiple compartment diffusion models suggest that diffusion kurtosis may be more sensitive than the simple diffusion coefficient to changes in the water exchange rate between two compartments [9], therefore RK may be more sensitive than RD in detecting changes to myelin integrity and intra- and extra-axonal water exchange rate. Yoshida et al. [33] first reported decreased MK as a more sensitive marker in MS patients compared to controls in normal-appearing white matter. Based on the DKI model, Fieremans et al. [34] derived a more microstructural and pathological specific white matter model to describe intra- and extra-axonal water diffusion property. In a rodent model of cuprizone induced demyelination and spontaneous remyelination, Guglielmetti et al. [35] showed histology proof of microgliosis associated with increased MK and RK during the acute inflammatory demyelination phase; and axonal water fraction (AWF) decrease associated with the spontaneous remyelination. They also reported strongly decreased intra-axonal diffusivity ( $D_a$ ) in cuprizone treated animal possibly due to axonal swelling or beading as a result of severe microglial activation and myelin breakdown. Using the same model, de Kouchkovsky et al. [36] reported MD and radial extra-axonal diffusivity increase along with FA, AWF,  $D_a$  decrease in MS patients compared to control subjects within the corpus callosum. AWF was also found to be significantly correlated with the expanded disability status scale score, indicating that the white matter model may provide a more pathologically specific and clinically meaningful index in detecting changes in normal-appearing white matter in MS patients. On the other hand, due to the increased sensitivity

of DKI to gray matter microstructure changes, reduced MK has been reported in MS patients both in the spinal cord gray matter [37, 38] and in the cortical gray matter [39], both of which correlated with cognitive deficits.

### 15.3.5 Other Neurodegenerative Disorders (Alzheimer's Disease, Parkinson Disease)

DKI has also been applied to other neurological disorders, where increasing MK is related to increased microstructural complexity resulting from increased glial activity and inflammation, and decreased kurtosis values are attributed to neuronal loss. Falangola et al. [40] and Gong et al. [41] both reported decreased MK and RK in Alzheimer's disease (AD) patients, possibly due to loss of neuron cell bodies, synapses, and dendrites. Struyfs et al. [42] found MK and MD being more sensitive than FA to detect differences between both MCI/AD and controls and suggested that DKI may offer early biomarkers for AD diagnosis complementing DTI. In a mice model of AD where the development of amyloid- $\beta$  ( $A\beta$ ) plaque was studied, which was thought to contribute to AD development, Praet et al. [43] observed a high correlation between the DK metrics (MK, AK, RK, and FA) and  $A\beta$ -induced pathology and neuroinflammation. They conclude that the combined metrics of DT and DK are better able of differentiating AD from MCI.

As a more sensitive tool to study gray matter microstructure changes, Wang et al. [44] investigated the usage of DKI in detecting pathological changes in basal ganglia region in patients with idiopathic Parkinson disease (PD) and found significantly increased MK in the absence of MD/FA changes in PD patients in the putamen and substantia nigra (SN). MK in the ipsilateral SN was also found to have the highest diagnostic performance in this group of early to middle stage

PD patients. As the region with most pathologic changes in PD patients, Zhang et al. [45, 46] also found increased MK in the SN along with reduced FA in PD patients. MK in SN was shown to have higher diagnostic accuracy, and correlated with PD symptom progression score measured with Hoehn–Yahr scale and unified Parkinson's disease rating scale (UPDRS), therefore has the potential to be a sensitive marker for early diagnosis and disease evaluation in PD. Studies of white matter changes in PD mostly reported MK and FA reduction that involved multiple brain regions [47, 48], and MK showed a wider extent of white matter abnormality including unique regions such as posterior corona radiata and superior longitudinal fascicle. Authors suggest the reduction of MK and FA could reflect white matter alterations caused by Lewy-related pathology, which is a hallmark for PD. Khairnar et al. [49, 50] offered pathological evidence for DKI parameters changes using an  $\alpha$ -Synuclein ( $\alpha$ -Syn) overexpressing transgenic TNWT-61 mice model, as  $\alpha$ -Synuclein ( $\alpha$ -Syn) is a major constituent of Lewy bodies. Khairnar et al. reported a positive correlation of  $\alpha$ -Syn accumulation with increased kurtosis values (MK, AK, RK) and decreased diffusivity values (MD, AD, RD) in the thalamus. In a follow-up study to evaluate diffusivity and kurtosis parameters in detecting early stage of  $\alpha$ -Syn accumulation-induced microstructural changes in young TNWT-61 mice, Khairnar et al. [51] found early MK increase in the striatum and thalamus in 3mo TNWT-61 mice without accompanying DTI parameter changes, supporting the notion that MK changes are sensitive to the accumulation of  $\alpha$ -Syn or Lewy body-like structures. At 6 months, increased MK was found in the SN, along with significant white matter changes, suggesting that " $\alpha$ -Syn accumulation-associated changes start in the gray matter and later progress to the white matter". Taken together DKI parameters may serve as a useful imaging marker to differentiate those patients that may progress to PD.

## 15.4 Practical Considerations and Limitations

There are some considerations with applying DKI in a clinical setting. DKI acquisition is longer in comparison to DTI acquisition. At least 2 non-zero  $b$ -values and 15 diffusion directions are required for full tensor estimation [52], and a typical DKI acquisition is about 7–10 min long ( $b$ -value of 1000, 2000–2500 s/mm<sup>2</sup> at 30 diffusion directions, 2.7 mm isotropic resolution and a  $b_0$  volume). The increased image acquisition time needs to be carefully considered, as long acquisition times are prone to increased motion artifact. Scan time reduction may be possible particularly if the only interest is to estimate MK parameters. This can be possible with the use of just one  $b_0$  and two non-zero  $b$ -values, with three directions at the  $b = 1000$  s/mm<sup>2</sup> level and nine directions at  $b = 2000$ –2500 s/mm<sup>2</sup> [53] in which case, the acquisition time can be as little as 2–3 min. It should be noted that both the diffusion tensor parameters and kurtosis tensor parameters can be reconstructed using the same data.

The choice of  $b$ -values is critical in estimating both the MD (AD, RD) and MK (AK, RK) parameters due to the non-monoexponential behavior of the diffusion-weighted signal as the sequence is made sensitive to shorter diffusion sentence through the use of higher  $b$ -values (Fig. 15.2). If the maximum  $b$ -value is too small, then the acquisition is sensitive only to diffusion over larger distances where the diffusion attenuation remains largely monoexponential. Therefore, performing kurtosis experiments using low  $b$ -values will result in erroneous/unreliable estimates and should be avoided. However on the other hand, if the maximum  $b$ -value is too high then the DKI model may expect the signal to actually increase with increased  $b$ -value (Eq. 15.2 is a quadratic equation of  $b$  so the DKI signal curve will be a concave one), which can never be true. So, a well-balanced use of  $b$ -values that stay within a range relevant to tissue properties is important, and this depends on the diffusion coefficient within a given anatomy of interest or pathology of interest. Most literature

supports the use of a  $b$ -value that is about twice that is used in DTI studies ( $b$ -value = 1000 s/mm<sup>2</sup>) and is around 2000–2500 s/mm<sup>2</sup> for the brain [9, 54]. Different pathology may lead to different choices of maximum  $b$ -values.

Higher  $b$ -value needed in DKI also leads to higher signal attenuation, and therefore to have enough signal, DKI acquisitions use slightly larger voxel size (~3 mm) than DTI (~2 mm), leading to reduced spatial resolution. The consequence of lost spatial resolution is the inability to identify smaller lesions. However, with the advent of new acquisition hardware, such as multiple channel RF-coil receivers and simultaneous multi-slice acquisition [55, 56], the spatial resolution will increase and acquisition times will be further reduced in the future.

---

## 15.5 Summary and Future Directions

DKI is a promising technique that expands the utility of diffusion-weighted imaging and diffusion tensor imaging by providing information on the status of microstructural changes within the tissue. Diffusion kurtosis metrics are unique and are independent of other diffusion imaging metrics and are believed to be generally proportional to tissue heterogeneity and complexity. Increased MK may indicate more densely packed cells, glial proliferation, which generally increases the cellular complexity. Decreased MK may indicate loss of cellular structure, white matter integrity, cell membrane, and myelin sheath. More importantly, DKI allows higher sensitivity than DTI in detecting microstructure changes within regions of isotropic diffusions, such as cortex, basal ganglia, or thalamus. Furthermore, fiber tracking based on the kurtosis tensor distribution allows for the differentiation of crossing fibers. It is quite likely that in the future DKI will find increased utility in understanding various disease processes and will provide complementary information to the information that is obtained from standard DTI methods.

## 15.6 Clinical Case (Fig. 15.6)

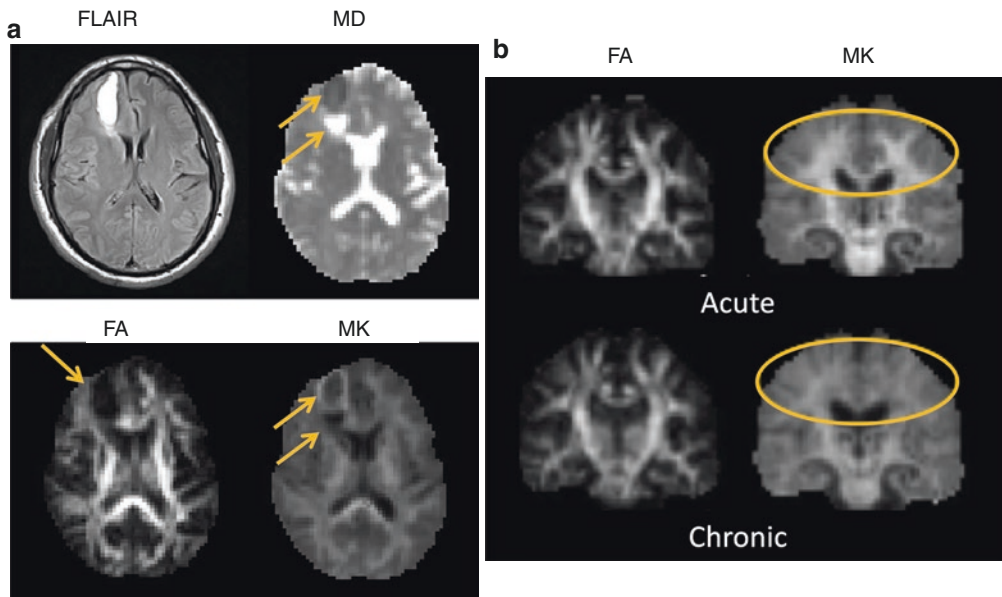


**Fig. 15.6** DKI maps of representative TBI patients. (a) 30 years old male with admission GCS 4 with multiple symptoms and cognitive deficits at 1 month. Homogeneous FLAIR lesion area shows both high and low diffusion components. Restricted diffusion region has a low MK center and high MK margin (possibly glial scar). (b)

22 years old male with admission GCS 7 recovered from injury with declined cognitive function and post-concussive symptoms at chronic stage post-injury, despite no visible. MK map showed an apparent loss of white matter structure. *DKI* diffusion kurtosis imaging, *GCS* Glasgow Coma Scale, *MK* mean kurtosis

## References

1. Wu EX, Cheung MM. MR diffusion kurtosis imaging for neural tissue characterization. *NMR Biomed.* 2010;23(7):836–48.
2. Jensen JH, Helpert JA, Ramani A, Lu H, Kaczynski K. Diffusional kurtosis imaging: the quantification of non-gaussian water diffusion by means of magnetic resonance imaging. *Magn Reson Med.* 2005;53(6):1432–40.
3. Hui ES, Du F, Huang S, Shen Q, Duong TQ. Spatiotemporal dynamics of diffusional kurtosis, mean diffusivity and perfusion changes in experimental stroke. *Brain Res.* 2012;1451:100–9.
4. Jensen JH, Falangola MF, Hu C, Tabesh A, Rapalino O, Lo C, Helpert JA. Preliminary observations of increased diffusional kurtosis in human brain following recent cerebral infarction. *NMR Biomed.* 2011;24(5):452–7.
5. Zhuo J, Xu S, Proctor JL, Mullins RJ, Simon JZ, Fiskum G, Gullapalli RP. Diffusion kurtosis as an in vivo imaging marker for reactive astrogliosis in traumatic brain injury. *NeuroImage.* 2012;59(1):467–77.
6. Tabesh A, Jensen JH, Ardekani BA, Helpert JA. Estimation of tensors and tensor-derived measures in diffusional kurtosis imaging. *Magn Reson Med.* 2011;65(3):823–36.
7. Lu H, Jensen JH, Ramani A, Helpert JA. Three-dimensional characterization of non-gaussian water diffusion in humans using diffusion kurtosis imaging. *NMR Biomed.* 2006;19(2):236–47.
8. Neto Henriques R, Correia MM, Nunes RG, Ferreira HA. Exploring the 3D geometry of the diffusion kurtosis tensor—impact on the development of robust tractography procedures and novel biomarkers. *NeuroImage.* 2015;111:85–99.
9. Jensen JH, Helpert JA. MRI quantification of non-gaussian water diffusion by kurtosis analysis. *NMR Biomed.* 2010;23(7):698–710.
10. Lazar M, Jensen JH, Xuan L, Helpert JA. Estimation of the orientation distribution function from diffusional kurtosis imaging. *Magn Reson Med.* 2008;60(4):774–81.
11. Descoteaux M, Angelino E, Fitzgibbons S, Deriche R. Regularized, fast, and robust analytical Q-ball imaging. *Magn Reson Med.* 2007;58(3):497–510.
12. Tuch DS. Q-ball imaging. *Magn Reson Med.* 2004;52(6):1358–72.
13. Wedeen VJ, Hagmann P, Tseng WY, Reese TG, Weisskoff RM. Mapping complex tissue architecture

- with diffusion spectrum magnetic resonance imaging. *Magn Reson Med*. 2005;54(6):1377–86.
14. Wedeen VJ, Wang RP, Schmahmann JD, Benner T, Tseng WY, Dai G, Pandya DN, Hagmann P, D'Arceuil H, de Crespigny AJ. Diffusion spectrum magnetic resonance imaging (DSI) tractography of crossing fibers. *NeuroImage*. 2008;41(4):1267–77.
  15. Cheung JS, Wang E, Lo EH, Sun PZ. Stratification of heterogeneous diffusion MRI ischemic lesion with kurtosis imaging: evaluation of mean diffusion and kurtosis MRI mismatch in an animal model of transient focal ischemia. *Stroke*. 2012;43(8):2252–4.
  16. Wang E, Wu Y, Cheung JS, Zhou IY, Igarashi T, Zhang X, Sun PZ. pH imaging reveals worsened tissue acidification in diffusion kurtosis lesion than the kurtosis/diffusion lesion mismatch in an animal model of acute stroke. *J Cereb Blood Flow Metab*. 2017;37(10):3325–33.
  17. Lu D, Jiang Y, Ji Y, Zhou IY, Mandeville E, Lo EH, Wang X, Sun PZ. JOURNAL CLUB: evaluation of diffusion kurtosis imaging of stroke lesion with hemodynamic and metabolic MRI in a rodent model of acute stroke. *AJR Am J Roentgenol*. 2018;210(4):720–7.
  18. Yin J, Sun H, Wang Z, Ni H, Shen W, Sun PZ. Diffusion kurtosis imaging of acute infarction: comparison with routine diffusion and follow-up MR imaging. *Radiology*. 2018;287(2):651–7.
  19. Guo YL, Zhang ZP, Zhang GS, Kong LM, Rao HB, Chen W, Wang GW, Shen ZW, Zheng WB, Wu RH. Evaluation of mean diffusion and kurtosis MRI mismatch in subacute ischemic stroke: comparison with NIHSS score. *Brain Res*. 2016;1644:231–9.
  20. Sugahara T, Korogi Y, Kochi M, Ikushima I, Shigematu Y, Hirai T, Okuda T, Liang L, Ge Y, Komohara Y, et al. Usefulness of diffusion-weighted MRI with echo-planar technique in the evaluation of cellularity in gliomas. *J Magn Reson Imaging*. 1999;9(1):53–60.
  21. Maier SE, Sun Y, Mulkern RV. Diffusion imaging of brain tumors. *NMR Biomed*. 2010;23(7):849–64.
  22. Raab P, Hattingen E, Franz K, Zanella FE, Lanfermann H. Cerebral gliomas: diffusional kurtosis imaging analysis of microstructural differences. *Radiology*. 2010;254(3):876–81.
  23. Van Cauter S, Veraart J, Sijbers J, Peeters RR, Himmelreich U, De Keyser F, Van Gool SW, Van Calenberg F, De Vleeschouwer S, Van Hecke W, et al. Gliomas: diffusion kurtosis MR imaging in grading. *Radiology*. 2012;263(2):492–501.
  24. Raja R, Sinha N, Saini J, Mahadevan A, Rao KN, Swaminathan A. Assessment of tissue heterogeneity using diffusion tensor and diffusion kurtosis imaging for grading gliomas. *Neuroradiology*. 2016;58(12):1217–31.
  25. Jiang R, Jiang J, Zhao L, Zhang J, Zhang S, Yao Y, Yang S, Shi J, Shen N, Su C, et al. Diffusion kurtosis imaging can efficiently assess the glioma grade and cellular proliferation. *Oncotarget*. 2015;6(39):42380–93.
  26. Falk Delgado A, Nilsson M, van Westen D, Falk DA. Glioma grade discrimination with MR diffusion kurtosis imaging: a meta-analysis of diagnostic accuracy. *Radiology*. 2018;287(1):119–27.
  27. Messe A, Caplain S, Paradot G, Garrigue D, Mineo JF, Soto Ares G, Duceux D, Vignaud F, Rozec G, Desal H, et al. Diffusion tensor imaging and white matter lesions at the subacute stage in mild traumatic brain injury with persistent neurobehavioral impairment. *Hum Brain Mapp*. 2011;32(6):999–1011.
  28. Niogi SN, Mukherjee P, Ghajar J, Johnson C, Kolster RA, Sarkar R, Lee H, Meeker M, Zimmerman RD, Manley GT, et al. Extent of microstructural white matter injury in postconcussive syndrome correlates with impaired cognitive reaction time: a 3T diffusion tensor imaging study of mild traumatic brain injury. *AJNR Am J Neuroradiol*. 2008;29(5):967–73.
  29. Yuh EL, Cooper SR, Mukherjee P, Yue JK, Lingsma HF, Gordon WA, Valadka AB, Okonkwo DO, Schnyer DM, Vassar MJ, et al. Diffusion tensor imaging for outcome prediction in mild traumatic brain injury: a TRACK-TBI study. *J Neurotrauma*. 2014;31:1457–77.
  30. Zhuo J, Keledjian K, Xu S, Pampori A, Gerzanich V, Simard JM, Gullapalli RP. Changes in diffusion kurtosis imaging and magnetic resonance spectroscopy in a direct cranial blast traumatic brain injury (dc-bTBI) model. *PLoS One*. 2015;10(8):e0136151.
  31. Stokum JA, Sours C, Zhuo J, Kane R, Shanmuganathan K, Gullapalli RP. A longitudinal evaluation of diffusion kurtosis imaging in patients with mild traumatic brain injury. *Brain Inj*. 2015;29(1):47–57.
  32. Song SK, Sun SW, Ramsbottom MJ, Chang C, Russell J, Cross AH. Demyelination revealed through MRI as increased radial (but unchanged axial) diffusion of water. *NeuroImage*. 2002;17(3):1429–36.
  33. Yoshida M, Hori M, Yokoyama K, Fukunaga I, Suzuki M, Kamagata K, Shimoji K, Nakanishi A, Hattori N, Masutani Y, et al. Diffusional kurtosis imaging of normal-appearing white matter in multiple sclerosis: preliminary clinical experience. *Jpn J Radiol*. 2013;31(1):50–5.
  34. Fieremans E, Jensen JH, Helpert JA. White matter characterization with diffusional kurtosis imaging. *NeuroImage*. 2011;58(1):177–88.
  35. Guglielmetti C, Veraart J, Roelant E, Mai Z, Daans J, Van Audekerke J, Naeyaert M, Vanhoutte G, Delgado Y, Palacios R, Praet J, et al. Diffusion kurtosis imaging probes cortical alterations and white matter pathology following cuprizone induced demyelination and spontaneous remyelination. *NeuroImage*. 2016;125:363–77.
  36. de Kouchkovsky I, Fieremans E, Fleysher L, Herbert J, Grossman RI, Inglese M. Quantification of normal-appearing white matter tract integrity in multiple sclerosis: a diffusion kurtosis imaging study. *J Neurol*. 2016;263(6):1146–55.
  37. Raz E, Bester M, Sigmund EE, Tabesh A, Babb JS, Jaggi H, Helpert J, Mitnick RJ, Inglese M. A better characterization of spinal cord damage in multiple sclerosis: a diffusional kurtosis imaging study. *AJNR Am J Neuroradiol*. 2013;34(9):1846–52.

38. Spampinato MV, Kocher MR, Jensen JH, Helpert JA, Collins HR, Hatch NU. Diffusional kurtosis imaging of the corticospinal tract in multiple sclerosis: association with neurologic disability. *AJNR Am J Neuroradiol.* 2017;38(8):1494–500.
39. Bester M, Jensen JH, Babb JS, Tabesh A, Miles L, Herbert J, Grossman RI, Inglese M. Non-gaussian diffusion MRI of gray matter is associated with cognitive impairment in multiple sclerosis. *Mult Scler.* 2015;21(7):935–44.
40. Fieremans E, Benitez A, Jensen JH, Falangola MF, Tabesh A, Dearnorff RL, Spampinato MV, Babb JS, Novikov DS, Ferris SH, et al. Novel white matter tract integrity metrics sensitive to alzheimer disease progression. *AJNR Am J Neuroradiol.* 2013;34(11):2105–12.
41. Gong NJ, Wong CS, Chan CC, Leung LM, Chu YC. Correlations between microstructural alterations and severity of cognitive deficiency in alzheimer's disease and mild cognitive impairment: a diffusional kurtosis imaging study. *Magn Reson Imaging.* 2013;31(5):688–94.
42. Struyfs H, Van Hecke W, Veraart J, Sijbers J, Slaets S, De Belder M, Wuyts L, Peters B, Slegers K, Robberecht C, et al. Diffusion kurtosis imaging: a possible MRI biomarker for AD diagnosis? *J Alzheimers Dis.* 2015;48(4):937–48.
43. Praet J, Manyakov NV, Muchene L, Mai Z, Terzopoulos V, de Backer S, Torremans A, Guns PJ, Van De Castele T, Bottelbergs A, et al. Diffusion kurtosis imaging allows the early detection and longitudinal follow-up of amyloid-beta-induced pathology. *Alzheimers Res Ther.* 2018;10(1):1. <https://doi.org/10.1186/s13195-017-0329-8>.
44. Wang JJ, Lin WY, Lu CS, Weng YH, Ng SH, Wang CH, Liu HL, Hsieh RH, Wan YL, Wai YY. Parkinson disease: diagnostic utility of diffusion kurtosis imaging. *Radiology.* 2011;261(1):210–7.
45. Zhang G, Zhang Y, Zhang C, Wang Y, Ma G, Nie K, Xie H, Liu J, Wang L. Striatal silent lacunar infarction is associated with changes to the substantia nigra in patients with early-stage Parkinson's disease: a diffusion kurtosis imaging study. *J Clin Neurosci.* 2016;33:138–41.
46. Zhang G, Zhang Y, Zhang C, Wang Y, Ma G, Nie K, Xie H, Liu J, Wang L. Diffusion kurtosis imaging of substantia nigra is a sensitive method for early diagnosis and disease evaluation in Parkinson's disease. *Parkinsons Dis.* 2015;2015:207624.
47. Kamagata K, Tomiyama H, Hatano T, Motoi Y, Abe O, Shimoji K, Kamiya K, Suzuki M, Hori M, Yoshida M, et al. A preliminary diffusional kurtosis imaging study of Parkinson disease: comparison with conventional diffusion tensor imaging. *Neuroradiology.* 2014;56(3):251–8.
48. Kamagata K, Tomiyama H, Motoi Y, Kano M, Abe O, Ito K, Shimoji K, Suzuki M, Hori M, Nakanishi A, et al. Diffusional kurtosis imaging of cingulate fibers in Parkinson disease: comparison with conventional diffusion tensor imaging. *Magn Reson Imaging.* 2013;31(9):1501–6.
49. Khairnar A, Latta P, Drazanova E, Ruda-Kucerova J, Szabo N, Arab A, Hutter-Paier B, Havas D, Windisch M, Sulcova A, et al. Diffusion kurtosis imaging detects microstructural alterations in brain of alpha-synuclein overexpressing transgenic mouse model of Parkinson's disease: a pilot study. *Neurotox Res.* 2015;28(4):281–9.
50. Khairnar A, Ruda-Kucerova J, Drazanova E, Szabo N, Latta P, Arab A, Hutter-Paier B, Havas D, Windisch M, Sulcova A, et al. Late-stage alpha-synuclein accumulation in TNWT-61 mouse model of Parkinson's disease detected by diffusion kurtosis imaging. *J Neurochem.* 2016;136:1259–69.
51. Khairnar A, Ruda-Kucerova J, Szabo N, Drazanova E, Arab A, Hutter-Paier B, Neddens J, Latta P, Starcuk Z Jr, Rektorova I. Early and progressive microstructural brain changes in mice overexpressing human alpha-synuclein detected by diffusion kurtosis imaging. *Brain Behav Immun.* 2017;61:197–208.
52. Tabesh A, Jensen JH, Ardekani BA, Helpert JA. Estimation of tensors and tensor-derived measures in diffusional kurtosis imaging. *Magn Reson Med.* 2011;65(3):823–36.
53. Hansen B, Lund TE, Sangill R, Jespersen SN. Experimentally and computationally fast method for estimation of a mean kurtosis. *Magn Reson Med.* 2013;69(6):1754–60. <https://doi.org/10.1002/mrm.24743>.
54. Yan X, Zhou M, Ying L, Yin D, Fan M, Yang G, Zhou Y, Song F, Xu D. Evaluation of optimized b-value sampling schemas for diffusion kurtosis imaging with an application to stroke patient data. *Comput Med Imaging Graph.* 2013;37(4):272–80.
55. Moeller S, Yacoub E, Olman CA, Auerbach E, Strupp J, Harel N, Ugurbil K. Multiband multislice GE-EPI at 7 tesla, with 16-fold acceleration using partial parallel imaging with application to high spatial and temporal whole-brain fMRI. *Magn Reson Med.* 2010;63(5):1144–53.
56. Setsompop K, Cohen-Adad J, Gagoski BA, Raji T, Yendiki A, Keil B, Wedeen VJ, Wald LL. Improving diffusion MRI using simultaneous multi-slice echo planar imaging. *NeuroImage.* 2012;63(1):569–80.



# Intravoxel Incoherent Motion (IVIM)

# 16

Denis Le Bihan and Sebastian F.-X. Winklhofer

## Contents

16.1	<b>Introduction</b> .....	229
16.2	<b>Principles of IVIM MRI</b> .....	230
16.3	<b>Processing of IVIM Data</b> .....	230
16.4	<b>IVIM and Classical Perfusion</b> .....	232
16.5	<b>Clinical Applications</b> .....	232
16.5.1	Ischemic Stroke Imaging.....	232
16.5.2	Brain Tumor Imaging.....	233
16.5.3	Other Clinical Applications.....	234
16.6	<b>Clinical Case</b> .....	235
	<b>References</b> .....	235

## 16.1 Introduction

While diffusion MRI has become a pillar of clinical MRI, especially in the field of neurological disorders, there is another subfield of diffusion MRI which is gaining popularity after a long sleep period: Intravoxel incoherent motion (IVIM) MRI allows tissue microcirculation (perfusion) to be

investigated in addition to tissue microstructure (from molecular diffusion) [1–3]. Perfusion imaging, as permitted with IVIM MRI, provides valuable information on neoangiogenesis, microvascular heterogeneity, on treatment efficacy of chemo- or radiotherapy, effectiveness of antiangiogenic drugs, and vascular targeting agents on brain tumors. The main reason for this “wake up” [4] is that vast progress has been made in MRI scanner hardware and sequence developments, satisfying the signal:noise ratio hungry IVIM method. Another reason is that IVIM MRI does not involve contrast agents, serving as an interesting alternative to perfusion MRI in some patients with contraindications for contrast agents, such as patients with renal failure at risk for nephrogenic systemic fibrosis (NSF). Recently, an accumula-

D. Le Bihan (✉)  
NeuroSpin/Joliot Institute/DRF/CEA-Saclay,  
Gif-sur-Yvette, France  
e-mail: [denis.lebihan@cea.fr](mailto:denis.lebihan@cea.fr)

S. F.-X. Winklhofer  
Department of Neuroradiology, University Hospital  
Zurich, University Zurich, Zurich, Switzerland  
e-mail: [sebastian.winklhofer@usz.ch](mailto:sebastian.winklhofer@usz.ch)

tion of gadolinium deposits in the brain or other organs in patients having received multiple injections of contrast agents has been demonstrated [5, 6]. The IVIM method, thus, appears particularly appealing for patients requiring multiple MRI scans, as well as for children or pregnant patients.

## 16.2 Principles of IVIM MRI

The IVIM concept was introduced in 1986 together with the foundation of diffusion MRI (DWI) [1, 2], as it was realized that flow of blood in capillaries (perfusion) would mimic a diffusion process and impact diffusion MRI measurements, although molecular diffusion and blood microcirculation refer to two completely different physical phenomena taking place at very different spatial and temporal scales. Apparent motion randomness for perfusion results from the geometry of the vessel network where blood circulates, under the hypothesis that the microvas-

cular network can be modeled by a series of straight segments randomly oriented in space. Hence, the motion of blood water molecules in the network, flowing from one capillary segment to the next can be seen as a *pseudo-diffusion* process. Given the mean capillary segment length and blood velocity in the network, one may estimate using Einstein's diffusion equation this pseudo-diffusion coefficient to be around  $10^{-2}$  mm<sup>2</sup>/s, just about 10 times the true diffusion coefficient on water in brain tissue so that diffusion and perfusion-driven pseudo-diffusion can be disentangled. In practice, because the fraction of the flowing blood is usually small (a few percentage) compared to the overall tissue water content, the perfusion-driven IVIM effect appears as a small deviation visible at low  $b$  values (parameter used to quantify the intrinsic degree of diffusion-weighting of a DWI sequence [1, 2]) on top of the overall tissue diffusion-driven DWI signal decay. More precisely, the IVIM/DWI signal attenuation,  $S(b)/S(0)$ , has been modeled as:

$$S(b)/S(0) = f \exp(-bD^*) + (1-f)F_{\text{diff}}(-bD) \quad (16.1)$$

where  $S(b)$  and  $S(0)$  are the DWI signals acquired at  $b$  and  $b = 0$ , respectively,  $f$  is the flowing blood fraction (sometimes also called  $fp$ ),  $D^*$  the pseudo-diffusion coefficient ascribed to blood random microcirculation (including the water diffusion coefficient in blood), and  $D$  the water diffusion coefficient in the tissue.  $F_{\text{diff}}(-bD)$  is also often modeled as a monoexponential decay,  $\exp(-bD)$ , assuming "free" (Gaussian) diffusion in tissues, resulting for Eq. (16.1) is the classical "biexponential model" [2] (Fig. 16.1). Many recent studies have pointed out, however, the non-Gaussian nature of diffusion in tissues, and more sophisticated models have been proposed to better describe diffusion in tissues [7, 8].

## 16.3 Processing of IVIM Data

A popular marker of DWI is the apparent diffusion coefficient, ADC, which is calculated from signals  $S(b)$  and  $S(0)$  as  $\ln[S(b)/S(0)]/b$ . In the

presence of perfusion-driven IVIM effects, the ADC is higher than the perfusion-free ADC. This difference is mostly seen when using small values for  $b$ . As  $f$  is usually small, one has  $\text{ADC} \sim D + f/b$ , and  $f$  simply appears as the (negative) intercept of the diffusion component of the signal decay in log plots with  $b$  values. Based on this observation, the flowing blood fraction,  $f$ , can be estimated just by using  $3b$  values [2], an approach which has gained popularity, as it minimizes acquisition times. However,  $D^*$  cannot be estimated with this simplistic approach. Another, more comprehensive and accurate approach is to acquire multiple DWI images with a range of  $b$  values covering "low"  $b$  values (0–200 s/mm<sup>2</sup>) to provide perfusion sensitivity and "high"  $b$  values (from 200 s/mm<sup>2</sup> to ideally above 2000 s/mm<sup>2</sup> to include non-Gaussian diffusion effects) to account for tissue diffusion. The signals from those images can then be fitted with the model of Eq. (16.1) to give estimates of  $f$ ,  $D^*$  and  $D$ . Although fitting can be performed in



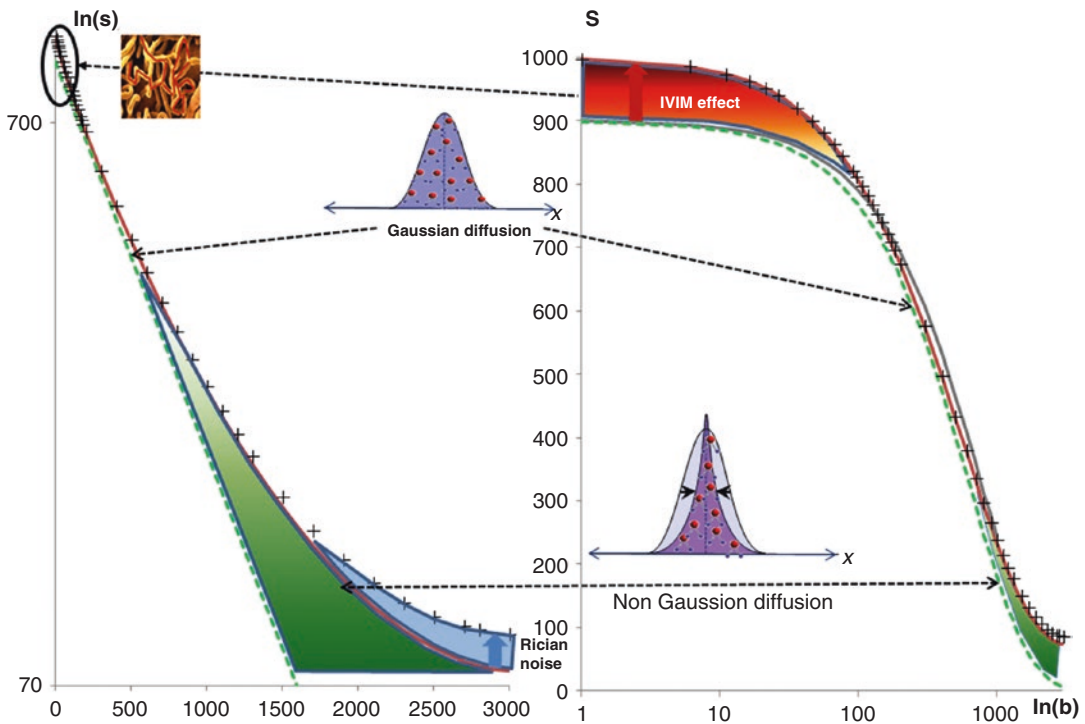


**Fig. 16.1** Perfusion-driven and diffusion signal attenuation. (Figure reprinted with permission from [7]). *Left*: The natural logarithm of the signal attenuation shows a triple curvature. At low  $b$  values ( $<200$  s/mm<sup>2</sup>) the curvature results from IVIM (blood microcirculation) effects. At very high  $b$  values the signal remains above a “noise floor” which produces a curvature which needs to be removed before signal analysis. The curvature visible at high  $b$  values after noise correction (deviation from the straight green line expected for free diffusion) is produced

by hindrance effects (notably from membranes) which make diffusion non-Gaussian. *Right*: As the IVIM effect is usually small, more images are often acquired at low  $b$  values than for diffusion at high  $b$  values. However, it may be difficult to visually qualify the goodness of the diffusion and IVIM fits using the standard attenuation plot ( $\ln(S)$  as a function of  $b$  value, as in the left plot). An attractive alternative would be to plot  $S$  as a function of  $\ln(b)$  to visually exaggerate the contribution of IVIM effects at very low  $b$  values

one step, it is often preferred to split the fitting process in two steps to relieve the pressure on signal:noise ratio, considering that the IVIM components become negligible at some point when  $b$  increases (as  $D^*$  is much higher than  $D$ ), typically around 200–400 s/mm<sup>2</sup> in the brain. The DWI signal at high  $b$  values is first fitted to estimate  $D$ . Then, the residual signal obtained after removing the diffusion component of the DWI signal at low  $b$  values is fitted to extract  $f$  and  $D^*$ .

Given the small size of  $f$  (typically 1–4% in the normal brain) an accurate estimation of perfusion-driven parameters requires, however, great care in data treatment. Any error in handling the tissue diffusion component of the signal will have deleterious effects on IVIM parameter estimates which could be either largely over-

underestimated. A first pitfall is to neglect non-Gaussian diffusion effects which result from the hindrance of water diffusion in tissue by many obstacles (cell membranes, fibers, etc.) in link with their microstructure. In the presence of non-Gaussian diffusion, a simple monoexponential model cannot be used for  $F_{\text{diff}}$  in Eq. (16.1) and one has to resort to more sophisticated models, out of the scope of this introductory review [7, 8]. Fitting the curved diffusion signal attenuation with a monoexponential model will systematically put the fitted diffusion signal decay too low, resulting in an overestimation of  $f$  and  $D^*$ . Another source of error in the mishandling of the noise in DWI signals especially at high  $b$  values. Signal of MRI images is magnitude reconstructed resulting in a Rician noise, as the

signal cannot go to 0 in the presence of noise. Rician noise is difficult to correct, especially when using phased-array MRI coils and parallel imaging, as noise patterns are different across space. Rician noise effects lead to an underestimation of IVIM effects, with  $f$  becoming sometimes “negative” [8]. It is thus particularly important to correct for this noise bias all IVIM MRI data, especially when using high  $b$  values. Several methods have been proposed to correct for those noise effects, however, this would be out of scope for this chapter.

The brain tissue itself adds another layer of complexity, especially for its white matter where water diffusion is anisotropic: Water diffusion is faster along the white matter tracks than perpendicularly to them. This anisotropy effect is handled and exploited by the diffusion tensor imaging (DTI) framework [9] to provide powerful markers of white matter integrity (such as the fractional anisotropy) and 3D images of brain connections. However, diffusion anisotropy effects represent another source of error, as artifactual IVIM effects may appear. Even in the absence of perfusion, tissue diffusion anisotropy results in nonzero  $f$  values, mimicking perfusion, when Eq. (16.1) is used. Furthermore, this artifactual IVIM effect looks anisotropic, with the  $f$  values depending on the measurement directions. This bias can be mitigated when taking the geometric mean of the DWI signals over specific acquisition directions before using Eq. (16.1).

## 16.4 IVIM and Classical Perfusion

One strength of IVIM MRI is that no tracer or contrast agent is used. Hence, it remains to be seen whether a bridge can be established between the IVIM parameters,  $f$  and  $D^*$ , and those which have been used with classical perfusion measurements [10–12], based on the delivery of tracers, as with PET or SPECT, or other MRI methods used to estimate tissue perfusion (arterial spin labeling or ASL, contrast-enhanced MRI). Classical perfusion parameters are, for instance, the cerebral blood volume, CBV, the cerebral blood flow, CBF, and the mean transit time, MTT. It can be shown that, under some hypotheses, one has [12]

$f = \text{CBV}/f_w$ ,  $\text{MTT} = Ll/6D^*$  and  $\text{CBF} = (6f_w/Ll)fD^*$ , where  $f_w$  is the MRI-visible water content fraction,  $L$  the total capillary length (from artery to vein) and  $l$  the mean capillary segment length. In short, the element bridging the classical perfusion and IVIM parameters is the capillary network geometry, and more especially two specific lengths characterizing this network: the capillary segment length and the total capillary length. Those quantities are constant for a given tissue, so that relative perfusion or blood flow can potentially be estimated from the product  $D^*f$ . Furthermore, the mean transit time could also be evaluated (at least in a relative manner) from  $D^*$  without the need to estimate an arterial “input function”, which is not a trivial methodological issue, and without the confound of the inclusion of the transit time of blood in the large feeding vessels.

In any case, the flowing blood fraction,  $f$ , appears correlated with vessel density [13, 14], and recent studies have shown a correlation between  $f$  and CBV (cerebral blood volume) derived from DSC (dynamic susceptibility contrast) MRI in gliomas [15, 16]. But other studies have failed to observe such a correlation [17]. One also has to keep in mind that IVIM imaging has a differential sensitivity to vessel sizes, according to the range of  $b$  values which are used, but is sensitive to all randomly flowing blood in each voxel. Direct comparison with other methods, such as ASL, is not straightforward, as ASL monitors only the transit of blood which has been labeled outside of the voxels, while IVIM reflects all randomly flowing blood in each voxel.

## 16.5 Clinical Applications

### 16.5.1 Ischemic Stroke Imaging

According to the World Health Organization (WHO), stroke (cerebrovascular accident) is the worldwide second leading cause of death and the third leading cause of long-term disability [18]. Next to computed tomography (CT), MRI is the modality of choice for imaging of ischemic stroke in the acute and subacute setting. Conventional MRI techniques, such as T1 weighted, T2 weighted, susceptibility-weighted imaging or fluid attenuation

inversion recovery (FLAIR) sequences and the more advanced DWI and perfusion-weighted sequences are established and routinely performed for the diagnostic workup of stroke patients. An increased hindrance in diffusion in DWI allows for the identification of brain tissue affected by cytotoxic edema, indicating irreversible damaged brain tissue and resembling the core of the ischemic infarction. Perfusion-weighted imaging (PWI), however, allows for the assessment of the perfusion of blood within the brain parenchyma. Depending on the applied PWI technique, an exogenous (i.e., gadolinium in dynamic susceptibility contrast (DSC) and dynamic contrast-enhanced (DCE) perfusion) or an endogenous contrast agent (i.e., blood in arterial spin labeling (ASL) perfusion) is required. Classic perfusion parameters are, as above mentioned, the cerebral blood volume (CBV), the cerebral blood flow (CBF), and the mean transit time (MTT). In patients with ischemic stroke, these parameters can be used to identify regions of diminished or reduced blood supply. Combining information from DWI and PWI enables a detailed analysis of the integrity of cerebral brain tissue in stroke imaging. The ischemic core with the irreversible damaged tissue can be assessed by DWI, whereas the tissue at risk or the salvageable parenchyma can be identified with the help of PWI. This concept is becoming increasingly important since ischemic stroke management (e.g., intravenous thrombolysis vs. mechanical thrombectomy) is currently rapidly changing and therapeutical decisions are increasingly based on advanced neuroimaging.

IVIM MRI can be applied in acute stroke imaging by using the IVIM perfusion fraction which is reduced in the infarcted brain tissue. Federau et al. showed, that IVIM perfusion fraction maps allow for the visualization of decreased perfusion fraction  $f$  in the region of decreased apparent diffusion coefficient from DWI and that quantitative analyses reveal a significant decrease in both IVIM perfusion fraction  $f$  and diffusion coefficient  $D$  compared with the contralateral cerebral hemisphere [19]. Another study investigated the potential utility of IVIM in characterizing brain diffusion and perfusion properties for clinical stroke. They found in 101 patients diagnosed with acute or subacute ischemic stroke, that ADC values in ischemic and normal regions significantly positively corre-

lated with  $D$  and  $f$  from IVIM and that a significant correlation was also found between ADC and  $fD^*$  in the ischemic region. They concluded that these findings may have clinical implications for the use of IVIM imaging in the assessment and management of acute or subacute stroke patients [20]. Furthermore, IVIM perfusion is feasible to measure the quality of the collateral blood flow in the penumbra in hyperacute stroke patients. IVIM  $f$  was found in a study to be significantly lower in the stroke core compared to the healthy contralateral brain region. Patients with a penumbra in IVIM perfusion had a larger infarct core at baseline, a larger infarct growth, and a larger final infarct size on follow-up images compared to the patients without. All IVIM penumbra perfusion lesions progressed to infarction despite thrombectomy treatment. From these results, it can be concluded that IVIM is a promising tool to assess the quality of the collateral blood flow in patients with a hyperacute stroke. The penumbra assessed by IVIM MRI may be a marker of non-salvageable tissue despite treatment with thrombectomy, suggesting that the IVIM penumbra perfusion lesion might be, together with the DWI lesion, counted to the stroke core [21].

### 16.5.2 Brain Tumor Imaging

Both DWI and PWI are helpful tools for the detection and grading as well as for predicting the patient's prognosis, choosing the optimal treatment, and for follow-up imaging of intracranial tumors. Based on quantitative and qualitative analysis of ADC images from DWI, the cellularity of tumors can be evaluated, with a known correlation between a high tumor cellularity and a higher tumor grading [22, 23]. Using imaging parameters from PWI allows to use MRI as a biomarker regarding tumor vascularization, which correlates with tumor classification and grading, prognosis and can be helpful for response assessment after chemo- or radiation therapy [24–26].

IVIM MRI has been shown several promising applications in tumor imaging. The parameters  $f_{max}$  and  $D_{min}$  from IVIM are significantly higher in glioblastoma (GBM) than in primary central nervous system lymphoma (PCNSL) and therefore, IVIM-MR imaging noninvasively pro-

vides useful quantitative information in distinguishing between PCNSL and GBM. Several studies have demonstrated the ability of IVIM to grade and to further specify gliomas including their isocitrate dehydrogenase 1 (IDH1) mutational status by using the diffusion and the perfusion information derived by IVIM imaging [27–30]. Furthermore, IVIM can be used as a potential biomarker for survival in glioma. In contrast-enhancing tumor regions,  $f$  and  $D^*$  from IVIM correlate with CBF derived from corresponding dynamic susceptibility contrast (DSC) perfusion images and moreover can be seen as promising biomarkers of survival in newly diagnosed glioblastoma [31]. Federau et al. showed that the IVIM perfusion fraction, similarly to maximal relative cerebral blood volume from DSC and minimal apparent diffusion coefficient from DWI, was prognostic for survival in patients with gliomas. Besides this, the maximal IVIM perfusion fraction and minimal apparent diffusion coefficient performed similarly in predicting survival, however, both slightly outperformed maximal relative cerebral blood volume from DSC [32].

Furthermore, IVIM MRI shows value for the peri- and post-therapeutic assessment of intracranial tumors: Tumor progression after bevacizumab treatment was successfully identified by decreasing relative  $D$  values from IVIM [33] and IVIM MRI demonstrated promise in differentiating recurrent tumor from radiation necrosis for brain metastases treated with radiosurgery [34]. However, these studies included only a low number of patients and further studies with larger patient cohorts are required for a final validation.

Besides glioma, meningiomas can also be assessed by using IVIM MRI: the  $f$  value measured by IVIM imaging shows a significant correlation and an excellent agreement with the histological vascular density in meningiomas. This parameter can therefore be used as a noninvasive and quantitative imaging measure to directly assess the volume fraction of capillaries in brain tumors [35].

### 16.5.3 Other Clinical Applications

Recently, more and more potential applications of IVIM MRI in neuroradiology are investi-

gated. Moyamoya disease is a rare cerebrovascular disease that primarily affects children and young adults. A study investigated whether IVIM could be used to evaluate the hemodynamic disturbance by comparison with the gold-standard  $^{15}\text{O}$ -gas positron emission tomography (PET) method. A significant correlation between IVIM parameters  $D^*$  and  $f$  were found to perfusion parameters derived by PET. The  $f$  values in the white matter were significantly higher in symptomatic Moyamoya patients than in healthy controls and they concluded that IVIM MRI may be used to investigate the cerebral hemodynamic impairment in those patients [36]. This is of particular interest for this often young patient group, since IVIM MRI is a noninvasive, radiation-free technique, which does not require the administration of contrast agents or tracers, which is an important advantage of IVIM MRI.

Other recent studies are dealing with the investigation of the perfusion and diffusion of brain parenchyma by IVIM in patients with cerebral small vessel disease [37] or with the prediction of delayed cerebral ischemia and vasospasm after aneurysm rupture [38].

In addition to potential applications in the brain, several promising studies have been published regarding IVIM MRI in the head and neck region. Similar to cerebral tumors, it was shown, that IVIM MRI successfully allows for the differentiation, characterization, and therapy monitoring of head and neck neoplasia, such as squamous cell carcinomas [39–43]. IVIM is feasible to identify metastatic lymph nodes and can therefore be used to separate benign from malignant lymph nodes.  $D$  is significantly decreased in malignant lymph nodes reflected by increased nuclear-to-cytoplasmic ratio tissue, and  $D^*$  is significantly increased reflected by increased blood vessel generation and parenchymal perfusion in malignant lymph nodes [44].

Another application for IVIM MRI includes the assessment of cerebrospinal fluid (CSF) by using cardiac-gating, an approach, which might provide future opportunities to further investigate the pathophysiology of various neurological disorders involving altered CSF [45, 46].

## 16.6 Clinical Case (Fig. 16.2)

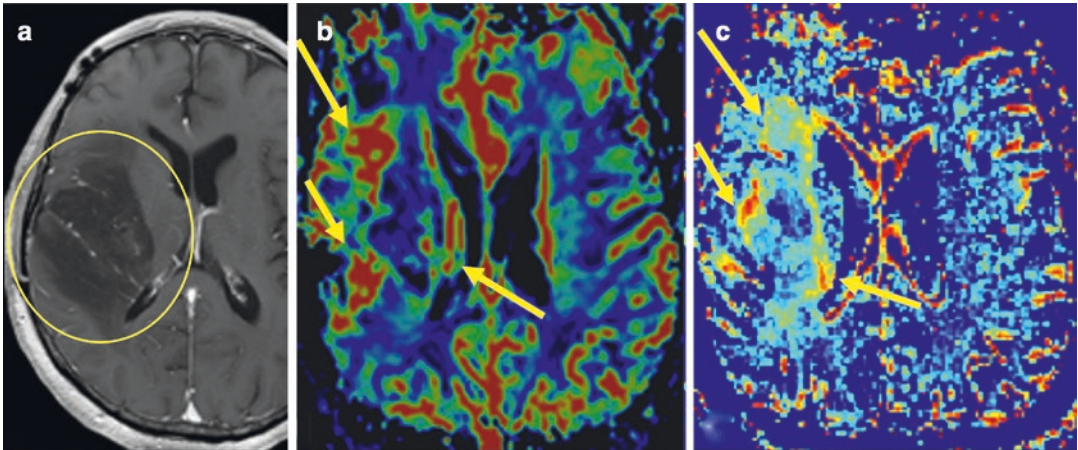


**Fig. 16.2** IVIM in tumor imaging. Glioblastoma located in the right cerebral hemisphere in a middle-aged woman. (a) Axial T1-weighted post-contrast MRI, (b) dynamic susceptibility contrast (DSC) MRI perfusion with cerebral blood volume map (CBV), and (c) IVIM  $f$ . T1 weighted

imaging demonstrates the tumor as a hypointense area with a faint contrast enhancement (circle). IVIM  $f$  correlates well with hyperperfused tumor components in the perfusion CBV map (arrows). (Case courtesy of PD Dr. Christian Federau)

## References

1. Le Bihan D, et al. MR imaging of intravoxel incoherent motions: application to diffusion and perfusion in neurologic disorders. *Radiology*. 1986;161(2):401–7.
2. Le Bihan D, et al. Separation of diffusion and perfusion in intravoxel incoherent motion MR imaging. *Radiology*. 1988;168(2):497–505.
3. Le Bihan D. Magnetic resonance imaging of perfusion. *Magn Reson Med*. 1990;14(2):283–92.
4. Le Bihan D. Intravoxel incoherent motion perfusion MR imaging: a wake-up call. *Radiology*. 2008;249(3):748–52.
5. Kanda T, et al. High signal intensity in the dentate nucleus and globus pallidus on unenhanced T1-weighted MR images: relationship with increasing cumulative dose of a gadolinium-based contrast material. *Radiology*. 2014;270(3):834–41.
6. Kanda T, et al. High signal intensity in dentate nucleus on unenhanced T1-weighted MR images: association with linear versus macrocyclic gadolinium chelate administration. *Radiology*. 2015;275(3):803–9.
7. Iima M, Le Bihan D. Clinical intravoxel incoherent motion and diffusion MR imaging: past, present, and future. *Radiology*. 2016;278(1):13–32.
8. Iima M, et al. Quantitative non-Gaussian diffusion and intravoxel incoherent motion magnetic resonance imaging: differentiation of malignant and benign breast lesions. *Investig Radiol*. 2015;50(4):205–11.
9. Basser PJ, Mattiello J, LeBihan D. MR diffusion tensor spectroscopy and imaging. *Biophys J*. 1994;66(1):259–67.
10. Zierler K. Indicator dilution methods for measuring blood flow, volume, and other properties of biological systems: a brief history and memoir. *Ann Biomed Eng*. 2000;28(8):836–48.
11. Henkelman RM. Does IVIM measure classical perfusion? *Magn Reson Med*. 1990;16(3):470–5.
12. Le Bihan D, Turner R. The capillary network: a link between IVIM and classical perfusion. *Magn Reson Med*. 1992;27(1):171–8.
13. Iima M, et al. Characterization of glioma microcirculation and tissue features using intravoxel incoherent motion magnetic resonance imaging in a rat brain model. *Investig Radiol*. 2014;49(7):485–90.
14. Lee HJ, et al. Tumor perfusion-related parameter of diffusion-weighted magnetic resonance imaging: correlation with histological microvessel density. *Magn Reson Med*. 2014;71(4):1554–8.
15. Federau C, et al. Perfusion measurement in brain gliomas with intravoxel incoherent motion MRI. *AJNR Am J Neuroradiol*. 2014;35(2):256–62.
16. Kim HS, et al. Histogram analysis of intravoxel incoherent motion for differentiating recurrent tumor from treatment effect in patients with glioblastoma:

- initial clinical experience. *AJNR Am J Neuroradiol.* 2014;35(3):490–7.
17. Bisdas S, et al. Correlative assessment of tumor microcirculation using contrast-enhanced perfusion MRI and intravoxel incoherent motion diffusion-weighted MRI: is there a link between them? *NMR Biomed.* 2014;27(10):1184–91.
  18. WHO methods and data sources for global causes of death 2000–2012. *Global Health Estimates Technical Paper WHO/HIS/HSI/GHE/2014.7.* World Health Organization; 2014.
  19. Federau C, et al. Intravoxel incoherent motion perfusion imaging in acute stroke: initial clinical experience. *Neuroradiology.* 2014;56(8):629–35.
  20. Suo S, et al. Stroke assessment with intravoxel incoherent motion diffusion-weighted MRI. *NMR Biomed.* 2016;29(3):320–8.
  21. Federau C, et al. Collateral blood flow measurement with intravoxel incoherent motion perfusion imaging in hyperacute brain stroke. *Neurology.* 2019;92(21):e2462–71.
  22. Yamasaki F, et al. Apparent diffusion coefficient of human brain tumors at MR imaging. *Radiology.* 2005;235(3):985–91.
  23. Sugahara T, et al. Usefulness of diffusion-weighted MRI with echo-planar technique in the evaluation of cellularity in gliomas. *J Magn Reson Imaging.* 1999;9(1):53–60.
  24. Brandao LA, Shiroishi MS, Law M. Brain tumors: a multimodality approach with diffusion-weighted imaging, diffusion tensor imaging, magnetic resonance spectroscopy, dynamic susceptibility contrast and dynamic contrast-enhanced magnetic resonance imaging. *Magn Reson Imaging Clin N Am.* 2013;21(2):199–239.
  25. Law M, et al. Gliomas: predicting time to progression or survival with cerebral blood volume measurements at dynamic susceptibility-weighted contrast-enhanced perfusion MR imaging. *Radiology.* 2008;247(2):490–8.
  26. Suh CH, et al. Perfusion MRI as a diagnostic biomarker for differentiating glioma from brain metastasis: a systematic review and meta-analysis. *Eur Radiol.* 2018;28(9):3819–31.
  27. Wang X, et al. Glioma grading and IDH1 mutational status: assessment by intravoxel incoherent motion MRI. *Clin Radiol.* 2019;74(8):651.e7–651.e14.
  28. Togao O, et al. Differentiation of high-grade and low-grade diffuse gliomas by intravoxel incoherent motion MR imaging. *Neuro Oncol.* 2016;18(1):132–41.
  29. Shen N, et al. Intravoxel incoherent motion diffusion-weighted imaging analysis of diffusion and microperfusion in grading gliomas and comparison with arterial spin labeling for evaluation of tumor perfusion. *J Magn Reson Imaging.* 2016;44(3):620–32.
  30. Bisdas S, et al. Intravoxel incoherent motion diffusion-weighted MR imaging of gliomas: feasibility of the method and initial results. *Neuroradiology.* 2013;55(10):1189–96.
  31. Puig J, et al. Intravoxel incoherent motion metrics as potential biomarkers for survival in glioblastoma. *PLoS One.* 2016;11(7):e0158887.
  32. Federau C, et al. IVIM perfusion fraction is prognostic for survival in brain glioma. *Clin Neuroradiol.* 2017;27(4):485–92.
  33. Miyoshi F, et al. Utility of intravoxel incoherent motion magnetic resonance imaging and arterial spin labeling for recurrent glioma after bevacizumab treatment. *Acta Radiol.* 2018;59(11):1372–9.
  34. Detsky JS, et al. Differentiating radiation necrosis from tumor progression in brain metastases treated with stereotactic radiotherapy: utility of intravoxel incoherent motion perfusion MRI and correlation with histopathology. *J Neuro-Oncol.* 2017;134(2):433–41.
  35. Togao O, et al. Measurement of the perfusion fraction in brain tumors with intravoxel incoherent motion MR imaging: validation with histopathological vascular density in meningiomas. *Br J Radiol.* 2018;91(1085):20170912.
  36. Hara S, et al. Intravoxel incoherent motion perfusion in patients with Moyamoya disease: comparison with (15)O-gas positron emission tomography. *Acta Radiol Open.* 2019;8(5):2058460119846587.
  37. Wong SM, et al. Simultaneous investigation of microvasculature and parenchyma in cerebral small vessel disease using intravoxel incoherent motion imaging. *Neuroimage Clin.* 2017;14:216–21.
  38. Heit JJ, et al. Reduced intravoxel incoherent motion microvascular perfusion predicts delayed cerebral ischemia and vasospasm after aneurysm rupture. *Stroke.* 2018;49(3):741–5.
  39. Hauser T, et al. Characterization and therapy monitoring of head and neck carcinomas using diffusion-imaging-based intravoxel incoherent motion parameters-preliminary results. *Neuroradiology.* 2013;55(5):527–36.
  40. Sumi M, Nakamura T. Head and neck tumours: combined MRI assessment based on IVIM and TIC analyses for the differentiation of tumors of different histological types. *Eur Radiol.* 2014;24(1):223–31.
  41. Fujima N, et al. Prediction of the treatment outcome using intravoxel incoherent motion and diffusional kurtosis imaging in nasal or sinonasal squamous cell carcinoma patients. *Eur Radiol.* 2017;27(3):956–65.
  42. Ai QY, et al. Distinguishing early-stage nasopharyngeal carcinoma from benign hyperplasia using intravoxel incoherent motion diffusion-weighted MRI. *Eur Radiol.* 2019;29:5627–34.
  43. Sumi M, Nakamura T. Head and neck tumors: assessment of perfusion-related parameters and diffusion coefficients based on the intravoxel inco-

- herent motion model. *AJNR Am J Neuroradiol.* 2013;34(2):410–6.
44. Liang L, et al. Lymph node metastasis in head and neck squamous carcinoma: Efficacy of intravoxel incoherent motion magnetic resonance imaging for the differential diagnosis. *Eur J Radiol.* 2017;90:159–65.
45. Becker AS, et al. Investigation of the pulsatility of cerebrospinal fluid using cardiac-gated Intravoxel Incoherent Motion imaging. *NeuroImage.* 2018;169:126–33.
46. Surer E, et al. Cardiac-gated intravoxel incoherent motion diffusion-weighted magnetic resonance imaging for the investigation of intracranial cerebrospinal fluid dynamics in the lateral ventricle: a feasibility study. *Neuroradiology.* 2018;60(4):413–9.



Lucy McGavin and Amoolya Mannava

## Contents

17.1	<b>Basic Physics of Proton Spectroscopy</b> .....	240
17.2	<b>Visible Metabolites</b> .....	240
17.2.1	Myo-Inositol (mI).....	241
17.2.2	Choline (Cho).....	242
17.2.3	Creatine (Cr).....	242
17.2.4	Glutamate (Glu) and Glutamine (Gln), Gamma-Aminobutyric Acid (GABA).....	242
17.2.5	<i>N</i> -Acetylaspartate (NAA).....	242
17.2.6	Lactate (Lac).....	243
17.2.7	Lipids.....	243
17.3	<b>Acquisition Parameters</b> .....	243
17.4	<b>Sequences</b> .....	243
17.4.1	Multivoxel Techniques.....	244
17.5	<b>Artefacts</b> .....	244
17.6	<b>Clinical Applications</b> .....	245
17.7	<b>CNS Neoplasms</b> .....	245
17.7.1	Role of Proton Spectroscopy in Diagnosis.....	245
17.7.2	Role of Proton Spectroscopy in Assessing Response to Treatment.....	246
17.7.3	Role of Proton Spectroscopy in Prognosis.....	246
17.8	<b>Hypoxic Neuronal Injury</b> .....	247
17.9	<b>Inborn Errors of Metabolism</b> .....	247
17.10	<b>Closing Remarks</b> .....	249
17.11	<b>Clinical Case</b> .....	249
	<b>References</b> .....	250

L. McGavin (✉) · A. Mannava  
University Hospitals Plymouth, NHS Trust,  
Plymouth, UK  
e-mail: [lucy.mcgavin@nhs.net](mailto:lucy.mcgavin@nhs.net)



## Abbreviations

GABA	Gamma-aminobutyric acid
Gln	Glutamine
Glu	Glutamate
Lac	Lactate
mI	Myo-inositol
NAA	<i>N</i> -acetyl aspartate
PRESS	Point-resolved spectroscopy
SNR	Signal-to-noise ratio
STEAM	Stimulated echo acquisition mode
tCho, Cho	Total choline, choline
tCr, Cr	Total creatine, creatine
TE	Time to echo

### 17.1 Basic Physics of Proton Spectroscopy

Both magnetic resonance imaging (MRI) and magnetic resonance spectroscopy (MRS) share a common origin from early developments in nuclear magnetic resonance (NMR) techniques. Nuclei such as hydrogen ( $^1\text{H}$ ), carbon ( $^{13}\text{C}$ ), fluorine ( $^{19}\text{F}$ ) and phosphorus ( $^{31}\text{P}$ ), with odd numbers of protons, neutrons or both have a net circulating nuclear charge which generates a magnetic dipole moment and spin. Nuclear magnetic resonance results from energy exchange and alteration of spin dynamics when these nuclei absorb energy from an applied radiofrequency pulse. MRI uses the electrical signal resulting from this resonance to perform spatial localisation; MRS analyses the signal for the component resonance frequencies derived from different molecules within the tissue. The geometry of the electron cloud surrounding a hydrogen nucleus (electron shielding) as a result of its chemical bonding to other atoms influences the magnetic field experienced by that hydrogen nucleus; this difference in local microenvironment leads to a small difference in resonating frequency termed “chemical shift” [1]. By plotting the unique chemical shift of molecules containing a hydrogen nucleus, proton spectroscopy builds a biochemical profile of tissue. In H-MRS, the focus is on molecules other than water which contain pro-

tons. It is necessary to suppress the signal from water in order to prevent the signal from these molecules from being overwhelmed in amplitude (and thus rendered invisible) by the much greater signal from water. Due to the low concentrations of molecules studied in MRS, the region of interest chosen has a typical spatial resolution of 1–10 cm<sup>3</sup> as compared to 1–10 mm<sup>3</sup> for MRI [2].

The chemical shift demonstrated by spectroscopy is not simply a function of the electron shielding effect described above; protons on adjacent molecules influence the net magnetisation experienced by each other and thereby their spins. Spins may align in the same or opposite directions to each other resulting in a greater or lesser net local magnetic field respectively; this phenomenon is described as spin–spin splitting or J-coupling. As a result, the spectra of certain metabolite groups may be represented as a single large peak or multiple small peaks clustered together as doublets, triplets or multiplets depending on their chemical bonding. The methyl group of lactate, for instance, produces a doublet peak. Oftentimes it is difficult to fully analyse a complex splitting pattern [2].

### 17.2 Visible Metabolites

In vivo spectroscopy is only able to visualise small, mobile molecules with concentrations  $\geq 0.5 \mu\text{mol/g}$  of tissue [2]. Most neurotransmitters, large, immobile molecules such as proteins, phospholipids, nucleic acids and myelin are not visualised. Concentrations of the visible metabolites described below are tightly regulated and remain constant in healthy tissue. If robust methodology is applied, acquisitions can be reproduced such that changes in spectra represent purely biochemical changes resulting from pathology. At commonly available field strengths of 1.5 or 3.0 T, choline (Cho), creatine (Cr) and *N*-acetyl aspartate (NAA) peaks are observed in healthy brain tissue at long echo times (e.g. 140 or 280 ms). At short echo times (e.g. 30 or 35 ms) compounds such as glutamate and glutamine (Glx), myo-inositol (mI), lipids and some macromolecules can also be seen. Metabolites such as

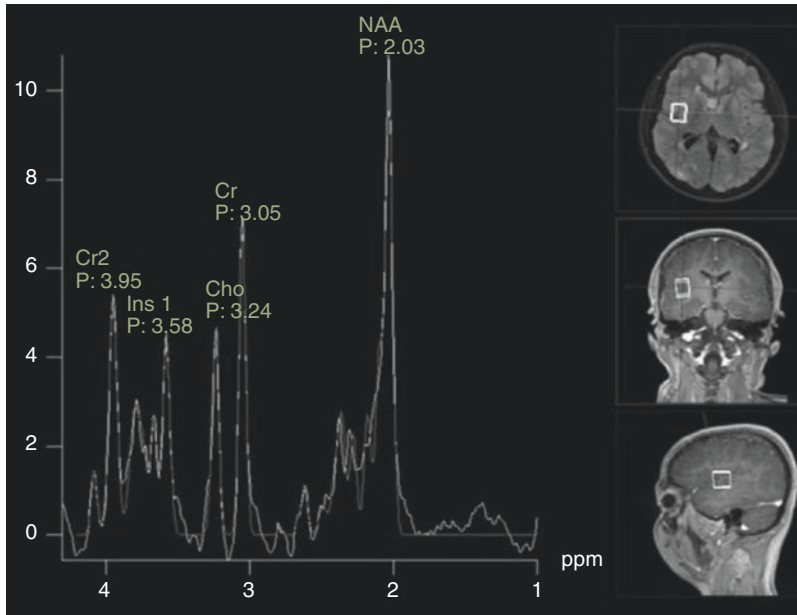


**Fig. 17.1** H-MRS spectrum of healthy brain tissue obtained with short TE sequence and corresponding MRI reference image. Cr2 indicates second peak of Creatine. In a normal spectrum, the resonances of metabolites myo-inositol, choline, creatine and *N*-acetylaspartate (NAA) are ascending in concentration. The line joining their

peaks subtends an angle to the  $x$ -axis of approximately  $45^\circ$ , referred to as Hunter's angle. When this angle is disturbed or the peaks do not make an ascending line, pathology is suspected. (Reproduced with permission from Ulmer et al. [6])

lactate, alanine or others may be detectable when pathological conditions increase their concentration [3]. Figure 17.1 illustrates a spectroscopy trace in healthy brain tissue. Resonance frequencies corresponding to chemical shift are plotted against metabolite concentration. The scale of chemical shift on the  $x$ -axis decreases from left to right. Commonly seen metabolites in healthy brain tissue and their metabolic role are summarised in Table 17.1.

Chemical shift is field-independent and is measured in parts per million (ppm). It is standardised by using the reference compound tetramethylsilane (TMS) for all proton spectroscopy [4]. On a reference scale where TMS = 0 ppm, water resonates at 4.7 ppm. Thus, even in the absence of TMS we can use the reference scale where water resonates at 4.7 ppm [5]. By using this unified scale, we can compare the concentrations of metabolites in different tissues and on different scanners. This allows MR spectroscopy to be a quantitative imaging tool.

**Table 17.1** Common metabolites seen in a proton spectrum

Metabolite	Chemical shift (ppm)	Metabolic role/indication
Water	4.7	
Myo-inositol	3.6	Glial cell marker
Choline	3.2	Cell membrane turnover
Creatine	3.0, 3.9	Energy metabolism
Glutamate and glycine	2.1–2.7, 3.7	Neurotransmitter
NAA	2.0	Neuronal integrity
Lactate	1.3	Anaerobic metabolism
Lipids	1.5–0.8	Breakdown of cell membranes

### 17.2.1 Myo-Inositol (mI)

Myo-inositol (mI) is a pentose sugar found abundantly in glial cells. It is an osmolyte and also participates in hormone receptor mechanisms. On short echo sequences, its representative peak

is seen at 3.56 ppm. mI levels are found to be negatively correlated with age from foetal life to adulthood. Findings in literature are inconsistent regarding levels in early adult life; levels are shown to increase in the elderly [7]. Myo-inositol is thought to be a glial cell marker; its levels are elevated in inflammatory and hyperosmolar states. Numerous studies and meta-analyses report elevated levels associated with low-grade glial tumours and Alzheimer's disease [8–10].

### 17.2.2 Choline (Cho)

Choline is a precursor of acetylcholine; in proton spectroscopy choline is used as an umbrella term embracing several soluble components of brain myelin and cell membranes such as glycerol phosphocholine, phosphocholine and choline. Choline resonance is seen at 3.22 ppm. High concentrations have been described in young infants [7, 11]. During childhood and adolescence, there is inconsistency of findings in literature; levels appear to increase in the elderly [7]. Higher concentrations of choline are found in the frontal lobes and in white matter when compared to grey matter. High choline levels are found in the cerebellum, pons, insular cortex, thalamus and hypothalamus [3, 12].

Being a metabolite of membrane synthesis and degradation, choline is often elevated in pathologies which result in high membrane turnover such as neoplasia, demyelination, inflammation and gliosis [13].

### 17.2.3 Creatine (Cr)

Creatine and phosphocreatine act as a surrogate for energy metabolism. As it is not possible to distinguish clearly the two separate peaks of creatine and phosphocreatine at 1.5 and 3 T they are often designated as tCr (total creatine), with resonance at 3.02 ppm. Creatine concentrations appear to positively correlate with age during a whole life [7]. Cr level is higher in grey matter than white matter [3]. Higher levels of Cr are

reported in the cerebellum compared to parieto-occipital cortex and pons [12].

Cr levels are relatively constant and were considered a good internal standard for comparisons with other metabolites. In recent years, however, it has been discovered that these peaks change in hypoxia, neurodegenerative disease, neuro AIDS and some tumours, and may not be as robust a standard for comparison as previously assumed [14].

### 17.2.4 Glutamate (Glu) and Glutamine (Gln), Gamma-Aminobutyric Acid (GABA)

Glutamate and GABA are major excitatory and inhibitory neurotransmitters in the brain respectively. Glycine (Gln) is the precursor of Glutamate (Glu) [13]. At 1.5 and 3 T, we may not clearly distinguish the separate peaks of Glutamine and Glutamate and together the spin system is frequently referred to as Glx (Glx = Glu + Gln) resonating between 2.1–2.5 and 2.75 ppm with a secondary peak at 3.7 ppm [15]. Several studies describe a reduction in Glx in neurodegenerative conditions [16, 17], and an increase is described in meningiomas [18] and Rett syndrome [19]. GABA peaks may overlap with other metabolites, particularly creatine and Glx. Newer spectral editing techniques and filtering methods are able to reproducibly isolate the GABA peak [20].

### 17.2.5 N-Acetylaspartate (NAA)

*N*-Acetylaspartate is an amino acid precursor for neurotransmitter *N*-acetylaspartylglutamate acid (NAAG) and being found almost exclusively in neurons, acting as a marker for neuronal health, density and viability. It is found in immature oligodendrocytes and astrocyte progenitor cells. The largest peak in proton spectroscopy is normally from NAA at 2.02 ppm. It increases in concentration during childhood neuronal development, plateaus and then decreases with ageing [7]. Apart from higher levels in the pons,

it has a relatively uniform regional distribution in the brain [12].

Decreased NAA is associated with almost all neurodegenerative conditions where there is loss or injury to neurons [9, 10] or in malignancy where healthy neurons are replaced by tumour tissue [21]. It is also reduced in hypoxia [22, 23] and demyelination [24, 25]. Canavan's disease is an interesting exception, where there is toxic accumulation of NAA secondary to a metabolic error [26].

### 17.2.6 Lactate (Lac)

Under normal conditions, lactate concentrations within the brain are too low to be detectable. Lactate becomes detectable when its concentrations increase as a result of anaerobic metabolism as seen in hypoxic brain tissue [23], certain mitochondrial diseases [27] and not infrequently in epilepsy [28, 29]. It is observed as a doublet resonating at 1.32 ppm. The lactate peak is inverted at TE of 144 ms due to spin–spin splitting or J-coupling. This can help to distinguish lactate resonance from adjacent lipid resonances.

### 17.2.7 Lipids

Lipids are best visualised on short TE acquisitions ( $\approx 35$  ms) resonating at 0.8–1.5 ppm. Lipids result from breakdown of cell membrane and are often seen elevated in radiation necrosis [30], high-grade tumours [8], metastasis [31], and demyelination [32].

---

## 17.3 Acquisition Parameters

The pivotal parameter in MRS is time to echo (TE). Short TE (TE  $\approx 35$  ms) provides good signal and captures metabolites with short TE properties such as mI and Glx. Proton spectra obtained at longer TE (TE of 135–288 ms) have poorer SNR but simpler spectra, with flat baselines. A

TR that is 1–1.5 times T1 relaxation time of metabolites is usually chosen [2].

With increasing field strength, baseline noise decreases and spectral peaks become more distinct. Single voxel techniques generally describe a voxel of 8 cc at 1.5 T. At a higher field strength a smaller voxel size can be used, thereby increasing relative spatial resolution and reducing partial volume effects [5].

Peak width is proportional to  $1/T_2$ . If the voxel contains molecules that shorten T2 such as blood breakdown products (hemosiderin), the spectral peak will broaden. The presence of bone and contrast can also result in susceptibility artefacts which degrade the spectra. Voxel placement is therefore crucial to the interpretation of spectra. One way to mitigate variations seen with development, ageing and brain region, is to obtain a second “control” spectrum from a voxel placed in the contralateral homologous brain region if the pathology is lateralised.

---

## 17.4 Sequences

Single voxel techniques: When specific regions of the brain need to be studied single voxel techniques are generally preferred. Two widely available, basic acquisition sequences are stimulated echo acquisition mode (STEAM) and point-resolved spectroscopy (PRESS) [33].

In a STEAM sequence, three orthogonal  $90^\circ$  narrow bandwidth frequency pulses are applied in sequence to a single voxel. As a result, four to five echoes are generated, one of which is the stimulated echo which is used to produce spectra. For many years, STEAM was the only MRS sequence available that could be done at short TE where metabolites such as mI and Glx could be observed. Compared to PRESS, STEAM yields a lower SNR and has longer acquisition. It also does not show the lactate inversion peak at TE 144 ms. It does, however, minimise chemical shift artefacts better [33, 34].

Point-resolved spectroscopy (PRESS) uses a  $90^\circ$  and  $180^\circ$  pulse followed by a refocusing  $180^\circ$  pulse. Each pulse has a slice-selective gradient

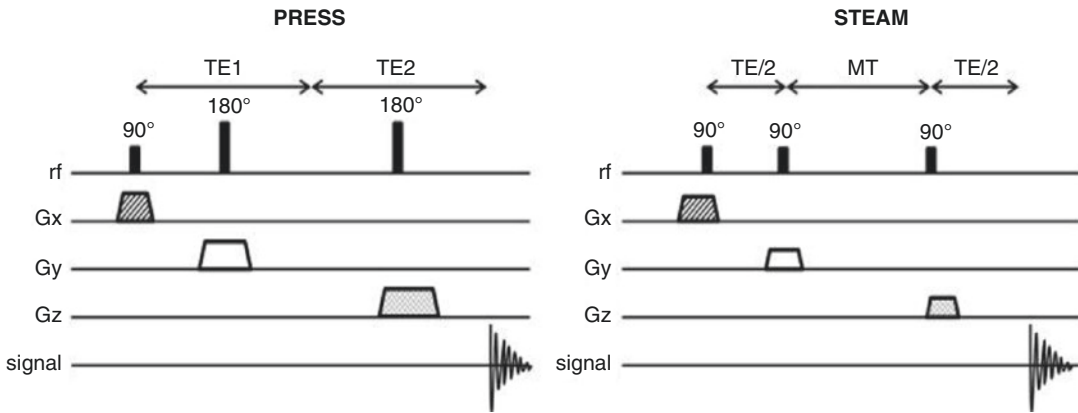


**Fig. 17.2** A schematic representation of PRESS and STEAM acquisition sequences. (Reproduced with permission from Bertholdo et al. [36])

acquired in sequence in orthogonal gradients such that only spins that intersect all three gradients are refocused to provide echoes for deriving spectra. The signal in PRESS depends on pulse spacing and TR. It can be used for short or long TE and has been popular in clinical use over the past decade [35]. Figure 17.2 demonstrates a schematic of PRESS and STEAM acquisition sequences.

### 17.4.1 Multivoxel Techniques

CSI (chemical shift imaging) or 3D MRSI (magnetic resonance spectroscopic imaging) is excellent for obtaining metabolic maps of large brain areas or different parts of a lesion. Tissue is imaged in slices and regions of interest (ROI) can be subsequently placed. Phase-encoding gradients are used to divide a slice into a grid of voxels and spectra are derived from each of these individual voxels. As a result, voxel size is small, but SNR can be made comparable to PRESS. Slices can be interleaved using parallel imaging techniques to reduce acquisition time [33]. CSI often uses colour maps in addition to spectra to represent metabolic profiles. This enables comparison between the anatomical and metabolic extent of a disease process. Maps must be correlated with respective spectra to identify artefacts e.g. due to poor shimming or poor water suppression (see below).

## 17.5 Artefacts

Spectral artefacts are often subtle and difficult to detect. Common artefacts encountered in MRS are due to motion, eddy currents, inadequate shimming or water suppression and spectral contamination.

- **Poor shimming:** The quality of shimming often dictates the quality of spectra. First-order shimming is generally automated while secondary shimming is introduced manually if needed. Poor shimming leads to peak broadening and increased baseline noise.
- **Incomplete water suppression:** This can result in loss of certain metabolic peaks. Skewing of the baseline to the left (i.e. towards water resonance of 4.7 ppm) generally indicates poor water suppression [5].
- **Chemical shift artefacts:** These can lead to spatial mis-mapping. Chemical shift artefacts are most problematic with single-voxel spectra at higher magnetic fields. The solution is often to employ larger bandwidth RF pulses and stronger imaging gradients.
- **Spectral contamination:** In multi-voxel spectroscopy, spectral contamination can occur such that spatial mis-mapping may extend many voxels away from the source. This is due to aliasing similar to Gibbs artefact seen in MRI. This effect can be reduced (but not completely eliminated) through digital filtering

techniques and by increasing the number of voxels [37, 38].

---

## 17.6 Clinical Applications

In the past two decades, there have been numerous studies published describing a wide range of neurological applications of MRS. In order to focus on those areas with high-level clinical evidence, a database search was conducted on PubMed and Embase from inception up to May 2018 for the terms: “magnetic resonance spectroscopy” OR “proton spectroscopy” OR “metabolic imaging” AND “brain” OR “CNS” OR “neurology”. Results were filtered for the following types: meta-analyses, systematic reviews and phase III, IV clinical trials published in the English language.

The resulting 356 articles were screened by title, followed by abstract to include 46 articles. A further 12 articles referenced in these studies were subsequently included. Technical reviews, reviews, non-proton spectroscopy, studies focusing on non-CNS carcinoma, single centre studies were excluded. Two systematic analysis reporting metabolic changes in normal ageing are referenced in the previous section. We reviewed the remaining 56 articles, categorising them into

- (a) *clinical applications with a clear role for MRS*; including CNS neoplasia (12 studies), hypoxic ischemic encephalopathy (4 studies);
- (b) *pre-clinical research applications* such as psychiatric illness (20 studies encompassing schizophrenia, bipolar mood disorders and major depression), neurodegeneration particularly Alzheimer’s disease (3 studies), chronic hepatitis C infection (1 study), substance abuse (3 studies) and diabetes mellitus (2 studies);
- (c) *clinical scenarios with limited evidence or equivocal conclusions* such as traumatic brain injury (3 studies), epilepsy (2 studies), migraine (1 study), multiple sclerosis (3 studies), chronic back pain (1 study) and drowning (1 study).

Drawing on this review of literature, we describe the application of MRS in answering specific questions in clinical management of CNS neoplasia and hypoxic neuronal injury. We have included a description of the role of MRS in management of children with certain inborn errors of metabolism. While the evidence basis for application is somewhat limited, likely due to rarity of conditions, we do observe its utility in clinical practice.

---

## 17.7 CNS Neoplasms

MRS is most useful in differentiating low- and high-grade gliomas [8, 21, 39], and tumour recurrence from radiation necrosis [21, 22, 30]. Meta-analyses examined its role in distinguishing neoplasia from non-neoplastic lesions [21, 40], defining tumour extent [21] and in follow-up monitoring for progression [41]. It holds promise as a method for reliably identifying IDH mutant gliomas [42, 43] and pituitary adenomas when compared to diagnostic utility of SPECT or PET [44] and in differentiating between pseudo-response and true response following chemotherapy [45, 46]. Nuclear medicine studies such as PET appear superior to MRS for diagnosis of CNS lymphoma in HIV patients [47]; MRS does not reliably differentiate metastasis from primary neoplasia [39].

### 17.7.1 Role of Proton Spectroscopy in Diagnosis

Glial tumours exhibit elevated choline and decreased NAA levels corresponding to the degree of malignancy [8, 39, 48]. As Cho/NAA describes glial cell proliferation this usually correlates with tumour infiltration, progression-free survival and contrast enhancement at recurrence in glioblastoma [49]. There is much heterogeneity in the literature regarding the threshold ratios for Cho/Cr, Cho/NAA and NAA/Cr needed to distinguish high- and low-grade gliomas. Lactate and lipids representing anaerobic metabolism and necrosis are often

seen with high-grade lesions and indicate a worse outcome [21, 50, 51]. Low-grade gliomas on the other hand are often associated with higher mI levels [13].

Several meta-analyses have established the value of in MRS for differentiating high- and low-grade gliomas [8, 21, 41]. Wang et al. demonstrated that the choice of Cho/NAA ratio was superior to Cho/Cr and NAA/Cr ratios in a meta-analysis of 30 studies [8]. Usinskeine et al. analysed 83 articles comparing MR metrics from relative cerebral blood volume (rCBV), normalised ADC and spectroscopic ratios of Cho/Cr, Cho/NAA, reporting greatest diagnostic accuracy with rCBV and ratios of Cho/Cr and Cho/NAA differentiating high- and low-grade gliomas. They report a significant difference between Cho/Cr and Cho/NAA ratios of low- and high-grade gliomas at both short and medium TE. The weighted mean of Cho/Cr (short TE), Cho/Cr (medium TE) and Cho/NAA ratios in low-grade gliomas were found to be 1.46, 1.71 and 2.36 respectively. This was significantly lower than weighted mean of Cho/Cr (short TE), Cho/Cr (medium TE) and Cho/NAA ratios in high-grade gliomas which were 2.4, 3.27 and 4.71 respectively [39].

Individual studies indicate associative characteristic spectral pattern in specific CNS neoplasia, which may provide additional information in lesions of uncertain origin. Untreated neuroectodermal tumours in children often show a taurine increase [13, 32]. Glycine increase may be seen in high-grade paediatric tumours [27]. Meningiomas and metastasis often have raised choline associated with near absent NAA [31, 52]. Meningiomas are also generally associated with a low mI and may exhibit raised alanine [53].

Other contrast-enhancing lesions such as abscess and tuberculomas may also exhibit an elevated lipid spectrum. Abscesses are often associated with elevated amino acids and absent NAA, Cho and creatinine [13]. Diffusion-weighted imaging (DWI) is better at distinguishing glioma from underactive MS, where MRS may provide equivocal results [54].

### 17.7.2 Role of Proton Spectroscopy in Assessing Response to Treatment

The pattern of enhancement on imaging is traditionally used to differentiate tumour recurrence from treatment response; recurrence is associated with pathological enhancement and response is associated with poor enhancement. The use of treatments that affect vascular permeability can produce patterns that mimic tumour response or progression. Cytotoxic therapies including radiotherapy can cause enhancement which mimics progression and is referred to as “pseudoprogression”. Approximately 30–40% of patients on anti-angiogenic agents such as bevacizumab and cediranib demonstrate non-enhancing tumour progression prior to changes in contrast enhancement [46]. This is termed “pseudoresponse”. Recent meta-analyses show that average Cho/Cr and Cho/NAA ratios are significantly higher in tumour recurrence than in tumour necrosis [30, 55]. While no absolute threshold is evident in available meta-analyses which quantitatively differentiated recurrence from radiation necrosis, many studies included use Cho/Cr and/or Cho/NAA >1.71 and/or Cho/Cr >2 with reduced NAA as an indication of recurrence [21, 30, 56]. On the other hand, necrotic tissue demonstrates elevated lactate which marks anaerobic glycolysis and elevated lipids. There are a few studies dedicated to the diagnostic utility of MRS in pseudo-response, but no meta-analysis is currently available supporting it [57].

### 17.7.3 Role of Proton Spectroscopy in Prognosis

The last decade of research, culminating in the revised 2016 WHO classification of CNS neoplasia, has shown that genetic and histological profiles of brain tumours are needed to both direct treatment and for prognostication. Isocitrate dehydrogenases (IDH) mutations are more frequent in secondary GBM than in the primary GBM and have a better prognosis. IDH mutation in grade II–IV gliomas are associated with a better

prognosis for survival [42, 58]. IDH mutation results in the high accumulation of 2-hydroxy glutarate (2HG), typically two to three orders greater than wild-type IDH or healthy tissue. 2HG molecules have multiplets which resonate at 4.02, 2.25 and 1.9 ppm of which the 2.25 ppm signal is typically the strongest at 3 T [42]. Prospective longitudinal trials (total of 161 patients) have shown that 2-HG peaks can be reliably detected on spectroscopy provided that appropriate spectral editing tools are used [42, 43]. This suggests there may be a promising clinical role for MRS in non-invasive IDH typing of gliomas.

---

## 17.8 Hypoxic Neuronal Injury

MRS and DWI are acutely sensitive to hypoxic brain injury. Indeed, some of the earliest applications of spectroscopy were in evaluation of neuronal ischemia. Thayyil et al. reported that raised Lac/NAA had better diagnostic accuracy for hypoxic ischaemic encephalopathy (HIE) than conventional MRI performed at any time during neonatal period, and was the best predictor of a poor outcome [23]. They suggest that Lac/NAA could be useful in early clinical management decisions and in counselling parents about prognosis.

Monitoring lactate and NAA during therapeutic hypothermia serves as a surrogate to treatment efficiency [23]. It may also serve as a surrogate end point in clinical trials evaluating new neuroprotective therapies.

There has been sustained interest in the role of MRS in traumatic brain injury (TBI) where prognostication with imaging remains a challenge. Brown et al. reported a significant decrease in NAA/Cr ratios and elevated Cho/Cr ratios in TBI in the subacute and chronic phases of injury but not in the acute phase [59]. Larger studies and multicentre trials with robust outcomes are lacking, making it difficult to evaluate clinical utility.

---

## 17.9 Inborn Errors of Metabolism

There are a number of relatively rare neurometabolic disorders whose diagnosis and monitoring can be improved using MRS. Typically, a genetic

mutation leads to a block in a metabolic pathway resulting in under production of one or more substrates and accumulation of another; the pathological effects may be due to the deficiency or toxic accumulation. Clinical presentation is often with non-specific symptoms in early life. In some disorders, specific treatment options are available and when instituted early, can prevent brain damage. Spectroscopy findings in some common inborn metabolic disorders are described here.

Maple syrup urine disease (MSUD) is an autosomal recessive disorder. A defect in oxidative decarboxylation of branched chain keto acids (BCKA) results in accumulation of the precursor amino acids and their corresponding keto acids, in the serum, CSF and urine. The more common, severe form of this disease presents in the neonate and if untreated leads to progressive neurological damage. Variant forms of the disease become apparent in childhood, with typically less severe symptoms that may only appear during times of fasting, stress or illness, but still involve neuro-cognitive insult. Earlier diagnosis and institution of therapy are critical for optimising prognosis. H-MRS demonstrates decreased NAA, methyl resonances of branched chain amino acids at 0.9 ppm and lactate in acute metabolic decompensation [60]. Cho and mI levels may be found elevated. The proton MR spectroscopic findings are positive even when structural imaging is negative and can be used to evaluate the state of disease in MSUD and its response to therapy [61].

Urea cycle disorders result in accumulation of nitrogenous compounds such as ammonia. Infantile Refsum disease is a milder form where spectra show increase in Cho and lipids but decreased NAA [60].

Mitochondrial disorders are a heterogeneous group of disorders, of which Leigh's disease and mitochondrial encephalomyopathy with lactic acidosis and stroke-like episodes (MELAS) are more common. Proton spectroscopy in Leigh's disease shows a large increase in lactate with fall in NAA [62]. MELAS presents with encephalomyopathy, lactic acidosis and stroke-like episodes, typically before the age of 30. MRS demonstrates very high lactate levels with reduced NAA, glutamate, mI and total creatinine in affected areas [27].



Other, rare leukodystrophies such as Canavan's disease and metabolic errors, such as creatinine deficiency and nonketotic hyperglycinaemia, also have characteristic spectra to aid diagnosis and management. Canavan's disease for instance

results in toxic accumulation of NAA leading to spongiform leukodystrophy and demonstrates characteristic high NAA spectra [63]. Figure 17.3 demonstrates a typical proton spectrum seen in Canavan's disease.

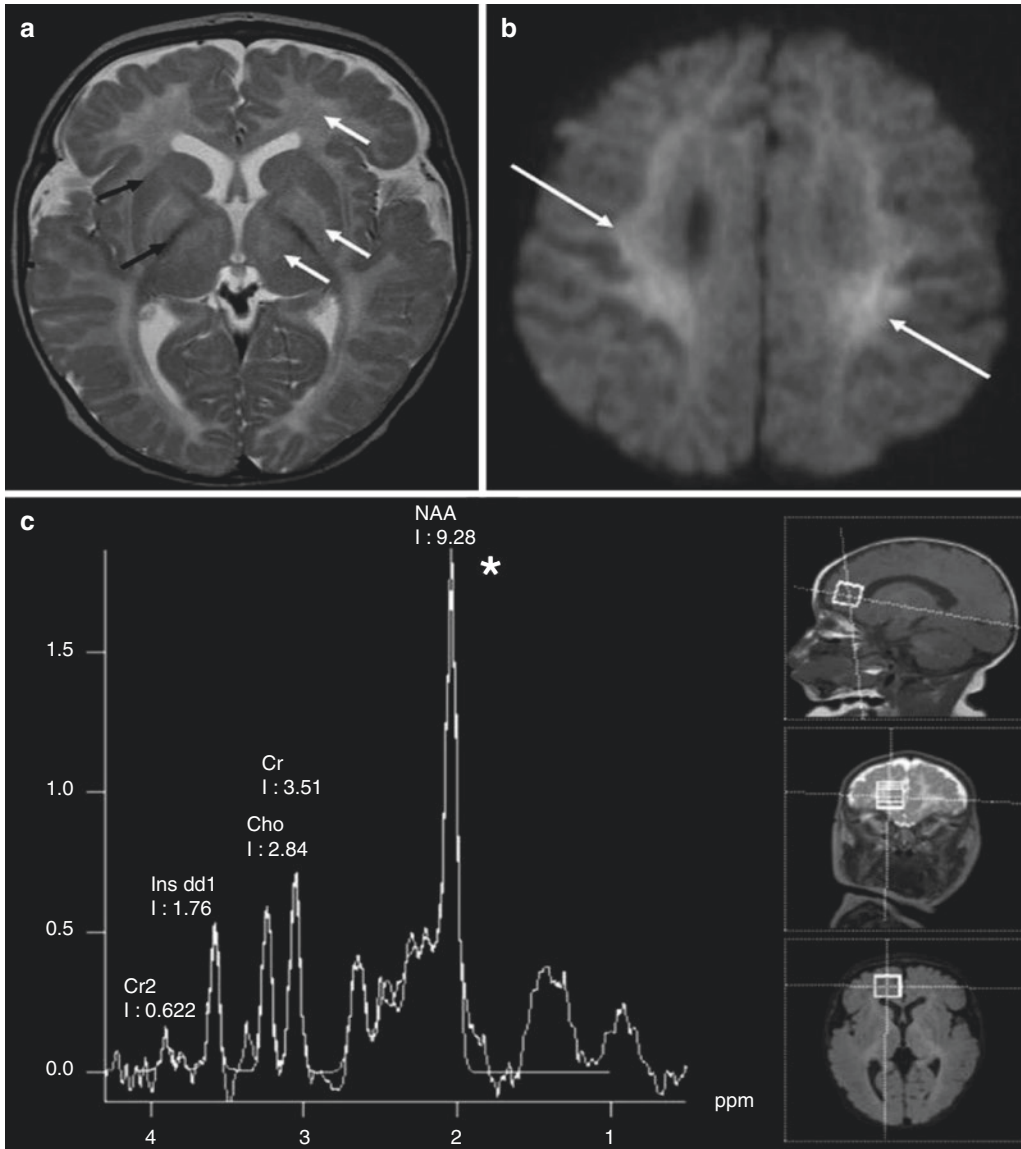


**Fig. 17.3** Canavan disease. An axial T2-weighted image (a) shows abnormal high signal in the thalami, globus pallidus, and the entire white matter (white arrows). There is relative sparing of the posterior limbs of internal capsules, caudate nuclei, and putamina (black arrows). An axial diffusion-weighted image (b) demonstrates uniformly restricted diffusion within the abnormal white matter compatible with intramyelinic edema (arrows). Spectroscopy

with TE = 35 ms (c), sampling voxel positioned in the right frontal white matter, shows markedly elevated NAA peak at 2.0 ppm (\*), considered pathognomonic of Canavan disease. Also note that decreased choline (Cho) and creatine (Cr) peaks, as well as slightly prominent myo-inositol peak (Ins dd1) at 3.54 ppm, labels computer generated. (Reproduced with permission from Atsina et al. [64])

## 17.10 Closing Remarks

MRS is a useful part of the diagnostic toolkit when the operator and reader are aware of its shortcomings and sources of potential error. As we accumulate more evidence on its clinical role it is likely that MRS will be used ever more widely in the management of neoplastic, inflammatory and degenerative disorders.

The literature to-date has tended to focus on defining precise metrics such as metabolite thresholds or ratios with which to distinguish between different disease states in what are perceived to be clinically useful sensitivities and specificities. It is our opinion that the use of simplified metrics risks missing a lot of the valuable data contained within MR spectra. In daily clinical practice, typically the whole spectrum is analysed and changes in patterns of spectra when compared to healthy brain tissue or over the course of a disease is considered. In agreement with Alger, we anticipate that the increased use of multi-dimensional analysis techniques, as embodied in data mining and machine learning literature and increased familiarity with biochemical aspects of disease within the radiology and neuroscience community will help address this issue and augment the clinical utility of MRS [66].

## 17.11 Clinical Case

We describe here the imaging findings of a 57-year-old lady with the working diagnosis of a low-grade primary brain tumour. She had opted out of surgical treatment of tumour in view of potential neurological insult being greater than benefit. She was being monitored annually for progression using MRI. Her initial surveillance studies suggested a stable tumour. Her latest surveillance MRI scan demonstrated that the tumour had increased in size with local mass effect. There was no pathological contrast enhancement. As structural MRI findings were equivocal, MRS and cerebral perfusion studies were also performed. There were no changes of note in the cerebral perfusion imaging. Her MRS, however, demonstrated a high Cho/NAA (highest=3.36) and Cho/Cr ratios with low NAA/Cr ratio within the core of the lesion. There was an associated small, insignificant rise in lactate. Proton spectra of the patient for corresponding sampling voxel placed within the brain lesion are shown in Fig. 17.4.

While structural MRI findings were equivocal, and cerebral perfusion studies negative, the MRS findings strongly suggested that the low-grade glioma had transformed to a high-grade lesion leading to a revision of management plan.

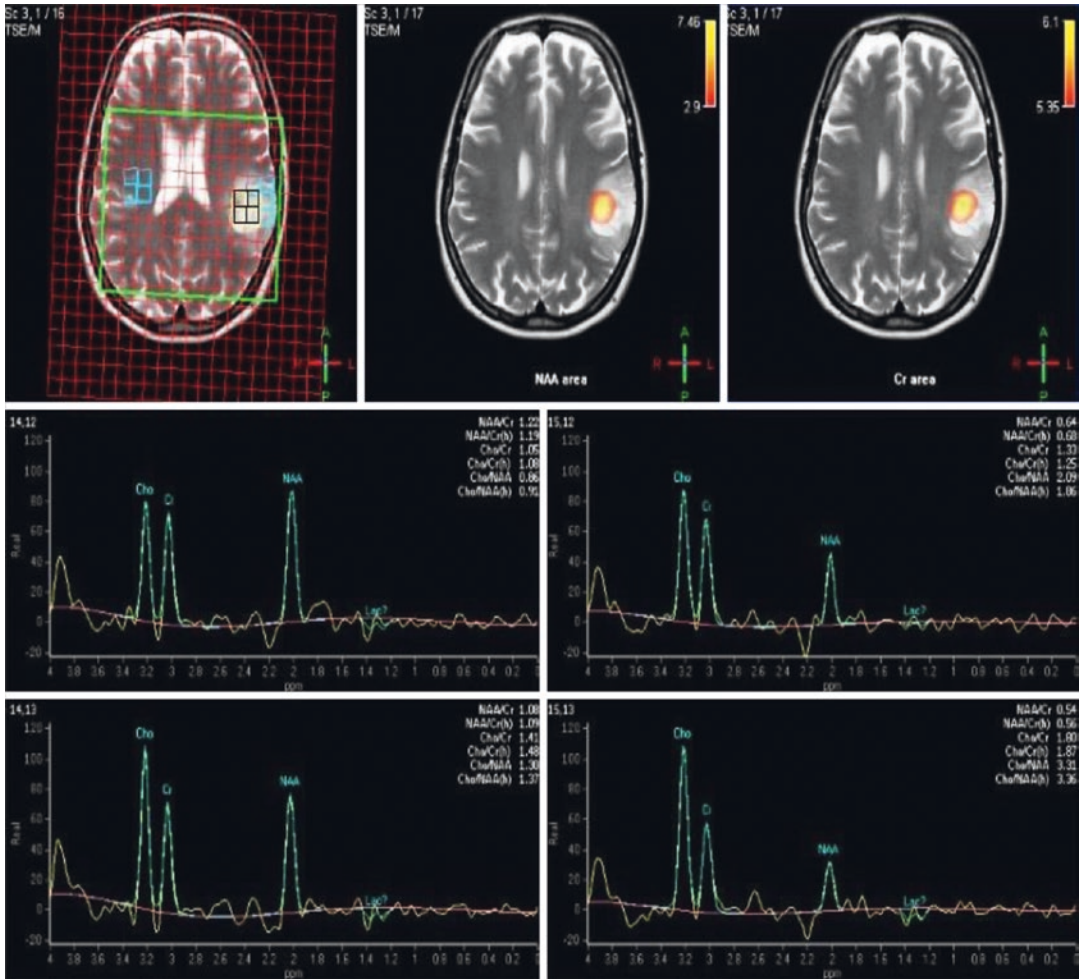


**Fig. 17.4** MRS spectra of sampling voxel (positioned in the core of left parietal lesion) show elevated choline peaks at 3.2 ppm and a markedly decreased NAA peak at 2 ppm. The resulting Cho/NAA ratio of 3.36 seen in spec-

tra 4 is significantly higher than the typical threshold of >2 used to distinguish high grade from low-grade glioma [65]

**References**

1. Roberts JD. Nuclear magnetic resonance. Applications to organic chemistry. New York: McGraw-Hill; 1959. p. 136.
2. Ross B, Bluml S. Magnetic resonance spectroscopy of the human brain. *Anat Rec.* 2001;265:54–84.
3. Barker PB. Fundamentals of MR spectroscopy. In: *Clinical MR neuroimaging: physiological and functional techniques*. 2nd ed. New York: Cambridge University Press; 2011. p. 5–20.
4. de Graaf RA. In vivo NMR spectroscopy: principles and techniques. 2nd ed. Chichester: Wiley; 2007. <https://doi.org/10.1002/9780470512968>.
5. Hashemi RH, Lisanti CJ, Bradley WG. MR spectroscopy in the Brain. In: *MRI: the basics*. Philadelphia: Wolters Kluwer; 2018.
6. Ulmer S, Backens M, Ahlhelm FJ. Basic principles and clinical applications of magnetic resonance spectroscopy in neuroradiology. *J Comput Assist Tomogr.* 2016;40:1–13.
7. Cichocka M, Bereś A. From fetus to older age: a review of brain metabolic changes across the lifespan. *Ageing Res Rev.* 2018;46:60–73.
8. Wang Q, Zhang H, Zhang J, Wu C, Zhu W, Li F, Chen X, Xu B. The diagnostic performance of magnetic resonance spectroscopy in differentiating high-from low-grade gliomas: a systematic review and meta-analysis. *Eur Radiol.* 2015;26:2670–84.
9. Wang H, Tan L, Wang H-F, Liu Y, Yin R-H, Wang W-Y, Chang X-L, Jiang T, Yu J-T. Magnetic resonance spectroscopy in Alzheimer’s disease: systematic review and meta-analysis. *J Alzheimers Dis.* 2015;46:1049–70. <https://doi.org/10.3233/JAD-143225>.

10. Tumati S, Martens S, Aleman A. Magnetic resonance spectroscopy in mild cognitive impairment: systematic review and meta-analysis. *Neurosci Biobehav Rev.* 2013;37:2571–86.
11. Haga KK, Khor YP, Farrall A, Wardlaw JM. A systematic review of brain metabolite changes, measured with 1H magnetic resonance spectroscopy, in healthy aging. *Neurobiol Aging.* 2009;30:353–63.
12. Jacobs MA, Horská A, Van Zijl PCM, Barker PB. Quantitative proton MR spectroscopic imaging of normal human cerebellum and brain stem. *Magn Reson Med.* 2001;46:699–705.
13. Ratai E-M, Gilberto González R. Clinical magnetic resonance spectroscopy of the central nervous system. *Handb Clin Neurol.* 2016;135:93–116.
14. Chang L, Ernst R, Witt MD, Ames N, Gaiefsky M, Miller E. Relationships among brain metabolites, cognitive function, and viral loads in antiretroviral-naïve HIV patients. *NeuroImage.* 2002;17:1638–48.
15. Ende G. Proton magnetic resonance spectroscopy: relevance of glutamate and GABA to neuropsychology. *Neuropsychol Rev.* 2015;25:315–25.
16. Griffith HR, den Hollander JA, Okonkwo OC, O'Brien T, Watts RL, Marson DC. Brain metabolism differs in Alzheimer's disease and Parkinson's disease dementia. *Alzheimers Dement.* 2008;4:421–7.
17. Rupsingh R, Borrie M, Smith M, Wells JL, Bartha R. Reduced hippocampal glutamate in Alzheimer disease. *Neurobiol Aging.* 2011;32:802–10.
18. Opstad KS, Provencher SW, Bell BA, Griffiths JR, Howe FA. Detection of elevated glutathione in meningiomas by quantitative in vivo 1H MRS. *Magn Reson Med.* 2003;49:632–7.
19. Farage L, Izbudak I, Nagae-Poetscher L, Bibat G, Kaufmann W, Barker P, Naidu S, Horska A. Age-dependence and clinical correlates of brain metabolism in Rett syndrome. In: *Proc. 14th sci. meet. int. soc. magn. reson. med.*; 2006. p. 245.
20. Mikkelsen M, Barker PB, Bhattacharyya PK, et al. Big GABA: edited MR spectroscopy at 24 research sites. *NeuroImage.* 2017;159:32–45.
21. Hollingworth W, Medina LS, Lenkinski RE, Shibata DK, Bernal B, Zurakowski D, Comstock B, Jarvik JG. A systematic literature review of magnetic resonance spectroscopy for the characterization of brain tumors. *AJNR Am J Neuroradiol.* 2006;27:1404–11.
22. Lin B, Zhang P, Cheng G, Zhou W, Wang L. [Meta-analysis of prognostic tests in neonates over 35-week gestational age with hypoxic-ischemic encephalopathy]. *Zhonghua Yi Xue Za Zhi.* 2014;94:115–21.
23. Thayyil S, Chandrasekaran M, Taylor A, Bainbridge A, Cady EB, Cheng WKK, Murad S, Omar RZ, Robertson NJ. Cerebral magnetic resonance biomarkers in neonatal encephalopathy: a meta-analysis. *Pediatrics.* 2010;125:e382–95.
24. Khan O, Seraji-Bozorgzad N, Bao F, et al. The relationship between brain MR spectroscopy and disability in multiple sclerosis: 20-year data from the U.S. Glatiramer Acetate Extension Study. *J Neuroimaging.* 2017;27:97–106.
25. Arnold DL, Narayanan S, Antel S. Neuroprotection with glatiramer acetate: evidence from the PreCISE trial. *J Neurol.* 2013;260:1901–6.
26. Cakmakci H, Pekcevik Y, Yis U, Unalp A, Kurul S. Diagnostic value of proton MR spectroscopy and diffusion-weighted MR imaging in childhood inherited neurometabolic brain diseases and review of the literature. *Eur J Radiol.* 2010;74:e161–71.
27. Möller HE, Kurlemann G, Pützler M, Wiedermann D, Hilbich T, Fiedler B. Magnetic resonance spectroscopy in patients with MELAS. *J Neurol Sci.* 2005;229–230:131–9.
28. Zhang L, Li H, Hong P, Zou X. Proton magnetic resonance spectroscopy in juvenile myoclonic epilepsy: a systematic review and meta-analysis. *Epilepsy Res.* 2016;121:33–8.
29. Caruso PA, Johnson J, Thibert R, Rapalino O, Rincon S, Ratai EM. The use of magnetic resonance spectroscopy in the evaluation of epilepsy. *Neuroimaging Clin N Am.* 2013;23:407–24.
30. Chuang MT, Liu YS, Tsai YS, Chen YC, Wang CK. Differentiating radiation-induced necrosis from recurrent brain tumor using MR perfusion and spectroscopy: a meta-analysis. *PLoS One.* 2016;11:1–13.
31. Ishimaru H, Morikawa M, Iwanaga S, Kaminogo M, Ochi M, Hayashi K. Differentiation between high-grade glioma and metastatic brain tumor using single-voxel proton MR spectroscopy. *Eur Radiol.* 2001;11:1784–91.
32. Oz G, Alger JR, Barker PB, et al. Clinical proton MR spectroscopy in central nervous system disorders. *Radiology.* 2014;270:658–79.
33. Posse S, Otazo R, Dager SR, Alger J. MR spectroscopic imaging: principles and recent advances. *J Magn Reson Imaging.* 2013;37:1301–25.
34. Bertholdo D, Watcharakorn A, Castillo M. Brain proton magnetic resonance spectroscopy. *Neuroimaging Clin N Am.* 2013;23:359–80.
35. Chong WK. Magnetic resonance neuroimaging. *Curr Paediatr.* 1995;5:208–12.
36. Bertholdo D, Watcharakorn A, Castillo M. Brain proton magnetic resonance spectroscopy: introduction and overview. *Neuroimaging Clin N Am.* 2013;23:359–80.
37. Kreis R. Issues of spectral quality in clinical 1H-magnetic resonance spectroscopy and a gallery of artifacts. *NMR Biomed.* 2004;17:361–81.
38. Elster AD. In: *Questions and answers in magnetic resonance imaging.* St. Louis: Mosby; 1994.
39. Usinskiene J, Ulyte A, Bjørnerud A, et al. Optimal differentiation of high- and low-grade glioma and metastasis: a meta-analysis of perfusion, diffusion, and spectroscopy metrics. *Neuroradiology.* 2016;58:339–50.
40. Wang W, Hu Y, Lu P, Li Y, Chen Y, Tian M, Yu L. Evaluation of the diagnostic performance of magnetic resonance spectroscopy in brain tumors: a systematic review and meta-analysis. *PLoS One.* 2014;9:e112577. <https://doi.org/10.1371/journal.pone.0112577>.

41. Fouke SJ, Benzinger T, Gibson D, Ryken TC, Kalkanis SN, Olson JJ. The role of imaging in the management of adults with diffuse low grade glioma. *J Neuro-Oncol.* 2015;125:457–79.
42. Choi C, Ganji SK, DeBardinis RJ, et al. 2-Hydroxyglutarate detection by magnetic resonance spectroscopy in IDH-mutated patients with gliomas. *Nat Med.* 2012;18:624–9.
43. Andronesi OC, Kim GS, Gerstner E, Batchelor T, Tzika AA, Fantin VR, Vander Heiden MG, Sorensen AG. Detection of 2-hydroxyglutarate in IDH-mutated glioma patients by in vivo spectral-editing and 2D correlation magnetic resonance spectroscopy. *Sci Transl Med.* 2012;4:116ra4. <https://doi.org/10.1126/scitranslmed.3002693>.
44. Yao A, Balchandani P, Shrivastava RK. Metabolic in vivo visualization of pituitary adenomas: a systematic review of imaging modalities. *World Neurosurg.* 2017;104:489–98.
45. Ryken TC, Aygun N, Morris J, Schweizer M, Nair R, Spracklen C, Kalkanis SN, Olson JJ. The role of imaging in the management of progressive glioblastoma: a systematic review and evidence-based clinical practice guideline. *J Neuro-Oncol.* 2014;118:435–60.
46. Cordova JS, Shu HKG, Liang Z, et al. Whole-brain spectroscopic MRI biomarkers identify infiltrating margins in glioblastoma patients. *Neuro-Oncology.* 2016;18:1180–9.
47. Yang M, Sun J, Bai HX, et al. Diagnostic accuracy of SPECT, PET, and MRS for primary central nervous system lymphoma in HIV patients. *Medicine (Baltimore).* 2017;96:e6676.
48. Howe FA, Opstad KS. 1H MR spectroscopy of brain tumours and masses. *NMR Biomed.* 2003;16:123–31.
49. Sawlani V, Taylor R, Rowley K, Redfern R, Martin J, Poptani H. Magnetic resonance spectroscopy for differentiating pseudo-progression from true progression in GBM on concurrent chemoradiotherapy. *Neuroradiol J.* 2012;25:575–86.
50. Hattingen E, Raab P, Franz K, Lanfermann H, Setzer M, Gerlach R, Zanella FE, Pilatus U. Prognostic value of choline and creatine in WHO grade II gliomas. *Neuroradiology.* 2008;50:759–67.
51. Chronaiou I, Stensjoen AL, Sjobakk TE, Esmaeili M, Bathen TF. Impacts of MR spectroscopic imaging on glioma patient management. *Acta Oncol (Madr).* 2014;53:580–9.
52. Arnold DL, Shoubridge EA, Villemure J-G, Feindel W. Proton and phosphorus magnetic resonance spectroscopy of human astrocytomas in vivo. Preliminary observations on tumor grading. *NMR Biomed.* 1990;3:184–9.
53. Gill SS, Thomas DGT, Van Bruggen N, et al. Proton MR spectroscopy of intracranial tumours: in vivo and in vitro studies. *J Comput Assist Tomogr.* 1990;14:497–504.
54. Law M, Yang S, Wang H, Babb JS, Johnson G, Cha S, Knopp EA, Zagzag D. Glioma grading: sensitivity, specificity, and predictive values of perfusion MR imaging and proton MR spectroscopic imaging compared with conventional MR imaging. *AJNR Am J Neuroradiol.* 2003;24:1989–98.
55. Wang X, Hu X, Xie P, Li W, Li X, Ma L. Comparison of magnetic resonance spectroscopy and positron emission tomography in detection of tumor recurrence in posttreatment of glioma: a diagnostic meta-analysis. *Asia Pac J Clin Oncol.* 2015;11:97–105.
56. Zhang H, Ma L, Wang Q, Zheng X, Wu C, Xu BN. Role of magnetic resonance spectroscopy for the differentiation of recurrent glioma from radiation necrosis: a systematic review and meta-analysis. *Eur J Radiol.* 2014;83:2181–9.
57. Ratai E, Zhang Z, Snyder BS, Yeh M, Heureux DL, Downs J, Boxerman JL, Safriel Y, Sorensen G, Gilbert MR. MR spectroscopy as an early indicator of response to anti-angiogenic therapy in patients with recurrent glioblastoma: ACRIN 6677/RTOG 0625. *Neuro-Oncology.* 2013;15:936–44.
58. Chaumeil MM, Lupo JM, Ronen SM. Magnetic resonance (MR) metabolic imaging in glioma. *Brain Pathol.* 2015;25:769–80.
59. Brown M, Baradaran H, Christos PJ, Wright D, Gupta A, Tsiouris AJ. Magnetic resonance spectroscopy abnormalities in traumatic brain injury: a meta-analysis. *J Neuroradiol.* 2018;45:123–9. <https://doi.org/10.1016/j.neurad.2017.09.004>.
60. Cecil KM, Kos RS. Magnetic resonance spectroscopy and metabolic imaging in white matter diseases and pediatric disorders. *Top Magn Reson Imaging.* 2006;17:275–93.
61. Cakir B, Teksam M, Kosehan D, Akin K, Koktener A. Inborn errors of metabolism presenting in childhood. *J Neuroimaging.* 2011;21:e117–33. <https://doi.org/10.1111/j.1552-6569.2011.00575.x>.
62. Valanne L, Ketonen L, Majander A, Suomalainen A, Pihko H. Neuroradiologic findings in children with mitochondrial disorders. *Am J Neuroradiol.* 1998;19:369–77.
63. Grodd W, Krägeloh-Mann I, Klose U, Sauter R. Metabolic and destructive brain disorders in children: findings with localized proton MR spectroscopy. *Radiology.* 1991;181:173–81.
64. Atsina K-B, Averill L, Kandula VVR. Neuroimaging of pediatric metabolic disorders with emphasis on diffusion-weighted imaging and MR spectroscopy: a pictorial essay. *Curr Radiol Rep.* 2017;5:60. <https://doi.org/10.1007/s40134-017-0251-7>.
65. Pirzkall A, McKnight TR, Graves EE, Carol MP, Sneed PK, Wara WW, Nelson SJ, Verhey LJ, Larson DA. MR-spectroscopy guided target delineation for high-grade gliomas. *Int J Radiat Oncol Biol Phys.* 2001;50:915–28.
66. Alger J. Quantitative proton magnetic resonance spectroscopy and spectroscopic imaging of the brain: a didactic review. *Top Magn Reson Imaging.* 2011;21:115–28.



# Magnetization Transfer Imaging

# 18

Paula Trujillo, Daniel O. Claassen,  
and Seth A. Smith

## Contents

18.1	<b>Principles of Magnetization Transfer</b> .....	253
18.2	<b>Magnetization Transfer Ratio</b> .....	255
18.3	<b>Quantitative Magnetization Transfer</b> .....	255
18.4	<b>Clinical Applications</b> .....	256
18.4.1	Magnetic Resonance Angiography (MRA) .....	256
18.4.2	Gadolinium-Enhanced MRI .....	256
18.4.3	Multiple Sclerosis .....	256
18.4.4	White Matter Disorders .....	257
18.4.5	Infectious Diseases .....	257
18.4.6	Tumors .....	257
18.4.7	Other CNS Disorders .....	257
18.5	<b>Clinical Case: qMT in the Cervical Spinal Cord—Application to MS</b> .....	257
	<b>References</b> .....	258

---

## 18.1 Principles of Magnetization Transfer

The magnetization transfer (MT) phenomenon [1] generically is the exchange (or transfer) of spin information between protons associated with macromolecules and surrounding water. The MT effect can be diagrammatically explained using a two-pool model, in which protons in tissues are associated with either free water (water pool) or semisolid macromolecules (macromolecular pool), which consists of protons bound to immobile proteins, large macromolecules, or cellular membranes [2]. The signal observed in con-

---

P. Trujillo (✉) · D. O. Claassen  
Department of Neurology, Vanderbilt University  
Medical Center, Nashville, TN, USA  
e-mail: [paula.trujillo.diaz@vumc.org](mailto:paula.trujillo.diaz@vumc.org);  
[daniel.claassen@vumc.org](mailto:daniel.claassen@vumc.org)

S. A. Smith  
Vanderbilt University Institute of Imaging Science,  
Vanderbilt University Medical Center, Nashville,  
TN, USA  
e-mail: [seth.smith@vanderbilt.edu](mailto:seth.smith@vanderbilt.edu)

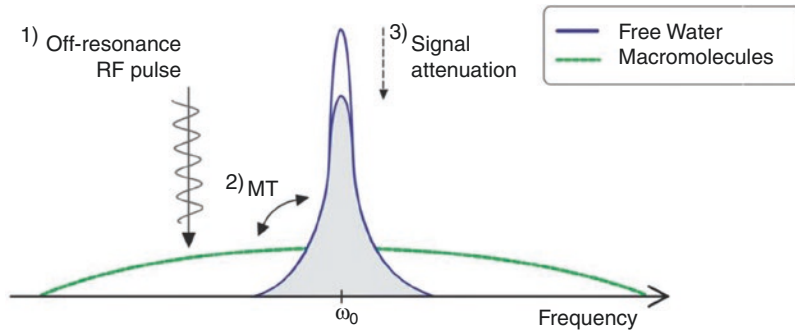


**Fig. 18.1** The water pool has a narrow spectrum, while the macromolecular pool has a broadened line. When a radiofrequency (RF) pulse is applied off-resonance (1), it will selectively saturate the macromolecular protons with-

out directly affecting the free water protons. This saturation is then transferred to the water protons (2), resulting in an observed signal attenuation (3)

ventional MRI comes from water protons that have sufficiently long  $T_2$  relaxation times (i.e. greater than 10 ms). Water protons have a specific resonance frequency ( $\omega_0$ ) and a narrow absorption lineshape (Fig. 18.1). Protons in the macromolecular pool are relatively immobile and strongly associated with each other, resulting in a broad absorption lineshape, and a very short  $T_2$  (in the order of 10  $\mu$ s), and therefore cannot be directly imaged with conventional MRI. However, the association and exchange between macromolecular protons and the free water allows the perturbation of the macromolecular pool to influence the water pool. In MRI, an MT experiment is as follows: MT preparation (saturation) is applied to selectively saturate the broad-lineshape macromolecular protons without directly affecting the water protons. The selective saturation of the macromolecular protons is exchanged throughout the semisolid proton pool (spin diffusion) and then is exchanged (through dipole–dipole or direct chemical exchange) with the surrounding water, resulting in an attenuation of the acquired MR (water) signal. Importantly, the magnitude of the MT effect depends on (1) sequence parameters (pulse power and frequency offset from water) and (2) physiological parameters (macromolecular-water exchange rate and concentration of macromolecules).

There are several methods to perform the MT preparation; it is beyond the scope of this chapter to discuss all the available methods, and readers

interested in further details on MT preparation techniques are encouraged to consult [3–9]. One of the more time-efficient methods to perform MT experiments is by using ‘off-resonance’ saturation [10, 11], which is outlined in Fig. 18.1, and in short applying an RF pulse to selectively saturate the broad macromolecular resonance (off-resonance with respect to water) sufficiently, minimizing direct water saturation and allowing MT to transfer saturation to water. Provided that the offset frequency is large enough to avoid direct saturation of water, the observed signal reduction is the result of MT and driven by macromolecular composition and exchange rate.

Practically, the amount of saturation is affected by the amplitude ( $B_1$ ) and the frequency offset of the RF pulse ( $\Delta\omega$ , with respect to water). Higher  $B_1$  results in greater saturation, and thus a greater MT-driven contrast, but saturation power is limited in practice by the Specific Absorption Rate (SAR) safety considerations. Lower offset frequencies will generate greater saturation of the macromolecular pool, but also directly saturates the water through the so-called direct saturation effect. A practical value for the offset frequency that will produce saturation of the macromolecular protons while minimizing the direct saturation of water protons is typically 2000 Hz (at  $\Delta\omega = 2000$  Hz, <10% direct saturation effect [11]).

It is worth noting that the duration of the MT preparation pulses can generally increase the

acquisition times, which could be a limitation depending on the clinical application. Finally, in addition to the method described above, where explicit MT preparation pulses are applied in a conventional MR sequence, it has also been shown that incidental MT contrast can be generated in many conventional imaging sequences [12]. This occurs, for example, in spin echo sequences, where the slice-selective excitation and refocusing pulses can be considered off-resonance pulse for neighboring slices, generating an implicit MT effect.

## 18.2 Magnetization Transfer Ratio

The most common approach to characterize the MT effect is the MT ratio (MTR), calculated as the relative change in intensity from an MT-prepared and nonprepared image pair:  $MTR = 1 - S(\Delta\omega)/S_0$ , where  $S(\Delta\omega)$  and  $S_0$  are the voxel intensities in the presence and absence of MT preparation, respectively (Fig. 18.2). The MTR combines all of the mechanistic factors contributing to the MT effect into a single semi-quantitative index [13], which is sensitive to macromolecular content. For example, white matter (WM) has higher MTR values (mostly due the abundance of myelin in these tissues), gray matter has intermediate MTR values, and the cerebrospinal fluid (CSF) has a MTR value close to zero. In addition, lesions that result in aberrations in macromolecular content typically have a different MTR than normal tissues.

Despite its easy implementation and calculation, MTR is not an intrinsic property of tissue, and thus, it is not only determined by the tissue itself, but is also sensitive to the pulse sequence design,  $B_1$  and  $B_0$  inhomogeneities, as well as tissue relaxation times, which limits the ability to create a standardized MTR metric to define pathology. Different off-resonance frequencies and different saturation powers generate different MTR values and, therefore, MTR cannot readily be used to quantitatively study tissue changes across sites.

## 18.3 Quantitative Magnetization Transfer

Quantitative MT (qMT) has been developed to overcome some of the limitations of MTR. The qMT model is still based on MT between water and the macromolecular pools [2], and can describe the MT effect by quantifying the constitutive parameters instead of a single summary MTR value. However, qMT typically utilizes multiple saturation offsets and powers to generate an MT z-spectrum, which is then fit to a model. In a two-pool model, the output of qMT analysis is as follows: equilibrium magnetization of the free water (<sup>f</sup>) and macromolecular (<sup>m</sup>) pools ( $M_0^f, M_0^m$ ), rates of the magnetization exchange between the pools ( $k_{fm}, k_{mf}$ ), and their relaxation times ( $T_1^f, T_1^m, T_2^f, T_2^m$ ). It is important to note that these values are intrinsic properties of tissues and therefore are independent of the pulse sequence.

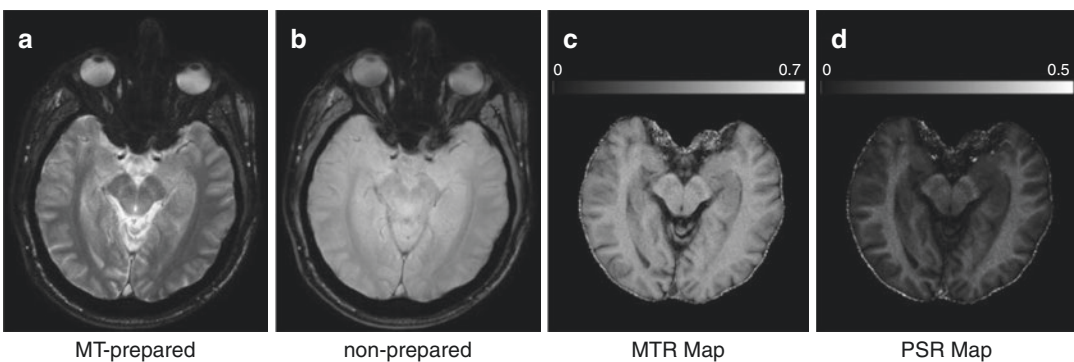


**Fig. 18.2** (a) MT-prepared image, (b) nonprepared image, (c) MTR map, (d) PSR map



Several techniques have been developed to estimate qMT-derived indices [4, 8, 9, 14–17]. However, robustly estimating all qMT parameters in a particular model necessitates the acquisition of a large number of data points (i.e. images acquired at different offset frequencies and/or powers), which results in long acquisition times, making it impractical for some clinical applications. To overcome this limitation, a new method to perform a qMT analysis using only a single MT acquisition and a reference measurement has been recently proposed [18]. In this case, only the macromolecular to water pool size ratio (PSR =  $M_0^m / M_0^f$ ) is estimated, while using physically reasonable constraints for the other parameters (Fig. 18.2d). The PSR allows straightforward biophysical interpretation as an indicator of the total macromolecular content in tissues [19]. Using this model, improved resolution or reduced sensitivity to motion can be achieved in clinical scan times, making it a viable approach for the study of multiple neurodegenerative disorders.

## 18.4 Clinical Applications

Since its discovery, several clinical applications of MT in the CNS have emerged [13, 20]. MT has been shown to be useful for tissue characterization, and improving image contrast, with the potential to guide differential diagnosis, quantify disease severity, and offer insight into prognosis and treatment response of different neurological conditions. The next paragraphs briefly describe some of the current and potential clinical applications of MT imaging.

### 18.4.1 Magnetic Resonance Angiography (MRA)

MRA uses specific MR sequences to evaluate intracranial blood vessels by suppressing the signal from static tissues while enhancing the signal from blood by means of inflow and phase effects. MT can be used to enhance the signal contrast between blood and other tissues by suppressing the background tissue signal [21]. When MT

preparation is applied, the signal from surrounding tissues is decreased due to MT effects, while the signal from blood vessels is not affected since blood is essentially in the fluid phase and does not contain immobilized macromolecular protons.

### 18.4.2 Gadolinium-Enhanced MRI

Gadolinium-based paramagnetic contrast agents in MRI are used to evaluate a variety of CNS lesions, by increasing the signal intensity in regions where the contrast agent accumulates due to a disruption of the blood–brain barrier. MT can be combined with contrast-enhanced  $T_1$ -weighted images to improve the contrast by suppressing the signal from background tissues and rendering Gd-enhanced areas more conspicuous [22]. The MT contrast enhancement has been shown to be useful to assess tumors, infarctions, and a variety of enhancing lesions [23].

### 18.4.3 Multiple Sclerosis

One of the most established applications of MT is in multiple sclerosis (MS). MS is an inflammatory and demyelinating disease that affects the CNS. While traditional MRI techniques can point to the location of the damage, they typically do not provide specific information on the microscopic pathology of the tissue, such as axonal loss and myelin damage. These abnormalities affect the macromolecular content, and MT provides a sensitive tool to detect these changes. MT has been shown to be useful for evaluating demyelination and the severity of intrinsic lesion damage [24, 25]. Using MT, MS lesions are more conspicuous, and MTR values provide valuable information on lesion evolution [26, 27]. Moreover, the MTR in normal-appearing white matter (NAWM) is also decreased in MS patients [28–30], which could represent the myelin thinning and axonal damage that can precede new lesion formation [31–33]. MTR has also been used to assess pathological changes in grey matter tissues of

MS patients [30] and has been shown to correlate with physical disability and cognitive impairment [34–36]. Recently, qMT techniques have been applied for the study of MS in the brain [19], spinal cord [37], and optic nerve [38]. These studies indicate that the PSR obtained from qMT enables an assessment of demyelination in NAWM and grey matter damage, outperforming MTR. qMT measures correlate with clinical status of MS patients, offering a valuable tool to quantitatively monitor disease progression and treatment efficacy.

#### 18.4.4 White Matter Disorders

MT imaging has also found clinical applications on different WM disorders and conditions associated with WM damage. MTR changes in cerebral WM have been detected in CNS vasculitis [39–41], stroke [42, 43], traumatic brain injury [44, 45], migraine [46, 47], cerebrotendinous xanthomatosis [48], Fabry's disease [49], and cerebral autosomal dominant arteriopathy with subcortical infarcts and leukoencephalopathy (CADASIL) [50]. MTR abnormalities have also been observed in the spinal cord of patients with isolated myelitis [51] and patients with CADASIL [52].

#### 18.4.5 Infectious Diseases

MT has been studied for the detection and diagnosis of a variety of CNS infections, including herpes simplex virus encephalitis [53], human immunodeficiency virus encephalitis [54], CNS tuberculosis [55], neurocysticercosis [56], brain abscess [57], and meningitis [58]. MT contrast has been shown to improve the conspicuity of CNS tuberculosis lesions, and MTR can be used to distinguish tuberculosis from similar-appearing infective lesions on conventional MR images [59]. Moreover, MT imaging has improved the sensitivity of detection of meningitis, and several studies have shown significantly different MTRs in meninges stemming from different causative agents [57, 59].

#### 18.4.6 Tumors

Several studies have shown that tumors have lower MTR values compared to normal brain tissue [60, 61]. Moreover, MTR was found to be useful in differentiating low-grade gliomas from high-grade gliomas and benign from malignant tumors, offering the opportunity to characterize tumors pre-surgically based on their macromolecular content.

#### 18.4.7 Other CNS Disorders

MT imaging has shown continuing promise for use in imaging other CNS diseases. In the last two decades, research studies in patients with neurological disorders including epilepsy [62–64], Alzheimer's disease [65, 66], Huntington's disease [67, 68], amyotrophic lateral sclerosis [69, 70], Parkinson's disease [71–73], multiple system atrophy [72], and progressive supranuclear palsy [72], and psychiatric disorders such as schizophrenia [74, 75] and bipolarism [76] have shown that MTR can be used to detect subtle changes that are not perceptible with traditional MRI. More recently, qMT techniques [77, 78] have been gaining ground as an attractive approach to quantitatively evaluate microstructural changes in CNS diseases.

---

### 18.5 Clinical Case: qMT in the Cervical Spinal Cord—Application to MS

In patients with MS, spinal cord lesions can result in a combination of sensory and/or motor deficits. Traditional MRI methods are not specific to the underlying macromolecular tissue changes (i.e. demyelination and axonal damage) that may precede or accompany an overt lesion. In a recent study [37], qMT was applied to provide high-resolution macromolecular to free pool size ratio (PSR) maps, sensitive to the underlying macromolecular composition of the spinal cord in clinically feasible scan times (5–8 min).

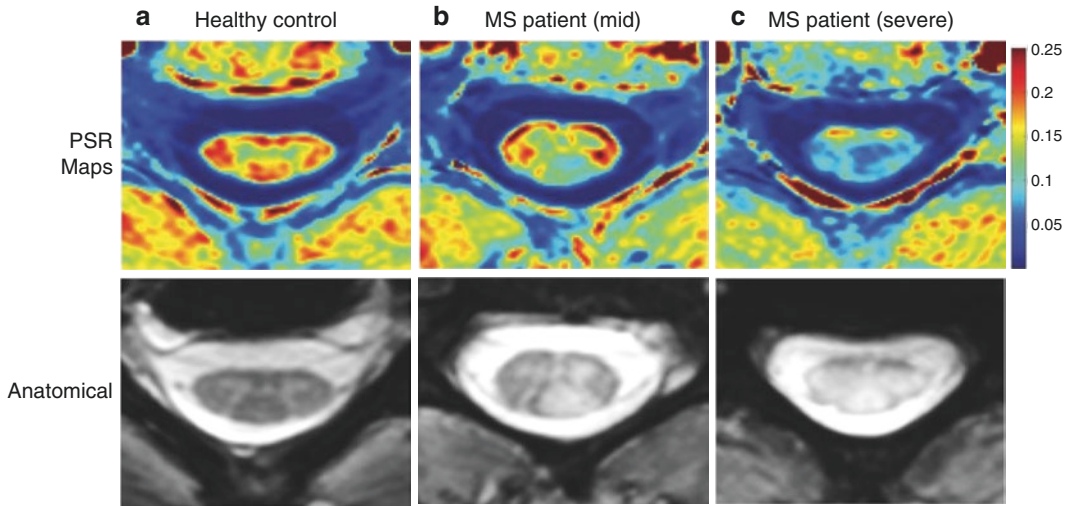


**Fig. 18.3** PSR maps (top) and high-resolution anatomical images (bottom) of the cervical spinal cord of a healthy control (a), a patient with mild MS (b), and a patient with more advance MS (c)

Figure 18.3 shows the PSR maps of the cervical spinal cord for (a) 25-year-old healthy control, (b) 31-year-old patient with mild sensory symptoms that were attributed to an MS lesion (EDSS score = 1.5), and (c) 25-year-old patient with severe sensory-motor symptoms who presented with a substantial clinical decline (EDSS score = 4). Both patients have relapsing–remitting MS and disease duration of less than 10 years. These figures illustrate a reduction of PSR localized to the location of an MS lesion, as well as surrounding the lesional area.

## References

1. Wolff SD, Balaban RS. Magnetization transfer contrast (MTC) and tissue water proton relaxation in vivo. *Magn Reson Med.* 1989;10:135–44.
2. Henkelman RM, Huang X, Xiang QS, Stanisz GJ, Swanson SD, Bronskill MJ. Quantitative interpretation of magnetization transfer. *Magn Reson Med.* 1993;29:759–66.
3. Schneider E, Prost RW, Glover GH. Pulsed magnetization transfer versus continuous wave irradiation for tissue contrast enhancement. *J Magn Reson Imaging.* 1993;3:417–23.
4. Dortch RD, Li K, Gochberg DF, Welch EB, Dula AN, Tamhane AA, Gore JC, Smith SA. Quantitative magnetization transfer imaging in human brain at 3 T via selective inversion recovery. *Magn Reson Med.* 2011;66:1346–52.
5. Smith AK, Dortch RD, Dethrage LM, Smith SA. Rapid, high-resolution quantitative magnetization transfer MRI of the human spinal cord. *NeuroImage.* 2014;95:106–16.
6. Henkelman RM, Stanisz GJ, Graham SJ. Magnetization transfer in MRI: a review. *NMR Biomed.* 2001;14:57–64.
7. Sled JG, Pike GB. Quantitative interpretation of magnetization transfer in spoiled gradient echo MRI sequences. *J Magn Reson.* 2000;145:24–36.
8. Yarnykh VL, Yuan C. Cross-relaxation imaging reveals detailed anatomy of white matter fiber tracts in the human brain. *NeuroImage.* 2004;23:409–24.
9. Gloor M, Scheffler K, Bieri O. Quantitative magnetization transfer imaging using balanced SSFP. *Magn Reson Med.* 2008;60:691–700.
10. Graham SJ, Henkelman RM. Understanding pulsed magnetization transfer. *J Magn Reson Imaging.* 1997;7:903–12.
11. Smith SA, Farrell JAD, Jones CK, Reich DS, Calabresi PA, van Zijl PCM. Pulsed magnetization transfer imaging with body coil transmission at 3 Tesla: feasibility and application. *Magn Reson Med.* 2006;56:866–75.
12. Dixon WT, Engels H, Castillo M, Sardashti M. Incidental magnetization transfer contrast in standard multislice imaging. *Magn Reson Imaging.* 1990;8:417–22.
13. van Buchem MA. Magnetization transfer: applications in neuroradiology. *J Comput Assist Tomogr.* 1999;23(Suppl 1):S9–18.
14. Ramani A, Dalton C, Miller DH, Tofts PS, Barker GJ. Precise estimate of fundamental in-vivo MT parameters in human brain in clinically feasible times. *Magn Reson Imaging.* 2002;20:721–31.

15. Sled JG, Pike GB. Quantitative imaging of magnetization transfer exchange and relaxation properties in vivo using MRI. *Magn Reson Med*. 2001;46:923–31.
16. Cercignani M, Symms MR, Schmierer K, Boulby PA, Tozer DJ, Ron M, Tofts PS, Barker GJ. Three-dimensional quantitative magnetisation transfer imaging of the human brain. *NeuroImage*. 2005;27:436–41.
17. Garcia M, Gloor M, Bieri O, Radue E-W, Lieb JM, Cordier D, Stippich C. Imaging of primary brain tumors and metastases with fast quantitative 3-dimensional magnetization transfer. *J Neuroimaging*. 2015;25:1007–14.
18. Yarnykh VL. Fast macromolecular proton fraction mapping from a single off-resonance magnetization transfer measurement. *Magn Reson Med*. 2012;68:166–78.
19. Yarnykh VL, Bowen JD, Samsonov A, Repovic P, Mayadev A, Qian P, Gangadharan B, Keogh BP, Maravilla KR, Jung Henson LK. Fast whole-brain three-dimensional macromolecular proton fraction mapping in multiple sclerosis. *Radiology*. 2015;274:210–20.
20. Filippi M, Rocca MA. Magnetization transfer magnetic resonance imaging of the brain, spinal cord, and optic nerve. *Neurotherapeutics*. 2007;4:401–13.
21. Thomas SD, Al-Kwif O, Emery DJ, Wilman AH. Application of magnetization transfer at 3.0 T in three-dimensional time-of-flight magnetic resonance angiography of the intracranial arteries. *J Magn Reson Imaging*. 2002;15:479–83.
22. Tanttu JI, Sepponen RE, Lipton MJ, Kuusela T. Synergistic enhancement of MRI with Gd-DTPA and magnetization transfer. *J Comput Assist Tomogr*. 1992;16:19–24.
23. Mehta RC, Pike GB, Haros SP, Enzmann DR. Central nervous system tumor, infection, and infarction: detection with gadolinium-enhanced magnetization transfer MR imaging. *Radiology*. 1995;195:41–6.
24. van Waesberghe JH, Kamphorst W, De Groot CJ, et al. Axonal loss in multiple sclerosis lesions: magnetic resonance imaging insights into substrates of disability. *Ann Neurol*. 1999;46:747–54.
25. Schmierer K, Tozer DJ, Scaravilli F, Altmann DR, Barker GJ, Tofts PS, Miller DH. Quantitative magnetization transfer imaging in postmortem multiple sclerosis brain. *J Magn Reson Imaging*. 2007;26:41–51.
26. Silver NC, Lai M, Symms MR, Barker GJ, McDonald WI, Miller DH. Serial magnetization transfer imaging to characterize the early evolution of new MS lesions. *Neurology*. 1998;51:758–64.
27. Campi A, Filippi M, Comi G, Scotti G, Gerevini S, Dousset V. Magnetisation transfer ratios of contrast-enhancing and nonenhancing lesions in multiple sclerosis. *Neuroradiology*. 1996;38:115–9.
28. Evangelou N, Esiri MM, Smith S, Palace J, Matthews PM. Quantitative pathological evidence for axonal loss in normal appearing white matter in multiple sclerosis. *Ann Neurol*. 2000;47:391–5.
29. Ge Y, Grossman RI, Udupa JK, Babb JS, Mannon LJ, McGowan JC. Magnetization transfer ratio histogram analysis of normal-appearing gray matter and normal-appearing white matter in multiple sclerosis. *J Comput Assist Tomogr*. 2002;26:62–8.
30. Davies GR, Altmann DR, Hadjiprocopis A, et al. Increasing normal-appearing grey and white matter magnetisation transfer ratio abnormality in early relapsing-remitting multiple sclerosis. *J Neurol*. 2005;252:1037–44.
31. Filippi M, Rocca MA, Martino G, Horsfield MA, Comi G. Magnetization transfer changes in the normal appearing white matter precede the appearance of enhancing lesions in patients with multiple sclerosis. *Ann Neurol*. 1998;43:809–14.
32. Pike GB, De Stefano N, Narayanan S, Worsley KJ, Pelletier D, Francis GS, Antel JP, Arnold DL. Multiple sclerosis: magnetization transfer mr imaging of white matter before lesion appearance on T2-weighted images. *Radiology*. 2000;215:824–30.
33. Fazekas F, Ropele S, Enzinger C, Seifert T, Strasser-Fuchs S. Quantitative magnetization transfer imaging of pre-lesional white-matter changes in multiple sclerosis. *Mult Scler*. 2002;8:479–84.
34. Ramió-Torrentà L, Sastre-Garriga J, Ingle GT, Davies GR, Ameen V, Miller DH, Thompson AJ. Abnormalities in normal appearing tissues in early primary progressive multiple sclerosis and their relation to disability: a tissue specific magnetisation transfer study. *J Neurol Neurosurg Psychiatry*. 2006;77:40–5.
35. Dehmeshki J, Chard DT, Leary SM, Watt HC, Silver NC, Tofts PS, Thompson AJ, Miller DH. The normal appearing grey matter in primary progressive multiple sclerosis. *J Neurol*. 2003;250:67–74.
36. Ge Y, Grossman RI, Udupa JK, Babb JS, Kolson DL, McGowan JC. Magnetization transfer ratio histogram analysis of gray matter in relapsing-remitting multiple sclerosis. *AJNR Am J Neuroradiol*. 2001;22:470–5.
37. Smith AK, By S, Lyttle BD, Dortch RD, Box BA, Mckeithan LJ, Thukral S, Bagnato F, Pawate S, Smith SA. Evaluating single-point quantitative magnetization transfer in the cervical spinal cord: application to multiple sclerosis. *NeuroImage Clin*. 2017;16:58–65.
38. Harrigan RL, Smith AK, Lyttle B, Box B, Landman BA, Bagnato F, Pawate S, Smith SA. Quantitative characterization of optic nerve atrophy in patients with multiple sclerosis. *Mult Scler J Exp Transl Clin*. 2017;3:205521731773009.
39. Rovaris M, Viti B, Ciboddo G, Gerevini S, Capra R, Iannucci G, Comi G, Filippi M. Brain involvement in systemic immune mediated diseases: magnetic resonance and magnetisation transfer imaging study. *J Neurol Neurosurg Psychiatry*. 2000;68:170–7.
40. Bosma GPT, Middelkoop HAM, Rood MJ, Bollen ELEM, Huizinga TWJ, van Buchem MA. Association of global brain damage and clinical functioning in neuropsychiatric systemic lupus erythematosus. *Arthritis Rheum*. 2002;46:2665–72.
41. Bosma GP, Rood MJ, Huizinga TW, de Jong BA, Bollen EL, van Buchem MA. Detection of cerebral involvement in patients with active neuropsychiatric

- systemic lupus erythematosus by the use of volumetric magnetization transfer imaging. *Arthritis Rheum.* 2000;43:2428–36.
42. Hanyu H, Imon Y, Sakurai H, Iwamoto T, Takasaki M, Shindo H, Abe K. Diffusion-weighted magnetic resonance and magnetization transfer imaging in the assessment of ischemic human stroke. *Intern Med.* 1998;37:360–5.
  43. Pendlebury ST, Lee MA, Blamire AM, Styles P, Matthews PM. Correlating magnetic resonance imaging markers of axonal injury and demyelination in motor impairment secondary to stroke and multiple sclerosis. *Magn Reson Imaging.* 2000;18:369–78.
  44. Bagley LJ, McGowan JC, Grossman RI, Sinson G, Kotapka M, Lexa FJ, Berlin JA, McIntosh TK. Magnetization transfer imaging of traumatic brain injury. *J Magn Reson Imaging.* 2000;11:1–8.
  45. McGowan JC, Yang JH, Plotkin RC, Grossman RI, Umile EM, Cecil KM, Bagley LJ. Magnetization transfer imaging in the detection of injury associated with mild head trauma. *AJNR Am J Neuroradiol.* 2000;21:875–80.
  46. Rocca MA, Colombo B, Pratesi A, Comi G, Filippi M. A magnetization transfer imaging study of the brain in patients with migraine. *Neurology.* 2000;54:507–9.
  47. Rovaris M, Bozzali M, Rocca MA, Colombo B, Filippi M. An MR study of tissue damage in the cervical cord of patients with migraine. *J Neurol Sci.* 2001;183:43–6.
  48. Inglese M, De Stefano N, Pagani E, Dotti MT, Comi G, Federico A, Filippi M. Quantification of brain damage in cerebrotendinous xanthomatosis with magnetization transfer MR imaging. *AJNR Am J Neuroradiol.* 2003;24:495–500.
  49. Marino S, Borsini W, Buchner S, Mortilla M, Stromillo ML, Battaglini M, Giorgio A, Bramanti P, Federico A, De Stefano N. Diffuse structural and metabolic brain changes in Fabry disease. *J Neurol.* 2006;253:434–40.
  50. Iannucci G, Dichgans M, Rovaris M, Brüning R, Gasser T, Giacomotti L, Yousry TA, Filippi M. Correlations between clinical findings and magnetization transfer imaging metrics of tissue damage in individuals with cerebral autosomal dominant arteriopathy with subcortical infarcts and leukoencephalopathy. *Stroke.* 2001;32:643–8.
  51. Rocca MA, Mezzapesa DM, Ghezzi A, Falini A, Agosta F, Martinelli V, Scotti G, Comi G, Filippi M. Cord damage elicits brain functional reorganization after a single episode of myelitis. *Neurology.* 2003;61:1078–85.
  52. Rocca MA, Filippi M, Herzog J, Sormani MP, Dichgans M, Yousry TA. A magnetic resonance imaging study of the cervical cord of patients with CADASIL. *Neurology.* 2001;56:1392–4.
  53. Burke JW, Mathews VP, Elster AD, Ulmer JL, McLean FM, Davis SB. Contrast-enhanced magnetization transfer saturation imaging improves MR detection of herpes simplex encephalitis. *AJNR Am J Neuroradiol.* 1996;17:773–6.
  54. Douset V, Armand JP, Lacoste D, Mièze S, Letenneur L, Dartigues JF, Caill JM. Magnetization transfer study of HIV encephalitis and progressive multifocal leukoencephalopathy. Groupe d'Epidémiologie Clinique du SIDA en Aquitaine. *AJNR Am J Neuroradiology.* 1997;18:895–901.
  55. Gupta RK, Husain N, Kathuria MK, Datta S, Rathore RKS, Husain M. Magnetization transfer MR imaging correlation with histopathology in intracranial tuberculomas. *Clin Radiol.* 2001;56:656–63.
  56. Kathuria MK, Gupta RK, Roy R, Gaur V, Husain N, Pradhan S. Measurement of magnetization transfer in different stages of neurocysticercosis. *J Magn Reson Imaging.* 1998;8:473–9.
  57. Gupta RK, Vatsal DK, Husain N, Chawla S, Prasad KN, Roy R, Kumar R, Jha D, Husain M. Differentiation of tuberculous from pyogenic brain abscesses with in vivo proton MR spectroscopy and magnetization transfer MR imaging. *AJNR Am J Neuroradiol.* 2001;22:1503–9.
  58. Runge VM, Wells JW, Williams NM, Lee C, Timoney JF, Young AB. Detectability of early brain meningitis with magnetic resonance imaging. *Investig Radiol.* 1995;30:484–95.
  59. Gupta RK, Kathuria MK, Pradhan S. Magnetization transfer MR imaging in CNS tuberculosis. *AJNR Am J Neuroradiol.* 1999;20:867–75.
  60. Okumura A, Takenaka K, Nishimura Y, Asano Y, Sakai N, Kuwata K, Era S. The characterization of human brain tumor using magnetization transfer technique in magnetic resonance imaging. *Neurol Res.* 1999;21:250–4.
  61. Thng CH, Tay KH, Chan LL, Lim EH, Khoo BK, Huin EL, Tan KP. Magnetic resonance imaging of brain metastases: magnetisation transfer or triple dose gadolinium? *Ann Acad Med Singap.* 1999;28:529–33.
  62. Ferini-Strambi L, Bozzali M, Cercignani M, Oldani A, Zucconi M, Filippi M. Magnetization transfer and diffusion-weighted imaging in nocturnal frontal lobe epilepsy. *Neurology.* 2000;54:2331–3.
  63. Rugg-Gunn FJ, Eriksson SH, Boulby PA, Symms MR, Barker GJ, Duncan JS. Magnetization transfer imaging in focal epilepsy. *Neurology.* 2003;60:1638–45.
  64. Tofts PS, Sisodiya S, Barker GJ, Webb S, MacManus D, Fish F, Shorvon S. MR magnetization transfer measurements in temporal lobe epilepsy: a preliminary study. *AJNR Am J Neuroradiol.* 1995;16:1862–3.
  65. Bozzali M, Franceschi M, Falini A, Pontesilli S, Cercignani M, Magnani G, Scotti G, Comi G, Filippi M. Quantification of tissue damage in AD using diffusion tensor and magnetization transfer MRI. *Neurology.* 2001;57:1135–7.
  66. Kabani NJ, Sled JG, Chertkow H. Magnetization transfer ratio in mild cognitive impairment and dementia of Alzheimer's type. *NeuroImage.* 2002;15:604–10.

67. Mascalchi M, Lolli F, Della Nave R, Tessa C, Petralli R, Gavazzi C, Politi LS, Macucci M, Filippi M, Piacentini S. Huntington disease: volumetric, diffusion-weighted, and magnetization transfer MR imaging of brain. *Radiology*. 2004;232:867–73.
68. Tambasco N, Nigro P, Romoli M, Simoni S, Parnetti L, Calabresi P. Magnetization transfer MRI in dementia disorders, Huntington's disease and parkinsonism. *J Neurol Sci*. 2015;353:1–8.
69. Kato Y, Matsumura K, Kinoshita Y, Narita Y, Kuzuhara S, Nakagawa T. Detection of pyramidal tract lesions in amyotrophic lateral sclerosis with magnetization-transfer measurements. *AJNR Am J Neuroradiol*. 1997;18:1541–7.
70. Tanabe JL, Vermathen M, Miller R, Gelinas D, Weiner MW, Rooney WD. Reduced MTR in the corticospinal tract and normal T2 in amyotrophic lateral sclerosis. *Magn Reson Imaging*. 1998;16:1163–9.
71. Tambasco N, Belcastro V, Sarchielli P, et al. A magnetization transfer study of mild and advanced Parkinson's disease. *Eur J Neurol*. 2011;18:471–7.
72. Eckert T, Sailer M, Kaufmann J, Schrader C, Peschel T, Bodammer N, Heinze HJ, Schoenfeld MA. Differentiation of idiopathic Parkinson's disease, multiple system atrophy, progressive supranuclear palsy, and healthy controls using magnetization transfer imaging. *NeuroImage*. 2004;21:229–35.
73. Anik Y, Iseri P, Demirci A, Komsuoglu S, Inan N. Magnetization transfer ratio in early period of Parkinson disease. *Acad Radiol*. 2007;14:189–92.
74. Antosik-Biernacka A, Peuskens H, De Hert M, Peuskens J, Sunaert S, Van Hecke P, Goraj B. Magnetization transfer imaging in chronic schizophrenia. *Med Sci Monit*. 2006;12:MT17–21.
75. Foong J, Symms MR, Barker GJ, Maier M, Woermann FG, Miller DH, Ron MA. Neuropathological abnormalities in schizophrenia: evidence from magnetization transfer imaging. *Brain*. 2001;124:882–92.
76. Bruno SD, Barker GJ, Cercignani M, Symms M, Ron MA. A study of bipolar disorder using magnetization transfer imaging and voxel-based morphometry. *Brain*. 2004;127:2433–40.
77. Ridha BH, Tozer DJ, Symms MR, Stockton KC, Lewis EB, Siddique MM, MacManus DG, Rossor MN, Fox NC, Tofts PS. Quantitative magnetization transfer imaging in Alzheimer disease. *Radiology*. 2007;244:832–7.
78. Trujillo P, Summers PE, Smith AK, Smith SA, Mainardi LT, Cerutti S, Claassen DO, Costa A. Pool size ratio of the substantia nigra in Parkinson's disease derived from two different quantitative magnetization transfer approaches. *Neuroradiology*. 2017;59:1251–63.



# Functional Magnetic Resonance Imaging

# 19

N. Hainc, J. Reinhardt, and C. Stippich

## Contents

19.1	<b>Introduction</b> .....	264
19.2	<b>From Brain Physiology to BOLD fMRI Signal</b> .....	264
19.2.1	Preprocessing the Acquired 4D Data.....	265
19.3	<b>Thresholding: How We Do It</b> .....	267
19.3.1	Thresholding.....	267
19.4	<b>Motor and Sensory fMRI</b> .....	267
19.4.1	Introduction.....	267
19.4.2	Cortical Motor Areas.....	268
19.5	<b>Language fMRI</b> .....	270
19.5.1	Introduction.....	270
19.5.2	Cortical Language Areas.....	272
19.6	<b>Optimization, Tips, and Pitfalls</b> .....	275
19.6.1	Not Everything That Activates Is Essential.....	275
19.6.2	Conversely, Absent BOLD Activation Does Not Mean Inactive Cortex.....	276
19.6.3	The Pathology Itself Can Nullify BOLD Activation.....	276
19.7	<b>Clinical Case</b> .....	276
	<b>References</b> .....	277

N. Hainc · C. Stippich (✉)  
Department of Neuroradiology, Clinical  
Neuroscience Center, University Hospital Zurich,  
University of Zurich, Zurich, Switzerland  
e-mail: [christoph.stippich@usz.ch](mailto:christoph.stippich@usz.ch)

J. Reinhardt  
Department of Neuroradiology, Clinical  
Neuroscience Center, University Hospital Zurich,  
University of Zurich, Zurich, Switzerland

Division of Neuroradiology, Institute for Radiology  
and Nuclear Medicine, University Hospital of Basel,  
Basel, Switzerland

## 19.1 Introduction

Neurosurgery aims to maximize the resection of brain tumors while minimizing involvement of eloquent cortex, thus improving survival while preventing lasting neurological deficits. Locating eloquent cortex presents a number of challenges: the unique anatomy of individual brains, tumor-induced distortion, and cortical reorganization render individual preoperative brain mapping essential [1, 2]. Current gold standards for brain mapping are highly invasive and consist of intraoperative electrocortical stimulation (ECS) [3] and the preoperative intracarotid amobarbital Wada test [4]—these techniques are by no means perfect and entail their own set of limitations. ECS, for example, is limited to the site of the craniotomy and to the superficial cortex exposed, as deeper sulci are poorly accessible. Functional magnetic resonance imaging (fMRI) [5, 6], on the other hand, combines whole-brain mapping with the safety of a non-invasive procedure and has been validated against ECS and Wada for motor mapping, language lateralization, and to a lesser extent language localization [7–18]. Furthermore, fMRI allows for assessment of operative feasibility, stratification of operative risk, guidance of surgical planning in terms of approach and craniotomy size, and selection of patients for ECS before an invasive procedure has been carried out.

Preoperative fMRI evaluates tumor resectability in terms of lesion-to-activation distance (LAD) for motor and language networks as well as language lateralization. In a surgical study comparing fMRI activation to ECS, resections with an LAD of less than 1 cm resulted in 50% postoperative deficits, dropping to 33% between 1 and 2 cm, with no deficits reported in LADs greater than 2 cm [7]. The LAD based on fMRI, however, cannot be regarded as absolute—depending on statistical parameters (thresholds) defined by the user fMRI activated cortical areas will increase or decrease in size; a further study recommends ECS be performed within an fMRI-based LAD of 10 mm [19]. Language lateralization has implications in patients with tumors and epilepsy, especially for pathologies in the temporal lobe. Furthermore, fMRI should be combined

with diffusion tensor imaging (DTI) whenever possible, as the preoperative evaluation of underlying white matter tracts is imperative. Still, fMRI has been shown to alter neurosurgical planning in up to 49% of cases [20] while decreasing craniotomy size in 15% cases. fMRI data can also be implemented into neuronavigation systems [21–23], but a brain shift of up to 20 mm can occur on craniotomy [24] and prediction of brain shift is impossible [25].

Presurgical motor fMRI is recommended in patients where tumor invasion of the precentral or postcentral gyrus is suspected or when structural landmarks are no longer distinguishable on anatomical MRI sequences [26]. For language fMRI, indications include patients presenting with tumor-induced language deficits. Keeping in mind the reported left hemispheric dominance in language processing (95% of right-handed individuals and 70% of left-handed individuals) [27], patients with left hemispheric tumors suspected of being in close proximity to essential language areas should be considered for presurgical fMRI. Furthermore, left-handed patients, especially those with right-sided brain tumors, should be considered to assess for atypical language dominance. This chapter focusses on task-based functional MRI only, in the preoperative setting in patients with brain tumors or epilepsy, accounting for the best established and validated clinical application of fMRI. The application of resting-state fMRI as a clinical diagnostic tool is not validated yet and therefore not addressed in this chapter.

---

## 19.2 From Brain Physiology to BOLD fMRI Signal

Functional magnetic resonance is a non-invasive imaging tool making use of magnetic changes induced by hemodynamic changes associated with brain activity. Activated neurons require a higher influx of metabolic substrates to meet increased energy and oxygen demands. The brain's response is to dilate local supplying arteries and capillaries for a greater blood inflow. For reasons not fully understood, the brain's response is over-proportionately strong [28], resulting in a



washout of the venous deoxyhemoglobin and a shift in the local (venous) ratio of blood in favor of oxyhemoglobin. This venous-based effect is the basis for the blood oxygen level-dependent (BOLD) fMRI signal. Paramagnetic deoxyhemoglobin results in magnetic field distortions and lower signal on MRI; its washout with diamagnetic oxyhemoglobin results in a signal increase [28]. The change in magnetism due to altered blood flow can be detected on MRI using pulse sequences designed to highlight these magnetic differences—generally, T2\*—echo-planar imaging (EPI) [29, 30] is used. Brain function on fMRI is therefore mapped using regional blood flow changes as surrogates of neuronal activity through a process known as neurovascular coupling [31] thought to be realized by astrocytes [32, 33]. Pathologies such as tumors and arteriovenous malformations (AVMs) can disrupt this process resulting in neurovascular uncoupling.

Vasodilatation and vasoconstriction are lethargic processes compared to the rapid response of neurons. This vascular response is known as the hemodynamic response function (HRF), showing an initial dip before increasing to a higher value and returning to baseline after 16–20 seconds [34, 35]. The signal from an fMRI experiment is, therefore, one of relatively low frequency correlating to these sluggish vascular changes.

For task-based activation studies, two major experimental designs exist to map brain function with fMRI; they are known as block designs and event-related designs. The block design basically consists of two alternating continuous conditions (or epochs) of predefined duration, one of which represents the experimental task (such as repetitive finger tapping) with the other representing control (e.g. rest). This creates differing brain activation states which are then statistically compared to each other. Block designs produce the larger relative BOLD signal change on fMRI [36], have increased statistical power [37], and are traditionally used in the preoperative setting. The event-related (ER) design, on the other hand, involves series of single stimuli being presented at random, reducing adaptation effects by the subject [38], and is preferential when higher temporal resolutions are required [39]. Due to the higher demands and difficult applicability in the

clinical setting, ER-fMRI has its domain more in neuroscientific functional imaging research.

A high signal to noise ratio (SNR) is essential to any imaging study, especially when it comes to diagnostic use in individual patients. However, on fMRI, noise can be even greater than the signal acquired with magnitudes of up to 2–4% [40] and represents a major challenge to a successful fMRI study. Major physical sources of noise include thermal noise from the subject as well as cardiac and respiratory noise [41] as well as variations in baseline neural metabolism. On fMRI, noise is increasingly pronounced at low frequencies [42] on the order of those alluded to in the HRF. Fortunately, fMRI signal is highest when low frequency changes occur [43, 44]. Power spectrum analysis comparing signal (from the HRF) to the noise reveals ideal epoch lengths of 15.5 s [45]. The block design fMRI experiment is therefore delicately planned into paradigms using epochs between 15 to 30 s in duration [46] traditionally run for around 4 min [41]; in our experience, the duration of a complete clinical fMRI examination consisting of multiple paradigms ranges between 10 and 20 min [47].

### 19.2.1 Preprocessing the Acquired 4D Data

Various problems arise when scanning a spherical, moving object with intrinsic inhomogeneities (such as a human's head) inside a magnetic tube. Here, proper preprocessing including artifact corrections of the acquired data is of utmost importance.

The combination of EPI sequences with magnetic field inhomogeneities caused by air-tissue interfaces results in geometric distortion. *Image distortion correction* is therefore required as images would otherwise suffer from stretching, pulling, and signal dropout. In comparison to anatomical images, displacements of 10 to 20 mm have been described in the functional data set, highlighting the importance of this data processing step [48–50].

Second, the 3D volume of the brain is scanned slice by slice at slightly different time points, either from top to bottom, vice versa or in an

interleaved fashion. The functional volume, however, is considered to be a single time point, as differences in regional blood flow across two (or more) neighboring slices occur simultaneously. To correct for these time differences, which can be up to several seconds [51], *slice timing correction* to a fixed time point is used.

Subsequently, *correction for patient motion* must be performed. Head motion and rotation are possible in all three axes ( $X$ ,  $Y$ ,  $Z$ ); therefore at least a six-parameter motion correction is warranted. Similar to slice acquisition correction, a reference is created for which all other displacements are aligned. Not all effects of patient motion can be undone as the magnetic field is distorted through motion. For this reason, we recommend data sets exceeding 2 mm of head motion to be rejected (rule of thumb: reject more than half the voxel size).

Finally, voxels are spatially smoothed by *convolution with a 3D Gaussian kernel*, improving signal to noise ratio by creating weighted averages with neighboring voxels. Statistical power is improved and the likelihood of obtaining significant results increases, all at the expense of spatial resolution.

Complex statistical modeling, for example, using the general linear model (GLM) [52–54] is

implemented to reveal the vital yet minor BOLD signal changes between the two activation states, which can be as low as 1–5% [55]. A discussion on the GLM is beyond the scope of this chapter, the interested reader is referred to the references provided.

Before reading, the functional data set must be overlaid onto anatomical images (e.g. a 3D-T1 weighted data set, 1 mm isotropic, sagittal acquisition) using dedicated software to determine the anatomical correlates of the different functional activations. Next, the statistical threshold used for interpretation of the functional data is set—this step is user-dependent and often of debate. We recommend a dynamic thresholding procedure when performing clinical fMRI studies on individual patients for diagnostic medical use [56–60] to localize the anatomical correlates of each activation precisely. Keep in mind we are locating the “center of gravity” (COG) of the activation clusters; thresholding (step-by-step instructions described later) results in COG growth (when reducing the statistical threshold) or shrinkage of the COG activation (when increasing the statistical threshold) and by no means represents true physiological boundaries of the activated cortex (Fig. 19.1).

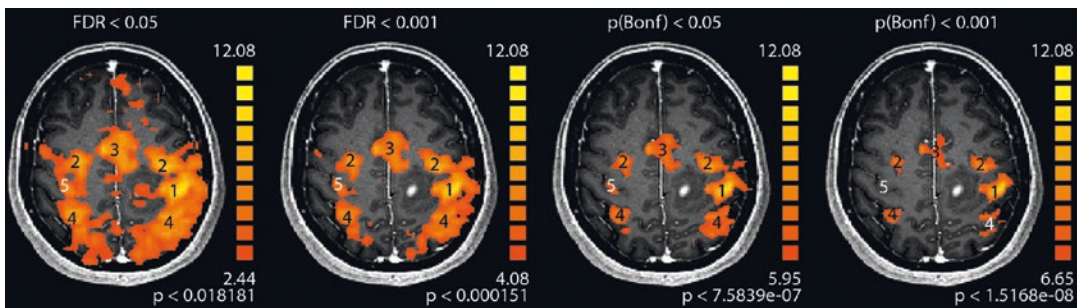


**Fig. 19.1** Changing the statistical threshold changes cluster size, using the motor network as an example in a patient with a left-sided tumor of the pre- and postcentral gyrus. Paradigm: finger tapping of the right hand. The statistical threshold (False Detection Rate FDR) increases from lowest (left) to highest (right)—the two images on

the right use the statistically more stringent Bonferroni method. Motor areas: (1) primary motor area M1/S1, (2) premotor cortex (PMC), (3) supplementary motor area (SMA), (4) superior parietal lobule (SPL), (5) co-activation of the primary motor area ipsilateral to movement

### 19.3 Thresholding: How We Do It

#### 19.3.1 Thresholding

1. First, set the false discovery rate (FDR) to 0.05.
2. Increase the threshold so that no functional activation is displayed. Gradually lower the threshold to the first cluster of activation with a predefined volume (our standard is 36 mm<sup>2</sup>).
3. Checkpoint: Does the cluster we see actually represent an expected hemodynamic response function (HRF)? Signal characteristics for this cluster are analyzed using the signal time course. The correlation coefficient ( $r$ ) of the signal time course for BOLD signal is compared to the modeled HRF. A minimal correlation ( $r$ ) of  $>0.40$  is recommended with  $p < 0.05$  (Bonferroni corrected) for cognitive paradigms and  $r > 0.6$  for motor paradigms. Unphysiologically high BOLD signal changes ( $\Delta S\%$ ) over 6% at 3 T—or 3% at 1.5 T respectively—are suspicious for a dominant venous origin (Fig. 19.2).

4. Continue lowering the threshold until activations are identified in all diagnostically relevant ROIs.

### 19.4 Motor and Sensory fMRI

#### 19.4.1 Introduction

fMRI for localization of brain motor areas has been validated in multiple studies but ultimately does not fully replace the gold standard ECS in tumor surgery. Early studies comparing fMRI to ECS reported accuracies in locating important motor areas of 100% [7, 8]; recent literature, however, reports accuracies at 91% [9] with sensitivities ranging between 85% and 97% [10–12]. Mapping of functional motor areas is generally accomplished by asking the patient to perform voluntary muscle movements such as finger tapping, tongue movements or lip putting, and toe flexion/extension; this way, three separate areas on the primary motor cortex can be located (Fig. 19.3). Supervised patient training before the examination is essential. The fol-

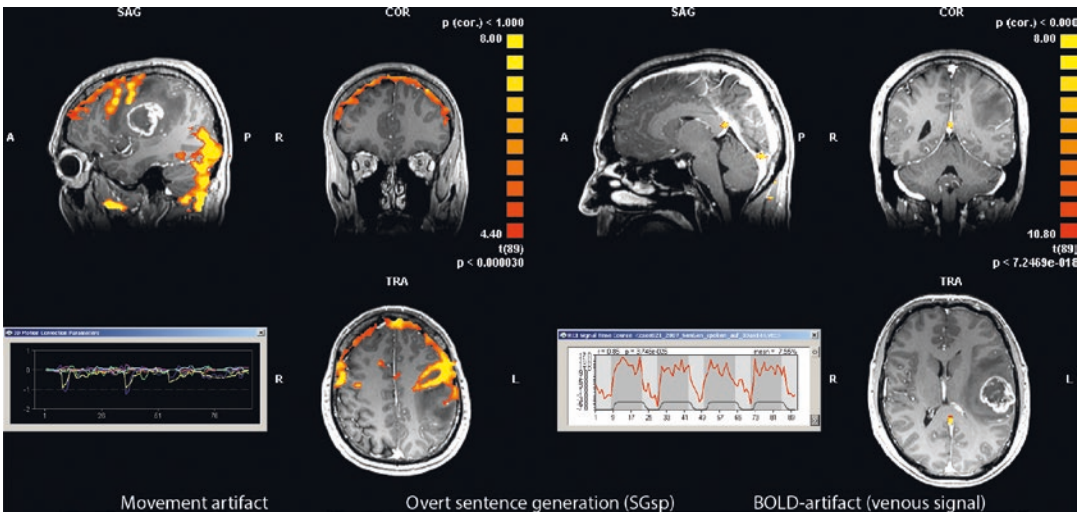


**Fig. 19.2** Artifacts: On the left, an example of motion-induced artifacts pronounced directly underneath the skull in a convex shape best appreciated in the coronal plane. In the bottom left corner, the corresponding motion correction parameter graph over time. On the right an example of a pulsating vein, in this case the vein of Galen. While

the correlation of the BOLD activation to the modeled hemodynamic response function is high ( $r = 0.85$ ), the mean signal change of 7.55% is above the acceptable limit—for this reason, this area of BOLD activation must be deemed an artifact

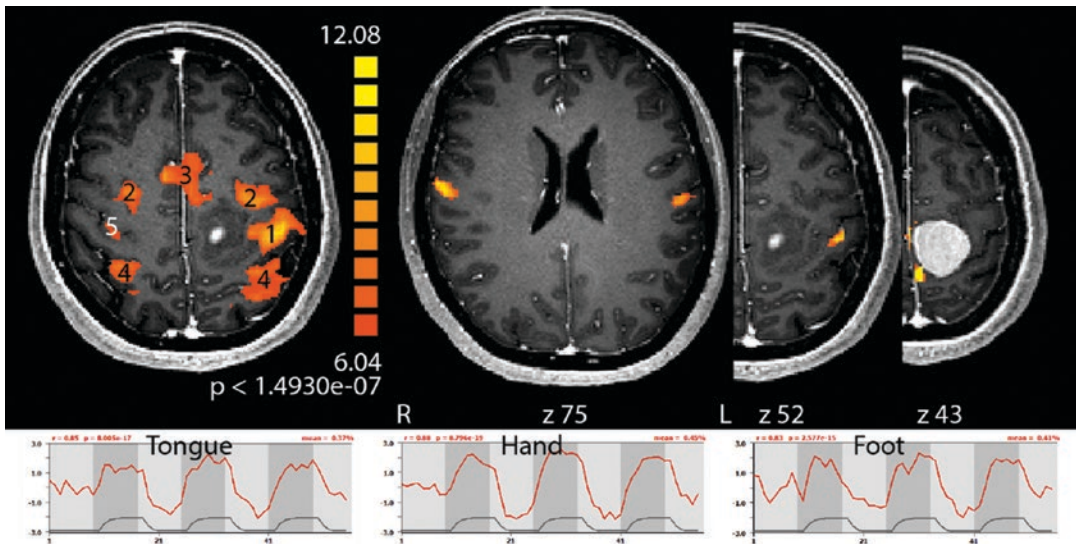


**Fig. 19.3** BOLD activation mapping of the motor network in a patient with a left-sided tumor of the pre- and postcentral gyrus: (1) Primary motor area M1/S1, (2) Premotor cortex (PMC), (3) Supplementary motor area (SMA), (4) Superior parietal lobule (SPL), (5) Co-activation of the primary motor area ipsilateral to

movement. Images on right: tongue (left), hand (middle), and foot (right). Signal-time courses of the BOLD activation (red) compared to the modelled hemodynamic response function (HRF, grey) for tongue (left), hand (middle), and foot (right)

lowing section is a summary and discussion of functional motor areas with practical tips for unusual situations.

## 19.4.2 Cortical Motor Areas

### 19.4.2.1 Primary Motor Area (M1)

The primary motor cortex is found on the pre-central gyrus and is arranged in a distorted, inverted body representation known as a homunculus—feet and toes are located dorsomedially near the central sulcus (paracentral lobule), the M1-hand representation is located further down the hemispheric surface in an anatomically distinct area known as the “hand knob” [61] and the face is represented on the lower hemispheric convexity. Focal defects of M1 result in complete paralysis of the contralateral muscle group with a limited chance of gradual recovery of proximal functions, but lasting deficits in fine motor control [62]. Self-triggered movements of the tongue or lips, hand or fingers, and foot or toes are used to locate M1 on fMRI. Unilateral

finger tapping activates the contralateral primary motor cortex as well as the premotor (PMA) and supplementary motor areas (SMA) in both hemispheres. Activation of the corresponding primary somatosensory (S1) somatotopic body representation of the postcentral gyrus is also intrinsically associated with voluntary movements. As a consequence, such fMRI BOLD-responses reflect the so-called primary sensorimotor activation. In cases where only primary sensorimotor cortex fMRI localization is desired, alternating movements of the right and left side of the body will lead to primary sensorimotor activation in both hemispheres without visualization of secondary cortical areas. This is due to the fact that the movements of either side activate the secondary areas (PMA, SMA) of the cortical motor network bilaterally. Such continuous activation leads to insignificant differences on statistical analysis, resulting in non-visualization on fMRI [63]. This is advantageous in patients with greatly distorted anatomy where undesired activation of the secondary motor areas could interfere with the identification of

the primary motor area. A word of caution with this technique is warranted as bilateral activation of the primary motor cortex upon unilateral voluntary movements has been described [56]. On the contrary, bilateral motor activation should be avoided if cortical reorganization needs to be addressed in clinical fMRI. Here, strictly unilateral movements are utilized to thoroughly study changes in primary and secondary cortical motor areas. As mentioned earlier, this is not possible when employing bilateral movements for motor cortex activation.

Patients with lesions involving eloquent motor areas are sometimes unable to perform fine motor movements due to paresis. In these cases, finger tapping can be replaced by larger movements such as hand clenching. Generally, movements involving larger muscle groups are

at higher risk for inducing motion artifacts, so the patient must be focused on keeping their head still. Options in fully paralytic patients include imagination of movements, showing activation of primary [57] and secondary motor areas [64], and passive motor movements [65] performed with the aid of a second individual (Fig. 19.4). Indirect mapping of the primary motor cortex through localization of the primary somatosensory cortex (S1) is also possible. Various stimuli such as fully automated pneumatically driven tactile stimulation [58, 59, 66] and manual stroking [63, 67] can map somatosensory cortex on the postcentral gyrus, obtaining indirect information on the location of the precentral gyrus [63]. Of note, tactile stimulation also elicits bilateral secondary (SII), integrative sensory areas [68].

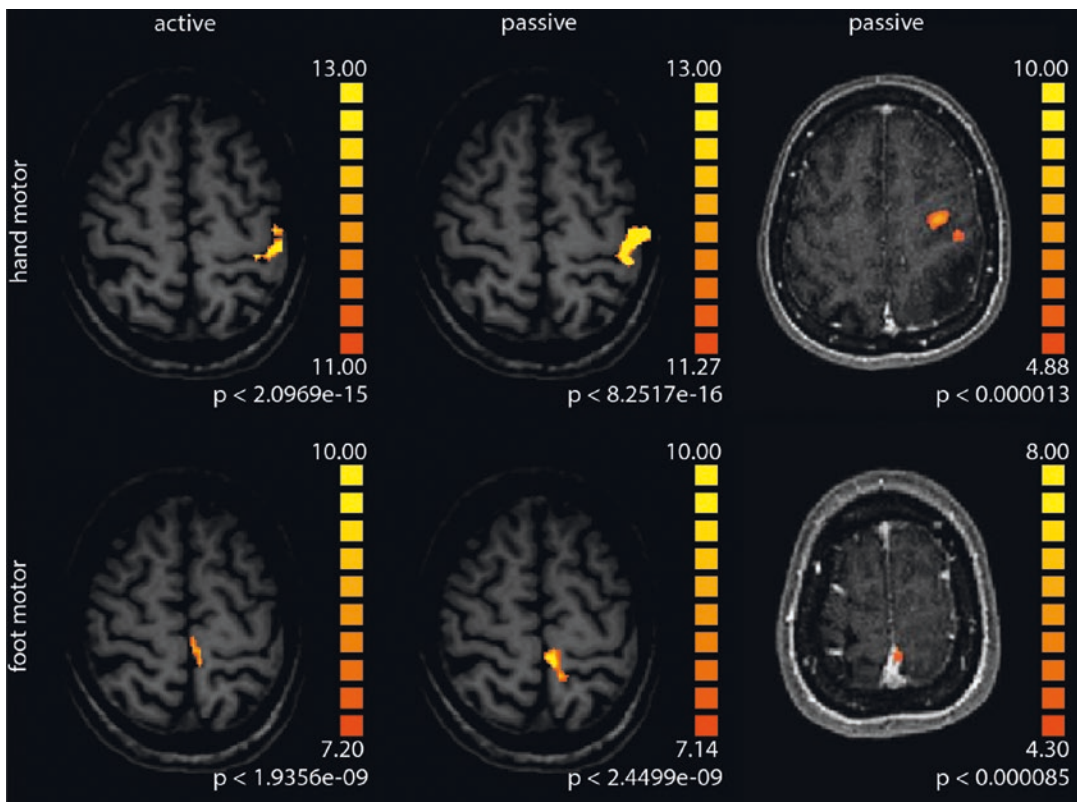


**Fig. 19.4** Active and passive movements for motor mapping: left row: BOLD activations can be seen in a volunteer actively moving their hand (above) and foot (below). Middle: passive movements of hand (above) and foot

(below) performed by a second individual in the same volunteer. Right: BOLD activations of passive movement of hand (above) and foot (below) in a highly uncoordinated patient, again performed by a second individual

### 19.4.2.2 Premotor Cortex (PMC)

The PMC is located anterior to the primary motor cortex on the anterior aspect of the precentral gyrus and posterior aspect of the middle frontal gyrus. The PMC appears to house coordinated, complex movements responding to visual cues [69], is activated bilaterally during unilateral muscle movement, and shows higher activations with increasingly complex movements [70]. These observations can be advantageous for locating the premotor cortex using the opposite limb [60] when voluntary movement of the contralateral limb is not possible. The PMC can also be activated during imagined complex movements [70] and while observing actions [71] without subsequent muscle movement. On postoperative resection, transient apraxia has been reported, with lasting deficits being attributed to subcortical lesions [72]. Naming deficits have also been described [73] on ECS which is elaborated in the language section.

### 19.4.2.3 Supplementary Motor Area (SMA)

The supplementary motor area is located on the medial aspect of the posterior superior frontal gyrus, essentially in continuation with the precentral gyrus located further laterally. The anterior SMA is involved in initiation, planning and temporal sequence selection of voluntary movements [74] and retrieval of motor memory [75], housing memorized programs, and has a large role in speech initiation in the dominant hemisphere. The posterior SMA shows activation during the executive component of movement tasks [76]. Postoperatively, the SMA syndrome has been described as transient akinetic mutism (speech arrest) and hemiparesis (or apraxia) with potential long-term disorders involving rapid alternating movements of both hands [77]. Like the premotor cortex, the SMA is activated bilaterally during unilateral muscle movement with increasing complexity showing higher activation and can be activated during imagined complex movements [70].

### 19.4.2.4 Further Motor fMRI Activations of Interest

Further activity on fMRI can be seen in the anterior cingulate cortex (ACC) and the superior parietal lobule (SPL). The ACC shows enhanced activity on self-initiated movements compared to externally triggered movements [78] and is activated in preparation of motor response [79] yet is not motor-specific as, for example, activations in pain studies have been reported [80]. The ACC is generally believed to function in a wide range of cognitive control [81] including motivation and execution of goal-directed behavior. SPL activation is routinely noted in motor studies such as simple finger-thumb opposition [74], yet stronger activation is seen in sequential tasks [82] with a main postulated function in spatial planning of motor movements [83] and movement sequences [74]. However, unilateral lesions induce deficits not specific to the motor system, and include hemineglect and altered visual representations of space [84] as well as tactile apraxia (isolated disturbance of hand movements for use of and interaction with an object) [85].

---

## 19.5 Language fMRI

### 19.5.1 Introduction

Language fMRI presents a much greater challenge than motor fMRI. First, the activations of differing regions heavily depend on the task presented to the patient. Second, patients may not be able to cooperate due to differences in education, language, or deficits induced by the brain lesion itself. Moreover, it is difficult to assess patient cooperation on silent language tasks and boredom associated with free-thinking during control (resting) tasks. For this, we recommend interviewing patients after the examination to assess these variables. Again, closely supervised patient training before the examination is essential. Finally, individual languages can be represented on distinct cortical areas in multilingual patients [86], therefore the examination should be

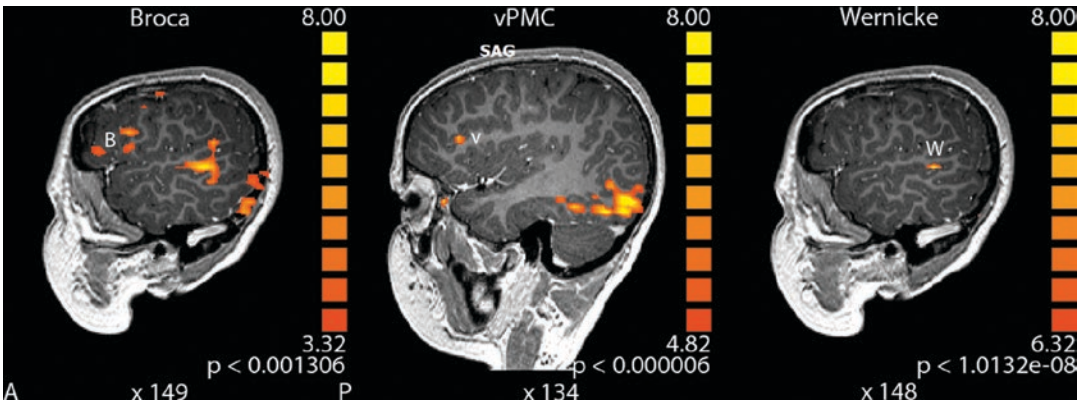


**Fig. 19.5** BOLD activations of Broca's area (left), the ventral premotor cortex (vPMC, middle), and Wernicke's area (right)

repeated for all languages of relevance for an individual patient. The fMRI language-tasks can be designed to investigate any language when patients are trained with a translating person; this is easily achieved when using pictures as triggers (Fig. 19.5).

Preoperative language mapping on fMRI has two main tasks: determining hemispheric dominance (language lateralization) and localizing areas functionally important to language. As the brain activation associated with cognitive functions (such as language) is widely distributed and task-dependent, preoperative fMRI target activation of language areas (ROIs) may be reduced pragmatically to the classical model of language (Wernicke-Lichtheim), namely to the Broca and Wernicke language areas and the anatomical homologs of the right hemisphere (for language lateralization). However, such simplistic models do no longer correctly reflect the current understanding of cortical language functions. Typically, further language associated activation can be identified in the ventral premotor cortex, Exner's, Dronker's, and Geschwind's language areas and distinct temporal areas (for further details see the following paragraphs). A combination of language fMRI with a DTI-tractography is recommended—at least of the arcuate fascicle. fMRI cannot currently replace the gold standard ECS in *language localization*, with a wide range of reported sensitivities (22–100%) [13, 14], a

marked variability between patients [87], a dependence on tumor grade [10] and a concordance lower than motor mapping (67–100%) [9, 15, 16]. *Language lateralization*, on the other hand, has shown strong concordance with ECS reportedly on the order of 80 to 90% [17, 18]. One study reports fMRI to have an even greater accuracy in the prediction of postoperative outcomes compared to ECS for cases where the two tests were discordant [88]. Binder et al. conclude that fMRI is a valid alternative to preoperative Wada testing [17].

The following section is separated into cortical language areas visible on fMRI based contemporary understanding of language function known as the dual-stream model [89]. Language is no longer thought of in terms of the traditional Broca (expressive) Wernicke (receptive) model, rather in terms of cognitive function separated into phonetics (speech sounds), semantics (meaning of words), orthography (representation of written characters), and syntax (combining words into sentence structure) [16]. Driving this evolution was a multitude of factors: lesions to Wernicke's area resulting in expressive language deficits [90], Broca's area showing receptive function [91], and similar lesions between patients resulting in a variety of aphasia syndromes [92]. Furthermore, cortex neighboring the traditional Broca and Wernicke areas was shown to be more characteristic of the traditional

area than the area itself! Corroborating these findings, Dronkers revealed the lesions in Broca's original brain studies to span greater territories than his namesake area with parietal, insular, and subcortical lesions [93] included. Finally, this section does not describe the executive motor components of speech, as these areas are thoroughly discussed in the previous motor section.

Of note:

1. Recommended paradigms including slides for download can be found at [www.asfnr.org](http://www.asfnr.org), the website for the American Society of Functional Neuroradiology. Generally, paradigms activating primarily frontal/expressive regions include silent word generation, antonym generation, and object naming while sentence completion and passive story listening activate the temporal/receptive areas [94] (Fig. 19.6).
2. Language lateralization can be assessed visually or through the laterality index (LI) formula [95, 96]:  $LI: (Right\ hemisphere - Left\ hemisphere) / (Right\ hemisphere + Left\ hemisphere)$ .
3. Neurosurgical priorities guiding resections based on ECS near language areas include

identifying cortical areas producing speech arrest and anomia [97].

## 19.5.2 Cortical Language Areas

### 19.5.2.1 Broca's Area (Pars Opercularis and Posterior Pars Triangularis)

Paul Broca's famous patients, Leborgne and Lelong, both presented with markedly reduced productive speech [98], attributed to lesions in the lateral left frontal lobe, resulting in the designation "Broca's aphasia." Broca's area is now precisely defined in terms of the pars triangularis and pars opercularis of the inferior frontal gyrus [93]. While speech arrest is reported on ECS of the Pars triangularis [97] and the Pars opercularis [99] recent studies have shown a higher rate of speech arrest in an area known as the ventral Premotor cortex [99]. Furthermore, normal speech function has been reported following removal of Broca's area [100, 101] but this is due to brain plasticity. For now, Broca's appears to have a much wider range of cognitive function than initially thought, including semantic [102], lexical, phonological, and syntax [102, 103] in

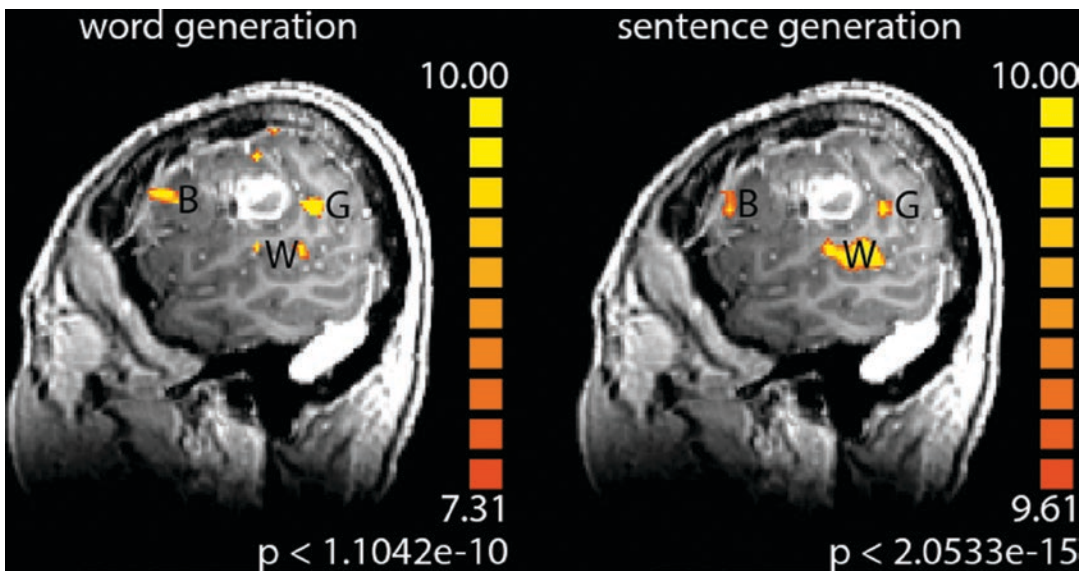


**Fig. 19.6** BOLD activations of the Broca (B), Wernicke (W), and Geschwind (G) areas in a patient with a perisylvian tumor. Left: word generation block design paradigm. Right: sentence generation block design paradigm



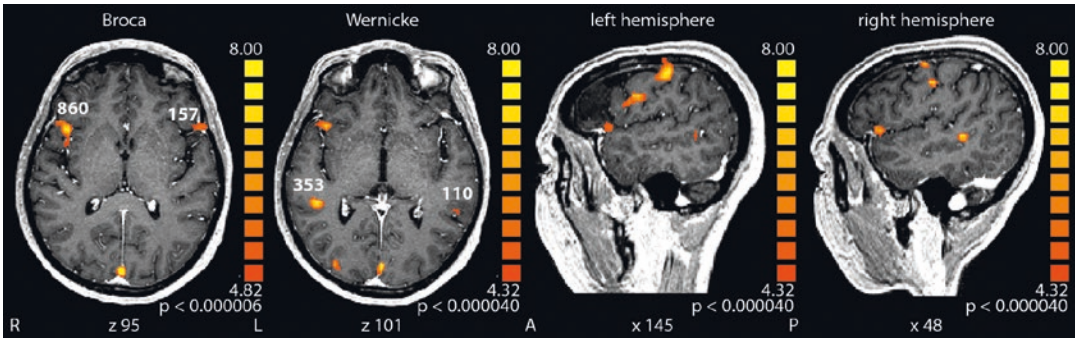


**Fig. 19.7** BOLD activations of the Broca and Wernicke areas on axial (left) and sagittal (right) images with voxel numbers or lateralization purposes in a patient with atypi-

cal right hemispheric dominance. Paradigm: silent word generation

expressive as well as receptive speech [91] and higher order processing [104]. ECS results in a range of deficits including anomia as well as phonological and semantic paraphasias [99]. Rhyming tasks produce robust activation of Broca's area [105]. For language lateralization producing robust activations of Broca's and Wernicke's area, word generation and silent word generation tasks are recommended [94, 106, 107] (Fig. 19.7).

### 19.5.2.2 Ventral Premotor Cortex (vPMC)

Located posterior and superior to the pars opercularis, the vPMC has been implicated in challenging Broca's classical area for speech production, demonstrating 83% incidence of speech arrest compared with 35% for the precentral gyrus and 4% of pars opercularis on ECS [99]. The vPMC has many subcortical connections with the perisylvian network [108] and forms an important part of the final pathway for speech synthesis [109] and planification of articulation [73]. These observations, combined with its limited plastic potential [110] makes it essential to locate preoperatively. Tool selective activation was reported in a paradigm including tools, animals, faces, and houses with phase-scrambled images as control stimuli [111], even in the absence of subsequent activity. The specific hand movements associated with tools was postulated to stimulate regions of the brain

(including the vPMC) housing information on the action associated with their use. Semantic tasks have also been shown to activate the vPMC [112]. While on the topic of the premotor cortex, a brief word of mention to Exner's area is warranted, with a recent summary recommending its localization on preoperative language fMRI [91]. Exner's area is located on the posterior aspect of the middle frontal gyrus with a reported function converging abstract orthographic representations into a planned motor sequence—isolated lesions were associated with deficits in the handwriting of words [113] while handwriting of numbers remained unaffected [114].

### 19.5.2.3 Dronkers' Area (Precentral Gyrus of the Insula, Fig. 19.8)

In a lesion-based study, Dronkers observed that all 25 stroke patients with lesions to the precentral gyrus of the insula displayed speech apraxia, while 19 stroke patients without lesions to this area had no signs of such deficits [115]. Further studies corroborate the idea with the area being involved in the coordination of complex articulatory movements before speech is executed [116]. A metaanalysis of verbal fluency tasks using fMRI data incorporates the anterior insula as a node in a network responsible for the formulation of an articulatory plan, receiving word selection, and planned speech phonetics from the pars opercularis and relaying it to the cerebellum and cau-

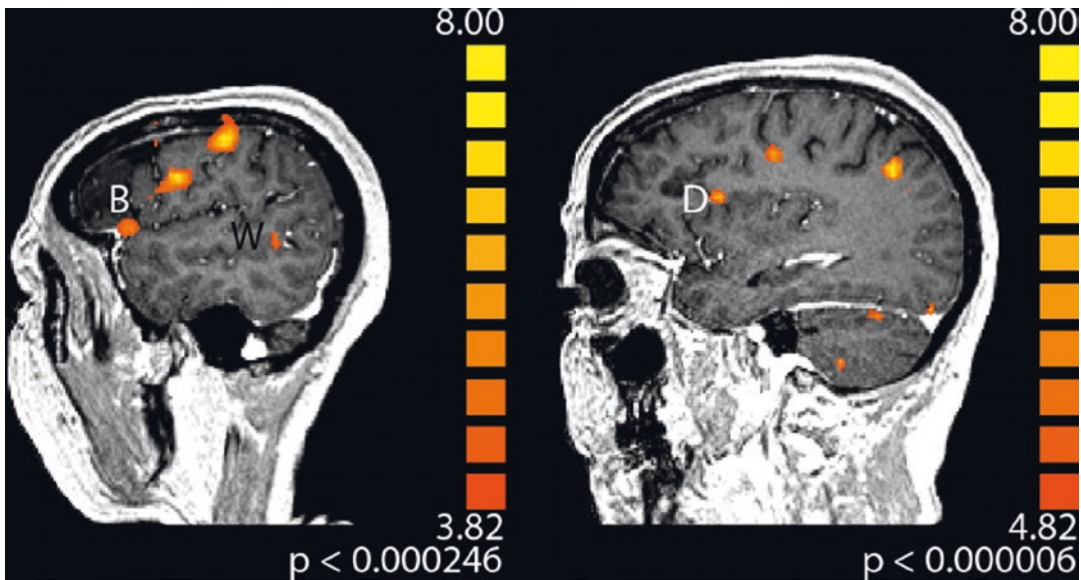


**Fig. 19.8** BOLD activations of the Broca (B), Wernicke (W), and Dronkers areas

date nucleus in a parallel fashion. From there, the modulated planned motor movement is integrated by the vPMC before being sent to M1 for execution [117]. Activation of the anterior insula can be seen, for example, in paradigms focusing on vocalized syllable complexity [118].

#### 19.5.2.4 Wernicke's Area

Wernicke's area is located at the posterior aspect of the superior temporal gyrus (pSTG, exact definitions vary [119]) and has a vital role in processing units of speech sound known as phonemes. Originally described as the site of the brain responsible for language comprehension [120], current literature attributes speech production to the forefront of the pSTG's function [90]. ECS, for example, has been shown to produce speech arrest [97, 99]. In fact, while areas around the classic Wernicke's area seem critical to comprehension (middle temporal gyrus, anterior superior temporal gyrus, superior temporal sulcus, and angular gyrus [121, 122]), the classical Wernicke area itself is not directly implicated. These observations parallel those seen in the evolution of our understanding of Broca's area: the neighboring cortex has become increasingly relevant and new functions have been attributed to the traditional area.

Specifically, the pSTG is responsible for retrieving phonemes [123] before speech is executed, with lesions resulting in an output disorder incorporating incorrectly chosen phonemes into words known as phonemic paraphasia [124, 125]. The cortex located directly anterior to Wernicke's area, the medial superior temporal gyrus (mSTG), has implications in the comprehension of phonemes. The mSTG receives low-level auditory information from the primary auditory cortex (rostral Heschl's gyrus [125, 126]) bilaterally—unilateral lesions are compensated by the contralateral hemisphere. Bilateral lesions, however, can cause pure word deafness [125]. Wernicke's is robustly activated during sentence completion tasks [127].

#### 19.5.2.5 Geschwind's Area (Angular and Supramarginal Gyrus)

While Geschwind's area is a combination of the angular and supramarginal gyrus, the two gyri have markedly different language functions: The angular gyrus is largely semantic [128] dealing with word meanings while the supramarginal gyrus is largely phonologic, dealing with word sounds [129]. The angular gyrus has a major role in reading and reading attainment [130] with lesions producing a range of cognitive deficits

including alexia [131], agraphia [13] (simultaneous occurrence of these deficits is known as Gerstmann syndrome) anomia [132], sentence comprehension impairment [121], and a high rate of naming errors on ECS [133]. ECS of the supra-marginal gyrus results in speech performance errors (apraxia) such as slurring or stuttering [133] as well as anomia [99]. Antonym generation tasks have been shown to activate these two areas [94].

### 19.5.2.6 Middle Temporal Gyrus

The middle temporal gyrus is part of the ventral semantic stream in the dual-stream model and is considered to be a major link between phonologic and semantic functions [134], integrating speech sounds from posterior temporal areas and relaying information to more anteriorly situated areas showing activation on higher, sentence-order levels [122]. Importantly, in a lesion based study, the MTG is one of only a few cortical areas shown critical to comprehension [121]. Activation on fMRI has been shown in phonetic studies such as speech versus non-speech sounds [135] and phoneme discrimination [136] with variable activation on silent word generation tasks [94].

### 19.5.2.7 Temporal Pole

The temporal pole has special implications in surgery of intractable temporal lobe epilepsy. Here, removal of the dominant anterior temporal lobe can result in naming difficulties (more specifically people and place) [128, 137] with little or no naming deficits reported after resection of the non-dominant temporal pole [138]. For this reason, language lateralization in the ATL is warranted preoperatively.

The temporal pole plays a role in sentence-level semantic cognition [139] yet reliable activation on fMRI has proven challenging due to observations of semantic processing during resting states [140]. The proposed solution is to substitute the resting state control task with an arithmetic task, effectively interrupting the default mode activity in the ATL showing

strong activation in the ATL across multiple centers [138].

### 19.5.2.8 Basal Temporal Language Area/Visual Word Form Area (BTLA/VWFA)

A discussion of naming deficits would not be complete without mentioning two areas on the fusiform gyrus known as the basal temporal language area (BTLA) and the visual word form area (VWFA). The BTLA is associated with a very high probability of lasting postoperative naming deficits [141], and while its exact function is not yet clear, suggestions of an important link between phonologic and semantic functions have arisen [134]. This is likely due to its proximity just anterior to the visual word form area (VWFA) housing representation of orthographic knowledge, showing activation during reading of printed words [142] when compared to pseudo-words or speech [143]; damage to the VWFA results in pure alexia [125, 144]. The VWFA can be activated in sentence completion tasks based on reading [125, 145].

---

## 19.6 Optimization, Tips, and Pitfalls

### 19.6.1 Not Everything That Activates Is Essential

From the previous sections, it has become apparent that not all areas of activation on fMRI represent no-touch cortex on surgery. fMRI cannot differentiate essential (eloquent) cortex from participating “non-essential” cortex, which activates but is not essential for the task at hand. Language fMRI, for example, involves a range of processes including working memory and attention; these activations represent general processes. Differentiation of these cortices can only be done on ECS. fMRI, an activation-based study, differs fundamentally from ECS and Wada-testing, which are transient inhibitory studies. Furthermore, activations within the contrast-enhanced region of brain tumors should

be considered artifacts until further research proves otherwise. The hemodynamic BOLD-response is prone to various tumor-induced alterations as compression of the vascular bed, neovascularization, and steal phenomena due to AV-shunting (details see below).

### 19.6.2 Conversely, Absent BOLD Activation Does Not Mean Inactive Cortex

fMRI is not an absolute study, it is a statistical, relative comparison of two functional states and many factors can lead to erroneous results. Furthermore, fMRI relies on assumptions such as intact neurovascular coupling. Medications such as acetazolamide [146] and ingested substances such as alcohol [147] decrease BOLD response by inducing vasodilatation while, as a side note, caffeine has actually been shown to boost the BOLD response [148]. The choice of paradigm also has an effect on fMRI results, in the preoperative context more importantly for language fMRI, as has been alluded to in the previous sections. While some factors can be optimized to increase the probability of a robust BOLD activation, some factors cannot be influenced. These include loss of vasodilatory response and impaired autoregulation in aging patients [149, 150], cerebrovascular disease with hypoperfused territories leading to ceiling effects [151], and susceptibility artifacts from hemorrhage causing signal drop out in postoperative and posttraumatic patients.

### 19.6.3 The Pathology Itself Can Nullify BOLD Activation

Finally, the pathology itself can render a study non-diagnostic. Tumors can decrease or even nullify BOLD signal through mass effect and edema, an effect shown to be dependent on distance to the tumor itself [152]. The neovascular structures induced by higher-grade tumors lose

their ability to autoregulate and may already be maximally dilated [153] resulting in neurovascular uncoupling [154, 155] and therefore lower MR signal changes. While these reduced signal changes more pronounced in higher grade tumors [156], the altered pH levels, abnormal astrocytes, and disruptions in neurotransmitters in lower grade tumors also result in neurovascular uncoupling [157]. Here, mapping of neurovascular uncoupling is advisable using a breath-hold induced hypercapnic state; normal vessels will dilate while chronically dilated or pathologic vessels will fail to respond [157, 158].

AVMs can also result in impaired BOLD activation through associated flow abnormalities such as lower perfusion pressure [159] and adjacent steal effects with a demonstrated return of BOLD activation after embolization [160]. Moreover, AVMs have been shown to induce cortical reorganization to the ipsilateral [161] and contralateral [162] hemisphere that should not be mistaken for absent activation in the expected anatomical region.

---

## 19.7 Clinical Case

A 70-year-old male patient presented to the emergency room with dizziness. After neurological workup, MRI revealed a tumor in the right insular region with a small focus of contrast enhancement likely representing a high-grade glioma. The patient was right-handed but had a family history of right-hemispheric language dominance, thus preoperative fMRI was performed. Silent sentence generation and word generation paradigms confirmed atypical right-hemispheric dominance. Consequently, the neurosurgical approach was changed from that of a radical resection to a focused resection of the contrast-enhancing (presumably more malignant) area of the tumor. Postoperatively, no language deficits were found. Histology confirmed the diagnosis of Glioblastoma (Fig. 19.9).

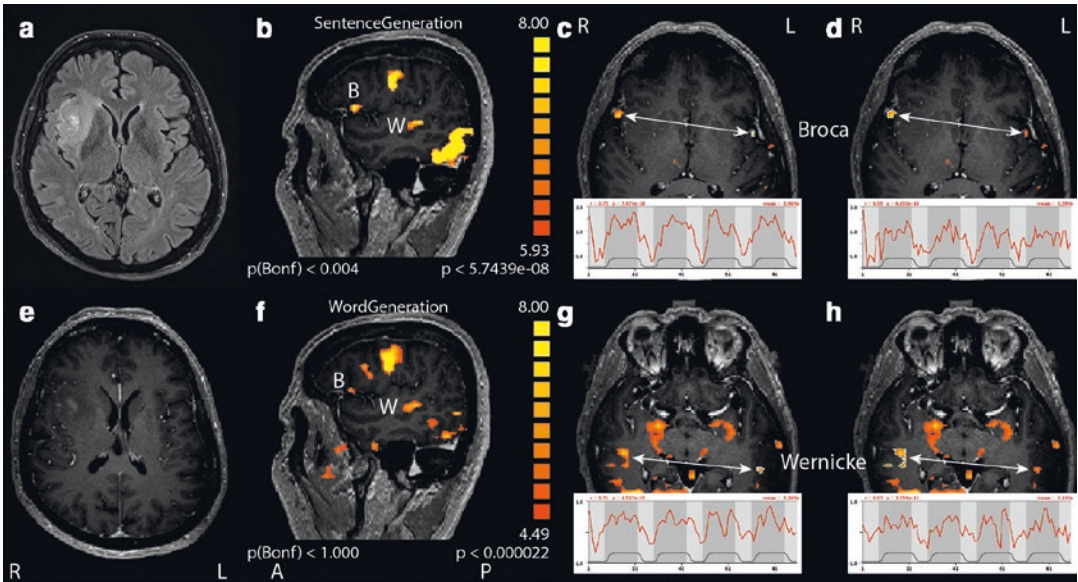


**Fig. 19.9** Morphological axial FLAIR (a) and T1 contrast-enhanced (T1-ce) (e) images revealing a small area of contrast-enhancement within a larger, non-enhancing subinsular tumor in the right hemisphere. Functional BOLD-MR images overlaid onto sagittal T1-ce images reveal Broca's (B) and Wernicke's (W) areas using silent sentence generation (b) and word generation (f) paradigms. Location and lateralization of

Broca's and Wernicke's areas on axial BOLD fMRI/T1-ce images with correlations of BOLD signal to modeled hemodynamic response function (HRF): left hemisphere image (c) (Broca's area) and (g) (Wernicke's area), right hemisphere image (d) (Broca's homolog) and (h) (Wernicke's homologue); graph beneath respective images

## References

- Bates E, Wilson SM, Saygin AP, Dick F, Sereno MI, Knight RT, et al. Voxel-based lesion–symptom mapping. *Nat Neurosci.* 2003;6(5):448–50.
- Duffau H. Lessons from brain mapping in surgery for low-grade glioma: insights into associations between tumour and brain plasticity. *Lancet Neurol.* 2005;4(8):476–86.
- Ojemann GA. Functional mapping of cortical language areas in adults. Intraoperative approaches. *Adv Neurol.* 1993;63:155–63.
- Wada J, Rasmussen T. Intracarotid injection of sodium amytal for the lateralization of cerebral speech dominance. *J Neurosurg.* 1960;17(2):266–82.
- Ogawa S, Lee TM, Kay AR, Tank DW. Brain magnetic resonance imaging with contrast dependent on blood oxygenation. *Proc Natl Acad Sci.* 1990;87(24):9868–72.
- Kwong KK, Belliveau JW, Chesler DA, Goldberg IE, Weisskoff RM, Poncelet BP, et al. Dynamic magnetic resonance imaging of human brain activity during primary sensory stimulation. *Proc Natl Acad Sci.* 1992;89(12):5675–9.
- Mueller WM, Yetkin FZ, Hammeke TA, Morris GL, Swanson SJ, Reichert K, et al. Functional magnetic resonance imaging mapping of the motor cortex in patients with cerebral tumors. *Neurosurgery.* 1996;39(3):515–20; discussion 520–1.
- Yousry TA, Schmid UD, Jassoy AG, Schmidt D, Eisner WE, Reulen HJ, et al. Topography of the cortical motor hand area: prospective study with functional MR imaging and direct motor mapping at surgery. *Radiology.* 1995;195(1):23–9.
- Kapsalakis IZ, Kapsalaki EZ, Gotsis ED, Verganelakis D, Toulas P, Hadjigeorgiou G, et al. Preoperative evaluation with fMRI of patients with intracranial gliomas [Internet]. *Radiol Res Pract.* 2012 [cited 2018 Aug 26]. Available from: <https://www.hindawi.com/journals/rp/2012/727810/>.
- Bizzi A, Blasi V, Falini A, Ferroli P, Cadioli M, Danesi U, et al. Presurgical functional MR imaging of language and motor functions: validation with intraoperative electrocortical mapping. *Radiology.* 2008;248(2):579–89.
- Krings T, Reinges MH, Erberich S, Kemeny S, Rohde V, Spetzger U, et al. Functional MRI for presurgical planning: problems, artefacts, and solution strategies. *J Neurol Neurosurg Psychiatry.* 2001;70(6):749–60.

12. Hirsch J, Ruge MI, Kim KH, Correa DD, Victor JD, Relkin NR, et al. An integrated functional magnetic resonance imaging procedure for preoperative mapping of cortical areas associated with tactile, motor, language, and visual functions. *Neurosurgery*. 2000;47(3):711–21; discussion 721–2.
13. Roux F-E, Boulanouar K, Lotterie J-A, Mejdoubi M, LeSage JP, Berry I. Language functional magnetic resonance imaging in preoperative assessment of language areas: correlation with direct cortical stimulation. *Neurosurgery*. 2003;52(6):1335–45; discussion 1345–7.
14. Pouratian N, Bookheimer SY, Rex DE, Martin NA, Toga AW. Utility of preoperative functional magnetic resonance imaging for identifying language cortices in patients with vascular malformations. *J Neurosurg*. 2002;97(1):21–32.
15. Petrovich N, Holodny AI, Tabar V, Correa DD, Hirsch J, Gutin PH, et al. Discordance between functional magnetic resonance imaging during silent speech tasks and intraoperative speech arrest. *J Neurosurg*. 2005;103(2):267–74.
16. Naidich TP, Hof PR, Gannon PJ, Yousry TA, Yousry I. Anatomic substrates of language: emphasizing speech. *Neuroimaging Clin N Am*. 2001;11(2):305–41, ix.
17. Binder JR. fMRI is a valid noninvasive alternative to Wada testing. *Epilepsy Behav*. 2011;20(2):214–22.
18. Swanson SJ, Sabsevitz DS, Hammeke TA, Binder JR. Functional magnetic resonance imaging of language in epilepsy. *Neuropsychol Rev*. 2007;17(4):491–504.
19. Krishnan R, Raabe A, Hattingen E, Szelényi A, Yahya H, Hermann E, et al. Functional magnetic resonance imaging-integrated neuronavigation: correlation between lesion-to-motor cortex distance and outcome. *Neurosurgery*. 2004;55(4):904–14; discussion 914–5.
20. Petrella JR, Shah LM, Harris KM, Friedman AH, George TM, Sampson JH, et al. Preoperative functional MR imaging localization of language and motor areas: effect on therapeutic decision making in patients with potentially resectable brain tumors. *Radiology*. 2006;240(3):793–802.
21. Cosgrove GR, Buchbinder BR, Jiang H. Functional magnetic resonance imaging for intracranial navigation. *Neurosurg Clin N Am*. 1996;7(2):313–22.
22. Nimsky C, Ganslandt O, Von Keller B, Romstöck J, Fahlbusch R. Intraoperative high-field-strength MR imaging: implementation and experience in 200 patients. *Radiology*. 2004;233(1):67–78.
23. Schulder M, Maldjian JA, Liu WC, Holodny AI, Kalnin AT, Mun IK, et al. Functional image-guided surgery of intracranial tumors located in or near the sensorimotor cortex. *J Neurosurg*. 1998;89(3):412–8.
24. Hartkens T, Hill DLG, Castellano-Smith AD, Hawkes DJ, Maurer CR, Martin AJ, et al. Measurement and analysis of brain deformation during neurosurgery. *IEEE Trans Med Imaging*. 2003;22(1):82–92.
25. Nimsky C, Ganslandt O, Hastreiter P, Fahlbusch R. Intraoperative compensation for brain shift. *Surg Neurol*. 2001;56(6):357–64; discussion 364–5.
26. Stippich C, Kress B, Ohmann H, Tronnier V, Sartor K. [Preoperative functional magnetic resonance tomography (fMRI) in patients with rolandic brain tumors: indication, investigation strategy, possibilities and limitations of clinical application]. *ROFO Fortschr Geb Rontgenstr Nuklearmed*. 2003;175(8):1042–50.
27. Lurito JT, Dziedzic M. Determination of cerebral hemisphere language dominance with functional magnetic resonance imaging. *Neuroimaging Clin N Am*. 2001;11(2):355–63, x.
28. Glover GH. Overview of functional magnetic resonance imaging. *Neurosurg Clin N Am*. 2011;22(2):133–9.
29. Boxerman JL, Bandettini PA, Kwong KK, Baker JR, Davis TL, Rosen BR, et al. The intravascular contribution to fMRI signal change: Monte Carlo modeling and diffusion-weighted studies in vivo. *Magn Reson Med*. 1995;34(1):4–10.
30. Mansfield P. Multi-planar image formation using NMR spin echoes. *J Phys C Solid State Phys*. 1977;10(3):L55.
31. Logothetis NK, Pauls J, Augath M, Trinath T, Oeltermann A. Neurophysiological investigation of the basis of the fMRI signal. *Nature*. 2001;412(6843):150–7.
32. Fox PT, Raichle ME, Mintun MA, Dence C. Nonoxidative glucose consumption during focal physiologic neural activity. *Science*. 1988;241(4864):462–4.
33. Magistretti PJ, Pellerin L, Rothman DL, Shulman RG. Energy on demand. *Science*. 1999;283(5401):496–7.
34. Aguirre GK, Zarahn E, D'Esposito M. The variability of human, BOLD hemodynamic responses. *NeuroImage*. 1998;8(4):360–9.
35. Menon RS, Kim SG. Spatial and temporal limits in cognitive neuroimaging with fMRI. *Trends Cogn Sci*. 1999;3(6):207–16.
36. Buxton RB, Wong EC, Frank LR. Dynamics of blood flow and oxygenation changes during brain activation: the balloon model. *Magn Reson Med*. 1998;39(6):855–64.
37. Friston KJ, Holmes AP, Price CJ, Büchel C, Worsley KJ. Multisubject fMRI studies and conjunction analyses. *NeuroImage*. 1999;10(4):385–96.
38. D'Esposito M, Zarahn E, Aguirre GK. Event-related functional MRI: implications for cognitive psychology. *Psychol Bull*. 1999;125(1):155–64.
39. Liu TT. Efficiency, power, and entropy in event-related fMRI with multiple trial types. Part II: design of experiments. *NeuroImage*. 2004;21(1):401–13.
40. Chen C-C, Tyler CW, Baseler HA. Statistical properties of BOLD magnetic resonance activity in the human brain. *NeuroImage*. 2003;20(2):1096–109.

41. Buxton RB. The physics of functional magnetic resonance imaging (fMRI). *Rep Prog Phys*. 2013;76(9):096601.
42. Zarahn E, Aguirre GK, D'Esposito M. Empirical analyses of BOLD fMRI statistics. I. Spatially unsmoothed data collected under null-hypothesis conditions. *NeuroImage*. 1997;5(3):179–97.
43. Glover GH. Deconvolution of impulse response in event-related BOLD fMRI. *NeuroImage*. 1999;9(4):416–29.
44. Boynton GM, Engel SA, Glover GH, Heeger DJ. Linear systems analysis of functional magnetic resonance imaging in human V1. *J Neurosci*. 1996;16(13):4207–21.
45. Chen C-C, Tyler CW. Spectral analysis of fMRI signal and noise. In: Onozuka M, Yen C-T, editors. *Novel trends in brain science: brain imaging, learning and memory, stress and fear, and pain* [Internet]. Tokyo: Springer Japan; 2008 [cited 2018 Aug 28]. p. 63–76. Available from: [https://doi.org/10.1007/978-4-431-73242-6\\_4](https://doi.org/10.1007/978-4-431-73242-6_4).
46. Maus B, van Breukelen GJP, Goebel R, Berger MPF. Optimization of blocked designs in fMRI studies. *Psychometrika*. 2010;75(2):373–90.
47. Stippich C, Heiland S, Tronnier V, Mohr A, Sartor K. [Functional magnetic resonance imaging: physiological background, technical aspects and prerequisites for clinical use]. *ROFO Fortschr Geb Rontgenstr Nuklearmed*. 2002;174(1):43–9.
48. Jezzard P, Balaban RS. Correction for geometric distortion in echo planar images from B0 field variations. *Magn Reson Med*. 1995;34(1):65–73.
49. Zaitsev M, Hennig J, Speck O. Point spread function mapping with parallel imaging techniques and high acceleration factors: fast, robust, and flexible method for echo-planar imaging distortion correction. *Magn Reson Med*. 2004;52(5):1156–66.
50. Zeng H, Constable RT. Image distortion correction in EPI: comparison of field mapping with point spread function mapping. *Magn Reson Med*. 2002;48(1):137–46.
51. Sladky R, Friston KJ, Tröstl J, Cunningham R, Moser E, Windischberger C. Slice-timing effects and their correction in functional MRI. *NeuroImage*. 2011;58(2):588–94.
52. Friston KJ, Holmes AP, Poline JB, Grasby PJ, Williams SC, Frackowiak RS, et al. Analysis of fMRI time-series revisited. *NeuroImage*. 1995;2(1):45–53.
53. Worsley KJ, Liao CH, Aston J, Petre V, Duncan GH, Morales F, et al. A general statistical analysis for fMRI data. *NeuroImage*. 2002;15(1):1–15.
54. Smith SM. Overview of fMRI analysis. *Br J Radiol*. 2004;77(2):S167–75.
55. Parrish TB, Gitelman DR, LaBar KS, Mesulam MM. Impact of signal-to-noise on functional MRI. *Magn Reson Med*. 2000;44(6):925–32.
56. Stippich C, Blatow M, Durst A, Dreyhaupt J, Sartor K. Global activation of primary motor cortex during voluntary movements in man. *NeuroImage*. 2007;34(3):1227–37.
57. Stippich C, Ochmann H, Sartor K. Somatotopic mapping of the human primary sensorimotor cortex during motor imagery and motor execution by functional magnetic resonance imaging. *Neurosci Lett*. 2002;331(1):50–4.
58. Stippich C, Romanowski A, Nennig E, Kress B, Sartor K. Time-efficient localization of the human secondary somatosensory cortex by functional magnetic resonance imaging. *Neurosci Lett*. 2005;381(3):264–8.
59. Stippich C, Romanowski A, Nennig E, Kress B, Hähnel S, Sartor K. Fully automated localization of the human primary somatosensory cortex in one minute by functional magnetic resonance imaging. *Neurosci Lett*. 2004;364(2):90–3.
60. Stippich C, Kapfer D, Hempel E, Borgulya G, Bongers A, Heiland S, et al. Robust localization of the contralateral precentral gyrus in hemiparetic patients using the unimpaired ipsilateral hand: a clinical functional magnetic resonance imaging protocol. *Neurosci Lett*. 2000;285(2):155–9.
61. Yousry TA, Schmid UD, Alkadhi H, Schmidt D, Peraud A, Buettner A, et al. Localization of the motor hand area to a knob on the precentral gyrus. A new landmark. *Brain J Neurol*. 1997;120(Pt 1):141–57.
62. Horsley V. The Linacre Lecture on the function of the so-called motor area of the brain. *Br Med J*. 1909;2(2533):121–32.
63. Stippich C, editor. *Clinical functional MRI: presurgical functional neuroimaging* [Internet]. 2nd ed. Berlin, Heidelberg: Springer-Verlag; 2015 [cited 2018 Aug 19]. (Diagnostic Imaging). Available from: [www.springer.com/de/book/9783662451229](http://www.springer.com/de/book/9783662451229)
64. Mizuguchi N, Nakata H, Hayashi T, Sakamoto M, Muraoka T, Uchida Y, et al. Brain activity during motor imagery of an action with an object: a functional magnetic resonance imaging study. *Neurosci Res*. 2013;76(3):150–5.
65. Blatow M, Reinhardt J, Riffel K, Nennig E, Wengenroth M, Stippich C. Clinical functional MRI of sensorimotor cortex using passive motor and sensory stimulation at 3 tesla. *J Magn Reson Imaging*. 2011;34(2):429–37.
66. Stippich C, Hofmann R, Kapfer D, Hempel E, Heiland S, Jansen O, et al. Somatotopic mapping of the human primary somatosensory cortex by fully automated tactile stimulation using functional magnetic resonance imaging. *Neurosci Lett*. 1999;277(1):25–8.
67. van der Zwaag W, Gruetter R, Martuzzi R. Stroking or buzzing? A comparison of somatosensory touch stimuli using 7 Tesla fMRI. *PLoS One*. 2015;10(8):e0134610.
68. Maldjian JA, Gottschalk A, Patel RS, Pincus D, Detre JA, Alsop DC. Mapping of secondary somatosensory cortex activation induced by vibrational stimulation: an fMRI study. *Brain Res*. 1999;824(2):291–5.
69. Halsband U, Ito N, Tanji J, Freund HJ. The role of premotor cortex and the supplementary motor area

- in the temporal control of movement in man. *Brain J Neurol.* 1993;116(Pt 1):243–66.
70. Rao SM, Binder JR, Bandettini PA, Hammeke TA, Yetkin FZ, Jesmanowicz A, et al. Functional magnetic resonance imaging of complex human movements. *Neurology.* 1993;43(11):2311–8.
  71. Manthey S, Schubotz RI, von Cramon DY. Premotor cortex in observing erroneous action: an fMRI study. *Brain Res Cogn Brain Res.* 2003;15(3):296–307.
  72. Shah KB, Hayman LA, Chavali LS, Hamilton JD, Prabhu SS, Wangaryattawanich P, et al. Glial tumors in Brodmann area 6: spread pattern and relationships to motor areas. *Radiographics.* 2015;35(3):793–803.
  73. Duffau H, Capelle L, Denvil D, Gatignol P, Sichez N, Lopes M, et al. The role of dominant premotor cortex in language: a study using intraoperative functional mapping in awake patients. *NeuroImage.* 2003;20(4):1903–14.
  74. Gordon AM, Lee J-H, Flament D, Ugurbil K, Ebner TJ. Functional magnetic resonance imaging of motor, sensory, and posterior parietal cortical areas during performance of sequential typing movements. *Exp Brain Res.* 1998;121(2):153–66.
  75. Tanji J. The supplementary motor area in the cerebral cortex. *Neurosci Res.* 1994;19(3):251–68.
  76. Van Oostende S, Van Hecke P, Sunaert S, Nuttin B, Marchal G. fMRI studies of the supplementary motor area and the premotor cortex. *NeuroImage.* 1997;6(3):181–90.
  77. Laplane D, Talairach J, Meininger V, Bancaud J, Orgogozo JM. Clinical consequences of corticectomies involving the supplementary motor area in man. *J Neurol Sci.* 1977;34(3):301–14.
  78. Wiese H, Stude P, Nebel K, de Greiff A, Forsting M, Diener HC, et al. Movement preparation in self-initiated versus externally triggered movements: an event-related fMRI-study. *Neurosci Lett.* 2004;371(2):220–5.
  79. Heun R, Jessen F, Klose U, Erb M, Granath DO, Grodd W. Response-related fMRI analysis during encoding and retrieval revealed differences in cerebral activation by retrieval success. *Psychiatry Res.* 2000;99(3):137–50.
  80. Kwan CL, Crawley AP, Mikulis DJ, Davis KD. An fMRI study of the anterior cingulate cortex and surrounding medial wall activations evoked by noxious cutaneous heat and cold stimuli. *Pain.* 2000;85(3):359–74.
  81. Umemoto A, Holroyd CB. Chapter 8—Exploring individual differences in task switching: Persistence and other personality traits related to anterior cingulate cortex function. In: Studer B, Knecht S, editors. *Progress in brain research* [Internet]. Amsterdam: Elsevier; 2016 [cited 2018 Aug 10]. p. 189–212. (Motivation; vol. 229). Available from: <http://www.sciencedirect.com/science/article/pii/S0079612316300632>.
  82. Boecker H, Kleinschmidt A, Requardt M, Hänicke W, Merboldt KD, Frahm J. Functional cooperativity of human cortical motor areas during self-paced simple finger movements. A high-resolution MRI study. *Brain J Neurol.* 1994;117(Pt 6):1231–9.
  83. Stephan KM, Fink GR, Passingham RE, Silbersweig D, Ceballos-Baumann AO, Frith CD, et al. Functional anatomy of the mental representation of upper extremity movements in healthy subjects. *J Neurophysiol.* 1995;73(1):373–86.
  84. Darling WG, Pizzimenti MA, Rizzo M. Unilateral posterior parietal lobe lesions affect representation of visual space. *Vis Res.* 2003;43(15):1675–88.
  85. Binkofski F, Kunesch E, Classen J, Seitz RJ, Freund HJ. Tactile apraxia: unimodal apractic disorder of tactile object exploration associated with parietal lobe lesions. *Brain J Neurol.* 2001;124(Pt 1):132–44.
  86. Kim KHS, Relkin NR, Lee K-M, Hirsch J. Distinct cortical areas associated with native and second languages. *Nature.* 1997;388(6638):171–4.
  87. Rutten GJM, Ramsey NF, van Rijen PC, Noordmans HJ, van Veelen CWM. Development of a functional magnetic resonance imaging protocol for intraoperative localization of critical temporoparietal language areas. *Ann Neurol.* 2002;51(3):350–60.
  88. Janeczek JK, Swanson SJ, Sabsevitz DS, Hammeke TA, Raghavan M, Mueller W, et al. Naming outcome prediction in patients with discordant Wada and fMRI language lateralization. *Epilepsy Behav.* 2013;27(2):399–403.
  89. Hickok G, Poeppel D. The cortical organization of speech processing. *Nat Rev Neurosci.* 2007;8(5):393–402.
  90. Binder JR. The Wernicke area: modern evidence and a reinterpretation. *Neurology.* 2015;85(24):2170–5.
  91. Benjamin CF, Walsham PD, Hale K, Gaillard WD, Baxter LC, Berl MM, et al. Presurgical language fMRI: mapping of six critical regions. *Hum Brain Mapp.* 2017;38(8):4239–55.
  92. Lazar RM, Antoniello D. Variability in recovery from aphasia. *Curr Neurol Neurosci Rep.* 2008;8(6):497–502.
  93. Dronkers NF, Plaisant O, Iba-Zizen MT, Cabanis EA. Paul Broca's historic cases: high resolution MR imaging of the brains of Leborgne and Lelong. *Brain J Neurol.* 2007;130(Pt 5):1432–41.
  94. Black DF, Vachha B, Mian A, Faro SH, Maheshwari M, Sair HI, et al. American Society of Functional Neuroradiology—recommended fMRI paradigm algorithms for presurgical language assessment. *Am J Neuroradiol.* 2017;38(10):E65–73.
  95. Binder JR, Swanson SJ, Hammeke TA, Morris GL, Mueller WM, Fischer M, et al. Determination of language dominance using functional MRI: a comparison with the Wada test. *Neurology.* 1996;46(4):978–84.
  96. Desmond JE, Sum JM, Wagner AD, Demb JB, Shear PK, Glover GH, et al. Functional MRI measurement of language lateralization in Wada-tested patients. *Brain J Neurol.* 1995;118(Pt 6):1411–9.
  97. Chang EF, Breshears JD, Raygor KP, Lau D, Molinaro AM, Berger MS. Stereotactic probability and variability of speech arrest and anomia sites dur-



- ing stimulation mapping of the language dominant hemisphere. *J Neurosurg.* 2017;126(1):114–21.
98. Broca P. Perte de la parole. Ramollissement chronique et destruction partielle du lobe antérieur gauche du cerveau. 1861 Jan 1 [cited 2018 Aug 3]. Available from: <https://www.scienceopen.com/document?vid=29af89a0-0d10-4792-ae83-f65355456d0d>.
  99. Tate MC, Herbet G, Moritz-Gasser S, Tate JE, Duffau H. Probabilistic map of critical functional regions of the human cerebral cortex: Broca's area revisited. *Brain J Neurol.* 2014;137(Pt 10):2773–82.
  100. Benzagmout M, Gatignol P, Duffau H. Resection of World Health Organization Grade II gliomas involving Broca's area: methodological and functional considerations. *Neurosurgery.* 2007;61(4):741–52; discussion 752–3.
  101. Plaza M, Gatignol P, Leroy M, Duffau H. Speaking without Broca's area after tumor resection. *Neurocase.* 2009;15(4):294–310.
  102. Friederici AD, Opitz B, von Cramon DY. Segregating semantic and syntactic aspects of processing in the human brain: an fMRI investigation of different word types. *Cereb Cortex (New York, NY: 1991).* 2000;10(7):698–705.
  103. Sahin NT, Pinker S, Cash SS, Schomer D, Halgren E. Sequential processing of lexical, grammatical, and phonological information within Broca's area. *Science.* 2009;326(5951):445–9.
  104. Tettamanti M, Weniger D. Broca's area: a supramodal hierarchical processor? *Cortex.* 2006;42(4):491–4.
  105. Lurito JT, Kareken DA, Lowe MJ, Chen SH, Mathews VP. Comparison of rhyming and word generation with fMRI. *Hum Brain Mapp.* 2000;10(3):99–106.
  106. Stippich C, Mohammed J, Kress B, Hähnel S, Günther J, Konrad F, et al. Robust localization and lateralization of human language function: an optimized clinical functional magnetic resonance imaging protocol. *Neurosci Lett.* 2003;346(1–2):109–13.
  107. Stippich C, Rapps N, Dreyhaupt J, Durst A, Kress B, Nennig E, et al. Localizing and lateralizing language in patients with brain tumors: feasibility of routine preoperative functional MR imaging in 81 consecutive patients. *Radiology.* 2007;243(3):828–36.
  108. Yagmurlu K, Middlebrooks EH, Tanriover N, Rhoton AL. Fiber tracts of the dorsal language stream in the human brain. *J Neurosurg.* 2016;124(5):1396–405.
  109. Ius T, Angelini E, Thiebaut de Schotten M, Mandonnet E, Duffau H. Evidence for potentials and limitations of brain plasticity using an atlas of functional resectability of WHO grade II gliomas: towards a “minimal common brain”. *NeuroImage.* 2011;56(3):992–1000.
  110. van Geemen K, Herbet G, Moritz-Gasser S, Duffau H. Limited plastic potential of the left ventral premotor cortex in speech articulation: evidence from intraoperative awake mapping in glioma patients. *Hum Brain Mapp.* 2014;35(4):1587–96.
  111. Chao LL, Martin A. Representation of manipulable man-made objects in the dorsal stream. *NeuroImage.* 2000;12(4):478–84.
  112. Fernández G, de Greiff A, von Oertzen J, Reuber M, Lun S, Klaver P, et al. Language mapping in less than 15 minutes: real-time functional MRI during routine clinical investigation. *NeuroImage.* 2001;14(3):585–94.
  113. Roux F-E, Dufor O, Giussani C, Wamain Y, Draper L, Longcamp M, et al. The graphemic/motor frontal area Exner's area revisited. *Ann Neurol.* 2009;66(4):537–45.
  114. Anderson SW, Damasio AR, Damasio H. Troubled letters but not numbers. Domain specific cognitive impairments following focal damage in frontal cortex. *Brain J Neurol.* 1990;113(Pt 3):749–66.
  115. Dronkers NF. A new brain region for coordinating speech articulation. *Nature.* 1996;384(6605):159–61.
  116. Baldo JV, Wilkins DP, Ogar J, Willock S, Dronkers NF. Role of the precentral gyrus of the insula in complex articulation. *Cortex J Devoted Study Nerv Syst Behav.* 2011;47(7):800–7.
  117. Eickhoff SB, Heim S, Zilles K, Amunts K. A systems perspective on the effective connectivity of overt speech production. *Philos Trans A Math Phys Eng Sci.* 2009;367(1896):2399–421.
  118. Riecker A, Brendel B, Ziegler W, Erb M, Ackermann H. The influence of syllable onset complexity and syllable frequency on speech motor control. *Brain Lang.* 2008;107(2):102–13.
  119. Tremblay P, Dick AS. Broca and Wernicke are dead, or moving past the classic model of language neurobiology. *Brain Lang.* 2016;162:60–71.
  120. Wernicke C. *Der aphasische Symptomencomplex: eine psychologische Studie auf anatomischer Basis.* Breslau: Cohn & Weigert; 1874. 80 p.
  121. Dronkers NF, Wilkins DP, Van Valin RD, Redfern BB, Jaeger JJ. Lesion analysis of the brain areas involved in language comprehension. *Cognition.* 2004;92(1–2):145–77.
  122. Leonard MK, Chang EF. Dynamic speech representations in the human temporal lobe. *Trends Cogn Sci.* 2014;18(9):472–9.
  123. Pillay SB, Stengel BC, Humphries C, Book DS, Binder JR. Cerebral localization of impaired phonological retrieval during rhyme judgment. *Ann Neurol.* 2014;76(5):738–46.
  124. Kurowski K, Blumstein SE. Phonetic basis of phonemic paraphasias in aphasia: evidence for cascading activation. *Cortex J Devoted Study Nerv Syst Behav.* 2016;75:193–203.
  125. Klein AP, Sabsevitz DS, Ulmer JL, Mark LP. Imaging of cortical and white matter language processing. *Semin Ultrasound CT MR.* 2015;36(3):249–59.
  126. Upadhyay J, Silver A, Knaus TA, Lindgren KA, Ducros M, Kim D-S, et al. Effective and structural connectivity in the human auditory cortex. *J Neurosci.* 2008;28(13):3341–9.
  127. Zacà D, Nickerson JP, Deib G, Pillai JJ. Effectiveness of four different clinical fMRI paradigms for preop-

- erative regional determination of language lateralization in patients with brain tumors. *Neuroradiology*. 2012;54(9):1015–25.
128. Binder JR, Desai RH, Graves WW, Conant LL. Where is the semantic system? A critical review and meta-analysis of 120 functional neuroimaging studies. *Cereb Cortex (New York, NY)*. 2009;19(12):2767–96.
  129. Hartwigsen G, Baumgaertner A, Price CJ, Koehnke M, Ulmer S, Siebner HR. Phonological decisions require both the left and right supramarginal gyri. *Proc Natl Acad Sci*. 2010;107(38):16494–9.
  130. Brennan NP, Peck KK, Holodny A. Language mapping using fMRI and direct cortical stimulation for brain tumor surgery: the good, the bad, and the questionable. *Top Magn Reson Imaging*. 2016;25(1):1–10.
  131. Maldonado IL, Moritz-Gasser S, de Champfleury NM, Bertram L, Moulinié G, Duffau H. Surgery for gliomas involving the left inferior parietal lobule: new insights into the functional anatomy provided by stimulation mapping in awake patients. *J Neurosurg*. 2011;115(4):770–9.
  132. Benson DF. Aphasia, alexia, and agraphia; 1928. Free Download, Borrow, and Streaming: Internet Archive [Internet] [cited 2018 Aug 16]. Available from: <https://archive.org/details/aphasiaalexiaagr00bens>.
  133. Corina DP, Loudermilk BC, Detwiler L, Martin RF, Brinkley JF, Ojemann G. Analysis of naming errors during cortical stimulation mapping: implications for models of language representation. *Brain Lang*. 2010;115(2):101–12.
  134. Middlebrooks EH, Yagmurlu K, Szaflarski JP, Rahman M, Bozkurt B. A contemporary framework of language processing in the human brain in the context of preoperative and intraoperative language mapping. *Neuroradiology*. 2017;59(1):69–87.
  135. Binder JR, Frost JA, Hammeke TA, Bellgowan PS, Springer JA, Kaufman JN, et al. Human temporal lobe activation by speech and nonspeech sounds. *Cereb Cortex (New York, NY)*. 1991;2000;10(5):512–28.
  136. Ashtari M, Lencz T, Zuffante P, Bilder R, Clarke T, Diamond A, et al. Left middle temporal gyrus activation during a phonemic discrimination task. *Neuroreport*. 2004;15(3):389–93.
  137. Bi Y, Wei T, Wu C, Han Z, Jiang T, Caramazza A. The role of the left anterior temporal lobe in language processing revisited: evidence from an individual with ATL resection. *Cortex J Devoted Study Nerv Syst Behav*. 2011;47(5):575–87.
  138. Binder JR, Gross WL, Allendorfer JB, Bonilha L, Chapin J, Edwards JC, et al. Mapping anterior temporal lobe language areas with fMRI: a multicenter normative study. *NeuroImage*. 2011;54(2):1465–75.
  139. Barnett A, Marty-Dugas J, McAndrews MP. Advantages of sentence-level fMRI language tasks in presurgical language mapping for temporal lobe epilepsy. *Epilepsy Behav*. 2014;32:114–20.
  140. Binder JR, Frost JA, Hammeke TA, Bellgowan PS, Rao SM, Cox RW. Conceptual processing during the conscious resting state. A functional MRI study. *J Cogn Neurosci*. 1999;11(1):80–95.
  141. Wilson SM, Lam D, Babiak MC, Perry DW, Shih T, Hess CP, et al. Transient aphasias after left hemisphere resective surgery. *J Neurosurg*. 2015;123(3):581–93.
  142. Cohen L, Lehericy S, Chochon F, Lemer C, Rivaud S, Dehaene S. Language-specific tuning of visual cortex? Functional properties of the Visual Word Form Area. *Brain J Neurol*. 2002;125(Pt 5):1054–69.
  143. Dehaene S, Le Clec'H G, Poline J-B, Le Bihan D, Cohen L. The visual word form area: a prelexical representation of visual words in the fusiform gyrus. *Neuroreport*. 2002;13(3):321–5.
  144. Gaillard R, Naccache L, Pinel P, Clémenceau S, Volle E, Hasboun D, et al. Direct intracranial, FMRI, and lesion evidence for the causal role of left inferotemporal cortex in reading. *Neuron*. 2006;50(2):191–204.
  145. Ischebeck A, Indefrey P, Usui N, Nose I, Hellwig F, Taira M. Reading in a regular orthography: an FMRI study investigating the role of visual familiarity. *J Cogn Neurosci*. 2004;16(5):727–41.
  146. Bruhn H, Kleinschmidt A, Boecker H, Merboldt K-D, Hänicke W, Frahm J. The effect of acetazolamide on regional cerebral blood oxygenation at rest and under stimulation as assessed by MRI. *J Cereb Blood Flow Metab*. 1994;14(5):742–8.
  147. Seifritz E, Bilecen D, Hänggi D, Haselhorst R, Radü EW, Wetzel S, et al. Effect of ethanol on BOLD response to acoustic stimulation: implications for neuropharmacological fMRI. *Psychiatry Res*. 2000;99(1):1–13.
  148. Laurienti PJ, Field AS, Burdette JH, Maldjian JA, Yen Y-F, Moody DM. Dietary caffeine consumption modulates fMRI measures. *NeuroImage*. 2002;17(2):751–7.
  149. Huettel SA, Singerman JD, McCarthy G. The effects of aging upon the hemodynamic response measured by functional MRI. *NeuroImage*. 2001;13(1):161–75.
  150. D'Esposito M, Zarahn E, Aguirre GK, Rypma B. The effect of normal aging on the coupling of neural activity to the bold hemodynamic response. *NeuroImage*. 1999;10(1):6–14.
  151. Carusone LM, Srinivasan J, Gitelman DR, Mesulam MM, Parrish TB. Hemodynamic response changes in cerebrovascular disease: implications for functional MR imaging. *AJNR Am J Neuroradiol*. 2002;23(7):1222–8.
  152. Krings T, Reinges MHT, Willmes K, Nuerk HC, Meister IG, Gilsbach JM, et al. Factors related to the magnitude of T2\* MR signal changes during functional imaging. *Neuroradiology*. 2002;44(6):459–66.
  153. Hou BL, Bradbury M, Peck KK, Petrovich NM, Gutin PH, Holodny AI. Effect of brain tumor neovascularity defined by rCBV on BOLD fMRI activation

- volume in the primary motor cortex. *NeuroImage*. 2006;32(2):489–97.
154. Ulmer JL, Krouwer HG, Mueller WM, Ugurel MS, Kocak M, Mark LP. Pseudo-reorganization of language cortical function at fMR imaging: a consequence of tumor-induced neurovascular uncoupling. *AJNR Am J Neuroradiol*. 2003;24(2):213–7.
155. Schreiber A, Hubbe U, Ziyeh S, Hennig J. The influence of gliomas and nonglial space-occupying lesions on blood-oxygen-level-dependent contrast enhancement. *AJNR Am J Neuroradiol*. 2000;21(6):1055–63.
156. Chen CM, Hou BL, Holodny AI. Effect of age and tumor grade on BOLD functional MR imaging in preoperative assessment of patients with glioma. *Radiology*. 2008;248(3):971–8.
157. Zacà D, Jovicich J, Nadar SR, Voyvodic JT, Pillai JJ. Cerebrovascular reactivity mapping in patients with low grade gliomas undergoing presurgical sensorimotor mapping with BOLD fMRI. *J Magn Reson Imaging*. 2014;40(2):383–90.
158. Li TQ, Kastrup A, Takahashi AM, Moseley ME. Functional MRI of human brain during breath holding by BOLD and FAIR techniques. *NeuroImage*. 1999;9(2):243–9.
159. Jungreis CA, Horton JA, Hecht ST. Blood pressure changes in feeders to cerebral arteriovenous malformations during therapeutic embolization. *AJNR Am J Neuroradiol*. 1989;10(3):575–7.
160. Lehericy S, Biondi A, Sourour N, Vlaicu M, du Montcel ST, Cohen L, et al. Arteriovenous brain malformations: is functional MR imaging reliable for studying language reorganization in patients? Initial observations. *Radiology*. 2002;223(3):672–82.
161. Lazar RM, Marshall RS, Pile-Spellman J, Hacein-Bey L, Young WL, Mohr JP, et al. Anterior translocation of language in patients with left cerebral arteriovenous malformation. *Neurology*. 1997;49(3):802–8.
162. Alkadhi H, Kollias SS, Crelier GR, Golay X, Hepp-Reymond MC, Valavanis A. Plasticity of the human motor cortex in patients with arteriovenous malformations: a functional MR imaging study. *AJNR Am J Neuroradiol*. 2000;21(8):1423–33.



# Positron Emission Tomography

# 20

Martin W. Huellner, Daniele A. Pizzuto,  
Philipp C. Mächler, and Tetsuro Sekine

## Contents

20.1	<b>PET: Technical Principles</b> .....	286
20.1.1	Radiotracers .....	286
20.1.2	Scanning .....	286
20.1.3	Detection .....	286
20.1.4	Crystals .....	287
20.1.5	Photodetectors .....	287
20.1.6	Signal Processing .....	287
20.1.7	Attenuation Correction .....	287
20.1.8	Scatter Coincidence and Random Coincidence Correction .....	288
20.1.9	Time of Flight (TOF) .....	288
20.1.10	Reconstruction Software .....	288
20.2	<b>Digital PET</b> .....	289
20.3	<b>Attenuation Correction Techniques</b> .....	289
20.4	<b>Motion Correction Techniques</b> .....	290
20.5	<b>Partial Volume Correction Using MRI</b> .....	290
20.6	<b>Dynamic PET Acquisition</b> .....	291
20.7	<b>PET Radiotracers for Neuroimaging</b> .....	292
20.7.1	FDG .....	292

M. W. Huellner (✉) · P. C. Mächler  
Department of Nuclear Medicine, University Hospital  
Zurich, University of Zurich, Zurich, Switzerland  
e-mail: [martin.huellner@usz.ch](mailto:martin.huellner@usz.ch); [philipp.maechler@usz.ch](mailto:philipp.maechler@usz.ch)

D. A. Pizzuto  
Department of Nuclear Medicine, University Hospital  
Zurich, University of Zurich, Zurich, Switzerland

Policlinico "A. Gemelli", Scuola di Specializzazione  
in Medicina Nucleare, Rome, Italy  
e-mail: [daniele.pizzuto@usz.ch](mailto:daniele.pizzuto@usz.ch)

T. Sekine  
Department of Radiology, Nippon Medical School,  
Tokyo General Hospital, Tokyo, Japan

20.7.2	Amino Acid Radiotracers .....	296
20.7.3	DOTA-Based Radiotracers .....	297
20.7.4	DOPA .....	298
20.7.5	Raclopride .....	299
20.7.6	Amyloid Radiotracers .....	300
20.7.7	Tau Radiotracers .....	301
20.7.8	Perfusion Radiotracers .....	301
20.7.9	Other PET Radiotracers for Neuroimaging .....	302
20.8	<b>Summary</b> .....	302
20.9	<b>Clinical Case</b> .....	303
	<b>References</b> .....	303

## 20.1 PET: Technical Principles

### 20.1.1 Radiotracers

PET imaging relies on different radiopharmaceuticals (thereafter termed “radiotracers”). A radiotracer consists of two parts, a molecule of interest to determine the distribution within the body, and a radioactive isotope that provides the signal that can be measured. The molecule of interest could provide information on various properties and functions of target tissues, such as glucose consumption, receptor expression, membrane turnover, or tissue perfusion. In some instances, e.g.  $^{15}\text{O}$ -labeled oxygen, both constituents of the radiotracer may be identical. The most commonly applied radiotracer is 2-deoxy-2-[ $^{18}\text{F}$ ]fluoroglucose ( $^{18}\text{F}$ -FDG), a glucose analog. For example,  $^{18}\text{F}$ -FDG may be used to discriminate benign from malignant neoplastic lesions or to assess response to therapy (e.g., chemotherapy, radiotherapy), mainly by determining the standardized uptake value (SUV) of a lesion. The SUV is the ratio of the radioactivity concentration (e.g., of  $^{18}\text{F}$ -FDG) within a region of interest (ROI) and the administered radioactivity, normalized to the body weight of a patient.

### 20.1.2 Scanning

After the intravenous injection of the radiotracer, a patient can be scanned directly, allowing dynamic processes to be analyzed. More com-

mon, however, a standardized uptake (or waiting) time is scheduled before the PET scan. This allows the radiotracer to distribute throughout the body, be taken up by cells, and/or connect to e.g. receptors of interest. Optimal uptake times are determined in clinical studies, taking into account the injected radiotracer dose, half-life of the radioisotope, and the time needed to reach an optimal target-to-background ratio (TBR).

After the uptake time, the patient is positioned in the PET scanner, inside a stationary ring of detectors with a diameter of 60–70 cm and an axial extent of approximately 15–25 cm. A whole-body scan then comprises several (usually eight to six) steps or bed positions to cover a region from the skull base to the mid thighs, although other acquisition methods do exist. The duration of a PET scan depends on several factors, such as the clinical question, the body region of interest, the injected dose, and the required signal to noise. It typically ranges from several minutes per bed position up to 1 h in dynamic scans. CT or MR scans can be acquired synchronously or sequentially in relation to the PET scan [1, 2]. Commonly scanned body regions in neuroimaging are the brain, head/neck, and spine.

### 20.1.3 Detection

The radioisotopes attached to the radiotracer continuously undergo radioactive decay, thereby emitting positrons. Depending on the radioisotope and tissue, the positron travels up to several

millimeters while slowing down, before it can interact and annihilate with an electron. Each annihilation phenomenon typically produces two high-energy (511 keV) gamma photons traveling at approximately opposite directions ( $\sim 180^\circ$ ) and with the speed of light. Two opposite detectors elements, located in the detector ring surrounding the patient, can then detect these two photons. The detection of the high-energy photons in a PET scanner is usually a two-step process: First, the high-energy photons are stopped and converted to (multiple) low-energy photons such as visible or ultraviolet light, in a so-called scintillator crystal. In the second step, the low-energy photons enter photodetectors, which convert the light signals into electrical signals.

#### 20.1.4 Crystals

Currently, the most widely used crystals are based on bismuth germinate (BGO). This material is often applied in conventional PET scanners. Cerium-doped lutetium oxyorthosilicate (LSO) and lutetium-yttrium oxyorthosilicate (LYSO) crystals are used in faster, but more expensive, detector systems [3].

#### 20.1.5 Photodetectors

Photomultiplier tubes (PMT) already exist for almost 100 years and are still the most commonly applied photodetectors. The major disadvantages of PMTs include their relatively large size, high voltage operation, power consumption, and their high sensitivity to magnetic fields. Due to the latter, PMTs are not compatible with integrated PET/MR systems. Early PET/MR systems therefore applied silicon, semiconductor-based, avalanche photodiodes (APDs) for photon detection. APDs are, however, relatively slow and have a low gain compared to modern PMTs. More recently, silicon photomultipliers (SiPMs) have been developed that have properties similar to PMTs (fast, high gain) [4]. A SiPM is basically an array containing 3k–8k miniature APDs operating in Geiger mode (G-APDs). Each cell in a SiPM

operates as an independent photon counter. The number of cells that “fire” within a short time frame is related to the energy of the detected photons. Adding all signals (or discharge currents) from these cells together results in an “analog” signal that is timed, measured, and converted to a digital signal in a following signal processing step. Fully digital detectors (dSiPMs) on the other hand, count the number of cells that fire within a short time frame, to generate these output signals. Although modern PMTs have excellent properties, SiPMs are increasingly applied also in PET/CT systems. The biggest disadvantage of silicon photomultipliers is their sensitivity to temperature. Therefore they are often (water) cooled to stabilize and control their temperature.

#### 20.1.6 Signal Processing

When two opposite detectors detect a photon within a specific coincidence time window, approximately 2 ns, and when the energy of the photons is around the expected 511 keV, the event is registered as a “true” coincidence event. In this case, the annihilation event took place somewhere along the virtual line connecting the two detectors, the line-of-response (LOR) [4]. After detecting many LORs, reconstruction software is able to estimate the actual activity distribution in the patient.

#### 20.1.7 Attenuation Correction

The further the high-energy (511 keV) gamma photons have to travel through the patient’s tissue, the higher the probability that at least one of the two photons interacts with the tissue. The most common interaction is Compton scattering, in which a photon loses energy and is deflected from its original path. As a result, it could be that the photon is scattered outside the field of view of the detector ring and thus not detected by a detector, or that the photon is rejected by the detector due to its lower remaining energy. In both cases, it means that the signal from this annihilation region is attenuated.

To correct for this signal loss, tissue attenuation factors can be obtained by acquiring a transmission scan. Previously,  $^{68}\text{Ge}$  sources were rotated around a patient for this purpose. This time-consuming process was later replaced by a *low-dose* CT acquisition. The approximately 70 keV X-ray photons in the obtained data set are then bilinear scaled to 511 keV gamma photons to obtain a PET attenuation map. In PET/MR, attenuation correction is more complicated. For the head region, atlas-based methods are often applied that register a population-averaged CT with the corresponding attenuation map to the scanned MR data set of the patient. In other body parts, Dixon-based methods are often applied to segment MR data sets into air/soft tissue/fat regions that are assigned corresponding attenuation factors to obtain a PET attenuation map. Latest PET/MR scanner software also includes zero time to echo (ZTE) protocols that enable bone tissue to be segmented and included into the MR-based attenuation map.

### 20.1.8 Scatter Coincidence and Random Coincidence Correction

The detection of one or two scattered photons results in an incorrect LOR. Single scatter simulation models and other complex techniques have been developed in an attempt to correct for these artifacts.

Random coincidences may occur when two photons that originated from different annihilation events are detected while their counterparts were, e.g., not detected. This will also result in an incorrect LOR. The random coincidence rate is proportional to the coincidence time window and the single rates of both detectors. Random coincidence correction can therefore be estimated from the measured data but it can also be obtained from models.

### 20.1.9 Time of Flight (TOF)

Conventional PET scanners with low coincidence timing resolution detectors ( $>1$  ns) can for each annihilation event only assume a uniform location proba-

bility along the LOR, within the patient body [5]. PET scanners with high coincidence timing resolution detectors on the other hand can measure the time difference between the two photons arriving in the detectors with a certain temporal accuracy. This “time-of-flight” (TOF) information can be used to “pinpoint” the location of annihilation along the LOR with a certain spatial precision [6, 7]. The spatial uncertainty for a conventional 1 ns detector is approximately 15 cm. Fast TOF detectors have a temporal resolution of approximately 400 ps, which corresponds to a 6 cm spatial uncertainty [8]. The improved localization of annihilation events leads to reduced noise correlation during image reconstruction.

### 20.1.10 Reconstruction Software

After detecting many coincidence events or LORs, image reconstruction software is applied to create image data sets that represent the estimated spatial distribution of activity in the patient. Filtered back projection is a basic reconstruction algorithm used since the mid-1970s [9]. In later years, maximum likelihood (ML) with expectation–maximization (EM)-based algorithms allowed the inclusion of accurate statistical Poisson-based noise models and physical modeling, which led to an improvement in artifacts, noise, and resolution [10–15]. The ML–EM algorithms are accurate but require significant computing power per iteration and many iterations before convergence is reached. Ordered subset expectation maximization (OSEM) algorithms were therefore developed [16]. These divide the measured data in subsets and apply the EM algorithm to each subset, before the next iteration starts [17]. This could lead to nonuniform recovery of activity as different image regions converge at different rates [18]. As a result, there can be inaccuracies in a quantitative assessment.

Another class of reconstruction algorithms is the regularized iterative reconstruction methods. These penalized likelihood image reconstruction methods, such as block sequential regularized expectation maximization (BSREM), add to the likelihood function a penalty function (e.g., Bayesian penalized likelihood) that can control image quality and noise within the iterative

reconstruction [17, 19–22]. BSREM is the algorithm that aims to solve this objective function. The penalty allows the BSREM algorithm to iterate until full convergence is reached. The penalty can be adjusted manually on the console by applying different  $\beta$ -factors. By this, one can balance image characteristics such as noise, smoothness of contours and SUV, and hence can “personalize” the reconstruction depending on positron energy, radiotracer dosage, body region of interest, and body size of the patient. Recent improvements on BSREM resulted in higher signal-to-noise ratio and higher SUV compared to OSEM [23–29]. The increased computing power needed for BSREM, however, requires a recent reconstruction computer.

---

## 20.2 Digital PET

A digital PET system either digitizes crystal scintillation pulses using analog-to-digital converters (ADC) and time-to-digital converters (TDC), or by direct photon counting without using ADC. Digital PET detectors are based on silicon and do work within the magnetic field of an MRI scanner, maintaining a high gain and a favorable coincidence timing resolution, leading to a high intrinsic system sensitivity. In PET/MR, these detectors have vastly replaced the older generation avalanche photodiodes, which also work in a magnetic field.

However, the main advantage of digital detectors is not their potential usage in a magnetic field, but their superior sensitivity and timing resolution compared to traditional analog detectors using PMTs. This is why there is an increasing implementation of both digital PET/CT and PET/MR scanners in clinical sites as of 2020. Digital PET has particularly advantages for the detection of small lesions, such as lymph node metastases or in-transit metastases [27, 30, 31].

---

## 20.3 Attenuation Correction Techniques

One of the most common physical effects preventing photon detection by PET scanners is photon attenuation. This degrades both quantification

and qualification of radiotracer uptake. Particularly in the head this effect becomes important because the bony skull has a high attenuation coefficient. Hence, photon attenuation needs to be corrected for precisely.

Traditionally, the attenuation coefficient for PET images was measured with an additional transmission scan using positron ( $^{68}\text{Ge}/^{68}\text{Ga}$ ) or gamma-ray ( $^{137}\text{Cs}$ ) sources [32, 33]. Such transmission scans prolong the acquisition time, which impairs clinical workflow. As an alternative, the transformation of attenuation values derived from CT into PET attenuation coefficients by hybrid or bilinear scaling was developed [34–36]. This method is reasonable in a clinical setting, because the CT scanner is an integral part of the PET/CT machine, and is clinically used to acquire anatomical information needed for exam interpretation. Hence, no additional equipment is needed. In an integrated PET/MR system, a different approach is required [37, 38]. Unlike conventional PET systems, it is difficult to implement a CT scanner or rotating point sources in a PET/MR system, owing to its strong magnetic field. As a consequence, no transmission measurements can be performed, and attenuation correction based on MR imaging is needed. As a clinically available method, four-class (i.e., air, lung, soft tissue, and fat) segmentation approaches using fat/water images derived from Dixon-based MR were initially developed [39]. However, these methods are not recommended for brain studies, because neglecting bone introduces a significant bias in the cortex [40]. It is difficult to segment bone with standard MR pulse sequences because bone tissue has very low proton density and heterogeneous structure causing fast dephasing of MR signals. Some manufacturers have clinically implemented more advanced techniques, which are classified into two groups: the direct segmentation using ultrashort time to echo (UTE) or zero time to echo (ZTE) MRI, and the indirect estimation using atlas/template methods. The first method directly captures the signal from bone as  $T2^*$  value or photon-density count, which highly corresponds to the attenuation coefficient of bone [41, 42]. The latter method utilizes low-resolution T1-weighted images to which nonrigid registration is performed from atlas or



template CT images [43–45]. The atlas/template images are predefined based on a cohort (some dozens) of normal subjects. The drawback of the atlas/template method is that it does not account for the interindividual variations of anatomy or pathology, e.g. different paranasal sinus architecture or postsurgical changes. Several novel methods have already been proposed by researchers, and recent multicenter trials validating them proved that the problem of attenuation correction based on MR images is going to be almost solved [46].

---

## 20.4 Motion Correction Techniques

Head motion during PET acquisition is an important issue because it reduces the spatial resolution and degrades image quality and quantitation capability of PET data. In addition, the misalignment between the PET raw image and the image used for attenuation correction causes severe bias in PET quantification. Particularly in PET scans for dementia patients, head motion becomes a clinical problem. Patients with Alzheimer's disease are known to present more head motion compared to normal subjects or patients with other neurodegenerative diseases (motion of  $\geq 8$  mm or  $\geq 4^\circ$ ) [47].

There are various approaches, which can reduce motion or compensate for motion. The simplest way is using head fixation devices, such as thermoplastic casts and foam head holders [48]. However, these devices cannot eliminate movement entirely, and such restrictive methods may be uncomfortable for patients. As alternative methods, motion correction based on hardware and software methods has been developed. One of the hardware methods that are used clinically is optical motion tracking during the PET scan by e.g. reflecting marks tracked by infrared cameras [49]. PET images are reconstructed combined with the position information derived from the optical device. The drawback of this method is that it impairs the clinical workflow by consuming time for setting up devices. The simplest software-based method is aligning PET images frame by

frame using a mutual information algorithm [47, 50]. For example, from a 30 min scan, six 5-min frame PET images may be generated and rigid registration may be performed with each one. However, this method does not account for motion within each frame. An additional drawback of software-based motion correction is its dependency on radiotracer activity. If the distribution of radiotracer activity changes drastically between frames, it would be difficult to co-register these frames. Currently, MR-based motion correction techniques at simultaneous PET/MR scanners are being developed [51]. During PET data acquisition, the position of the head is estimated by repeated MR scanning. Therefore, echo-planar imaging with short acquisition time (i.e., 2–3 s), or navigator echo imaging inserted in every repetition time of high-resolution MR acquisition (e.g., 3D T1-weighted imaging), is used [52].

---

## 20.5 Partial Volume Correction Using MRI

The limited spatial resolution of PET scanners leads to biased radiotracer activity due to partial volume effect (PVE). This is caused by cross-contamination between different image regions. The degree of PVE depends on the size and shape of the target and nearby regions. Particularly in patients with brain atrophy, PVE is increasingly noted because the gray matter (GM) is widely surrounded by cerebrospinal fluid (CSF) with relatively low uptake. The impact of PVE has been repeatedly evaluated in the last two decades. In 1998, Ibanez et al. applied partial volume correction (PVC) technique and revealed that cerebral glucose metabolism decline in elderly patients remains even after performing PVC, while they later reported that the decline in healthy aging is caused by atrophy, not by true metabolic reduction [53, 54]. Several partial volume correction (PVC) techniques have been proposed to recover the true activity distribution [55, 56]. These methods may be classified into two groups, the post-reconstruction methods and the reconstruction-based methods [56]. The former ones have the advantage of being easier to imple-

ment with off-line software. They are, however, inferior compared to the latter ones with regard to bias versus noise trade-off [57]. Most of these methods are image domain anatomical-based PVC techniques, which utilize other anatomical images, such as CT and MR, in order to split a voxel with mixed tissue (e.g., GM and CSF) into a single tissue type. In this anatomy-guided PVC method, accurate co-registration between PET and anatomical images is required. Hence, the benefit of PVC is expected to be higher with a PET/MR scanner, which allows for precise matching of anatomical and functional information derived from MR and PET, respectively. Moreover, the clinical workflow to use and validate PVC might be improved using a PET/MR system, where PET and MR are acquired simultaneously, and an operator could perform PVC much more easily compared to the conventional workflow (e.g., PET and MR scan acquired separately and PVC performed off-line) [56]. As a limitation, different PVC techniques and different PVC settings within one technique potentially lead to diverse results and conclusions [58]. In addition, CSF was recently found to have a surprisingly high radiotracer activity, although the vast majority of PVC methods account for CSF radiotracer activity as zero [58].

---

## 20.6 Dynamic PET Acquisition

In general clinical practice, static PET images are acquired at one single time point (e.g., 1 h after injection of FDG) for a certain time frame (e.g., 20 min). However, net uptake at a certain time after injection is a complex interplay between delivery, uptake, retention, and clearance [59]. From a single static scan, it is impossible to separate the various components that contribute to the total signal. In order to quantify physiological parameters, such as metabolism, blood flow, and neuroreceptor function, dynamic PET acquisition combined with compartment model analysis is performed [60].

In these analyses, zero-, single-, and two-tissue compartment models are used as basis for radiotracer kinetic modeling [59]. The simplest

model is a zero-tissue compartment model. For example, this model is used to quantify cerebral blood flow or volume from a  $C^{15}O$  or  $^{11}CO$  PET study [61]. CO binds to red blood cells and remains in the vascular space (no tissue compartment). The single-tissue compartment model is used where the radiotracer is taken up by an isolated tissue compartment without further interaction within the tissue (e.g.,  $C^{15}O_2$  and  $^{11}C$ -flumazenil) [62, 63]. In a two-tissue compartment model, generally the first compartment represents free and nonspecifically bound radiotracer and the second compartment represents “metabolized” (e.g.,  $^{18}F$ -FDG) or bound radiotracer (e.g.,  $^{11}C$ -raclopride) [64, 65]. All of these quantification methods require an input function from arterial blood sampling, which limits their clinical usability. As an alternative, in case of neuroreceptor studies, the reference tissue model, using a region free of the specific receptor binding can be applied [66]. In addition, image-driven arterial input function (IDAIF) methods that use the counts on the PET image itself have been developed. IDAIF may be more representative of the radiotracer concentration in local arteries and may outperform the blood AIF in some cases [67]. However, the accuracy of conventional IDAIF is limited due to partial volume effect and the difficulty of carotid artery segmentation [68]. One novel IDAIF method currently being developed is using a TOF-PET/MR system [69]. The information of magnetic resonance angiography acquired simultaneously with PET enables a segmentation of the carotid artery that is unrestricted by its movement (pulsation) or torsion based on the head position. In addition, it combines the benefit of high sensitivity and TOF capability using SiPM detectors, which provide sufficient PET image quality with low partial volume effect and background noise even with a short PET acquisition time frame.

Novel dynamic PET imaging is no more limited to one single body region, but can cover the whole body by using a stepwise repeated (dynamic) acquisition in all bed positions. Therefore, the patient is not only moved through the PET gantry and scanned once, but repeatedly.

## 20.7 PET Radiotracers for Neuroimaging

### 20.7.1 FDG

Glucose is the main energetic substrate for brain metabolism. Hence,  $^{18}\text{F}$ -FDG background uptake in the brain is very high (particularly in the cortical and deep gray matter), which interferes with the detection of metabolically active brain lesions, such as certain glial tumors, central nervous system lymphoma, or metastases. On the other hand, abnormal low  $^{18}\text{F}$ -FDG uptake is expected in brain areas affected by neurodegenerative disease and seizures in interictal state.

#### 20.7.1.1 Glial Tumors

Despite these aforementioned limitations, some evidence suggest a positive correlation between  $^{18}\text{F}$ -FDG uptake and the grade of malignancy and poorer prognosis in patients with astrocytic tumors [70]. Overall, other radiotracers such as  $^{18}\text{F}$ -fluoroethyltyrosine and  $^{18}\text{F}$ -fluorothymidine, which are imaging biomarkers of protein synthesis and cell proliferation, respectively, provide better diagnostic performance (see below) [71, 72].

#### 20.7.1.2 Central Nervous System Lymphoma

Similar to systemic lymphoma, the assessment of therapy response in patients with central nervous system (CNS) lymphoma by  $^{18}\text{F}$ -FDG PET could affect patient management and disease-specific survival. An early detection of a metabolic response (i.e., before a response is seen with morphological imaging) or lack thereof, may allow to either confirm the success of an ongoing treatment or advocate switching to a second-line treatment in the latter case [73–75]. In selected cases,  $^{18}\text{F}$ -FDG PET may be able to distinguish between glial tumors and CNS lymphoma. CNS lymphomas usually exhibit a comparably high  $\text{SUV}_{\text{max}}$  ( $>15$ ), while glial tumors and brain metastases usually have a lower  $\text{SUV}_{\text{max}}$  [76].

#### 20.7.1.3 Epilepsy

The lifetime prevalence of epilepsy is estimated to be 7–8 per 1000 persons, with an annual cumu-

lative incidence rate of 61 per 100,000 person-years [77–79]. Approximately one-third of epilepsy patients develop drug-resistant seizures after appropriate therapy [80, 81]. Surgical excision of epileptogenic foci for individuals with drug-resistant seizures was proven effective and was associated with a positive outcome with regard to seizure recurrence [82, 83]. In epilepsy, MR imaging in conjunction with electroencephalography serves as the standard of reference for localizing epileptic foci prior to surgery. MR can detect morphological abnormalities associated with epilepsy, such as mesial temporal sclerosis (MTS). However, despite an overall favorable diagnostic performance of MR [84–86], it is estimated that 20–30% of drug-resistant epilepsy patients have an equivocal or negative MR scan [87, 88].

PET with  $^{18}\text{F}$ -FDG might be helpful in the presurgical management of patients with drug-resistant epilepsy and equivocal or negative MR scan.  $^{18}\text{F}$ -FDG PET is usually performed in the interictal state, i.e. in between two seizures. While the true epileptogenic focus cannot be precisely localized in most cases, a comparably large hypometabolic area is seen surrounding around the focus, involving connected brain areas as well. Thereby, the approximate location of the seizure focus can be estimated, or at least the sidedness may be determined. Evidence of unilateral hypometabolism is considered predictive for a good outcome in patients with temporal lobe epilepsy (TLE) undergoing surgical excision.  $^{18}\text{F}$ -FDG PET also helps to rule out extratemporal epileptogenic foci prior to surgery [89].

The cause of the interictal hypometabolism is still somewhat unclear [90]. Hypometabolism may be due to neuronal loss and to the dysfunction of neuronal electric activity [91]. The lack of perfect overlap between morphological abnormalities and the hypometabolic area is related to the presence of neuronal cross-connection [92].

Opposed to temporal lobe epilepsy,  $^{18}\text{F}$ -FDG PET is limited in predicting the success of surgical procedures in patients with extra-temporal epilepsy [93]. Therefore, more invasive diagnostic tests, i.e. deep electroencephalography (DEEG) are required in extra-temporal epilepsy.

Several radiotracers may serve as alternatives to  $^{18}\text{F}$ -FDG PET in epilepsy, mainly SPECT radiotracers. One clinically used non-FDG PET radiotracer in epilepsy is  $^{11}\text{C}$ -flumazenil, which is an imaging biomarker for cerebral benzodiazepine receptor density and neuronal loss.  $^{11}\text{C}$ -flumazenil was demonstrated to provide complementary information to  $^{18}\text{F}$ -FDG PET in patients with TLE, because it allows to more precisely determine the potential epileptogenic focus [94]. However, a widespread clinical use of  $^{11}\text{C}$ -flumazenil is limited owing to availability issues, mainly due to technical and financial challenges of  $^{11}\text{C}$  radiochemistry.

#### 20.7.1.4 Neurodegenerative Diseases

Most neurodegenerative diseases that affect the brain lead to hypometabolism that can be detected using  $^{18}\text{F}$ -FDG PET. Brain atrophy, which can be detected using MR imaging, usually occurs later in the course of disease than hypometabolism. Certain neurodegenerative diseases may be diagnosed by their rather specific regional hypometabolism patterns, although this may be impaired in early disease, or may be confounded by overlap with another co-existing neurodegenerative disease [95]. Typically, patients with equivocal neuropsychological examination and without specific pathological findings on MR imaging are referred to an  $^{18}\text{F}$ -FDG PET scan.

Cerebral neurodegenerative diseases can be broadly classified into dementia and movement disorders. Dementias can further be classified into those affecting primarily the gray matter (“neurodegenerative dementia,” such as Alzheimer disease and frontotemporal lobar degeneration), those affecting primarily the white matter, e.g. metabolic disorders and encephalopathies such as multiple sclerosis or HIV encephalopathy, and those with combined gray and white matter involvement, such as vascular dementia. Movement disorders are primarily deep gray matter diseases, such as the Parkinsonian syndromes.

The most common type of neurodegenerative dementia is Alzheimer’s disease (AD). Pathogenetic events that lead to the disease start more than one decade before first clinical symptoms are seen [96]. Histopathologic hallmarks of

AD consist of extracellular deposits of  $\beta$ -amyloid plaques ( $\text{A}\beta_{40/42}$ ) and intracellular neurofibrillary tangles (NFT) of hyperphosphorylated tau proteins deposits. This finally leads to neuronal cell death (by then, extracellular NFT are seen), neurotransmission system dysfunction and parenchymal atrophy, manifesting clinically with memory loss and cognitive impairment [95, 97–99]. Several specific non-FDG PET radiotracers exist to detect pathological amyloid plaque burden and tau burden in the brains of patients (see below).

$^{18}\text{F}$ -FDG PET is the most commonly used radiotracer in AD patients. AD patients typically show profound hypometabolism in the temporoparietal area, with the posterior cingulate cortex and the precuneus being involved early on [100–104]. While in advanced disease also frontal hypometabolism is seen, the basal ganglia, the occipital cortex, and the motor cortex are typically spared. Exceptions to that rule are early-onset AD (parietal pattern) and posterior cortical atrophy (PCA, parietooccipital and temporoccipital pattern).

$^{18}\text{F}$ -FDG PET may also have a prognostic role, since it was shown able to distinguish subjects with mild cognitive impairment (MCI, a condition characterized by a single cognitive domain impairment without loss of autonomy in daily life) who are more likely to convert to AD and non-converting MCI subjects [105, 106]. However, there is some debate about the accuracy of  $^{18}\text{F}$ -FDG PET to detect MCI/AD converters, which might rather be related to the definition of MCI criteria, heterogeneous study design, and data analysis [107, 108].

$^{18}\text{F}$ -FDG PET is also used to discriminate typical and atypical AD as well as AD and other neurodegenerative dementia (see Table 20.1).

Although  $^{18}\text{F}$ -FDG PET is a feasible tool for diagnosing AD, a multidisciplinary approach consisting of neurological examination, neuropsychological tests, and brain MR imaging is recommended, mainly because  $^{18}\text{F}$ -FDG PET provides rather complementary or confirmatory information [109].

Vascular dementia (VD) is the second most common type of dementia. VD may sometimes have a sudden clinical onset and is characterized by alternating periods of relative stability and

**Table 20.1** Overview of regional PET changes of neurodegenerative diseases affecting the brain

	AD	bvFTLD	lvFTLD	VD	DLB	PD	MSA	PSP	CBD	HD
FDG PET (hypometabolism)	Temporal and parietal cortex	Frontal and temporal cortex	Frontal and temporal cortex, often asymmetric	No specific pattern, often inhomogeneous and asymmetric	Frontal and occipital cortex > temporal and parietal cortex	–	Cerebellum and bilateral putamen	Brainstem, midline frontal cortex	Parietal frontal, asymmetric	Striatum and caudate nucleus
Amyloid PET (pathologic burden)	Temporal and parietal cortex	–	–	–/+ (positive if concomitant AD)	Temporal and parietal cortex, occipital cortex	–	N/A	N/A	N/A	N/A
Tau PET (pathologic burden)	Medial inferior temporal gyrus, strong correlation with cognitive impairment	Frontal cortex	Temporal cortex	–/+ (positive if concomitant AD)	Temporal and parietal cortex, occipital cortex [214]	–	– [215]	Globus pallidum, midbrain [214]	Motor cortex, basal ganglia [214]	N/A
DOPA PET (AADC activity)	–	–	–	–	<b>Low uptake</b> in striatum	<b>Decreased</b> striatal uptake, more pronounced on clinically less affected side	Homogenous <b>low uptake</b> in striatum	Homogenous <b>low uptake</b> in striatum	<b>Low uptake</b> in striatum	– / <b>low uptake</b> in striatum
Raclopride PET (D2 receptor density)	–	–	–	–	<b>Low uptake</b> in striatum [216, 217]	<b>Increased</b> striatal uptake, more pronounced on clinically less affected side, <b>upregulation</b>	<b>Low uptake</b> in striatum [218]	<b>Low uptake</b> in striatum [218]	<b>Low uptake</b> in striatum	<b>Low uptake</b> in striatum [219]

AD Alzheimer's disease, bvFTLD behavioral variant of frontotemporal lobar degeneration, lvFTLD language variant of frontotemporal lobar degeneration, VD vascular dementia, DLB dementia with Lewy bodies, bvFTLD behavioral variant of frontotemporal lobar degeneration, MSA multiple system atrophy, PSP progressive supranuclear palsy, CBD corticobasal degeneration, HD Huntington disease

cognitive decline. Hypertension is an important risk factor for developing VD. White matter changes on MR imaging involve more than 25% of the white matter, where demyelinations and lacunes can be seen [110]. VD has no specific pattern of hypometabolism and has frequently an asymmetric involvement of cortical, subcortical, and deep structures of the brain.

Frontotemporal lobar degeneration (FTLD) represents the overall third most common type of dementia and the second most common one in patients younger than 65 years [111]. As the name implies, the typical hypometabolism pattern of FTLD involves the frontal and temporal lobes. The involved areas are responsible for behavior, personality, and speech; memory loss is mostly absent in the beginning. There are two distinct subtypes of FTLD: the behavioral variant (bvFTLD) with symmetric involvement of the

frontal and temporal lobes, and the language variant (lvFTLD), with typical asymmetric involvement (predominantly left-sided of the temporal lobe and insula). The latter variety is also termed primary progressive aphasia (PPA). It consists of three distinct subtypes with clinical and radiological differences, i.e. semantic dementia (SD, Fig. 20.1), primary non-fluent aphasia (PNFA), and logopenic PPA [112, 113]. The latter one is considered an atypical variant of Alzheimer's disease, and as such shows frequently amyloid deposition in the cortex (see below).  $^{18}\text{F}$ -FDG-PET was particularly proven reliable to discriminate between FTLD and AD, as well as between bvFTLD and lvFTLD [114].

Dementia with Lewy bodies (DLB) represents approximately 10–20% of dementias in patients older than 65 years, and is one of the atypical Parkinsonian syndromes. Besides signs of

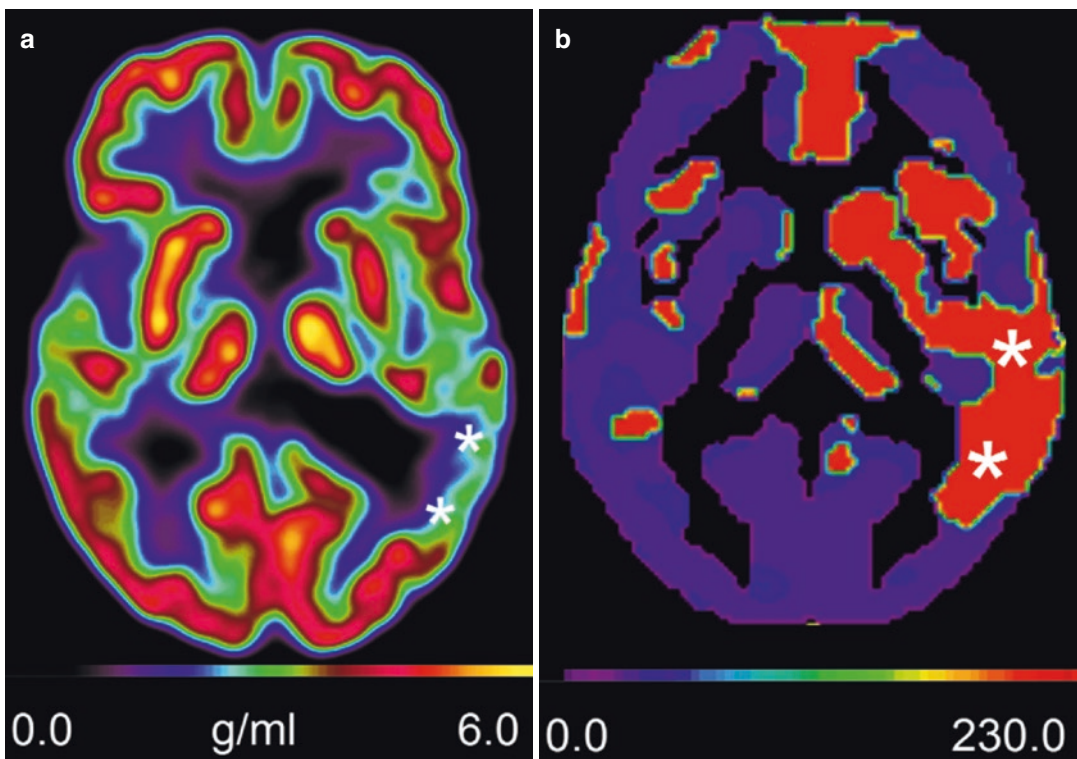


**Fig. 20.1** A 62 year-old man with semantic dementia. On the  $^{18}\text{F}$ -FDG PET image (a), asymmetric hypometabolism is seen involving the temporal lobe and the insula on the left side (asterisks). The coregistration with an age-

adjusted normals' database and Z score calculation (b) reveals that this hypometabolism (asterisks) is highly significant ( $p < 0.001$ ). The left-sided basal ganglia are affected as well

dementia, the hallmarks of DLB are optical symptoms, such as hallucinations (visual cortex involvement) or Parkinson-like symptoms (basal ganglia involvement).  $^{18}\text{F}$ -FDG-PET often reveals to some degree hypometabolism in the parietal and temporal lobes, but compared to AD, a more pronounced involvement of the frontal and occipital lobes is seen as well [115].

Multisystem atrophy of the cerebellar type (MSA-C) is characterized by varying degrees of Parkinsonism, cerebellar symptoms such as ataxia and autonomic dysfunction.  $^{18}\text{F}$ -FDG PET reveals profound hypometabolism in the cerebellum and pons, in the lentiform nuclei, and eventually in varying cortical areas [116, 117].

Patients with progressive supranuclear palsy (PSP), another atypical Parkinsonian syndrome, suffer from an upward gaze paralysis, bradykinesia, postural instability, and rigidity.  $^{18}\text{F}$ -FDG PET shows bilateral hypometabolism in the superior and medial frontal cortex, in the cingulate cortex, insula, and bilateral caudate nuclei as well as in the midbrain [116].

Corticobasal degeneration (CBD) is a rare entity and is clinically characterized by Parkinsonism symptoms associated with neurocognitive impairment. Occasionally, patients present with an alien-limb syndrome. Asymmetric hypometabolic is seen particularly in the parietal lobes. Hypometabolism may also be seen in the frontal lobes, in the cingulate cortex, in the thalamus, and striatum [116]. CBD and PSP are thought to represent different phenotypes of the same underlying disease.

Huntington disease (HD) is an uncommon type of dementia, which has an autosomal dominant pattern of inheritance with genetic anticipation. HD is typically seen in younger patients. Patients exhibit unintentional choreathetoid movements, dementia, psychosis, and emotional lability [111]. HD is a subcortical dementia with atrophy and hypometabolism, particularly of the caudate, which may lead to a widening of frontal horns of the lateral ventricles.

While  $^{18}\text{F}$ -FDG PET is a useful tool to support a clinical diagnosis of dementia or to discriminate different types of dementia by their metabolic pattern, other PET radiotracers are able to more specifically assess the viability of certain pathways involved in patients with neurodegen-

eration, such as the dopaminergic function, or amyloid and tau deposition, thereby providing complementary information in order to reach a proper diagnosis (Table 20.1).

### 20.7.1.5 Head and Neck Cancer

$^{18}\text{F}$ -FDG PET is recommended by several guidelines for the staging and restaging of patients with head and neck cancer, particularly for assessing the N and M status, and for differentiating postradiogenic changes from tumor persistence or recurrence.  $^{18}\text{F}$ -FDG PET may alter the TNM classification at initial staging in as many as 30–34% of patients [118, 119]. Also, patients with CT or MR findings suspicious for metastases may benefit from  $^{18}\text{F}$ -FDG PET before salvage treatment is initiated.  $^{18}\text{F}$ -FDG PET/CT has a high sensitivity, specificity, and accuracy (92%, 95%, and 97%, respectively) with regard to the detection of distant metastases in head and neck cancer patients [120]. Beyond the staging and restaging of known head and neck tumors,  $^{18}\text{F}$ -FDG PET may also detect second primary malignancies in up to 10% of patients [121].  $^{18}\text{F}$ -FDG PET/CT has a high accuracy in the treatment response assessment of patients with locally advanced head and neck squamous cell carcinoma (HNSCC), which directly affects the decision-making process [122].  $^{18}\text{F}$ -FDG PET/CT offers also prognostic insights, with a negative PET on 3 months follow-up after completion of radiochemotherapy indicating a low likelihood for disease recurrence within the next 2 years. Conflicting data exist about the usefulness of interim PET, i.e. PET performed after a few treatment cycles, for early response evaluation in HNSCC patients [121]. On the one hand, an SUV decrease by more than 65% at interim was reported to positively correlate with complete response. On the other hand, end of therapy PET was shown to outperform interim PET in terms of sensitivity and negative predictive value [123, 124].

### 20.7.2 Amino Acid Radiotracers

Protein synthesis and amino acid turnover are significantly altered in various brain pathologies such as malignant tumors [125]. The most common clinically used amino acid tracers are  $^{18}\text{F}$ -fluoroethyl-*L*-

tyrosine ( $^{18}\text{F}$ -FET) and  $^{11}\text{C}$ -S-methyl-*L*-methionine ( $^{11}\text{C}$ -MET) [126]. In the brain,  $^{18}\text{F}$ -FET has a favorable signal-to-background-ratio compared to  $^{18}\text{F}$ -FDG and has the benefit to accumulate to a lesser extent in inflammatory tissue [127]. However, only high-grade gliomas (WHO grade III and IV) and some low-grade oligodendrogliomas consistently exhibit increased  $^{18}\text{F}$ -FET uptake with an  $\text{SUV}_{\text{max}}$  above 2.5 and a tumor-to-background ratio (background:  $\text{SUV}_{\text{mean}}$  of contralateral cortex) above 2.0 [128]. These parameters may be used to differentiate high-grade glial tumors and lymphoma from low-grade glial tumors and non-neoplastic lesions (Fig. 20.2) [128]. They may also be used as prognostic indicators for tumor progression, as has been demonstrated for brain stem glioma [129]. In cases of equivocal static  $^{18}\text{F}$ -FET uptake, the dynamic  $^{18}\text{F}$ -FET uptake curve may be of help [130]. The dynamic PET series should cover at least the time interval from 10 to 30 min or from 20 to 40 min after radiotracer injection. An early peak activity followed by a decrease in activity (washout pattern) suggests a high-grade glioma, a lymphoma or a metastasis rather than low-grade gliomas or radionecrosis [131, 132].

A large number of other amino acid tracers such as  $^{11}\text{C}$ -carboxyl-*L*-leucine and  $^{18}\text{F}$ -fluorophenylalanine were demonstrated to accumulate significantly in brain tumors as a result of the increased expression and transport of amino acid transporters in malignant cells [133].

However, increased amino acid uptake may also be present in macrophages and gliotic tissue. This explains the accumulation of FET in non-neoplastic lesions, such as ischemia, infarcts, postradiogenic changes, and demyelinating lesions, although usually to a lesser extent than with high-grade glioma, lymphoma or brain metastasis [134, 135].

### 20.7.3 DOTA-Based Radiotracers

After the discovery that somatostatin receptor type 2 is not only expressed by neuroendocrine tumors but also by meningioma, the usage of specific ligands such as  $^{68}\text{Ga}$ -DOTA(0)-Phe(1)-Tyr(3)-octreotate (DOTATATE) and  $^{68}\text{Ga}$ -DOTA(0)-phe(1)-tyr(3)-octreotide (DOTATOC) has increased in recent years for brain PET imaging of patients with meningiomas [136]. The comparably high tumor-to-background ratio of meningioma allows an improved detection of local tissue infiltration and residual tumor after treatment. It also helps detecting tumor infiltration of structures that are sometimes difficult to assess with MR imaging after surgery, such as the venous sinuses and the skull base. DOTA-based radiotracers are also suitable for radiotherapy planning and for dose calculation before radionuclide therapy [137].

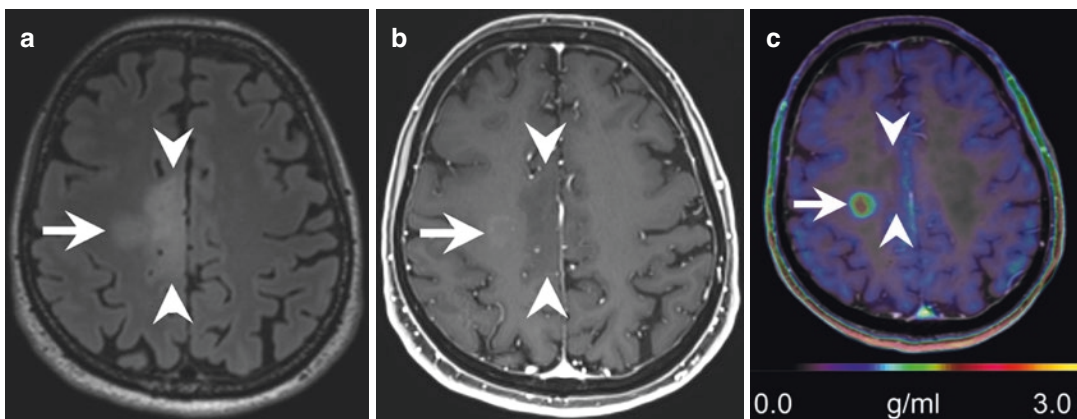


**Fig. 20.2** A 71 year-old woman with an anaplastic astrocytoma. The high-grade (WHO grade III, arrow) components of the tumor in the right-sided corona radiata exhibit high signal intensity on FLAIR-weighted MR image (a), faint contrast enhancement on T1-weighted MR image (b)

and intense uptake ( $\text{SUV}_{\text{max}}$  2.6) of  $^{18}\text{F}$ -FET on the T1-weighted PET/MR image (c). While the voluminous low-grade (WHO grade II, arrowheads) components of the tumor are hyperintense on FLAIR (a), no contrast enhancement (b) or  $^{18}\text{F}$ -FET uptake (c) is seen



### 20.7.4 DOPA

Dihydroxyphenylalanine (DOPA), synthesized from the amino acid tyrosine, represents a substrate of the synthesis of dopamine (DA), a monoamine neurotransmitter that plays a central role in dopaminergic pathways regulating movement and reward and gratification circuits. DOPA is converted into DA by the enzyme amino acid decarboxylase (AADC). DA is stored in presynaptic vesicles by vesicular monoamine transporters (VMAT) or released into the synaptic cleft or extrasynaptic space where it binds to D1 or D2 type receptors. From the synaptic cleft, DA is recycled by dopamine transporters (DAT) residing on the presynaptic membrane and is again stored by VMAT for reuse. Alternatively, dopamine may be catabolized by the enzymes monoamine oxidase (MAO) or catechol-O-methyltransferase (COMT).

$^{18}\text{F}$ -DOPA is an *L*-DOPA analog that follows the same steps in dopamine synthesis as *L*-DOPA. It is a neuroimaging marker of the integrity of dopaminergic pathways, because it reflects the activity of AADC [138]. The evaluation of dopaminergic pathways is important in patients with Parkinson disease (PD), which is characterized by a decreased availability of DA in nigrostriatal pathways, as well as in other Parkinsonian syndromes [139, 140].

Resting tremor, bradykinesia, postural instability, and rigidity are the cardinal symptoms of PD. These are often accompanied by disorders of cognition, mood, sleep, as well as olfactory and autonomic problems. The preclinical stage of PD lasts usually less than 7 years [141].

$^{18}\text{F}$ -DOPA may detect neuronal dysfunction in dopaminergic pathways even in early disease stages, and may allow differentiating Parkinsonian syndromes, including Parkinson disease, from essential tremor (ET), which might have clinical similarities. Patients with Parkinsonian syndromes show an absence of the typical comma-shaped and symmetric  $^{18}\text{F}$ -DOPA uptake in the striatum. Studies showed an inverse correlation of decreased uptake with the severity of symptoms in patients with suspected PD [142]. Dopaminergic neuronal loss was reported to be faster in PD patients than in healthy control sub-

jects. In early stages, abnormal low uptake starts to be seen in the posterior putamen, with a relative sparing of the anterior putamen and caudate nucleus [141]. Owing to fiber crossing in the brainstem, the striatum affected more severely is the one contralateral to the clinically predominant sidedness in patients with Parkinsonian syndromes [143–145].

$^{18}\text{F}$ -DOPA PET was also suggested to be useful for detecting patients with PD who are more likely to develop *L*-DOPA induced dyskinesia (LID). Patients with high dopamine turnover (owing to an imbalance between DA synthesis, storage, and release) at the baseline assessed by  $^{18}\text{F}$ -DOPA PET were shown to more likely develop LID at follow-up [146].

In clinical practice, a differential diagnosis between PD and other Parkinsonian syndromes, such as multiple system atrophy (MSA), progressive supranuclear palsy (PSP), and corticobasal degeneration (CBD) is important, because only PD patients typically respond to *L*-DOPA treatment and will have a better prognosis [116, 117]. PD and other Parkinsonian syndromes cannot reliably be differentiated based on the presynaptic dopaminergic pathway that is represented by  $^{18}\text{F}$ -DOPA, because it is impaired in all kinds of Parkinsonian syndromes. However, one study reported a different pattern of signal loss, with a homogeneously decreased  $^{18}\text{F}$ -DOPA uptake in both caudate nuclei and the putamen in MSA patients compared to an asymmetric decrease in PD patients [147]. Additional information may be derived from  $^{18}\text{F}$ -FDG PET, where usually increased uptake is seen in the striatum in PD patients, compared to decreased uptake in the striatum and other somewhat specific brain areas (see above) in patients with other Parkinsonian syndromes [116, 148, 149]. In summary, differences among MSA, PSP, and CBD in  $^{18}\text{F}$ -DOPA PET are subtle—if visible at all—in comparison to more obvious differences of hypometabolism in  $^{18}\text{F}$ -FDG PET in these diseases (see Table 20.1).

If  $^{18}\text{F}$ -FDG PET is equivocal,  $^{18}\text{F}$ -DOPA PET may help differentiate AD from DLB, which might have clinical similarities. While the hypometabolism pattern may show some overlap between these two diseases, DLB typically shows an impaired

dopaminergic pathway on  $^{18}\text{F}$ -DOPA PET, while this finding is absent in AD patients. However, differentiating DLB and PD with dementia (PDD) is challenging, both clinically and by PET imaging using  $^{18}\text{F}$ -DOPA and  $^{18}\text{F}$ -FDG [150].

Dopaminergic mesocorticolimbic pathways are involved in the gratification and reward circuit, and alterations in dopamine transmission represent an important biological substrate of pathological behavior.  $^{18}\text{F}$ -DOPA PET may be used for assessing the dopaminergic “status” of patients with neuropsychiatric disorders, such as drug or alcohol addiction or gambling. Either low or normal dopamine synthesis capacity was reported in patients with drug abuse disorders, alcohol addiction, or smokers [151–153]. Higher striatal  $^{18}\text{F}$ -DOPA uptake was demonstrated in patients with gambling addiction compared to healthy control subjects, and a positive correlation was shown between  $^{18}\text{F}$ -DOPA uptake and the duration of gambling disorders and craving [154–156]. However, altered dopaminergic pathways do not represent the whole extent of these psychiatric disorders, since other neurotransmission systems are involved as well, e.g. the GABAergic system. Hence,  $^{18}\text{F}$ -DOPA is considered a simplistic approach to these diseases.

Since DOPA and other amino acids share the same amino acid transport systems [157] and generally have a higher target-to-background ratio compared to  $^{18}\text{F}$ -FDG in the brain,  $^{18}\text{F}$ -DOPA may play a role in the assessment of brain tumors (e.g., astrocytoma and glioblastoma). Comparable diagnostic accuracy of  $^{18}\text{F}$ -DOPA and other amino acid radiotracers has been reported in patients with malignant brain lesions [158]. One important limitation of  $^{18}\text{F}$ -DOPA in this context is that lesions located close to the basal ganglia are somewhat hard to detect, owing to high physiological background uptake there.  $^{18}\text{F}$ -DOPA PET is more useful than  $^{18}\text{F}$ -FDG for the detection of head and neck paraganglioma (HNPGs), mainly owing to a lower number of false positives [159–163]. Paragangliomas are a rare neuroendocrine neoplasia that arises from parasympathetic paraganglia [164]. HNPGs typically lack the characteristic norepinephrine and epinephrine production of pheochromocytomas (“intraadrenal

paragangliomas”), but have high AADC activity, which supports the thesis that these kinds of tumors are capable of DA synthesis [165].

### 20.7.5 Raclopride

While  $^{18}\text{F}$ -DOPA PET allows for an assessment of the integrity of the presynapse and may hence differentiate Parkinsonian syndromes including PD from non-Parkinsonian diseases, it is clinically not useful for differentiating PD and other Parkinsonian syndromes. The latter task requires an assessment of the postsynapse, which is defective in atypical Parkinsonian syndromes. Hence, specific radiotracers binding postsynaptic receptors (e.g., D2) in human brain have been developed, with the first PET radiotracer used in clinical practice for dopaminergic postsynaptic imaging in humans brain being  $^{11}\text{C}$ -raclopride [166].

Owing to reduced presynaptic dopamine synthesis and reduced dopamine secretion into the synaptic cleft in PD patients, there is an overexpression of postsynaptic D2 receptors in early disease stages in order to compensate for the lack of dopamine. Hence, a  $^{11}\text{C}$ -raclopride image in a PD patient represents sort of a mirror image compared to this patient’s  $^{18}\text{F}$ -DOPA image, with high D2 receptor density seen with  $^{11}\text{C}$ -raclopride in the putamen contralateral to the clinically predominantly affected side, and a relative sparing of the ipsilateral caudate nucleus [167, 168]. Evidence suggests that there is no difference in postsynaptic receptor density before and after short-term (3–4 months) treatment with *L*-DOPA or lisuride [169]. Conversely, long-term treatment (3–5 years) may result in a loss of whole dopaminergic nerve terminals both in presynaptic and postsynaptic neurons [170].

Hence, long-term treatment may eventually lead to a loss of dopaminergic nerve terminals in presynaptic and postsynaptic neurons [171]. Patients with early-stage PD who are more likely to develop LIDs after *L*-DOPA treatment were shown to have a reduced putaminal  $^{11}\text{C}$ -raclopride binding potential, which mirrors their comparably high dopamine turnover [146, 172].

Unlike PD patients, where postsynaptic  $^{11}\text{C}$ -raclopride binding is typically upregulated, patients with other Parkinsonian syndromes, such as MSA, DLB, and PSP, show decreased postsynaptic  $^{11}\text{C}$ -raclopride binding [147] (see Table 20.1). Evidence about  $^{11}\text{C}$ -raclopride PET in CBD patients is lacking. Results of other postsynaptic radiotracers in CBD patients are controversial, and were reported as either normal or decreased striatal binding [173–175].

While high  $^{18}\text{F}$ -DOPA uptake was seen in gambling patients [154–156], several studies on this topic failed to reveal differences between D2/D3 receptor availability among gambling patients and healthy controls [155, 156, 176–178], suggesting other monoaminergic pathways may play a role here. Similarly, it is not well understood if differences in D2/D3 receptor availability are cause or consequence of addiction in drug abusers, although a positive correlation was found between D2/D3 receptor availability and trait impulsivity that induces drug-abusive behavior [154, 179, 180].

### 20.7.6 Amyloid Radiotracers

As outlined above, the preclinical stage of patients who finally develop AD may last for approximately 10–15 years. Earlier than morphological changes on MR imaging, such as atrophy, and even earlier than functional changes, such as hypometabolism seen on  $^{18}\text{F}$ -FDG PET, an abnormal deposition of A $\beta$  amyloid in the gray matter (GM) of subjects who will develop AD may be seen from early preclinical stages on [95]. Pathologic cortical A $\beta$  deposition needs to be distinguished from A $\beta$  deposition in the white matter (WM), which occurs in normal aging. Cortical A $\beta$  deposition is not specific for AD and may be seen in other neurodegenerative diseases as well, such as DLB, cerebral amyloid angiopathy (CAA), or logopenic primary progressive aphasia. On the other hand, cortical A $\beta$  deposition is seen in up to 25% of cognitively normal subjects older than 50 years and in half of normal subjects older than 80 years.

PET radiotracers that specifically bind to A $\beta$  plaques are  $^{11}\text{C}$ -Pittsburgh compound B (PIB),  $^{18}\text{F}$ -florbetapir,  $^{18}\text{F}$ -flutemetamol, and  $^{18}\text{F}$ -florbetaben [95, 181–184]. Standardized qualitative and quantitative assessment is needed to properly distinguish normal and abnormal A $\beta$  burden. Qualitative assessment refers to detection of pathological presence of A $\beta$  plaques based on loss of GM/WM contrast or higher GM signal than WM in a region greater than a cortical gyrus. The  $^{18}\text{F}$ -labeled radiotracers such as flutemetamol and florbetapir are comparable to  $^{11}\text{C}$ -PIB with regard to GM and WM retention [185].

Besides a (qualitative) visual assessment, quantification of A $\beta$  burden may help to distinguish positive and negative scans. Quantitative assessment is based on an SUV ratio between an ROI covering the suspected pathological A $\beta$  burden and an ROI of a reference region in apparently healthy brain tissue. Typical reference regions are the cerebellum (whole cerebellum or only cerebellar GM), which is used for  $^{11}\text{C}$ -PiB,  $^{18}\text{F}$ -florbetapir, and  $^{18}\text{F}$ -florbetaben PET scans [186–190], or the pons that is used for  $^{18}\text{F}$ -flutemetamol PET [191, 192]. An SUV ratio above or below a certain cut-off value allows to categorize scans as negative or positive for cortical amyloid deposition with good agreement with histopathologic classification.

An amyloid PET may be performed if knowledge of the amyloid status of a patient will potentially alter the treatment, which may be the case in subjects with equivocal findings on MR imaging,  $^{18}\text{F}$ -FDG PET, and clinical and neuropsychological tests.

Amyloid PET may be useful to discriminate AD and FTLT patients, if other modalities failed to do so. Given that the latter entity belongs to the tauopathies, an amyloid PET scan is typically negative in most FTLT patients and positive in most AD patients [193]. However, with thorough clinical and MR imaging workup, the diagnostic performance of an amyloid PET scan and an  $^{18}\text{F}$ -FDG PET scan was shown to be comparable for this task. The former is more sensitive, the latter more specific if a quantitative analysis is performed [194].

The indication for an amyloid PET scan needs to be selected carefully. For example, amyloid PET scans typically fail to distinguish DLB and AD patients, both of which showing pathological cortical A $\beta$  deposition. Patients with PDD, however, with clinical symptomatology often overlapping with AD, are more likely negative on amyloid PET [195].

In summary, amyloid imaging is very sensitive to exclude AD in early stages, but has low specificity for AD.  $^{18}\text{F}$ -FDG PET is more reliable to differentiate among neurodegenerative dementias.

### 20.7.7 Tau Radiotracers

Tau proteins play a significant role for neuronal microtubule stability, which is based on their phosphorylation status. Microtubule regulation is responsible for plasticity and integration by means of regulating axonogenesis, polarization, outgrowth, and myelination [196]. Abnormal presence of neurofibrillary tangles (NT) that derive from hyperphosphorylated tau proteins leads to various neurodegenerative disorders. NT may be present in AD, in variants of FTL, PSP, CBD, and chronic traumatic encephalopathy (CTE) [197]. Tau protein aggregates are initially found intracellularly and then also extracellularly after the death of neurons.

As outlined above, the presence of A $\beta$  plaque deposition on amyloid PET does not necessarily correlate with cognitive impairment, owing to its low specificity. Since a couple of years, tau radiotracers are increasingly used in research, but are currently not used clinically. Tau radiotracers are expected to assume a prognostic role and link functional imaging to cognitive impairment.  $^{18}\text{F}$ -AV1451 and  $^{18}\text{F}$ -THK5351 were shown able to discriminate healthy controls from AD patients, preclinical AD subjects, and subjects with MCI, with higher uptake seen in the medial and inferior temporal gyrus in AD and MCI [198–202].

Tau radiotracers may become helpful in clinical practice not only owing to their comparably high specificity to detect MCI and AD, or their strong correlation with cognitive impairment and prognosis of patients (i.e., conversion from MCI to AD), but also for understanding normal aging [196].

### 20.7.8 Perfusion Radiotracers

Perfusion can be measured with any radiotracer using a dynamic acquisition. However, there are some PET radiotracers with special characteristics, such as short half-life or binding capability to vascular contents, which make them ideal substrates for measuring perfusion, even when using a static acquisition.

While MRI is the preferred clinical method to assess cerebral ischemia, PET allows the quantification of regional cerebral blood flow (rCBF), regional cerebral blood volume (rCBV), and the cerebral perfusion reserve (PR). A brain PET with arterial blood activity sampling using  $^{15}\text{O}$  products allows for the quantification of rCBF in absolute measures (mL/100 mg/min). For clinical applications, the arterial blood sampling can be avoided using estimations of the arterial blood activity [203]. However, the short half-life of  $^{15}\text{O}$  of approximately 2 min requires an on-site cyclotron close to the PET scanner.

$\text{H}_2^{15}\text{O}$  is the most widely used tracer in PET to measure rCBF.  $\text{H}_2^{15}\text{O}$  additionally provides the measure PR, which is the calculated difference (or ratio) of rCBF under hypercapnia-induced vasodilation compared to a baseline condition. Vasodilation can be achieved either by the intravenous application of the carbonic anhydrase inhibitor acetazolamide or by inhalation of air with increased  $\text{CO}_2$  content. A stenosis of a brain artery, e.g., by an atherosclerotic plaque, can lead to symptoms such as transient ischemic attacks (TIA) or stroke. A post-stenotic reduction of blood flow can induce a compensatory vasodilation to maintain tissue

perfusion. Because regional vasodilation has an upper limit, the PR is reduced in the post-stenotic area. Patients with reduced PR have been shown to benefit from revascularization procedures such as endarterectomy, stenting, or bypass surgery [204]. Most vascular pathologies of the brain such as Moyamoya disease spare the cerebellum, which can therefore be used as a reference region indicating the normal PR of approximately 20%.

Alternative methods to quantify local cerebral blood flow are  $^{99m}\text{Tc}$ -coupled radiotracers used in SPECT imaging, such as HMPAO (hexamethylpropyleneamineoxime) and ECD (ethyl cysteinate dimer). These radiotracers get trapped intracellularly, and their accumulation can be measured between 2 min and up to 4 h after the venous injection to quantify blood flow using estimates of the extraction rate. However, estimates of the extraction rate are only relative, as they are not independent of blood flow.

The bolus inhalation of the radiotracer  $^{15}\text{O}_2$  allows for the measurement of the regional cerebral oxygen extraction fraction and the estimation of the regional cerebral metabolic rate of oxygen ( $\text{CMRO}_2$ ), which has been shown to be reduced in stroke and traumatic brain injuries [205].

The radiotracer  $\text{C}^{15}\text{O}$  allows for the measurement of rCBV. After inhalation,  $\text{C}^{15}\text{O}$  binds to intravascular hemoglobin. The ratio of brain-to-blood activity then indicates rCBV [206]. Specifically, the rCBV is pathologically increased in post-stenotic brain tissue.

### 20.7.9 Other PET Radiotracers for Neuroimaging

Several other PET radiotracers were shown to have an abnormal and often disease-specific distribution in the brain of subjects with different types of pathology. For example, ligands for receptors and transporters of the serotonin and

cholinergic system have been tested for detecting neurodegenerative disorders, such as Alzheimer's disease [207]. Another example is radiotracers for central benzodiazepine receptors, such as  $^{11}\text{C}$ -flumazenil, which have been used e.g., in epilepsy patients to localize the epileptogenic focus [208]. More recently, the cortical expression of different glutamate receptors was shown to be altered in various neurological and psychiatric diseases. This led to the development of novel PET ligands such as  $^{11}\text{C}$ -ABP688 or  $^{18}\text{F}$ -PSS232 that label metabotropic glutamate receptors subtype 5 (mGluR5) [209, 210]. Other radiotracers that have recently entered preclinical trials target  $\alpha$ -synuclein, a misfolded protein which builds up in the brains of e.g. Parkinson disease patients, and radiotracers for the synaptic density, such as  $^{11}\text{C}$ -UCB-J [211–213]. One characteristic of many PET radiotracers that are in development and/or have limited clinical indications is their complex  $^{11}\text{C}$  radiochemistry, which in turn limits their accessibility and prevents a more widespread clinical use.

---

## 20.8 Summary

In many regards, PET imaging is still an underutilized diagnostic neuroimaging modality. Its potential mainly lies in providing complementary information with regard to morphological imaging. PET is able to specifically trace pathologic changes of the CNS that are out of reach for conventional imaging such as CT or MR, e.g., glucose metabolism, postsynaptic D2 receptor density, or amyloid deposition. PET may be combined with either CT or MR imaging using a simultaneous acquisition, the latter representing the smarter approach in neuroimaging. Knowledge of specific indications for PET imaging and familiarity with the normal and abnormal distribution of specific radiotracers in the CNS will help coin-ing a proper diagnosis for your patient.

## 20.9 Clinical Case (Fig. 20.3)

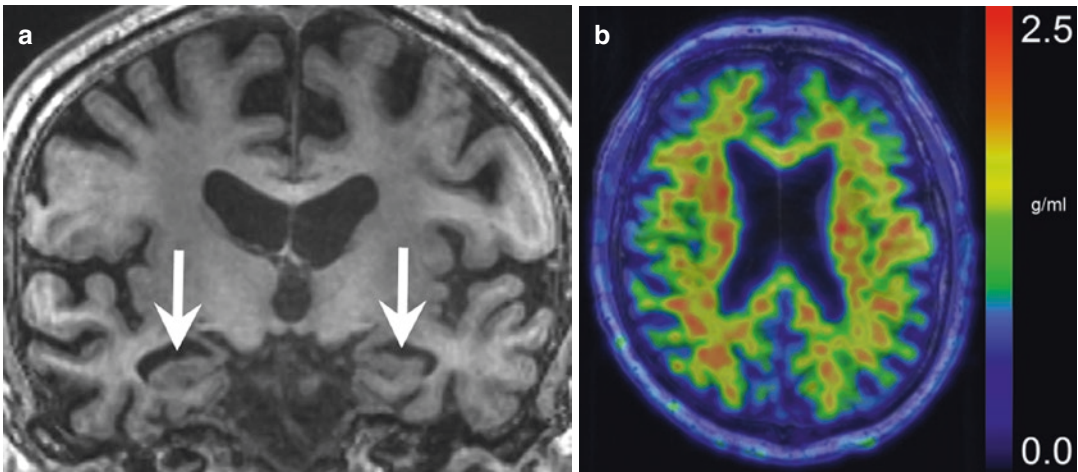


**Fig. 20.3** A 70 year-old man with high clinical suspicion of Alzheimer disease, supported by MR imaging. Global cortical atrophy is seen on the coronal T1-weighted MR image (a), with particular loss of hippocampal volume (arrows) on the left side. The T1-weighted  $^{18}\text{F}$ -flutemetamol

PET/MR image (b) reveals absence of pathologic cortical amyloid deposition, which changes the diagnosis of the patient to suspected non-Alzheimer pathology (SNAP) and alters the treatment plan

**Acknowledgment** The authors of this chapter are indebted to Edwin E.G.W. ter Voert, PhD.

### References

1. Beyer T, Townsend DW, Brun T, Kinahan PE, Charron M, Roddy R, et al. A combined PET/CT scanner for clinical oncology. *J Nucl Med.* 2000;41(8):1369–79.
2. Ng TS, Procissi D, Wu Y, Jacobs RE. A robust coregistration method for in vivo studies using a first generation simultaneous PET/MR scanner. *Med Phys.* 2010;37(5):1995–2003. <https://doi.org/10.1118/1.3369447>.
3. Nemallapudi MV, Gundacker S, Lecoq P, Auffray E, Ferri A, Gola A, et al. Sub-100 ps coincidence time resolution for positron emission tomography with LSO:Ce codoped with Ca. *Phys Med Biol.* 2015;60(12):4635–49. <https://doi.org/10.1088/0031-9155/60/12/4635>.
4. Surti S. Update on time-of-flight PET imaging. *J Nucl Med.* 2015;56(1):98–105. <https://doi.org/10.2967/jnumed.114.145029>.
5. Moses WW. Recent advances and future advances in time-of-flight PET. *Nucl Instrum Methods Phys Res A.* 2007;580(2):919–24. <https://doi.org/10.1016/j.nima.2007.06.038>.
6. Ter-Pogossian MM, Ficke DC, Hood JT Sr, Yamamoto M, Mullani NA. PETT VI: a positron emission tomograph utilizing cesium fluoride scintillation detectors. *J Comput Assist Tomogr.* 1982;6(1):125–33.
7. Ter-Pogossian MM, Ficke DC, Yamamoto M, Hood JT. Super PETT I: a positron emission tomograph utilizing photon time-of-flight information. *IEEE Trans Med Imaging.* 1982;1(3):179–87. <https://doi.org/10.1109/TMI.1982.4307570>.
8. Surti S, Karp JS. Advances in time-of-flight PET. *Phys Med.* 2016;32(1):12–22. <https://doi.org/10.1016/j.ejmp.2015.12.007>.
9. Radon J. On the determination of functions from their integral values along certain manifolds. *IEEE Trans Med Imaging.* 1986;5(4):170–6. <https://doi.org/10.1109/tmi.1986.4307775>.
10. Rockmore AJ, Macovski A. A maximum likelihood approach to emission image reconstruction from projections. *IEEE Trans Nucl Sci.* 1976;23(4):1428–32. <https://doi.org/10.1109/TNS.1976.4328496>.

11. Shepp LA, Vardi Y. Maximum likelihood reconstruction for emission tomography. *IEEE Trans Med Imaging*. 1982;1(2):113–22. <https://doi.org/10.1109/tmi.1982.4307558>.
12. Boellaard R, van Lingen A, Lammertsma AA. Experimental and clinical evaluation of iterative reconstruction (OSEM) in dynamic PET: quantitative characteristics and effects on kinetic modeling. *J Nucl Med*. 2001;42(5):808–17.
13. Johnson CA, Seidel J, Carson RE, Gandler WR, Sofer A, Green MV, et al. Evaluation of 3D reconstruction algorithms for a small animal PET camera. *IEEE Trans Nucl Sci*. 1997;44(3):1303–8. <https://doi.org/10.1109/23.597005>.
14. Shepp LA, Vardi Y, Ra JB, Hilal SK, Cho ZH. Maximum likelihood PET with real data. *IEEE Trans Nucl Sci*. 1984;31(2):910–3. <https://doi.org/10.1109/TNS.1984.4333398>.
15. Tsoumpas C, Turkheimer FE, Thielemans K. Study of direct and indirect parametric estimation methods of linear models in dynamic positron emission tomography. *Med Phys*. 2008;35(4):1299–309. <https://doi.org/10.1118/1.2885369>.
16. Hudson HM, Larkin RS. Accelerated image reconstruction using ordered subsets of projection data. *IEEE Trans Med Imaging*. 1994;13(4):601–9. <https://doi.org/10.1109/42.363108>.
17. Qi J, Leahy RM. Iterative reconstruction techniques in emission computed tomography. *Phys Med Biol*. 2006;51(15):R541–78. <https://doi.org/10.1088/0031-9155/51/15/r01>.
18. Liow JS, Strother SC. The convergence of object dependent resolution in maximum likelihood based tomographic image reconstruction. *Phys Med Biol*. 1993;38(1):55–70.
19. Asma E, Manjeshwar R, editors. Analysis of organ uniformity in low count density penalized likelihood PET images. In: 2007 IEEE Nuclear science symposium conference record, 26 Oct–3 Nov 2007.
20. Geman S, Geman D. Stochastic relaxation, Gibbs distributions, and the bayesian restoration of images. *IEEE Trans Pattern Anal Mach Intell*. 1984;6(6):721–41.
21. Geman S, McClure D, editors. Bayesian image analysis methods: an application to single photon emission computed tomography. In: Proc. statistical computation section, 1985.
22. Mumcuoglu EU, Leahy RM, Cherry SR. Bayesian reconstruction of PET images: methodology and performance analysis. *Phys Med Biol*. 1996;41(9):1777–807.
23. Ahn S, Ross SG, Asma E, Miao J, Jin X, Cheng L, et al. Quantitative comparison of OSEM and penalized likelihood image reconstruction using relative difference penalties for clinical PET. *Phys Med Biol*. 2015;60(15):5733.
24. Asma E, Ahn S, Ross SG, Chen A, Manjeshwar RM, editors. Accurate and consistent lesion quantitation with clinically acceptable penalized likelihood images. In: 2012 IEEE Nuclear science symposium and medical imaging conference record (NSS/MIC), 27 Oct–3 Nov 2012.
25. Sah BR, Stolzmann P, Delso G, Wollenweber SD, Hullner M, Hakami YA, et al. Clinical evaluation of a block sequential regularized expectation maximization reconstruction algorithm in 18F-FDG PET/CT studies. *Nucl Med Commun*. 2017;38(1):57–66. <https://doi.org/10.1097/mnm.0000000000000604>.
26. Teoh EJ, McGowan DR, Macpherson RE, Bradley KM, Gleeson FV. Phantom and clinical evaluation of the Bayesian penalized likelihood reconstruction algorithm Q.Clear on an LYSO PET/CT system. *J Nucl Med*. 2015;56(9):1447–52. <https://doi.org/10.2967/jnumed.115.159301>.
27. Aljared A, Alharbi AA, Huellner MW. BSREM reconstruction for improved detection of In-transit metastases with digital FDG-PET/CT in patients with malignant melanoma. *Clin Nucl Med*. 2018;43(5):370–1. <https://doi.org/10.1097/RLU.0000000000002024>.
28. Messerli M, Stolzmann P, Egger-Sigg M, Trinckauf J, D'Aguanno S, Burger IA, et al. Impact of a Bayesian penalized likelihood reconstruction algorithm on image quality in novel digital PET/CT: clinical implications for the assessment of lung tumors. *EJNMMI Phys*. 2018;5(1):27. <https://doi.org/10.1186/s40658-018-0223-x>.
29. Messerli M, Kotasidis F, Burger IA, Ferraro DA, Muehlemaier Urs J, Weyeremann C, et al. Impact of different image reconstructions on PET quantification in non-small cell lung cancer: A comparison of adenocarcinoma and squamous cell carcinoma. *Br J Radiol*. 2019;92(1096):20180792. <https://doi.org/10.1259/bjr.20180792>. Epub 2019 Feb 26.
30. Baratto L, Park SY, Hatami N, Davidzon G, Srinivas S, Gambhir SS, et al. 18F-FDG silicon photomultiplier PET/CT: a pilot study comparing semi-quantitative measurements with standard PET/CT. *PLoS One*. 2017;12(6):e0178936. <https://doi.org/10.1371/journal.pone.0178936>.
31. Schwyzler M, Martini K, Benz DC, Burger IA. Artificial intelligence for detecting small FDG-positive lung nodules in digital PET/CT: impact of image reconstructions on diagnostic performance. *Eur Radiol*. 2020;30(4):2031–40. <https://doi.org/10.1007/s00330-019-06498-w>.
32. Karp JS, Muehlelehner G, Qu H, Yan XH. Singles transmission in volume-imaging PET with a <sup>137</sup>Cs source. *Phys Med Biol*. 1995;40(5):929–44.
33. Bailey DL. Transmission scanning in emission tomography. *Eur J Nucl Med*. 1998;25(7):774–87.
34. Burger C, Goerres G, Schoenes S, Buck A, Lonn AH, Von Schulthess GK. PET attenuation coefficients from CT images: experimental evaluation of the transformation of CT into PET 511-keV attenuation coefficients. *Eur J Nucl Med Mol Imaging*. 2002;29(7):922–7. <https://doi.org/10.1007/s00259-002-0796-3>.
35. Kinahan PE, Hasegawa BH, Beyer T. X-ray-based attenuation correction for positron emission tomography/computed tomography scanners. *Semin Nucl*

- Med. 2003;33(3):166–79. <https://doi.org/10.1053/snuc.2003.127307>.
36. Carney JP, Townsend DW, Rappoport V, Bendriem B. Method for transforming CT images for attenuation correction in PET/CT imaging. *Med Phys*. 2006;33(4):976–83. <https://doi.org/10.1118/1.2174132>.
  37. Delso G, Nuyts J. PET/MRI: attenuation correction. In: Iagaru A, Hope T, Veit-Haibach P, editors. *PET/MRI in oncology: current clinical applications*. Cham: Springer International Publishing; 2018. p. 53–75.
  38. Werner P, Barthel H, Drzezga A, Sabri O. Current status and future role of brain PET/MRI in clinical and research settings. *Eur J Nucl Med Mol Imaging*. 2015;42(3):512–26. <https://doi.org/10.1007/s00259-014-2970-9>.
  39. Wollenweber SD, Ambwani S, Lonn AHR, Shanbhag DD, Thiruvankadam S, Kaushik S, et al. Comparison of 4-class and continuous fat/water methods for whole-body, MR-based PET attenuation correction. *IEEE Trans Nucl Sci*. 2013;60(5):3391–8. <https://doi.org/10.1109/tns.2013.2278759>.
  40. Andersen FL, Ladefoged CN, Beyer T, Keller SH, Hansen AE, Hojgaard L, et al. Combined PET/MR imaging in neurology: MR-based attenuation correction implies a strong spatial bias when ignoring bone. *NeuroImage*. 2014;84:206–16. <https://doi.org/10.1016/j.neuroimage.2013.08.042>.
  41. Aasheim LB, Karlberg A, Goa PE, Haberg A, Sorhaug S, Fagerli UM, et al. PET/MR brain imaging: evaluation of clinical UTE-based attenuation correction. *Eur J Nucl Med Mol Imaging*. 2015;42(9):1439–46. <https://doi.org/10.1007/s00259-015-3060-3>.
  42. Sekine T, Ter Voert EE, Warnock G, Buck A, Huellner M, Veit-Haibach P, et al. Clinical evaluation of zero-echo-time attenuation correction for brain 18F-FDG PET/MRI: comparison with atlas attenuation correction. *J Nucl Med*. 2016;57(12):1927–32. <https://doi.org/10.2967/jnumed.116.175398>.
  43. Koesters T, Friedman KP, Fenchel M, Zhan Y, Hermosillo G, Babb J, et al. Dixon sequence with superimposed model-based bone compartment provides highly accurate PET/MR attenuation correction of the brain. *J Nucl Med*. 2016;57(6):918–24. <https://doi.org/10.2967/jnumed.115.166967>.
  44. Sekine T, Burgos N, Warnock G, Huellner M, Buck A, Ter Voert EE, et al. Multi-atlas-based attenuation correction for brain 18F-FDG PET imaging using a time-of-flight PET/MR scanner: comparison with clinical single-atlas- and CT-based attenuation correction. *J Nucl Med*. 2016;57(8):1258–64. <https://doi.org/10.2967/jnumed.115.169045>.
  45. Sekine T, Buck A, Delso G, Ter Voert EE, Huellner M, Veit-Haibach P, et al. Evaluation of atlas-based attenuation correction for integrated PET/MR in human brain: application of a head atlas and comparison to true CT-based attenuation correction. *J Nucl Med*. 2016;57(2):215–20. <https://doi.org/10.2967/jnumed.115.159228>.
  46. Ladefoged CN, Law I, Anazodo U, St Lawrence K, Izquierdo-Garcia D, Catana C, et al. A multi-centre evaluation of eleven clinically feasible brain PET/MRI attenuation correction techniques using a large cohort of patients. *NeuroImage*. 2017;147:346–59. <https://doi.org/10.1016/j.neuroimage.2016.12.010>.
  47. Ikari Y, Nishio T, Makishi Y, Miya Y, Ito K, Koeppe RA, et al. Head motion evaluation and correction for PET scans with 18F-FDG in the Japanese Alzheimer's disease neuroimaging initiative (J-ADNI) multi-center study. *Ann Nucl Med*. 2012;26(7):535–44. <https://doi.org/10.1007/s12149-012-0605-4>.
  48. Beyer T, Tellmann L, Nickel I, Pietrzyk U. On the use of positioning aids to reduce misregistration in the head and neck in whole-body PET/CT studies. *J Nucl Med*. 2005;46(4):596–602.
  49. Studholme C, Hill DL, Hawkes DJ. Automated three-dimensional registration of magnetic resonance and positron emission tomography brain images by multiresolution optimization of voxel similarity measures. *Med Phys*. 1997;24(1):25–35. <https://doi.org/10.1118/1.598130>.
  50. Montgomery AJ, Thielemans K, Mehta MA, Turkheimer F, Mustafovic S, Grasby PM. Correction of head movement on PET studies: comparison of methods. *J Nucl Med*. 2006;47(12):1936–44.
  51. Catana C. PET/MRI: motion correction. In: Iagaru A, Hope T, Veit-Haibach P, editors. *PET/MRI in oncology: current clinical applications*. Cham: Springer International Publishing; 2018. p. 77–96.
  52. Catana C, Benner T, van der Kouwe A, Byars L, Hamm M, Chonde DB, et al. MRI-assisted PET motion correction for neurologic studies in an integrated MR-PET scanner. *J Nucl Med*. 2011;52(1):154–61. <https://doi.org/10.2967/jnumed.110.079343>.
  53. Ibanez V, Pietrini P, Furey ML, Alexander GE, Millet P, Bokde AL, et al. Resting state brain glucose metabolism is not reduced in normotensive healthy men during aging, after correction for brain atrophy. *Brain Res Bull*. 2004;63(2):147–54. <https://doi.org/10.1016/j.brainresbull.2004.02.003>.
  54. Ibanez V, Pietrini P, Alexander GE, Furey ML, Teichberg D, Rajapakse JC, et al. Regional glucose metabolic abnormalities are not the result of atrophy in Alzheimer's disease. *Neurology*. 1998;50(6):1585–93.
  55. Erlandsson K, Buvat I, Pretorius PH, Thomas BA, Hutton BF. A review of partial volume correction techniques for emission tomography and their applications in neurology, cardiology and oncology. *Phys Med Biol*. 2012;57(21):R119–59. <https://doi.org/10.1088/0031-9155/57/21/R119>.
  56. Erlandsson K, Dickson J, Arridge S, Atkinson D, Ourselin S, Hutton BF. MR imaging-guided partial volume correction of PET data in PET/MR imaging. *PET Clin*. 2016;11(2):161–77. <https://doi.org/10.1016/j.cpet.2015.09.002>.
  57. Nuyts J, Baete K, Beque D, Dupont P. Comparison between MAP and postprocessed ML for image



- reconstruction in emission tomography when anatomical knowledge is available. *IEEE Trans Med Imaging*. 2005;24(5):667–75. <https://doi.org/10.1109/tmi.2005.846850>.
58. Greve DN, Salat DH, Bowen SL, Izquierdo-Garcia D, Schultz AP, Catana C, et al. Different partial volume correction methods lead to different conclusions: an (18)F-FDG-PET study of aging. *NeuroImage*. 2016;132:334–43. <https://doi.org/10.1016/j.neuroimage.2016.02.042>.
  59. Lammertsma AA. Tracer kinetic modelling. In: Dierckx R, Otte A, de Vries EFJ, van Waarde A, Leenders KL, editors. *PET and SPECT in neurology*. Berlin: Springer; 2014. p. 59–73.
  60. Gunn RN, Gunn SR, Cunningham VJ. Positron emission tomography compartmental models. *J Cereb Blood Flow Metab*. 2001;21(6):635–52. <https://doi.org/10.1097/00004647-200106000-00002>.
  61. Phelps ME, Huang SC, Hoffman EJ, Kuhl DE. Validation of tomographic measurement of cerebral blood volume with C-11-labeled carboxy-hemoglobin. *J Nucl Med*. 1979;20(4):328–34.
  62. Frackowiak RS, Lenzi GL, Jones T, Heather JD. Quantitative measurement of regional cerebral blood flow and oxygen metabolism in man using 15O and positron emission tomography: theory, procedure, and normal values. *J Comput Assist Tomogr*. 1980;4(6):727–36.
  63. Koeppe RA, Holthoff VA, Frey KA, Kilbourn MR, Kuhl DE. Compartmental analysis of [11C]flumazenil kinetics for the estimation of ligand transport rate and receptor distribution using positron emission tomography. *J Cereb Blood Flow Metab*. 1991;11(5):735–44. <https://doi.org/10.1038/jcbfm.1991.130>.
  64. Phelps ME, Huang SC, Hoffman EJ, Selin C, Sokoloff L, Kuhl DE. Tomographic measurement of local cerebral glucose metabolic rate in humans with (F-18)2-fluoro-2-deoxy-D-glucose: validation of method. *Ann Neurol*. 1979;6(5):371–88. <https://doi.org/10.1002/ana.410060502>.
  65. Farde L, Eriksson L, Blomquist G, Halldin C. Kinetic analysis of central [11C]raclopride binding to D2-dopamine receptors studied by PET—a comparison to the equilibrium analysis. *J Cereb Blood Flow Metab*. 1989;9(5):696–708. <https://doi.org/10.1038/jcbfm.1989.98>.
  66. Blomqvist G, Pauli S, Farde L, Eriksson L, Persson A, Halldin C. Maps of receptor binding parameters in the human brain—a kinetic analysis of PET measurements. *Eur J Nucl Med*. 1990;16(4–6):257–65. <https://doi.org/10.1007/bf00842777>.
  67. Richard MA, Fouquet JP, Lebel R, Lepage M. MRI-guided derivation of the input function for PET kinetic modeling. *PET Clin*. 2016;11(2):193–202. <https://doi.org/10.1016/j.cpet.2015.09.003>.
  68. Zanotti-Fregonara P, Fadaili el M, Maroy R, Comtat C, Souloumiac A, Jan S, et al. Comparison of eight methods for the estimation of the image-derived input function in dynamic [(18)F]-FDG PET human brain studies. *J Cereb Blood Flow Metab*. 2009;29(11):1825–35. <https://doi.org/10.1038/jcbfm.2009.93>.
  69. Khalighi MM, Deller TW, Fan AP, Gulaka PK, Shen B, Singh P, et al. Image-derived input function estimation on a TOF-enabled PET/MR for cerebral blood flow mapping. *J Cereb Blood Flow Metab*. 2018;38(1):126–35. <https://doi.org/10.1177/0271678X17691784>.
  70. Del Sole A, Moncayo R, Tafuni G, Lucignani G. Position of nuclear medicine techniques in the diagnostic work-up of brain tumors. *Q J Nucl Med Mol Imaging*. 2004;48(2):76–81.
  71. Dunet V, Prior JO. Diagnostic accuracy of F-18-fluoroethyltyrosine PET and PET/CT in patients with brain tumor. *Clin Transl Imaging*. 2013;1(2):135–44. <https://doi.org/10.1007/s40336-013-0017-z>.
  72. Bertagna F, Biasiotto G, Giubbini R. The role of F-18-fluorothymidine PET in oncology. *Clin Transl Imaging*. 2013;1(2):77–97. <https://doi.org/10.1007/s40336-013-0014-2>.
  73. Mikhaeel NG, Hutchings M, Fields PA, O'Doherty MJ, Timothy AR. FDG-PET after two to three cycles of chemotherapy predicts progression-free and overall survival in high-grade non-Hodgkin lymphoma. *Ann Oncol*. 2005;16(9):1514–23. <https://doi.org/10.1093/annonc/mdi272>.
  74. Palmedo H, Urbach H, Bender H, Schlegel U, Schmidt-Wolf IGH, Matthies A, et al. FDG-PET in immunocompetent patients with primary central nervous system lymphoma: correlation with MRI and clinical follow-up. *Eur J Nucl Med Mol Imaging*. 2006;33(2):164–8. <https://doi.org/10.1007/s00259-005-1917-6>.
  75. Kawai N, Zhen H-N, Miyake K, Yamamoto Y, Nishiyama Y, Tamiya T. Prognostic value of pre-treatment 18F-FDG PET in patients with primary central nervous system lymphoma: SUV-based assessment. *J Neuro-Oncol*. 2010;100(2):225–32. <https://doi.org/10.1007/s11060-010-0182-0>.
  76. Kosaka N, Tsuchida T, Uematsu H, Kimura H, Okazawa H, Itoh H. 18F-FDG PET of common enhancing malignant brain tumors. *AJR Am J Roentgenol*. 2008;190(6):W365–9. <https://doi.org/10.2214/AJR.07.2660>.
  77. Fiest KM, Sauro KM, Wiebe S, Patten SB, Kwon CS, Dykeman J, et al. Prevalence and incidence of epilepsy: a systematic review and meta-analysis of international studies. *Neurology*. 2017;88(3):296–303. <https://doi.org/10.1212/WNL.0000000000003509>.
  78. Sillanpaa M, Gissler M, Schmidt D. Efforts in epilepsy prevention in the last 40 years: lessons from a large nationwide study. *JAMA Neurol*. 2016;73(4):390–5. <https://doi.org/10.1001/jamaneurol.2015.4515>.
  79. Hauser WA, Annegers JF, Kurland LT. Incidence of epilepsy and unprovoked seizures in Rochester, Minnesota: 1935-1984. *Epilepsia*. 1993;34(3):453–68.
  80. Epilepsy in adults and access to care—United States, 2010. *MMWR Morb Mort Wkly Rep*. 2012;61(45):909–13.
  81. Kwan P, Brodie MJ. Clinical trials of antiepileptic medications in newly diagnosed patients with epilepsy. *Neurology*. 2003;60(11 Suppl 4):S2–12.

82. Engel J Jr, Wiebe S, French J, Sperling M, Williamson P, Spencer D, et al. Neocortical parameter: temporal lobe and localized neocortical resections for epilepsy. *Epilepsia*. 2003;44(6):741–51.
83. Wiebe S, Blume WT, Girvin JP, Eliasziw M. A randomized, controlled trial of surgery for temporal-lobe epilepsy. *N Engl J Med*. 2001;345(5):311–8. <https://doi.org/10.1056/nejm200108023450501>.
84. Cascino GD, Jack CR Jr, Parisi JE, Sharbrough FW, Hirschorn KA, Meyer FB, et al. Magnetic resonance imaging-based volume studies in temporal lobe epilepsy: pathological correlations. *Ann Neurol*. 1991;30(1):31–6. <https://doi.org/10.1002/ana.410300107>.
85. Duncan JS. Imaging in the surgical treatment of epilepsy. *Nat Rev Neurol*. 2010;6(10):537–50. <https://doi.org/10.1038/nrneurol.2010.131>.
86. Kuzniecky RI, Bilir E, Gilliam F, Faught E, Palmer C, Morawetz R, et al. Multimodality MRI in mesial temporal sclerosis: relative sensitivity and specificity. *Neurology*. 1997;49(3):774–8.
87. Theodore WH, Gaillard WD, De Carli C, Bhatia S, Hattaj J. Hippocampal volume and glucose metabolism in temporal lobe epileptic foci. *Epilepsia*. 2001;42(1):130–2.
88. Theodore WH, Sato S, Kufta C, Balish MB, Bromfield EB, Leiderman DB. Temporal lobectomy for uncontrolled seizures: the role of positron emission tomography. *Ann Neurol*. 1992;32(6):789–94. <https://doi.org/10.1002/ana.410320613>.
89. Lamusuo S, Forss N, Ruottinen HM, Bergman J, Makela JP, Mervaala E, et al. [18F]FDG-PET and whole-scalp MEG localization of epileptogenic cortex. *Epilepsia*. 1999;40(7):921–30.
90. Wieser HG. PET and SPECT in epilepsy. *Eur Neurol*. 1994;34(Suppl 1):58–62. <https://doi.org/10.1159/000119511>.
91. DeCarli C, McIntosh AR, Blaxton TA. Use of positron emission tomography for the evaluation of epilepsy. *Neuroimaging Clin N Am*. 1995;5(4):623–45.
92. Willmann O, Wennberg R, May T, Woermann FG, Pohlmann-Eden B. The contribution of 18F-FDG PET in preoperative epilepsy surgery evaluation for patients with temporal lobe epilepsy: A meta-analysis. *Seizure*. 2007;16(6):509–20. <https://doi.org/10.1016/j.seizure.2007.04.001>.
93. Benbadis SR, So NK, Antar MA, Barnett GH, Morris HH. The value of PET scan (and MRI and Wada test) in patients with bitemporal epileptiform abnormalities. *Arch Neurol*. 1995;52(11):1062–8.
94. Vivash L, Gregoire MC, Lau EW, Ware RE, Binns D, Roselt P, et al. 18F-flumazenil: a gamma-aminobutyric acid A-specific PET radiotracer for the localization of drug-resistant temporal lobe epilepsy. *J Nucl Med*. 2013;54(8):1270–7. <https://doi.org/10.2967/jnumed.112.107359>.
95. Jack CR Jr, Knopman DS, Weigand SD, Wiste HJ, Vemuri P, Lowe V, et al. An operational approach to National Institute on Aging-Alzheimer's Association criteria for preclinical Alzheimer disease. *Ann Neurol*. 2012;71(6):765–75. <https://doi.org/10.1002/ana.22628>.
96. Villemagne VL, Burnham S, Bourgeat P, Brown B, Ellis KA, Salvado O, et al. Amyloid beta deposition, neurodegeneration, and cognitive decline in sporadic Alzheimer's disease: a prospective cohort study. *Lancet Neurol*. 2013;12(4):357–67. [https://doi.org/10.1016/S1474-4422\(13\)70044-9](https://doi.org/10.1016/S1474-4422(13)70044-9).
97. Hardy J, Allsop D. Amyloid deposition as the central event in the aetiology of Alzheimer's disease. *Trends Pharmacol Sci*. 1991;12(10):383–8.
98. Hardy JA, Higgins GA. Alzheimer's disease: the amyloid cascade hypothesis. *Science*. 1992;256(5054):184–5.
99. Sperling RA, Aisen PS, Beckett LA, Bennett DA, Craft S, Fagan AM, et al. Toward defining the preclinical stages of Alzheimer's disease: recommendations from the National Institute on Aging-Alzheimer's Association workgroups on diagnostic guidelines for Alzheimer's disease. *Alzheimers Dement*. 2011;7(3):280–92. <https://doi.org/10.1016/j.jalz.2011.03.003>.
100. Friedland RP, Budinger TF, Ganz E, Yano Y, Mathis CA, Koss B, et al. Regional cerebral metabolic alterations in dementia of the Alzheimer type: positron emission tomography with [18F]fluorodeoxyglucose. *J Comput Assist Tomogr*. 1983;7(4):590–8.
101. Herholz K, Carter SF, Jones M. Positron emission tomography imaging in dementia. *Br J Radiol*. 2007;80(2):S160–7. <https://doi.org/10.1259/bjr/97295129>.
102. Jagust W, Reed B, Mungas D, Ellis W, Decarli C. What does fluorodeoxyglucose PET imaging add to a clinical diagnosis of dementia? *Neurology*. 2007;69(9):871–7. <https://doi.org/10.1212/01.wnl.0000269790.05105.16>.
103. Reiman EM, Caselli RJ, Yun LS, Chen K, Bandy D, Minoshima S, et al. Preclinical evidence of Alzheimer's disease in persons homozygous for the epsilon 4 allele for apolipoprotein E. *N Engl J Med*. 1996;334(12):752–8. <https://doi.org/10.1056/NEJM199603213341202>.
104. Small GW, Ercoli LM, Silverman DH, Huang SC, Komo S, Bookheimer SY, et al. Cerebral metabolic and cognitive decline in persons at genetic risk for Alzheimer's disease. *Proc Natl Acad Sci U S A*. 2000;97(11):6037–42. <https://doi.org/10.1073/pnas.090106797>.
105. Yuan Y, Gu ZX, Wei WS. Fluorodeoxyglucose-positron-emission tomography, single-photon emission tomography, and structural MR imaging for prediction of rapid conversion to Alzheimer disease in patients with mild cognitive impairment: a meta-analysis. *AJNR Am J Neuroradiol*. 2009;30(2):404–10. <https://doi.org/10.3174/ajnr.A1357>.
106. Anchisi D, Borroni B, Franceschi M, Kerrouche N, Kalbe E, Beuthien-Beumann B, et al. Heterogeneity of brain glucose metabolism in mild cognitive impairment and clinical progression to Alzheimer disease. *Arch Neurol*. 2005;62(11):1728–33. <https://doi.org/10.1001/archneur.62.11.1728>.

107. Smailagic N, Vacante M, Hyde C, Martin S, Ukoumunne O, Sachpekidis C. (1)(8)F-FDG PET for the early diagnosis of Alzheimer's disease dementia and other dementias in people with mild cognitive impairment (MCI). *Cochrane Database Syst Rev.* 2015;1:CD010632. <https://doi.org/10.1002/14651858.CD010632.pub2>.
108. Morbelli S, Garibotto V, Van De Giessen E, Arbizu J, Chetelat G, Drezgza A, et al. A Cochrane review on brain [(1)(8)F]FDG PET in dementia: limitations and future perspectives. *Eur J Nucl Med Mol Imaging.* 2015;42(10):1487–91. <https://doi.org/10.1007/s00259-015-3098-2>.
109. Teipel S, Drezgza A, Grothe MJ, Barthel H, Chetelat G, Schuff N, et al. Multimodal imaging in Alzheimer's disease: validity and usefulness for early detection. *Lancet Neurol.* 2015;14(10):1037–53. [https://doi.org/10.1016/S1474-4422\(15\)00093-9](https://doi.org/10.1016/S1474-4422(15)00093-9).
110. van Straaten EC, Scheltens P, Knol DL, van Buchem MA, van Dijk EJ, Hofman PA, et al. Operational definitions for the NINDS-AIREN criteria for vascular dementia: an interobserver study. *Stroke.* 2003;34(8):1907–12. <https://doi.org/10.1161/01.STR.0000083050.44441.10>.
111. Ratnavalli E, Brayne C, Dawson K, Hodges JR. The prevalence of frontotemporal dementia. *Neurology.* 2002;58(11):1615–21.
112. Mesulam MM. Slowly progressive aphasia without generalized dementia. *Ann Neurol.* 1982;11(6):592–8. <https://doi.org/10.1002/ana.410110607>.
113. Gorno-Tempini ML, Dronkers NF, Rankin KP, Ogar JM, Phengrasamy L, Rosen HJ, et al. Cognition and anatomy in three variants of primary progressive aphasia. *Ann Neurol.* 2004;55(3):335–46. <https://doi.org/10.1002/ana.10825>.
114. Cerami C, Dodich A, Lettieri G, Iannaccone S, Magnani G, Marcone A, et al. Different FDG-PET metabolic patterns at single-subject level in the behavioral variant of fronto-temporal dementia. *Cortex.* 2016;83:101–12. <https://doi.org/10.1016/j.cortex.2016.07.008>.
115. Minoshima S, Foster NL, Sima AA, Frey KA, Albin RL, Kuhl DE. Alzheimer's disease versus dementia with Lewy bodies: cerebral metabolic distinction with autopsy confirmation. *Ann Neurol.* 2001;50(3):358–65.
116. Eckert T, Barnes A, Dhawan V, Frucht S, Gordon MF, Feigin AS, et al. FDG PET in the differential diagnosis of parkinsonian disorders. *NeuroImage.* 2005;26(3):912–21. <https://doi.org/10.1016/j.neuroimage.2005.03.012>.
117. Eidelberg D, Takikawa S, Moeller JR, Dhawan V, Redington K, Chaly T, et al. Striatal hypometabolism distinguishes striatonigral degeneration from Parkinson's disease. *Ann Neurol.* 1993;33(5):518–27. <https://doi.org/10.1002/ana.410330517>.
118. Pauwels EK, Coumou AW, Kostkiewicz M, Kairemo K. [(1)(8)F]fluoro-2-deoxy-d-glucose positron emission tomography/computed tomography imaging in oncology: initial staging and evaluation of cancer therapy. *Med Princ Pract.* 2013;22(5):427–37. <https://doi.org/10.1159/000346303>.
119. Connell CA, Corry J, Milner AD, Hogg A, Hicks RJ, Rischin D, et al. Clinical impact of, and prognostic stratification by, F-18 FDG PET/CT in head and neck mucosal squamous cell carcinoma. *Head Neck.* 2007;29(11):986–95. <https://doi.org/10.1002/hed.20629>.
120. Gao S, Li S, Yang X, Tang Q. 18FDG PET-CT for distant metastases in patients with recurrent head and neck cancer after definitive treatment. A meta-analysis. *Oral Oncol.* 2014;50(3):163–7. <https://doi.org/10.1016/j.oraloncology.2013.12.002>.
121. Gallamini A, Zwarthoed C, Borra A. Positron emission tomography (PET) in oncology. *Cancers (Basel).* 2014;6(4):1821–89. <https://doi.org/10.3390/cancers6041821>.
122. Prestwich RJ, Subesinghe M, Gilbert A, Chowdhury FU, Sen M, Scarsbrook AF. Delayed response assessment with FDG-PET-CT following (chemo) radiotherapy for locally advanced head and neck squamous cell carcinoma. *Clin Radiol.* 2012;67(10):966–75. <https://doi.org/10.1016/j.crad.2012.02.016>.
123. Yoon DH, Cho Y, Kim SY, Nam SY, Choi SH, Roh JL, et al. Usefulness of interim FDG-PET after induction chemotherapy in patients with locally advanced squamous cell carcinoma of the head and neck receiving sequential induction chemotherapy followed by concurrent chemoradiotherapy. *Int J Radiat Oncol Biol Phys.* 2011;81(1):118–25. <https://doi.org/10.1016/j.ijrobp.2010.04.034>.
124. Ceulemans G, Voordeckers M, Farrag A, Verdries D, Storme G, Everaert H. Can 18-FDG-PET during radiotherapy replace post-therapy scanning for detection/demonstration of tumor response in head-and-neck cancer? *Int J Radiat Oncol Biol Phys.* 2011;81(4):938–42. <https://doi.org/10.1016/j.ijrobp.2010.07.019>.
125. Langen KJ, Watts C. Neuro-oncology: amino acid PET for brain tumours—ready for the clinic? *Nat Rev Neurol.* 2016;12(7):375–6. <https://doi.org/10.1038/nrneuro.2016.80>.
126. Moulin-Romsee G, D'Hondt E, de Groot T, Goffin J, Sciort R, Mortelmans L, et al. Non-invasive grading of brain tumours using dynamic amino acid PET imaging: does it work for 11C-methionine? *Eur J Nucl Med Mol Imaging.* 2007;34(12):2082–7. <https://doi.org/10.1007/s00259-007-0557-4>.
127. Dunet V, Pomoni A, Hottinger A, Nicod-Lalonde M, Prior JO. Performance of 18F-FET versus 18F-FDG-PET for the diagnosis and grading of brain tumors: systematic review and meta-analysis. *Neuro-Oncology.* 2016;18(3):426–34. <https://doi.org/10.1093/neuonc/nov148>.
128. Rapp M, Heinzl A, Galldiks N, Stoffels G, Felsberg J, Ewelt C, et al. Diagnostic performance of 18F-FET PET in newly diagnosed cerebral lesions suggestive of glioma. *J Nucl Med.* 2013;54(2):229–35. <https://doi.org/10.2967/jnumed.112.109603>.
129. Albatly AA, Alsamarah AT, Alhawas A, Veit-Haibach P, Buck A, Stolzmann P, et al. Value of (18)F-FET PET in adult brainstem glioma. *Clin Imaging.* 2018;51:68–75. <https://doi.org/10.1016/j.clinimag.2018.01.015>.

130. Jansen NL, Suchorska B, Wenter V, Eigenbrod S, Schmid-Tannwald C, Zwergal A, et al. Dynamic 18F-FET PET in newly diagnosed astrocytic low-grade glioma identifies high-risk patients. *J Nucl Med*. 2014;55(2):198–203. <https://doi.org/10.2967/jnumed.113.122333>.
131. Galldiks N, Stoffels G, Filss CP, Piroth MD, Sabel M, Ruge MI, et al. Role of O-(2-(18)F-fluoroethyl)-L-tyrosine PET for differentiation of local recurrent brain metastasis from radiation necrosis. *J Nucl Med*. 2012;53(9):1367–74. <https://doi.org/10.2967/jnumed.112.103325>.
132. Akhoundova D, Hiltbrunner S, Mader C, Förster R, Kraft J, Schwanhäusser B, et al. 18F-FET PET for diagnosis of pseudoprogression of brain metastases in patients with non-small cell lung cancer. *Clin Nucl Med*. 2020;45(2):113–17. <https://doi.org/10.1097/RLU.0000000000002890>.
133. Sun A, Liu X, Tang G. Carbon-11 and fluorine-18 labeled amino acid tracers for positron emission tomography imaging of tumors. *Front Chem*. 2017;5:124. <https://doi.org/10.3389/fchem.2017.00124>.
134. Hutterer M, Nowosielski M, Putzer D, Jansen NL, Seiz M, Schocke M, et al. [18F]-fluoro-ethyl-L-tyrosine PET: a valuable diagnostic tool in neuro-oncology, but not all that glitters is glioma. *Neuro-Oncology*. 2013;15(3):341–51. <https://doi.org/10.1093/neuonc/nos300>.
135. Barbagallo M, Albatly AA, Hayward-Könnecke HK, Schreiner S, Buck A, Kollias SS, et al. Value of 18F-FET PET in patients with suspected tumefactive demyelinating disease—preliminary experience from a retrospective analysis. *Clin Nucl Med*. 2018;43:e385–91.
136. Johnbeck CB, Knigge U, Kjaer A. PET tracers for somatostatin receptor imaging of neuroendocrine tumors: current status and review of the literature. *Future Oncol*. 2014;10(14):2259–77. <https://doi.org/10.2217/fon.14.139>.
137. Rachinger W, Stoecklein VM, Terpolilli NA, Haug AR, Ertl L, Poschl J, et al. Increased 68Ga-DOTATATE uptake in PET imaging discriminates meningioma and tumor-free tissue. *J Nucl Med*. 2015;56(3):347–53. <https://doi.org/10.2967/jnumed.114.149120>.
138. Weingarten CP, Sundman MH, Hickey P, Chen NK. Neuroimaging of Parkinson's disease: expanding views. *Neurosci Biobehav Rev*. 2015;59:16–52. <https://doi.org/10.1016/j.neubiorev.2015.09.007>.
139. Galvan A, Wichmann T. Pathophysiology of parkinsonism. *Clin Neurophysiol*. 2008;119(7):1459–74. <https://doi.org/10.1016/j.clinph.2008.03.017>.
140. DeLong MR. Primate models of movement disorders of basal ganglia origin. *Trends Neurosci*. 1990;13(7):281–5. [https://doi.org/10.1016/0166-2236\(90\)90110-V](https://doi.org/10.1016/0166-2236(90)90110-V).
141. Morrish PK, Rakshi JS, Bailey DL, Sawle GV, Brooks DJ. Measuring the rate of progression and estimating the preclinical period of Parkinson's disease with [18F]dopa PET. *J Neurol Neurosurg Psychiatry*. 1998;64(3):314–9.
142. Otsuka M, Ichiya Y, Kuwabara Y, Hosokawa S, Sasaki M, Yoshida T, et al. Differences in the reduced 18F-Dopa uptakes of the caudate and the putamen in Parkinson's disease: correlations with the three main symptoms. *J Neurol Sci*. 1996;136(1–2):169–73.
143. Cropley VL, Fujita M, Bara-Jimenez W, Brown AK, Zhang XY, Sangare J, et al. Pre- and post-synaptic dopamine imaging and its relation with frontostriatal cognitive function in Parkinson disease: PET studies with [11C]NNC 112 and [18F]FDOPA. *Psychiatry Res*. 2008;163(2):171–82. <https://doi.org/10.1016/j.psychres.2007.11.003>.
144. Hilker R, Schweitzer K, Coburger S, Ghaemi M, Weisenbach S, Jacobs AH, et al. Nonlinear progression of Parkinson disease as determined by serial positron emission tomographic imaging of striatal fluorodopa F 18 activity. *Arch Neurol*. 2005;62(3):378–82. <https://doi.org/10.1001/archneur.62.3.378>.
145. Sawle GV, Playford ED, Burn DJ, Cunningham VJ, Brooks DJ. Separating Parkinson's disease from normality. Discriminant function analysis of fluorodopa F 18 positron emission tomography data. *Arch Neurol*. 1994;51(3):237–43.
146. Löhle M, Mende J, Wolz M, Beuthien-Baumann B, Oehme L, van den Hoff J, et al. Putaminal dopamine turnover in de novo Parkinson disease predicts later motor complications. *Neurology*. 2016;86(3):231–40. <https://doi.org/10.1212/wnl.0000000000002286>.
147. Antonini A, Leenders KL, Vontobel P, Maguire RP, Missimer J, Psylla M, et al. Complementary PET studies of striatal neuronal function in the differential diagnosis between multiple system atrophy and Parkinson's disease. *Brain*. 1997;120(Pt 12):2187–95.
148. Burn DJ, Sawle GV, Brooks DJ. Differential diagnosis of Parkinson's disease, multiple system atrophy, and Steele-Richardson-Olszewski syndrome: discriminant analysis of striatal 18F-dopa PET data. *J Neurol Neurosurg Psychiatry*. 1994;57(3):278–84.
149. Sawle GV, Brooks DJ, Marsden CD, Frackowiak RS. Corticobasal degeneration. A unique pattern of regional cortical oxygen hypometabolism and striatal fluorodopa uptake demonstrated by positron emission tomography. *Brain*. 1991;114(Pt 1B):541–56.
150. Klein JC, Eggers C, Kalbe E, Weisenbach S, Hohmann C, Vollmar S, et al. Neurotransmitter changes in dementia with Lewy bodies and Parkinson disease dementia in vivo. *Neurology*. 2010;74(11):885–92. <https://doi.org/10.1212/WNL.0b013e3181d55f61>.
151. Bloomfield MAP, Morgan CJA, Kapur S, Curran HV, Howes OD. The link between dopamine function and apathy in cannabis users: an [18F]-DOPA PET imaging study. *Psychopharmacology*. 2014;231(11):2251–9. <https://doi.org/10.1007/s00213-014-3523-4>.
152. Bloomfield MAP, Pepper F, Egerton A, Demjaha A, Tomasi G, Mouchlianitis E, et al. Dopamine function in cigarette smokers: an [18F]-DOPA PET study. *Neuropsychopharmacology*. 2014;39:2397. <https://doi.org/10.1038/npp.2014.87>.
153. Heinz A, Siessmeier T, Wrase J, Buchholz HG, Gründer G, Kumakura Y, et al. Correlation of alcohol

- craving with striatal dopamine synthesis capacity and D2/3 receptor availability: a combined [18F]DOPA and [18F]DMFP PET study in detoxified alcoholic patients. *Am J Psychiatr*. 2005;162(8):1515–20. <https://doi.org/10.1176/appi.ajp.162.8.1515>.
154. van Holst RJ, Sescousse G, Janssen LK, Janssen M, Berry AS, Jagust WJ, et al. Increased striatal dopamine synthesis capacity in gambling addiction. *Biol Psychiatry*. 2017. <https://doi.org/10.1016/j.biopsych.2017.06.010>.
  155. Joutsa J, Johansson J, Niemelä S, Ollikainen A, Hirvonen MM, Piepponen P, et al. Mesolimbic dopamine release is linked to symptom severity in pathological gambling. *NeuroImage*. 2012;60(4):1992–9. <https://doi.org/10.1016/j.neuroimage.2012.02.006>.
  156. Linnet J, Møller A, Peterson E, Gjedde D, Doudet D. Dopamine release in ventral striatum during Iowa Gambling Task performance is associated with increased excitement levels in pathological gambling. *Addiction*. 2011;106(2):383–90. <https://doi.org/10.1111/j.1360-0443.2010.03126.x>.
  157. Oldendorf WH, Szabo J. Amino acid assignment to one of three blood-brain barrier amino acid carriers. *Am J Phys*. 1976;230(1):94–8. <https://doi.org/10.1152/ajplegacy.1976.230.1.94>.
  158. Becherer A, Karanikas G, Szabo M, Zetting G, Asenbaum S, Marosi C, et al. Brain tumour imaging with PET: a comparison between [18F]fluorodopa and [11C]methionine. *Eur J Nucl Med Mol Imaging*. 2003;30(11):1561–7. <https://doi.org/10.1007/s00259-003-1259-1>.
  159. Charrier N, Deveze A, Fakhry N, Sebag F, Morange I, Gaborit B, et al. Comparison of [111In]pentetretotide-SPECT and [18F]FDOPA-PET in the localization of extra-adrenal paragangliomas: the case for a patient-tailored use of nuclear imaging modalities. *Clin Endocrinol*. 2011;74(1):21–9. <https://doi.org/10.1111/j.1365-2265.2010.03893.x>.
  160. Gabriel S, Blanchet EM, Sebag F, Chen CC, Fakhry N, Deveze A, et al. Functional characterization of nonmetastatic paraganglioma and pheochromocytoma by 18F-FDOPA PET: focus on missed lesions. *Clin Endocrinol*. 2013;79(2):170–7. <https://doi.org/10.1111/cen.12126>.
  161. King KS, Chen CC, Alexopoulos DK, Whatley MA, Reynolds JC, Patronas N, et al. Functional imaging of SDHx-related head and neck paragangliomas: comparison of 18F-fluorodihydroxyphenylalanine, 18F-fluorodopamine, 18F-fluoro-2-deoxy-d-glucose PET, 123I-metaiodobenzylguanidine scintigraphy, and 111In-pentetretotide scintigraphy. *J Clin Endocrinol Metabol*. 2011;96(9):2779–85. <https://doi.org/10.1210/jc.2011-0333>.
  162. Miederer M, Fottner C, Rossmann H, Helisch A, Papaspyrou K, Bartsch O, et al. High incidence of extraadrenal paraganglioma in families with SDHx syndromes detected by functional imaging with [18F]fluorodihydroxyphenylalanine PET. *Eur J Nucl Med Mol Imaging*. 2013;40(6):889–96. <https://doi.org/10.1007/s00259-013-2346-6>.
  163. Timmers HJLM, Chen CC, Carrasquillo JA, Whatley M, Ling A, Havekes B, et al. Comparison of 18F-fluoro-L-DOPA, 18F-fluoro-deoxyglucose, and 18F-fluorodopamine PET and 123I-MIBG scintigraphy in the localization of pheochromocytoma and paraganglioma. *J Clin Endocrinol Metabol*. 2009;94(12):4757–67. <https://doi.org/10.1210/jc.2009-1248>.
  164. Tischler AS, Kimura N, McNicol AM. Pathology of pheochromocytoma and extra-adrenal paraganglioma. *Ann NY Acad Sci*. 2006;1073:557–70. <https://doi.org/10.1196/annals.1353.059>.
  165. Osinga TE, Korpershoek E, de Krijger RR, Kerstens MN, Dullaart RP, Kema IP, et al. Catecholamine-synthesizing enzymes are expressed in parasympathetic head and neck paraganglioma tissue. *Neuroendocrinology*. 2015;101(4):289–95. <https://doi.org/10.1159/000377703>.
  166. Farde L, Hall H, Ehrin E, Sedvall G. Quantitative analysis of D2 dopamine receptor binding in the living human brain by PET. *Science*. 1986;231(4735):258–61.
  167. Rinne JO, Laihinena A, Nagren K, Bergman J, Solin O, Haaparanta M, et al. PET demonstrates different behaviour of striatal dopamine D-1 and D-2 receptors in early Parkinson's disease. *J Neurosci Res*. 1990;27(4):494–9. <https://doi.org/10.1002/jnr.490270409>.
  168. Shinotoh H, Calne DB. The use of pet in Parkinsons-disease. *Brain Cogn*. 1995;28(3):297–310. <https://doi.org/10.1006/brcg.1995.1259>.
  169. Antonini A, Schwarz J, Oertel WH, Beer HF, Madeja UD, Leenders KL. [11C]Raclopride and positron emission tomography in previously untreated patients with Parkinson's disease: Influence of L-dopa and lisuride therapy on striatal dopamine D2-receptors. *Neurology*. 1994;44(7):1325–9.
  170. Antonini A, Schwarz J, Oertel WH, Pogarell O, Leenders KL. Long-term changes of striatal dopamine D2 receptors in patients with Parkinson's disease: a study with positron emission tomography and [11C]raclopride. *Mov Disord*. 1997;12(1):33–8. <https://doi.org/10.1002/mds.870120107>.
  171. Antonini A, Vontobel P, Psylla M, Gunther I, Maguire PR, Missimer J, et al. Complementary positron emission tomographic studies of the striatal dopaminergic system in Parkinson's disease. *Arch Neurol*. 1995;52(12):1183–90.
  172. Pavese N, Evans AH, Tai YF, Hotton G, Brooks DJ, Lees AJ, et al. Clinical correlates of levodopa-induced dopamine release in Parkinson disease. A PET study. *Neurology*. 2006;67(9):1612–7. <https://doi.org/10.1212/01.wnl.0000242888.30755.5d>.
  173. Klaffke S, Kuhn AA, Plotkin M, Amthauer H, Harnack D, Felix R, et al. Dopamine transporters, D2 receptors, and glucose metabolism in corticobasal degeneration. *Mov Disord*. 2006;21(10):1724–7. <https://doi.org/10.1002/mds.21004>.
  174. Plotkin M, Amthauer H, Klaffke S, Kuhn A, Ludemann L, Arnold G, et al. Combined 123I-FP-CIT and 123I-IBZM SPECT for the diagnosis of parkinsonian syndromes: study on 72 patients. *J Neural Transm (Vienna, Austria)*. 1996. 2005;112(5):677–92. <https://doi.org/10.1007/s00702-004-0208-x>.

175. Stover NP, Watts RL. Corticobasal degeneration. *Semin Neurol.* 2001;21(1):49–58.
176. Boileau I, Payer D, Chugani B, Lobo D, Behzadi A, Rusjan PM, et al. The D2/3 dopamine receptor in pathological gambling: a positron emission tomography study with [11C]-(+)-propyl-hexahydro-naphtho-oxazin and [11C]raclopride. *Addiction.* 2013;108(5):953–63. <https://doi.org/10.1111/add.12066>.
177. Clark L, Stokes PR, Wu K, Michalczuk R, Benecke A, Watson BJ, et al. Striatal dopamine D2/D3 receptor binding in pathological gambling is correlated with mood-related impulsivity. *NeuroImage.* 2012;63(1):40–6. <https://doi.org/10.1016/j.neuroimage.2012.06.067>.
178. Peterson E, Møller A, Doudet DJ, Bailey CJ, Hansen KV, Rodell A, et al. Pathological gambling: relation of skin conductance response to dopaminergic neurotransmission and sensation-seeking. *Eur Neuropsychopharmacol.* 2010;20(11):766–75. <https://doi.org/10.1016/j.euroneuro.2010.07.010>.
179. Kim J-H, Son Y-D, Kim H-K, Lee S-Y, Kim Y-B, Cho Z-H. Dopamine D2/3 receptor availability and human cognitive impulsivity: a high-resolution positron emission tomography imaging study with [11C] raclopride. *Acta Neuropsychiatr.* 2013;26(1):35–42. <https://doi.org/10.1017/neu.2013.29>.
180. Reeves SJ, Polling C, Stokes PRA, Lappin JM, Shotbolt PP, Mehta MA, et al. Limbic striatal dopamine D2/3 receptor availability is associated with non-planning impulsivity in healthy adults after exclusion of potential dissimulators. *Psychiatry Res.* 2012;202(1):60–4. <https://doi.org/10.1016/j.psychres.2011.09.011>.
181. Barthel H, Gertz HJ, Dresel S, Peters O, Bartenstein P, Buerger K, et al. Cerebral amyloid-beta PET with florbetaben (18F) in patients with Alzheimer's disease and healthy controls: a multicentre phase 2 diagnostic study. *Lancet Neurol.* 2011;10(5):424–35. [https://doi.org/10.1016/S1474-4422\(11\)70077-1](https://doi.org/10.1016/S1474-4422(11)70077-1).
182. Klunk WE, Engler H, Nordberg A, Wang Y, Blomqvist G, Holt DP, et al. Imaging brain amyloid in Alzheimer's disease with Pittsburgh Compound-B. *Ann Neurol.* 2004;55(3):306–19. <https://doi.org/10.1002/ana.20009>.
183. Vandenberghe R, Van Laere K, Ivanoiu A, Salmon E, Bastin C, Triau E, et al. 18F-flutemetamol amyloid imaging in Alzheimer disease and mild cognitive impairment: a phase 2 trial. *Ann Neurol.* 2010;68(3):319–29. <https://doi.org/10.1002/ana.22068>.
184. Wong DF, Rosenberg PB, Zhou Y, Kumar A, Raymont V, Ravert HT, et al. In vivo imaging of amyloid deposition in Alzheimer disease using the radioligand 18F-AV-45 (florbetapir [corrected] F 18). *J Nucl Med.* 2010;51(6):913–20. <https://doi.org/10.2967/jnumed.109.069088>.
185. Landau SM, Thomas BA, Thurfjell L, Schmidt M, Margolin R, Mintun M, et al. Amyloid PET imaging in Alzheimer's disease: a comparison of three radiotracers. *Eur J Nucl Med Mol Imaging.* 2014;41(7):1398–407. <https://doi.org/10.1007/s00259-014-2753-3>.
186. Ewers M, Insel P, Jagust WJ, Shaw L, Trojanowski JQ, Aisen P, et al. CSF biomarker and PIB-PET-derived beta-amyloid signature predicts metabolic, gray matter, and cognitive changes in nondemented subjects. *Cereb Cortex (New York, NY: 1991).* 2012;22(9):1993–2004. <https://doi.org/10.1093/cercor/bhr271>.
187. Fleisher AS, Chen K, Liu X, Roontiva A, Thiyyagura P, Ayutyanont N, et al. Using positron emission tomography and florbetapir F18 to image cortical amyloid in patients with mild cognitive impairment or dementia due to Alzheimer disease. *Arch Neurol.* 2011;68(11):1404–11. <https://doi.org/10.1001/archneurol.2011.150>.
188. Joshi AD, Pontecorvo MJ, Clark CM, Carpenter AP, Jennings DL, Sadowsky CH, et al. Performance characteristics of amyloid PET with florbetapir F 18 in patients with Alzheimer's disease and cognitively normal subjects. *J Nucl Med.* 2012;53(3):378–84. <https://doi.org/10.2967/jnumed.111.090340>.
189. Mormino EC, Kluth JT, Madison CM, Rabinovici GD, Baker SL, Miller BL, et al. Episodic memory loss is related to hippocampal-mediated beta-amyloid deposition in elderly subjects. *Brain.* 2009;132(Pt 5):1310–23. <https://doi.org/10.1093/brain/awn320>.
190. Villemagne VL, Ong K, Mulligan RS, Holl G, Pejoska S, Jones G, et al. Amyloid imaging with (18)F-florbetaben in Alzheimer disease and other dementias. *J Nucl Med.* 2011;52(8):1210–7. <https://doi.org/10.2967/jnumed.111.089730>.
191. Leinonen V, Rinne JO, Wong DF, Wolk DA, Trojanowski JQ, Sherwin PF, et al. Diagnostic effectiveness of quantitative [(1)(8)F]flutemetamol PET imaging for detection of fibrillar amyloid beta using cortical biopsy histopathology as the standard of truth in subjects with idiopathic normal pressure hydrocephalus. *Acta Neuropathol Commun.* 2014;2:46. <https://doi.org/10.1186/2051-5960-2-46>.
192. Thurfjell L, Lilja J, Lundqvist R, Buckley C, Smith A, Vandenberghe R, et al. Automated quantification of 18F-flutemetamol PET activity for categorizing scans as negative or positive for brain amyloid: concordance with visual image reads. *J Nucl Med.* 2014;55(10):1623–8. <https://doi.org/10.2967/jnumed.114.142109>.
193. Rabinovici GD, Furst AJ, O'Neil JP, Racine CA, Mormino EC, Baker SL, et al. 11C-PIB PET imaging in Alzheimer disease and frontotemporal lobar degeneration. *Neurology.* 2007;68(15):1205–12. <https://doi.org/10.1212/01.wnl.0000259035.98480.ed>.
194. Rabinovici GD, Rosen HJ, Alkalay A, Kornak J, Furst AJ, Agarwal N, et al. Amyloid vs FDG-PET in the differential diagnosis of AD and FTLD. *Neurology.* 2011;77(23):2034–42. <https://doi.org/10.1212/WNL.0b013e31823b9c5e>.
195. Villemagne VL, Okamura N, Pejoska S, Drago J, Mulligan RS, Chetelat G, et al. Differential diagnosis in Alzheimer's disease and dementia with Lewy bodies via VMAT2 and amyloid imaging.

- Neurodegener Dis. 2012;10(1–4):161–5. <https://doi.org/10.1159/000334535>.
196. Choi Y, Ha S, Lee YS, Kim YK, Lee DS, Kim DJ. Development of tau PET imaging ligands and their utility in preclinical and clinical studies. *Nucl Med Mol Imaging*. 2018;52(1):24–30. <https://doi.org/10.1007/s13139-017-0484-7>.
  197. McKee AC, Cantu RC, Nowinski CJ, Hedley-Whyte ET, Gavett BE, Budson AE, et al. Chronic traumatic encephalopathy in athletes: progressive tauopathy after repetitive head injury. *J Neuropathol Exp Neurol*. 2009;68(7):709–35. <https://doi.org/10.1097/NEN.0b013e3181a9d503>.
  198. Cho H, Choi JY, Hwang MS, Kim YJ, Lee HM, Lee HS, et al. In vivo cortical spreading pattern of tau and amyloid in the Alzheimer disease spectrum. *Ann Neurol*. 2016;80(2):247–58. <https://doi.org/10.1002/ana.24711>.
  199. Wang L, Benzinger TL, Su Y, Christensen J, Friedrichsen K, Aldea P, et al. Evaluation of tau imaging in staging Alzheimer disease and revealing interactions between beta-amyloid and tauopathy. *JAMA Neurol*. 2016;73(9):1070–7. <https://doi.org/10.1001/jamaneurol.2016.2078>.
  200. Ossenkoppele R, Schonhaut DR, Scholl M, Lockhart SN, Ayakta N, Baker SL, et al. Tau PET patterns mirror clinical and neuroanatomical variability in Alzheimer’s disease. *Brain*. 2016;139(Pt 5):1551–67. <https://doi.org/10.1093/brain/aww027>.
  201. Betthausen TJ, Lao PJ, Murali D, Barnhart TE, Furumoto S, Okamura N, et al. In vivo comparison of tau radioligands (18)F-THK-5351 and (18)F-THK-5317. *J Nucl Med*. 2017;58(6):996–1002. <https://doi.org/10.2967/jnumed.116.182980>.
  202. Harada R, Okamura N, Furumoto S, Furukawa K, Ishiki A, Tomita N, et al. 18F-THK5351: a novel PET radiotracer for imaging neurofibrillary pathology in Alzheimer disease. *J Nucl Med*. 2016;57(2):208–14. <https://doi.org/10.2967/jnumed.115.164848>.
  203. Treyer V, Jobin M, Burger C, Teneggi V, Buck A. Quantitative cerebral H<sub>2</sub>(15)O perfusion PET without arterial blood sampling, a method based on wash-out rate. *Eur J Nucl Med Mol Imaging*. 2003;30(4):572–80. <https://doi.org/10.1007/s00259-002-1105-x>.
  204. Schmiedek P, Piepgras A, Leinsinger G, Kirsch CM, Einhuß K. Improvement of cerebrovascular reserve capacity by EC-IC arterial bypass surgery in patients with ICA occlusion and hemodynamic cerebral ischemia. *J Neurosurg*. 1994;81(2):236–44. <https://doi.org/10.3171/jns.1994.81.2.0236>.
  205. Altman DI, Lich LL, Powers WJ. Brief inhalation method to measure cerebral oxygen extraction fraction with PET: accuracy determination under pathologic conditions. *J Nucl Med*. 1991;32(9):1738–41.
  206. Mintun MA, Raichle ME, Martin WR, Herscovitch P. Brain oxygen utilization measured with O-15 radiotracers and positron emission tomography. *J Nucl Med*. 1984;25(2):177–87.
  207. Sander CY, Hesse S. News and views on in-vivo imaging of neurotransmission using PET and MRI. *Q J Nucl Med Mol Imaging*. 2017;61(4):414–28. <https://doi.org/10.23736/S1824-4785.17.03019-9>.
  208. Richardson MP, Koeppe MJ, Brooks DJ, Duncan JS. 11C-flumazenil PET in neocortical epilepsy. *Neurology*. 1998;51(2):485–92.
  209. Majo VJ, Prabhakaran J, Mann JJ, Kumar JS. PET and SPECT tracers for glutamate receptors. *Drug Discov Today*. 2013;18(3–4):173–84. <https://doi.org/10.1016/j.drudis.2012.10.004>.
  210. Sephton SM, Herde AM, Mu L, Keller C, Rudisuhli S, Auberson Y, et al. Preclinical evaluation and test-retest studies of [(18)F]PSS232, a novel radioligand for targeting metabotropic glutamate receptor 5 (mGlu5). *Eur J Nucl Med Mol Imaging*. 2015;42(1):128–37. <https://doi.org/10.1007/s00259-014-2883-7>.
  211. Mathis CA, et al. Small-molecule PET tracers for imaging proteinopathies. *Semin Nucl Med*. 2017;47(5):553–75.
  212. Eberling JL, et al.  $\alpha$ -synuclein imaging: a critical need for Parkinson’s disease research. *J Parkinsons Dis*. 2013;3(4):565–7.
  213. Chen MK, et al. Assessing synaptic density in Alzheimer disease with synaptic vesicle glycoprotein 2A positron emission tomographic imaging. *JAMA Neurol*. 2018;75(10):1215–24.
  214. Lyoo CH, Cho H, Choi JY, Ryu YH, Lee MS. Tau positron emission tomography imaging in degenerative Parkinsonisms. *J Mov Disord*. 2018;11(1):1–12. <https://doi.org/10.14802/jmd.17071>.
  215. Jellinger K. Unusual tau in MSA. *Neuropathology*. 2012;32(1):110–1. <https://doi.org/10.1111/j.1440-1789.2011.01246.x>.
  216. Sun J, Cairns NJ, Perlmutter JS, Mach RH, Xu J. Regulation of dopamine D<sub>3</sub> receptor in the striatal regions and substantia nigra in diffuse Lewy body disease. *Neuroscience*. 2013;248:112–26. <https://doi.org/10.1016/j.neuroscience.2013.05.048>.
  217. Piggott MA, Marshall EF, Thomas N, Lloyd S, Court JA, Jaros E, et al. Striatal dopaminergic markers in dementia with Lewy bodies, Alzheimer’s and Parkinson’s diseases: rostrocaudal distribution. *Brain*. 1999;122(Pt 8):1449–68.
  218. Loane C, Politis M. Positron emission tomography neuroimaging in Parkinson’s disease. *Am J Transl Res*. 2011;3(4):323–41.
  219. Day M, Wokosin D, Plotkin JL, Tian X, Surmeier DJ. Differential excitability and modulation of striatal medium spiny neuron dendrites. *J Neurosci*. 2008;28(45):11603–14. <https://doi.org/10.1523/jneurosci.1840-08.2008>.



L. Michels

## Contents

21.1	<b>Electroencephalography</b> .....	314
21.2	<b>Brainwaves</b> .....	314
21.2.1	Delta Waves.....	315
21.2.2	Theta Waves.....	315
21.2.3	Alpha Waves.....	315
21.2.4	Beta Waves.....	315
21.2.5	Gamma Waves.....	316
21.3	<b>EEG Recordings</b> .....	316
21.4	<b>Event-Related Potentials (ERP) Analysis</b> .....	317
21.5	<b>Spectral EEG Analysis</b> .....	317
21.5.1	Power and Spatial Factor Analysis.....	317
21.5.2	Time–Frequency Analysis.....	318
21.5.3	Synchronicity, Connectivity and Information Flow.....	318
21.5.4	Microstate Analysis.....	318
21.5.5	Deep Learning.....	319
21.6	<b>Dipole and Source Localization of EEG Activity</b> .....	319
21.7	<b>Artefacts</b> .....	320
21.8	<b>Limitations</b> .....	320
21.9	<b>Clinical Applications</b> .....	320
21.9.1	Epilepsy.....	320
21.9.2	ADHD.....	321
21.9.3	Dementia.....	322
21.9.4	Addiction and Drug Abuse.....	322
21.9.5	OCD.....	323
21.9.6	Depression.....	323
21.9.7	Schizophrenia.....	324
21.9.8	Chronic Pain.....	324
21.9.9	Panic Disorder.....	326

---

L. Michels (✉)  
Department of Neuroradiology,  
University Hospital of Zurich, Zurich, Switzerland  
e-mail: [lars.michels@usz.ch](mailto:lars.michels@usz.ch)



21.9.10	Tumour.....	326
21.9.11	Stroke.....	326
21.10	<b>Clinical Cases</b> .....	327
21.10.1	Epilepsy.....	327
	<b>References</b> .....	328

---

## 21.1 Electroencephalography

In the eighteenth century, physiologists discovered the electrical properties of living tissue. In the brain, electric potentials are generated by neurons that can be modelled by dipoles. The electroencephalogram (EEG) is a non-invasive electrophysiological imaging technique to record electrical activity of the brain, as EEG generators are electrical dipoles. In 1929, the German psychiatrist Hans Berger demonstrated that electrical activity of the brain could be measured by few electrodes on the human scalp (e.g. from his son), amplifying the signals and plotting variations in voltage over time [1] called EEG. He was also the inventor of the alpha wave rhythm (“Berger wave”). After some initial disbelief in the validity of EEG, research in the 1930s led to the recognition of EEG as real phenomenon (e.g. [2]). As stated by Coles and Rugg, it is generally accepted that the EEG reflects activity originating in the brain [3]. The EEG reflects voltages generated (mostly) by excitatory postsynaptic potentials from apical dendrites of massively synchronized neocortical pyramidal cells. Hence, there is no EEG at a single location, and EEG does not measure activity from single neurons, asynchronous activity, glial cells and subcortical structures. Compared to other imaging techniques, the EEG is a coarse measure of brain activity due to its poor spatial resolution and cannot be used in its raw form. The latter is due to the fact that the EEG reflects a mixed-up conglomeration of numerous different neuronal and non-neuronal sources of activity, making it difficult to isolate, e.g. neurocognitive processes. Compared to other neuroimaging techniques, EEG or magnetoencephalography (MEG) offer a superior temporal resolution in the millisecond range and

direct access to neuronal signalling compared to the 1–2 s resolution and indirect metabolic signals seen with, e.g. functional magnetic resonance imaging (fMRI). However, there is a strong limitation of the EEG/MEG tomography, which is the precise localization of electrical neuronal generators in 3D due to the inverse problem (see Sect. 21.6). Yet, as described in the following sections, it is possible to characterize EEG signals quantitatively (qEEG) by, e.g. averaging techniques, time–frequency analyses and source localization approaches. The EEG is commonly used to study neuronal processes related to sleep, resting (awake) states, task conditions or brain disorders (see Sect. 21.9).

---

## 21.2 Brainwaves

Brainwaves (neural oscillations), measured as variations in electrical potentials, can be tuned to become an ideal “observer” of the environment due to an organized system of brain rhythms. Brainwaves can be examined in different frequency bands and they can reflect endogenous activity, e.g. related to internal mental processes, such as mind wandering or interoception. However, they can also reflect on the plethora of on-going occurring mental activity due to the processing of exogenous sensory stimuli. Brainwaves can also represent age-related activity or can index abnormal activity, as e.g. in epilepsy [4–6], which is the most common clinical application for EEG, in psychosis [7] or neurodegeneration [8–10] or other disease states. One important consideration for any physiological interpretation of EEG oscillatory patterns is that the thalamus (and other subcortical regions) have an impact on cortical EEG patterns, as it acts as a

pacemaker and is bilaterally connected to the cortex by the thalamocortical radiations. This is especially relevant to consider for slow EEG rhythms (as the delta and alpha wave, see below), whereas the origin of the theta and gamma waves are less clear.

### 21.2.1 Delta Waves

Delta waves occur in all mammals and potentially in all animals and are the slowest (infra-slow) recorded brainwaves in human beings. They were first described by Walter in the 1930s, who improved upon Hans Berger's electroencephalograph machine to detect alpha and delta waves. The delta oscillation likely has two different components, one of which originates in the neocortex and the other in the thalamus. They are found most often in infants and young children and are associated with the deepest levels of relaxation and restorative, healing sleep. During slow-wave sleep (SWS) and some types of anaesthesia, the dominant activity pattern is a slow oscillation (sub-delta), with a frequency of 0.3–1 Hz [11, 12], which has most probably an intracortical origin. Also during sleep, another slow-wave brain activity is visible (called delta wave) with a frequency of oscillation between 0.5 and 4 Hz. Delta waves begin to occur (i.e. the EEG shows less than 50% delta wave activity) in stage 3 of NREM sleep and at stage 4 nearly all spectral activity is dominated by delta waves. SWS may be essential for memory consolidation and memory formation [13–16]. Clinically, delta waves are prominently seen in brain injuries, learning problems, inability to think, chronic pain and severe attention-deficit hyperactivity disorder (ADHD). If delta activity is suppressed, it leads to poor sleep and an inability to rejuvenate the body and revitalize the brain.

### 21.2.2 Theta Waves

The activity between 4 and 8 Hz is called theta wave activity. This activity arising from the hippocampus is manifested during, e.g. short-term

memory tasks [17–19]. Several studies suggest that these rhythms reflect the “on-line” state of the hippocampus; one of readiness to process-incoming signals [20]. Conversely, theta oscillations have been correlated to various voluntary behaviours such as spatial learning and navigation [21], and alert states (e.g. goose bumps) in rats [22]. It has been proposed that theta waves may reflect the integration of sensory information with motor output [23].

### 21.2.3 Alpha Waves

Alpha waves are neural oscillations in the frequency range of 8–13 Hz, generated from synchronous and coherent (in phase) electrical activity of thalamic pacemaker cells in humans. They predominantly originate from the occipital lobe during alert, wakeful relaxation (resting) with closed eyes. Alpha waves are reduced with open eyes, drowsiness and sleep. Initially, alpha waves were thought to represent the activity of the visual cortex in an idle state. However, more recent studies have claimed that they inhibit areas of the cortex not in use, or alternatively playing an active role in network coordination and communication [24]. An alpha-like variant called mu ( $\mu$ ) can be found over the motor cortex (central scalp) which is shown to be reduced with movement, or the intention to move. Alpha waves seem not to appear until 3 years of age [25] and can be modulated by attention [26, 27], working memory [28] and other processes.

### 21.2.4 Beta Waves

Beta waves are neural oscillations in the brain with a frequency range of 13–30 Hz and can be split into three sub-bands: low beta waves (13–16 Hz, “beta1 power”); beta waves (16–20 Hz, “beta2 power”) and high beta waves (20–30 Hz, “beta3 power”). Beta states are associated with motor planning [29] and normal waking consciousness. Low amplitude beta waves with multiple and varying frequencies are often associated with active busy or anxious thinking and active

concentration [30]. Over the motor cortex, beta waves are associated with the muscle contractions that happen in isotonic movements and are suppressed prior to and during movement changes [31]. Bursts of beta activity are associated with a strengthening of sensory feedback in static motor control and reduced when there is movement change [32]. Beta wave activity is elevated when movement has to be voluntarily suppressed or resisted [33]. The artificial induction of increased beta waves over the motor cortex by a form of electrical stimulation (transcranial alternating-current stimulation) is consistent with its link to isotonic contraction as it produces a slowing of motor movements [34]. Synchronization in the low beta wave range is essential for multimodal semantic processing [19].

### 21.2.5 Gamma Waves

Gamma waves reflect neural oscillations in humans with a frequency between 30 and 100 Hz. According to a popular theory, gamma waves can be reliability induced by visual stimuli and may be implicated in creating the unity of conscious perception (called “the binding problem”) [35]. The binding-by-gamma-oscillation hypothesis has a clear prediction: every part of the cortex should be able to support gamma oscillations under the right conditions. MEG studies indicate that there is a significant coupling of the gamma frequency band in the waking brain as well as during REM sleep. Gamma-related REM sleep activity cannot be perturbed by a sensory stimulus. However, there is no agreement on the “the binding problem” theory. “Whether or not gamma wave activity is related to subjective awareness is a difficult question that cannot be answered with confidence at the present time”. In humans, gamma oscillations are present during visual search [36], short-term working memory [37, 38], and object representation [39]. For example, local synchronization during visual processing evolved in the gamma frequency range [19]. In contrast, beta synchronization during multimodal

semantic processing evolved in the beta1 frequency range, and long-range fronto-parietal interactions during working memory retention and mental imagery evolved in the theta and alpha frequency range. EEG/MEG gamma band activity is altered in patients, e.g. in patients schizophrenia during mental (arithmetic) tasks or short-term working memory [40, 41]. Yet, gamma amplitudes are generally small, compared to other EEG frequency bands, and deserve careful post-processing to minimize artefacts (e.g. head motion) that could mimic gamma band activity.

## 21.3 EEG Recordings

Currently, EEG analyses are performed using 19–256 electrodes that are embedded in an electrode cap of different sizes. For high-density EEG (>64 channels) particular EEG caps are available that need only a short setup time. However, some researchers prefer to “record very clean data from a relatively modest number of electrodes rather than to record noisier data from a large number of electrodes” (Steven J. Luck, *An introduction to the event-related potential technique*, 2nd edition). The position of the electrodes on the cap most often follows the international 10–20 system [42]. This system uses four reference points: Inion, nasion and two preauricular positions. One or two letters are used to indicate the general brain region (e.g. C for central), numbers are used indicate the hemisphere (even for right and odd for left) and the distance from midline (larger numbers correspond to more distant electrodes). Recordings require a ground electrode and a single or multiple reference electrodes. There is still a quest for the “ideal” position of the reference electrode(s). Many researchers prefer the reference from electrodes near the mastoids or using the average of all electrode measurements as a reference. Theoretically, one could select an “inactive” electrode as reference electrode, as it is the assumption that recordings electrodes are close to the “generator” and the reference electrode is “far” from the generator. However,

whether an inactive electrode may or may not be a valid selection as a reference electrode depends on the size of the generator region. For example, alpha activity is optimally recorded from a posterior electrode with an anterior reference. For all EEG recordings, the EEG signal needs to be amplified (i.e., by a factor of 20,000 or more) and then converted into a digital form for storage on an EEG digitization computer. Event or trigger codes of the presented stimuli are usually sent from the stimulation PC to the digitization computer, where they were stored along with the EEG data.

---

## 21.4 Event-Related Potentials (ERP) Analysis

ERPs are measured by means of EEG. The ERP is the measured brain response from the direct result of a specific sensory, cognitive, motor or other mental event. More formally, it is any stereotyped electrophysiological response prior, during or after the stimulus. The MEG equivalent of ERP is the ERF or event-related field. Evoked potentials and induced potentials are subtypes of ERPs. Most ERPs are not directly visible from raw EEG data and thus, post-processing steps are required to identify them. They were first discovered in the Hallowell Davis' lab at Harvard in the 1930s, who observed a strong negative potential about 100–200 ms after an auditory event (the first computer-averaged ERP waveforms were published by Galambos and Sheatz [43]). The repetitive occurrence of the same event should result in similar amplitudes (in case stimuli are spaced apart large enough), whereas the background EEG should be distributed randomly in power. Hence, a simple signal averaging procedure across multiple trials (of the same experimental condition) is performed to extract the ERP waveform for single or multiple electrode sites, background EEG activity is also minimized by this approach. For most task situations, not only a single early ERP complex is observed but is accompanied by additional ERPs. The averaged ERP can be observed as deflection (which is

called peak, component or wave) with different polarities (positive or negative). Usually, ERPs can be identified and quantified with respect to the time of occurrence, latency and amplitude. In healthy adults (or animals), they should show the same characteristics in case of identical experimental conditions; and any deviation from the reflection of the ERPs must be interpreted with caution. Depending on the polarity and time of occurrence, they are labelled differently. The peaks are labelled P1, N1, P2, N2 and P3. P and N are traditionally used to indicate positive and negative peaks; the number indicates the temporal occurrence of the peaks (and thus the flow of information through the brain). Alternatively, the number is associated to the latency of the peak, e.g. post-stimulus response at 100 ms is called N100 in case of a negative response and P300 for a positive peak 300 ms after stimulus onset. Sometimes, ERPs can be named according to the function or paradigm, such as error-related negativity (ERN, seen if subjects perform an error) or no-go response (i.e. during a go/no-go task). Nowadays, ERP-related waveforms are plotted with positive upward and negative downward (although some researchers still prefer the opposite ways of plotting ERPs, as used in the early days of ERP research). As mentioned, ERP responses can already be seen prior to a sensory event, can be stronger for infrequent stimuli (e.g. the P3 during an oddball task, see [44]), and could be observed even for subliminal stimuli (but with a lower amplitude).

---

## 21.5 Spectral EEG Analysis

### 21.5.1 Power and Spatial Factor Analysis

Once the EEG is recorded, post-processing steps are required to visualize spectral power changes for a particular condition of interest or to compare EEG parameter differences between groups. EEG power spectra are computed by means of fast Fourier transformation (FFT) that decomposes the EEG signals into a series of sinusoidal

functions with different frequencies, amplitude and phases. Spectra demonstrate the dependency of amplitude, phase and power of the sinusoidal harmonic on the sinusoid's frequency in the EEG signal. The common idea of the spatial factor analysis is to produce factors constituted as a weighted sum of the recorded EEG channels. The simple and most commonly used spatial factor analysis is the principal component analysis (PCA). Here, the first factors account for the maximum possible amount of data variance and every subsequent factor explains the maximum possible residual variance. A PCA leads to signal decorrelations, as the cross-correlations between EEG activities (corresponding to different factors) are minimized. Another method is the independent component analysis (ICA) that separates the EEG signal in independent components (often 20 components are set as default in the available software packages). One advantage of the ICA is that it separates noise (respiration, pulse, eyes blinks, motion) from "real" EEG components. Yet, one has to examine both the topography of a component alongside its spectral plot to judge about the most likely origin of the component. Depending on the experimental design, analysis of variance (ANOVA) analysis or *t*-test analysis can be performed for group or condition comparisons in most of the commonly available software packages (see below).

### 21.5.2 Time–Frequency Analysis

EEG frequencies are never present as sinusoids in actual EEG data. Instead, they always reflect a mixture of such frequencies. Running a simple FFT on EEG data will provide a way to detect the most dominant peaks for one or more frequency bands of interest. With a time–frequency analysis (wavelet analysis), it is possible to analyse when which frequencies will occur. It is possible to decompose such signal into a superposition of signal at different sinusoidal signal at different frequencies using the real part of the EEG signal. Time–frequency plots are shown in 3D, most commonly with the frequency band on the *y*-axis,

the time on the *x*-axis and the amplitude on the *z*-axis, using a multi-colour-coding scheme to index amplitude variations.

### 21.5.3 Synchronicity, Connectivity and Information Flow

Without the presence of synchronous ("in-phase") events of the thalamus or other cortical regions, field potentials at the scalp would be small and would not produce any meaningful EEG, as field potentials of single cells are too weak. In fact, the activity of multiple (pyramidal) cells has to be synaptically active at the same time to be detected as EEG potentials. Synchronicity can be expressed by functional connectivity that can be used as an index for the temporal similarity between two or more channel locations (−1: fully anti-correlated, 1: fully correlated). For example, synchronous gamma band activity can be seen in cortical regions during in task-relevant stimuli [45]. It is also known that phase coupling between different frequency bands is a neural mechanism important for attention and to predict task performance (even on a single trial basis) [46]. One way to analyse the direction of information flow between cerebral regions or networks is to implement directed connectivity analysis. This method can be applied to EEG (or MEG) data and is computed by, e.g. renormalized partial directed coherence [47–49].

### 21.5.4 Microstate Analysis

Microstates are transient (quasi-stable) states or patterns of an EEG, tending to last from milliseconds to seconds, and are hypothesized to be the most basic initializations of human neurological tasks, and are thus nicknamed "the atoms of thought" [50]. Microstate estimation and analysis were originally done using alpha band activity, though broader bandwidth EEG bands are now typically used. The quasi-stability of microstates means that the "global EEG topography is fixed, but strength might vary and polarity invert" [51].

Microstate alterations have been reported in patients with panic disorder [52], schizophrenia [53–55], mild and moderate dementia of the Alzheimer type (AD) [56], epilepsy [57] and obsessive-compulsive disorder (OCD) [58].

### 21.5.5 Deep Learning

Deep learning with convolutional neural networks has revolutionized computer vision through end-to-end learning, that is, learning from the raw data [59]. For deep learning, there are no requirements for prior assumptions to guide extraction of particular features of the EEG/MEG to be used for classification, in contrast to machine learning techniques. Deep learning applicability has been demonstrated in clinical practice, e.g. for the detection of focal epileptiform discharges from scalp EEG recordings [60] but also for classifying sex and specific brain activity [61], emotion recognition [62], motor imagery classification [63] or sleep spindle detection [64].

---

## 21.6 Dipole and Source Localization of EEG Activity

In fact, many tiny dipoles result in an equivalent current dipole. The dipole results in a topography at the scalp. Scalp topography does not reflect source activity. The apparent visual of EEG signals is influenced by distance, volume conduction, dipole orientation and the superposition of sources. For example, for a radial dipole the source is reflected as the maximum on the topographic map. Yet, for two or more dipoles, the source is somewhere else and for a tangential dipole, the source is where topography reverses. Any dipole produces a certain scalp topography (forward problem). Any topography could have been produced by an infinite number of possible sources (inverse problem). Thus, it is difficult to infer EEG sources from EEG topographies. Activity from multiple electrodes can be visualized on so-called 2D topographic plots. Yet,

insufficient coverage but also additional problems, e.g. related to the “inverse problem”, limit the interpretation of EEG signals from subcortical and cortical structures, such as the thalamus or hippocampus. In addition, EEG signals are orchestrated by multiple brain regions or networks; thus, the strongest potential difference does not necessarily reflect the task-relevant brain area. As shown by several studies, it can even reflect inhibition, i.e. it shows task-unrelated activity, enabling other brain areas to be engaged in particular task situations. EEG has a high temporal resolution but lacks in spatial resolution compared to fMRI, but promising approaches for the accurate localization of EEG signals have been proposed. Clearly, it is advantageous to use high-density recordings for a better spatial localization of EEG signals. However, as trials with short temporal gaps can be reliably assessed by EEG, a precise 3D location of these events is highly recommendable to improve the interpretability of EEG signals. Source analysis was first performed in the 1980s, and improved a lot since then [65, 66]. Using discrete, 3D distributed, linear imaging methods were possible to estimate activity as the statistically standardized current density, referred to dynamic statistical parametric maps or noise-normalized current density [67]. Yet, it was shown that this method has significant non-zero localization errors even under quasi-ideal conditions with minimal measurement noise [68, 69]. More recently, programs have been developed (e.g. EEGLAB, fieldtrip, brainstorm, TAPEEG, e/sLORETA, SESAME, CARTOOL, Curry, MNE, BCILAB, dSPM (dynamic statistical parametric mapping), LCMV, DICS, BESA, MNE) that not only consider noise (from the current density) in the EEG/MEG measurements but also from possible biological noise, i.e. the variance in the actual electric neuronal activity. In this context, biological noise is assumed due to electrical neuronal activity that is independent and identically distributed all over the cortex [70]. Most of the described programs are open source, freely available and user-friendly (graphic user interface).

## 21.7 Artefacts

Several internal and external artefacts can compromise the EEG or MEG signal. The most prominent and constant artefact is produced by the electrical hum (50 or 60 Hz). However, this artefact can be easily removed by a sharp (Notch) filter. Other, more irregular artefacts are produced by eye movements, blinks, heartbeat, muscle tension or head motion. Muscle tensions (most often from the face) are very delicate artefacts, as they fall within frequency bands, which are of particular interest, e.g. during cognitive, motor or sensory tasks and as the strength of muscle tension could correlate to task-related activity [71]. In most software packages, automatic artefact rejection algorithms (e.g. based on an independent component analysis) are implemented to remove the described artefacts. However, as some of them show an irregular temporal and spatial pattern, manual correction steps are heavily warranted.

## 21.8 Limitations

The most important limitation of EEG (and MEG) is its poor spatial resolution. In addition, EEG is most sensitive to a particular set of post-synaptic potentials: those generated in superficial layers of the cortex, on the crests of gyri directly abutting the skull and radial to the skull. Dendrites, which are deeper in the cortex, inside sulci, in midline or deep structures (such as the hippocampus), or producing currents that are tangential to the skull, have far less contribution to the EEG signal. EEG recordings do not directly capture axonal action potentials. An action potential can be accurately represented as a current quadrupole, meaning that the resulting field decreases more rapidly than the ones produced by the current dipole of post-synaptic potentials. In addition, since EEGs represent averages of thousands of neurons, a large population of cells in synchronous activity is necessary to cause a significant deflection on the recordings. Action potentials are very fast and, therefore, the chances of field summation are slim. However, neural

backpropagation, as a typically longer dendritic current dipole, can be picked up by EEG electrodes and is a reliable indication of the occurrence of neural output. Not only do EEGs capture dendritic currents almost exclusively as opposed to axonal currents, they also show a preference for activity on populations of parallel dendrites and transmitting current in the same direction at the same time. Pyramidal neurons of cortical layers II/III and V extend apical dendrites to layer I. Currents moving up or down these processes underlie most of the signals produced by the EEG, and thus, the EEG provides information with a large bias to select neuron types. Therefore, EEG should generally not be used to make claims about global brain activity. The meninges, cerebrospinal fluid and skull “smear” the EEG signal, obscuring its intracranial source. It is mathematically impossible to reconstruct a unique intracranial current source for a given EEG signal, as some currents produce potentials that cancel each other out. This is referred to as the inverse problem. Yet, much work has been done to produce remarkably good estimates of, at least, a localized electric dipole that represents the recorded currents [65].

## 21.9 Clinical Applications

Brain disorders are not classified on the basis of neurophysiological data but on the basis of behaviour (e.g. DSM-5 or ICD-10). However, it is a pertinent question to look into the neurophysiological alterations seen in various brain disorders. The brain systems can roughly be divided into the following parts: sensory system, attentional system, affective system, executive system and memory system. The EEG has been used in various brain disorders demonstrating alternations in one or more of the systems, as a sign of neuronal dysfunction.

### 21.9.1 Epilepsy

There are many types of epilepsy, each presenting its own particular combination of seizure form

and location, age of onset and EEG correlates. The EEG can be used to monitor seizure-related and inter-ictal activity as well as to localize the epileptic focus. Studies in the 1930s demonstrated abnormal EEG activity with epilepsy. Nowadays, most of the modern qEEG software packages have tools for automatic spike detection that help practitioners for detecting and analysing paroxysmal events from particular electrodes. Spectral analysis can be used to visualize abnormal EEG activity in patients with epilepsy. As shown in Fig. 21.1, brain wave activity could be atypically elevated in children with generalized cryptogenic epilepsy. Spectral analysis revealed that global (whole-scalp) delta, alpha and beta band activity was greater in children without epilepsy compared to adults, and even further elevated for children with epilepsy. This might be an interesting neurophysiological finding but for clinicians, it is more important to understand how spike-related activity is associated with cortical and subcortical activity to achieve a better pre-surgical planning for resection procedures. In this context, EEG–fMRI represents a method for simultaneous recordings of electrical activity and oxygen changes. This method thus allows identifying the spatial origin of the epileptogenic zone and the temporal evolution of spike-related activity. Since 2003, EEG–fMRI has been applied in >100 publications (status: 2020) in the context of epilepsy [72–75].

### 21.9.2 ADHD

Attention-deficit hyperactivity disorder (ADHD) is the most common developmental disorder that affects about 3–9% of children worldwide. Patients with ADHD show behavioural abnormalities in the executive system, e.g. in the maintenance of working memory and attention, action selection, action inhibition and action monitoring. A common finding from qEEG studies is an increase in absolute slow wave activities (power) and a decrease in beta waves amplitudes in patients with ADHD in comparison to normal children. As absolute values of the spectra exhibit a big variation dependent on several brain unrelated features (e.g. thickness of the skull), a relative parameter, known as the theta/beta ratio, has been introduced. During brain development, this index shows that the strongest changes occur from centro-parietal electrodes in children below 9 years to fronto-central location in adults. This change in electrode position during normal development needs to be accounted for, if someone wants to discriminate patients with ADHD from controls. However, not all studies consistently reported differences in the theta/beta ratio comparing patients with ADHD and controls [76], which is consistent with the evidence that ADHD is a heterogeneous disorder. In addition, it has been demonstrated using qEEG, that chil-

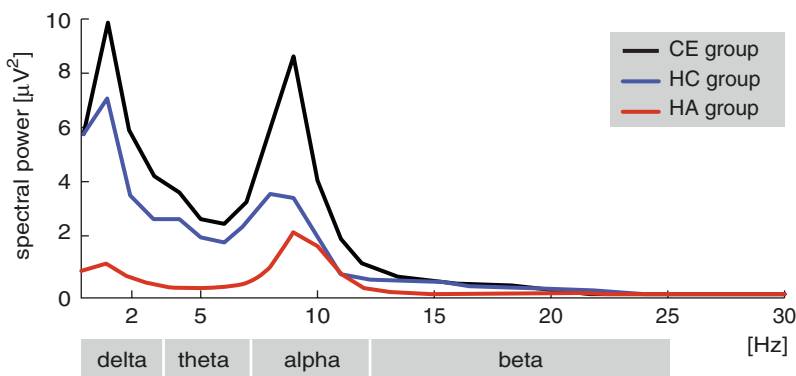


**Fig. 21.1** Absolute spectral power averaged across all electrodes for children with cryptogenic epilepsy (CE group, black curve) and the healthy control groups: healthy children (HC group, blue curve) and healthy adult

(HA group, red curve). The grey-shaded areas on the x-axis indicate the different frequency domains. (Printed with permission from *Brain Topogr* (2011) 24:78–89)



dren with ADHD show a slowing in the alpha frequency combined with a higher power in lower alpha and beta band activity. Power and central frequency from all frequency bands lead to a moderate cross-validated sensitivity and specificity to discriminate adults with ADHD from healthy adults. Using ERPs, various and inconsistent results have been reported since the early ERP studies in ADHD in the 1970s (for a review see [77, 78]). The lack of unequivocal ERP effects might be explained by the small ADHD sub-groups (e.g. attention-deficit vs. hyperactivity group) and heterogeneity of ADHD population examined in these studies.

### 21.9.3 Dementia

The slow dying of neuronal cells with age can be dramatically accelerated in the case of abnormally fast neurodegenerative processes, such as dementia of Alzheimer type (AD). QEEG measures are a sensitive index of degree of cognitive impairment, especially reflected in increased absolute and relative power in the theta band, with delta increasing in later stages of deterioration [79]. Using qEEG during resting states, Steven and co-authors found an increase in theta power at topographically widespread positions and decrease in coherence (the temporal similarity between two or more EEG signals) in mild AD patients [80]. In fact, eyes-open coherence was the most reliable parameter to discriminate patients from age- and sex-matched controls. In people with subject cognitive complaint, Prichep and co-workers [81] found that qEEG could be used to predict the cognitive decline within the next 7 years. In contrast to individuals with stable cognition, decliners showed elevated absolute and relative theta brain waves, a slowing of the mean frequency and alterations in coherence between multiple electrode sites [81]. Regarding microstates, people with mild or moderate probable AD showed a significant anteriorization of the centres of gravity of the microstate fields and a reduced duration of sustained microstates and

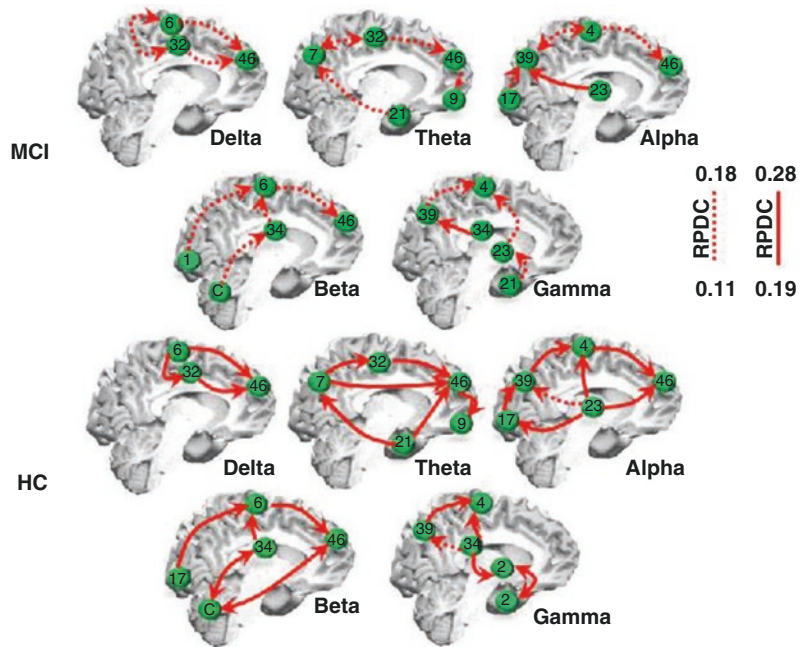
these differences were significantly correlated with the cognitive decline [56]. Using resting-state EEG, it has been demonstrated that directed connectivity is disturbed in people with mild cognitive impairment (MCI) [47]. Especially, the information flow of the hippocampus was weaker in different frequency bands and unilateral in patients with MCI compared to age- and sex-matched controls (Fig. 21.2). Using ERP analysis it could be shown that dementia was associated with a decreased accuracy and decreased ERN as compared to age-matched healthy controls during a picture–name verification task [82].

### 21.9.4 Addiction and Drug Abuse

Addiction is a compulsive, out-of-control drug use despite serious negative consequences. Addictive drugs can change directly (cocaine) or indirectly (e.g. opiates) the level of synaptic dopamine in reward centres of the brain such as the nucleus accumbens. The anterior cingulate cortex (ACC) plays an important role in monitoring behaviour and hyperactivity can result in compulsive pattern of drug seeking. An impairment in monitoring operation can be seen in addicted patients seen as alterations of the P400 using ERP recordings in a Go/no-go paradigm. After stereotactic cingulotomy, the P400 was suppressed and resulted to lower craving activity [83]. In addition, relaxation protocols of neuro-feedback might be useful e.g. for alcohol abuse, such as the alpha–theta brain wave training [84, 85]. Here, patients need to relax while alpha and theta activity is recorded simultaneously or they need to selectively increase activity of these brain waves at certain time points (“Peniston and Kulkosky protocol”). This EEG-based “treatment” resulted in sustained prevention of relapse in alcoholics.

Cannabis decreases in particular REM sleep time and disturbs the EEG. In a recent study with cannabis users, decreased resting-state (closed eyes) delta and increased theta to gamma power is observed compared to controls, indicating an

**Fig. 21.2** EEG renormalized partial directed coherence (RPDC) results. Top two rows: RPDC for mild cognitive impairment (MCI) participants. Bottom two rows: RPDC for healthy controls (HC). RPDC ranges between 0 and 1 and can be unidirectional or bidirectional (visualized by two red arrows). The labels indicate Brodmann areas (Bas). (Printed with permission from Front Aging Neurosci. 2017 Sep 20;9:304. <https://doi.org/10.3389/fnagi.2017.00304>. eCollection 2017)



abnormally high cortical activation and a disinhibition of inhibitory functions that may interrupt cognitive processes [86]. Cannabis users exhibited increased frequency–band dependent coherence and clustering coefficient in some brain regions, suggesting a loss of neural refinement and efficiency (“noisy” brain). Because measures related to cannabis use were correlated with spectral band power and functional connectivity measures, these results could inform about the effectiveness of intervention programs. Cocaine alters the EEG, and leads – as cannabis – to a decrease in delta–theta power and an increase in beta wave activity [87], the latter being most likely a consequence of the direct stimulation of a central noradrenergic arousal system.

**21.9.5 OCD**

Obsessive-compulsive disorders (OCD) can affect both cognition and motor behaviour. Using qEEG, hyperactivity has been reported in the frontal cortex in the OCD [88]. In addition, alpha wave activity appears to be decreased at frontal

electrodes. In fact, a change in alpha power was negatively correlated to executive function scores, whereas beta waves were positively correlated to characteristics of OCD. Yet, the frontal hyperactivity has also been reported in patients with phobias and posttraumatic stress disorder (under symptom provocation). This suggests that this hyperactivity could reflect the anxiety component of OCD more than its specific neuronal correlate. Using ERP, patients with OCD show a reduction in the P3 no-go component at anterior electrode locations, most likely in the ACC region [89]. In addition, the level of anteriorization was negatively associated with OCD symptomatology.

**21.9.6 Depression**

Major depression is a disorder of the affective system and is mainly characterized by a triad of symptoms: (1) low or depressed mood, (2) anhedonia, (3) low energy or fatigue. As shown by Henriques and Davidson [90], patients with depression demonstrated elevated left midfrontal

alpha power compared to never-depressed individuals [90]. During task-related EEG, non-depressed controls had a pattern of relative left-sided activation during the verbal task and relative right-sided activation during the spatial task. In contrast, depressed subjects failed to show activation in posterior right hemisphere regions during spatial task performance, indication of a deficit in posterior function in patients with depression [91]. Functional asymmetry appears to occur already early in life and might be a biological marker of a familiar or even genetic risk for mood disorders. Using ERP analysis, it could be shown that healthy adults demonstrated an asymmetry (right hemisphere > left hemisphere) of the amplitude of the N200 component during an auditory oddball task, which was not observed in individuals with sub-clinical depressed subjects [92].

### 21.9.7 Schizophrenia

In schizophrenic patients, the following three systems are affected: (a) executive system (e.g. leading to disorganized speech or thinking), (b) sensory system (e.g. leading to auditory hallucinations) and (c) affective system (e.g. leading to blunted emotions). EEG studies yield very inconsistent results, ranging from power elevations (reductions) in the beta band and reductions (elevations) on the alpha band to negative findings. This divergence can be most likely attributed to the heterogeneous and small sample size as well as to the impact of drug intake that influences the EEG pattern. Yet, for psychosis, which can be caused by schizophrenia, an increase of beta power was associated with the occurrence of hallucinations at (left) temporal electrodes [93]. Using ERPs, there is a consistent finding, which is the reduction of the amplitude of the mismatch negativity (an automatic response of the temporal cortex to a rare change in a repetitive stimulus/sound) in

patients with schizophrenia compared to controls [94]. However, this observation is not made in first-episode patients but only in patients with chronic- or recent-onset schizophrenia [95].

### 21.9.8 Chronic Pain

Chronic pain is caused by many conditions, but the aetiology and the maintenance of pain symptoms over time remain a scientific challenge. Recent evidence supports the idea that chronic pain can be understood not only as an altered perceptual state but also because of several changes produced in neural processing after body injury or stress. QEEG has been applied to assess brain functioning in several chronic pain syndromes [96–98]. Technical protocols for EEG recordings varied widely among studies related to chronic pain. Electrode placement followed the 10–20 International System in all studies and the number of electrodes for EEG recordings varied from 4 to 64 electrodes. The most frequently analysed parameters of brain activity were EEG power spectra at rest and the magnitude of different components of the ERP elicited by sensory stimulation or cognitive tasks. Chronic pain patients (including patients with migraine and spinal cord injury) displayed increased resting-state theta [98–101], alpha [100–102], beta [98, 100], or delta band power [100]. Some studies reported ERP changes when comparing patients with chronic pain and healthy controls [101, 103–108]. Some studies stated significant reductions of several ERP components in response to different sensory and cognitive tasks [101, 103, 104, 106]. In addition, qEEG can be used to study the impact of an interventional therapy on brain wave activity in chronic pain patients. As shown in Fig. 21.3, patients with chronic neuropathic pain showed almost a normal EEG power spectrum 3 and 12 months

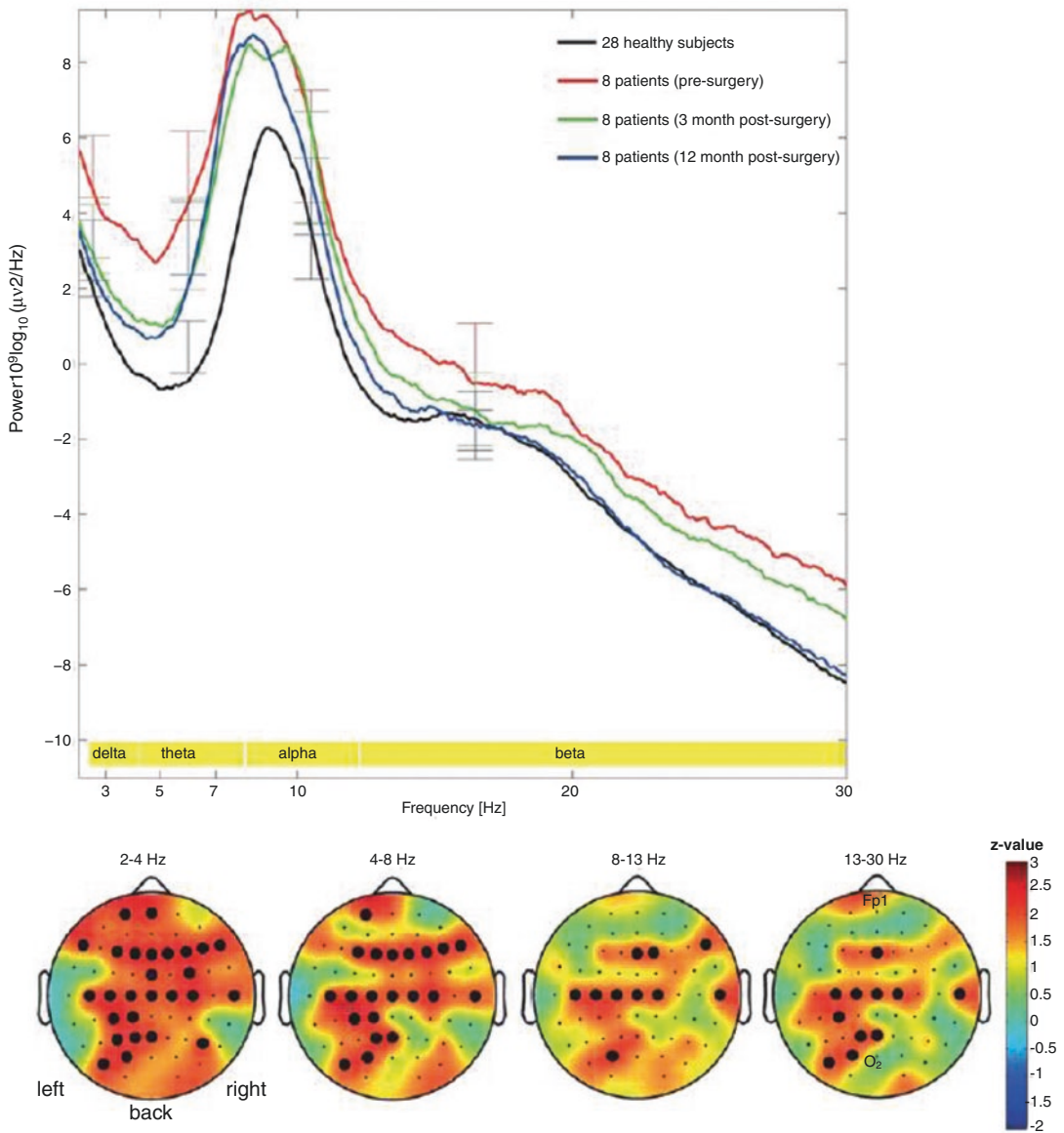


**Fig. 21.3** Upper row: graph showing power spectral curves of the patients before and after surgery with standard deviations of the means (vertical bars). Black curve is for controls. Frequency bands are shown in yellow at the bottom of the graph. Lower row: topoplots showing

electrode-wise comparisons. Black dots indicate the electrodes, which showed significantly higher spectral power before surgery as compared with 12 months after surgery. (Printed with permission from *Neurosurg Focus* 32(1):E1, 2012)

after non-invasive (ultrasound) central lateral thalamotomy.

### 21.9.9 Panic Disorder

Panic disorder is an anxiety disorder characterized by reoccurring unexpected panic attacks. In one of the first EEG studies to panic disorder, only 14% of the patients showed non-specific and abnormal EEGs and none displayed EEG evidence supportive of an ictal process related to epilepsy [109]. More recently, it has been reported that patients with panic disorder showed elevated overall absolute power in the delta–alpha frequency bands and reduced relative beta power compared to controls. Absolute delta and theta power can be positively associated with observer ratings of anxiety, while relative beta power can be related to self-ratings of anxiety [110].

### 21.9.10 Tumour

qEEG is often performed in tumour patients in the co-occurrence of epilepsy. For example, Hughes and Zak [111] performed EEGs in patients with chronic seizures associated with slowly growing (3–36 years) brain tumours [111]. When all EEGs were considered together without regard to their changes, no significant differences were found between patients and controls, especially with respect to the high incidence (60%) of EEG abnormalities both ipsilateral and contralateral to the tumour. Exact localization of the tumour by EEG (within one electrode) was found in 88% of patients. When changes in time were considered, the tumour group showed increasing slow waves, increasing sharp-wave discharges, depression of normal rhythms, a change in type of seizures, increase in frequency of seizures and a change in neurological signs and symptoms, especially motor. Using a visual stimulation design, Fukushima [112] found that a reduction of photic driving response

in brain tumour cases was not specific to the localization of the tumour and rather represents the diminution of the general cerebral reactivity, corresponding to the severity of the brain damage [112].

### 21.9.11 Stroke

In order to deepen our knowledge of the brain's ability to react to a cerebral insult, it is fundamental to obtain a "snapshot" of the acute phase, both for understanding the neural condition immediately after the insult and as a starting point for follow-up and clinical outcome prognosis. In an early work by Melamed and colleagues [113], regional cerebral blood flow (rCBF) and EEG frequency were investigated in the contralateral hemisphere of patients with acute cerebral infarction. Apart from a general decrease in rCBF, the authors found a slowing in the EEG frequency (from 10 to 6 Hz) in about 25% of the patients. In patients with acute cerebrovascular disease (mostly with ischemic stroke), neurological symptoms were scored repeatedly and related to EEG abnormalities quantified by frequency analysis. A correspondence between location of neurologic lesion and EEG focus was found in 87%, but correlation between neurologic score and the degree of EEG abnormality was low. Changes of clinical defects were not significantly related to qEEG parameters, indicating that qEEG analysis has to be used with caution for quantifying the clinical course of stroke patients [114]. It is known that transient ischemic attacks are characterized by stroke-like neurologic signs and symptoms in the absence of demonstrable structural neuropathology. Recently, Rogers et al. [115] performed a single electrode EEG during resting-state and auditory oddball conditions in patients within 72 h of admission to the acute stroke ward. Stroke patients exhibited pronounced left frontal delta activity, whereas alpha and beta power was increased in patients with transient ischaemic attacks. Theta power was attenuated in both patient groups compared to healthy controls

[115]. EEG and MEG can be used to increase the accuracy of predicting sensorimotor upper limb recovery (for a systematic review, see [116]); especially using theta, beta and gamma network features [117] or delta dipole density [118]. Using MEG, patients who had a recent (previous 10 days) unilateral stroke in the middle cerebral artery territory showed increased absolute delta band and lower beta–gamma power in the affected than in the unaffected hemisphere [119]. These values in both hemispheres differed from

control values. In addition, clinical severity correlated with the affected hemisphere decrease of gamma band power and individual alpha frequency. Larger lesions were also associated with a worse clinical picture and stronger MEG alterations.

## 21.10 Clinical Cases

### 21.10.1 Epilepsy (Figs. 21.4 and 21.5)

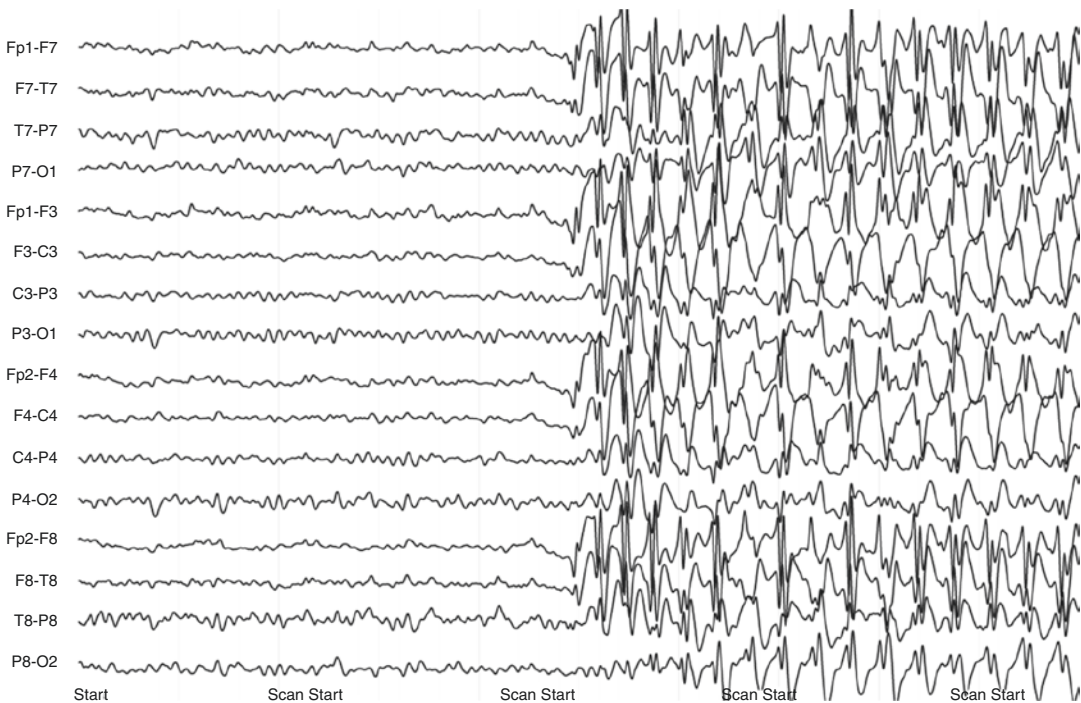


**Fig. 21.4** As shown in this figure, the EEG demonstrates an example of a childhood absence epilepsy in a 6-year-old child suffering from absence seizures accompanied by very short episodes of abrupt and severe impairment (loss) of consciousness. The seizures are paralleled by ictal discharges of generalized high-amplitude spikes and by some double spike- and slow-wave complexes. The paroxysms are rhythmic at around 3 Hz with a gradual and

regular slowdown from the initial to the terminal phase of the discharge. The duration of absence of seizures varies between 4 and 20 s. Absence epilepsy represents a typical form of a generalized epilepsy. Most children with this form of epilepsy have a normal neurological state and a normal development. (Courtesy of Prof. Dr. M. Siniatchkin, Evangelisches Klinikum Bethel, Germany)



**Fig. 21.5** This is an EEG of a 7-year-old child suffering from the Benign Epilepsy with Rolandic or Centro-Temporal Spikes or BECTS—a partial epilepsy of childhood characterized by absence of neurological deficits, motor partial seizures, peculiar EEG centro-temporal spikes and spontaneous recovery. The EEG shows epileptic discharges originating from the right central region (C4, Laplacian montage) distributing to the parietal brain

areas (P4). BECTS is the most common form of idiopathic epilepsy in children with the typical electro-clinical picture (centro-temporal spikes) and favourable outcome. This child has seizures started in the fourth year of his life, which consisted of unilateral facial paresthesia, hemifacial jerks involving lips and tongue as well as speech arrest. (Courtesy of Prof. Dr. M. Siniatchkin, Evangelisches Klinikum Bethel, Germany)

## References

- Berger H. Electroencephalogram in humans. *Arch Psychiatr Nervenkr.* 1929;87:527–70. <https://doi.org/10.1007/BF01797193>.
- Jasper HH, Carmichael L. Electrical potentials from the intact human brain. *Science.* 1935;81(2089):51–3. <https://doi.org/10.1126/science.81.2089.51>.
- Coles MD, Rugg. *Electrophysiology of mind.* Oxford: Oxford University Press; 1996.
- Belnap WD, Toman JE, Goodman LS. Tridione-diphenylhydantoin combination therapy in grand mal with slow-wave EEG dysrhythmia. *Fed Proc.* 1947;6(1):308.
- Glaser MA, Irons M. Is the epileptic a safe motor vehicle driver? With some remarks relative to the clinical application of the EEG. *J Nerv Ment Dis.* 1946;103:21–36.
- Goodwin JE. The significance of alpha variants in the EEG, and their relationship to an epileptiform syndrome. *Am J Psychiatry.* 1947;104(6):369–79. <https://doi.org/10.1176/ajp.104.6.369>.
- Bonnet H, Chabot E. EEG and clinical manifestations observed in a case of anxiety psychosis during the period of treatment with various drugs. *Electroencephalogr Clin Neurophysiol.* 1955;7(1):151.
- Guntekin B, Emek DD, Kurt P, Yener GG, Basar E. Beta oscillatory responses in healthy subjects and subjects with mild cognitive impairment upon application of stimuli with cognitive load. *Biol Psychiatry.* 2013;73(9):82s.
- Liddell DW. Investigations of EEG findings in presenile dementia. *J Neurol Neurosurg Psychiatry.* 1958;21(3):173–6. <https://doi.org/10.1136/jnmp.21.3.173>.
- Yener GG, Kurt P, Cavusoglu B, Emek DD, Aktas G, Ada E, Guntekin B, Basar E. The auditory event-related oscillations are diminished, and correlate with hippocampal volumetry in mild cognitive impairment. *Ann Neurol.* 2012;72:S126.
- Steriade M, Nunez A, Amzica F. A novel slow (< 1 Hz) oscillation of neocortical neurons in vivo: depolarizing and hyperpolarizing components. *J Neurosci.* 1993;13(8):3252–65.
- Steriade M, Timofeev I, Grenier F. Natural waking and sleep states: a view from inside neocortical neurons. *J Neurophysiol.* 2001;85(5):1969–85. <https://doi.org/10.1152/jn.2001.85.5.1969>.

13. Gais S, Plihal W, Wagner U, Born J. Early sleep triggers memory for early visual discrimination skills. *Nat Neurosci.* 2000;3(12):1335–9. <https://doi.org/10.1038/81881>.
14. Huber R, Ghilardi MF, Massimini M, Tononi G. Local sleep and learning. *Nature.* 2004;430(6995):78–81. <https://doi.org/10.1038/nature02663>.
15. Maquet P. The role of sleep in learning and memory. *Science.* 2001;294(5544):1048–52. <https://doi.org/10.1126/science.1062856>.
16. Stickgold R, Whidbee D, Schirmer B, Patel V, Hobson JA. Visual discrimination task improvement: a multi-step process occurring during sleep. *J Cogn Neurosci.* 2000;12(2):246–54.
17. Koenig T, Lehmann D, Saito N, Kuginuki T, Kinoshita T, Koukkou M. Decreased functional connectivity of EEG theta-frequency activity in first-episode, neuroleptic-naive patients with schizophrenia: preliminary results. *Schizophr Res.* 2001;50(1–2):55–60.
18. Vertes RP. Hippocampal theta rhythm: a tag for short-term memory. *Hippocampus.* 2005;15(7):923–35. <https://doi.org/10.1002/hipo.20118>.
19. von Stein A, Sarnthein J. Different frequencies for different scales of cortical integration: from local gamma to long range alpha/theta synchronization. *Int J Psychophysiol.* 2000;38(3):301–13.
20. Buzsáki G. Theta oscillations in the hippocampus. *Neuron.* 2002;33(3):325–40. [https://doi.org/10.1016/S0896-6273\(02\)00586-X](https://doi.org/10.1016/S0896-6273(02)00586-X).
21. Buzsáki G. Theta rhythm of navigation: Link between path integration and landmark navigation, episodic and semantic memory. *Hippocampus.* 2005;15(7):827–40. <https://doi.org/10.1002/hipo.20113>.
22. Vanderwolf CH. Hippocampal electrical activity and voluntary movement in rat. *Electroencephalogr Clin Neurophysiol.* 1969;26(4):407–18. [https://doi.org/10.1016/0013-4694\(69\)90092-3](https://doi.org/10.1016/0013-4694(69)90092-3).
23. Bland BH, Oddie SD. Theta band oscillation and synchrony in the hippocampal formation and associated structures: the case for its role in sensorimotor integration. *Behav Brain Res.* 2001;127(1–2):119–36. [https://doi.org/10.1016/S0166-4328\(01\)00358-8](https://doi.org/10.1016/S0166-4328(01)00358-8).
24. Palva S, Palva JM. New vistas for alpha-frequency band oscillations. *Trends Neurosci.* 2007;30(4):150–8. <https://doi.org/10.1016/j.tins.2007.02.001>.
25. Kolev V, Basar-Eroglu C, Aksu F, Basar E. EEG rhythmicities evoked by visual stimuli in three-year-old children. *Int J Neurosci.* 1994;75(3–4):257–70.
26. Daniel RS. Alpha and theta EEG in vigilance. *Percept Mot Skills.* 1967;25(3):697–703. <https://doi.org/10.2466/pms.1967.25.3.697>.
27. Mulholland T. The concept of attention and the EEG alpha-rhythm. *Electroencephalogr Clin Neurophysiol.* 1968;24(2):188.
28. Gale A, Spratt G, Christie B, Smallbone A. Stimulus complexity, EEG abundance gradients, and detection efficiency in a visual recognition task. *Br J Psychol.* 1975;66(3):289–98.
29. Jasper HH, Penfield W. Electroencephalograms in man: effect of voluntary movement upon the electrical activity of the precentral gyrus. *Arch Psychiatr Zeitschr Neurol.* 1949;83:163–74.
30. Baumeister J, Barthel T, Geiss KR, Weiss M. Influence of phosphatidylserine on cognitive performance and cortical activity after induced stress. *Nutr Neurosci.* 2008;11(3):103–10. <https://doi.org/10.1179/147683008X301478>.
31. Baker SN. Oscillatory interactions between sensorimotor cortex and the periphery. *Curr Opin Neurobiol.* 2007;17(6):649–55. <https://doi.org/10.1016/j.conb.2008.01.007>.
32. Lalo E, Gilbertson T, Doyle L, Di Lazzaro V, Cioni B, Brown P. Phasic increases in cortical beta activity are associated with alterations in sensory processing in the human. *Exp Brain Res.* 2007;177(1):137–45. <https://doi.org/10.1007/s00221-006-0655-8>.
33. Zhang Y, Chen Y, Bressler SL, Ding M. Response preparation and inhibition: the role of the cortical sensorimotor beta rhythm. *Neuroscience.* 2008;156(1):238–46. <https://doi.org/10.1016/j.neuroscience.2008.06.061>.
34. Pogosyan A, Gaynor LD, Eusebio A, Brown P. Boosting cortical activity at beta-band frequencies slows movement in humans. *Curr Biol.* 2009;19(19):1637–41. <https://doi.org/10.1016/j.cub.2009.07.074>.
35. Singer W, Gray CM. Visual feature integration and the temporal correlation hypothesis. *Annu Rev Neurosci.* 1995;18:555–86. <https://doi.org/10.1146/annurev.ne.18.030195.003011>.
36. Tallon-Baudry C, Bertrand O, Delpuech C, Pernier J. Oscillatory gamma-band (30–70 Hz) activity induced by a visual search task in humans. *J Neurosci.* 1997;17(2):722–34.
37. Howard MW, Rizzuto DS, Caplan JB, Madsen JR, Lisman J, Aschenbrenner-Scheibe R, Schulze-Bonhage A, Kahana MJ. Gamma oscillations correlate with working memory load in humans. *Cereb Cortex.* 2003;13(12):1369–74.
38. Tallon-Baudry C, Bertrand O, Peronnet F, Pernier J. Induced gamma-band activity during the delay of a visual short-term memory task in humans. *J Neurosci.* 1998;18(11):4244–54.
39. Tallon-Baudry C, Bertrand O. Oscillatory gamma activity in humans and its role in object representation. *Trends Cogn Sci.* 1999;3(4):151–62.
40. Basar-Eroglu C, Brand A, Hildebrandt H, Karolina Kedzior K, Mathes B, Schmiedt C. Working memory related gamma oscillations in schizophrenia patients. *Int J Psychophysiol.* 2007;64(1):39–45. <https://doi.org/10.1016/j.ijpsycho.2006.07.007>.
41. Kissler J, Muller MM, Fehr T, Rockstroh B, Elbert T. MEG gamma band activity in schizophrenia patients and healthy subjects in a mental arithmetic task and at rest. *Clin Neurophysiol.* 2000;111(11):2079–87.
42. Jasper HH. The ten-twenty electrode system of the international federation. *Electroencephalogr Clin Neurophysiol Suppl.* 1958;10:371–75.



43. Galambos R, Sheatz GC. An electroencephalograph study of classical conditioning. *Am J Phys.* 1962;203:173–84. <https://doi.org/10.1152/ajplegacy.1962.203.1.173>.
44. Polich J. Neuropsychology of P300. In: Kappenman ES, Luck SJ (eds.), *The oxford handbook of event-related potential components*. Oxford University Press, 2012; pp. 159–88.
45. Haig AR, Gordon E, Wright JJ, Meares RA, Bahramali H. Synchronous cortical gamma-band activity in task-relevant cognition. *Neuroreport.* 2000;11(4):669–75.
46. Hanslmayr S, Aslan A, Staudigl T, Klimesch W, Herrmann CS, Bauml KH. Prestimulus oscillations predict visual perception performance between and within subjects. *NeuroImage.* 2007;37(4):1465–73. <https://doi.org/10.1016/j.neuroimage.2007.07.011>.
47. Michels L, Muthuraman M, Anwar AR, Kollias S, Leh SE, Riese F, Unschuld PG, Siniatchkin M, Gietl AF, Hock C. Changes of functional and directed resting-state connectivity are associated with neuronal oscillations, ApoE genotype and amyloid deposition in mild cognitive impairment. *Front Aging Neurosci.* 2017;9:304. <https://doi.org/10.3389/fnagi.2017.00304>.
48. Michels L, Muthuraman M, Luchinger R, Martin E, Anwar AR, Raethjen J, Brandeis D, Siniatchkin M. Developmental changes of functional and directed resting-state connectivities associated with neuronal oscillations in EEG. *NeuroImage.* 2013;81:231–42. <https://doi.org/10.1016/j.neuroimage.2013.04.030>.
49. Schelter B, Sommerlade L, Platt B, Plano A, Thiel M, Timmer J. Multivariate analysis of dynamical processes with applications to the neurosciences. *Conf Proc IEEE Eng Med Biol Soc.* 2011;2011:5931–4. <https://doi.org/10.1109/IEMBS.2011.6091467>.
50. Koenig T, Lehmann D, Merlo MC, Kochi K, Hell D, Koukkou M. A deviant EEG brain microstate in acute, neuroleptic-naïve schizophrenics at rest. *Eur Arch Psychiatry Clin Neurosci.* 1999;249(4):205–11.
51. Van de Ville D, Britz J, Michel CM. EEG microstate sequences in healthy humans at rest reveal scale-free dynamics. *Proc Natl Acad Sci U S A.* 2010;107(42):18179–84. <https://doi.org/10.1073/pnas.1007841107>.
52. Kikuchi M, Koenig T, Munesue T, Hanaoka A, Strik W, Dierks T, Koshino Y, Minabe Y. EEG microstate analysis in drug-naïve patients with panic disorder. *PLoS One.* 2011;6(7):e22912. <https://doi.org/10.1371/journal.pone.0022912>.
53. Lehmann D, Faber PL, Galderisi S, Herrmann WM, Kinoshita T, Koukkou M, Mucci A, Pascual-Marqui RD, Saito N, Wackermann J, Winterer G, Koenig T. EEG microstate duration and syntax in acute, medication-naïve, first-episode schizophrenia: a multi-center study. *Psychiatry Res.* 2005;138(2):141–56. <https://doi.org/10.1016/j.psychres.2004.05.007>.
54. Soni S, Muthukrishnan SP, Sood M, Kaur S, Sharma R. Hyperactivation of left inferior parietal lobule and left temporal gyri shortens resting EEG microstate in schizophrenia. *Schizophr Res.* 2018;201:204–7. <https://doi.org/10.1016/j.schres.2018.06.020>.
55. Strelets V, Faber PL, Golikova J, Novototsky-Vlasov V, Koenig T, Gianotti LR, Gruzeliev JH, Lehmann D. Chronic schizophrenics with positive symptomatology have shortened EEG microstate durations. *Clin Neurophysiol.* 2003;114(11):2043–51.
56. Strik WK, Chiaramonti R, Muscas GC, Paganini M, Mueller TJ, Fallgatter AJ, Versari A, Zappoli R. Decreased EEG microstate duration and anteriorisation of the brain electrical fields in mild and moderate dementia of the Alzheimer type. *Psychiatry Res.* 1997;75(3):183–91.
57. Raj VK, Rajagopalan SS, Bhardwaj S, Panda R, Reddam VR, Ganne C, Kenchaiah R, Mundlamuri RC, Kandavel T, Majumdar KK, Parthasarathy S, Sinha S, Bharath RD. Machine learning detects EEG microstate alterations in patients living with temporal lobe epilepsy. *Seizure.* 2018;61:8–13. <https://doi.org/10.1016/j.seizure.2018.07.007>.
58. Yoshimura M, Pascual-Marqui RD, Nishida K, Kitaura Y, Mii H, Saito Y, Ikeda S, Katsura K, Ueda S, Minami S, Isotani T, Kinoshita T. Hyperactivation of the frontal control network revealed by symptom provocation in obsessive-compulsive disorder using EEG microstate and sLORETA analyses. *Neuropsychobiology.* 2019;77:176–85. <https://doi.org/10.1159/000491719>.
59. Schirrmester RT, Springenberg JT, Fiederer LDJ, Glasstetter M, Eggenesperger K, Tangermann M, Hutter F, Burgard W, Ball T. Deep learning with convolutional neural networks for EEG decoding and visualization. *Hum Brain Mapp.* 2017;38(11):5391–420. <https://doi.org/10.1002/hbm.23730>.
60. Tjepkema-Cloostermans MC, de Carvalho RCV, van Putten M. Deep learning for detection of focal epileptiform discharges from scalp EEG recordings. *Clin Neurophysiol.* 2018;129(10):2191–6. <https://doi.org/10.1016/j.clinph.2018.06.024>.
61. van Putten M, Olbrich S, Arns M. Predicting sex from brain rhythms with deep learning. *Sci Rep.* 2018;8(1):3069. <https://doi.org/10.1038/s41598-018-21495-7>.
62. Jirayuchareonsak S, Pan-Ngum S, Israsena P. EEG-based emotion recognition using deep learning network with principal component based covariate shift adaptation. *ScientificWorldJournal.* 2014;2014:627892. <https://doi.org/10.1155/2014/627892>.
63. Chiarelli AM, Croce P, Merla A, Zappasodi F. Deep learning for hybrid EEG-fNIRS brain-computer interface: application to motor imagery classification. *J Neural Eng.* 2018;15(3):036028. <https://doi.org/10.1088/1741-2552/aaaf82>.
64. Dakun T, Rui Z, Jinbo S, Wei Q. Sleep spindle detection using deep learning: a validation study based on crowdsourcing. *Conf Proc IEEE Eng Med Biol Soc.* 2015;2015:2828–31. <https://doi.org/10.1109/EMBC.2015.7318980>.
65. Pascual-Marqui RD, Lehmann D, Koukkou M, Kochi K, Anderer P, Saletu B, Tanaka H, Hirata

- K, John ER, Prichep L, Biscay-Lirio R, Kinoshita T. Assessing interactions in the brain with exact low-resolution electromagnetic tomography. *Philos Trans A Math Phys Eng Sci.* 2011;369(1952):3768–84. <https://doi.org/10.1098/rsta.2011.0081>.
66. Pascual-Marqui RD, Michel CM, Lehmann D. Low resolution electromagnetic tomography: a new method for localizing electrical activity in the brain. *Int J Psychophysiol.* 1994;18(1):49–65.
67. Dale AM, Liu AK, Fischl BR, Buckner RL, Belliveau JW, Lewine JD, Halgren E. Dynamic statistical parametric mapping: combining fMRI and MEG for high-resolution imaging of cortical activity. *Neuron.* 2000;26(1):55–67.
68. Pascual Marqui RD. Standardized low-resolution brain electromagnetic tomography (sLORETA): technical details. *Methods Find Exp Clin Pharmacol.* 2002;24(Suppl C):5–12.
69. Sekihara K, Sahani M, Nagarajan SS. Localization bias and spatial resolution of adaptive and non-adaptive spatial filters for MEG source reconstruction. *NeuroImage.* 2005;25(4):1056–67. <https://doi.org/10.1016/j.neuroimage.2004.11.051>.
70. Michel C, Koenig T, Brandeis D, Gianotti LR, Wackermann J. *Electrical neuroimaging.* Cambridge: Cambridge University Press; 2009.
71. Van Boxtel A, Jessurun M. Amplitude and bilateral coherency of facial and jaw-elevator EMG activity as an index of effort during a two-choice serial reaction task. *Psychophysiology.* 1993;30(6):589–604.
72. Al-Asmi A, Benar CG, Gross DW, Khani YA, Andermann F, Pike B, Dubeau F, Gotman J. fMRI activation in continuous and spike-triggered EEG-fMRI studies of epileptic spikes. *Epilepsia.* 2003;44(10):1328–39.
73. Bagshaw AP, Aghakhani Y, Benar CG, Kobayashi E, Hawco C, Dubeau F, Pike GB, Gotman J. EEG-fMRI of focal epileptic spikes: analysis with multiple haemodynamic functions and comparison with gadolinium-enhanced MR angiograms. *Hum Brain Mapp.* 2004;22(3):179–92. <https://doi.org/10.1002/hbm.20024>.
74. Hamandi K, Salek-Haddadi A, Laufs H, Liston A, Friston K, Fish DR, Duncan JS, Lemieux L. EEG-fMRI of idiopathic and secondarily generalized epilepsies. *NeuroImage.* 2006;31(4):1700–10. <https://doi.org/10.1016/j.neuroimage.2006.02.016>.
75. Kang JK, Benar C, Al-Asmi A, Khani YA, Pike GB, Dubeau F, Gotman J. Using patient-specific hemodynamic response functions in combined EEG-fMRI studies in epilepsy. *NeuroImage.* 2003;20(2):1162–70.
76. Liechti MD, Valko L, Müller UC, Döhnert M, Drechsler R, Steinhausen Hans-Christoph, Brandeis D. Diagnostic value of resting electroencephalogram in attention-deficit/hyperactivity disorder across the lifespan. *Brain Topogr.* 2013;26(1):135–51. <https://doi.org/10.1007/s10548-012-0258-6>.
77. Barry RJ, Stuart JJ, Clarke AR. A review of electrophysiology in attention-deficit/hyperactivity disorder: II. event-related potentials. *Clin Neurophysiol.* 2003;114(2):184–98. [https://doi.org/10.1016/s1388-2457\(02\)00363-2](https://doi.org/10.1016/s1388-2457(02)00363-2).
78. Barry RJ, Clarke AR, Stuart JJ. A review of electrophysiology in attention-deficit/hyperactivity disorder: I. Qualitative and Quantitative Electroencephalography. *Clin Neurophysiol.* 2003;114(2):171–83. [https://doi.org/10.1016/s1388-2457\(02\)00362-0](https://doi.org/10.1016/s1388-2457(02)00362-0).
79. Prichep LS, John ER, Ferris SH, Reisberg B, Almas M, Alper K, Cancro R. Quantitative EEG correlates of cognitive deterioration in the elderly. *Neurobiol Aging.* 1994;15(1):85–90.
80. Stevens A, Kircher T, Nickola M, Bartels M, Rosellen N, Wormstall H. Dynamic regulation of EEG power and coherence is lost early and globally in probable DAT. *Eur Arch Psychiatry Clin Neurosci.* 2001;251(5):199–204.
81. Prichep LS, John ER, Ferris SH, Rausch L, Fang Z, Cancro R, Torossian C, Reisberg B. Prediction of longitudinal cognitive decline in normal elderly with subjective complaints using electrophysiological imaging. *Neurobiol Aging.* 2006;27(3):471–81. <https://doi.org/10.1016/j.neurobiolaging.2005.07.021>.
82. Mathalon DH, Bennett A, Askari N, Gray EM, Rosenbloom MJ, Ford JM. Response-monitoring dysfunction in aging and Alzheimer's disease: an event-related potential study. *Neurobiol Aging.* 2003;24(5):675–85.
83. Ryzhenkova YY, Ponomarev VA, Anichkov AD, Konenkov SY, Polyakov YI, Melnichuk KV, Kropotov JD. P3 monitoring component decrease after bilateral crio-cingulotomy in heroin drug addicts. *Int J Psychophysiol.* 2008;69(3):314. <https://doi.org/10.1016/j.ijpsycho.2008.05.334>.
84. Peniston EG, Kulkosky PJ. Alpha-theta-brainwave training and beta-endorphin levels in alcoholics. *Alcohol Clin Exp Res.* 1989;13(2):271–9. <https://doi.org/10.1111/j.1530-0277.1989.tb00325.x>.
85. Saxby E, Peniston EG. Alpha-theta brainwave neurofeedback training—an effective treatment for male and female alcoholics with depressive symptoms. *J Clin Psychol.* 1995;51(5):685–93. [https://doi.org/10.1002/1097-4679\(199509\)51:5<685::Aid-Jclp2270510514>3.0.Co;2-K](https://doi.org/10.1002/1097-4679(199509)51:5<685::Aid-Jclp2270510514>3.0.Co;2-K).
86. Prasad S, Dedrick ES, Filbey FM. Cannabis users exhibit increased cortical activation during resting state compared to non-users. *NeuroImage.* 2018;179:176–86. <https://doi.org/10.1016/j.neuroimage.2018.06.031>.
87. Herning RI, Jones RT, Hooker WD, Mendelson J, Blackwell L. Cocaine increases EEG beta: a replication and extension of Hans Berger's historic experiments. *Electroencephalogr Clin Neurophysiol.* 1985;60(6):470–7.
88. Bucci P, Mucci A, Volpe U, Merlotti E, Galderisi S, Maj M. Executive hypercontrol in obsessive-

- compulsive disorder: electrophysiological and neuropsychological indices. *Clin Neurophysiol.* 2004;115(6):1340–8. <https://doi.org/10.1016/j.clinph.2003.12.031>.
89. Herrmann MJ, Jacob C, Unterecker S, Fallgatter AJ. Reduced response-inhibition in obsessive-compulsive disorder measured with topographic evoked potential mapping. *Psychiatry Res.* 2003;120(3):265–71.
  90. Henriques JB, Davidson RJ. Regional brain electrical asymmetries discriminate between previously depressed and healthy control subjects. *J Abnorm Psychol.* 1990;99(1):22–31.
  91. Henriques JB, Davidson RJ. Brain electrical asymmetries during cognitive task performance in depressed and nondepressed subjects. *Biol Psychiatry.* 1997;42(11):1039–50.
  92. Sumich AL, Kumari V, Heasman BC, Gordon E, Brammer M. Abnormal asymmetry of N200 and P300 event-related potentials in subclinical depression. *J Affect Disord.* 2006;92(2–3):171–83. <https://doi.org/10.1016/j.jad.2006.01.006>.
  93. Lee SH, Wynn JK, Green MF, Kim H, Lee KJ, Nam M, Park JK, Chung YC. Quantitative EEG and low resolution electromagnetic tomography (LORETA) imaging of patients with persistent auditory hallucinations. *Schizophr Res.* 2006;83(2–3):111–9. <https://doi.org/10.1016/j.schres.2005.11.025>.
  94. McCarley RW, O'Donnell BF, Niznikiewicz MA, Salisbury DF, Potts GF, Hirayasu Y, Nestor PG, Shenton ME. Update on electrophysiology in schizophrenia. *Int Rev Psychiatry.* 1997;9(4):373–86.
  95. Umbricht DS, Bates JA, Lieberman JA, Kane JM, Javitt DC. Electrophysiological indices of automatic and controlled auditory information processing in first-episode, recent-onset and chronic schizophrenia. *Biol Psychiatry.* 2006;59(8):762–72. <https://doi.org/10.1016/j.biopsych.2005.08.030>.
  96. Boord P, Siddall PJ, Tran Y, Herbert D, Middleton J, Craig A. Electroencephalographic slowing and reduced reactivity in neuropathic pain following spinal cord injury. *Spinal Cord.* 2008;46(2):118–23. <https://doi.org/10.1038/sj.sc.3102077>.
  97. Schmidt S, Naranjo JR, Brenneisen C, Gundlach J, Schultz C, Kaube H, Hinterberger T, Jeanmonod D. Pain ratings, psychological functioning and quantitative EEG in a controlled study of chronic back pain patients. *PLoS One.* 2012;7(3):e31138. <https://doi.org/10.1371/journal.pone.0031138>.
  98. Stern J, Jeanmonod D, Sarneathin J. Persistent EEG overactivation in the cortical pain matrix of neurogenic pain patients. *NeuroImage.* 2006;31(2):721–31. <https://doi.org/10.1016/j.neuroimage.2005.12.042>.
  99. Bjork MH, Stovner LJ, Engstrom M, Stjern M, Hagen K, Sand T. Interictal quantitative EEG in migraine: a blinded controlled study. *J Headache Pain.* 2009;10(5):331–9. <https://doi.org/10.1007/s10194-009-0140-4>.
  100. Sarneathin J, Stern J, Aufenberg C, Rousson V, Jeanmonod D. Increased EEG power and slowed dominant frequency in patients with neurogenic pain. *Brain.* 2006;129(Pt 1):55–64. <https://doi.org/10.1093/brain/awh631>.
  101. Vuckovic A, Hasan MA, Fraser M, Conway BA, Nasseroleslami B, Allan DB. Dynamic oscillatory signatures of central neuropathic pain in spinal cord injury. *J Pain.* 2014;15(6):645–55. <https://doi.org/10.1016/j.jpain.2014.02.005>.
  102. van den Broeke EN, Wilder-Smith OHG, van Goor H, Vissers KCP, van Rijn CM. Patients with persistent pain after breast cancer treatment show enhanced alpha activity in spontaneous EEG. *Pain Med.* 2013;14(12):1893–9. <https://doi.org/10.1111/pme.12216>.
  103. Bjork M, Hagen K, Stovner L, Sand T. Photic EEG-driving responses related to ictal phases and trigger sensitivity in migraine: a longitudinal, controlled study. *Cephalalgia.* 2011;31(4):444–55. <https://doi.org/10.1177/0333102410385582>.
  104. Gonzalez-Roldan AM, Munoz MA, Cifre I, Sitges C, Montoya P. Altered psychophysiological responses to the view of others' pain and anger faces in fibromyalgia patients. *J Pain.* 2013;14(7):709–19. <https://doi.org/10.1016/j.jpain.2013.01.775>.
  105. Mendonca-de-Souza M, Monteiro UM, Bezerra AS, Silva-de-Oliveira AP, Ventura-da-Silva BR, Barbosa MS, de Souza JA, Criado EC, Ferrarezi MC, Alencar Gde A, Lins OG, Coriolano M, Costa BL, Rodrigues MC. Resilience in migraine brains: decrease of coherence after photic stimulation. *Front Hum Neurosci.* 2012;6:207. <https://doi.org/10.3389/fnhum.2012.00207>.
  106. Sitges C, Bornas X, Llabres J, Noguera M, Montoya P. Linear and nonlinear analyses of EEG dynamics during non-painful somatosensory processing in chronic pain patients. *Int J Psychophysiol.* 2010;77(2):176–83. <https://doi.org/10.1016/j.ijpsycho.2010.05.010>.
  107. Sitges C, Garcia-Herrera M, Pericas M, Collado D, Truyols M, Montoya P. Abnormal brain processing of affective and sensory pain descriptors in chronic pain patients. *J Affect Disord.* 2007;104(1–3):73–82. <https://doi.org/10.1016/j.jad.2007.02.024>.
  108. Veldhuijzen DS, Kenemans JL, van Wijck AJ, Olivier B, Kalkman CJ, Volkerts ER. Processing capacity in chronic pain patients: a visual event-related potentials study. *Pain.* 2006;121(1–2):60–8. <https://doi.org/10.1016/j.pain.2005.12.004>.
  109. Stein MB, Uhde TW. Infrequent occurrence of EEG abnormalities in panic disorder. *Am J Psychiatry.* 1989;146(4):517–20. <https://doi.org/10.1176/ajp.146.4.517>.
  110. Knott VJ, Bakish D, Lusk S, Barkely J, Perugini M. Quantitative EEG correlates of panic disorder. *Psychiatry Res.* 1996;68(1):31–9.
  111. Hughes JR, Zak SM. EEG and clinical changes in patients with chronic seizures associated with slowly growing brain tumors. *Arch Neurol.* 1987;44(5):540–3.
  112. Fukushima T. Application of EEG-interval-spectrum-analysis (EISA) to the study of photic driv-

- ing responses. A preliminary report. *Arch Psychiatr Nervenkr* (1970). 1975;220(2):99–105.
113. Melamed E, Lavy S, Portnoy Z, Sadan S, Carmon A. Correlation between regional cerebral blood flow and eeg frequency in the contralateral hemisphere in acute cerebral infarction. *J Neurol Sci*. 1975;26(1):21–7. [https://doi.org/10.1016/0022-510x\(75\)90110-0](https://doi.org/10.1016/0022-510x(75)90110-0).
114. Hossmann KA, Heiss WD, Bewermeyer H, Mies G. EEG frequency analysis in the course of acute ischemic stroke. *Neurosurg Rev*. 1980;3(1):31–6.
115. Rogers JM, Bechara J, Middleton S, Johnstone SJ. Acute EEG patterns associated with transient ischemic attack. *Clin EEG Neurosci*. 2018. <https://doi.org/10.1177/1550059418790708>.
116. Tedesco Triccas L, Meyer S, Mantini D, Camilleri K, Falzon O, Camilleri T, Verheyden G. A systematic review investigating the relationship of electroencephalography and magnetoencephalography measurements with sensorimotor upper limb impairments after stroke. *J Neurosci Methods*. 2019;311:318–30. <https://doi.org/10.1016/j.jneumeth.2018.08.009>.
117. Chen CC, Lee SH, Wang WJ, Lin YC, Su MC. EEG-based motor network biomarkers for identifying target patients with stroke for upper limb rehabilitation and its construct validity. *PLoS One*. 2017;12(6):e0178822. <https://doi.org/10.1371/journal.pone.0178822>.
118. Zappasodi F, Tombini M, Milazzo D, Rossini PM, Tecchio F. Delta dipole density and strength in acute monohemispheric stroke. *Neurosci Lett*. 2007;416(3):310–4. <https://doi.org/10.1016/j.neulet.2007.02.017>.
119. Tecchio F, Zappasodi F, Pasqualetti P, Tombini M, Salustri C, Oliviero A, Pizzella V, Vernieri F, Rossini PM. Rhythmic brain activity at rest from rolandic areas in acute mono-hemispheric stroke: a magnetoencephalographic study. *NeuroImage*. 2005;28(1):72–83. <https://doi.org/10.1016/j.neuroimage.2005.05.051>.



# Artificial Intelligence and Radiomics: Outlook into the Future

# 22

Tommaso Di Noto, Manoj Mannil, Hugo Aerts,  
and Chandini Kadian

## Contents

22.1	<b>Machine Learning in Radiology</b> .....	335
22.1.1	Introduction .....	335
22.1.2	Machine Learning in Radiology .....	336
22.1.3	Unmet Needs .....	337
22.1.4	Risks, Responsibilities and Ethical Dilemmas .....	337
22.2	<b>Introduction to Deep Learning</b> .....	338
22.3	<b>Deep Learning</b> .....	339
22.3.1	Convolutions .....	339
22.3.2	Activation Function .....	339
22.3.3	Pooling .....	340
22.4	<b>Training</b> .....	340
22.5	<b>Learning</b> .....	340
22.6	<b>Deep Learning in Alzheimer's Disease</b> .....	340
22.7	<b>Clinical Application</b> .....	341
	<b>References</b> .....	341

---

T. Di Noto (✉)  
Radiology Department (CHUV), Lausanne  
University Hospital, Lausanne, Switzerland

M. Mannil  
University Clinic for Radiology, University Hospital  
Münster, Münster, Germany

H. Aerts  
Department of Radiation Oncology, Dana-Farber  
Cancer Institute, Brigham and Women's Hospital,  
Harvard Medical School, Boston, MA, USA

C. Kadian  
Department of Biochemistry, University of Zurich,  
Zürich, Switzerland

---

## 22.1 Machine Learning in Radiology

### 22.1.1 Introduction

Machine learning is a type of artificial intelligence (AI) where we teach machines how to solve problems without explicitly programming them to do so. Instead, existing data are provided to the algorithms in order to learn a function that can identify statistical patterns within the input data and then make a prediction (return an output) to given new input samples. More

specifically, a popular methodology that has been established in this field, divides the available data into *training* and independent *test* examples. When facing a prediction problem, the machine learning model is usually given a data set of known labelled data for training (*training* data set), and a data set of unknown data (or first seen data) against which the model can be tested (*test* data set). Nowadays, machine learning comprises an extensive class of statistical algorithms that aim at building models for autonomous predictions. Among the most widespread, we can recall linear models, quadratic models, kernel-based models, probabilistic models, neural networks, ensemble and boosting algorithms. On top of these “more traditional” systems, the newest and predominant algorithms that undeniably revolutionized the field of image analysis are Deep learning neural networks. More specifically, convolutional neural networks (CNNs) are specialized deep networks that have proven to be extremely effective in tasks such as image recognition, image segmentation and image registration [1, 2]. These algorithms have started to gain compelling notoriety in 2012 when AlexNet, one of the most popular CNN proposed in the field of computer vision, drastically outperformed all contestants in the famous ImageNet competition [3]. Since 2012, novel CNNs have been built and the achieved accuracy of the competition has constantly improved, reaching levels of precision comparable to human visual recognition.

### 22.1.2 Machine Learning in Radiology

Radiology has witnessed an impressive transformation over the last 20 years. This innovative trend was not only driven by the technological advancements achieved by the major vendors for CT and MRI scanners-resulting in faster acquisition times, improved resolution, hybrid imaging [4], but also by the increasing emerging opportunities created by artificial intelligence. The first aspect that makes radiology a fertile territory for machine learning algorithms is the increasing amount of digital medical imaging data routinely

generated in public and private healthcare facilities worldwide. While the input data consist of tens of millions radiology reports plus the associated billions of images of patients, outputs in radiologic applications are a set of specific conditions (e.g. benign vs. malignant tumour) with some associated probabilities [5].

The fundamental question that arose in the medical community was, whether AI could add significant value to routine radiologic practice. Indeed, the trend towards which the medical community is shifting, is that of personalized precision medicine, in which the best-targeted treatment is provided to each patient, by trying to combine low costs with outcome efficacy. Machine learning and AI algorithms could support this trend, for instance by improving work lists handling and prioritizing most urgent cases (ideally performing this filtering automatically in the scanning machine) [6]. Moreover, since human readers tend to be prone to fatigue when facing high-volume data sets and monotonous tasks, machine learning algorithms can be run as a pre-analytical tool for these large data archives in order to speed up the decision making processes.

In addition, the field of “radiomics” has emerged in the last years: this entails the quantification of the radiographic phenotype of e.g. a tumour using AI approaches. This high-throughput quantification of tumour characteristics can be automated and it captures the 3D complexity of solid tumors. It also brings important benefits such as, it is easy to perform, it is non-invasive, and low-cost. In other words, radiomics can be defined as the analysis of standard clinical images to uncover radiographic information that goes beyond human interpretation (*more-than-meets-the-eye*) [7]. Hence, what can be envisioned in the forthcoming future are machine learning systems that, either trained with radiomics algorithms (e.g. histogram-based, shape and texture features) or with specific features extracted by custom deep neural networks, will help expert physicians (or act independently, see Sect. 22.1.4) in the clinical decision process providing faster, more robust and more accurate results - that are not achievable by humans alone.

### 22.1.3 Unmet Needs

Even though the above-mentioned applications may indeed help to improve current clinical practice, there are still some unmet standard criteria and reliability issues that must be met before starting to adopt such solutions. First, there exists an urgent need of shared image databases [6], both within healthcare facilities and with possible third parties such as universities, companies, etc. This is because, needless to say, the wider and more heterogeneous the input data set is, the more generalizable and robust will be the outputs for each clinical case. Therefore, a joint effort is needed to create such shared reference data sets of proven cases against which machine learning models could be validated and tested. Ideally, the demographics of the affected patients should be preserved while building these data sets; moreover, standardization criteria should be set when labelling the images (i.e. when defining the true diagnosis/prognosis/findings for each image), especially because many scenarios might often require patient symptoms, clinical follow-up, comparison with other imaging modalities, genomic or histologic data [5]. In addition, a common lexicon should be established during the labelling step and the shared images utilized for creating the data set should not be corrupted during transmission and storage, in order to maintain image integrity and to allow post hoc comparisons [6]. For tuning the hyperparameters (i.e. the architecture) of the chosen algorithms is necessary to obtain generalizable results [8]. When dividing the whole data set into *training*, *tuning* and *test* set; one should always specify also the possible cross-validation (programmatically alternation of data set portions) in order to avoid the recurrent problem of overfitting in artificial intelligence. Similarly, for deep learning networks, all selected hyperparameters such as filter sizes, stride, padding, activation functions, learning rate, regularization terms, weight initialization and epochs should be reported and validated.

### 22.1.4 Risks, Responsibilities and Ethical Dilemmas

Even once the above-mentioned data sets will be created, there will still be a strong concern regarding the source of truth for validating the results: since medicine is not always a field of complete certainty, there will always be the dilemma of normal vs. abnormal cases in continuously variable biological data [6], meaning that machine learning algorithms would also have to keep the pace with the newest discoveries and findings for each case study. For instance, ranges for distinguishing normal from pathological in a specific condition today might be adjusted and fine-tuned in the future, and AI should therefore move along with medical research keeping the algorithms updated, adapting the image labels and, if necessary, re-train the models from scratch every time the diagnosis standard criteria have slightly been modified.

In addition, the drastic shift towards deep learning architectures of recent years also entails some ethical dilemmas: indeed, there is the need for interpreting, monitoring and understanding what happens inside each hidden layer of deep networks and overcome the recurrent licit critique of “black box architecture” of these systems. Many research groups are trying to face this issue [9, 10] which is indeed of vital importance in medical applications, in comparison with other image classifications (e.g. ImageNet) where classes to be distinguished are every-day objects such as cats, dogs, airplanes, etc. This is also why the application of transfer learning (utilizing pre-trained networks, refining and adapting them to different tasks) in medical images is limited and not yet regulated [5]. Moreover, legal responsibility has also become a crucial topic with the advent of AI: currently, experts envision AI only supporting doctors who would eventually take their decision, therefore retaining the major responsibility for any patient outcome. Nonetheless, as AI models become more accurate and advanced, this responsibility could gradually

shift towards the algorithm developers and, more broadly, to the companies deploying and commercializing such systems. In forthcoming years, it is expected that entities such as the FDA or the EMA will release rules about data set creation, transparency, verification processes, responsibilities, etc. even if no similar guidelines have been officialized yet.

## 22.2 Introduction to Deep Learning

The increase in computing power, digital imaging, readily available large data sets, decreasing hardware costs and a world-wide collaborative effort to promote open source software frameworks are factors that have given rise to the recent influx of artificial intelligence (AI) research in medical imaging. In its sub-form of machine learning, AI generates algorithms by learning patterns instead of being explicitly programmed to perform classification tasks. Deep learning is another sub-form of AI characterized by use of so-called neuronal networks of multiple layers. These neural networks are inspired by simplified biologic neurons. Each artificial neuron or node uses an input of a set of values representing features, which are multiplied by a corresponding weight. In so-called multilayer perceptron architecture, multiple neurons are grouped to form a layer. Layers are then being stacked together. The first layer represents the input and the last layer represents the desired output classification. The intermediate layers are so-called hidden layers, which are the hallmark of neural networks and deep learning. The hidden layers autonomously compute intermediate representations of input features, which are then used in the inference process (Fig. 22.1).

The generated algorithms utilize higher level abstractions of input data. The extracted features are not manually engineered but generated by breaking down images into their different components, for instance signal intensity, shape, texture or lesions. Obtaining a prediction from a

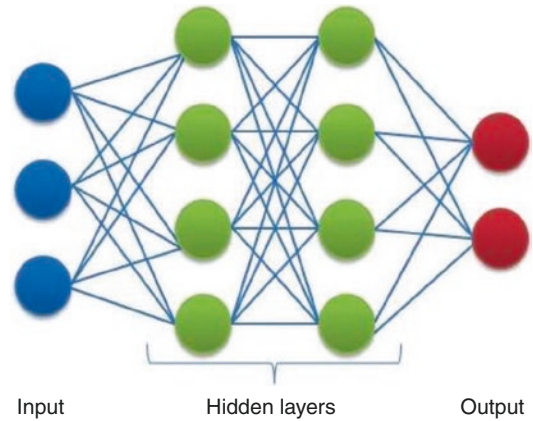


**Fig. 22.1** Basic deep learning architecture. Circles represent nodes/artificial neurons. Vertical arrays of nodes represent layers

sample observation (e.g. an image) using a neural network involves the activation of each node of each layer, starting from the input layer, a process called forward propagation. In the setting of a classification task, the activation of the output layer is typically submitted to a softmax function, a function that maps a vector of real values to a probability distribution. A neural network is trained by adjusting the parameters, which consist of the weights and biases of each node. Modern neural networks contain millions of such parameters. Starting from a random initial configuration, the parameters are adjusted via an optimization algorithm called gradient descent, which attempts to find a set of parameters that performs well on a training data set. Each time predictions are computed with forward propagation, the performance of the network is assessed through a loss (error) function that quantitatively measures the inaccuracy of the prediction (Fig. 22.2).

Each parameter of the network is adjusted by small increments in the direction that minimizes the loss, a process called back-propagation. Owing to memory limitations and algorithmic advantages, the update of parameters is computed from a randomly selected subset of the training data at each iteration, a commonly used optimization method called stochastic gradient descent [11].



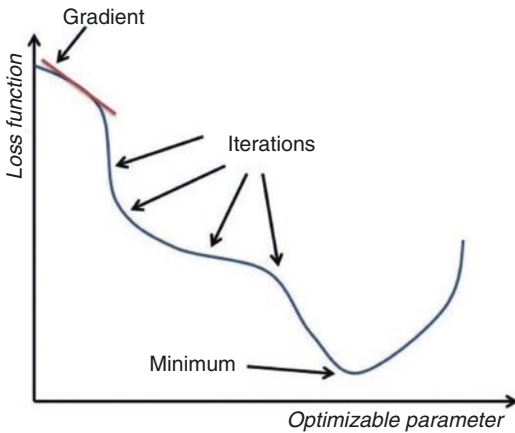


**Fig. 22.2** Example of a loss (error) function in deep learning

## 22.3 Deep Learning

In deep neural networks, the composition of features is enabled by inherent image characteristics. So-called *convolutional neural networks* (CNN) exploit these properties to process larger and more variable inputs as compared to a multi-layer perceptron. The latter perform poorly on images in which the object of interest tends to vary in shape, orientation and position because they must encode redundant representations for the many feature arrangements.

CNNs introduce reliability to these variations by passing each feature detector over every part of the image in a convolution operation. Each feature detector is then limited to detect local features in its immediate input, which is acceptable for natural images. Thus, deep CNNs (with more than two hidden layers) exploit the compositional structure of natural images. As a result, shifts and deformations of objects in these images do not significantly affect the overall performance of the network. Image classification in deep CNN can be achieved with following components: (1) convolutions, (2) activation functions, (3) pooling and (4) softmax function.

### 22.3.1 Convolutions

Deep CNN relies on convolution operations: The linear application of a filter/kernel to local neighbourhoods of points in an input. Common image filters in PACS (picture archiving and communication system) workstations, such as those for image sharpening and smoothing, work using such operations. Filters representing features are usually defined by a small grid of weights (such as  $3 \times 3$ ). If an input has  $n$  channels (e.g. different colour channels), then the size of the filters would be  $n \times 3 \times 3$ . Since a feature may occur anywhere in the image, the filters' weights are shared across all the image positions. Thus, image features can be modelled with fewer parameters, increasing model efficiency. Typically, multiple different convolutional filters are learned for each layer, yielding many different automatically generated feature maps, each highlighting where different characteristics of the input image or the previously hidden layer have been detected [11].

### 22.3.2 Activation Function

An activation function is a nonlinear function that is applied to the outputs of linear operations, e.g. convolutions. Stacking these allows the input to be mapped to a representation that is linearly separable by a linear classifier. The activation function is inspired by biologic neurons. The role of an activation function in a neural network layer is typically that of a selection function, which allows some features to pass through to the output.

Historically, sigmoidal and hyperbolic tangent functions were used, as they were considered to be biologically plausible. Nowadays, most CNNs use a rectified linear unit (ReLU) in their hidden layers. This activation function is perfectly linear for positive inputs, passing them through unchanged and blocks negative inputs (i.e. evaluates to zero) [12, 13].

### 22.3.3 Pooling

Pooling groups feature map activations into a lower resolution feature map. It increases the effective scope of subsequent filters. Moreover, combined with convolutions, this operation also reduces the model's sensitivity to small shifts of the objects, since deeper layers rely increasingly on spatially low-resolution, but contextually rich, information. An added benefit of pooling is the reduction of a model's size. For instance, the size of each feature map will decrease by factor 4 each time a  $2 \times 2$  pooling operator is applied. A common subform is *max pooling*, which propagates the maximum activation within a pooling region into a lower resolution feature map. Successive pooling operations result in maps that have progressively lower resolution but represent increasingly richer information on the structure of interest.

---

### 22.4 Training

Two different approaches are usually utilized to train deep learning models: *supervised learning* and *unsupervised learning*. With supervised learning, each entry of the data set is labelled, for instance to the correct diagnosis.

In unsupervised learning, the data examples are not labelled, instead the model aims to cluster images into groups based on their inherent variability. The machine learning algorithm then discovers structures within the data set that might later be used to solve a task (e.g. classification, segmentation). There is also a hybrid approach called *semi-supervised learning*, which makes use of a large quantity of unlabelled data usually combined with a smaller number of labelled data [14].

Deep learning methods scale well with the quantity of data and can often leverage extremely large datasets for good performance. While a large quantity of data is desirable, obtaining high-quality labelled data can be time-consuming. One approach to artificially increase the available data to an adequate size is data augmentation. Data augmentation applies random transformations to the data that do not change the label assignments. Possible random transformations that can be applied to images

include rotation, translation, zooming, skewing, flipping and elastic deformation.

To avoid overfitting (see below) of deep learning models, it is common practice to divide available data into three subsets: (1) a training set, (2) a validation set and (3) a test set. The training set is used to train and optimize the parameters of the neural network. This training involves repeatedly running training images through it and using the errors to adjust the weights of the network connections. The validation set is used to monitor the performance of the model during the training process; this data set should also be used to perform model selection. Once all the parameters of the model are fixed, test performance is measured on the test data set.

---

### 22.5 Learning

Designing neural network architectures requires consideration of numerous parameters that are not learned by the model (hyperparameters), such as the network topology, the number of filters at each layer and the optimization parameters. Hyperparameters are typically selected through random search, where each configuration is arbitrarily set and then trained to compare performances. Once a neural network architecture is established, learning the model parameters can commence. An important machine learning pitfall is overfitting, where a model learns idiosyncratic statistical variations of the training set rather than generalizable patterns for the task at hand. Overfitting is usually detected by analysis of model accuracy on the training and validation sets. If the model performs well on the training set and poorly on the validation set, the model has overfit the training data.

---

### 22.6 Deep Learning in Alzheimer's Disease

Novel feature attribution techniques, e.g. based on Wasserstein Generative Adversarial Networks (WGAN), enable the identification of disease effects at the subject-specific level. In contrast to backdrop-based methods, it can cap-

ture multiple regions affected by disease effects and predictions thereof. It will allow disentangling complex pathologies like schizophrenia or Alzheimer's disease, while currently strikingly different clinical symptoms are seen as mere variations of these common neurological disorders [15].

---

## 22.7 Clinical Application

An application of AI in the field of neuroradiology is the task of brain tumour segmentation. Even if brain tumours are not very common, they are among the most lethal [16]. Segmentation of brain tumours consists in delineating regions that separate tumour tissue from healthy brain tissues including gray matter, white matter and CSF. In current clinical practice, this operation is performed manually by one or more expert readers, but it is undoubtedly a time-consuming task and frequently prone to fatigue-induced error when dealing with high-volume data sets. Moreover, the manual segmentation has the downside of being radiologist dependent, hence subject to inter- and intra-reader variability (neither objective nor scalable). Even though traditional segmentation methods such as discriminative and generative models have proven to be rather satisfactory with the well-accepted BRATS data set until around 2015, the advent of deep learning has shifted the interest towards CNNs. In contrast to older methods which extracted hand-crafted features and fed them to a set of classifiers, CNNs are capable of iteratively learning features from the data itself, fine-tuning the weights and biases of the network through backpropagation [17]. Therefore, research on segmentation performed with CNNs mainly focuses on the network architecture rather than on image pre-processing or feature extraction itself. In 2017, [18] designed an ensemble algorithm which combined different types of CNNs in order to make the overall model configuration-invariant, trying to marginalize out the biased behaviour introduced by different configuration choices of the deep net-

works. This solution proved to be the most accurate on the BRATS-2017 test set reaching a Dice score (DSC) of 72.9%, 88.6% and 78.5% when classifying Gadolinium-enhanced tumour, peritumoral oedema and non-enhanced tumour pixels, respectively [18] obtained similar classification results also in the validation set, therefore highlighting the actual robustness of the ensemble. Along with standard segmentation of glioblastomas and glioma images, the BRATS-2018 competition focussed on the prediction of patients' overall survival.

---

## References

1. LeCun Y, Bengio Y, Hinton G. Deep learning. *Nature*. 2015;521(7553):436.
2. Shen D, Wu G, Suk HI. Deep learning in medical image analysis. *Annu Rev Biomed Eng*. 2017;19:221–48.
3. Krizhevsky A, Sutskever I, Hinton GE. Imagenet classification with deep convolutional neural networks. In: *Advances in neural information processing systems*. 2012. p. 1097–105.
4. Wang S, Summers RM. Machine learning and radiology. *Med Image Anal*. 2012;16(5):933–51.
5. Kohli M, Prevedello LM, Filice RW, Geis JR. Implementing machine learning in radiology practice and research. *Am J Roentgenol*. 2017;208(4):754–60.
6. Thrall JH, Li X, Li Q, Cruz C, Do S, Dreyer K, Brink J. Artificial intelligence and machine learning in radiology: opportunities, challenges, pitfalls, and criteria for success. *J Am Coll Radiol*. 2018;15(3):504–8.
7. Aerts HJ, Velazquez ER, Leijenaar RT, Parmar C, Grossmann P, Carvalho S, Bussink J, Monshouwer R, Haibe-Kains B, Rietveld D, Hoebers F. Decoding tumour phenotype by noninvasive imaging using a quantitative radiomics approach. *Nat Commun*. 2014;5:4006.
8. Cawley GC, Talbot NL. On over-fitting in model selection and subsequent selection bias in performance evaluation. *J Mach Learn Res*. 2010;11:2079–107.
9. Yosinski J, Clune J, Nguyen A, Fuchs T, Lipson H. Understanding neural networks through deep visualization. 22 June 2015. arXiv:1506.06579.
10. Zeiler MD, Fergus R. Visualizing and understanding convolutional networks. In: *European conference on computer vision*, 6 Sept 2014. Cham: Springer; 2014. p. 818–33.
11. Gabriel Chartrand, Phillip M. Cheng, Eugene Vorontsov, Michal Drozdal, Simon Turcotte, Christopher J. Pal, Samuel Kadoury, An Tang. *Deep Learning: A Primer for Radiologists*. *RadioGraphics* 2017;37(7):2113–31.

12. Hochreiter S, Schmidhuber J. Long short-term memory. *Neural Comput.* 15;9(8):1735–80. <https://doi.org/10.1162/neco.1997.9.8.1735>.
13. Chartrand G, Cheng PM, Vorontsov E, Drozdal M. Deep learning: a primer for radiologists. *Radiographics.* 2017;37(7):2113–31. <https://doi.org/10.1148/rg.2017170077>.
14. Qian G, Wu Y, Ferrari D, Qiao P, Hollande F. Semisupervised clustering by iterative partition and regression with neuroscience applications. *Comput Intell Neurosci.* 2016;4037380. <https://doi.org/10.1155/2016/4037380>. Epub 2016 Apr 26.
15. Baumgartner, Christian F, et al. “Visual feature attribution using wasserstein gans.” *Proceedings of the IEEE Conference on Computer Vision and Pattern Recognition.* 2018.
16. Lisa M. DeAngelis. *Brain Tumors.* *New England Journal of Medicine.* 2001;344(2):114–23.
17. Ali Işın, Cem Direkoğlu, Melike Şah. Review of MRI-based Brain Tumor Image Segmentation Using Deep Learning Methods. *Procedia Computer Science.* 2016;102:317–24.
18. Kamnitsas, Konstantinos, et al. “Ensembles of multiple models and architectures for robust brain tumour segmentation.” *International MICCAI Brainlesion Workshop.* Springer, Cham, 2017.